30 November 2007 | $10

Science

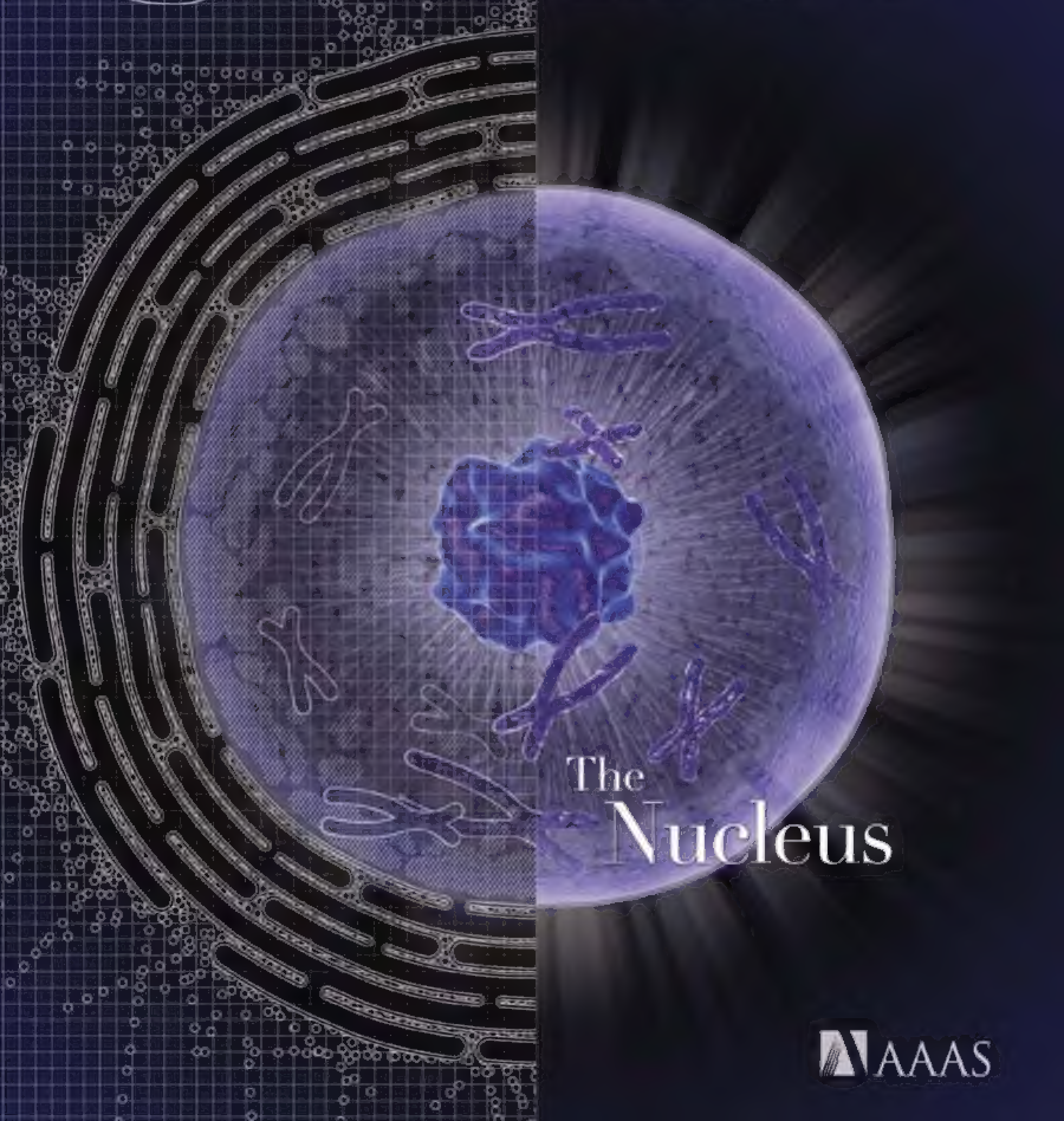

CONTENTS

Volume 318, Issue 5855

COVER

The cell nucleus houses the genetic blueprint, but it is also a dynamic organelle that interacts with the rest of the cell on many levels. A special section beginning on page 1399 focuses on the cell biology of the nucleus.

Image: Chris Bickel/Science

DEPARTMENTS

EDITORIAL

SPECIAL SECTION

The Nucleus

INTRODUCTION

NEWS

REVIEWS

See Science's STKE material p. 1343 or at www.sciencemag.org/sciext/subnuclear/

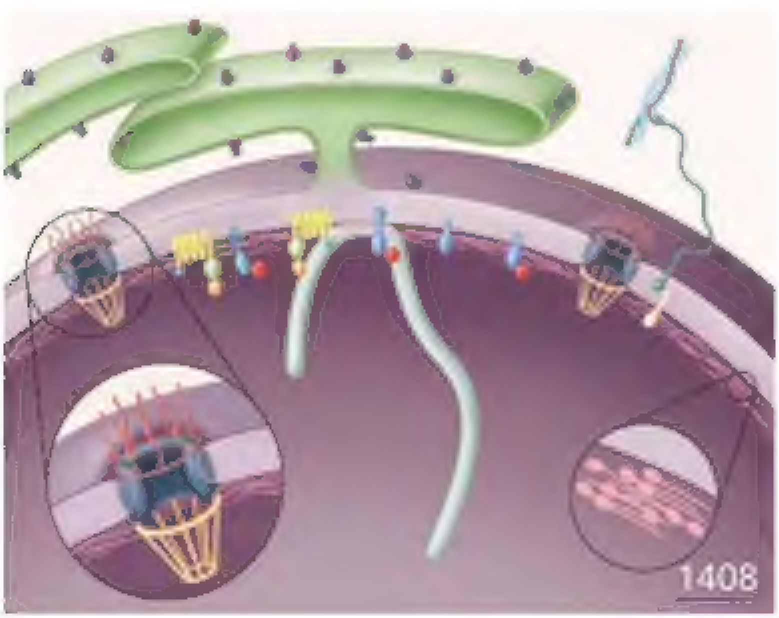

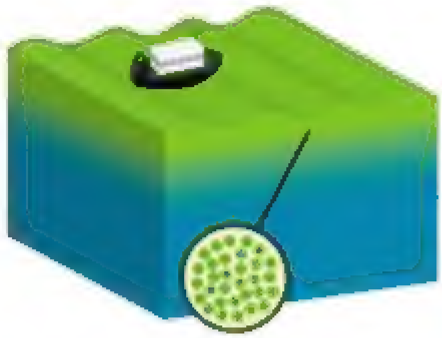

1368

NEWS OF THE WEEK

NEWS FOCUS

LETTERS

CONTENTS continued >>

Science

SCIENCE EXPRESS

BOOKS *ET AL.*

POLICY FORUM

EDUCATION FORUM

PERSPECTIVES

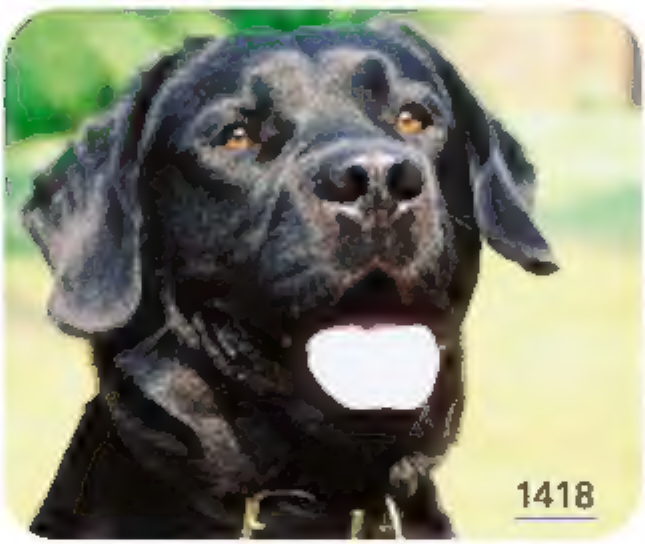

1418

TECHNICAL COMMENT ABSTRACTS

BREVIA

RESEARCH ARTICLES

CONTENTS continued >>

REPORTS

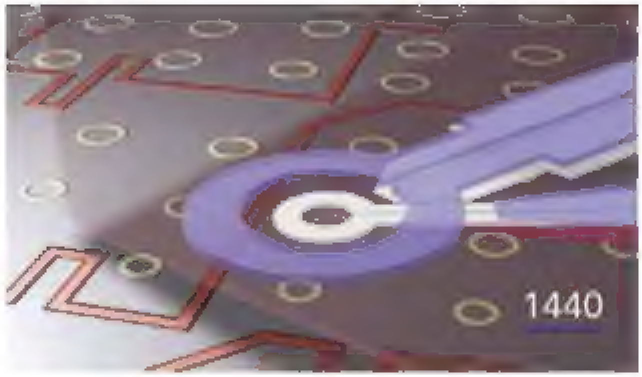

AAAS
ADVANCING SCIENCE, SERVING SOCIETY

SCIENCE (ISSN 0036-8075) is published weekly on Friday, except the last week in December, by the American Association for the Advancement of Science, 1200 New York Avenue, NW, Washington, DC 20005. Periodicals Mail postage (publication No. 484460) paid at Washington, DC, and additional mailing offices. Copyright © 2007 by the American Association for the Advancement of Science. The title SCIENCE is a registered trademark of the AAAS. Domestic individual membership and subscription (51 issues): $142 ($74 allocated to subscription). Domestic institutional subscription (51 issues): $710; Foreign postage extra: Mexico, Caribbean (surface mail) $55; other countries (air assist delivery) $85. First class, airmail, student, and emeritus rates on request. Canadian rates with GST available upon request, GST #1254 88122. Publications Mail Agreement Number 1069624. SCIENCE is printed on 30 percent postconsumer recycled paper. **Printed in the U.S.A.**

Change of address: Allow 4 weeks, giving old and new addresses and 8-digit account number. **Postmaster:** Send change of address to AAAS, P.O. Box 96178, Washington, DC 20090–6178. **Single-copy sales:** $10.00 current issue, $15.00 back issue prepaid includes surface postage; bulk rates on request. **Authorization to photocopy** material for internal or personal use under circumstances not falling within the fair use provisions of the Copyright Act is granted by AAAS to libraries and other users registered with the Copyright Clearance Center (CCC) Transactional Reporting Service, provided that $18.00 per article is paid directly to CCC, 222 Rosewood Drive, Danvers, MA 01923. The identification code for Science is 0036-8075. Science is indexed in the *Reader's Guide to Periodical Literature* and in several specialized indexes.

Printed on 30% post-consumer recycled paper.

CONTENTS continued >>

Tangled webs.

SCIENCE NOW

www.sciencenow.org DAILY NEWS COVERAGE

Untangling an Artistic Spider Web
Argiope spiders weave complex patterns to attract prey, but they pay a price.

An Environmental Contaminant Invades the Womb
Mothers may pass the ill effects of arsenic exposure on to their offspring.

Lyme Disease's Unusual Suspects
Mice, usually blamed for the disease, turn out to be only one of many culprits.

SPECIAL SECTION

The Nucleus

SCIENCE'S STKE

www.stke.org SIGNAL TRANSDUCTION KNOWLEDGE ENVIRONMENT

EDITORIAL GUIDE: Focus Issue—Mastering Nuclear Dynamics
N. R. Gough
The nucleus is connected to cytoplasmic signaling networks and has its own complex signaling environment.

PERSPECTIVE: Genomic Maintenance—The p53 Poly(ADP-ribosyl)ation Connection
R. Alvarez Gonzalez
In response to DNA damage, p53 is modified by poly(ADP-ribose) polymerase-1 (PARP-1) and accumulates in the nucleus.

PERSPECTIVE: Nuclear Localization of Growth Hormone Receptor—Another Age of Discovery for Cytokine Action?
S. M. Swanson and J. J. Kopchick
Translocation of the growth hormone receptor to the nucleus is linked with tumorigenesis.

Scientists' salaries in Europe.

SCIENCE CAREERS

www.sciencecareers.org CAREER RESOURCES FOR SCIENTISTS

EUROPE: To Have and Have Not
A. Swarup
Salaries for European scientists vary greatly by country and region.

MISCINET: Big Science at a Small College
P. Shulman
Haverford's Andrea Morris is the first small-college faculty member to win an NIH Career Development Award.

US: Tooling Up—Overcoming Conflicts in the Lab and Beyond
D. Jensen
If you face conflicts squarely and calmly, you can transform them into better relationships and personal growth.

US: GREAT Expectations
B. Benderly
A new organization aims to focus national attention on issues facing medical postdocs.

SCIENCE PODCAST

Download the 30 November *Science* Podcast to hear about sexual dimorphism in male fossil hominins, hot plasma outflow from the Orion Nebula, iron fertilization experiments, and more.
www.sciencemag.org/about/podcast.dtl

CREDITS: (SCIENCE [redacted] JIH-NAN HUANG AND REN-CHUNG CHENG; (SCIENCE CAREERS) [redacted] MUIR, CREATIVE COMMONS

Separate individual or institutional subscriptions to these products may be required for full-text access.

EDITED BY STELLA HURTLEY AND PHIL SZUROMI

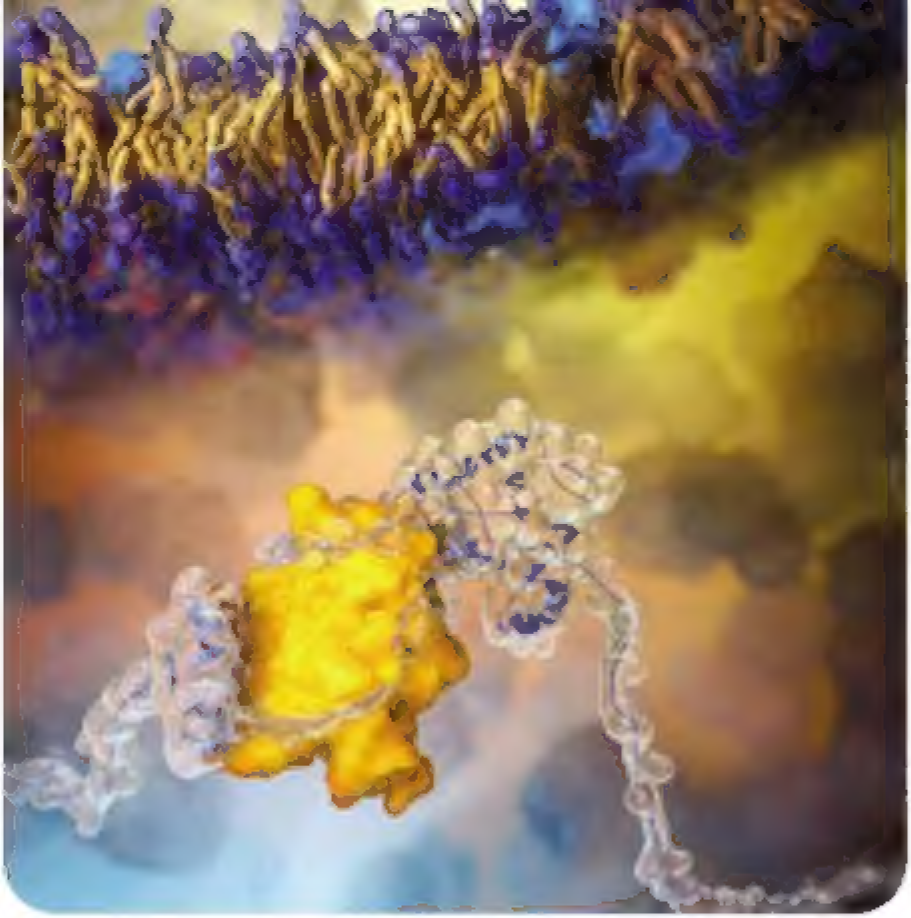

<< To Fold or Not to Fold...

Molecular chaperones not only prevent misfolding of proteins but also play an active role in protein folding pathways. However, how protein folding pathways are affected by chaperones remains poorly understood. **Bechtluft *et al.*** (p. 1458) used a combination of experimental and computational approaches to study the effect of the chaperone SecB on the folding and unfolding pathways of maltose binding protein (MBP) at the single-molecule level. SecB retains MBP in a molten globule-like structure so that no energy will be needed to disrupt stable tertiary interactions during translocation across the cell membrane.

Breathing Conductivity into Diamonds

Diamond is an excellent electrical insulator, but for nearly 20 years, researchers have puzzled over observations that the surface of hydrogen-terminated diamonds becomes conducting after exposed to air. The phenomenon has recently been applied to device design, but a compelling explanation of the underlying chemistry remained elusive. Through careful electrochemical measurements, **Chakrapani *et al.*** (p. 1424; see the Perspective by **Nebel**) show that the positive hole carriers responsible for conduction arise from electron transfer to oxygen dissolved in aqueous films on the surfaces. Similar interfacial charge transfer equilibria could be active in other semiconducting solids.

Controlling Spin Electrically

Manipulation of the spin of a single electron stored on a quantum dot is a strong contender as the basis for quantum information processing. Coherent manipulation of the spin has been demonstrated for a locally applied magnetic field, but scaling up to larger ensemble systems of spins and the individual manipulation of spin with magnetic field present significant experimental problems. **Nowack *et al.*** (p. 1430, published online 1 November) now show that coherent manipulation of the spin state can be achieved using a locally applied electric field to the quantum dot. They argue that the observation of coherent Rabi oscillations arises from electrical modulation of the spin-orbit interaction experienced by the confined electron.

Helium Tracing of Rising Mantle Fluids

Mantle helium has a high $^3He/^4He$ ratio but is diluted by ^4He from other crustal isotopic processes. **Kennedy and van Soest** (p. 1433; see the Perspective by **Hilton**) investigated the geographic distribution of helium isotopes across the Basin and Range province of North America. A gradient in $^3He/^4He$ correlates with rates of active deformation of the crust, and the highest ratios occur where the extension and shear strain rates are greatest. This finding indicates that deformation enhances the permeability of the lithosphere and allows fluid from the mantle to penetrate even in the absence of local magmatism. Local spots with high isotope ratios may also pinpoint areas of high crustal permeability that maybe valuable for geothermal energy development.

Snapshots of Crystal Growth

When complex alloys crystallize, partitioning of elements can be expected between the liquid and solid phases, but measuring these changes is a challenging experimental task. **Eswaramoorthy *et al.*** (p. 1437) used energy-dispersive, x-ray spectroscopy during in situ transmission electron microscopy observations to follow crystallization of an Al-Si-Cu-Mg alloy used in automobile and aerospace applications. They heated nanoscale particles to different temperatures and observed stable and metastable phase boundaries, as well as measured the chemical composition in each phase. This technique may be of use in clarifying the growth mechanisms of nanowires and related structures.

Parsing Extinct Primate Dynamics

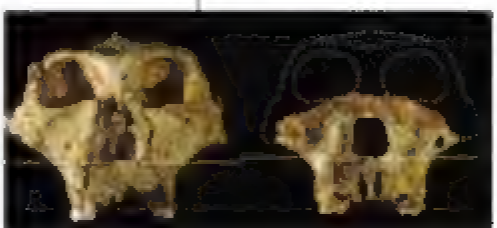

Inferring the social characteristics of early hominins is difficult, in part because fossils are few, scattered, and rarely reveal group dynamics. One more reliable indicator may be the developmental patterns between males and females and, by inference with other primate species, what such findings might imply about social and reproductive strategies. **Lockwood *et al.*** (p. 1443) used a large sample of facial fossils from *Paranthropus robustus* to show that males of this species, extant about 2 million years ago, developed much more slowly than did females.

Continued on page 1347

CREDITS (TOP TO BOTTOM): SOURCE: SANDER TANS, ILLUSTRATED BY GRAHAM T. JOHNSON ©2007; LOCKWOOD ET AL.

Continued from page 1345

In primates, this pattern implies that social groups were mostly female (with only one or a few males), and that the mortality of most of the males was high.

Defensins and Dog's Coats

Inheritance of "dominant black" coat color in domestic dogs involves a gene that is distinct from, but interacts with, genes encoding components of conventional pigmentation systems. Variation in this so-called K locus accounts for differences between yellow, black, and brindle colors in more than 38 dog breeds. Using genetic strategies that exploit the evolutionary history of dogs, **Candille *et al.*** (p. 1418, published online 18 October; see the Perspective by **Dorin and Jackson**) make the remarkable discovery that this locus encodes a member of the β-defensins, a protein family that in other species has been implicated in the defense against microbes. Mechanistic studies revealed that CBD103 is a ligand for melanocortin receptors, proteins that control pigment type-switching.

Boron and Plants

For reasons that remain unclear, boron is a key micronutrient for plants. However, boron toxicity is particularly apparent in agriculture of equatorial and arid regions. **Sutton *et al.*** (p. 1446) have cloned a boron transporter from barley and find that forms of barley that are unusually tolerant of boron have extra copies of this gene. **Miwa *et al.*** (p. 1417) find that *Arabidopsis* plants engineered to overexpress a related boron transporter are also more tolerant of boron. Thus, it may be possible to engineer boron tolerance into crops to improve growth on marginally suitable lands.

Putting Weight on DNA Methylation State

Recently, genome-wide association studies have identified genetic variants that affect one's risk of developing common disorders. Among the most interesting are obesity-associated sequence variants in the *FTO* (fat mass and obesity associated) gene, whose functional role has been unknown. **Gerken *et al.*** (p. 1469, published online 8 November) now show that *FTO* encodes a 2-oxoglutarate–dependent nucleic acid demethylase, an enzyme that removes methyl groups from DNA. The subcellular and tissue expression patterns of FTO are consistent with the protein's potential roles in DNA modification and in organismal energy balance, but precisely how these roles are linked mechanistically remains unclear.

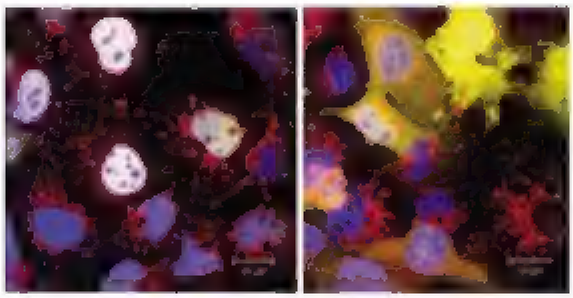

Neandertal Redheads

The melanocortin 1 receptor is involved in the pathway that produces melanin and is a major determinant of skin color in humans. **Lalueza-Fox *et al.*** (p. 1453, published online 25 October; see the 26 October news story by **Culotta**) analyzed Neandertal DNA corresponding to the human gene and found evidence of a novel allele unknown in modern humans. Functional analyses of this variant showed reduced function at a level similar to that seen in humans of European descent. Thus, some Neandertals may have had reduced pigmentation levels, possibly leading to similar pale skin color or red hair in modern humans.

Reducing When Wet

In a puzzling case of structural economy, nature manages to use the same iron-sulfur cluster motif in proteins for both oxidative and reductive electron shuttling. **Dey *et al.*** (p. 1464) used x-ray absorption spectroscopy and theoretical modeling to explore the environmental factors that shift the oxidation potential of high-potential iron-sulfur proteins (HiPIPs) and the reduction potential of ferredoxins into physiological range. They found that hydration from exposure to water accounts for a large part of the change. Ferredoxins have more hydrated active sites, but a desiccated sample showed iron-sulfur covalency (which correlates with ease of oxidation) that approaches the level seen in HiPIPs. Similarly, HiPIPs evidenced reduced covalency upon exposure to water through denaturing.

CREDIT: GERKEN ET AL.

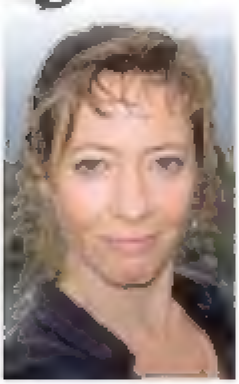

Kathy Sykes is professor of Sciences and Society at the University of Bristol, UK. She works in the field of public engagement and dialogue and chairs the independent advisory panel of Sciencewise. E-mail: kathy.sykes@bristol.ac.uk

The Quality of Public Dialogue

SCIENTISTS ARE INCREASINGLY ASKED BY FUNDERS AND GOVERNMENTS TO ENGAGE THE public. They are no longer expected merely to "teach" the public what they are presumed to need to know. Rather, we now know that a less hierarchical process, in which both parties listen and learn, has greater impact. A critical strand of this public engagement with science involves policy-makers, who are increasing their dialogue with the public to help make wiser decisions about how society uses science. These changes in communication are important because issues like climate change and health are in the political mainstream and affect everyone. But these dialogues must be of a high standard; otherwise, time is wasted, the public lose trust in science, and bad policy decisions result. So, what constitutes good dialogue?

Public dialogue is valuable when it helps policy-makers hear the views of people who have no prior or vested interest. It can challenge assumptions, explore long-term impacts, generate ideas, tease out the nature of public concerns before polarized positions emerge, and help broaden consideration of the issues. Dialogue is not about the public making decisions about science policy; that is for policy-makers. Neither is it formal public consultation, nor is it an open platform for debates that can polarize participants or be hijacked by lobby groups or stakeholders (although their perspectives are important to consider).

For public dialogue to be credible, the public need to be given realistic expectations about what will happen after the process concludes, as well as feedback about its impact. And the conversations must begin early enough to inform decisions. Greenpeace and Friends of the Earth recently criticized how the UK government engaged the public this year on nuclear power, saying that decisions had already been made, thus potentially shaking public confidence in science.

There needs to be good practice in dialogue. Participants should have time to think issues through, and to become well-informed through reliable and balanced resources. Different viewpoints and expert input—not just from scientists, but from others such as journalists, stakeholders, social scientists, and ethicists—are essential. Participants should explore aspirations and concerns, and ultimately, questions should be open ("How do we provide for our energy needs in the future?"), rather than closed ("Should we build new nuclear power stations?").

What is being done to improve public dialogue? In December 2006, the British government committed funding for an Expert Resource Centre for Public Dialogue in Science, led by the program Sciencewise. The goal is to help the United Kingdom produce better policies. So far, over 3000 people have been involved, around £2 million has been spent, and learning is being shared across government departments. UK Prime Minister Gordon Brown also launched a series of citizens' juries in September 2007, promising to harness the "experience and wisdom" of the British people to tackle policy challenges. And a month earlier in the United States, thousands of people from all backgrounds and ages gathered in small groups to discuss health care. Through "CaliforniaSpeaks," the public was enabled to tell state lawmakers about desired reforms, and as a result, the governor is reconsidering health policies. These are good starts.

What about scientists involved in dialogue as experts? In the case of Sciencewise, good interaction with scientists is described by participants as a "privilege," whereas a pompous scientist presenting issues obscurely can be the "worst aspect." Scientists should give clear explanations, be open-minded rather than defensive, and be prepared to discuss their ethical views. Although relatively few scientists are involved in dialogue, the wider scientific community gains from hearing about such discussions; it helps them to better understand the public and may even inspire research ideas.

As with any successful dialogue, the parties involved need to rise to the occasion. If governments are to make wise science-policy decisions—national and global—and are seriously open to public views, then they must engage the public at the right time, based on good practice. And if the public take the time to think, discuss, and become informed about issues, their observations can help science to better serve society.

–Kathy Sykes

10.1126/science.1151332

CREDITS (TOP TO BOTTOM): GERRY DAWSON; GETTY IMAGES

IMMUNOLOGY

Gut Reaction

The intestine, as well as providing the wherewithal to digest food, is a dynamic immunological site—and indeed, is the largest in the body. The oral delivery of vaccines has the potential to provide an extremely effective means of immunizing against infection. However, to improve on the few currently successful oral vaccines, new approaches will be needed to deliver antigens selectively to the relevant intestine-situated immune cells. A distinct class of epithelial cells, called M cells, have been seen as ideal targets for some time, because they are specialists in the transfer of antigens from the lumen of the gut to the underlying mucosa. By attaching antigens to a monoclonal antibody that is able to latch selectively onto M cells, Nochi *et al.* achieved specific delivery to these cells. When compared with antigens that had been coupled to nonspecific immunoglobulin, oral administration of the antigen-conjugated monoclonal led to an increase in elicited antibodies and protection from a normally lethal bacterial challenge. The M-cell specificity of the monoclonal was due to a difference associated with a carbohydrate moiety present on epithelial cells, suggesting that looking for similar targets on human M cells might be beneficial in human vaccine development. — SJS

J. Exp. Med. 10.1084/jem.20070607 (2007).

Sniffing mice.

ECOLOGY

Nothing to Sniff at…

In many animals, the major histocompatibility complex (MHC) has been thought to be responsible for the generation of signals that inform the status of relationship among individuals. The similarity of MHC complexes, which is detectable by scent, were believed to be a means by which mice, and potentially other mammals, recognize and avoid breeding with close relatives. However, Cheetham *et al.* now find that female mice could not differentiate between individuals that differed solely on the basis of their MHC type. Instead, the mice showed preferences between a choice of half-sibling males on the basis of direct contact with another set of species-specific variable markers—their major urinary proteins. This suggests that the factors used by many animals to recognize specific individuals may not in fact be controlled by their MHC profile. — LMZ

Curr. Biol. **17**, 1771 (2007).

BIOPHYSICS

Shining Light on Hydration

Proteins derive a substantial degree of their form and function from the presence or absence of water molecules swarming about the amino acids in various parts of the structure. The hydration process is highly dynamic, and ultrafast laser spectroscopy has recently proved useful in exploring the detailed interactions between protein and solvent. In this vein, Zhang *et al.* undertook a systematic study of water motion in distinct regions of the eight helices constituting the native conformation of apomyoglobin, as well as the molten globular form of the protein accessed at low pH. To introduce local probes, they prepared a series of mutants with tryptophan (Trp) residues substituted at 16 different sites; excitation with a femtosecond ultraviolet pulse then induced Trp fluorescence that varied with the hydration environment. Increased exposure to water led to a higher Stokes shift (i.e., longer wavelength emission), as well as a shorter fluorescence lifetime. In general, the emission decays were biexponential, with a fast time constant that ranged from ~1 to 8 ps and a slow component ranging from ~20 to 200 ps. The fast process could be attributed to short-range fluctuations of the hydrogen-bonded water network, and the slower process to more collective restructuring as exchange with bulk solvent starts to come into play. — JSY

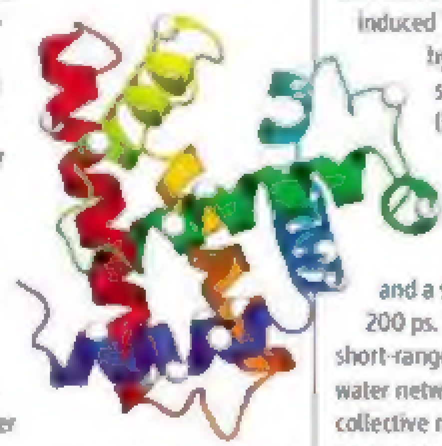

Mutated sites (white) in myoglobin.

Proc. Natl. Acad. Sci. U.S.A. **104**, 18461 (2007).

CHEMISTRY

Triangle Triumph

How does an extra proton latch onto an ethylene? If one thinks about the $H_2C{=}CH_2$ molecule grasping H^+, the logical structure would seem to be a triangle with the proton shared between the two carbons, because that's where the electrons doing the grasping are already mostly confined. On the other hand, the same cation should result from stripping H^- off ethane ($H_3C\text{-}CH_3$), and in that context it seems as though the extra H should stay on one carbon or the other, in a more classical bonding arrangement. Chemists have long puzzled over this question, and the highest-level quantum mechanical calculations favor the triangular H-sharing structure. However, direct experimental evidence has been elusive. Andrei *et al.* have now measured the vibrational spectrum of the $C_2H_5^+$ cation in gas phase and confirmed the nonclassical geometry. The experiment relied on a highly sensitive technique in which an argon atom loosely bound to the cation is ejected (and the naked cation then mass-detected) by the energy dissipated when C-H

Continued on page 1353

CREDITS (TOP TO BOTTOM): MICHAEL THOM, UNIVERSITY OF LIVERPOOL; ZHANG ET AL., PROC. NATL. ACAD. SCI. U.S.A. 104, 18461 (2007)

Continued from page 1351

bonds in the compound resonantly absorb infrared light. Spectral shifts of the primary bands relative to ethylene were relatively small ($<50\ cm^{-1}$). — JSY

Angew. Chem. Int. Ed. **46**, 10.1002/anie.200704163 (2007).

CHEMISTRY

Tougher Liposomes

Although liposomes can be used for drug delivery, efforts continue toward improving both the stability of these spherical bilayer structures and the control over how they release their aqueous contents. Lee *et al.* describe a **method to generate caged liposomes surrounded by a cholesterol-anchored polymer** coating whose stability is pH dependent. Cholesterol-terminated poly(acrylic acid) was mixed with dipalmitoyl-phosphatidylcholine liposomes. After an overnight incubation period, these coated liposomes, which had a mean diameter of 90 nm, were cross-linked with 2,2′-(ethylenedioxy)-bis(ethylamine). The coated vesicles retained their spherical shape after freeze-drying and were resistant to leakage after 500 hours in bovine calf serum. However, the carboxylic acid cross-links helped facilitate release of the vesicles' content through compressive rupture after introduction into modestly acidic solutions (pH range of 4.0 to 5.5) over periods of 150 hours. This type of modified liposome has the potential to provide a stable, controllable drug-delivery vehicle. — PDS

J. Am. Chem. Soc. **129**, 10.1021/ja0707481 (2007).

BIOMEDICINE

Another Case of Cellular Identity Theft

Solid tumors use a variety of crafty mechanisms to optimize their growth, invasion, and metastasis. One unusual mechanism that has attracted much recent interest is a form of cellular identity theft whereby tumor cells morph into a different cell type or induce surrounding normal cells to do so. The best characterized of these phenotypic changes is EMT, or "epithelial-mesenchymal transition," a process thought to endow tumor epithelial cells with migratory and invasive features and/or provide the tumor with a pool of activated fibroblasts that produce molecules required for metastasis. Zeisberg *et al.* describe a new variation on this theme. Using genetically marked transgenic mice, they show that proliferating endothelial cells (the cells that form the inner layer of blood vessels) can also morph into mesenchymal cells resembling activated fibroblasts and that the latter cells are present in at least two distinct tumor types in mice. This "endothelial-mesenchymal" transition is promoted by transforming growth factor–1β1, a cytokine that also promotes EMT and that is abundant in many tumors. The next question is whether and how these intriguing cells contribute to tumor progression. — PAK

Cancer Res. **67**, 10123 (2007).

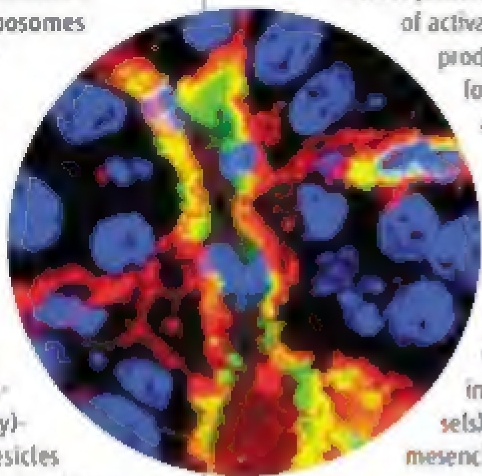

Multicolor "endothelial-mesenchymal" transition–derived cells.

Science stke AAAS

www.stke.org

<< PINK Participates in Parkinson's Pathway

Mice expressing missense mutations in a serine protease known as HtrA2 (also called Omi) exhibit a neurodegenerative disease that shows similarities to Parkinson's disease in humans. Plun-Favreau *et al.* describe a connection between this protein and PINK1, a mitochondrial protein kinase that is mutated in certain forms of Parkinson's disease. HtrA2 functions to detect damaged or misfolded proteins caused by stress in the mitochondria. Misfolded proteins bind to a regulatory domain and activate the protease. HtrA2 may also be regulated by phosphorylation in response to the stress-activated p38 MAP (mitogen-activated protein) kinase pathway. Although PINK1 binds to HtrA2 and was required for p38-activated phosphorylation and activation of HtrA2, PINK appeared not to phosphorylate HtrA2 directly. Furthermore, phosphorylation of HtrA2 was increased in samples of brain from patients with idiopathic Parkinson's disease—as might be expected if mitochondrial stress in the diseased cells caused activation of the p38 pathway and consequent phosphorylation and activation of HtrA2. — LBR

Nat. Cell Biol. **9**, 1243 (2007).

CREDIT: ZEISBERG ET AL., CANCER RES. 67, 10123 (2007)

www.sciencemag.org

Science

1200 New York Avenue, NW
Washington, [redacted]
Editorial: 202-326-6550, FAX 202-289-7562
News: 202-326-6581, FAX 202-371-9227

Bateman House, 82-88 Hills Road
Cambridge, UK CB2 1LQ
+44 (0) 1223 326500, FAX +44 (0) 1223 326501

Subscription Services For change of address, missing issues, new orders and renewals, and payment questions: 866-434-AAAS (2227) or 202-326-6417, FAX 202-842-1065. Mailing addresses: AAAS, P.O. Box 96178, Washington, DC 20090-6178 or AAAS Member Services, 1200 New York Avenue, NW, Washington, DC 20005

Institutional Site Licenses please call 202-326-6755 for any questions or information

Reprints: Author Inquiries 800-635-7181
Commercial Inquiries 803-359-4578

Permissions 202-326-7074, FAX 202-682-0816

Member Benefits AAAS/Barnes&Noble.com bookstore www.aaas.org/bn; AAAS Online Store http://www.apisource.com/aaas/ code MKB6; AAAS Travels: Betchart Expeditions 800-252-4910; Apple Store www.apple/eppstore/aaas; Bank of America MasterCard 1-800-833-6262 priority code FAA3YU; Cold Spring Harbor Laboratory Press Publications www.cshlpress.com/affiliates/aaas.htm; GEICO Auto Insurance www.geico.com/landingpage/go51.htm?logo=17624; Hertz 800-654-2200 CDP#343457; Office Depot https://bsd.officedepot.com/portalLogin.do; Seabury & Smith Life Insurance 800-424-9883; Subaru VIP Program 202-326-6417; VIP Moving Services http://www.vipmayflower.com/domestic/index.html; Other Benefits: AAAS Member Services 202-326-6417 or www.aaasmember.org.

science_editors@aaas.org	(for general editorial queries)
science_letters@aaas.org	(for queries about letters)
science_reviews@aaas.org	(for returning manuscript reviews)
science_bookrevs@aaas.org	(for book review queries)

Published by the American Association for the Advancement of Science (AAAS), *Science* serves its readers as a forum for the presentation and discussion of important issues related to the advancement of science, including the presentation of minority or conflicting points of view, rather than by publishing only material on which a consensus has been reached. Accordingly, all articles published in *Science*—including editorials, news and comment, and book reviews—are signed and reflect the individual views of the authors and not official points of view adopted by the AAAS or the institutions with which the authors are affiliated.

AAAS was founded in 1848 and incorporated in 1874. Its mission is to advance science and innovation throughout the world for the benefit of all people. The goals of the association are to: foster communication among scientists, engineers and the public; enhance international cooperation in science and its applications; promote the responsible conduct and use of science and technology; foster education in science and technology for everyone; enhance the science and technology workforce and infrastructure; increase public understanding and appreciation of science and technology; and strengthen support for the science and technology enterprise.

Information for Authors

See pages 120 and 121 of the 5 January 2007 issue or access www.sciencemag.org/feature/contribinfo/home.shtml

editor-in-chief **Donald Kennedy**
executive editor **Monica M. Bradford**
deputy editors **R. Brooks Hanson, Barbara R. Jasny, Katrina L. Kelner**
news editor **Colin Norman**

Editorial supervisory senior editors Phillip D. Szuromi; senior editor/perspectives Lisa D. Chong; senior editors Gilbert J. Chin, Pamela J. Hines, Paula A. Kiberstis (Boston), Marc S. Lavine (Toronto), Beverly A. Purnell, L. Bryan Ray, Guy Riddihough, H. Jesse Smith, Valda Vinson, David Voss; associate editors Jake S. Yeston, Laura M. Zahn; online editor Stewart Wills; associate online editors Robert Frederick, Tara S. Marathe; book review editor Sherman J. Suter; associate letters editor Jennifer Sills; editorial manager Cara Tate; senior copy editors Jeffrey E. Cook, Cynthia Howe, Harry Jach, Barbara P. Ordway, Trista Wagoner; copy editors Lauren Kmec, Peter Mooreside; editorial coordinators Carolyn Kyle, Beverly Shields; publications assistants Ramatoulaye Diop, Chris Filiatreau, Joi S. Granger, Jeffrey Hearn, Lisa Johnson, Scott Miller, Jerry Richardson, Brian White, Anita Wynn; editorial assistants Emily Guise, Patricia M. Moore, Jennifer A. Seibert; executive assistant Sylvia S. Kihara; administrative support Maryrose Madrid

News senior correspondent Jean Marx; deputy news editors Robert Coontz, Eliot Marshall, Jeffrey Mervis, Leslie Roberts; contributing editors Elizabeth Culotta, Polly Shulman; news writers Yudhijit Bhattacharjee, Adrian Cho, Jennifer Couzin, David Grimm, Constance Holden, Jocelyn Kaiser, Richard A. Kerr, Eli Kintisch, Andrew Lawler (New England), Greg Miller, Elizabeth Pennisi, Robert F. Service (Pacific NW), Erik Stokstad; intern Benjamin Lester; contributing correspondents Barry A. Cipra, Jon Cohen (San Diego, CA), Daniel Ferber, Ann Gibbons, Robert Irion, Mitch Leslie, Charles C. Mann, Evelyn Strauss, Gary Taubes; copy editors Rachel Curran, Linda B. Felaco, Melvin Gatling; administrative support Scherraine Mack, Fannie Groom; bureaus New England: 207-549-7755, San Diego, CA: 760-942-3252, FAX 760-942-4979, Pacific Northwest: 503-963-1940

Production director James Landry; senior manager Wendy K. Shank; assistant manager Rebecca Doshi; senior specialists Jay Covert, Chris Redwood; specialist Steve Forrester; preflight director David M. Tompkins; manager Marcus Spiegler; specialist Jessie Mudjitaba

Art director Kelly Buckheit Krause; associate art director Aaron Morales; illustrators Chris Bickel, Katharine Sutliff; senior art associates Holly Bishop, Laura Creveling, Preston Huey, Nayomi Kevitiyagala; associate Jessica Newfield; photo editor Leslie Blizard

Science International

Europe (science@science-int.co.uk) editorial: international managing editor Andrew M. Sugden; senior editor/perspectives Julia Fahrenkamp-Uppenbrink; senior editors Caroline Ash, Stella M. Hurtley, Ian S. Osborne, Stephen J. Simpson, Peter Stern; associate editor Joanne Baker; editorial support Deborah Dennison, Rachel Roberts, Alice Whaley; administrative support Janet Clements, Jill White; news: international news editor John Travis; deputy news editor Daniel Clery; contributing correspondents Michael Balter (Paris), John Bohannon (Vienna), Martin Enserink (Amsterdam and Paris), Gretchen Vogel (Berlin); intern Elizabeth Quill

Asia Japan Office: Asca Corporation, Eiko Ishioka, Fusako Tamura, 1-8-13, Hirano-cho, Chuo-ku, Osaka-shi, Osaka, 541-0046 Japan; +81 (0) 6 6202 6272, FAX +81 (0) 6 6202 6271; asca@os.gulf.or.jp; asia news editor Richard Stone (Beijing: rstone@aaas.org); contributing correspondents Dennis Normile (Japan: +81 (0) 3 3391 0630, FAX 81 (0) 3 5936 3531; dnormile@gol.com); Hao Xin (China: + 86 (0) 10 6307 4439 or 6307 3676, FAX +86 (0) 10 6307 4358; cindyhao@gmail.com); Pallava Bagla (South Asia: +91 (0) 11 2271 2896; pbagla@vsnl.com)

Africa Robert Koenig (contributing correspondent, rob.koenig@gmail.com)

executive publisher **Alan I. Leshner**
publisher **Beth Rosner**

Fulfillment Systems and Operations (membership@aaas.org) director Waylon Butler; customer service supervisor Pat Butler; specialists Laurie Baker, Latoya Casteel, Lavonda Crawford, Vicki Linton; data entry supervisor Cynthia Johnson; specialists Tomeka Diggs, Tarrika Hill, Erin Layne, Sheila Thomas; systems analyst Tim Popoola

Business Operations and Administration director Deborah Rivera-Wienhold; assistant director, business operations Randy Yi; senior financial analysts Michael LoBue, Jessica Tierney; financial analysts [illegible], Farida Yeasmin; rights and permissions: administrator Emilie David; associate Elizabeth Sandler; marketing: director John Meyers; marketing managers Darryl Walter, Allison Pritchard; marketing associates Julianne Wielga, Mary Ellen Crowley, Alison Chandler, Marcia Leach, Wendy Wise; international marketing manager Wendy Sturley; marketing executive Jennifer Reeves; marketing/member services executive Linda Rusk; japan sales Jason Hannaford; site license sales director Tom Ryan; sales manager Russ Edra; sales and customer service Mehan Dossani, Iquo Edim, Kiki Forsythe, Catherine Holland, Phillip Smith, Philip Tsolakidis; electronic media: manager Lizabeth Harman; project manager Trista Snyder; assistant manager Lisa Stanford; senior production specialist Walter Jones; production specialists Nichele Johnston, Kimberly Oster

Advertising director worldwide ad sales Bill Moran

Product (science_advertising@aaas.org); midwest & southeast sales manager Tina Morra: 202-326-6542; midwest Rick Bongiovanni: 330-405-7080, FAX 330-405-7081; west coast/w. canada Teola Young: 650-964-2266; east coast/e. canada Christopher Breslin: 443-512-0330, FAX 443-512-0331; uk/europe/asia Michelle Field: +44 (0) 1223-326-524, FAX +44 (0) 1223-325-532; japan Mashy Yoshikawa: +81 (0) 33235 5961, FAX +81 (0) 33235 5852; senior traffic associate Dejandra Simms

Commercial Editor Sean Sanders: 202-326-6430

Classified (advertise@sciencecareers.org); u.s.: recruitment sales manager Ian King: 202-326-6528, FAX 202-289-6742; inside sales manager: midwest/canada Daryl Anderson: 202-326-6543; northeast Alexis Fleming: 202-326-[illegible]; southeast Tina Burks: 202-326-6577; west Nicholas Hintibidze: 202-326-6533; sales coordinators Erika Foard, Rohan Edmonson, Shirley Young; international: sales manager Tracy Holmes: +44 (0) 1223 326525, FAX +44 (0) 1223 326532; sales Marium Hudda, Alex Palmer, Alessandra Sorgente; sales assistant Louise Moore; japan: Jason Hannaford: +81 (0) 52 757 5360, FAX +81 (0) 52 757 5361; advertising production operations manager Deborah Tompkins; senior production specialists Robert Buck, Amy Hardcastle; senior traffic associate Christine Hall; publications assistant Mary Lagnaoui

AAAS Board of Directors retiring president, chair John P. Holdren; president David Baltimore; president-elect James J. McCarthy; treasurer David E. Shaw; chief executive officer Alan I. Leshner; board John E. Dowling, Lynn W. Enquist, Susan M. Fitzpatrick, Alice Gast, Linda P. B. Katehi, Cherry A. Murray, Thomas D. Pollard, Kathryn D. Sullivan

ADVANCING SCIENCE, SERVING SOCIETY

Hunting and Gathering Data

Anthropologist Thomas Headland and his wife Janet, have spent most of the past 45 years among the Agta, a hunter-gatherer group in the northern Philippines. This week, the Headlands announced at the meeting of the American Anthropological Association in Washington, D.C., they put their unique database on the tribe—covering some 4000 people over 100 years—online.

Today's Agta number only 600. High infant mortality offsets the high birthrate, so life expectancy is only 23 years. "When I first started working with the Agta, they didn't wear clothes, they didn't eat farmed food," says Headland, now based at SIL International in Dallas, Texas. "Now, some of them use cell phones."

The disappearance of groups like the Agta means that such an effort will never be duplicated, he notes. The database, at www.sil.org/silepubs/abstract.asp?id=49227, covers information on births, deaths, marriages, migrations, physical characteristics, genealogies, and cultural and food-gathering practices that will allow anthropologists, archaeologists, economists, and geneticists to test questions about societies before agriculture and metal tools.

Goals Rock Nation

Seismology grad student Garrett Euler of Washington University in St. Louis, Missouri, was mystified by perplexing squiggles he and colleagues had recorded early in 2006 in the West African nation of Cameroon. As they will report at next month's meeting of the American Geophysical Union, they want to paint an image of Earth's interior by listening for seismic waves sent under a line of local volcanoes by distant earthquakes. But Euler's seismic waves, instead of sweeping across the land, were showing up simultaneously at a score of seismometers around the country.

Euler's nonseismologist girlfriend solved the mystery with a Google search combining Cameroon and one of the dates of the squiggles. "The first thing that came up was a soccer match," says Euler. Then the light bulb went on: "Every city we had a seismometer in was going crazy at a goal." The Cameroon Lions football team scored eight goals in the African Cup of Nations, each of which triggered a countrywide "footquake" as TV-watching fans jumped and stomped for joy. The more crucial the goal, the stronger the footquake.

What the Skull Tells

Some psychometricians enjoy estimating the IQs of great men in history: Galileo, for example, purportedly would have scored an astronomical 185. Now researchers have for the first time tried doing it from skull measurements.

Robert the Bruce, 14th century king of Scots, died in Scotland in 1329 at age 55. A highly accurate cast of his skull (right), made when his tomb was rediscovered in 1819, now sits in the anatomy department of the University of Edinburgh.

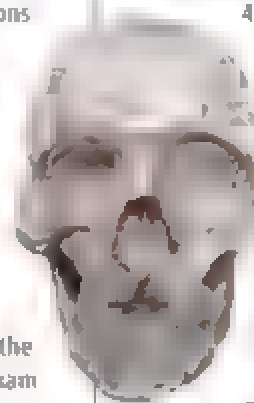

Studies have shown that brain, and therefore skull, sizes have modest but significant correlations with IQ. So Edinburgh psychologist Ian Deary and colleagues decided to use the cast to estimate Bruce's intellectual wattage. They compared his skull measurements with those of 48 Scotsmen who took an IQ-like reading test. The men's scores correlated well—at around 0.5—with brain-imaging measurements of their intracranial space. Applying the same relationship to Bruce's high-browed cranium, the researchers report in the November issue of *Intelligence* that his IQ probably hovered around 128.

"The results are very interesting," says psychologist Philip A. Vernon of the University of Western Ontario in London, Canada. Although Bruce's brain volume could not be directly measured, Vernon notes, "the estimated IQ is in the same ballpark as [those of] other leaders and is corroborated by suggestions that [Bruce] spoke several languages and was a master of national and international politics."

Dino in the Basement

Last spring, paleontologist David Evans was scouting for a long-necked sauropod to serve as centerpiece in the dinosaur hall at the newly renovated Royal Ontario Museum in Toronto. He flew to Wyoming in search of a *Barosaurus* to excavate and even considered buying a replica.

But this fall, he found that the real thing was already in the basement. Scattered in various dusty museum drawers, the fossils include vertebrae from the neck, back, and tail, the pelvis, and various limb bones. A now-deceased curator had acquired the 150-million-year-old bones in a 1962 museum trade, but they were never cataloged. Evans was clued in when he spotted a reference in a 2005 journal article.

Misplaced fossils turn up in museums all the time, but not gigantic sauropods. "The scale of this is what makes this funny," Evans says. The *Barosaurus*, with its skull and other missing bones modeled after a close relative, *Diplodocus*, will measure about 24 meters. The exhibit opens 15 December.

CREDITS (TOP TO BOTTOM): IAN DEARY; THOMAS HEADLAND; ROYAL ONTARIO MUSEUM

Politics

STILL BOSS. Enrico Garaci, the president of Italy's premier health research institute, has been appointed to a third term despite the protests of some biomedical researchers.

Garaci (right in photo, with NIH Director Elias Zerhouni) has led the Istituto Superiore di Sanità (ISS) since 2001. He has generated controversy in the past by endorsing the manifesto of the conservative Science and Life group, which opposes embryonic stem cell research. And he drew flak earlier this year after ISS gave out $4.5 million for stem cell research without holding a public competition or conducting peer review, raising questions about the type of research being supported.

In September, stem cell biologist Paolo Bianco of the University of Rome "La Sapienza" and others complained to Health Minister Livia Turco about the way the program had been managed and why ISS had not publicly announced the grantees. "Scientists are not supposed to negotiate with government officials in order to receive grants," he says. Turco did not reply. Immunologist Fernando Aiuti of the University of Rome "La Sapienza" calls Garaci's reappointment "a dismaying decision."

MONEY MATTERS

GIVING BACK. A mining magnate and his wife have donated $25 million to West Virginia University (WVU) in Morgantown to fund breast cancer care and research and a number of other health and academic programs. Benjamin Statler, who studied mining engineering at WVU, and his wife, Jo, want a portion of the gift to fund a mobile mammography unit to provide free services across rural West Virginia. The donation will also help the university recruit physician scientists for its cancer center, beef up programs in the College of Engineering and Mineral Resources, and put up a new scoreboard at the WVU Coliseum.

FAMILY-FRIENDLY FELLOWSHIP. What does a $25,000 fellowship mean to molecular geneticist Irena Pekker? "It makes our life completely different," says Pekker. She is one of 11 Israeli women who have won a new award created by the Weizmann Institute of Science in Rehovot to allow young female researchers to pursue world-class postdoctoral experiences overseas without sacrificing their family lives.

Pekker says the money, when added to her $40,000 postdoc salary, made it possible for her husband and two children to join her in Worcester, where she is doing a 2-year postdoc to work with Philip Zamore on gene silencing at the University of Massachusetts Medical School. Pekker's husband works for an Israeli aerospace firm and for security reasons would find it difficult to find a comparable position with a U.S. company. "The reason such a small percentage of Israeli women do a postdoc is because of the economic situation," Pekker says.

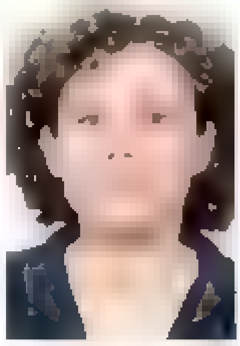

She intends to return home at the end of her training to pursue an academic career. That's exactly what Weizmann officials hope every grantee will do: A press release says the goal of the new award, funded by the Clore Foundation and S. Donald Sussman, is to create a "feminine leadership within the Israeli research community."

THEY SAID IT

"I'm male, in my 40s, have a Ph.D. in physics, and work as a professor at a university in California. I view my Wikipedia writings as a form of procrastination from real work, so I'd prefer to remain anonymous and not reveal the extent of my procrastination to colleagues."

—A Wikipedia contributor whose entry on the 1996 bombing of the Khobar Towers in Saudi Arabia was reproduced nearly verbatim—without attribution—in a recently published book by George Orwel titled *Black Gold: The New Frontier in Oil for Investors*. Source: *The New York Times*

<< MOVERS

CHANGE AT HARVARD. Barry Bloom, the outspoken dean of the Harvard School of Public Health since 1999, will step down from the post in June. Bloom, 71, a tuberculosis vaccine researcher, has expanded the school's international reach and programs in areas such as genes and the environment. He has also been a vocal commentator on various hot topics, including developing an AIDS vaccine, publishing biodefense research, and politicizing science. He plans to remain on the Harvard faculty and continue his research on vaccine development and other topics.

CREDITS (TOP TO BOTTOM): PLINIO LEPRI/AP PHOTO; SOURCE: IRENA PEKKER; RICHARD FRIEDMAN

Got a tip for this page? E-mail people@aaas.org

EPIDEMIOLOGY

New Estimates Scale Back Scope Of HIV/AIDS Epidemic

On the surface, it looked like very good news. Two United Nations groups reported last week that the estimated number of people infected with HIV worldwide has fallen from 39.5 million to 33.2 million, a drop of 16% from last year. The annual number of new infections has also plummeted since 2006, says the report, from 4.3 million to 2.5 million. The new analysis suggests that global incidence peaked in the late 1990s at just over 3 million per year.

A large part of the steep decline, however, reflects the fact that numbers for previous years had been overestimated. The new figures are based on improved methods to estimate HIV prevalence and a better understanding of the disease's dynamics, the Joint United Nations Programme on HIV/AIDS (UNAIDS) and the World Health Organization (WHO) explain in their December 2007 update. Behavior change contributed to the drop in some locales but overall was not a major factor.

Epidemiologists at UNAIDS categorically deny that the agencies had jacked up previous estimates to increase funding for HIV/AIDS, as sources alleged in a *Washington Post* story on 20 November. "We find that accusation absurd," says UNAIDS epidemiologist Paul De Lay. Tim Brown of the East-West Center in Honolulu, Hawaii, an epidemiologist who has worked closely with UNAIDS on its estimates, also rejects the charge. "There was no inflation of the numbers," says Brown. "We were trying to use the best scientific information available at the time."

Seventy percent of the downward shift comes from Angola, India, Kenya, Mozambique, Nigeria, and Zimbabwe. Of these, India accounts for the biggest change—a drop from 5.7 million to 2.5 million—which was first reported this summer (*Science*, 13 July, p. 179).

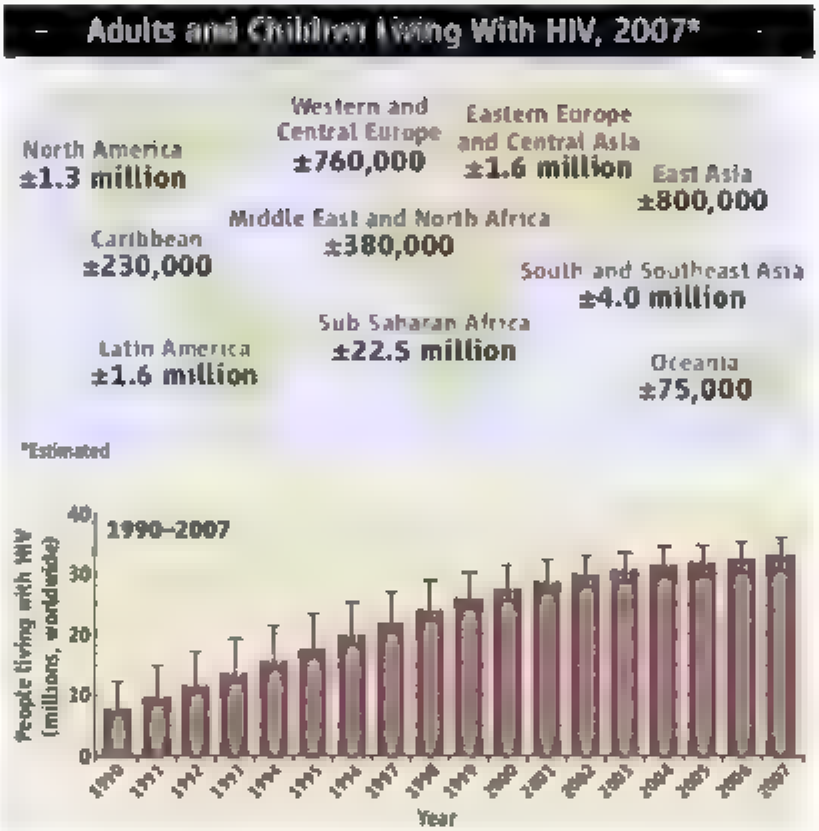

Ups and downs. Estimates of the number of HIV-infected people worldwide have dropped because of new methodologies, but taking these into account, a revised look back shows that the number has steadily increased (*bottom*).

Evidence suggests that declines occurred in Kenya and Zimbabwe in part because people engaged in less of the risky behavior that can expose them to HIV. In other countries, the lower figures reflect data from a growing number of sites that report results from HIV tests. (India alone went from 155 in 1998 to 1100 in 2006.) Additionally, 30 countries since 2001 have done household surveys that document HIV prevalence in large swaths of the population. These population-based surveys revealed that urban prenatal clinics, which have served as a major source of countrywide estimates in the past, generally inflate actual infection rates by about 20%, prompting experts to lower the latest estimates. One reason for the inflation is that in places such as South Africa—which has more infected people than any country—young women are more likely to be infected than young men. Another is that such surveys do not capture the status of women who are not sexually active or routinely use condoms.

Executive Director Peter Piot explains that UNAIDS now realizes the importance of using different tools to track the epidemic in different locales. "We should be connecting all these different approaches very, very early on," says Piot. Specifically, in countries that have a "generalized" epidemic—in which the virus infects more than 1% of adults—population surveys are probably the most accurate gauge, he says. But in countries with an epidemic "concentrated" in groups such as sex workers, injection drug users, and men who have sex with men, it makes more sense to focus on those high-risk groups.

Not all estimates decreased. In eastern and central Asia, prevalence increased 150% since 2001, with nearly 90% of the new infections occurring in Russia and Ukraine. Similarly, prevalence doubled in Vietnam between 2000 and 2005, and the report says the epidemic in Indonesia "is among the fastest growing in Asia."

The update also reported the surprising finding that, on average, it takes 11 years rather than 9 for HIV infection to cause symptomatic disease in untreated people. This slower disease course affects calculations of the new infection rate and of mortality. Anti-HIV drugs, which more than 2 million infected people now receive in poor and middle-income countries, also have contributed to decreasing mortality, which dropped from 2.9 million deaths in 2006 to 2.1 million in 2007.

AIDS epidemiologist Thomas Quinn, who directs the Johns Hopkins Center for Global Health in Baltimore, Maryland, ▶

CREDIT: ADAPTED FROM WHO AND UNAIDS

stresses that like all infectious-disease estimates, the new figures have their own degree of uncertainty. "I certainly hope this change in statistics doesn't alter anyone's concerns about how we're going to manage this epidemic," says Quinn. "It doesn't really matter whether it's 33 million or 39 million when it's that high of a number. It's a massive epidemic that continues to grow."

Kevin De Cock, head of WHO's HIV/AIDS program, says the 16% reduction in prevalence will not change the amount of money needed for anti-HIV drugs. "We're not going to see a substantial reduction in treatment needs, and for various reasons, it's likely to go up," he says. Two forces in particular will offset the cost savings from the prevalence reduction, he says: People are surviving longer without treatment, and people in developing countries are beginning to start treatment earlier. "Where this will end up is not entirely clear," he says.

The same holds true for estimating HIV's incidence and prevalence. "I hope we don't have to adjust in a big way in the future," says Piot of UNAIDS. "But we're no longer simply documenting the natural history of HIV infection. There are treatment and prevention effects to consider now. That's great, but it's a nightmare to document." **–JON COHEN**

INFLUENZA

Tense Meeting Produces Some Hope for Flu-Sharing Deal

It's too early to call it a breakthrough. But a marathon meeting in Geneva, Switzerland, last week has resulted in what participants hope will be a way to salvage the international system for sharing influenza virus samples. After 4 days of feverish debate and diplomacy, often stretching late into the night, participants agreed to embark on an overhaul of the system that Indonesia and other developing nations had demanded. They also agreed to some immediate measures, including a way to help countries keep track of what happens to their samples. "It's more progress than I have seen at any meeting to date," a member of the U.S. delegation says.

At stake during the Intergovernmental Meeting on Pandemic Influenza Preparedness was the Global Influenza Surveillance Network (GISN), which helps monitor viral evolution and prepare the production of vaccines against seasonal and pandemic flu strains. Indonesia has for the past year refused to share samples from its human H5N1 influenza victims with the network, saying those viruses are its own property and demanding guarantees that it will get the benefits—such as pandemic vaccines—that sharing can help produce.

Other developing countries, such as Egypt, Nigeria, Vietnam, and Thailand, have stopped short of boycotting GISN but sympathize with Indonesia. The result was a "very tense and polarized meeting," says Christianne Bruschke, a bird flu expert at the World Organisation for Animal Health in Paris.

In the end, participants from more than 100 countries agreed to a 50-plus-page document that will form the basis for a new set of principles and rules for the sharing system, to be worked out at the next meeting in 2008. The text still has many dozens of disputed passages and even conflicting ideas, which nobody believes will be easy to resolve. "But at least now we have a process to start solving the problem," says Edward Hammond of the Sunshine Project, a nongovernmental organization based in Austin, Texas, that has supported the developing nations.

In a separate two-page statement that was awaiting approval from African countries as *Science* went to press, the meeting also agreed to set up a database to help countries track where their viruses, "and the parts thereof," go after submission to a GISN lab. Details are unclear—one key question, for instance, is whether those "parts" include genetic information—but the system would alleviate complaints that viruses sent in by affected countries are shared among labs and vaccine companies without the countries' knowledge. In addition, the statement announces that WHO Director-General Margaret Chan will set up a new advisory body to address the sharing issue.

"As a tangible demonstration of good will," the statement also says, virus sharing will continue until the issue is resolved. Whether Indonesia will resume its contributions is unclear, however. The country's laws require so-called material transfer agreements to ship biological samples, says Indonesian delegation member Widjaja Lukito, a physician at the University of Indonesia in Jakarta. But those aren't currently issued within GISN, and the meeting did not reach an agreement on them.

Hammond says the country hasn't been "entirely coherent" in its demands. "Indonesia has brought us to this point, but they're not showing the leadership to take it to the next level," he says. "It may be the Brazilians and the Nigerians and the Thai that move this issue forward." **–MARTIN ENSERINK**

With reporting by Dennis Normile.

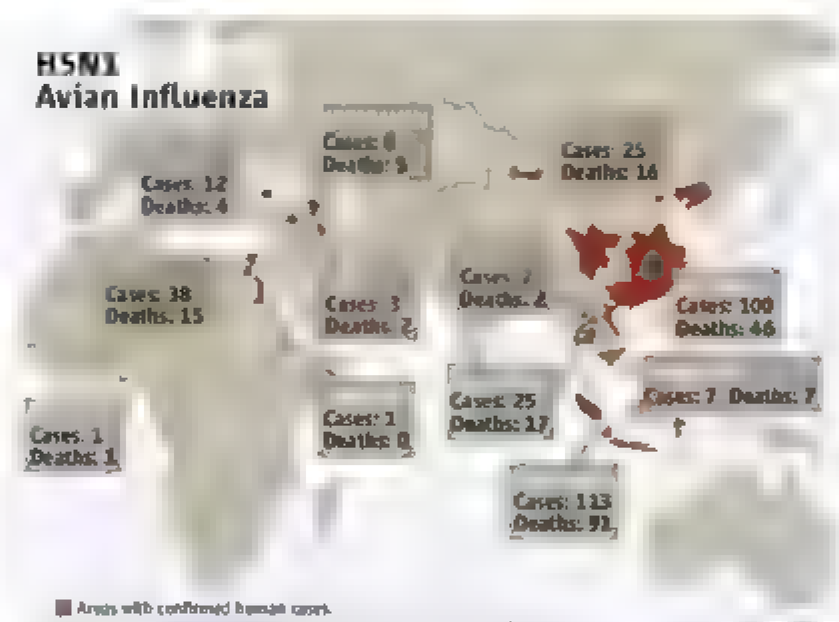

Epicenter. Indonesia has been the hardest hit by H5N1 avian influenza.

CREDIT: ADAPTED FROM WHO 2007

PALEOANTHROPOLOGY

Hominid Harems: Big Males Competed For Small Australopithecine Females

Among living people, men are usually bigger than women—but not by much, averaging 5% to 10% larger. Now a study on page 1443 finds that the males of an extinct species of hominid in South Africa took longer to grow up than females—and got much larger. This suggests that these robust australopithecines chose a risky mating strategy. Top males invested energy in bodybuilding in order to possess a harem of females, much like silverback gorillas do today.

Although this species, *Paranthropus robustus*, is not on the human line, the study is the first to offer solid evidence of the mating strategies of an early hominid, says paleoanthropologist J. Michael Plavcan of the University of Arkansas in Fayetteville, who was not part of the study. The males' facial features were on average 17% larger than females', suggesting a haremlike mating strategy. "You don't get that kind of sexual dimorphism unless you are polygamous. Males don't get that big unless they get a big payoff," Plavcan explains. That suggests diverse social strategies in the hominid family and perhaps the relatively recent adoption of low sexual dimorphism by humans. "This is not the human pattern," says lead author Charles Lockwood of University College London.

Lockwood made the discovery while examining 19 skulls and 16 jawbones of *P. robustus* from caves in South Africa, where they had been consumed by predators between 1.5 million and 2 million years ago. The adult males clustered into two groups, smaller specimens with less dental wear and larger ones with worn teeth and more robust features, such as pillars of bone alongside the nose. Lockwood cites this as evidence that the smaller males were younger and hadn't reached full size. In many primates, males don't achieve full maturity until years after equal-aged females have started to have offspring. This pattern is found in primates in which one male dominates a group of females and wards off other males. In contrast, female humans and chimps are only slightly smaller than their male counterparts, reflecting different mating strategies. "I think [the study] is very convincing," says biological anthropologist Steven R. Leigh of the University of Illinois, Urbana-Champaign.

The finding challenges a theory that early hominids had a relatively low level of sexual dimorphism, inherited from a common ancestor shared with chimpanzees,

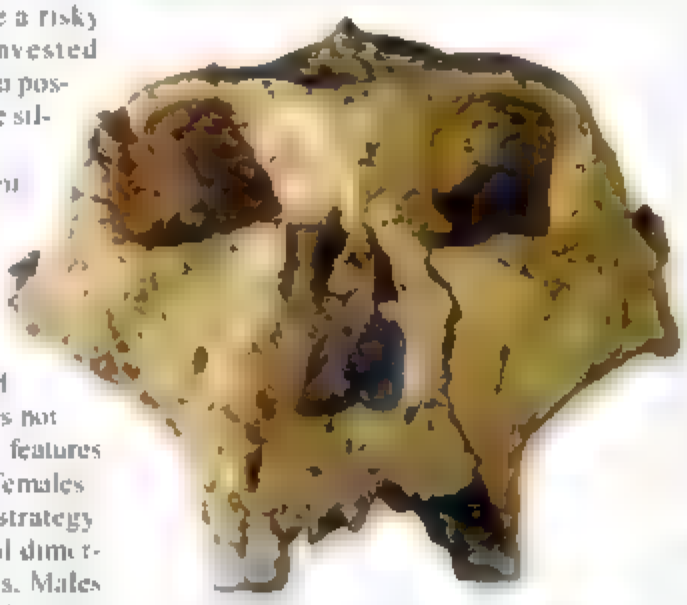

Bachelor boy? Male robust australopithecines took longer to grow up and mated later than females, leaving young males on their own.

CREDIT: C. A. LOCKWOOD

says Plavcan. Instead, the primitive condition may have been more gorillalike, and our female ancestors may not have closed the gap until recently, perhaps in *Homo erectus* in the past 2 million years.

But those who have championed the early theory remain skeptical. Paleoanthropologist C. Owen Lovejoy of Kent State University in Ohio isn't convinced that *P. robustus* males were actually much bigger than the females. He warns that using dental wear to estimate age can be risky, as is estimating soft-tissue body mass based on skeletal size. And researchers hold conflicting opinions on the amount of sexual dimorphism in what most consider our closest australopithecine ancestor, *Australopithecus afarensis*. Lockwood plans to apply this type of analysis to that and other species to detect when the sexes grew closer in size, a signal that males were investing more in offspring and in longer-term bonds with females. "This is the $64,000 question: When did human dimorphism get smaller?" says Plavcan.

—ANN GIBBONS

Gene Therapy Trial Back On

Federal regulators have given a green light to a gene-therapy arthritis trial that was halted in July after a patient died. The decision comes as a relief to researchers who had worried that the treatment was to blame.

The trial, conducted by Targeted Genetics Corp., located in Seattle, Washington, was put on hold after the 24 July death of 36-year-old Jolee Mohr of Taylorville, Illinois, who had recently received a gene-therapy injection to treat rheumatoid arthritis in her knee. Mohr apparently died mainly from a fungal infection called histoplasmosis that her immune system was unable to fight off (*Science*, 21 September, p. 1665).

New tests confirm that the gene therapy didn't contribute to Mohr's death, neither through replication of the adeno-associated viral vector nor by raising levels of an immune system–suppressing protein in her blood, the company says. It announced this week that the U.S. Food and Drug Administration has lifted its hold on the trial. The federal Recombinant DNA Advisory Committee will issue its conclusions about the case at a meeting next week.

—JOCELYN KAISER

Italian Cold Cuts

The heads of Italy's four major research institutes are protesting unexpected last-minute cuts in their 2007 budgets, saying they will force them to slash ongoing projects and could harm international collaborations.

As part of its National Fund for Research, Italy had committed €1.6 billion to the nation's research institutes for 2007, which represented a €50 million increase over 2006's budget. Scientists had wanted more but were promised another increase in 2008. Last week, however, Italy's Ministry of Economy announced it would allocate only €1.5 billion to the institutes for 2007.

The research heads are meeting next month with Italy's research minister to plead their cases, but there's little optimism that the cut can be reversed—and fears that the 2008 boost won't come through. Roberto Petronzio, president of the Italian National Institute for Nuclear Physics, says that his organization might have to reduce its contributions to the CERN accelerator near Geneva, Switzerland. "European countries like Spain are increasing research funds at level of 20% while Italy is stuck. That's really worrying," he says. The Ministry of Economy declined comment.

—FRANCESCO DE PRETIS

MUSEUMS

Smithsonian Struggles to Strike a Balance With Sponsors

When the Smithsonian National Museum of Natural History (NMNH) opens a new exhibition hall on the oceans next fall, a key component—an elaborate educational Web site—will still be on the drawing board. It lost its sole sponsor last week when the American Petroleum Institute (API) withdrew a promised $5 million gift in the wake of questions about whether the Smithsonian should take money from oil companies. The withdrawal comes at a time when the Smithsonian's leaders are about to launch a capital campaign to shore up the institution's 19 museums and more than a half-dozen research centers. The fuss about API's gift hints at how challenging the campaign may be, and the episode has sent the Smithsonian's leaders scrambling to avoid future embarrassments.

"We will take a look at the guidelines to make sure they are clear enough," says Smithsonian acting Secretary Cristián Samper. In addition, the institution's governing Board of Regents plans to get involved earlier in negotiations with potential donors. "It was [a] mistake in not raising the questions [about the API donation] sooner," notes Roger Sant, head of the board's executive committee.

Mixed message. A disagreement between Smithsonian acting Secretary Cristián Samper *(left)* and Regents member Roger Sant about a gift for a natural history museum *(above)* Web site led to the withdrawal of $5 million.

The natural history museum's $75 million ocean initiative includes a $49 million exhibit, an endowed research chair, and research support, in addition to the threatened Web site, which should have extensive educational and research components as well as daily updates. "I am hoping it will become the site everyone in the world will go to when they want to learn something about the oceans," says NMNH marine biologist David Pawson, who is helping to design the site.

The U.S. government has agreed to foot about 60% of the total bill for the oceans initiative, and more than a dozen private donors are chipping in. In 2005, the natural history museum approached API—an oil and gas industry trade association that sometimes supports outside research and education programs—for help in funding the Web site. A detailed agreement was hammered out by the end of August 2007: API's logo would appear for 2 seconds during the Web site's opening sequence and there would be a link on the site to API's own ocean information, but the institute would have no say in the content or publicity surrounding the site.

Everyone up the Smithsonian chain of command, including Samper, signed off on the plan. "My assumption was that it would be approved," says Paul Risser, acting director of NMNH. But when, as required for any gift of more than $1 million, the agreement was sent to the Board of Regents for the final go-ahead, Sant and board member Senator Patrick Leahy (D–VT) questioned whether it was appropriate for API to be a sponsor in light of the problems created by oil spills. An article about these concerns appeared in the *Washington Post* on 3 November. In mid-November, API withdrew its gift with a one-sentence letter to Risser. "Once it became discussed in public, in some ways [the loss] was inevitable," Risser explains. He is confident, however, that new sponsors will step in. API officials would only say that conditions had changed recently at the Smithsonian, prompting API to withdraw the gift.

Typically, Smithsonian scientists are quick to complain about possible blemishes to the Smithsonian's reputation. They sharply criticized former secretary Lawrence Small's business-oriented style and the naming of exhibit space and auditoriums after corporate and private donors. Yet in this case, *Science* found, researchers weren't objecting. "Most people were sorry to see it fail. I am sorry," says Pawson. NMNH paleontologist Brian Huber agrees, adding, "It's unfortunate that we send these mixed messages [to donors]."

The API fiasco comes at a time when the Smithsonian is being squeezed for funds to replace or renovate old buildings and exhibits and revitalize programs. The federal government pays for about 70% of the institution's $1 billion budget, which includes capital and operations expenses. However, the cost of repairing and renovating buildings alone over the next 6 years is expected to top $2.5 billion; based on previous appropriations, some are predicting a $1 billion shortfall. Moreover, Samper has been pressing hard for improvements to exhibits. "[That cost] is probably the same order of magnitude as the facilities deficit," says Sant.

On 19 November, the regents approved in principle the first pan-Smithsonian capital campaign, the details of which will be worked out next year, when a permanent secretary is in place. The flap over the API donation suggests that this fundraising effort could be full of land mines. "The Smithsonian, because it's such a national icon, does have a higher level of scrutiny," says Risser. "There's a need to set rules on what we will and will not accept."

—ELIZABETH PENNISI

CREDITS (TOP TO BOTTOM): GERALD MARTINEAU/THE WASHINGTON POST; STEPHANIE KUYKENDAL/BLOOMBERG NEWS/LANDOV

PUBLIC SCIENCE

Pilot NSF Program Flies Into Stiff Community Headwinds

A novel program at the U.S. National Science Foundation (NSF) to support innovative ways of communicating science faces an uncertain fate. The 4-year-old Discovery Corps Fellowship (DCF) program has attracted few applicants, and in a time of tight funding, a new program solicitation that's about to hit the streets could be its last. Fellows say one big obstacle is that the scientific community, for all its handwringing about a scientifically illiterate public, still views outreach as a dubious activity for those on an academic career path.

"My department chair calls it 'that weird thing you do,'" says a current postdoctoral fellow at a major research university who requested anonymity. "It's like we're wearing a scarlet O on our chests." For many faculty members, outreach can be "something that you shove off onto somebody else ... so we can stick to the science," says senior fellow Carl Batt, a chemistry professor at Cornell University. But that's the wrong attitude, according to Batt, who works on self-assembling nanoscale arrays and has developed a touring show on nanotechnology called "Too Small to See." "I run a huge research lab, and I still have the time," he says.

The DCF program, which gives 2-year $200,000 grants to both postdocs and experienced investigators for research and outreach, was begun by Arthur Ellis when he headed NSF's chemistry division. Ellis saw it as a potential model for the $6 billion foundation, which embraces outreach as one of its core missions. "New Ph.D.s were telling us that they wanted to do something different as a postdoc—something with a science component but not strictly research," recalls Ellis, now vice chancellor for research at the University of California, San Diego. "And senior investigators had ideas that they wanted to pursue, but they couldn't find the right way to go about it. Traditional models work well for most people," he adds, "but DCF was supposed to attract those who wanted to go in a different direction."

Tami Lasseter Clare, a postdoctoral fellow at the Philadelphia Museum of Art, is one of those people. She knew after one interview that she didn't want to work for the chemical industry, and a full-time academic position didn't sound appealing either. Instead, her love of art and historical preservation landed her a part-time position at the art museum, doing work that included restoring a set of century-old bronze sculptures atop city hall. Now she's designing new protective coatings for metallic works of art as well as teaching high school students about the chemistry of such coatings. "It might lead me back into academia," she says about her career plans, "but in a ►

CREDIT: STEVEN CROSSOT

Polished science. Discovery Corps fellow Tami Clare teaches silvering to high school students at the Philadelphia Museum of Art in a workshop on the chemistry of metalworking.

Baghdad Museum to Reopen

Two galleries of Baghdad's Iraq Museum, shut since the U.S. invasion in 2003, are set to reopen in December, a move that some archaeologists worry could imperil its artifacts. The museum was badly damaged and looted during the start of the war, and more than 10,000 objects are still missing. Now Iraqi authorities plan to reopen two of the 16 galleries, which have been restored with Italian assistance, reports *The Art Newspaper*.

But former director Donny George and other archaeologists oppose the reopening. "Opening any part of the museum is a dangerous move," says George. A U.S. officer in Baghdad recently told the American Forces Press Service that the military was eager to reopen the museum. "Can they really be sure that a suicide bomber does not go into the galleries?" asks Elizabeth Stone of Stony Brook University in New York state. —**ANDREW LAWLER**

Wanted: More Tongues

The U.S. National Science Foundation (NSF) has cheered linguists by strengthening its commitment to a federal effort to record and analyze dying languages. Since 2005, NSF, the National Endowment for the Humanities, and the Smithsonian Institution have spent $10 million on the Documenting Endangered Languages initiative, and this month NSF said it would make the project a permanent program at the foundation. "Much remains to be done," says program director Douglas Whalen, who estimates that nearly half of the world's 6500 languages could disappear in the next century. NSF hopes to spend $2 million to $3 million next year on the project; last year's contribution was $3.7 million. —**MICHAEL ERARD**

Bonobo Reserve Established

The Democratic Republic of the Congo has designated the world's largest contiguous reserve for the bonobo, spanning 30,570 square kilometers. Although the government is not paying for the reserve, the Bonobo Conservation Initiative (BCI), which helped conduct initial surveys, says the official designation will make it easier to raise funds from international NGOs, which will help efforts to develop sustainable agriculture and curb the bush-meat trade. Craig Sholley of the African Wildlife Foundation worries that biological surveys and consultations with local chiefs were incomplete, but BCI's Michael Hurley expects to finish the remaining accords in the next year. Another reserve to the north, Kokolopori, is due for official designation within the coming months. —**ERIK STOKSTAD**

much more interdisciplinary way."

Other fellows—the class of 2007–08 consists of five postdoctoral DC fellows and four senior fellows—are doing everything from running biofuels workshops for high school teachers to developing movie-quality visualizations on the origins of life and how cells evolve. Liam Pingree, a chemistry postdoc at the University of Washington, Seattle, has enlisted art students and Web site designers to help him put placards about solar power on city buses in the hope that daily commuters will be drawn to a Web site with more information on the topic. But Pingree, who hopes his research on the structure and function of organic solar cells will win him a tenure-track faculty position, admits that sometimes he has to curb his enthusiasm for his bus project. "You don't want to be flagged as someone who does outreach," he says. "Somehow, it makes you look like something less of a scientist."

NSF's Kathy Covert, who runs the DCF program, says it takes time for scientists to become familiar with any new NSF initiative, especially one that deliberately goes against the grain. "This is different enough that it has what chemists might call a really low sticking coefficient," she says. Still, she's disappointed that only 29 people applied for funding last year, and she doesn't know whether DCF will survive despite her best efforts to promote it. "If that's the most we can get from this vast community of chemists from academia, industry, and the national labs, then ..." her voice trails off.

—JEFFREY MERVIS

SCIENCE ADVICE

Germany Finally Picks a National Science Academy

The world's oldest scientific academy has a new job. Ending years of discussion, German Science Minister Annette Schavan unexpectedly announced earlier this month that the Leopoldina, founded in 1652 and named after Holy Roman Emperor Leopold I, would serve as the new German Academy of Sciences and as science adviser to the federal government.

Germany currently has a system of eight regional science academies, an engineering academy called acatech, and the Leopoldina, which draws its members from across the nation as well as from 30 foreign countries. But science leaders and federal officials have worried that there is no single organization set up to advise the government on scientific questions and to represent the German science community in international affairs.

Schavan's announcement, which came as part of a radio interview on 16 November, took Germany's research community—and the academies, including the Leopoldina—by surprise. The Leopoldina's president, Volker ter Meulen, a virologist at the University of Würzburg, was at a conference in India and says his cell phone connection was so intermittent that he was unable to comment—or speak with Schavan—until his return more than a week later. Representatives from the other academies quickly complained in German newspapers that they had been snubbed.

A plan for a new national advisory body to be made up of members elected from the eight regional academies plus acatech and the Leopoldina, "was ready a year ago," says Gerhard Gottschalk, president of the Union of the German Academies of Sciences and Humanities, which represents the regional academies. "We received no reaction." On the radio show, Schavan made her reaction clear, saying that the Leopoldina was "predestined" to take on this new role.

This is not the first time the Leopoldina has been offered the job. Shortly after reunification, the science minister at the time asked the academy, based in Halle in the former East Germany, if it would be willing to serve as a national academy. But although it had received praise for remaining independent under Communist rule (*Science*, 15 October 1999, p. 394), Leopoldina's leaders declined the promotion, saying the organization was not yet ready.

Decision time. German research minister Annette Schavan announced that the Leopoldina should become Germany's national academy of sciences.

CREDIT: FRITZ REISS/AP PHOTO

In 2003, Germany's Science Council recommended that a new body be formed, with representatives from all the existing academies. For nearly 4 years, the academies and German research organizations discussed various possibilities, settling on the proposal Schavan rejected.

Despite bruised egos among the other academies, many in the scientific community welcome Schavan's decision. The proposal "would be the realization of a long-discussed idea, without the need to found a new institution," said Matthias Kleiner, head of the German research funding organization the DFG. Ter Meulen says that although he had no problem with establishing a new institution, the idea "didn't convince the politicians." "All those involved were tired" of the discussions, he says. "It is now time to stop going in circles."

The Leopoldina is already well-connected internationally, with ter Meulen currently serving as chair of the European Academies Science Advisory Council, which brings together the national science academies of European Union member states. In preparation for the G8 meeting in Germany in May, the Leopoldina organized a meeting of the national academies from 13 countries on climate change.

To bolster any weaknesses, the Leopoldina should cooperate with the other academies, Schavan says, especially with acatech on issues involving technology and engineering and with the Berlin-Brandenburg Academy of Sciences and Humanities for questions involving the humanities and social sciences.

The science minister said in her announcement that she plans to be "generous" with new funding for the academy, but she did not give any solid figures beyond saying that the federal government will provide 80% of the budget and the state of Saxony-Anhalt, where the Leopoldina is located, will cover the rest. Funding and organizational details are expected to be ironed out at a meeting of Germany's state and federal science ministries in February.

—GRETCHEN VOGEL

Should Oceanographers Pump Iron?

Companies and countries are planning a series of controversial experiments to help determine if seeding the ocean with iron can mitigate global warming

Ambling down to the winch room after a midday nap, German oceanographer Victor Smetacek realized immediately that the instruments aboard the RV *Polarstern* were registering something important. The water hundreds of meters below a massive algal bloom that Smetacek was monitoring was surprisingly turbid, with particles clumping up everywhere. A handful of samples revealed that the clumps consisted of dead algae.

The phenomenon surprised the 50 scientists on the European Iron Fertilization Experiment operating in the Southern Ocean 2000 km off the Antarctic coast. Six weeks earlier, the participants in the 2004 cruise had dumped nearly 3 metric tons of iron into the frigid sea. The algal bloom from the iron was expected. But the widespread, rapid sinking of dead matter was a surprise. "We were quite stunned," Smetacek says. "I went up and down the ship ... shouting, 'The bloom is sinking, the bloom is sinking!' "

EIFEX offered preliminary confirmation of one method for sucking carbon dioxide from the atmosphere. The researchers hoped to demonstrate that iron would fertilize the growth of phytoplankton, which, like nearly all plants, form carbon compounds from CO_2. If the algal bloom promptly sank to the sea floor, taking the carbon with it, fertilizing the oceans with iron might help remove some of the greenhouse gases that humans are pouring into the atmosphere. But Smetacek's excitement soon gave way to frustration. The EIFEX team was focused on the surface plankton bloom and lacked instruments to measure what was happening deep underwater or to collect more than a few samples. "We were not prepared for what we saw," says Smetacek. Next time, he vowed, that wouldn't happen.

He may soon get another chance. Last month, scientists from the National Institute of Oceanography in Goa, India, visited Smetacek's lab at the Alfred Wegener Institute for Polar and Marine Research in Bremerhaven, Germany. The Indian team is planning a 2009 cruise to explore the impact of a fertilization experiment on krill stocks and to determine how much of the algae's carbon actually reaches the depths without being recycled through the food web. Dubbed LOHAFEX—*loha* means iron in Hindi—the cruise is one of a new generation of iron fertilization experiments (see table, p. 1370).

Earlier projects like EIFEX confirmed that iron fertilization stimulates algal blooms. The new experiments will explore what happens to those blooms and whether they can be carbon sinks for atmospheric carbon dioxide. There's a lot scientists don't know, including why some blooms fall so rapidly, how much of them are devoured by microbes and other sea life on the way down, and which locations and plankton species do the best job of sequestering carbon. Larger experiments could more effectively track carbon that makes it to the deep and help to quantify the impact of the technique on climate.

The strong interest of commercial companies and governments is driving academic experiments like LOHAFEX. Companies are hoping to make money by selling credits for carbon sequestered, using the Kyoto international climate system, smaller trading schemes, or voluntary ones. On 6 November, a ship leased by one company, Foster City, California–based Planktos, set sail from Florida toward an undisclosed area in the equatorial Atlantic that it plans to fertilize. (The secrecy is due to threats from environmental activists to disrupt the mission.) Climos, a competitor based in San Francisco, California, says on its Web site that the technique has "the highest greenhouse gas mitigation potential of all available methods."

These plans are generating a backwash of concerns. Scientists have been divided for years about not only whether large-scale

Day 1
Researchers distribute tons of dissolved iron on the ocean surface.

Day 21
The iron catalyzes rapid growth of algae, turning a patch of ocean green.

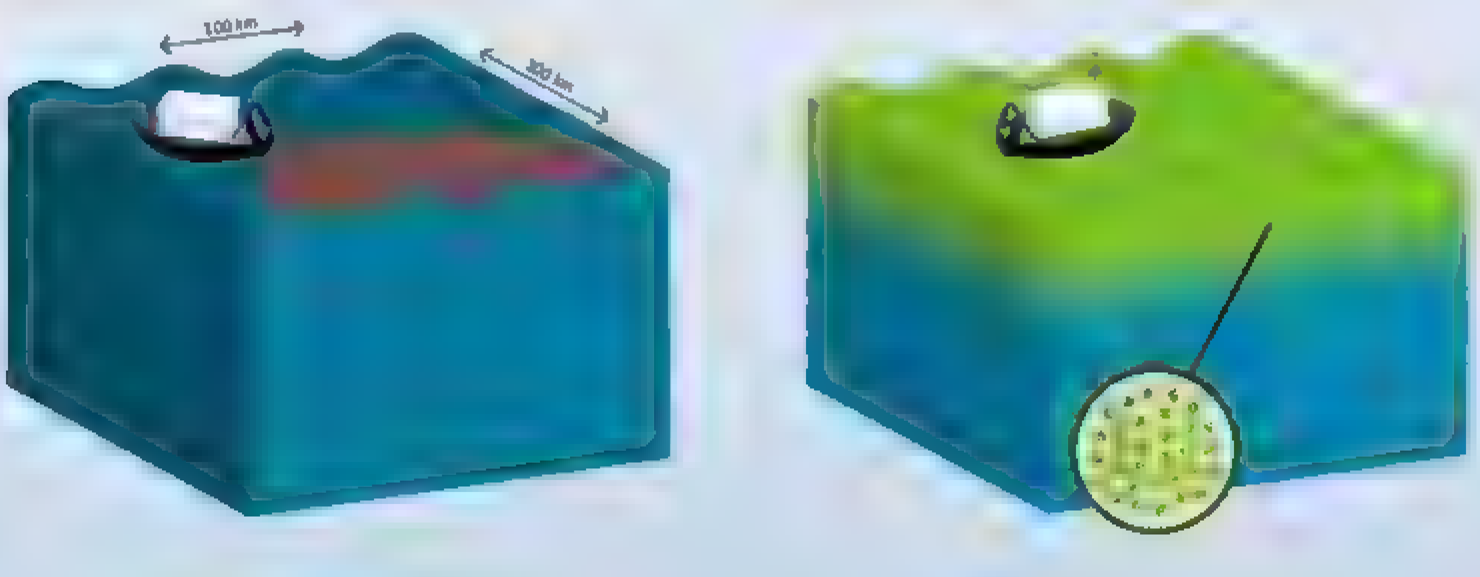

CREDIT: J. NEWFIELD/SCIENCE; SOURCE: PHILIP BOYD, UNIVERSITY OF OTAGO, NEW ZEALAND

ocean fertilization is feasible but also whether it should be done at all. One worry is that such ocean engineering could disrupt ocean food webs. Another is that jump-starting ocean ecosystems with an iron jolt could lead to emissions of methane and N_2O, both potent greenhouse gases that could limit the total climate benefit of a big uptake in carbon. At a recent meeting at Woods Hole Oceanographic Institution (WHOI) in Massachusetts, several scientists questioned whether large-scale fertilization could ever provide the data needed for a credible credits program. And earlier this month, the parties to the international antidumping London Convention declared that "given the present state of knowledge regarding ocean fertilization, such large-scale operations are currently not justified." (Experts say that the treaty may be easy to circumvent, however, and that it's not clear iron fertilization is even a form of "dumping.")

Key Questions

Surface

Would large-scale plankton seeding spur the growth of harmful algal blooms? Scientists will monitor for toxins.

Middle Depth ~0 to 1000 m

Is methane or N_2O produced? These greenhouse pollutants could offset the benefit of taking in CO_2.

Does rapid plankton growth at large scale deplete dissolved oxygen and nitrogen? Such dead zones can disrupt fish ecosystems, so scientists will look for these nutrients.

The Deep ~4000 m

Can the amount of carbon sequestered be quantified? Mixing along the edge of experiments could complicate the measurements.

Location, location

Behind the current buzz about ocean fertilization is one of the biggest oceanographic discoveries of the past 50 years, namely, that iron from terrestrial dust controls the growth of extensive marine ecosystems. Scientists had long puzzled over why huge swaths of surface oceans lacked phytoplankton, the plants that form the foundation of global ocean ecosystems, despite relatively high levels of two important nutrients—nitrate and phosphate. In 1990, biogeochemist John Martin of Moss Landing Marine Laboratories in California proposed an answer: Iron is the limiting factor in determining the abundance of life in the ocean, and those marine deserts contained too little of it.

The first successful test of this "iron hypothesis" was carried out in 1993—just months after Martin's death—by oceanographers on a cruise southwest of the Galápagos Islands in the Pacific. Since then, nearly a dozen experiments in the southern, equatorial, and northern Pacific and South Atlantic oceans have shown that iron, dissolved into seawater, could catalyze algal blooms. Some blooms were so huge, they were visible by satellite.

Oceanographers don't understand exactly how iron influences the blooms. But ice cores suggest that the oceans have taken up as much as 100 billion tons of carbon during a series of ice ages. Smetacek calls the quest to understand how the oceans took in so much carbon "the Holy Grail" of paleoceanography because of its significance for the history of Earth's climate.

But iron fertilization experiments have not simply opened a window into the past, he says. They have also given researchers the unique ability to perturb an ocean ecosystem with small amounts of a single chemical and then watch the effects. "All the rest [of oceanography] are simple observations," says Smetacek. "This is the way to really understand the system."

Can that system be used to fight global warming? The first order of business, according to oceanographer Philip Boyd of the University of Otago in Dunedin, New Zealand, is to get a better handle on where to conduct such experiments. "Location, location, location," Boyd said at the Woods Hole meeting. The key is to find ocean sites that are fertile enough to grow algae on the surface but that offer the environmental, ecological, and physical traits needed for the carbon to sink quickly to the deep and stay there.

Planktos later plans to take advantage of warm waters and nutrients in the equatorial Pacific in hopes of spurring rapid algal growth. Russ George of Planktos says the company will be looking for areas that feature the best nutrient cycling. But WHOI marine geochemist Ken Buesseler questions whether it would be appropriate to sell credits based on work at the site. "It's quick and easy [there] to get a quick green patch," he says. But nutrients from the deep are recycled infrequently in those areas, he adds, and those nutrients "would have been used anyway" by carbon-sipping plants growing naturally.

To avoid that potential problem, the India-funded team is focusing on the Southern

Day 35

The bloom dies. For carbon sequestration to work, the algae must sink or be eaten by microorganisms and zooplankton, whose carbonaceous waste falls to depth.

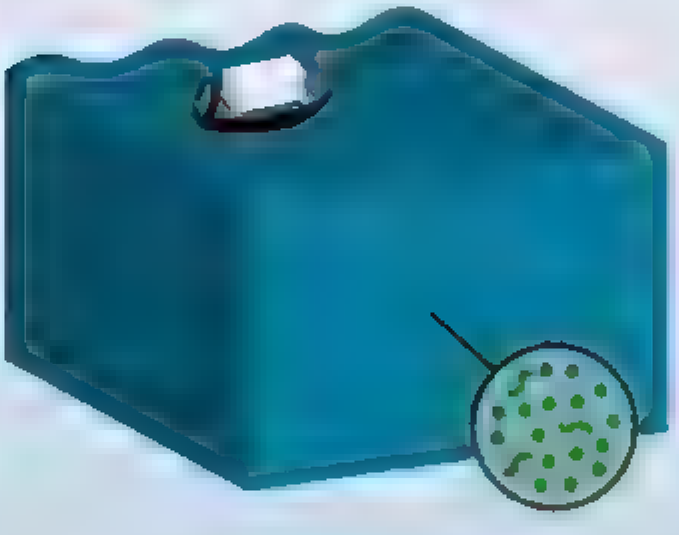

Day 365

The carbon waste is recycled back to CO_2 but remains dissolved in deep water that could take centuries to return to the surface.

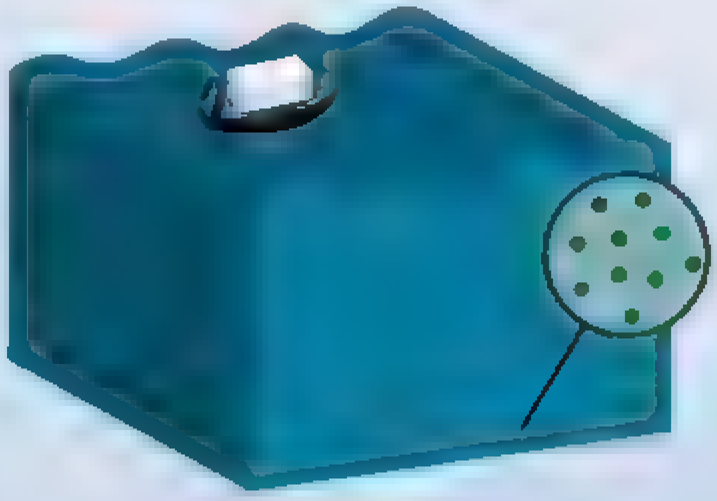

CREDIT (TOP): J. NEWFIELD/SCIENCE

Ocean. Although the cold and seasonally dark conditions are less conducive to algal growth, its surface nutrients are more regularly replenished by upwelling. That allows successive iron-fertilized blooms to take in carbon using nutrients that would have otherwise returned to the deep.

Larger experiments of longer duration could make it easier to track the humanmade blooms, which get stretched and diluted by currents, downwelling, and storms. During a 12-day experiment in 1999, says Boyd, "we invest[ed] about half our time just keeping track of where [the patch] is." Scientists have calculated that the next generation of experiments should be bigger by a factor of 10 and occur within a relatively enclosed, recirculating area called an eddy to keep the fertilized area intact.

Counting the carbon

The trick to sequestering carbon is to have it fall below what oceanographers call the 100-year horizon. That's the point, starting at 500 m, beyond which the water will not come into contact with the surface for a century. That duration is the international standard for commercial carbon-storage projects. As much of the carbonaceous material grown on the surface falls, microorganisms and animals called zooplankton below invariably eat it, creating, among other things, CO_2 that eventually returns to the surface within a year. By getting more carbon beyond the 100-year line, fertilization buffs hope to bypass that process.

Scientists don't know exactly why some of the dead algae clumps and falls, and only three of the 11 experiments to date have shown evidence of carbon being transported below the surface. It's possible that the experiments were too short or too small for scientists to measure the amount of carbon transported. A more ambitious effort should, many scientists think, send more carbon to the deep. Researchers also need better measurements to quantify how much carbon is gone for good after a bloom dies or gets eaten up. Climos plans to deploy devices, called sediment traps, just below the 100-year horizon to catch that harvest.

To know where the magic line is, says oceanographer Andrew Watson of the University of East Anglia in Norwich, U.K., modelers need a better understanding of how water moves within their ocean models. "The physics is as important as the biology," he says. Another task is to monitor more accurately the potent greenhouse gases produced by microbes in such an altered ocean ecosystem. Although only two of the 11 experiments thus far have detected nitrous oxide and none methane, any company that hopes to claim carbon credits from a fertilization project must first measure these gases and subtract their impact.

There's also the problem of tracing carbon that doesn't make it past the 100-year line, says John Cullen of Dalhousie University in Halifax, Canada. The water below the surface moves turbulently and gets mixed up, so any N_2O generated later could turn up far from the original. "There could be ill effects we simply could not see," says Cullen. "It's a legitimate concern," agrees Margaret Leinen of Climos.

A Growing Field

The Players	Their Plans
Planktos	This public U.S. company plans six seeding experiments (the largest 31,000 km²). Its ship left Florida on 6 November for an undisclosed location in the equatorial Atlantic.
Climos	This private U.S. company is funded by Silicon Valley tycoon Dan Whaley; his mother, oceanographer Margaret Leinen, is leading development of a scientific plan. It's released a draft code of conduct for the field.
China	Scientists aboard its research icebreaker, *Xuelong*, are headed to the Southern Ocean to perform small-scale studies. The government is also seeking collaborations with U.S. experts.
India	Scientists plan to carry out experiments in the Southern Ocean in 2009 aboard the *Polarstern*, Germany's research icebreaker.
GreenSea Ventures	This private U.S. company owns several of the original patents on the fertilization technique. But it has not announced any plans to conduct experiments.

But she believes that observational data suggesting a problem with N_2O levels are "equivocal" and that modeling studies show that only a portion of the positive impact of the bloom would be offset by the additional levels of the potent greenhouse gas.

A sea of unknowns

Scientists must find a way of linking specific downstream impacts to specific experiments. Otherwise, says Buesseler, once several companies begin working in the same region, "it starts to get very difficult to work out who's responsible for some of these effects."

Those consequences could be considerable. The next generation of experiments must improve monitoring of nitrate and phosphate to measure whether an algal bloom could deplete these nutrients from the site of the experiments or adjacent areas. Overfed bacteria, for instance, can create dead zones that could deplete fish stocks. So the next experiments need better technology to track nutrients and oxygen levels indicative of dead zones. Right now, the error bars are too large. The problem is "somewhere between trivial and bad," says Climos adviser Anthony Michaels of the University of Southern California in Los Angeles. Researchers are also on the lookout for toxic algae strains from blooms.

Leinen says "a mix of indicators" on robots and boats could help track the algal blooms. It would be a big improvement over the first generation of experiments, she says, which had little ability to monitor their blooms over a broad tract. The increasing variety of buoys, undersea gliders, and autonomous samplers can now follow a bloom and report data to satellites at regular intervals. But the tools are still limited. Remote sensors can't yet measure N_2O and have limited battery life. The thousands of buoys needed to keep an eye on greenhouse gases returning to the surface for roughly a year would be prohibitively expensive, notes Watson.

Even if individual projects could account for the carbon that they're sequestering, says oceanographer James Bishop of the University of California, Berkeley, their combined impact could alter the carbon uptake of the world's oceans in ways that are very hard to quantify. That could stymie efforts to balance the terrestrial, atmospheric, and ocean segments of the global carbon budget, he says, and make it harder for policymakers "to know if carbon management is working."

Despite considerable reservations, a growing number of oceanographers expect ocean fertilization to be among the proposed solutions to global warming. "China has 500 years of coal and intends to burn it at 3 cents a kilowatt hour," Brian Von Herzen of the Climate Foundation said at the Woods Hole conference. In response, he says, "as a community, we can do nothing. Or [we can] play an active role by exploring this second generation of [fertilization] experiments."

Cullen predicts that scientists will be unable to quantify the greenhouse impacts of fertilization but that policymakers will want to use the method anyway. Before that happens, Cullen says, scientists should have collected as much data as possible. "It's the only ocean we have," he says. "Society needs clearer answers on what the risks are."

–ELI KINTISCH

Worldly. To gain stature beyond Korea, KAIST has lured students from Vietnam, China, and Rwanda among other countries.

HIGHER EDUCATION

MIT Engineer Shakes Korean Academia to Its Core

Radical measures from the new president of the Korea Advanced Institute of Science and Technology are roiling a tradition-bound system

DAEJEON, SOUTH KOREA—When the Korea Advanced Institute of Science and Technology (KAIST) announced on 19 November that an entrepreneur had donated $2.5 million to the university with promises of more to follow, it marked the latest in a string of coups for the new president, Suh Nam Pyo. A mechanical engineer on leave from the Massachusetts Institute of Technology (MIT) in Cambridge, Suh has raised an unprecedented amount—$12.5 million—in a country where donations to universities are rare. He's challenging other traditions as well. For example, KAIST's latest tenure review turned down several candidates, a shocking move by Korean standards.

Suh says he is aiming to make KAIST "as good as the best [universities], including MIT." Many faculty members agree that Suh's "overall philosophy and vision are correct," says KAIST systems biologist Lee Sang Yup. But there are concerns about how Suh will implement that vision at the 36-year-old university.

The KAIST community has reason to be cautious. In 2004, the university hired Nobel physics laureate Robert Laughlin as president—the first foreigner to lead a Korean university—with a mandate to transform KAIST into a world-class institution. Laughlin, on leave from Stanford University in Palo Alto, California, proposed privatizing KAIST and charging tuition, focusing on commercialization, and tripling undergraduate enrollment (*Science*, 25 February 2005, p. 1181; 20 January 2006, p. 321). But when Laughlin's plans failed to materialize, "the faculty was disappointed," says KAIST molecular biologist Chung Jongkyeong. In 2006, the board of trustees decided to seek a new president.

The board turned to Suh. Born in Gyeongju, South Korea, in 1936, Suh moved to the United States with his family as a teenager and earned a doctorate in mechanical engineering from Carnegie Mellon University in Pittsburgh, Pennsylvania. As an MIT professor, Suh has won plaudits for his engineering design theories, earned more than 50 patents, and helped start several companies. In the early 1980s, he was assistant director for engineering at the U.S. National Science Foundation, and he headed MIT's Department of Mechanical Engineering from 1991 until 2001.

Since arriving at KAIST in July 2006, Suh has opened undergraduate education to non-Korean students for the first time by insisting that many courses be taught in English. Suh decided that students who maintain "B" or better grades would continue to pay no tuition, whereas those with a "C" or below must pay about $16,000 per year starting in February. "We want students to take responsibility for their actions," Suh says.

Agent of change. KAIST's faculty supports Suh Nam Pyo's reforms, so far.

A new admissions process may also have broad impact. Previously, KAIST, like most of Korea's top universities, selected the top scorers in a written exam. Most high school students spend their free time prepping for these tests in cram schools. But Suh says that scores "are a one-dimensional measure" that fails to identify leaders. So candidates for KAIST's next incoming class were invited to campus this fall for interviews, to give presentations, and to engage in discussions while being observed by faculty members, who made selections based on scores and personal impressions. "We're looking for future Einsteins and future Bill Gateses," says Suh.

An even more radical step was putting teeth into tenure reviews. Traditionally, faculty members in Korea gain tenure after logging enough years. Suh insisted that KAIST professors up for tenure gather endorsements from experts in their field around the world. In September, 11 of 33 applicants were denied tenure and were given a year to find new jobs.

The tenure review "is the beginning of an educational revolution," says KAIST chemist Ryoo Ryong. But he and others worry about the fate of those denied tenure. Suh understands their predicament but is standing firm. The professors who didn't make tenure "are very good people, but in terms of the standard we set, they're not as good as we expect our professors to be." He is asking other universities to consider giving these professors a chance.

At the same time, Suh is looking to inject fresh blood—including foreigners—into the 418-strong faculty with a plan to add 300 professors over the next 4 to 5 years. (To expand the school, Suh is striving to win government approval for a doubling of KAIST's base governmental support of $108 million.) His first catch is Mary Kathryn Thompson, who completed her Ph.D. in mechanical engineering at MIT last year. "It's an exciting time to be here," says Thompson, who just started studying Korean when she arrived last August.

Although they support Suh's initiatives, some faculty members chafe at his blunt public comments implying that Korea's professors take life too easy. "I cannot agree," says Choi Yang-Kyu, an electrical engineer. "Most professors here are working very hard." Biomolecular engineer Kim Hak-Sung adds: "President Suh should have sticks and carrots, not just sticks."

Carrots don't come cheap. "I'm spending most of my time trying to raise money," Suh says. Part of that effort is wooing private donors. "Giving to universities is not prevalent in Asia, but it is something I'm trying to nurture in Korea," he says. That's a precedent all of Korea's universities might want to embrace.

–DENNIS NORMILE

CREDITS (TOP TO BOTTOM): D. NORMILE/SCIENCE; KAIST

VETERINARY MEDICINE

Camel Scientists Ask: What's Sinking the Ships of the Desert?

A wave of deaths among Saudi Arabian camels is the latest reason for a surge in research into these rugged, unusual, and highly valuable animals

When more than 2000 camels perished in Saudi Arabia this year, the mysterious die-offs caused a nationwide furor. Investigations were launched and camel "beauty contests" suspended. And when evidence mounted that the killer was not an infectious disease but rather a toxic substance in the animals' feed, a government council demanded punishments and reforms.

Camels are serious business in the Middle East and North Africa. And, increasingly, camel research has become a hot topic. "Camels are amazing animals," says Ulrich Wernery, scientific director of Dubai's Central Veterinary Research Laboratory, which has a staff of 15 camel experts and a herd of 50 dromedaries. (The camelid group includes one-humped dromedaries, Asia's two-humped species, and South America's llamas and alpacas.) Educated in Germany, Wernery first treated camels during a veterinary stint in Somalia in the 1970s, and he has been hooked ever since. "They have fantastic qualities, able to survive without water for 2 weeks in temperatures of 50° centigrade in the shade. They can drink water that is 3% salt." The animals also make unusual antibodies that may have applications including human diagnostics and snake antivenins (see sidebar, p. 1373).

But just as scientists in North Africa and the Middle East are expanding research into these seemingly impregnable desert juggernauts, the animals appear to be increasingly vulnerable to disease and toxins. Although epidemiological data are scarce—especially in the camel-rich but politically troubled nations of Somalia and Sudan—some scientists argue that the illnesses sinking camels are changing. "We are seeing new diseases in camels, and we often don't have a good explanation," says Bernard Faye, chair of the newly formed International Society of Camelids Research and Development (ISOCARD).

Dromedary die-offs

In North Africa, there have been several unexplained dromedary die-offs during the past decade, but the incidents have not shown a consistent pattern so far. In the late 1990s, hundreds of camels perished in Ethiopia, followed by isolated incidents of dying animals showing similar symptoms—pneumonia and fevers, for example—in Kenya and Sudan over the past 7 years. Faye, who is working with Kenyan scientists to investigate the deaths there, says a small ruminant virus that normally infects cattle and sheep was the likely cause, but other pathogens were also found in the dead animals. "The biggest problem is getting blood and organ samples," says Faye, a veterinary scientist with the French Agricultural Research Centre for International Development in Montpellier.

Another scourge of dromedaries, camelpox, is also a perennial suspect. The disease has been controlled with a vaccine in some regions, but Saudi scientists say it does not protect all camel populations. Other persistent or emerging camel diseases being scrutinized by North African investigators include tuberculosis, sleeping sickness, brucellosis, and rotavirus infections. There are no vaccines for such camel diseases, complains biochemist Mohamed Bengoumi of the Hassan II Institute of Agronomy and Veterinary Medicine in Rabat, Morocco.

In both North Africa and the Middle East, scientists have also noted an increase in the number of "food intoxications," camel deaths or sickness caused by harmful substances in plants or in the livestock fodder the animals eat. Bengoumi says camels are highly susceptible to high-nitrogen plants as well as fungal mycotoxins, neither of which are typically found in dry regions.

Faye collaborates with camelid scientists from Mongolia to Morocco, and he suspects that climate change in the Sahel region—the transition between the Sahara desert and wetter areas of central Africa—may be altering disease patterns among camels there. "There are two major factors affecting camels in North Africa: desertification and changes in the rainy seasons that tend to increase insect disease vectors," he says.

Other scientists suggest that changes in how people use camels—these days, more for their milk and meat and less for long-range desert transport—could make the animals susceptible to new illnesses. Yet another reason may be the expanding geographical range of dromedaries, now found as far south on the African continent as Nigeria and Tanzania.

Although he shares the perception that camel pathologies are slowly changing, Ghaleb Alhadrami, dean of the agriculture college at United Arab Emirates University in Al Ain, which hosted ISOCARD's first conference last year, says there is not enough evidence to link any shifts to climate change. He speculates that increased stress from keeping ever-larger herds in confined spaces and from camel racing—a multimillion-dollar industry in the Middle East—weakens the immune systems of many camels. But Alhadrami, like other researchers, says more data are needed, especially from North

Desert mystery. The recent deaths of more than 2000 camels in Saudi Arabia, such as this one near the capital city of Riyadh, belies their image as rugged desert juggernauts.

CREDIT: ISSA ABDUL/AFP/GETTY IMAGES

'Camelized' Antibodies Make Waves

When biologists at the Vrije University in Brussels by chance substituted leftover camel serum for mouse serum in a laboratory experiment, they made a startling discovery: The camel antibodies were fundamentally different from their murine counterparts.

"We were amazed," recalls Belgian biochemist Serge Muyldermans. Instead of being composed of two "heavy-chain" subunits and two "light-chain" subunits, the camel antibodies have only two heavy chains, making them smaller and more durable than typical antibodies.

Since this discovery—first reported in 1993—more than 130 papers have been published on the properties of camel antibodies and their uses, which include diagnostic tests and biodefense assays. At least two companies are trying to develop clinical products using antibodies from camels or related species, such as llamas and alpacas.

Muyldermans says these camelid antibodies pose lower risks to humans than antibodies from other animals, and they can survive elevated temperatures, are highly soluble, and can penetrate more quickly than normal antibodies through cell layers in tissue to reach their targets. Because of those and other qualities, drug companies are already using camel antibodies to speed identification of leads for therapeutics. And at the University of Munich in Germany, Heinrich Leonhardt's group is fusing fluorescent markers to camelid antibody fragments and using them to target and trace molecules in living cells.

The heat resistance of camelid antibodies has attracted the interest of the U.S. Naval Laboratory and the Southwest Foundation for Biomedical Research. They are testing the antibodies in biosensors designed to detect bioterrorism agents in hot environments. Another group, at Washington University School of Medicine in St. Louis, Missouri, has used the antibodies to develop a simple test to measure the caffeine content of hot beverages.

Ulrich Wernery of Dubai's Central Veterinary Research Laboratory, speculates that dromedaries developed heat-resistant antibodies to survive in harsh desert conditions. But Muyldermans says scientists don't truly know why the animals have such odd antibodies, which probably resulted from mutations about 50 million years ago, after cameloids split from ruminants and pigs.

One unusual application of camelid antibodies comes from Wernery's lab, where camels are used to produce antibodies to the venom of poisonous animals. The researchers obtain the antivenin by exposing a group of 15 dromedaries to venom from cobras, spitting vipers, and other poisonous snakes. Some people have severe reactions to traditional antivenins produced in horses, but Wernery says, "there is no problem with camel antivenins." The first clinical trial is scheduled for next year in Nigeria.

–R.K.

Africa. "There are few reliable statistics on camel disease trends," Bengoumi notes.

Furor in Arabia

Although mysterious camel deaths have occurred elsewhere in the Middle East and North Africa, no recent event matches the extent of this year's Saudi die-off, during which at least 2000 dromedaries perished in a region mainly south of Riyadh, Saudi Arabia. One unofficial estimate placed the death toll at 5000.

Initial reports focused on the possibility of an infectious disease or intentional poisonings. But after an investigation by the nation's agriculture ministry—which sent camel blood and fodder samples to both Saudi and outside labs—government officials asserted that the camels succumbed to contaminants found in their bran fodder: the antibiotic salinomycin, a supplement in chicken feed that is toxic to camels, and a fungal species whose mycotoxins can damage some animals' nervous systems.

The Saudi government has shared few details of its investigation with outside experts, which has puzzled camel scientists who felt they could have contributed. "Many questions remain open," says Faye. He suggests that the deaths may involve several factors, possibly including viral infections that suppress camels' immune systems. But Saudi Arabia's deputy agriculture minister for research, Abdullah Al-Obeid, says the lab tests showed no evidence of infectious disease. Steps are now being taken to improve the transport and storage of fodder for the nation's half-million camels, he says.

Although Wernery's lab hasn't yet studied tissue samples from the recent deaths, he says, "neither mycotoxins nor any known disease could have killed 5000 camels in that short span of time." He favors the antibiotic explanation, noting that the Saudi die-off appeared similar in symptoms to the deaths of about 120 racing camels in Dubai a few years ago. The cause was also later determined to be salinomycin in the fodder.

Whatever its origins, the Saudi debacle may help energize camel studies in the region. ISOCARD has been attracting new members, and Sudan has opened a camel research lab in Khartoum. In Saudi Arabia, Al-Obeid says his ministry plans to strengthen camel research, which is under way at several centers, including King Faisal University, where infectious-disease expert Abdulsalam Abdulah Bakhsh is investigating camel maladies.

Also, in January, the newest phase of the Camel Breeding, Protection, and Improvement Center—built with help from the U.N.'s Food and Agriculture Organization—will open in northern Saudi Arabia. Its technical director, veterinary scientist Mukhtar Taha Abu-Samra, says the facility will boast a camel hospital with seven diagnostic labs, a radiology and ultrasound room, and a surgery theater. By training camel specialists and upgrading research programs, he says the center aims to "bridge major gaps" in our knowledge of dromedaries.

Certainly many gaps remain. Camels' desert survival skills include kidneys that release very little urine in order to preserve water, an intestinal system that recycles water, and a nasal "air-conditioning system" that cools the blood vessels heading to their brains. And scientists suspect they will find more quirks of dromedary physiology, some that might even eventually benefit human medicine.

"Camels are wonderful research subjects," says Wernery, "and we can learn a great deal from them."

–ROBERT KOENIG

CREDIT: COURTESY OF BERNARD FAYE

SPACE

Columbus Injects Science Into Station

... Europe's Columbus laboratory on the launch pad— [illegible]

Next week, Florida's weather and aging space-shuttle technology permitting, Europe's main contribution to the International Space Station (ISS) will thunder into orbit. The European Space Agency's (ESA's) Columbus laboratory, a multipurpose experimental module, should dramatically increase the capacity for research on the station—and perhaps quiet those who have called the space station a job-creation scheme for aerospace companies rather than a productive scientific platform.

The €1 billion Columbus, which will be attached to the space station during the course of the three spacewalks of the 11-day mission, is the crowning achievement of ESA's human space-flight effort—its first crewed facility in space. "Columbus opens a new page for us. Now we will have real estate in orbit," says Bernardo Patti, ESA's Columbus project manager. But it has been a long and frustrating process for European scientists and engineers to get this far. Columbus arrives at the station some 5 years later than originally planned, because of construction delays and 2003's Columbia shuttle disaster. And, like the rest of the space station, Columbus is more modest than what was on ESA's drawing board early last decade.

Despite the scaled-back ambitions, European researchers believe Columbus will bring something new to the station. NASA's ability to use the space station as a laboratory has been hamstrung by the increasing cost of its construction, problems with the shuttle, and President George W. Bush's 2004 realignment of the U.S. agency toward exploring the moon and Mars. As a result, most NASA research on board the space station concerns the effects of long-duration space flights on the human body.

ESA managers say Columbus will restore part of the station's original rationale, providing a platform for basic research in biology, fluids, and materials, as well as for medical research and technological development. "We haven't followed the United States in narrowing our objectives," says Alan Thirkettle, ESA's space-station program manager.

The launch next spring of the main part of Japan's Kibo laboratory should continue to expand the station's scientific potential, as will 2009's planned increase of the station's resident crew from three to six. This doubling, and dwindling construction demands upon the crew, should create "an order of magnitude more experiment time," says Thirkettle. Adds physicist Gregor Morfill of the Max Planck Institute for Extraterrestrial Physics in Garching, Germany, "Columbus and the Japanese module will complete the transformation of the space station from a political point in space to a real laboratory."

Standing tall. Columbus is Europe's main contribution to ISS, but it came close to being left behind.

Indeed, with the words of space-station critics fresh in their minds, scientists and space-agency officials are hoping they can finally show what the station is capable of. "Now we have to prove ourselves," says Patti.

Being there

After President Ronald Reagan formally invited international partners in 1984 to join NASA in building a space station, Europe developed a plan consisting of several elements: a laboratory attached to the station; a free-flying module that would house automated experiments and occasionally dock with the station for repairs and restocking; and a polar-orbiting Earth observation satellite that would share computer and communications technology with the station. European astronauts would travel to and from the station in Hermes, a minishuttle that could carry three people and 3 metric tons of cargo.

The first cost estimates produced by contractors in 1989 were much higher than ESA had expected, and European governments began to put the squeeze on ESA's space-station program. The Hermes shuttle and free-flying module were abandoned. The polar satellite was handed over to ESA's Earth observation directorate. The program that emerged in the mid-1990s comprised the Columbus module—smaller than originally planned but still containing 10 phone-booth-sized payload racks—and a series of pilotless cargo ships called Automated Transfer Vehicles (ATV). Launched atop a European Ariane 5 rocket, an ATV would carry about 7.5 metric tons of air, water, food, fuel, scientific equipment, and personal items to resupply all parts of the station. Once emptied, filled with waste, and jettisoned, it would burn up on reentry. The first ATV is due to fly in February.

CREDITS (TOP TO BOTTOM): NASA; ESA/NASA

The ATV is also part of the complex barter arrangements through which NASA's international partners buy into the space station. "It pays our rent," Thirkettle says. To reimburse NASA for the shuttle launch of Columbus, European companies have built two "nodes" connecting modules for the station. The first is Node 2, also known as Harmony, which the shuttle carried aloft last month. Columbus and Japan's Kibo will both dock to Node 2. In addition, to pay for the air, water, power, and other station services that Columbus needs, five of its 10 payload racks will be devoted to NASA's use.

Although construction of the 19-metric-ton, 7-meter-long Columbus was well under way by the late 1990s, its trials were far from over. In 2001, with station costs spiraling out of control, legislators in Congress and NASA officials began to consider building the ISS to the minimum viable configuration. "They questioned the entire premise of the station and didn't give a damn for the partners," says Thirkettle. The crisis passed, but delays in building Russian elements of the station bumped Columbus's planned launch from 2002 to 2004.

Then the Columbia shuttle disintegrated during reentry in February 2003, and all station construction was put on hold. Two years later, with the shuttle fleet still grounded, NASA again debated drastically cutting back the number of shuttle flights to complete the station. Some scenarios would have left Columbus and Kibo on the ground. "This lasted for a few weeks. It was very, very messy," Thirkettle says.

But then, he notes, Michael Griffin was appointed NASA administrator and turned out to be a keen proponent of the station. As *Science* went to press, Columbus was in the hold of Atlantis and on the pad ready for a weeklong launch window starting 6 December.

A lab in space

Planning, designing, and building such a space facility takes roughly a decade, so Columbus's technology was never going to be cutting-edge. But the 5-year delay has made Columbus even more outdated, with computer technology and data-transfer speeds falling behind what's available on Earth. Patti says ESA has upgraded Columbus's avionics system and installed a 100-megabit-per-second computer network. Equipment with such speeds can now be bought in any computer store, but Columbus's network will still be the fastest in space.

Personnel issues have also been a challenge, as ESA tried to retain essential staff and keep "the scientific community on the ball and interested," says Thirkettle. A significant number of researchers who prepared experiments for Columbus were Ph.D. students at the time and have since graduated and found other jobs.

Just as in the United States, many researchers in Europe think the science they get from a crewed facility in space is not worth the huge cost of building it. The money spent on the space station and Columbus, they argue, would have been better spent on robotic probes. Astronomers dislike the station, for example, because with whirring machinery and people moving around it isn't still enough to point a telescope accurately. "It goes up and down like a roller coaster," says George Fraser, director of the Space Research Centre at the University of Leicester in the U.K.

But Patti says many researchers in Europe, mostly at universities and government labs, are eager to conduct microgravity research. He hopes a few years of good results out of Columbus will trigger more curiosity among industrial researchers. According to Marc Heppener, head of science and applications in ESA's human space-flight directorate, the last call for experiment proposals in 2004 attracted three times as many as the agency could fund.

Max Planck's Morfill attests to the promise of Columbus, having already had experiments performed by cosmonauts on the Russian segment of the station. His area of interest is "dusty plasmas," microscopic particles mixed into a plasma that can be coaxed into repeating patterns, akin to a macroscopic crystal and other states of matter. These experiments could be automated, Morfill says, but "with cosmonauts doing the experiments, you're able to go into regimes not anticipated before. It's been enormously successful. We've got 100 publications out of it."

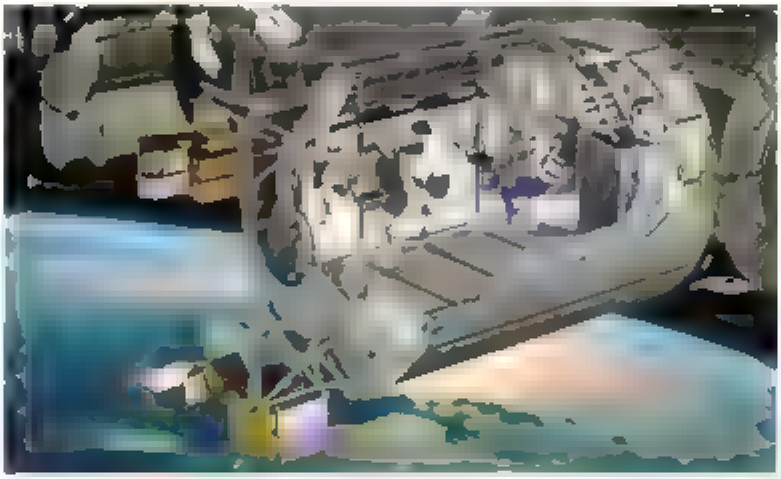

People power. With Columbus (illustration) and a Japanese lab module in place, and larger crews by 2009, space-station science should take off.

Columbus will take off with a full complement of experiments already installed. Its racks include a fluid science laboratory, a set of physiology modules, and a basic biology lab, among others. On the outside of Columbus, there are two sites for external experiments. Initially, one will hold a facility to expose various pieces of technology to the harsh conditions of space; the other will be home to a solar telescope.

Although some Columbus experiments will follow NASA's lead and examine the effects of microgravity on humans, many others will be more fundamental. "Columbus should return fascinating data that will advance physiological science in general," says physiologist Kevin Fong of University College London, who has just completed a 9-month fellowship at NASA's Johnson Space Center. Experiments will look at, for example, how bone remodels after a break. Removing gravity allows researchers to see the remodeling process more clearly. "No one really understands this at a fundamental level," Fong says.

Researchers in Japan are looking forward to a similarly eclectic mix of experiments once Kibo arrives at the station next year. The size of a luxury tour bus and weighing nearly 23 metric tons, Kibo, which means "hope" in Japanese, will be the biggest of the space station's research modules. It will take three shuttle flights to deliver all its components: a pressurized module with racks for experiments conducted by astronauts, an exposed platform, and an external storage compartment.

Japanese scientists have plans for eight internal experiments covering various aspects of protein crystallization, fluid mechanics, and cell biology. Later, three payloads will be fixed to the exposed facility, including an x-ray scanner to catch novae and gamma ray bursts, an atmospheric monitor, and a material-exposure facility. "From the beginning, science was intended to be a key factor for the ISS. I'd like to see that direction pursued," says astrophysicist Shoji Torii of Waseda University in Tokyo, who is designing an instrument for Kibo.

Once Columbus and Kibo are in place, fans of the space station will finally have a chance to do the unique science they promised. That opportunity is all ESA's Thirkettle wants. "I'm looking forward with anticipation, not trepidation," to the launch of Columbus, he says. "Now we have an opportunity to really exploit this gorgeous piece of hardware."

–DANIEL CLERY

With reporting by Dennis Normile

CREDIT: D. DUCROS/ESA

LETTERS

edited by Jennifer Sills

Global and Local Conservation Priorities

Community empowerment. A local fisherman sets up a buoy marking a boundary of a community-enforced total protection zone near Rolas Island in the northern part of Quirimbas National Park.

IN THEIR POLICY FORUM, "GLOBALIZATION OF CONSERVAtion: A view from the South" (10 August, p. 755), J. P. Rodríguez *et al.* claim that international nongovernmental organizations (INGOs) promote conservation from the top down, through global biodiversity priority-setting, rather than from the bottom up, by supporting local groups or building local capacity in areas of high biological importance. They also liken INGOs to transnational corporations. We respectfully disagree with both assertions.

Perhaps the best example of support from an INGO to community-based conservation is World Wildlife Fund's (WWF's) program in Namibia, where 50 communal conservancies operating over 119,000 km² allow indigenous groups to directly benefit from increased control over wildlife resources. Rather than top-down, this initiative devolves user rights to groups previously marginalized under apartheid. Another example is Quilalea Island, Quirimbas National Park, Mozambique, the largest marine reserve on the east coast of Africa, which was established with WWF support to local communities to better manage local fisheries (see photo).

Conservation organizations are not faceless transnational corporations; rather, they are led by passionate defenders of the natural world who are devoted to helping local communities and building local conservation capacity. Three outstanding examples draw from the work of Henri Nsanjama, Mingma Norbu Sherpa, and Chandra Gurung (*1*, *2*). During his lifetime, Nsanjama was Head of the African College of Wildlife Management before joining WWF, and in his tenure as Vice President for Africa he did more to build local capacity among African professionals than virtually any of his contemporaries. Mingma Sherpa and Chandra Gurung were world-renowned conservationists who helped create the first locally managed conservation area in Asia, in the Annapurna region. In September 2006, they and 22 others—including some of the region's leading conservationists—perished in a helicopter crash after successfully handing over the largest community-run nature conservation area, Kanchenjunga, to a local management committee. The memories of Henri, Mingma, and Chandra inspire all conservationists committed to supporting local conservation efforts.

ERIC DINERSTEIN

Conservation Science Program, World Wildlife Fund, Washington, DC 20037, USA.

References

1. E. Dinerstein, P. Yonzon, *Conserv. Biol.* 21, 278 (2007).
2. E. Dinerstein, *Pachyderm* 41, 107 (2007).

IN THE POLICY FORUM "GLOBALIZATION OF conservation: A view from the South" (10 August, p. 755), J. P. Rodríguez and colleagues argue that large international nongovernmental organizations (INGOs) set the global conservation agenda by using tools to define worldwide priorities of conservation. As a result, they assert, INGOs increase their own fundraising capacity, investments in biodiversity conservation by local governments decline, and local NGOs (LNGOs) are forced out of the market. Thus, they compare INGOs to transnational corporations.

Current experience in Brazil is otherwise. First, the executed budget of the Brazilian Ministry for Environment has doubled between 1999 and 2006 (*1*), which parallels the range of increase in expenditures (shown by Rodríguez *et al.*) for global actions fostered by Conservation International (CI) and World Wildlife Fund (WWF)—INGOs with strong Brazilian branches.

Second, the argument that conservation training is insufficiently supported by INGOs does not hold true in Brazil. Graduate training, which has recently been credited with boosting Brazilian scientific productivity (*2*), is traditionally fostered by governmental agencies. However, INGOs and LNGOs now occupy a central role in graduate training on biodiversity sciences, with no niche overlap. Funding for field courses, research projects, and infrastructure is provided by both INGOs (such as CI and WWF) and LNGOs (such as Fundação Biodiversitas, Fundação O Boticário, and Instituto Internacional de Educação do Brasil) (*3*–*6*). The LNGO Instituto de Pesquisas Ecológicas (IPE) will soon pioneer a professional masters program focused on conservation (*7*). CI is providing funds, grants, and personnel to a graduate program on tropical biodiversity at the Federal University of Amapá in partnership with federal and local governments (*8*). Both IPE and CI are promoting high-quality training to conservationists and academics.

I agree with Rodríguez and colleagues' idea that conservation leadership ought to be decentralized and integrated into local conditions. In Brazil, however, this is a governmental issue, as defined by the federal constitution.

CREDIT: PETER BECHTEL/WWF

There is plenty of room for both INGOs and LNGOs to help Brazil reach higher scientific standards in biodiversity sciences and to bridge scientific knowledge and decision-making (6).

F. R. SCARANO

Departamento de Ecologia, Universidade Federal do Rio de Janeiro, 21941-970 Rio de Janeiro, Brazil.

[redacted]

1. Ministerio do Meio Ambiente, "Relatório de Gestão 2003-2006—Política Ambiental Integrada para o Desenvolvimento Sustentável" (Brasília, Brazil, 2007); [redacted] 07032007_relatoriodegestao2003_2006.pdf [in Portuguese].
2. W. Glanzel et al., *Scientometrics* **67**, 67 (2006).
3. http://ecologia.icb.ufmg.br/~ecmvs/exportar/manual_aluno.htm [in Portuguese].
4. Postgraduate Program in Ecology and Conservation, [redacted] www.dbi.ufms.br/mstecopan/ [in Portuguese].
5. Postgraduate Program in Ecology and Conservation, Universidade Federal do Paraná; www.bio.ufpr.br/ecologia/ [in Portuguese].
6. Instituto Internacional de Educação do Brasil; www.ieb.org.br/ [in Portuguese].
7. F. R. Scarano, *Sci. Agric.* **64**, 439 (2007).
8. Postgraduate Program in Tropical Biodiversity; www.unifap.br/ppgbio/historico.htm [in Portuguese].

IN THEIR POLICY FORUM, "GLOBALIZATION OF conservation: A view from the South" (10 August, p. 755), J. P. Rodriguez *et al.* call upon Southern scholars to promote self-governing local institutions, enhance human capacity, and secure local participation in conservation. These goals cannot be met without certain prerequisites.

In order for the participation of local people and institutions to flourish, it is necessary to build local community capital (1), improve local governance (2), and enhance equity in benefit and burden sharing. Only 6% of biological scientists live in the South, which is home to more than 85% of the world's biodiversity (3); without bolstering human capital, our efforts in achieving these goals might be counterproductive. Moreover, in light of the cuts in university scholarships and the small percentage of the INGOs' budgets that is devoted to building capacity in developing countries, regional-level efforts are needed to generate scholarship. To improve training efficiency, online training and in-country or on-site trainings should be encouraged.

The South is home to some renowned universities and highly competent scientists. Other countries should send scholars to those universities, and regional scientists should mentor university students. More interaction between southern countries is crucial to achieving self-sustainability goals, but short- and long-term alliances between northern and southern countries can still reduce redundancy and improve efficiency. Let's work together to translate the slogan "think globally, act locally" into action.

PASHUPATI CHAUDHARY

Department of Biology, University of Massachusetts Boston, Boston, MA 02125, USA.

[redacted]

1. J. N. Pretty, *Science* **302**, 1912 (2003).
2. T. Dietz, E. Ostrom, P. C. Stern, *Science* **302**, 1907 [redacted]
3. J. Sarukhan, R. Dirzo, in *Encyclopaedia of Biodiversity*, S. A. Levin, Ed. (Academic Press, San Diego, CA, 2001), vol. 1, pp. 419–436.

J. P. RODRIGUEZ *ET AL.* (POLICY FORUM, 10 August, p. 755) highlight the need for increased funding and training for local conservation institutions to achieve biodiversity conservation on the ground—a conclusion with which we emphatically agree. They also claim that global conservation prioritization templates are equivalent to top-down development plans, but do not acknowledge that one purpose of global priority-setting is channeling globally flexible resources to the regions that need it most (1).

Conservation International (CI) and other global conservation organizations act as conduits for financial support, capacity-building, and technical assistance within countries. Over the past 5 years, CI has provided more than $100 million in funding to more than 1000 partners. Arguably, these resources come from sources that would not have been available without global conservation NGO action.

Global conservation priorities also serve as a scientific blueprint for governments to adapt and link local and national priorities with global ones. Madagascar provides one such powerful example. President Marc Ravalomanana's government has used CI's Hot Spots concept as a way to engage the international community in supporting a plan to triple the country's protected area coverage. Such national leadership combined with local implementation capacity has led to the creation of a national conservation trust fund that now has a capitalized value of over U.S. $30 million.

We agree with Rodriguez *et al.* that "solutions must integrate extremely diverse natural, socioeconomic, and cultural systems and usually require a sense of community ownership," which is why CI supports local groups in developing responses they deem appropriate. Approaches often support existing organizations in building others at scales below them. For example, CI's Critical Ecosystem Partnership Fund provides funds to the Liberia Conservation Action Fund, which then makes grants to small NGOs.

A fundamental pillar of our business model is to create partnerships for more lasting and

powerful conservation results. These partnerships include a long-term component of capacity-building and learning so that CI can eventually divest from an area when local leadership is strong. Often, these solutions mean that CI funds organizations and programs well outside of universities or the biological sciences, believing instead that the "strong local institutions and individuals" that Rodriguez *et al.* call for must span civil society. It is precisely these strengthened sectors and partnerships, from local to global scales, that are needed to bring about conservation successes.

RUSSELL A. MITTERMEIER, CLAUDE GASCON, LEON RAJAOBELINA, JATNA SUPRIATNA, JOSE MARIA CARDOSO DA SILVA, CARLOS MANUEL RODRIGUEZ, LU ZHI, KATRINA BRANDON

Conservation International, Arlington, VA 22202, USA.

Reference

1. T. M. Brooks *et al.*, *Science* 313, 58 (2006).

Response

THE LETTERS BY DINERSTEIN, SCARANO, AND Chaudhary focus on the capacity-building elements of our article, rather than on our critique of branding strategies of international nongovernmental organizations (INGOs). While we are grateful to the authors for providing cases of successful capacity-building, it remains unclear whether this is a prevalent trend among biodiversity conservation INGOs or governmental organizations worldwide. Investment in local capacity has not been a funding priority (*1*), even though the existing cadre of conservation professionals is substantially below the level required for biodiversity-rich countries (*2*, *3*). Additionally, strengthening local capacity is not identified in the mission statements of major INGOs (*4*), nor is it systematically assessed. Philanthropic organizations that fund these INGOs have not prioritized building local capacity, which may partially explain the reluctance of the INGOs to embrace this as a primary goal. Many institutions in developed countries rely on individual donations and endowments to cover core operating costs, sources rarely available in the developing world. Therefore, local organizations often depend on international funds for their projects, which are frequently tied to priorities set by the INGOs.

As Dinerstein and Scarano demonstrate, there is anecdotal evidence of local capacity-building. We recommend a sector-wide, systematic evaluation of investments in strengthening local scientific and institutional capacity for conservation as a basis for developing indicators to guide improvements. Commonly tracked variables in conservation, such as number of hectares protected, deforestation rates, species population trends, legislation passed, and policies changed, are not as useful for this purpose as metrics that track investment in capacity-building. We further recommend that donors create incentives so that grants given to INGOs are implemented directly by local organizations; fund more training at local universities, as suggested by Chaudhary; help local organizations raise funds for their home priorities; and provide management assistance. Better yet, developed country donors could mount a major fundraising effort and provide endowments for core support to local organizations that meet and maintain performance standards, the funds would be distributed based on conservation needs worldwide.

As the examples of Dinerstein and Scarano underscore, INGOs employ many dedicated and talented conservation scientists. Scarano

shows that Brazil is among the vanguard of countries assigning high priority to building their conservation science sectors, but it is an outlier (along with Mexico) in Latin America. As of 2005, of the 40 formal programs offering conservation biology courses in the region, 67% were registered in either Brazilian or Mexican universities (2). Had the tragic event mentioned by Dinerstein occurred in a developed country, it would have remained an immense human tragedy, but the impact on conservation efforts would have been short-lasting: numerous qualified professionals would be available to follow in the tracks of those who died. This is not the case in Nepal or in the vast majority of the developing world.

Mittermeier *et al.* agree that large INGO branding strategies are useful for fundraising, but they offer no scientific evidence to support the prioritizing templates used in the brands. By devoting the large sums they raise to areas selected on grounds that are not the product of scientific consensus (such as Hot Spots) (5), they exclude many regions of high biodiversity importance (6). Moreover, if only Hot Spots are protected in a sea of development, they will not survive intact in the face of climate change and invasive species, including pathogens. Finally, we are pleased that Mittermeier *et al.* agree with us on the importance of local leadership and capacity-building; we believe that strong local leadership merits major, long-term investment.

J. P. RODRÍGUEZ,[1] A. B. TABER,[2*] P. DASZAK,[2,3] R. SUKUMAR,[4,5] C. VALLADARES-PADUA,[6] S. PADUA,[6] L. F. AGUIRRE,[7,8] R. A. MEDELLÍN,[9] M. ACOSTA,[10] A. A. AGUIRRE,[3] C. BONACIC,[11] P. BORDINO,[12] J. BRUSCHINI,[3] D. BUCHORI,[13] S. GONZÁLEZ,[14] T. MATHEW,[5] M. MÉNDEZ,[12,15] L. MUGICA,[10] A. P. DOBSON,[16] M. PEARL[3]

[1]Instituto Venezolano de Investigaciones Científicas and PROVITA, Caracas, Venezuela. [2]Wildlife Trust, New York, NY USA. [3]Consortium for Conservation Medicine, New York, NY USA. [4]Indian Institute of Science, Bangalore, India. [5]Asian Nature Conservation Foundation, Bangalore, India. [6]IPÊ—Instituto de Pesquisas Ecológicas, Nazaré Paulista, São Paulo, Brazil. [7]Centro de Biodiversidad y Genética, Universidad Mayor de San Simón, Cochabamba, Bolivia. [8]Centro de Estudios en Biología Teórica y Aplicada—BIOTA, La Paz, Bolivia. [9]Instituto de Ecología, Universidad Nacional Autónoma de México and BioConciencia, Mexico City, Mexico. [10]Universidad de la Habana, Cuba. [11]Fauna Australis and Pontificia Universidad Católica de Chile, Santiago, Chile. [12]AquaMarina—Centro de Estudios en Ciencias Marinas, Pinamar, Argentina. [13]Bogor Agricultural University and PEKA Indonesia Foundation, Bogor, Indonesia. [14]IIBCE, Facultad de Ciencias, Universidad de la República Montevideo, Uruguay. [15]Department of Ecology, Evolution and Environmental Biology, Columbia University, New York, NY USA. [16]Department of Ecology and Evolutionary Biology, Princeton University, Princeton, NJ, USA.

*Corresponding author. E-mail: taber@wildlifetrust.org

References and Notes

1. G. Castro, I. Locker, "Mapping conservation investments: An assessment of biodiversity funding in Latin America and the Caribbean" (Biodiversity Support Program, Washington, DC, 2000).
2. J. P. Rodríguez, J. A. Simonetti, A. Premoli, M. A. Marini, *Conserv. Biol.* **19**, 969 (2005).
3. J. P. Rodríguez, K. M. Rodríguez-Clark, M. A. Oliveira-Miranda, T. Good, A. Grajal, *Conserv. Biol.* **20**, 1340 (2006).
4. This includes mission statements of World Wildlife Fund (www.worldwildlife.org/about/), The Nature Conservancy (www.nature.org/aboutus/?src=l5), Wildlife Conservation Society (www.wcs.org/sw-our_mission), and Conservation International (http://web.conservation.org/xp/CIWEB/about/).
5. G. M. Mace *et al.*, *Nature* **405**, 393 (2000).
6. G. Ceballos, P. R. Ehrlich, *Science* **296**, 904 (2002).

CORRECTIONS AND CLARIFICATIONS

Reports: "A 'silent' polymorphism in the *MDR1* gene changes substrate specificity" by C. Kimchi-Sarfaty *et al.* (26 January, p. 525). Based on an inquiry from Jack Kornblatt, the authors wish to clarify that the protein sequence was obtained from a detailed mass spectrometric study performed at the Harvard Microchemistry Facility (HMF) by microcapillary reverse-phase HPLC nano-electrospray tandem mass spectrometry. HMF performed both chymotryptic

and pronase digestions of the protein. In all, 82 peptides (representing 37% of the Pgp sequence by amino acid count) were identified and sequenced (see Supporting Online Material at www.sciencemag.org/cgi/content/full/318/5855/1382/DC1). Each of these sequences was identical to the sequence of haplotype P-glycoprotein. Moreover, several different peptides encoded by the synonymous SNP (3435C>T), which is the key polymorphism linked to the functional change in Pgp, were sequenced and found to be unchanged. In addition, the analysis of codon usage, table S1 in the original Supporting Online Material (see www.sciencemag.org/cgi/data/1135308/DC1/1) contains for each codon around the three polymorphisms the frequency of this codon per 1000 codons in the human genome instead of RSCU values, as stated in the text. These values were obtained from the codon usage Web site (www.kazusa.or.jp/codon/cgi-bin/showcodon.cgi?species=Homo+sapiens+%5Bgbpri%5D). Figure 1, panels D to F, shows results in the presence of cyclosporin A (+CsA), not (+/CsA), as indicated in the body of the figure. This is correctly stated in the legend. These clarifications do not affect the conclusions of the paper.

TECHNICAL COMMENT ABSTRACTS

Comment on "Decagonal and Quasi-Crystalline Tilings in Medieval Islamic Architecture"

Emil Makovicky

Lu and Steinhardt (Reports, 23 February 2007, p. 1106) claimed the discovery of a large, potentially quasi-crystalline Islamic tiling in the Darb-i Imam shrine but regard the earlier Maragha tiling, previously described as quasiperiodic, as a small isolated motif. We demonstrate that the Darb-i Imam pattern is periodic and that the quasi-crystalline discs superimposed on its lattice are derivatives of the Maragha pattern.

Full text at www.sciencemag.org/cgi/content/full/318/5855/1383a

Response to Comment on "Decagonal and Quasi-Crystalline Tilings in Medieval Islamic Architecture"

Peter J. Lu and Paul J. Steinhardt

Our study showed that both Gunbad-i Kabud and Darb-i Imam tessellations belong to a sequence of Islamic tilings that resolve into a common set of girih tiles, so local similarities are expected. However, historically accurate reconstructions show that Darb-i Imam is unique: the only known example that does not repeat periodically and that displays a self-similar transformation enabling its continuation ad infinitum to a perfect quasi-crystalline pattern.

Full text at www.sciencemag.org/cgi/content/full/318/5855/1383b

Letters to the Editor

PSYCHOLOGY

Learning from Words

Robin Lakoff

Language comes naturally to humans, but understanding how it works, much less so. How come you can drive on a parkway, and park on a driveway, but not park on a parkway? Conundrums like this fill some of us with delight and others with unease: language should, some feel, work logically.

Both parties will find pleasure and elucidation in Steven Pinker's new book, *The Stuff of Thought: Language as a Window into Human Nature*. Pinker, a cognitive psychologist at Harvard University, brings an engaging and witty style to the study of subject matter that—were it not as important to us as it is complex—might otherwise be off-putting. His overall theme is the way in which linguistic forms are in some sense inevitable rather than chaotic: intrinsically bound to the way our brains are wired.

In a sense, the work of Pinker and his colleagues is a continuation of Chomsky's revolution of a half-century ago. Chomsky, after all, famously called language a window into the mind, a statement Pinker's subtitle echoes. But where Chomsky justified his theories intuitively, creating his example sentences and testing their grammaticality in his own mind, Pinker and his colleagues are empiricists, proving their claims by experimentation.

Pinker discusses language at all levels, from sounds, to words and phrases, to larger units (sentences and beyond). There is a set of English words that begin with gl-: glare, glow, glass, gleam, and glimpse (among many others). Is the similarity due to mere coincidence? Pinker says that all such words have as part of their meaning the suggestion of "emission of light." Even in those areas that some might want to banish from the domains of orderly reason, like four-letter words, language works according to general principles. Pinker cites the work of the fictitious linguist Quang Fuc Dong (an alter ego of the very real linguist James D. McCawley), who argued against the common assumption that "Fuck you!" is an imperative. In a true imperative, a second-person direct object must be reflexive: yourself, not you. Of course, this discussion (in the chapter "The seven words you can't say on television") is good clean (if titillating) fun, but Pinker deepens the discussion to illustrate important properties of language. The fun aspects of linguistic theory are inseparable from its deeply serious nature. This necessary connection between depth and wit is echoed in Pinker's style. Where the discussion might bog down of its own weight, he leavens the dough with humor: quips, anecdotes, jokes, and comic strips. Chomsky and other cognitive theorists are often cited, as we would expect, but so, to good effect, are Groucho Marx, Lewis Carroll, and Dorothy Parker.

The Stuff of Thought

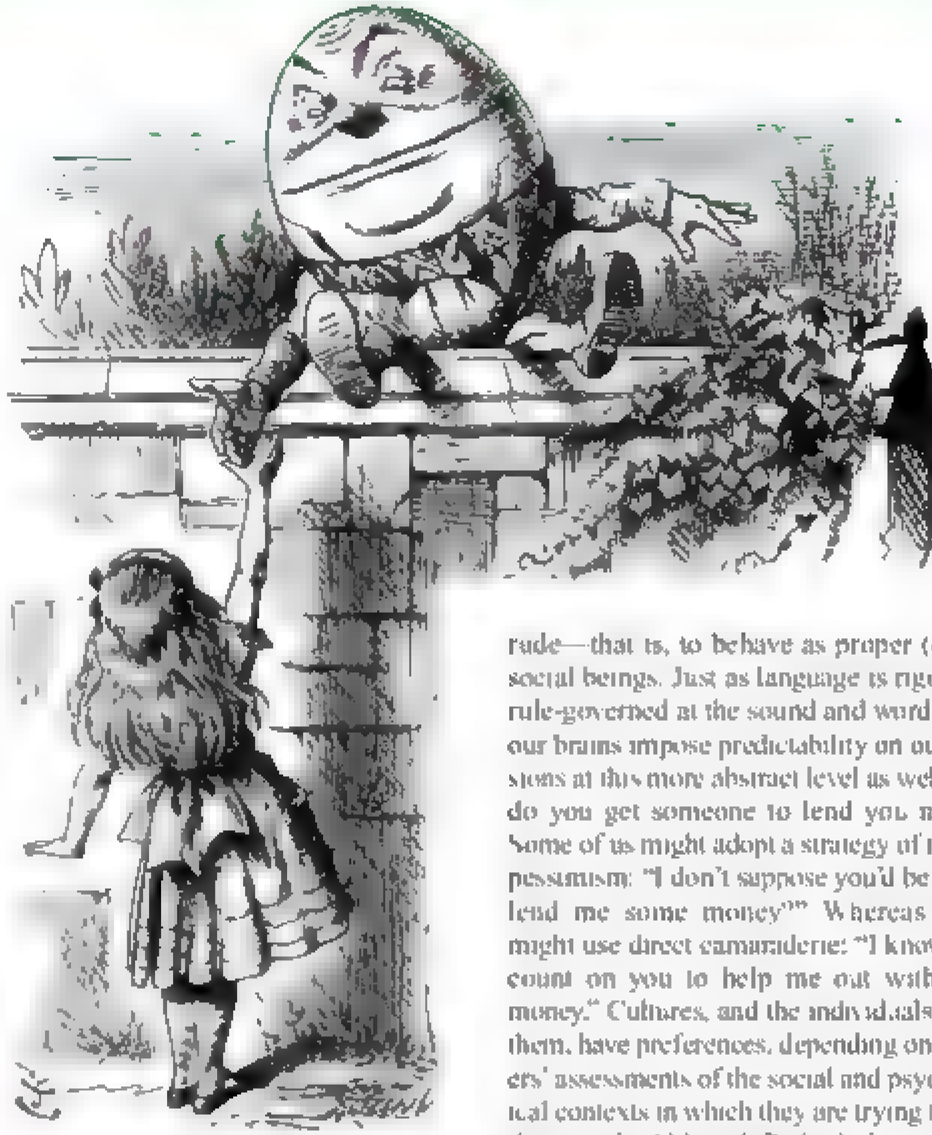

Alice finds Humpty Dumpty very clever at explaining words.

CREDIT: JOHN TENNIEL, ILLUSTRATION FOR THE SIXTH CHAPTER OF LEWIS CARROLL'S THROUGH THE LOOKING GLASS (1865)

The chapter "Games people play" looks at some of the larger and more abstract uses of language: the way we use it interactively, choosing to be direct or indirect, polite or rude—that is, to behave as proper (or not) social beings. Just as language is rigorously rule-governed at the sound and word levels, our brains impose predictability on our decisions at this more abstract level as well. How do you get someone to lend you money? Some of us might adopt a strategy of indirect pessimism: "I don't suppose you'd be able to lend me some money?" Whereas others might use direct camaraderie: "I know I can count on you to help me out with some money." Cultures, and the individuals within them, have preferences, depending on speakers' assessments of the social and psychological contexts in which they are trying to meet their needs. Although Pinker's discussion of this topic is generally informative and engaging, here is one place where he might have gone beyond the fields in which he claims expertise. Interactional sociolinguists like John Gumperz, Deborah Tannen, and Deborah Schiffrin have had a great deal of interest to say on these topics. Likewise, the work of William Labov in a great many areas of sociolinguistics would provide Pinker with additional evidence of the rationality and logic of linguistic choices. But the book is curiously lacking in any discussion of sociolinguistics whatsoever.

Although the author generally shows a perfect intuition for how much to say about complex topics, occasionally he falters. His discussion of meaning and naming in the chapter "What's in a name?", while useful in leading up to his detailed examination of naming conventions of all kinds, goes into too much formal detail, at least for my taste. On the other hand, despite its length his discussion of politeness and indirectness, as noted above, oversimplifies the questions it explores.

But these are mere quibbles when discussing such an inviting and important

The reviewer is at the Department of Linguistics, 1203 Dwinelle Hall, University of California, Berkeley, CA 94720–2650, USA. E-mail: rlakoff@berkeley.edu

book. Everyone with an interest in language and how it gets to be how it is—that is, everyone interested in how we get to be human and do our human business—should read *The Stuff of Thought*.

10.1126/science.1150869

GEOSCIENCE

Dancing Continents

Kevin Burke

Some of the world's ocean basins, like the Atlantic, are currently opening, while others, like the Pacific, are closing. Plate tectonic data recording the rotation of rigid objects across Earth's surface mean that we can analyze the plate motions associated with these openings and closings. Forty years ago, Tuzo Wilson pointed out that because similar analyses are impossible for times before the age of the oldest ocean floor, the best we can do is to interpret the older geological record in terms of cycles (now called Wilson cycles) of the opening and the closing of ocean basins (*1*). The way of describing how and when continents were broken up and younger continents or supercontinents were later assembled has been to map and date sutures within continents that mark the places where ancient ocean basins have opened and closed. Ted Nield's imagination has been captured by one aspect of these cycles. He writes, "The Earth's landmasses are locked in a stately quadrille that geologists call the Supercontinent Cycle, the grandest of all the patterns in nature." I have too many astronomer friends to be able to accept that, but it does show that the idea of supercontinents has hooked Nield, and it accounts for the book's title being in the singular.

Nield (the editor of the Geological Society of London's magazine *Geoscientist*) has responded to being hooked by writing a book that is both informative and entertaining. He has thought well outside any academic box, touching on a huge diversity of topics. He writes of a future Earth with a single supercontinent visited by a spacecraft from far in the galaxy (that accounts for his book's subtitle), and he tells of fictional and postulated continents as well as their colorful and, in some cases, disreputable protagonists. Nield relates many subjects that are currently major foci of research in Earth history to his theme. For example, he provides clear and well-informed treatments of evidence from Australia for the existence of abundant continental material about four billion years ago; evidence for a snowball Earth, at the end of the Proterozoic; and evidence for the, very likely related, origin of complex life forms after the end of that extraordinary episode of cooling.

Although I enjoyed the book and learned much from it, I remain puzzled about how to recognize a supercontinent. I came to the book assuming that supercontinents contain all the continental crust of the Earth. The illustrated future example, boldly constructed by Roy Livermore, contains all continental material in a single roughly elliptical body, and Nield describes Pangea as a supercontinent that contained nearly all continental crust. Imagine my surprise when I read "Pangaea consisted of two smaller supercontinents joined at the hip in the region of the Equator: Laurasia in the Northern Hemisphere … and Gondwanaland in the Southern… ." I was left asking what a supercontinent is. I do not think it is simply something assembled from smaller continental blocks, because that would make all continents supercontinents. Even Greenland (only two million km^2) is crossed by two sutures, which indicate its assembly from three smaller continental blocks. I suggest a testable property for identifying supercontinents would be "contains nearly all extant continental crust."

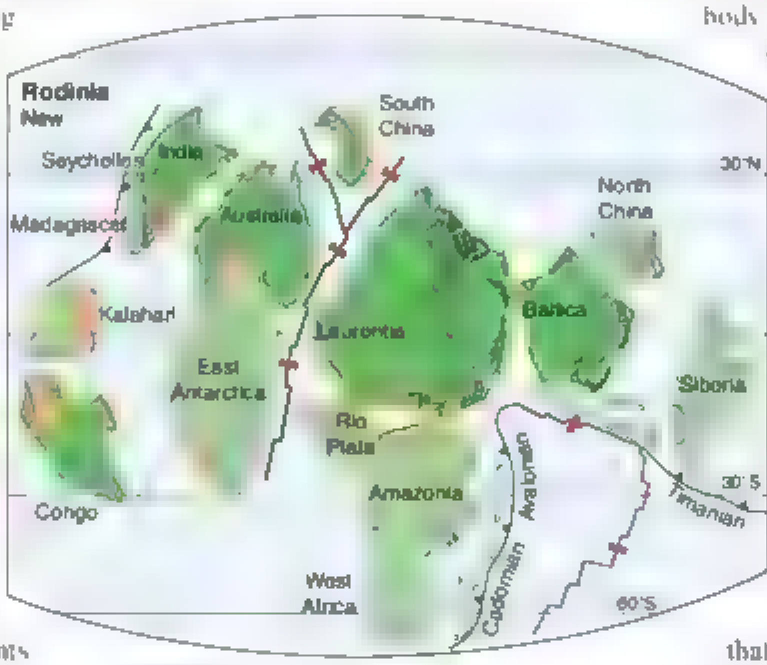

Rodinia reconstruction.

Rodinia has been suggested to have been a supercontinent assembled through collisions of various fragments with an already-ancient Laurentia about one billion years ago, although my estimate of the area of its assembled blocks makes it only about half as large as the younger Pangea. Nield writes a lot about Rodinia, mostly emphasizing its breakup, but does not include a map of it—perhaps because there is no consensus about what Rodinia looked like. Assembled continental fragments have been arranged around Laurentia in a variety of ways; the figure shows a version drawn by Trond Torsvik (*2*).

The difficulties in recognizing ancient supercontinents involve not only estimating how much of then-extant continental crust was incorporated into the newly assembled body but also obtaining high-resolution age determinations and distinguishing other convergent plate boundary phenomena from continental collisions. An even harder problem is determining where the objects involved in an assembly were, not only with respect to each other but also with respect to Earth's spin axis. Ancient latitudes and longitudes are essential. There has been progress in estimating ancient latitudes using paleomagnetism: thus a few continental blocks now have credible poles for as long ago as one billion years. But resolving ancient longitudes is not yet feasible.

Nield has not persuaded me that there is yet a case for the existence of ancient supercontinents (other than Pangea) that contained all of the Earth's continental crust—let alone evidence of cycles of supercontinent assembly. Nevertheless, I think that *Supercontinent* is a good book because of its lively and stimulating perspective on many topical aspects of Earth's history. A robust foundation is not, after all, essential for a good book. Proust's masterpiece rested on no more than the smell of a pastry fragment soaked in tea.

References

1. J. T. Wilson, *Proc. Am. Philos. Soc.* **112**, 309 (1968).
2. T. H. Torsvik, *Science* **300**, 1379 (2003).

10.1126/science.1151202

The reviewer is at the Department of Geosciences, SRI, University of Houston, Houston, TX 77204–5503, USA. E-mail: Kevin.Burke@mail.uh.edu

CREDIT: FROM (2)

CLIMATE CHANGE

Climate Assessment: What's Next?

Future international scientific climate change assessments should be faster, more integrated, and more directly linked to policy questions.

Frank Raes[1]* and Rob Swart[2]

The Fourth Assessment Report of the Intergovernmental Panel on Climate Change (IPCC) (*1*) is a milestone for climate-change science and policy. It concludes that global greenhouse gas emissions must peak and decline within the next decade to keep the increase of global mean temperature below limits accepted by some parties. By 2009, there should be an agreement on how to proceed with emission cuts after the Kyoto Protocol's first commitment period ends in 2012. Is the IPCC still sufficiently equipped to support the United Nations Framework Convention on Climate Change (UNFCCC) in directing the required action?

The IPCC is not a UNFCCC body, but the UNFCCC's Subsidiary Body on Scientific and Technical Advice (SBSTA) considers the IPCC a main source of independent information. We believe that comprehensive IPCC reports every 5 to 6 years (which also require additional years to filter through the SBSTA) are not sufficient to adequately inform policy. In addition, key questions are likely to cut across the boundaries of the current Working Group (WG) structure of the IPCC: WG1 deals with the scientific understanding of the climate system, WG2 with climate-change impacts, adaptation, and vulnerability, and WG3 with mitigation of climate change. Topics such as large-scale biofuel use and the regional and global costs of adapting to climate change will require better integration among the natural, economic, and social sciences and, hence, among WGs.

The IPCC could learn from an assessment process that is faster and more integrated and that supports the U.N. Convention on Long-Range Transboundary Air Pollution (UNCLRTAP)(*2*). Both the UNFCCC and the UNCLRTAP went through an initial phase in which science was mainly used to provide the foundation for requesting action by the decision-makers. The UNCLRTAP has moved to the next stage, using science to support the identification and design of policy responses, while the UNFCCC is presently making that transition.

The UNCLRTAP was signed in 1979 after the observation of lake acidification in Scandinavia caused by pollutants emitted elsewhere. The first Sulfur Protocol (1985) involved a flat rate 30% emissions reduction, based on economic and technical feasibility rather than on scientific. However, to justify further emission reductions, a quantitative analysis of the link between emissions and acidification was required, as well as a scientific basis for developing new targets and cost-effective measures.

A policy-oriented research and assessment community was formed around formal working groups, task forces, and centers under the UNCLRTAP, reporting annually to its subsidiary bodies. They developed simplified descriptions of atmospheric transport, ecosystem and health impacts indicators, and information on emission controls, feeding into integrated assessment models. Pragmatically, the number of models and data sources was kept limited. Cutting-edge research was not included, but procedures for review and resolution of disagreement were developed that involved scientists and relevant stakeholders. This extended peer review broadened the quality of the assessments from purely scientific to "fit-for-purpose."

During the 1990s, a parallel community in atmospheric science made advances, but without structural links to policy-making groups. As a consequence, new tools, knowledge, and alternative views were not systematically included for consideration. Now, the gap between those focusing on policy and on basic science has started to shrink. The UNCLRTAP's scientific support bodies are more open to partnering with the scientific community. In particular, the Task Force and Centre for Integrated Assessment Modeling has been key to fostering integration and stakeholder interaction. Simultaneously, basic research programs are increasingly bringing new problems to the attention of policy-makers, such as hemispheric transport of air pollution, and providing a scientific basis for addressing policy questions (*3*).

The IPCC does not have the same relevance to climate policy as do the scientific assessments for air pollution policies. Cross-cutting issues cannot currently be addressed comprehensively and in a timely fashion because of the divided working group structure of the IPCC. A systematic comparison of the costs and benefits of different levels of intervention was tackled outside the IPCC by the Stern review (*4*). However, it lacked global legitimacy, coming from only one country, and did not have the scientific credibility of IPCC's more thoroughly reviewed assessments.

The IPCC procedures already allow for special reports with a 2- to 3-year production cycle. A faster procedure might be achieved by creating a group dedicated to integrated assessment that marries the more immediate policy relevance of the UNCLRTAP scientific bodies with the scientific credibility of the IPCC. It would interact directly with the SBSTA and would address specific issues simultaneously if needed, covering the diverse priorities and concerns of all countries and stakeholders.

Fully comprehensive science updates will still be needed to inform policy, although perhaps less frequently. Here, too, it is possible to learn from other organizations. The Millennium Ecosystems Assessment developed an approach linking different geographical scales. The Technical and Economic Advisory Panel (TEAP) of the Montreal Protocol involves private-sector stakeholders better than the IPCC does.

With the emphasis shifting to response options, the IPCC could collaborate more systematically with international organizations in the area of development, economy, and technology. The scientific community has already organized itself within the Earth System Science Partnership (*5*) to underpin such assessments with the required integrated scientific knowledge.

[1]Institute for Environment and Sustainability, Directorate-General Joint Research Centre, European Commission 21020 Ispra (VA), Italy. [2]MNP (the Netherlands Environmental Assessment Agency), 3720 AH Bilthoven, Netherlands.

*Author for correspondence. E-mail: frank.raes@jrc.it

References and Notes

1. *Climate Change 2007*, Fourth Assessment Report, Working Group reports I to III (IPCC, Cambridge Univ. Press, Cambridge, 2007); www.ipcc.ch/.
2. J. Sliggers, W. Kaakebeeke, *Clearing the Air: 25 Years of the Convention on Long-Range Transboundary Air Pollution* (United Nations, New York, 2004).
3. F. Raes, J. Hjorth, Eds., *Answers to the Urbino Questions: ACCENT's First Policy-Driven Synthesis* (ACCENT Project Office, Urbino, Italy, 2006); www.accent-network.org/portal/publications/accent-series-reports.
4. N. Stern, *The Economics of Climate Change* (Cambridge Univ. Press, Cambridge, 2007).
5. Earth System Science Partnership, www.essp.org.
6. The authors thank two anonymous reviewers; Bert Metz and Rob Maas (MNP) and Terry Keating (U.S. EPA), for comments. The ideas expressed by the authors are not necessarily those of their organizations.

10.1126/science.1147873

THE EARLY YEARS

Preschool Program Improves Cognitive Control

Cognitive control skills important for success in school and life are amenable to improvement in at-risk preschoolers without costly interventions.

Adele Diamond,[1*] W. Steven Barnett,[2] Jessica Thomas,[2] Sarah Munro[1]

Executive functions (EFs), also called cognitive control, are critical for success in school and life. Although EF skills are rarely taught, they can be. The Tools of the Mind (Tools) curriculum improves EFs in preschoolers in regular classrooms with regular teachers at minimal expense. Core EF skills are (i) inhibitory control (resisting habits, temptations, or distractions), (ii) working memory (mentally holding and using information), and (iii) cognitive flexibility (adjusting to change) (*1, 2*).

Significance

EFs are more strongly associated with school readiness than are intelligence quotient (IQ) or entry-level reading or math skills (*3, 4*). Kindergarten teachers rank skills like self-discipline and attentional control as more critical for school readiness than content knowledge (*5*). EFs are important for academic achievement throughout the school years. Working memory and inhibition independently predict math and reading scores in preschool through high school [e.g., (*3, 6, 7*)].

Many children begin school lacking in EF skills (*5*). Teachers receive little instruction in how to improve EF and have preschoolers removed from class for poor self-control at alarming rates (*8, 9*). Previous attempts to improve children's EF have often been costly and of limited success (*10–12*). Poor EFs are associated with such problems as ADHD, teacher burnout, student dropout, drug use, and crime (*2*). Young lower-income children have disproportionately poor EFs (*13, 14*). They fall progressively farther behind in school each year (*15*).

The Study

The opportunity to evaluate Tools of the Mind (Tools) and another curriculum arose when a low-income, urban school district agreed to randomly assign teachers and children to these two curricula. Our study included 18 classrooms initially and added 3 more per condition the next year. Quality standards were set by the state. All classrooms received exactly the same resources and the same amounts of teacher training and support (*2*). Stratified random assignment of teachers and assistants minimized confounds due to teacher characteristics.

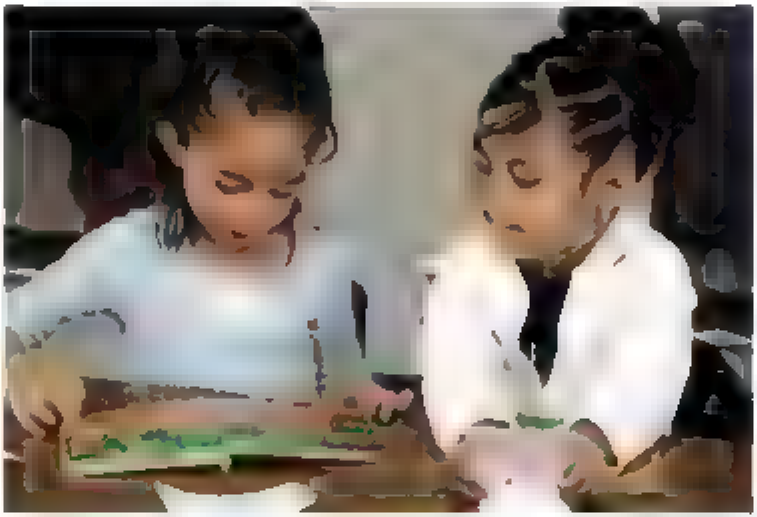

"Buddy reading." Two preschoolers engaged in Tools activity. The ear line-drawing held by one guides her attention (*2*).

EF-training curriculum: Tools. The Tools curriculum (*16*) is based on Vygotsky's insights into EF and its development. Its core is 40 EF-promoting activities, including telling oneself out loud what one should do ("self-regulatory private speech") (*17*), dramatic play (*18*), and aids to facilitate memory and attention (*19*). Tools teachers spent ~80% of each day promoting EF skills. Tools has been refined through 12 years of research in preschools and kindergartens. Only when EFs were challenged and supported by activities throughout the day did gains generalize to new contexts (*2*).

District's version of Balanced Literacy curriculum (dBL). The curriculum developed by the school district was based on balanced literacy and included thematic units. Tools and dBL covered the same academic content, but dBL did not address EF development. [For teacher training and fidelity, see (*2*).]

Participants. Data are reported on 147 preschoolers (62 in dBL and 85 in Tools) in their second year of preschool (average age ≈ 5.1 years in both) who received dBL or Tools for 1 or 2 years. Those who entered in year 2 had attended other preschools for a year. All came from the same neighborhood and were randomly assigned to Tools or dBL with no self-selection into either curriculum. All came from low-income families; 78% with yearly income <$25,000 (*2*).

After year 1, so convinced were educators in one school that Tools children were doing substantially better than dBL children that they halted the experiment in their school, reducing our sample of dBL children.

Measures of EF. Outcome measures (the Dots task and a Flanker task) were quite different from what any child had done before. These measures are appropriate for ages 4 through adults, assess all three EF components, and require prefrontal cortex (*20, 21*). They were administered in May and June of year 2.

In all conditions of the Dots task (*20*), a red heart or flower appeared on the right or left. In the congruent condition, one rule applied ("press on the same side as the heart"). Dots-Incongruent also required remembering a rule ("press on the side opposite the flower") plus it required inhibition of the tendency to respond on the side where the stimulus appeared. In Dots-Mixed, incongruent and congruent trials were intermixed (taxing all three core EFs). Children were given a lot of time to respond [over five times as long as preschoolers usually take (*20*)].

The central stimulus for our Flanker task was a circle or triangle. Memory demands were minimized by a triangle atop the right-hand key and at the bottom right of the screen, with similar aids for the left-hand circle response. The image to focus on was the small shape in the center; the distractor (or flanker) to be ignored was the larger shape surrounding it. Congruent (e.g., ○ inside ○) and incongruent (e.g., △ inside ○) trials were intermixed. Next came "Reverse" Flanker, where children had to focus on the outside shape, inhibiting attention to the inside, plus flexibly switching

[1]Department of Psychiatry, University of British Columbia, Vancouver, BC V6T 2A1, BC Children's Hospital, Vancouver, BC, Canada. [2]National Institute for Early Education Research (NIEER), Rutgers University, New Brunswick, NJ, USA.

*Author for correspondence. E-mail: adele.diamond@ubc.ca

mindsets and attentional focus. The rules were still "press right for Δ and left for ▽." Again, children were encouraged to take their time and not to rush.

Independently, NIEER administered academic measures to Tools children only. These are described in (2).

Results

We report accuracy rather than speed because, for young children, accuracy is the more sensitive measure (23). We conducted multiple regression analyses with age, gender, curriculum and years in curriculum as independent variables. Interaction terms were insignificant and were dropped. On Dots-Congruent, which had minimal EF demands, children performed similarly regardless of curriculum, year in a curriculum, or gender, though older children performed better.

When an inhibition demand was added (Dots-Incongruent), Tools children significantly outperformed dBL children (see the figure, left of above). Dots-Mixed taxed all three EF skills and was too difficult for most dBL children: Almost twice as many Tools as dBL children achieved >75% correct on training trials (see the figure, right of above).

Our Flanker task, like Dots-Incongruent, taxed inhibition (with minimal memory or flexibility demands). Tools children significantly outperformed dBL children (figure above). On Reverse Flanker, dBL children performed near chance (65% correct), but Tools children averaged 84% correct (see figure, above). Thus, the most demanding Dots and Flanker conditions showed the largest effects; those effects are socially significant because they are sizeable.

Tasks that were more demanding of EFs correlated more strongly with standardized academic measures. For example, "Get Ready to Read" scores correlated 0.05, 0.32, and 0.42 with Dots-Congruent, -Incongruent, and -Mixed, respectively (2).

Tools accounted for more variance in EFs than did age or gender and remained significant when we controlled for those. These findings of superior scores by Tools children compared with closely matched peers on objective, neurocognitive EF measures are consistent with teachers' observations (24).

Although play is often thought frivolous, it may be essential. Tools uses mature, dramatic play to help improve EFs. Yet preschools are under pressure to limit play.

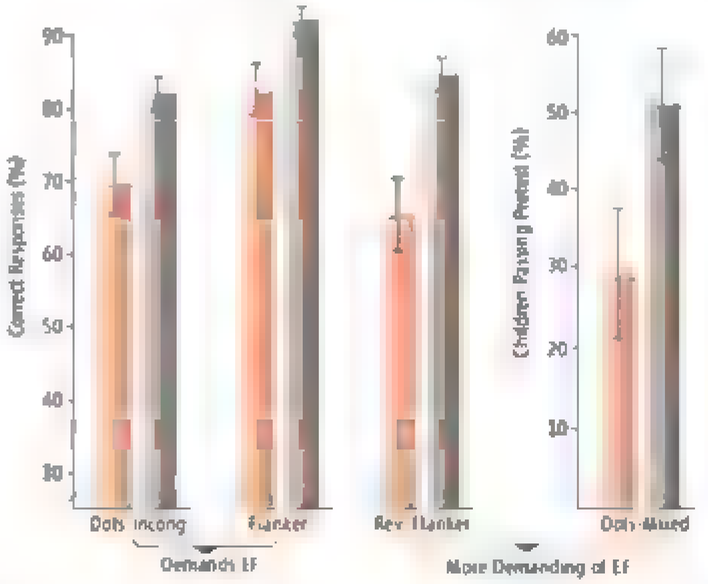

Tools children (blue) performed better on measures of EF than dBL children (red) did. (A) The dependent measure is percentage of correct responses. Dots-Incongruent, Flanker, and Reverse Flanker tasks are described in the text. **(B)** The dependent measure is percentage of children passing the pretest for this task. Statistics are reported in the SOM (2).

If, throughout the school day, EFs are supported and progressively challenged, benefits generalize and transfer to new activities. Daily EF "exercise" appears to enhance EF development much as physical exercise builds bodies (2).

The more EF-demanding the task, the more highly it correlated with academic measures. Superior academic performance has been found for Tools children in other schools and states, with other teachers and comparison curricula (24, 25). EFs [especially self-discipline (inhibition)] predict and account for unique variance in academic outcomes independent of and more robustly than does IQ (2, 3, 26).

Tools successfully moves children with poor EFs to a more optimal state. It is not known how much it would help children who begin with better EFs.

No study is perfect, and ours is no exception. Before and after measures of EFs, as well as academic measures in dBL children, would have strengthened it. Strengths include random assignment and use of objective measures. No authors or testers had a stake in either curriculum. Many competing explanations have been ruled out (2).

Most interventions for at-risk children target consequences of poor EFs rather than seeking prevention, as does Tools. We hypothesize that improving EFs early may have increasing benefits over time and may reduce needs for costly special education, societal costs from unregulated antisocial behavior and the number of diagnoses of EF disorders [e.g., ADHD and conduct disorder (2)].

Conclusions

Some think preschool is too early to try to improve EFs. Yet it can be done. EFs can be improved in 4- to 5-year-olds in regular public school classes with regular teachers. Being in

References and Notes

1. A. Diamond, in *Lifespan Cognition: Mechanisms of Change*, E. Bialystok, F. Craik, Eds. (Oxford Univ. Press, New York, 2006), pp. 70–95.
2. See supporting online material for more information.
3. C. Blair, R. P. Razza, *Child Dev.* **78**, 647 (2007).
4. M. M. McClelland, F. J. Morrison, D. L. Holmes, *Early Child. Res. Q.* **15**, 307 (2000).
5. S. E. Rimm-Kaufman, R. C. Pianta, M. J. Cox, *Early Child. Res. Q.* **15**, 147 (2000).
6. R. Bull, G. Scerif, *Dev. Neuropsychol.* **19**, 273 (2001).
7. S. E. Gathercole, C. Tiffany, J. Briscoe, A. Thorn, ALSPAC team, *J. Child Psychol. Psychiatry* **46**, 598 (2005).
8. T. Lewin, "Research finds a high rate of expulsions in preschool," *New York Times*, 17 May 2005, p. A12.
9. W. S. Gilliam, *Prekindergarteners Left Behind: Expulsion Rates in State Prekindergarten Systems* (Yale Child Studies Center, New Haven, CT, 2005).
10. K. A. Kerns, K. Eso, J. Thompson, *Dev. Neuropsychol.* **16**, 273 (1999).
11. S. M. Dowsett, D. J. Livesey, *Dev. Psychobiol.* **36**, 161 (2000).
12. M. R. Rueda, M. K. Rothbart, B. D. McCandliss, L. Saccomanno, M. I. Posner, *Proc. Natl. Acad. Sci. U.S.A.* **102**, 14931 (2005).
13. K. G. Noble *et al.*, *Dev. Sci.* **10**, 464 (2007).
14. K. G. Noble *et al.*, *Dev. Sci.* **8**, 74 (2005).
15. T. O'Shaughnessy *et al.*, *Remedial Spec. Educ.* **24**, 27 (2003).
16. E. Bodrova, D. J. Leong, *Tools of the Mind: The Vygotskian Approach to Early Childhood Education* (Merrill/Prentice-Hall, New York, ed. 2, 2007).
17. A. R. Luria, in *Reading in the Psychology of Cognition*, R. C. Anderson, D. P. Ausubel, Eds. (Holt, Rinehart and Winston, New York, 1965), pp. 350–363.
18. L. S. Vygotsky, *Soviet Psychol.* **7**, 6 (1967).
19. L. S. Vygotsky, *Mind in Society: The Development of Higher Psychological Processes* (Harvard Press, Cambridge, MA, 1978).
20. M. C. Davidson *et al.*, *Neuropsychologia* **44**, 2037 (2006).
21. M. R. Rueda *et al.*, *Neuropsychologia* **42**, 1029 (2004).
22. S. Durston *et al.*, *Neuroimage* **20**, 2135 (2003).
23. A. Diamond, N. Kirkham, *Psychol. Sci.* **16**, 291 (2005).
24. W. S. Barnett, *et al.*, "Educational effectiveness of the Tools of the Mind curriculum: A randomized trial" (National Institute of Early Education Research, Rutgers University, New Brunswick, NJ, 2006).
25. S. Saifer, paper presented at the 17th Annual Conference of the European Early Childhood Education Research Association, Prague, Czech Republic, 29 August 2007.
26. A. L. Duckworth, M. E. P. Seligman, *Psychol. Sci.* **16**, 939 (2005).

27. This research was made possible by funding to A.D. from HELP (the Human Early Learning Partnership) and National Institute on Drug Abuse (R01 DA19685).

Supporting Online Material
www.sciencemag.org/cgi/content/full/318/5855/1387/DC1

10.1126/science.1151148

GEOCHEMISTRY

The Leaking Mantle

The flow of mantle fluids through Earth's crust reveals fundamental geophysical processes and may help pinpoint sources of geothermal energy.

David R. Hilton

Earth's mantle (the massive silicate shell located between the crust and core) is an important reservoir for volatiles such as water, carbon dioxide, and the noble gases. It combines volatiles captured during Earth's formation with those added later by nuclear reactions or by recycling from the surface. Consequently, mantle-derived volatiles provide a key means to learn about Earth's early history and its continuing evolution (*1*). Although Earth's crustal carapace limits access to the mantle, sampling its volatiles has been pretty straightforward: Researchers target regions where mantle-derived melts (magmas) invade the crust, such as mid-ocean ridges, volcanic arcs, and hot spots. But can volatiles escape the mantle without the help of magma? On page 1433 of this issue, Kennedy and van Soest (*2*) show that the Basin and Range province (which covers much of the southwestern continental United States) is leaking mantle volatiles over a wide area, despite little magmatic activity. Moreover, they propose that the lower crust, usually considered a barrier to volatiles, shows an enhanced permeability caused by the Pacific and North American plates sliding past one another. These observations, and their proposed explanation, have far-reaching implications for the origins of earthquakes and finding new geothermal resources.

Researchers trace mantle volatiles by analyzing the isotopic composition of the lightest noble gas, helium (*3*). Both isotopes, ^3He and ^4He, are produced in the crust at a ratio of ~0.02 R_A (where R_A is the $^3He/^4He$ ratio in air). Higher values indicate the presence of helium from a reservoir enriched in ^3He. The only viable possibility is the mantle, which stores ^3He captured during planetary accretion. Hence, $^3He/^4He$ values between 0.1 and 3 R_A throughout the Basin and Range signify mantle-derived volatiles. What is so unusual about this finding is the lack of magmatic activity in the Basin and Range, except at the westernmost transition to the Cascades magmatic arc. How can mantle volatiles traverse the ductile lower crust and brittle upper crust without melts?

Maps of the deformation dynamics of the western United States may provide the answer (*4*). Plate motion between the Pacific and North American plates drives east-west extension of the Basin and Range province across most of the Central Nevada Seismic Belt (east of 242°E) at rates between 3 and 4 mm year^{-1}. In this region, $^3He/^4He$ ratios define minimum (baseline) values of ~0.1 to 0.2 R_A. West of 242°E, strain rates and corresponding flow velocities increase sharply (up to 13 to 14 mm year^{-1}), their direction changes to the northwest, and baseline $^3He/^4He$ values also increase to as high as 3 R_A. The increase in $^3He/^4He$ values must reflect increased flow of mantle-derived volatiles through the crust. Therefore, the pattern of increasing baseline $^3He/^4He$ values toward the west is tracking the increase in permeability of the crust, including the ductile lower crust and its transition to the source of the high $^3He/^4He$ values: the lithospheric mantle.

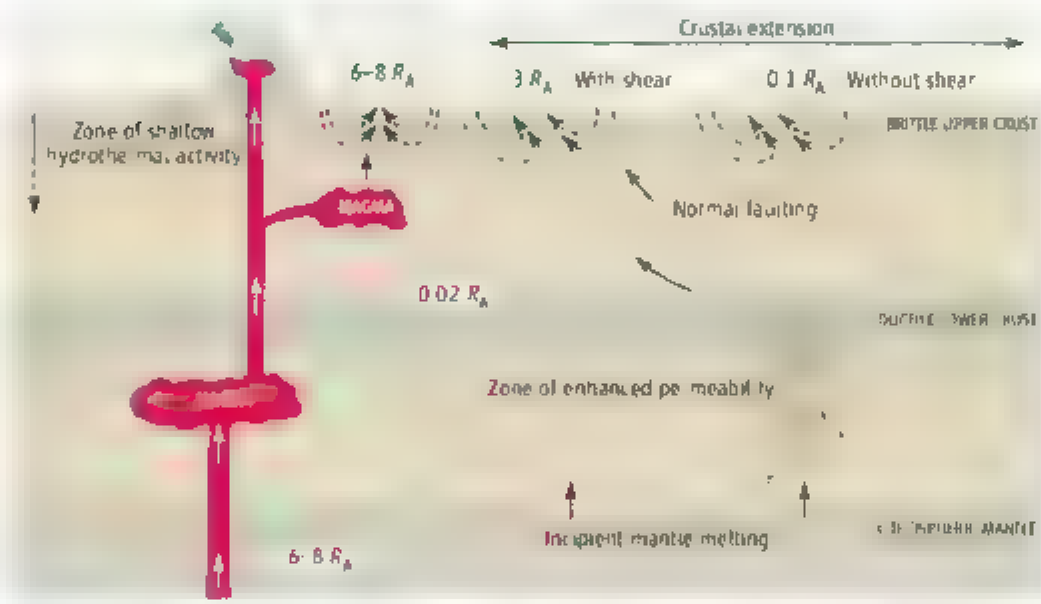

Escape routes. Schematic cross section of continental crust showing escape routes of mantle volatiles to the surface. Zones of enhanced permeability in the ductile lower crust, formed as a result of shear stresses imposed on areas of crustal extension, may provide an additional connection to the mantle to supplement that provided by volcanic and magma-driven hydrothermal activity. Helium isotope ratios are in boxes.

Two ingredients are required to explain this enhanced permeability. First, fractures that can act as conduits for the mantle volatiles must be present. Kennedy and van Soest suggest that the shear force twisting the regional strain to the northwest generates vertical faults that link the brittle upper crust with the ductile lower crust. Extension alone produces normal faults that are refracted to near-horizontal positions at the brittle-ductile transition (see the figure). Second, these pathways must remain open, at least for part of the time, to maintain a connection between the surface and the mantle source of the high $^3He/^4He$ values. Therefore, fluid pressures within the conduits must be extremely high. Continuous connection from the surface to the mantle is not required. Changes in fluid pressure may facilitate growth or sealing of fractures so that the flow could be episodic rather than steady-state.

The realization that helium isotopes can identify zones of enhanced crustal permeability may open new lines of inquiry. For example, Kennedy and van Soest point to $^3He/^4He$ anomalies in the Basin and Range (areas where the $^3He/^4He$ values are much greater than the baseline) as areas of enhanced geothermal potential. They argue that high helium isotope ratios mark localities such as Dixie Valley, Nevada (*5*), as possessing the enhanced crustal permeability and deep fluid production necessary for geothermal energy development. Mapping helium isotope ratios may thus be a valuable tool for finding new geothermal energy sources.

Another prospect concerns earthquakes. Nonvolcanic tremor (quasicontinuous ground vibration) has been detected in southwest Japan (*6*) and beneath the San Andreas Fault (*7*). The former case reflects movement of aqueous fluids through the mantle (*8*); in the latter, such events may reveal the presence of fluids below the seismogenic zone (i.e., brittle upper crust where earthquakes occur) (*7*). The role of deep fluid movement in changing

The author is at the Scripps Institution of Oceanography, La Jolla, CA 92093, USA. E-mail: drhilton@ucsd.edu

stresses in the upper crust and triggering earthquakes remains unclear, yet these two very different tectonic regimes share a common feature: $^3He/^4He$ ratios much higher than expected for regions virtually devoid of mantle melting (8, 9). Looking more closely at the helium isotope characteristics of such regions—spatially and temporally—may provide evidence coupling the leaking mantle to one of our greatest natural hazards.

References

1. R. O. Pepin, D. Porcelli, *Rev. Mineral. Geochem.* **47**, 191 (2002).
2. B. M. Kennedy, M. C. van Soest, *Science* **318**, 1433 (2007).
3. J. E. Lupton, H. Craig, *Earth Planet. Sci. Lett.* **26**, 133 (1975).
4. L. M. Flesch, W. E. Holt, A. J. Haines, B. Shen-Tu, *Science* **287**, 834 (2000).
5. B. M. Kennedy, M. C. van Soest, *Geothermics* **35**, 26 [redacted].
6. K. Obara, *Science* **296**, 1679 (2002).
7. R. M. Nadeau, D. Dolenc, *Science* **307**, 389 (2005); published online 9 December 2004 (10.1126/science.1107142).
8. K. Umeda, G. F. McCrank, A. Ninomiya, *J. Geophys. Res.* **112**, B10206 (2007).
9. B. M. Kennedy *et al.*, *Science* **278**, 1278 (1997).

10.1126/science.1151983

GENETICS

Paradigm for Life

Lateral gene transfer may have spurred microbial evolution, producing a pattern of evolution that resembles a network, rather than a tree.

James O. McInerney and Davide Pisani

It has been known for more than 60 years that prokaryotes can swap their DNA through the processes of conjugation, transformation, and transduction (1). This acquisition of foreign genes is generally referred to as horizontal gene transfer (as opposed to vertical inheritance, in which an organism receives DNA from an ancestor). The consequence is that each prokaryotic chromosome is a mosaic of vertically inherited and horizontally acquired genes (2). On page 1449 of this issue, Sorek *et al.* (3) report the first large-scale empirical analysis of the transferability of genes by analyzing the introduction of almost a quarter of a million genes from other eubacterial and archaebacterial species into the eubacterium *Escherichia coli*. The findings provide insight into the likely evolutionary history of prokaryotes and indicate that interspecies gene transfer is not restricted to special categories of genes, nor are there categories of genes that cannot be transferred.

The role of horizontal gene transfer in evolution has raised fierce debate about the relevance of the Tree of Life, a long-accepted representation of the interrelatedness of living things through evolutionary time, based primarily on the sequence of the genes that encode the small subunit of ribosomal RNA (4). The question is whether this depiction should be replaced with a network, or Web of Life (5) (see the figure). Whereas a tree reflects evolution as a process in which new species arise, or branch, from specific ancestors, a web may more accurately portray microbial evolution based on the rise of variation (and new species) through the lateral transfer of genetic information between distantly related species.

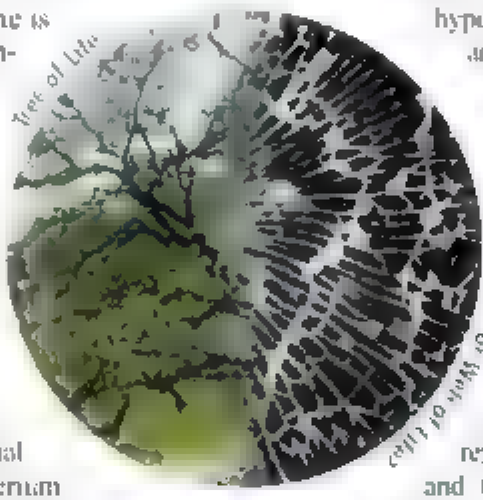

Tree or Web? There is an ongoing debate about whether the genetic relationship of life on the planet should be depicted as a Tree or Web of Life.

Using phylogenetic methods, it has been proposed under the complexity hypothesis that not all genes are equally affected by horizontal gene transfer (6). Two classes of genes have been identified. Informational genes—those involved in DNA replication, transcription, and translation—are part of more complex protein-interaction networks and are thus less likely to be involved in horizontal gene transfer. So-called operational genes—those involved in day-to-day processes of cell maintenance, such as genes that control energy metabolism and the biosynthesis of nucleotides and amino acids—may be more prone to transfer (6). This has led to the notion that a core of nontransferred or rarely transferred genes might have kept track of the clonal history of prokaryotes. If this prediction were true, the Tree of Life hypothesis would hold, even in the presence of rampant horizontal gene transfer (5).

Up to now, a major obstacle to understanding the role of horizontal gene transfer in evolution was the lack of large-scale experimental evidence that might corroborate or reject the existence of a core set of genes. Sorek *et al.* have gone a considerable way in providing data to test this idea. The authors found that among 246,045 genes from 79 different species of prokaryotes, there was no single gene that, along with all its prokaryotic homologs, resisted transfer by way of a plasmid (thus, gene transfer by transduction) into *E. coli*. However, whereas all gene families could be cloned into *E. coli*, some genes were not easily transferred. Members of informational gene families represent a substantial fraction of those resilient to cloning, lending more weight to the complexity hypothesis (6). And even though 1402 genes were impossible to transfer, favoring the existence of core genes, transferable orthologs of these genes were found, thus opposing the core hypothesis.

There are currently almost 6000 accepted prokaryotic species, but the analysis by Sorek *et al.* could only deal with *E. coli*, because adequate data are currently available only for this species. It is possible that if a different host was used, a different set of untransferable genes might have been identified.

Sorek *et al.* also report that genes from prokaryotic genomes enriched in the nucleotide bases guanine (G) and cytosine (C) are more transferable, consistent with the observation that the synonymous usage pattern of codons (triplets of nucleotide bases that encode amino acids) in recently acquired genes in *E. coli* is different from that of native genes (2). The explanation might be that promoter regions (DNA sequences that control the transcription of a gene) in the *E. coli* genome are GC-poor; hence, GC-rich promoters might not work well and would result in nontranscription. It is thought that one of the most important ways to introduce foreign DNA into an organism is by stealth: repressing the expression of the introduced gene until

The authors are in the Department of Biology, National University of Ireland Maynooth, Maynooth, County Kildare, Ireland. E-mail: james.o.mcinerney@nuim.ie

PHOTO CREDIT: JUPITER IMAGES

it is widely distributed in the host species and then allowing expression (7). The stealth model of successful horizontal gene transfer implies that it may be easier to introduce DNA from a distant relative with different nucleotide base composition and different promoter characteristics than from a closer relative. For example, Sorek *et al.* show that γ-proteobacterial genes are more difficult to transfer into *E. coli*, which is itself a γ-proteobacterium. This is consistent with the observation that a well-supported tree seems to exist only toward the tips of the Tree of Life (within bacterial phyla, there is a strong phylogenetic signal associated with vertically inherited genes) (8, 9).

The question now is whether experimentally forced horizontal gene transfer is a fair comparison to that in nature. In the laboratory, cloned genes carried on a plasmid remain in an *E. coli* cell under strong selection conditions for the plasmid (such as antibiotic resistance). In such conditions, only highly deleterious genes would be absent from the set of cloned genes. The nontransferred genes must therefore be a subset of those that would never successfully propagate in *E. coli* in a natural setting.

Many of the forced horizontally transferred genes would never remain in *E. coli* outside the laboratory because they would not be associated with the selection genes used in experimental analyses, such as those that confer antibiotic resistance. Evolutionary biologist W. Ford Doolittle stated that if horizontal gene transfer was not limited to special categories of genes, then no system of classification could be considered natural (5). The results of Sorek *et al.* show that even if some barriers to horizontal gene transfer into *E. coli* exist (they seem to be associated with dosage-toxicity effects), they are rather low. Data on more than one host would answer whether the results are peculiar to *E. coli*.

For now, we know the profile of gene resistance to lateral transfer in one organism, but the existence of a prokaryotic Tree of Life remains an open question. Sorek *et al.* do not address the issue of horizontal transfer and genomic fusions in eukaryotes. However, recent analyses show that eukaryotes have a chimeric nature (9, 10). When eukaryotes are included in our considerations of evolution, the phylogeny of life seems better represented by a network than a tree, making any core genes-based argument in favor of the Tree of Life essentially irrelevant.

References

1. J. Lederberg, E. L. Tatum, *Nature* **158**, 558 (1946).
2. R. A. Welch *et al.*, *Proc. Natl. Acad. Sci. U.S.A.* **99**, 17020 (2002).
3. R. Sorek *et al.*, *Science* **318**, 1449 (2007); published online 18 October 2007 (10.1126/science.1147112).
4. C. R. Woese, G. E. Fox, *Proc. Natl. Acad. Sci. U.S.A.* **74**, 5088 (1977).
5. W. F. Doolittle, *Science* **284**, 2124 (1999).
6. R. Jain, M. C. Rivera, J. A. Lake, *Proc. Natl. Acad. Sci. U.S.A.* **96**, 3801 (1999).
7. M. Doyle *et al.*, *Science* **315**, 251 (2007).
8. C. J. Creevey *et al.*, *Proc. Biol. Sci.* **271**, 2551 (2004).
9. D. Pisani, J. A. Cotton, J. O. McInerney, *Mol. Biol. Evol.* **24**, 1752 (2007).
10. J. A. Lake, *Nature* **446**, 983 (2007).

10.1126/science.1151657

CHEMISTRY

Surface-Conducting Diamond

Experiments reveal the mechanism by which diamond surfaces can become conducting.

Christoph E. Nebel

On page 1424 of this issue, Chakrapani *et al.* (1) prove experimentally that an insulator—diamond—can become a metal by charge transfer from the solid to the liquid (2). A similar type of charge transfer has long been known to occur in solid-solid junctions used in ultrafast transistors (3). The effect should find application, for example, in chemical and biological sensors.

In solid/solid junctions, electrons migrate from the semiconductor with the larger band gap (a band of "forbidden" energies that cannot be occupied by electrons) into the semiconductor with the lower band gap, thereby losing energy and becoming trapped because they cannot climb back over the interfacial barrier. This motion separates the negatively charged electrons from their positively charged donors and is one of the reasons for the ultrahigh mobility of electrons in this two-dimensional system.

Chakrapani *et al.* now prove that a similar phenomenon takes place at the solid/liquid interface, based on the migration of carriers from the solid (diamond) into the liquid (electrolyte). The authors show unambiguously that electrons from diamond transfer into redox electronic states of the electrolyte. This transfer generates a highly conductive surface layer in diamond, which originates from missing electrons (termed "holes").

In 1989, Landstrass and Ravi showed that diamond can be reversibly transformed from insulating to metallic (3). The work attracted much attention and controversy. Two groups developed electrochemical models to explain the observations (4, 5), but both teams focused on water layers adsorbed in the diamond surface. These layers are ill-defined and their electrochemical properties are thus difficult to pin down. Therefore, the electrochemical basis for the observed effect has not been understood until the present work.

The migration (or tunneling) of electrons from diamond into the electrolyte requires that empty electronic states exist in the liquid and that they can be reached without having to cross a substantial energy barrier. In semiconductors, the valence band is filled with electrons and therefore can be considered the main electron source in this process. However, most semiconductors have a valence-band maximum lower in energy than corresponding electrochemical levels (5). To reverse this scenario, a strong electronic surface-dipole layer is required. In the case of diamond, the properties of this dipole layer—and hence the electron affinity of the diamond surface—can be tuned by using hydrogen and oxygen atoms to terminate carbon bonds at the surface (6).

With changing termination from oxygen to hydrogen, the valence-band maximum shifts continuously to higher energies (see the figure). This continuous variation of the surface energy can be used to tune the energetic levels of diamond with respect to redox molecular levels at the solid-liquid interface. It is comparable to the band-gap engineering at the solid-solid interface of semiconductors and will be important for the optimization of bioelectronic devices; diamond is a highly promising material for such devices, because it provides strong bonding to biomolecules like DNA and proteins (7).

The surface conductivity properties generated by this "transfer doping" are interesting, because the holes in diamond are confined to a fairly deep yet very narrow energy well (8, 9). Theoretically, holes can propagate in this

The author is in the Diamond Research Center, National Institute of Advanced Industrial Science and Technology (AIST), Tsukuba 305-8568, Japan. E-mail: christoph.nebel@aist.go.jp

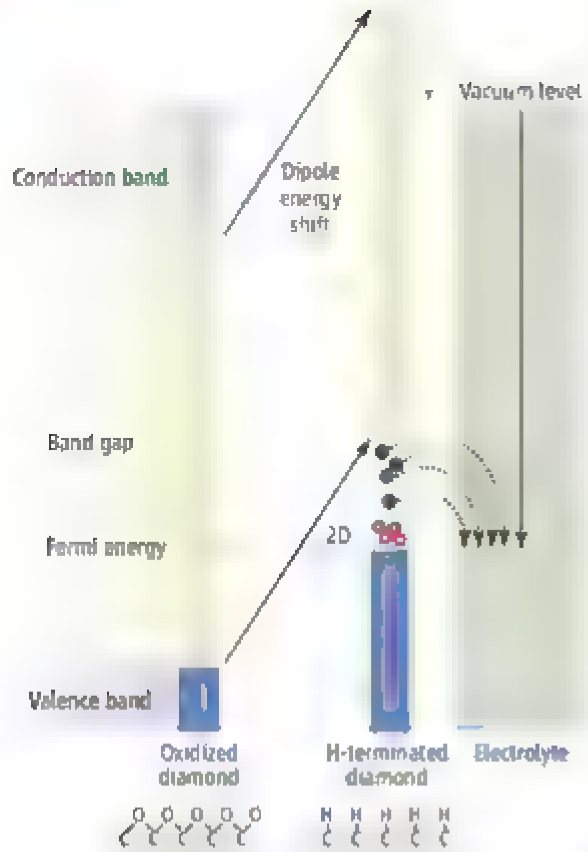

Transfer doping. The energy of valence-band electrons can be increased with respect to the electrolyte by changing the surface coverage from oxygen to hydrogen. As shown experimentally by Chakrapani *et al.*, valence-band electrons transfer into the electrolyte if their energy is above that of electronic states of the electrolyte that can be occupied (Fermi energy, dashed red line). This transfer gives rise to surface conductivity.

well with ultrahigh mobilities, but measured mobilities are orders of magnitude lower than predicted (*10*). The low mobility is a result of the strong, highly efficient scattering in electronic fields that arises from ions in the liquid.

The surface conductivity increases or decreases depending on the detailed properties of the liquid. This effect can thus be used to measure properties of liquids in contact with diamond, for example, using in-plane gate transistor structures in which a hydrogen-terminated diamond surface is the gate of the sensor (*11*). Such devices can detect variations of pH close to the Nernst limit (59 mV pH) and show promise as fast and sensitive chemical and biological sensors (*12*).

Diamond biosensors—based on transfer doping and related effects—are currently developed by an increasing number of research teams for cancer screening, human DNA decoding, and use as ultrasensitive enzyme-protein detectors. The future of such applications will strongly depend on the chemical stability especially of hydrogen-terminated diamond in aqueous environments, where solids like silicon and gold degrade rapidly. However, C-H bonds are chemically more stable than, for example, Si-H bonds, and experiments on DNA-functionalized surfaces of diamond, silicon, and gold have shown that carbon is more stable than all other transducers (*13*).

References

1. V. Chakrapani *et al.*, *Science* **318**, 1424 (2007).
2. H. Ehrenreich, D. Turnbull, in *Solid State Physics*, H. Ehrenreich, D. Turnbull, Eds. (Academic Press, Boston, 1991), vol. 44, pp. 10–16.
3. M. I. Landstrass, K. V. Ravi, *Appl. Phys. Lett.* **55**, 957 (1989).
4. R. S. Gi *et al.*, *Jpn. J. Appl. Phys.* **34**, 5550 (1995).
5. M. Maier, B. Riedel, J. Mantel, J. Ristein, L. Ley, *Phys. Rev. Lett.* **85**, 3472 (2000).
6. J. Ristein, M. Riedel, L. Ley, *J. Electrochem. Soc.* **151**, 1315 (2004).
7. M. Stutzmann, J. A. Garrido, M. Eickhoff, M. S. Brandt, *Phys. Stat. Sol. (a)* **203**, 3424 (2006).
8. C. E. Nebel, B. Rezek, A. Zrenner, *Diamond Relat. Mater.* **13**, 2031 (2004).
9. B. Rezek *et al.*, *Appl. Phys. Lett.* **82**, 2266 (2003).
10. C. E. Nebel *et al.*, *Appl. Phys. Lett.* **79**, 4541 (2001).
11. B. Rezek, D. Shin, H. Watanabe, C. E. Nebel, *Sensors Actuators B* **122**, 596 (2007).
12. C. E. Nebel, B. Rezek, D. Shin, H. Uetsuka, N. Yang, *J. Phys. D Appl. Phys.* **40**, 6443 (2007).
13. W. Yang *et al.*, *Nat. Mater.* **1**, 253 (2002).

10.1126/science.1151314

CHEMISTRY

Metal-Based Therapeutics

Metals and metal complexes can make multiple contributions to drug development, but are not receiving the attention they merit.

Trevor W. Hambley

Metals and metal complexes have played key roles in the development of pharmacy and modern chemotherapy (*1–3*). For example, platinum drugs appear in more chemotherapy regimes than any other class of anticancer agent and have contributed substantially to the successes in treating cancer achieved over the past three decades. The importance of this area and the potential for metals to contribute more widely to the treatment of disease is recognized by the National Institutes of Health Metals in Medicine program (*4*). However, metal-based therapeutics remain a tiny minority of all drugs in the market today.

Several meetings over the past few years—including a recent meeting in Durham (*5*)—have addressed the reasons for the limited development of metal-based therapeutics. A hot topic of debate has been the relative emphasis that should be placed on molecularly targeted metal-based drugs—designed to bind to and inhibit a single molecular target with high specificity—versus new cytotoxics and broad-spectrum agents.

The expectation was that molecularly targeted drugs would have low toxicity and high efficacy, but the results to date have been disappointing. Even those compounds with the best activity—such as the COX-2 class of anti-inflammatories (*6*), matrix metalloproteinase inhibitors (*7*), and the highly successful Glivec used to treat chronic myeloid leukemia (*8*)—have unexpected side effects. Furthermore, many molecularly targeted drugs, such as those designed to inhibit angiogenesis, have measurable benefit only when combined with a cytotoxic or less targeted agent. The number of new substances approved as drugs in 2006 was less than half that of a decade ago, and the number of new chemical entities approved has dropped even more dramatically (*9*), perhaps in part because of the focus on molecular targeting.

Molecular targeting is generally achieved by structure-based design of molecules that bind tightly and selectively to the protein target. To date, these molecules have been constructed from organic fragments. Meggers and colleagues have shown that metal complexes can serve as scaffolds for developing drug molecules that are at least as active and selective as existing drugs at inhibiting protein kinases (*10*). Metal complexes are relatively easy to prepare, and the additional geometric possibilities resulting from the use of six-coordinate

The author is at the Centre for Heavy Metals Research, School of Chemistry, University of Sydney, Sydney, NSW 2006, Australia. E-mail: t.hambley@chem.usyd.edu.au

metal centers (compared to four-coordinate carbon) make this an attractive approach for the rapid development of new species, either as drugs or as probes of the geometric requirements of the active sites. Furthermore, some metals and metal complexes within existing drugs have previously unidentified molecular targets [such as the inhibition of thioredoxin by gold-containing species (*11*)]; this molecular targeting could be optimized based on detailed knowledge of the drug target interaction.

Metals can play an important role in modifying the pharmacological properties of known drugs, most of which can be coordinated to a metal. The resulting "prodrugs" have different physical and pharmacological properties, allowing the drug to be released in a controlled fashion or location. This approach may lead to the "rescue" of drugs that have failed because of poor pharmacology or high toxicity, an approach that has received surprisingly little attention. For example, complexation of nonsteroidal anti-inflammatory drugs to copper overcomes some of the gastric side effects of these drugs (*12*). Release of cytotoxins such as nitrogen mustards from redox-active metals such as cobalt—if achieved mainly in the hypoxic regions of solid tumors—has the potential to improve drug activity and reduce toxicity (see the figure) (*13*).

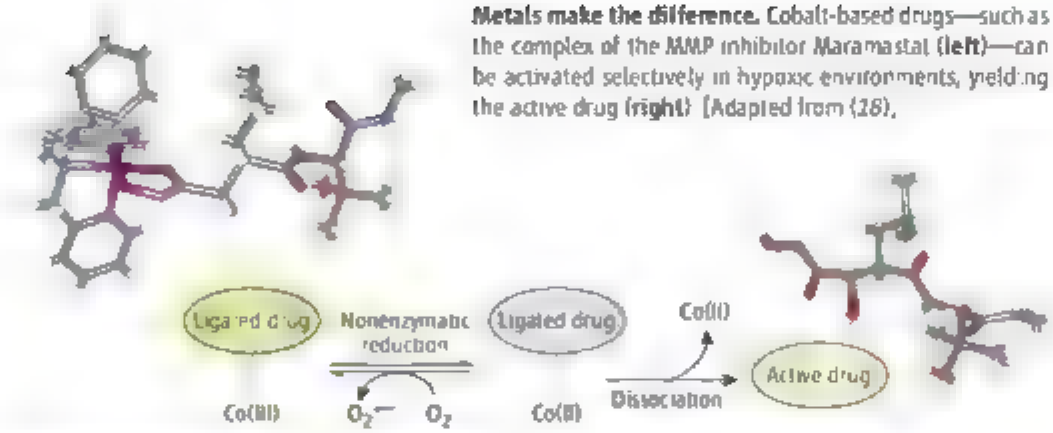

Metals make the difference. Cobalt-based drugs—such as the complex of the MMP inhibitor Maramastat (**left**)—can be activated selectively in hypoxic environments, yielding the active drug (**right**). [Adapted from (*18*).]

Most metal-based anticancer therapeutics are not molecularly targeted but belong to the class of "shotgun" cytotoxics, typified by the platinum drug cisplatin. Because of the focus on molecularly targeted agents, less work has been done on the development of new cytotoxics. Yet, some key developments in cancer chemotherapy in recent years have been the emergence of oxaliplatin (eloxatin) for treating colon cancer and of arsenic trioxide for treating acute myeloid leukemia. The success of oxaliplatin has encouraged a rethink. Two compounds that had been under clinical investigation but were then sidelined (satraplatin and picoplatin) are now in clinical trials; satraplatin is in the late stages of consideration for approval by the U.S. Food and Drug Administration.

Efforts to develop additional platinum-based cytotoxics are focusing on three areas: the largely unmet need for agents that are active in tumors with mutant p53 (*14*), the use of carrier groups to deliver platinum to tumors (*15*, *16*), and the exploitation of unique aspects of the tumor physiology to increase selectivity (*17*). In all these areas, platinum-based drugs can provide insights that are not readily achievable with organic molecules, by virtue of the unique spectroscopic techniques that can be used to determine the location and chemical state of metal ions. Thus, even metal complexes that do not lead to new therapeutics can contribute substantially to the development of the next generation of anticancer drugs, whether they be cytotoxics or molecularly targeted agents.

The history of drug development is dominated by organic and biologically derived molecules; knowledge and expertise in the pharmaceutical industry lie almost entirely in these areas. Successful metal-based therapeutics have nearly all originated from university research and/or small companies. Unless larger pharmaceutical companies develop expertise in these areas, many opportunities for drug development will continue to be lost.

References

1. M. Gielen, E. R. T. Tiekink, Eds., *Metallotherapeutic Drugs and Metal-Based Diagnostic Agents: The Use of Metals in Medicine* (Wiley, Chichester, 2005).
2. J. L. Sessler, S. R. Doctrow, T. J. McMurry, S. J. Lippard, Eds., *Medicinal Inorganic Chemistry* (American Chemical Society, Washington, DC, 2005).
3. K. H. Thompson, C. Orvig, *Science* **300**, 936 (2003).
4. For details on the Metals in Medicine initiative, see www.nigms.nih.gov/Initiatives/metals.html.
5. *Dalton Discussion 10: Applications of Metals in Medicine and Healthcare* (3 to 5 September 2007, Durham University, Durham, U.K.); see www.rsc.org/ConferencesAndEvents/RSCConferences/DD10/index.asp
6. N. M. Davies, F. Jamali, *J. Pharm. Pharmaceut. Sci.* **7**, 332 (2004).
7. D. R. A. Sang et al., *Curr. Top. Med. Chem.* **6**, 289 (2006).
8. E. Hutchinson, *Nat. Rev. Drug Disc.* **5**, 720 (2006).
9. J. Grimley, *Chem. Eng. News* **84**, 17 (4 December 2006).
10. K. S. M. Smalley et al., *Cancer Res.* **67**, 209 (2007).
11. P. J. Barnard, S. J. Berners-Price, *Coordination Chem. Rev.* **251**, 1889 (2007).
12. J. E. Weder et al., *Coord. Chem. Rev.* **232**, 95 (2002).
13. D. C. Ware et al., *J. Chem. Soc. Dalton Trans.* 925 (2000).
14. P. Kabolizadeh, J. Ryan, N. Farrell, *Biochem. Pharmacol.* **73**, 1270 (2007).
15. K. R. Barnes, A. Kutikov, S. J. Lippard, *Chem. Biol.* **11**, 557 (2004).
16. W. H. Ang, I. Khalaila, C. S. Allardyce, L. Juillerat-Jeanneret, P. J. Dyson, *J. Am. Chem. Soc.* **127**, 1382 (2005).
17. T. W. Hambley, *J. Chem. Soc. Dalton Trans.* **2007**, 4929 (2007).
18. T. Failes et al., *Chem. Eur. J.* **13**, 2974 (2007).

10.1126/science.1150504

PHYSICS

Precision Without Entanglement

Jeremy L. O'Brien

A recent experiment shows that exotic quantum processes are not necessary to reach the ultimate limits of measurement.

All science is founded on measurement, and improvements in precision have led not just to more detailed knowledge but also to new fundamental understanding. The quest to realize ever more precise measurements leads one to ask whether the laws of physics impose fundamental limits. This is indeed the case, and it turns out that to reach these firm limits requires the use of quantum mechanical systems (*1*).

Optical phase measurements are used in all fields of science to routinely measure distances smaller than the wavelength of light. The ultimate precision is dictated by the Heisenberg uncertainty principle, which places fundamental limits on measurement. Previously it was thought that quantum entanglement—the exotic cooperative behavior of many quantum systems—is essential in going right to this limit. The problem is that harnessing entanglement in the lab is a real challenge,

The author is at the Centre for Quantum Photonics, H. H. Wills Physics Laboratory and Department of Electrical and Electronic Engineering, University of Bristol, Bristol, BS8 1UB, UK. E-mail: Jeremy.OBrien@bristol.ac.uk

and consequently the Heisenberg limit has been out of reach. Contrary to expectation, Higgins *et al.* (2) have now experimentally shown that the Heisenberg limit can be reached even in the absence of entanglement, and their result paves the way for new kinds of ultrahigh precision measurements.

The basis of optical phase measurements is an interferometer (see the figure). A laser beam is split in two at a beamsplitter (or semitransparent mirror) and then recombined at a second beamsplitter. The wave nature of light means that the two beams interfere at the second beamsplitter. If the path lengths c and d are exactly equal (i.e., phase difference $\phi = 0$), they interfere constructively and all of the light comes out at f; if the path lengths are different by half a wavelength ($\phi = \pi$), they interfere destructively and all of the light comes out at e; and if the path lengths differ by less than half a wavelength, some of the light comes out at e and some at f. By measuring the intensity I_f of light at output f, this path-length difference, or phase shift ϕ, can be measured—as ϕ is varied, I changes sinusoidally with period 2π (see the graph in the figure).

The precision with which we can determine ϕ depends on the slope of I_f. By increasing I, we can increase this slope and so increase the precision without limit. However, in reality the laser intensity is limited and the object causing the phase shift may be damaged or modified by intense light passing through it. The essential question is: With given resources (i.e., energy, as quantified by the number of photons), what is the maximum sensitivity with which we can determine ϕ? If we use a laser pulse with an average of N photons, then the precision $\Delta\phi$ is proportional to $1/\sqrt{N}$, which is known as the shot noise or standard quantum limit (SQL) and is due to quantization of the electromagnetic field and statistical fluctuations in the (classical) light beam. The overarching goal of quantum metrology is to reach the more fundamental Heisenberg limit where $\Delta\phi$ is proportional to $1/N$, which would allow much more precise measurements.

This is where entanglement comes in. Operating the interferometer one photon at a time for N repetitions enables us to measure the phase, but statistical fluctuations limit the precision to the SQL. However, if we prepare the N photons in an entangled state, we can reduce the period by a factor of N, making the slope of the intensity curve greater, and thereby reach the Heisenberg limit. In essence, entanglement makes the oscillations in the curve shown in the figure much closer together, enabling a much more precise measurement.

Observations of this reduction in period has been reported for three (3) and four (4) photons. However, it turns out that a reduced period alone, which can be achieved without quantum mechanics (5), does not guarantee you've reached the Heisenberg limit. Recently, my colleagues and I reported a phase measurement beating the standard quantum limit for four entangled photons (6), and similar results were previously achieved with trapped ions (7, 8). However, entangling hundreds of photons or ions to gain a substantial advantage is an incredibly daunting task, and this obstacle has now been circumvented by Higgins *et al.*

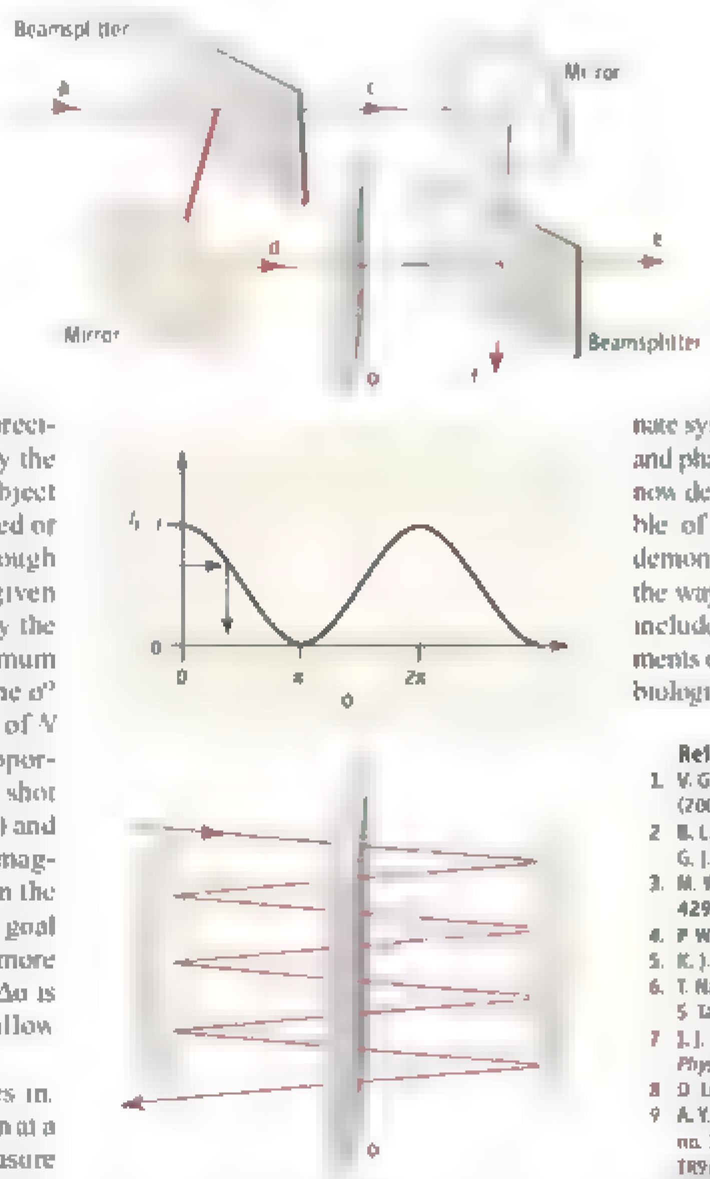

Reaching the limit. (Top) Conventional interferometer and **(middle)** the intensity curve produced by introducing a phase shift ϕ into one arm of the interferometer. **(Bottom)** Higgins *et al.* (2) passed a single photon multiple times through the phase shifter rather than using a single pass of multiple entangled photons.

Higgins *et al.* use a scheme in which single unentangled photons go through the interferometer one at a time but pass through the phase shift either 1, 2, 4, 8, 16, or 32 times, as shown in the figure. Applying the phase shift multiple times on a single photon, rather than putting multiple entangled photons through a single phase shift, allows them to reach the Heisenberg limit.

This improved sensitivity is based on an idea from quantum computing. Kitaev developed a quantum computing circuit that outputs the binary digits for the estimate of a phase one by one (9). With this algorithm, phase estimation can be done using a single photon at a time for sequentially estimating each bit of the phase. In the optical implementation of Higgins *et al.*, these single photons are repeatedly passed through the phase element, with the number of passes determined by which bit of the phase is being estimated. Through a clever "adaptive" strategy that generalizes Kitaev's algorithm to use more than one photon for each bit, they were able to achieve a Heisenberg limited estimate of an optical phase.

Gaining a quantum advantage through multipass protocols was first proposed for aligning coordinate systems (10), clock synchronization (11), and phase estimation (12). Higgins *et al.* have now described the first practical scheme capable of reaching the Heisenberg limit and demonstrated it experimentally. This opens the way to important applications that could include gravity-wave detection, measurements of material properties, and medical and biological sensing.

References

1. V. Giovannetti, S. Lloyd, L. Maccone, *Science* **306**, 1330 (2004).
2. B. L. Higgins, D. W. Berry, S. D. Bartlett, H. M. Wiseman, G. J. Pryde, *Nature* **450**, 393 (2007).
3. M. W. Mitchell, J. S. Lundeen, A. M. Steinberg, *Nature* **429**, 161 (2004).
4. P. Walther *et al.*, *Nature* **429**, 158 (2004).
5. K. J. Resch *et al.*, *Phys. Rev. Lett.* **98**, 223601 (2007).
6. T. Nagata, R. Okamoto, J. L. O'Brien, K. Sasaki, S. Takeuchi, *Science* **316**, 726 (2007).
7. J. J. Bollinger, W. M. Itano, D. J. Wineland, D. J. Heinzen, *Phys. Rev. A* **54**, 4649 (1996).
8. D. Leibfried *et al.*, *Nature* **438**, 639 (2005).
9. A. Y. Kitaev, *Electr. Coll. Comput. Complex.* **1996**, article no. 3 (1996); http://eccc.hpi-web.de/eccc-reports/1996/TR96-003/Paper.pdf
10. T. Rudolph, L. Grover, *Phys. Rev. Lett.* **91**, 217905 (2003).
11. M. de Burgh, S. D. Bartlett, *Phys. Rev. A* **72**, 042301 (2005).
12. V. Giovannetti, S. Lloyd, L. Maccone, *Phys. Rev. Lett.* **96**, 010401 (2006).

10.1126/science.1152581

GENETICS

β-Defensin Repertoire Expands

How does a peptide involved in fighting microbial infections also control hair color in mammals?

Julie R. Dorin and Ian J. Jackson

β-Defensins are antimicrobial peptides of key interest because they operate in both innate and adaptive immune responses in mammals (*1*). Now, these peptides have become more intriguing. On page 1418 of this issue, Candille *et al.* (*2*) identify a role for a β-defensin in pigmentation. The peptide, CBD103, binds to melanocortin 1 receptor, one of a protein family that controls pigmentation, inflammation, and feeding behavior. This expands the functional repertoire of β-defensins and opens new avenues of research with potential implications for human disease (see the figure).

How does a gene implicated in mammalian immune responses alter pigmentation? A mutation at the K^B locus was identified as the cause of dominant inheritance of a black coat in dogs (*3*). Candille *et al.* identify the gene at this locus as *CBD103*, the dog ortholog of human *DEFB103*, which encodes the β-defensin HBD3. The K^B mutation results in loss of the predicted first amino acid of mature CBD103. Mutant CBD103 is more efficiently secreted from cells and has a higher affinity than the wild-type peptide for the dog melanocortin 1 receptor, which controls production of eumelanin, the black/brown hair pigment.

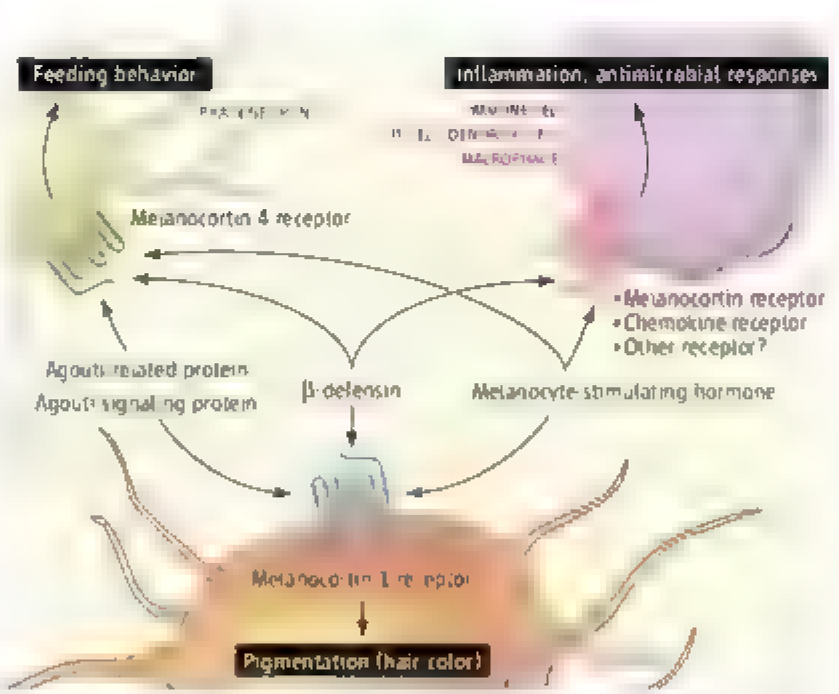

Beyond defense. β-Defensins bind to melanocortin receptors, extending the influence they may have on biological processes.

CBD103 also competes with agouti signaling protein for binding to this receptor. Agouti signaling protein antagonizes the melanocortin 1 receptor, resulting in the production of pheomelanin, a red/yellow pigment. Wild-type and mutant CBD103 suppressed agouti signaling protein in transgenic mice, resulting in black hair rather than agouti (hair with a yellow stripe). A reasonable conclusion is that increased abundance and stronger affinity for the melanocortin 1 receptor allows mutant β-defensin to competitively inhibit agouti signaling protein in melanocytes, enabling the production of eumelanin and black hair.

There is a conundrum, as the β-defensin also competes with α-melanocyte–stimulating hormone (a melanocortin) to bind melanocortin 1 receptor, yet it does not itself elicit adenosine 3′, 5′-monophosphate signaling that characterizes this receptor's activation. So how does this receptor elicit black pigment production in response to CBD103? Perhaps the dog receptor has ligand-independent signaling, as seen in the mouse (but not human), in which lack of α-melanocyte-stimulating hormone has little effect on pigmentation (*4*). Alternatively, CBD103 may activate different effectors through the melanocortin 1 receptor.

Two human β-defensins, HBD1 and HBD3, bind to the melanocortin 1 receptor, but there is little sequence similarity between them (though tertiary structure is conserved) (*1*). There are some structural similarities between agouti signaling protein and β-defensins—both are cationic, with antiparallel β sheets stabilized by cysteine bridges. These properties may be important for receptor interaction.

Although HBD3 is highly expressed and present in inflamed psoriatic skin (*5*), patients do not show hyperpigmentation to indicate melanocortin 1 receptor activation. HBD3 attracts certain immune cells (including monocytes, macrophages, and mast cells) through an as yet unidentified receptor, and immature dendritic cells and memory T cells through chemokine receptor 6 (*1*). HBD3 expression increases in response to proinflammatory agents, and it also induces production of proinflammatory cytokines (*1*). Some melanocortins suppress inflammation (*6*). β-defensins may act at melanocortin receptors to modulate inflammation.

Candille *et al.* also observed that transgenic mice overexpressing the dog β-defensin have lower body weight. It's possible that CBD103 activates the melanocortin 4 receptor, suppressing feeding behavior. Alternatively, reduced body size might reflect peptide toxicity due to overexpression. Determining immune dysfunction in these transgenic mice should tease out the answer.

Does the mutated β-defensin alter host defense? Transgenic mice that overexpress human α-defensin show increased resistance to pathogens (*7*). But the amino-terminal residues of β-defensin are important for antimicrobial action against *Staphylococcus aureus*, a common skin pathogen, so mutant CBD103 could have lost function. In mice, loss of β-defensin 1 reduces clearing of *S. aureus* and *Haemophilus influenzae* (*8*, *9*). The immune phenotype of dogs carrying the mutation warrants investigation. Variation in copy-number and expression of human defensins is seen in normal populations and in patients with Crohn's disease, an inflammatory disorder of the intestinal tract (*10*). Interaction of β-defensins with pleiotropic melanocortin receptors may cause subtle phenotypic changes with direct relevance to human disease.

References

1. M. Pazgier *et al.*, *Cell. Mol. Life Sci.* **63**, 1294 (2006).
2. S. I. Candille *et al.*, *Science* **318**, 1418 (2007); published online 18 October 2007 (10.1126/science.1147880).
3. J. A. Kerns *et al.*, *Mamm. Genome* **15**, 798 (2004).
4. I. J. Jackson *et al.*, *Hum. Mol. Genet.* **16**, 2341 (2007).
5. I. Nomura *et al.*, *J. Immunol.* **171**, 3262 (2003).
6. C. Maaser, K. Kannengiesser, T. Kucharzik, *Ann. N.Y. Acad. Sci.* **1072**, 123 (2006).
7. N. H. Salzman *et al.*, *Nature* **422**, 522 (2003).
8. G. Morrison *et al.*, *Infect. Immun.* **70**, 3053 (2002).
9. E. Moser *et al.*, *Infect. Immun.* **70**, 3068 (2002).
10. K. Fellermann *et al.*, *Am. J. Hum. Genet.* **79**, 439 (2006).

10.1126/science.1151370

The authors are in the MRC Human Genetics Unit, Western General Hospital, Crewe Road, Edinburgh EH4 2XU, UK. E-mail: ian.jackson@hgu.mrc.ac.uk

SCIENCE AND ENVIRONMENT

Abelson Seminar: Searching for Climate Change's "Tipping Points"

Earth's poles are no longer the terra incognita of ancient maps, thanks to unprecedented scrutiny by those tracking the effects of global climate change in these vulnerable areas. But scientists still face unknowns about when and how polar warming will have an irrevocable effect on the rest of the planet, said speakers at the annual Philip Hauge Abelson Advancing Science Seminar.

The population of Adelie penguins in Antarctica has declined sharply.

The researchers gathered at AAAS on 30 October offered several glimpses of the rapidly changing polar regions at which ice sheets crumble, animals like the Antarctic Adelie penguin dwindle in number and the exotic tusked narwhal change their migration patterns, and native communities relinquish their hold on centuries-old cultural and economic traditions.

Humans have enjoyed a relatively stable global climate over the past 10,000 years. But there are abundant signs that this "sweet spot" may be coming to an end, brought on largely by human causes, said keynote speaker Robert W. Corell, director of the Global Change Program for the H. John Heinz Center for Science, Economics and the Environment.

Corell said the troublesome signs—from bark beetles that turn Alaska forests into tinder and shrinking support for ice sheets—are already visible across the polar regions. Once these events occur, "a return to the past looks virtually impossible, at least on the time scales we know," he cautioned.

The "New Horizons in Polar Science" seminar was planned in recognition of the International Polar Year and in honor of Philip Abelson, who served as editor of the journal *Science* for 22 years, and then as senior advisor to AAAS until shortly before his death at the age of 91.

Several of the speakers mentioned personal connections to Abelson, including James G. Anderson, a Harvard University professor of atmospheric chemistry whose father taught Abelson. Anderson's presentation included several maps of a drowned Harvard Square—a likelihood dependent on different models of Greenland ice sheet melting.

Several other speakers presented studies on the human dimension of climate change as one focus of International Polar Year research. Shrinking Arctic sea ice is opening up new possibilities for offshore fishing, shipping lanes, and oil and gas development at the same time that key traditional resources such as caribou herds are disappearing, the scientists noted. But almost nothing is known about "the critical thresholds of adaptability and resilience"—the human tipping points—for Arctic people in a post-warming world, according to research by Norwegian anthropologist Grete K. Hovelsrud of the Center for International Climate and Environmental Research.

As climate studies continue at an urgent pace, the poles have become a laboratory for some unusual experiments probing the unseen in space and on Earth. For instance, the South Pole is one of the best places on the planet to collect data on the infant universe, according to John R. Carlstrom, professor of astronomy and astrophysics at the University of Chicago.

"If you want a better site, you better launch your experimental satellite," Carlstrom said. The dry, cold, and clear atmosphere at his Antarctic telescope station offers a relatively unimpeded look at the cosmic microwave background radiation, the fingerprint of the Big Bang, as well as signs of dark matter and dark energy, he explained.

Nearby on the continent, an international team of neutrino researchers is hard at work on IceCube, a massive "crystal ball" of thousands of detectors dangled two kilometers deep within the ultrapure ice sheet. In the next 10 years, the scientists hope to capture a million of the elusive subatomic particles as they bombard Earth at energies higher than those produced in the laboratory, explained Francis Halzen, a professor of physics at the University of Wisconsin.

In his 1911 expedition journal, British explorer Robert Falcon Scott called the Antarctic's Lake Bonney region "the Valley of the Dead." But modern explorers like John C. Priscu, a professor of ecology at Montana State University, see instead "an oasis of life in a polar desert" below the ice sheet. Priscu said that by using DNA sequencing, he and others have identified a diverse microbial community that may contain "museums of ancient DNA" and a new set of clues to how life evolved on Earth.

AAAS's Chief Executive Officer Alan I. Leshner said the seminar's founder would have been pleased by the cutting-edge polar research. Abelson "had almost no interest in the past," said Leshner, executive publisher of *Science*. "He was a man who was only interested in where science was going."

—*Becky Ham*

INTERNATIONAL

AAAS, Rwandan Leaders Discuss S&T Development

With Rwanda working to address chronic poverty and the legacy of its 1994 genocide, AAAS President David Baltimore met with Rwandan President Paul Kagame to discuss how science-related development and education could contribute to peace and prosperity.

Romain Murenzi, Minister of Science, Technology and Scientific Research; AAAS President David Baltimore; Rwandan President Paul Kagame; and Tom Wang, AAAS director for International Cooperation.

CREDIT: (TOP) JAIME RAMOS/NSF

Lacking natural resources such as oil or minerals, the African nation has an ambitious development plan that aims instead to build a knowledge-based economy. Kagame has

pledged to double research spending from the current 1.6% of gross domestic product to 3% over the next 5 years.

Baltimore visited Rwanda from 10 to 13 October, joined by Tom Wang, AAAS director for International Cooperation, to better understand its S&T capacity and needs. Hosted by Romain Murenzi, Rwanda's minister for Science, Technology, and Scientific Research, they visited education and research institutions and health facilities—and came away deeply impressed with the nation's commitment.

Rwandan leaders see science-related development "as an engine of economic progress and understand that this involves both a widening of scientific literacy and an indigenous research capability," Baltimore said after the visit. "Our hope is that a continuing relationship between Rwanda and AAAS will allow our organization to act as an intermediary between African countries and the skills available within our membership."

During an hour-long meeting, Kagame detailed Rwanda's S&T development and education priorities, noting that building institutions is critical for building capacity. He also discussed energy issues and the importance of partnerships that address development priorities of Rwanda.

Baltimore described AAAS and its interest in the globalization of the science enterprise. He expressed support for Rwanda's efforts and suggested that it also has an opportunity to become a cutting-edge center for primate studies. In addition, he discussed the importance of education in preventing HIV transmission. Baltimore, a molecular biologist and 1975 Nobel laureate, is president emeritus and Robert Andrews Millikan Professor of Biology at the California Institute of Technology.

After the meeting, Murenzi said that Rwandan leaders "look forward to the ongoing support and collaboration with AAAS." His Excellency Paul Kagame and his government "have committed themselves to meeting the challenges of building an economy based on science, technology, and innovation and making Rwanda a sub-Saharan technology hub," he added. "In the words of His Excellency, 'We will continue to invest in our people, and we will strive to open up the frontiers of science, technology and research as we broaden our trade links with our neighboring countries and beyond.'"

Baltimore and Wang met with other senior officials, including Health Minister Jean Damascène Ntawukuliryayo; Minister of State in charge of HIV/AIDS Innocent Nyaruhirira; Kigali Institute of Science and Technology Rector Chrysologue Karangwa; and Kigali Health Institute Rector Desire Ndushabandi, as well as U.S. Ambassador to Rwanda Michael Arietti. The trip received extensive coverage in Rwandan news media.

Most residents of the small, landlocked nation are subsistence farmers, and gross per capita income is less than $1 a day. Rwanda continues to deal with the aftermath of civil war that culminated in genocide in 1994, leaving some 800,000 people dead, mainly ethnic Tutsis as well as politically moderate Hutus. As a result, there remains a significant shortage of educated workers.

Recently, there has been much positive momentum. Between 1995 and 2005, annual economic growth averaged 7.4%, the World Bank says. Both the World Bank and the U.K. Department for International Development are assisting Rwanda's effort to build S&T and education capacity.

"When people hear the word 'Rwanda,' the first thing they think is 'genocide,'" Baltimore said. "What they don't realize is that the country is on a trajectory to go beyond that.... It is very impressive how 13 years later, the leaders have calmed down the passions and are thinking and working very hard for the future of their country."

COMMUNICATION

Science Receives Prince of Asturias Award

The journal *Science* received the 2007 Prince of Asturias Award in Communication and Humanities on 26 October after a week of welcome for the journal and the rest of this year's prize winners in Oviedo, Spain. *Science* shares this year's award with the journal *Nature* for their pivotal roles in communicating scientific research to the international community.

At a grand ceremony held at the Teatro Campoamor de Oviedo and attended by Her Majesty Queen Sofía, *Science* International Managing Editor Andrew Sugden and News Editor Colin Norman accepted the award from His Royal Highness Prince Felipe de Borbón, honorary president of the Foundation and heir to the throne of Spain.

The Foundation, formed in 1980, honors scientific, technical, cultural, social, and humanitarian work carried out internationally by individuals, groups, or organizations, across eight categories.

This year's winners include American musician Bob Dylan, Israeli novelist Amos Oz, and former U.S. Vice President and recent Nobel Peace Prize recipient Al Gore, among others.

"The Prince of Asturias Foundation awards are unusual in honoring such a broad diversity of endeavors, and that's part of what makes them special," Norman said.

"It was a huge honor to be on the same stage as all the other prize winners," said Sugden, who recalled moving speeches from several of the winners and remarks by the Prince at the ceremony "that wove together the various awards in a common and optimistic thread."

At least one connection was recognized by Gore himself, this year's winner of the International Cooperation Award. In his acceptance speech, he acknowledged a "special debt" owed to *Science* and *Nature* for publishing much of the research behind his famed slide show on the effects of global climate change.

Andrew Sugden and Prince Felipe de Borbon

Sugden and Norman attended two formal press conferences and other events associated with the awards in Oviedo, including a discussion of the challenges of scientific publishing at the University of Oviedo library.

"The university itself is celebrating its 400th anniversary this year, and it was a real treat to discuss modern scientific communications in such a historical setting," Norman said.

As part of the award, *Science* received a bronze sculpture—designed by Spanish artist Joan Miró before his death in 1983—and 25,000 euros in prize money, which *Science* will use to make the journal more accessible to non-English speakers, including Spanish speakers. For more information about this year's prize, including a video statement from *Science* Executive Editor Monica Bradford, see www.fundacionprincipedeasturias.org.

Becky Ham

2008 ELECTION

A Call for Nominations

AAAS members may suggest nominees (including themselves) for president-elect and the Board of Directors for election in the fall of 2008. For a list of this year's candidates, see AAAS News and Notes in the 31 August 2007 issue of *Science*; for a list of current Board members, see the masthead page of any recent issue of *Science*.

Please send the suggested nominee's curriculum vitae no later than 30 December to Gretchen Seiler, AAAS Executive Office, 1200 New York Avenue, N.W., Washington, DC, 20005. Suggested nominees will be considered by the AAAS Committee on Nominations at their winter meeting.

CREDIT: IVÁN MARTÍNEZ/FPA

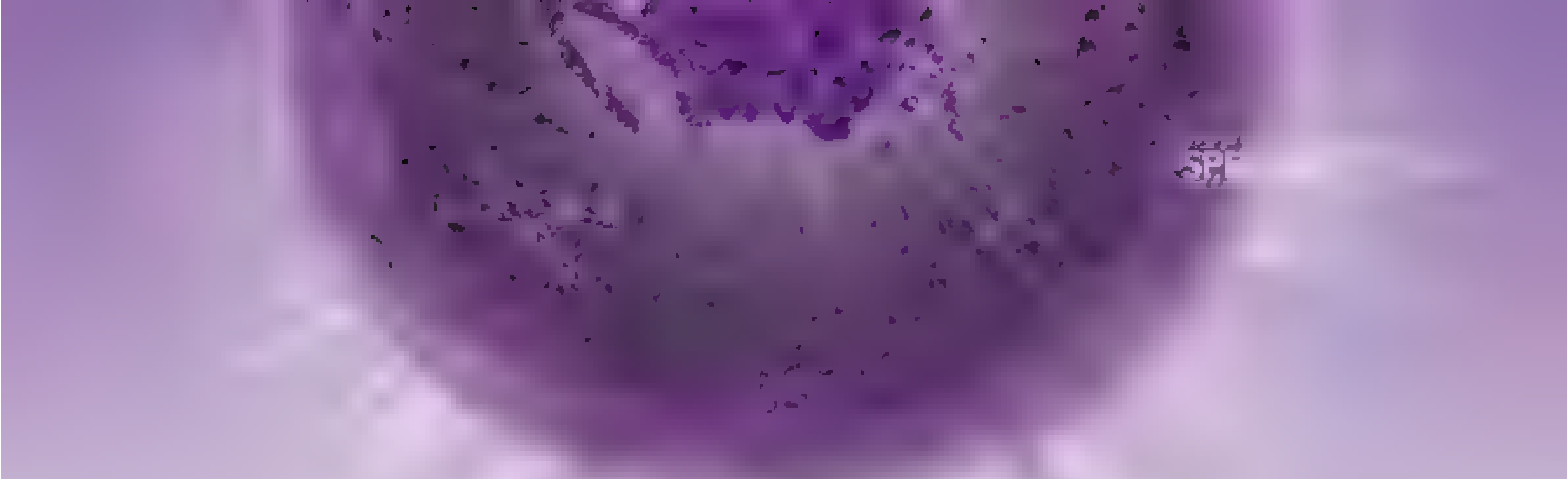

INTRODUCTION

Journey to the Center of the Cell

THE ANIMAL CELL NUCLEUS HOUSES THE GENETIC MATERIAL OF THE ORGANISM and therefore protects and maintains the blueprint for the cell and all its progeny. However, the nucleus is more than a simple repository for chromosomes. A dynamic organelle, the nucleus goes through astonishing transformations during each cell cycle, breaking down completely during mitosis and reforming afresh in each daughter cell after cell division. Within the nucleus, chromosomes are replicated and their DNA is transcribed to provide information that programs the physiology of the cell. Also, ribosomes assemble in the nucleus, then leave and carry out protein translation in the cytoplasm. All of this activity requires complex machineries that can respond to the changing needs of the cell throughout the cell cycle and may vary during development and by cell type.

One of the defining features of the nucleus is its unique architecture. The nucleus is bounded by a nuclear envelope, a double layer of membranes punctuated by nuclear pores, which allow the passage of a huge variety of molecules into and out of the nucleus. The nuclear envelope is contiguous with the endoplasmic reticulum, a membranous labyrinth that provides the entry portal to the secretory pathway. The nuclear envelope is lined with a protein meshwork known as the nuclear lamina, which is composed of lamin proteins related to cytoplasmic intermediate filament proteins. Defects in the nuclear lamina have been linked to progeric diseases.

In this issue, three Reviews examine various aspects of nuclear organization and dynamics. Trinkle-Mulcahy and Lamond (p. 1402) describe how a combination of state-of-the-art proteomics and imaging technologies is contributing to a greater understanding of the dynamics of nuclear function in living cells in real time. Stewart *et al.* (p. 1408) describe how the nuclear envelope influences events within the nucleus and throughout the cell. Terry *et al.* (p. 1412) explain how the bidirectional transport of proteins and nucleic acids through nuclear pores can be regulated at many levels, from individual cargoes to global changes in nuclear pore transport characteristics.

In a News story, Travis (p. 1400) describes how a few researchers are making the case that proteins from the nucleus do double duty as components of a spindle matrix, a controversial structure alleged to help move chromosomes during cell division.

Two Perspectives at *Science*'s Signal Transduction Knowledge Environment (http://www.sciencemag.org/sciext/subnucleus/) highlight mechanisms controlling nuclear transport. Alvarez-Gonzalez describes how poly(ADP-ribosyl)ation of p53 in response to DNA damage interferes with its nuclear export, and Swanson and Kopchick describe how the cytokine receptor GHR may traffic to the nucleus to regulate gene expression.

In the future, it will be important to continue to advance our understanding of how the nucleus interacts with the rest of the cytoplasm throughout the cell cycle and how these interactions program organismal physiology and development.

– STELLA M. HURTLEY AND ELIZABETH PENNISI

CREDIT: CHRIS BICKEL/SCIENCE

The Nucleus

CONTENTS

News

Reviews

See also related online material on page 1343 or at http://www.sciencemag.org/sciext/subnucleus/

Science

The Nucleus

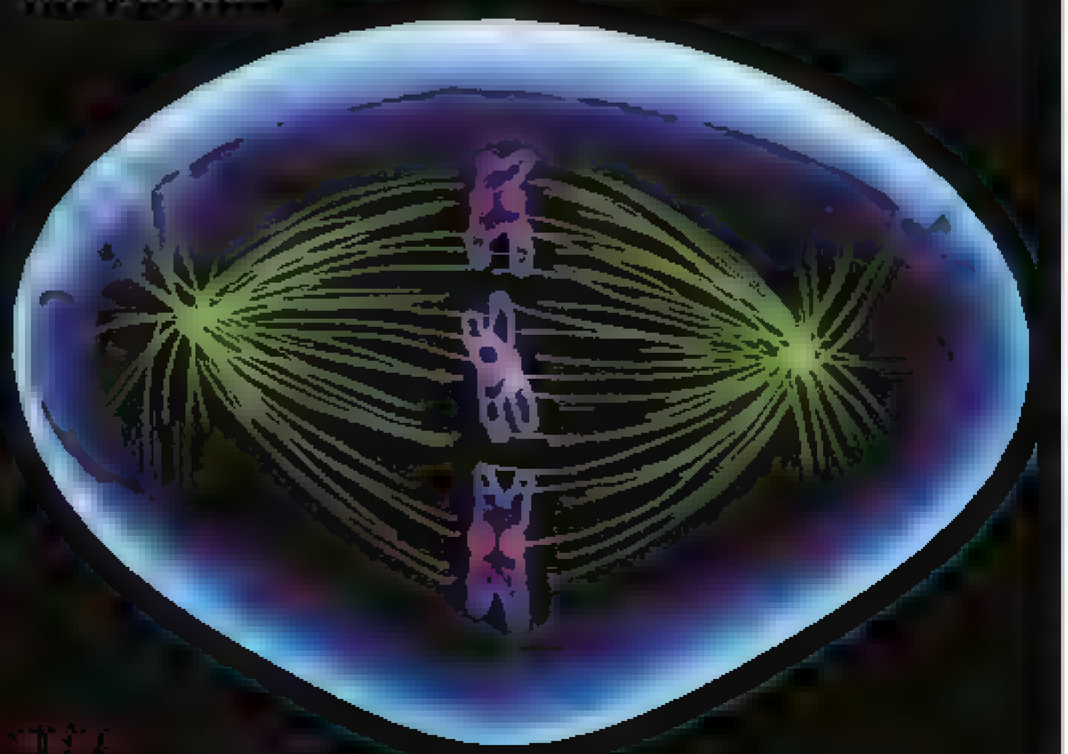

Good alignment. During cell division (artist illustration), the spindle's microtubules (green) line up the chromosomes (blue) before separating them.

Return of the Matrix

A few cell biologists are trying to convince skeptics that they have missed a molecular matrix that helps a dividing cell move its chromosomes around

It's tough to get money to study something that most biologists doubt exists. Kristen Johansen of Iowa State University in Ames learned that firsthand in 1999 when the U.S. National Institutes of Health (NIH) in Bethesda, Maryland, rejected her grant application to investigate a hypothetical cellular structure called the spindle matrix. As one reviewer bluntly put it, recalls Johansen, "'If it existed, it would have already been discovered.'"

The spindle itself is well-known to cell biologists. This array of protein filaments separates a dividing cell's two sets of chromosomes during mitosis, ensuring that each daughter cell has the right DNA. In the 1960s, a few scientists proposed that the spindle required a molecular underlayer—a spindle "matrix"—in order to work. But the idea never took hold, as cell biologists concentrated instead on the spindle filaments that they could observe and manipulate.

Fortunately for Kristen Johansen and Jørgen Johansen, her collaborator and husband, the grant reviewers at the National Science Foundation (NSF) were more open-minded than NIH's about the spindle matrix. Since 2001, NSF has funded the pair as they try to breathe new life into this old idea. So far the Johansens have pinpointed four matrix protein candidates. They are now working with mutant fruit flies to verify that these proteins are important to spindle function. Another researcher has identified at least one more matrix contender through her studies of spindles in a cell-free system. "I don't think anyone rejects [the spindle matrix] out of hand anymore," says Kristen Johansen.

However, because these proteins appear to be pulling double shifts—also having crucial roles in the nucleus of nondividing cells—researchers have had trouble assessing just how important these proteins are to the spindle during cell division. And, says Jonathan Scholey of the University of California, Davis, until these "matrix" proteins are proven to have a role in cell division, he and many other cell biologists will remain skeptical. "It's certainly an interesting topic that merits further research and discussion," he says. "There has been progress, but the jury is still out."

Unexplained forces

The spindle's filaments, known as microtubules, are made of the protein tubulin. After a cell has duplicated its DNA and begun breaking down its nucleus in preparation for dividing, free tubulins polymerize into these filaments, arranging into an oval network. The cell relies on the spindle to segregate the two sets of chromosomes before it can pinch in at the middle to create two distinct cells.

Since the 1920s, cell biologists have produced stunning pictures of spindles. They really started to see spindles in action in the 1970s, when they observed live cells in which the protein tubulin and DNA were lit up with fluorescent markers. Once the spindle forms, chromosomes line up perpendicular to the spindle's main filaments, at the midpoint between the spindle's two ends, or poles. Sites on each chromosome called kinetochores attach to microtubules, which extend out to the poles. The chromosomes then start their march toward the spindle poles.

The spindle images that grace journal covers and textbook pages are so attractive that few cell biologists felt a need to look for something more to explain chromosome segregation, contends Yixian Zheng, a Howard Hughes Medical Institute investigator at the Carnegie Institution for Science in Baltimore, Maryland. "Nothing is as good looking as microtubules and kinetochores," she says.

But what actually moves the chromosomes? Microtubules can lengthen or contract through

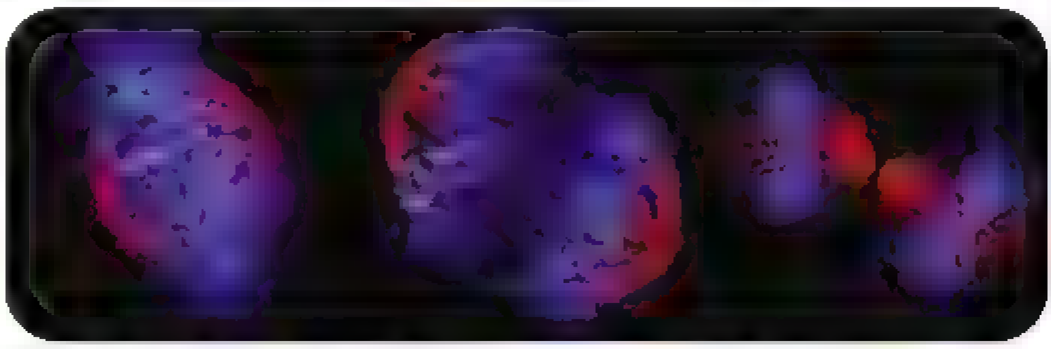

Splitting up. In a dividing cell, spindle filaments (red) first attach to DNA (blue) at chromosome structures called kinetochores (green). Then the spindle somehow moves the DNA apart so that each daughter cell has its own set of chromosomes.

CREDITS (TOP TO BOTTOM): BENEDICT CAMPBELL/WELLCOME IMAGES; LAURA TURNLE AND LAURA HEWELL/WELLCOME IMAGES

the addition or removal of tubulin subunits. At first, researchers thought such changes might move the DNA. If a microtubule anchored at a spindle pole slowly shortened, it could reel in a chromosome. Alternatively, microtubules extending from the cell's middle could push a chromosome out toward the pole as they added more tubulin subunits.

There are also motor proteins such as dynein attached to spindles, suggesting another way to move chromosomes. These molecules utilize a cell's energy to change shape and inch along a substrate. They can transport tethered cargo and may push or pull chromosomes—or microtubules bearing DNA—toward the opposite ends of the cell.

Most mitosis researchers contend that microtubule growth and contraction, perhaps in combination with motor proteins, are all a dividing cell needs to get chromosomes to the right places. But a few cell biologists, chief among them Arthur Forer of York University in Toronto, Canada, and Jeremy Pickett-Heaps of the University of Melbourne, Australia, have long argued that microtubules and motor proteins don't fully explain the movement of chromosomes along a spindle. As evidence, they point to what happens when they use a beam of ultraviolet light to sever spindle microtubules in dividing cells. "You would expect a chromosome to stop moving," says Forer. Yet both the chromosome and the severed microtubules keep sliding toward the cell edge. "It looks like something is pushing them," adds Forer.

For a motor protein to do the pushing, it "has to attach to something," Forer points out. That something, he, Pickett-Heaps, and others argue, is the spindle matrix.

Reasonable doubts

Over the past decade, researchers have proposed various matrix ingredients, but none have yet convinced the skeptics. For example, Timothy J. Mitchison of Harvard Medical School in Boston and his colleagues reported in the 2 December 2004 issue of *Nature* that a polymer composed of sugars and nucleotides was needed to assemble the spindle. But his team has since found no evidence that the polymer is part of a spindle matrix. Mitchison calls himself "agnostic" on the matrix hypothesis.

The Johansens entered the matrix debate in 1996 when an antibody intended for a membrane protein instead bound to chromosomes in the nucleus. During the early stages of mitosis, these proteins left the chromosomes and, before any tubulin had started to form microtubules, created a suspiciously familiar filamentous oval. "It looked like a spindle was forming within the nucleus," recalls Kristen Johansen.

The researchers ultimately identified the tagged nuclear protein, dubbing it skeletor. Since then, they have fished out megator, chromator, and EAST, three other nuclear proteins that, like skeletor, redistribute into a filamentous oval before the spindle itself takes shape. These ovals persist even if a chemical that breaks up microtubules is added to a dividing cell. To the Johansens, these results are suggestive of a nontubulin mesh of molecules that provides a platform upon which the spindle can assemble. The mesh may also offer a substrate for motor proteins to move along.

And this summer, Forer's group, working with the Johansens, reported in the 1 July 2007 *Journal of Cell Science* that a muscle protein called titin appears in many of the same places within a dividing cell as skeletor, megator, chromator, and microtubules. Given that titin's distribution seems to mirror the spindle, Forer considers the protein an excellent candidate to provide musclelike elasticity to a spindle matrix.

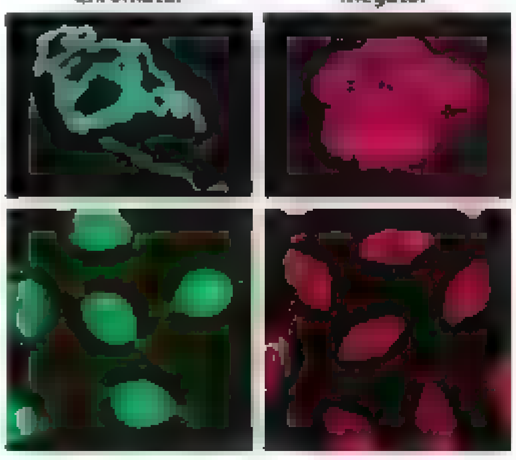

Moonlighting. In nondividing cells, the proteins chromator and megator reside in the nucleus, either on chromosomes (*top, left*) or dispersed (*top, right*). But as cells start to divide, each protein rearranges into an oval spindlelike structure (*bottom*).

CREDIT: K. JOHANSEN

All this is provocative but far from proof that there is a spindle matrix composed of titin, skeletor, or anything else. One problem is that scientists have looked carefully for gene mutations that perturb spindle assembly, shape, or function, and thus far none of the genes for the Johansens' proteins has popped up. "What has been lacking up till now, and what people are clamoring for, is better evidence for a direct role of the matrix in spindle function," acknowledges Kristen Johansen.

That proof isn't easy to come by, she and other spindle-matrix fans stress. Because some of the key proteins have additional jobs in the nucleus—megator is part of the complex that regulates traffic across the nuclear membrane, for example—mutating them or depriving cells of the proteins may simply cause cells to die or have other problems that obscure any spindle defects.

Smoking gun?

Still, in work to be presented at the American Society for Cell Biology meeting in Washington, D.C., next week, the Johansens and their colleagues will describe strains of fruit flies with subtle mutations in chromator's gene. These flies exhibit spindle defects—poorly organized microtubules or improper chromosome segregation, for example—as cells divide. The researchers further show that introducing the normal gene into cells corrects the problems. Finally, they provide evidence that chromator actually binds to microtubules and to a motor protein. "Hopefully, when these experiments are complete, we will be close to having a 'smoking gun,' " says Kristen Johansen.

Zheng has taken another approach in an attempt to sway spindle-matrix skeptics. She adds a protein called RanGTPase to the extracts of frog eggs, which triggers the formation of spindles. With this simplified system, Zheng can concentrate on spindle function alone.

Last year, using this strategy, Zheng and her colleagues added a new name to the list of candidate spindle-matrix proteins: lamin B (*Science*, 31 March 2006, p. 1887). According to Zheng, this filamentous protein looks a bit like the putative matrix proteins studied by the Johansens. It's likewise found in the nucleus, as part of the protein mesh that underlies the nuclear envelope.

Other researchers had shown that when this envelope breaks down at the beginning of mitosis, lamin B disperses and some of it ends up on spindle filaments. Using her egg-extract system, Zheng and her colleagues showed that lamin B is required for spindle creation and forms a matrix that harbors spindle assembly factors.

Zheng is now chasing down other possible spindle-matrix proteins using her system. And she proposes that as a nucleus dissolves for mitosis, many of its components likely become part of the spindle matrix. Still, she knows all too well how unfashionable the spindle matrix remains. Zheng recently lost her NIH funding and decided to downplay mention of her work on the matrix in a recent NIH grant application. "We're not at the tipping point yet," she says.

—JOHN TRAVIS

REVIEW

Toward a High-Resolution View of Nuclear Dynamics

Laura Trinkle-Mulcahy* and Angus I. Lamond

The nucleus is the defining feature of eukaryotic cells. It is a highly dynamic, membrane-bound organelle that encloses chromatin and thereby partitions gene transcription from sites of protein translation in the cytoplasm. Major cellular events, including DNA replication, messenger RNA synthesis and processing, and ribosome subunit biogenesis, take place within the nucleus, resulting in a continuous flux of macromolecules into and out of the nucleus through dedicated nuclear pore complexes in the nuclear envelope. Here, we review the impact of new technologies, especially in areas of fluorescence microscopy and proteomics, which are providing major insights into dynamic processes affecting both structure and function within the nucleus.

All eukaryotic cells enclose their genome within a dedicated organelle termed the nucleus. Nuclear chromatin is the template for two of the cell's major metabolic activities, DNA replication and transcription, necessitating a huge flux of macromolecules into and out of the nucleus. For example, import of histones is required during S phase of the cell cycle to package the newly replicated DNA, and both ribosome subunits and mRNA transcripts must be regularly exported from the nucleus for ribosome assembly and protein translation in the cytoplasm. Nuclear functions can vary at different stages of interphase, while during mitosis, in most eukaryotes, the entire nucleus is disassembled (Fig. 1). This involves chromosome condensation, disassembly of the nuclear lamina and envelope, and complete or partial disassembly of subnuclear bodies such as nucleoli and Cajal bodies.

Despite the importance of nuclear functions and extensive research into many aspects of mechanisms affecting nuclear processes, our understanding of the structure and function of the nucleus is still surprisingly limited. In part this has reflected technological limitations, which have made it difficult to resolve dynamic nuclear events at the cell biological level.

Methodological advances have provided new opportunities to investigate how complex nuclear mechanisms, which have largely been studied in vitro, take place within the context of a living cell. Live cell fluorescence imaging techniques, especially those involving the use of fluorescent protein (FP)-tagged reporters, now allow the localization, dynamic properties, and interactions of proteins and ribonuclear protein (RNP) complexes in the nucleus to be studied quantitatively. Concurrent with this, advances in the sensitivity and time resolution of global approaches, particularly mass spectrometry (MS)-based proteomics, now permit quantitative analyses of complex proteomes and their changes in response to cell growth and perturbations. Importantly, this includes the direct analysis of endogenous proteins and their complex posttranslation modification states.

Here, we highlight recent examples of the application of both imaging and proteomics approaches to uncover mechanisms involved in the dynamic organization of nuclear structure and function throughout the cell cycle. We focus on transcription, replication, and condensation of chromatin and on the regulated assembly and disassembly of nuclear structures during mitosis.

Wellcome Trust Centre for Gene Regulation and Expression, College of Life Sciences, University of Dundee, Dundee DD1 5EH, UK.

*To whom correspondence should be addressed. E-mail: l.trinklemulcahy@dundee.ac.uk

Emerging Technologies: Imaging and Proteomics

Green fluorescent protein (GFP) and its many variants have been major driving forces in enabling the visualization of nuclear structure and function in live cells. There is now an entire "toolbox" of fluorescent proteins with different chromatic and structural properties [reviewed in (1)]. Combinations of chromatic variants can be visualized in the same cell, and specific pairs permit protein-protein interactions to be measured in vivo by fluorescence resonance energy transfer (FRET). In fluorescence complementation, the direct interaction of two proteins, each fused to a nonfluorescent fragment of a fluorophore, is reflected by formation of the intact fluorescent complex (2). Other interesting variants are photoactivatable GFP (paGFP) and similar fluorophores (3). Both GFP and photoactivatable tags, when combined with either laser photobleaching or photoactivation, respectively, allow rates of protein movement within cells to be measured under a wide range of conditions.

A major advantage of fluorescent proteins is that events can be analyzed at the level of a single cell and in the same cell throughout the cell cycle. By fusing FP tags to DNA or RNA binding domains, the movement of specific DNA loci and RNP complexes can be visualized, facilitating the in vivo analysis of gene expression [reviewed in (4, 5)]. A caveat with all FP-tagging techniques, however, is that the presence of the tag can alter the properties and function of the molecule being visualized. Therefore, it is important to control for the effect of the tag in the experiment design and, where possible, validate the results obtained using other methods. An interesting parallel approach developed recently involves "chromobodies," i.e., epitope-recognition fragments of antibody heavy chains fused to fluorophores that can be expressed in living cells and allow live-cell imaging of endogenous proteins (6).

Proteomics. An important goal in characterizing nuclear organization is to identify proteins concentrated on chromatin and in each of the different subnuclear domains, which can guide future functional experiments. The method of choice for such analyses is MS-based proteomics, although non–MS-based techniques have also proved useful.

In the case of the nucleus, proteomic analyses have been performed on purified nucleoli, enriched preparations of interchromatin granule clusters, nuclear envelope and pore complexes, and various purified chromatin and chromosome fractions (7–10). A major limitation, however, is that the resulting "static" proteome provides an averaged view, which does not take into account dynamic changes in the protein composition of an organelle or structure, either at different cell cycle stages or in response to specific stimuli. Furthermore, this first-generation proteome does not distinguish between proteins that are predominantly located within a specific structure, and other components, which are only present in low amounts and/or transiently under specific conditions.

Detailed information concerning the dynamic properties of nuclear structures can be obtained with quantitative techniques such as stable isotope labeling of amino acids in cell culture (SILAC) and isotope tagging for relative and absolute protein quantitation (iTRAQ) [reviewed in (11)]. These techniques are based on differential isotope labeling of proteins from cells under two or more different experimental conditions, which allows quantitation of the relative amounts of protein found in each condition. This provides for a "second generation" proteomics approach, which couples protein identification with a quantitative annotation of protein properties, including dynamics, turnover, and interaction partners. For example, isotope labeling in combination with MS has been used to determine the flux of proteins through nucleoli and to measure the turnover rates of many nucleolar proteins (7, 12), while a combination of SILAC-based quantitative proteomics with immunoprecipitation revealed differences in binding partners for two different isotopes of the same nuclear protein phosphatase, PP1 (13). In addition, these methods permit dynamic assessment of changes in the

posttranslational modification state of proteins under a wide range of conditions (*14*).

The sensitivity of proteomics has not yet reached the point where measurements can be performed at the single-cell level. However, it is already possible to combine the advantages of high-throughput proteomics in studying endogenous, untagged proteins in cell populations with the advantages of studying FP-tagged proteins at the single-cell level using fluorescence microscopy. These complementary techniques can be applied in parallel, providing a "dual strategy" with which to analyze the same biological process (Fig. 2). This allows a direct comparison of the behavior of FP-tagged and endogenous forms of the same protein in stable cell lines, which determines if the tagged protein is a valid reporter for the behavior of the endogenous form.

An alternative to proteomics is to adopt a function-based approach, where gene expression is knocked down using RNA interference (RNAi) libraries and cells screened for phenotypes affecting either a specific process or structure of interest. For example, large-scale RNAi screens have been performed to identify mammalian proteins involved in chromosome condensation and apoptosis (*15*). There is considerable scope in the future for applying a combination of RNAi and proteomics to identify proteins required for a range of nuclear activities.

Functional Studies on the Nucleus

Within the nucleus, DNA is highly packaged through its association with histone proteins to form nucleosomes, which in turn are further compacted into higher-order structures [reviewed in (*16*)]. This chromatin complex is important both for controlling the compaction of chromosomes and for regulating access to specific DNA sequences during gene transcription and DNA replication. Both global and localized changes in structure are driven, at least in part, by posttranslational modifications, including methylation and acetylation of specific histone residues. Modification of the DNA itself, such as base methylation of cytosine residues, is also important and is involved in the epigenetic marking of gene loci.

The condensation state of chromatin, which can vary regionally in chromosomes during interphase, changes dramatically at the onset of mitosis when all chromosomes become highly condensed to facilitate accurate segregation to daughter cells. There is still debate over what mechanisms are primarily responsible for the condensation of chromatin, because detailed results from in vitro studies have not correlated completely with in vivo results [reviewed in (*16*)]. For example, although topoisomerase II and the condensin complexes are absolutely required for mitotic chromosome condensation in vitro, pronounced condensation occurs in vivo even after knockdown or genetic knockout of these proteins, although segregation defects are observed. It has been suggested that their primary effect may be on chromosome stability or architecture or that redundant mechanisms exist. The debate has also raised the important issue of how to measure chromatin condensation accurately. To improve upon subjective measurements based on visual inspection of microscopy images, new approaches have been developed, including measurement of changes in the volume and density of chromatin with fluorescent probes (*17*).

Dynamic studies of transcription and replication have been enabled by the development of a method for visualizing specific DNA sequences, involving a tandem array of lac operator binding sites integrated into the genome and detected by the binding of FP-tagged lac repressor fusion proteins (*18*). This system has been used successfully

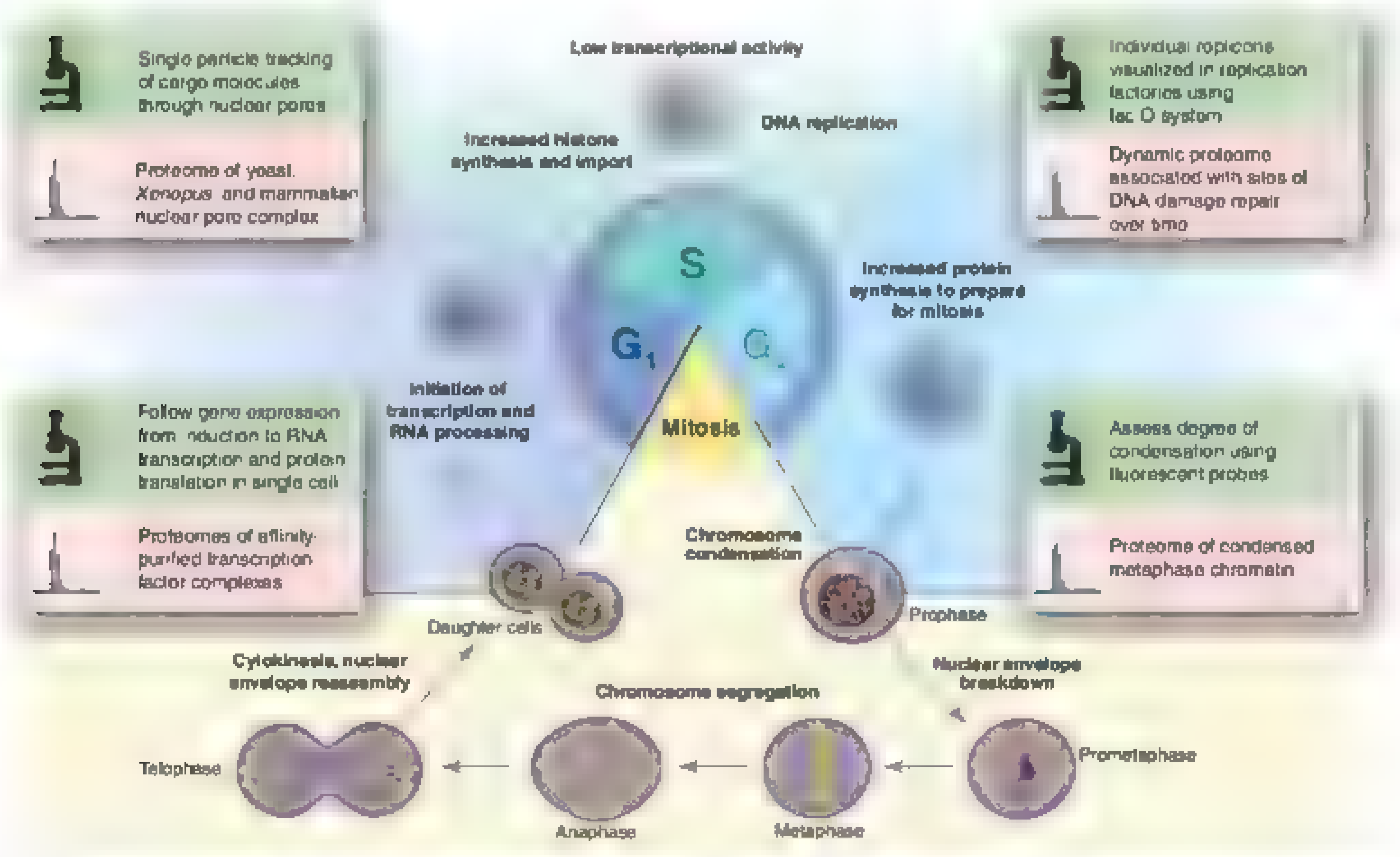

Fig. 1. Dynamic nuclear events. The cell cycle is divided broadly into interphase and mitosis, with cell growth and duplication of chromosomes occurring during interphase and segregation of chromosomes into two new daughter cells occurring during mitosis. Interphase is further divided into three distinct stages—G_1, S, and G_2—with specific functions carried out at each stage and advancement to the next stage dependent on proper progression and completion of the previous one. Recent uses of imaging (green) and proteomics (pink) techniques to study specific nuclear events are highlighted.

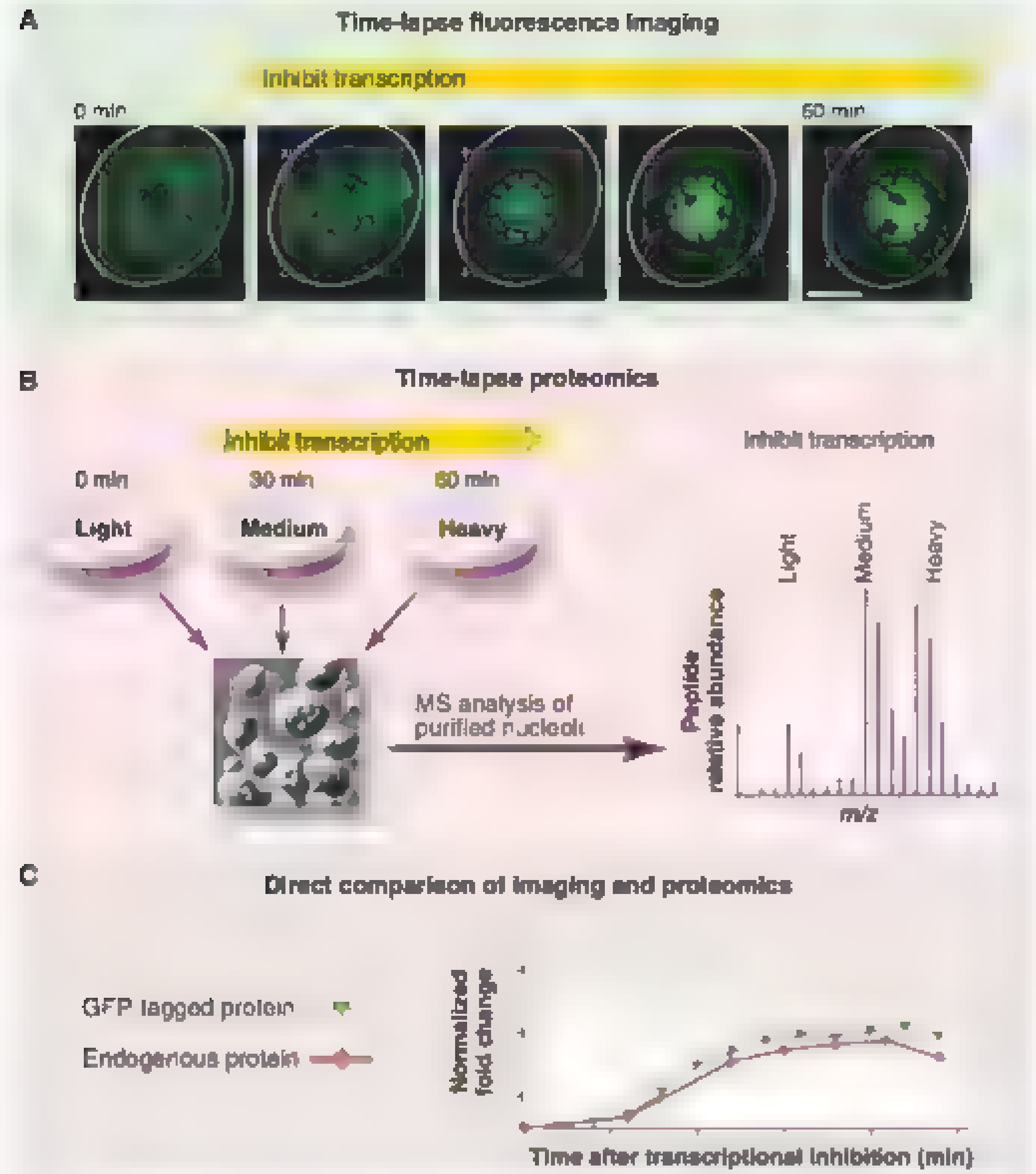

Fig. 2. Dual-strategy imaging and proteomics approach. Fluorescence imaging and MS-based proteomics are complementary methods, which can be used together in a "dual strategy." Time-lapse fluorescent imaging of an FP-tagged protein in a single cell nucleus (**A**) (ellipse) is used here to quantitate the fluorescence intensity within the nucleolus (hashed circle) over time, following inhibition of transcription. The results correlate with time-lapse proteomics data (**B**), in which the relative abundance of the endogenous protein within purified nucleoli was determined by metabolic labeling of cell populations at different time points following transcriptional inhibition. Cells were labeled either with light (^{12}C), medium (^{13}C/^{4}D), or heavy (^{13}C/^{15}N) isotopes of arginine and lysine, respectively, which cause a measurable shift in the mass of peptides containing these amino acids. When combined for purification of nucleoli and MS analysis, the changing proteome of the nucleolus following transcriptional inhibition is determined by calculating isotopic arginine and lysine ratios for each protein identified. Thus, the increase in fluorescence intensity of the FP-tagged protein within the nucleolus upon inhibition of transcription matches the increase in relative abundance of the endogenous protein within purified nucleoli [plotted together in (**C**)].

in a range of organisms from *Escherichia coli* to eukaryotes and was adapted to analyze quantitatively the kinetics of gene transcription by RNA polymerase II (Pol II) in live mammalian cells (*19*) (Fig. 3A). Using a combination of photobleaching and photoactivation coupled with mathematical modeling, single-cell kinetic measurements were made of promoter binding, initiation, and elongation events. This shows that single-cell analysis of gene expression is already feasible. Further improvement in the sensitivity of detection of fluorescent signals should facilitate characterization of smaller arrays, or even single-copy genes, allowing more gene templates to be analyzed at the single-cell level.

The study of individual DNA replicons in *Saccharomyces cerevisiae* replication factories was also made possible with the lac operon system (*20*). By combining quantitative fluorescence imaging of lac operon- and tet operon-tagged gene loci with an independent label for replication sites, i.e., DNA polymerase, the increase in fluorescence that accompanies duplication of the inserted arrays could be monitored relative to the site of replication. Time-lapse imaging of these two separate foci supports the idea that sister replication forks generated from the same origin remain associated within a replication factory while the DNA moves through it. A related concept of a "transcription factory," in which RNA Pol II remains tethered while the transcribed genes move through, has also been proposed [reviewed in (*21*)].

Chromatin also shows dynamic, localized changes in response to different forms of DNA damage, as factors are recruited to identify and repair the resulting lesions. The dynamic association of repair proteins with chromatin following DNA damage events has been analyzed in vivo with time-lapse fluorescence imaging and photobleaching techniques (*22*). Using a combination of lac and tet operator arrays detected by the binding of their respective FP-tagged repressors, the movement of individual double-strand chromosome breaks was analyzed in live mammalian cells after DNA damage (*23*). The resulting broken ends do not move extensively within the nucleus, and this immobilization requires the DNA-end binding protein Ku80. In addition, ends resulting from double-strand breaks preferentially undergo translocations with other chromosomes in their local vicinity. The DNA repair process has also been analyzed by measuring the increased mobility of chromatin marked by paGFP-tagged histone H2B at sites undergoing DNA damage repair (*24*). The results were consistent with a local change in the condensation state of chromatin, facilitating access of repair factors to sites of damage.

A quantitative proteomics approach based on stable-isotope labeling and affinity purification was used to characterize protein complexes associating with chromatin containing a tagged form of the histone variant H2AX, which is phosphorylated at sites of double-strand DNA breaks (*25*). Through comparison of irradiated and nonirradiated cells, specific proteins were found to leave damaged regions of chromatin, while known repair factors transiently accumulated at H2AX sites, indicating that the H2AX chromatin complex undergoes dynamic changes after DNA damage and resulting DNA repair.

In most cases, the large-scale proteomic analysis of specific DNA-associated protein complexes has proven to be a technically difficult task, albeit an essential one for characterizing active genes and the mechanisms of their activation or repression. Chromatin immunoprecipitation techniques have helped to localize proteins to specific genes and can be combined with MS-based proteomics to identify both the DNA binding site(s) for a tagged protein and its associated protein binding partners [reviewed in (*26*)].

It has proven difficult to isolate transcription factories and to extract engaged RNA Pol II

complexes in native form. However, purification and MS analysis of tandem affinity protein-tagged RNA Pol II holoenzyme complexes identified a minimum stable complex of both known and novel proteins (27). The absence of certain expected proteins, such as elongation factors, likely highlights the technical difficulties in isolating intact protein complexes from relatively insoluble chromatin fractions. Recently, a method based on in vivo biotinylation tagging was used to identify transcription and chromatin remodeling factors associated with the essential hematopoietic transcription factor GATA-1 (28). A proteomics approach has also been used to identify the protein components of the Mediator complex, which links transcriptional activators with the general transcriptional machinery. It was shown that a common core of proteins is shared by alternate forms of the complex that differentially associate with components of the transcription machinery (29).

Major changes are expected in the composition of chromatin-associated proteins during mitosis, and thus mitosis-specific chromatin proteins may have roles in either maintaining or regulating the unique condensed state that occurs during chromosome segregation. Proteomics methods have been used to identify proteins associated with mitotic chromatin and to map protein interactions and posttranslational modifications in mitotic kinases, anaphase-promoting complex, centrosomes, and kinetochores [reviewed in (10)]. MS analysis of histone-depleted mitotic chromosomes identified several novel chromosome-associated proteins, including borealin, a component of the chromosomal passenger protein complex. Borealin helps target this essential regulatory complex, which includes aurora B kinase, INCENP and survivin, to centromeres and the central spindle during mitosis (30).

Nucleoli and nuclear bodies. Many nuclear factors involved in events such as DNA replication, transcription, RNA processing, and ribosome subunit biogenesis are organized in spatially distinct nuclear domains. These domains include chromosome territories, interchromatin granule clusters, nucleoli, and assorted nuclear bodies. Although many of the mechanisms controlling the formation, organization, and movement of these domains remain unclear, live-cell experiments with FP-tagged fusion proteins suggest that the interaction of many factors with these domains is highly dynamic (31).

FP-tagging and time-lapse imaging strategies have identified protein-trafficking pathways within the nucleus. The use of heterokaryon formation to distinguish between newly assembled and mature components showed that two major classes of nuclear RNPs, i.e., small nucleolar RNAs (snoRNAs) and small nuclear RNAs (snRNAs) complexed with specific proteins, initially concentrate in nuclear domains distinct from their final sites of function. Maturation of both splicing snRNPs and nucleolar snoRNPs and movement to their respective sites of function in nucleoplasmic splicing and ribosomal RNA (rRNA) modification was shown to involve a transient localization in Cajal bodies [reviewed in (32)]. More recently, this has been extended to include a role for the nuclear export factor CRM1 in the directed nuclear movement of both snRNPs and snoRNPs (33, 34).

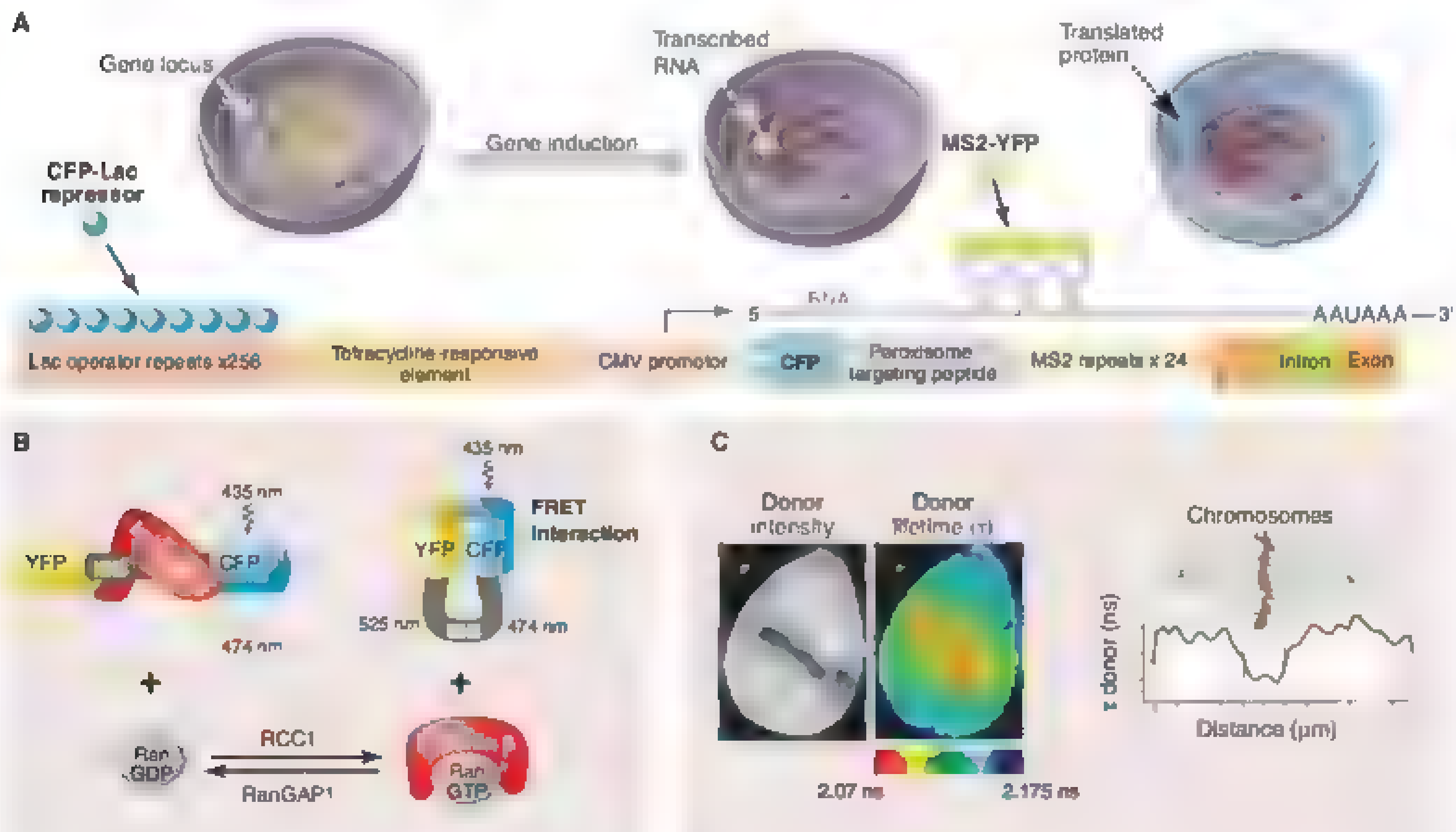

Fig. 3. Fluorescent probes for cellular mechanisms. **(A)** Plasmid used to visualize and quantitatively assess the kinetics of gene expression. The gene locus is marked by cotransfected CFP-lac repressor binding to multiple lac operon repeats, whereas cotransfected MS2-YFP binds transcribed RNA. The translated CFP fusion protein targets to cytoplasmic peroxisomes. **(B)** The biosensor Rango, used to monitor changes in RanGTP/GDP gradients in cells, consists of an importin β binding domain (IBB) flanked by CFP and YFP. Binding of importin β to Rango sterically hinders the FRET interaction between CFP and YFP. Where levels of RanGTP are high, release of importin β relieves this steric hindrance, and FRET can occur. This is observed as a decrease in the fluorescence lifetime of CFP. **(C)** A gradient of fluorescence lifetime is observed for the Rango probe in a metaphase mammalian cell, with shorter lifetimes (red) around chromosomes indicating FRET/free Rango and hence a high level of RanGTP, which is maintained by chromatin-bound RCC1.

Upon entry into mitosis, most nuclear bodies partially or fully disassemble, and nuclear functions such as transcription and pre-mRNA processing shut down. These processes, and reassembly of nuclear complexes and domains at the end of mitosis, have been studied by time-lapse imaging of FP-tagged proteins, including analysis of the sequential entry of components of the gene expression machinery, i.e., RNA Pol II subunits and pre-mRNA processing factors, into daughter nuclei after nuclear envelope (NE) formation (35). The initiation-competent form of RNA Pol II and general transcription factors are imported first, with pre-mRNA splicing factors recruited only after transcription is initiated. This suggests that a mechanism, most likely at the level of nuclear import, exists to coordinate transcription and pre-mRNA splicing during the transition from telophase to the establishment of the interphase nucleus.

The best-studied nuclear body is the nucleolus, which forms around the tandemly repeated clusters of ribosomal DNA and is the site of rRNA transcription, processing, and ribosome subunit assembly [reviewed in (36)]. Quantitative kinetic analysis of the breakdown and reassembly of the nucleolus with FP-tagged proteins demonstrated that disassembly starts before the onset of NE breakdown with the loss of RNA Pol I subunits from the fibrillar centers (37). These subunits, originally believed to remain associated with nucleolar organizing regions (NORs) throughout mitosis, were shown to transiently leave NORs during metaphase. Dissociation of proteins from the remaining nucleolar subcompartments occurred at a faster rate and was coincident with NE breakdown. Reassembly of nucleoli also followed a defined temporal sequence, although not necessarily in the same order, as the proteins were imported into newly formed nuclei. Time-lapse FRET analysis between FP-tagged nucleolar proteins has extended such live-cell imaging experiments to include information about protein-protein interactions during nucleolar reformation (38). Both early and late rRNA processing factors pass through the same prenucleolar bodies, and during translocation of these factors, interactions between protein partners from the same rRNA processing machinery can occur and may even induce formation of prenucleolar bodies.

Although proteomics studies have been carried out on various nuclear protein complexes and enriched fractions of interchromatin granule clusters (8), nucleoli have proven the most amenable of the nuclear bodies to biochemical purification and detailed proteomic analysis to define their protein composition in both mammalian and plant cells. Nucleoli have also been used to develop the "time-lapse proteomics" strategy, in which, using the SILAC isotope-labeling procedure, changes in the relative levels of nucleolar proteins were systematically evaluated by repeated proteomic analysis at multiple time points after treatment of cells with inhibitors affecting either transcription, proteasome activity, or specific kinases (7). Pulse labeling with heavy isotopes has also been used to characterize the different turnover rates of nucleolar proteins (12). These studies in the nucleolus have provided the first global characterization of the flux of proteins through a cellular organelle. It will clearly be important in the future to apply similar approaches to study other nuclear bodies and defined complexes.

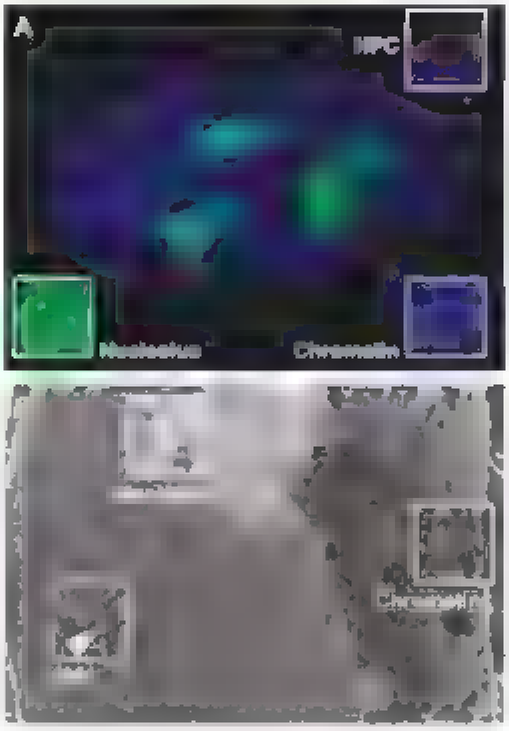

Fig. 4. Visualization of nuclear structures. (A) Conventional wide-field fluorescence micrograph of a paraformaldehyde-fixed HeLa cell stained with markers for the NPC (red), nucleolus (green), and chromatin (blue). A resolution limit of 200 nm is imposed by the wavelength of visible light. **(B)** Field-emission scanning electron micrograph of a dry fractured HeLa cell, which permits spatial resolution of structures within 3 to 5 nm. The fracture exposed NPCs (arrowhead), which are clearly visible on the surface of the nucleus, while a fracture across the surface exposes the chromatin within the nucleus. The paler, brighter circular area at the top center is a result of the increased backscatter electron signal from the dense nucleolar region.

Nuclear envelope and transport. The NE and associated nuclear pore complexes (NPCs) provide a barrier between the genome and the cytoplasm and play a major role in controlling entry and exit of the wide range of molecules that must continually move between these cellular compartments [reviewed in (39)]. In addition to regulating nucleocytoplasmic exchange, the NE has also been linked to control of both signaling and mitotic progression [reviewed in (40)].

Recent advances in imaging and single particle tracking have been applied to study cargo transport, permitting visualization of single molecules interacting with NPCs. Cargo molecules were shown to randomly diffuse within a NPC, exiting as a result of a single rate-limiting step (41). The small guanosine triphosphatase (GTPase) Ran plays a central role in the transport mechanism and is also required during mitosis when the NE is no longer present. The common feature is that Ran signals the location of chromatin within the cell through establishment of a gradient in the relative levels of RanGTP:GDP, with a higher RanGTP:GDP ratio occurring in the vicinity of chromatin as Ran interacts with the chromatin-bound GTP exchange factor RCC1. Away from chromatin, hydrolysis of GTP bound to Ran is stimulated by a Ran GTPase activating protein (RanGAP). This gradient defines the directionality of nucleocytoplasmic transport during interphase, is required for the correct formation of bipolar mitotic spindles during mitosis (42), and defines the sites where NE and nuclear re-formation will occur at the end of telophase. FRET probes have been used to visualize the RanGTP:GDP gradient in both cell-free systems and in live mammalian cells (42, 43). As shown in Fig. 3, B and C, an importin β binding domain flanked by cyan (CFP) and yellow fluorescent protein (YFP) on opposite ends provides an elegant visual readout that indirectly reflects the relative level of RanGTP by monitoring the RanGTP-dependent cargo release from importin β at different sites within the cell. This convenient assay for monitoring changes in the Ran GTP/GDP gradient upon specific perturbations has been used to probe the contribution of Ran to transport and chromosome segregation mechanisms (42).

In most eukaryotes, chromosome segregation during mitosis occurs in the absence of a defined nuclear structure. Thus, an open mitosis is characterized by the breakdown of the NE and associated structures before association of condensed chromosomes with the spindle and their subsequent segregation during anaphase. NE breakdown is a complex process involving disassembly of the underlying nuclear lamina, tearing apart of the membranous NE, and disassembly of the NPCs (44). Advanced fluorescence and electron microscopy techniques have been applied to visualize NPC disassembly and membrane fenestration. In starfish embryos, NPCs were seen to expand and likely contribute to tearing of the membrane (45), while in *Xenopus* the NPCs were dismantled and the pore closed before membrane rupturing (46). These apparently conflicting results could be attributable either to differences between species or to technical limitations. Many details of the mechanisms involved in NPC assembly also remain to be characterized. NPCs were recently shown to form de novo from both sides of the NE in pre-assembled *Xenopus* nuclei (47), supporting the view that once assembled, an NPC remains stable throughout interphase, with

little or no exchange of nucleoporins (Nups) between separate NPCs.

Considerable work has also been aimed at identifying the detailed protein composition of NPCs in yeast, *Xenopus*, and mammals. Combinations of biochemical fractionation and subtractive proteomics have produced the current inventory of Nups, which includes ~30 proteins, a subset of which share phenylalanine-glycine (FG) repeat domains that bind transport factors and coordinate active transport through the NPC [reviewed in (9)]. The proteomics data on NPCs have in turn facilitated large-scale imaging studies aimed at localizing Nups within the NPC by both fluorescence and immunoelectron microscopy, examining FRET interactions between Nup pairs to build a network map of Nup-Nup interactions (48), and assessing the effects of RNAi knockdown of various Nups on NPC formation and integrity [reviewed in (49)]. Through the use of photobleaching analysis of GFP-tagged Nups to compare residence times, the dynamic organization of the NPC was also mapped (44). Nups known to localize to central parts of the NPC were more stable, whereas peripheral components were more dynamic, consistent with their having primarily structural and regulatory roles, respectively. Taken together, these studies demonstrate the complementary contributions of proteomics and imaging approaches to the study of the NE and NPCs.

Conclusion

Both proteomics and imaging technologies have contributed to the recent progress in analyzing dynamic events connected with nuclear structure and function. Proteomics, for example, is rapidly moving away from the simple generation of lists of proteins toward providing quantitative annotation of protein properties, including intracellular distributions, concentrations, turnover dynamics, interaction partners, and posttranslational modifications. As the sensitivity continues to improve, it may yet be possible to reach the goal of performing proteomics studies on material from a single cell. With the major emphasis shifting toward quantitation and the analysis of protein dynamics, proteomics is rapidly evolving into a mainstream research tool for cell biology.

Fluorescence imaging technology also continues to improve, both in sensitivity and resolution. Improvements in instrumentation have brought us closer to bridging the gap between the 1- to 5-nm resolution of electron microscopy and the 200-nm resolution of light microscopy (Fig. 4). With techniques such as stimulated emission depletion (STED) and photoactivated localization microscopy subdiffraction-limit imaging by stochastic optical reconstruction microscopy (PALM STORM) that exploit reversibly saturable or photoswitchable transitions of fluorescent probes, a resolution of ~20 nm has been achieved with light microscopy (50). Higher-resolution imaging will also drive the further development of techniques exploiting the unique properties of GFP and related fluorophores.

Currently, a major roadblock for the proteomic study of nuclear bodies and complexes is the difficulty in isolating enough pure and intact material for analysis. Progress in this area is likely to come both from improvements in fractionation methods and also from further advances in MS technology that will allow proteomic analysis of complexes isolated from smaller numbers of cells. One promising approach is the development of protein correlation profiling (51), which does not rely on absolute purity of the structure or organelle of interest. In this technique, cell lysates are fractionated by density gradient centrifugation and analyzed by liquid chromatography-based MS. Organelle localization is assigned by comparing the ion intensity profiles (based on peptide mass and elution time from the column) of peptides from an unknown protein to those of known marker proteins for particular organelles across the separated fractions.

Another important future goal for proteomics studies is detailed mapping of posttranslational modifications. A large-scale nuclear phosphoproteome has already been mapped (45), and SILAC can be used to quantify, in parallel, thousands of changes in phosphorylation sites in response to a cellular perturbation (46). Other global proteomics studies are addressing the significance and mechanism of complex posttranslational modifications that occur on DNA-associated proteins in addition to phosphorylation, including methylation, ADP-ribosylation, ubiquitination, and acetylation [reviewed in (52)].

A major goal of proteomics now is to quantitate protein abundance, dynamics, modifications, and interactions at the single-cell level. A parallel goal of imaging is time-lapse fluorescence microscopy of living cells with a sensitivity sufficient to detect single molecules and a resolution approximating that of electron microscopy. Improvements in mathematical modeling may also allow a detailed quantitative understanding of specific steps in the mechanism of nuclear events to be derived and analyzed at the single-cell level.

References and Notes

1. B. N. Giepmans, S. R. Adams, M. H. Ellisman, R. Y. Tsien, *Science* **312**, 217 (2006).
2. T. K. Kerppola, *Nat. Rev. Mol. Cell Biol.* **7**, 449 (2006).
3. K. A. Lukyanov, D. M. Chudakov, S. Lukyanov, V. V. Verkhusha, *Nat. Rev. Mol. Cell Biol.* **6**, 885 (2005).
4. Y. Shav-Tal, X. Darzacq, R. H. Singer, *EMBO J.* **25**, 3469 (2006).
5. S. Tyagi, *Nat. Methods* **4**, 391 (2007).
6. U. Rothbauer et al., *Nat. Methods* **3**, 887 (2006).
7. J. S. Andersen et al., *Nature* **433**, 77 (2005).
8. M. Saitoh et al., *Mol. Biol. Cell* **15**, 3876 (2004).
9. E. C. Schirmer, L. Gerace, *Trends Biochem. Sci.* **30**, 551 (2005).
10. V. Archambault, *Expert Rev. Proteomics* **2**, 615 (2005).
11. J. S. Andersen, M. Mann, *EMBO Rep.* **7**, 874 (2006).
12. Y. W. Lam, A. I. Lamond, M. Mann, J. S. Andersen, *Curr. Biol.* **17**, 749 (2007).
13. L. Trinkle-Mulcahy et al., *J. Cell Biol.* **172**, 679 (2006).
14. J. Dengjel et al., *Nat. Biotechnol.* **25**, 566 (2007).
15. B. Neumann et al., *Nat. Methods* **3**, 385 (2006).
16. A. S. Belmont, *Curr. Opin. Cell Biol.* **18**, 632 (2006).
17. F. Mora-Bermudez, J. Ellenberg, *Methods* **41**, 158 (2007).
18. A. S. Belmont, *Trends Cell Biol.* **11**, 250 (2001).
19. X. Darzacq, *Nat. Struct. Biol.* **9**, 796 (2007).
20. E. Kitamura, J. J. Blow, T. U. Tanaka, *Cell* **125**, 1297 (2006).
21. D. A. Jackson, *Brief. Funct. Genomic. Proteomic.* **4**, 143 (2005).
22. M. J. Mone et al., *Proc. Natl. Acad. Sci. U.S.A.* **101**, 15933 (2004).
23. E. Soutoglou et al., *Nat. Cell Biol.* **9**, 675 (2007).
24. M. J. Kruhlak et al., *J. Cell Biol.* **172**, 823 (2006).
25. Y. C. Du et al., *Mol. Cell. Proteomics* **5**, 1033 (2006).
26. X. Le Guezennec et al., *BJU Int.* **96**, 16 (2005).
27. C. Jeronimo et al., *Mol. Cell. Biol.* **24**, 7043 (2004).
28. P. Rodriguez et al., *Methods Mol. Biol.* **338**, 305 (2006).
29. A. C. Paoletti et al., *Proc. Natl. Acad. Sci. U.S.A.* **103**, 18928 (2006).
30. R. Gassmann et al., *J. Cell Biol.* **164**, 179 (2004).
31. T. Misteli, *Science* **291**, 843 (2001).
32. A. I. Lamond, J. E. Sleeman, *Curr. Biol.* **13**, R825 (2003).
33. S. Boulon et al., *Mol. Cell* **16**, 777 (2004).
34. J. Sleeman, *J. Cell Sci.* **120**, 1540 (2007).
35. K. V. Prasanth, P. A. Sacco-Bubulya, S. G. Prasanth, D. L. Spector, *Mol. Biol. Cell* **14**, 1043 (2003).
36. F. M. Boisvert, S. van Koningsbruggen, J. Navascues, A. I. Lamond, *Nat. Rev. Mol. Cell Biol.* **8**, 574 (2007).
37. A. K. Leung et al., *J. Cell Biol.* **166**, 787 (2004).
38. M. Angelier et al., *Mol. Biol. Cell* **16**, 2862 (2005).
39. L. J. Terry, E. B. Shows, S. R. Wente, *Science* **318**, 1412 (2007).
40. C. L. Stewart, K. J. Roux, B. Burke, *Science* **318**, 1408 (2007).
41. W. Yang, S. M. Musser, *Methods* **39**, 316 (2006).
42. P. Kalab, A. Pralle, E. Y. Isacoff, R. Heald, K. Weis, *Nature* **440**, 697 (2006).
43. P. Kalab, K. Weis, R. Heald, *Science* **295**, 2452 (2002).
44. G. Rabut, V. Doye, J. Ellenberg, *Nat. Cell Biol.* **6**, 1114 (2004).
45. S. A. Beausoleil et al., *Proc. Natl. Acad. Sci. U.S.A.* **101**, 12130 (2004).
46. J. V. Olsen et al., *Cell* **127**, 635 (2006).
47. M. A. D'Angelo, D. J. Anderson, E. Richard, M. W. Hetzer, *Science* **312**, 440 (2006).
48. M. Damelin, P. A. Silver, *Biophys. J.* **83**, 3626 (2002).
49. B. Fahrenkrog, J. Koser, U. Aebi, *Trends Biochem. Sci.* **29**, 175 (2004).
50. S. W. Hell, *Science* **316**, 1153 (2007).
51. L. J. Foster et al., *Cell* **125**, 187 (2006).
52. S. L. Berger, *Nature* **447**, 407 (2007).

53. We thank K. Weis, P. Kalab, and T. Allen for providing images and help in preparing figures, and also members of the Lamond laboratory for their critical reading of this manuscript. Regrettably, owing to space limitations, we were unable to include all recent examples of the elegant uses of imaging and proteomics techniques to probe dynamic nuclear events. A.I.L. is a Wellcome Trust Principal Research Fellow.

10.1126/science.1142033

REVIEW

Blurring the Boundary: The Nuclear Envelope Extends Its Reach

Colin L. Stewart,[1] Kyle J. Roux,[2] Brian Burke[2]*

The past decade has seen a complete rethinking of the traditional view of the nuclear envelope as simply a passive enclosure for the chromosomes. The convergence of several lines of clinical and basic research has revealed additional roles in both signaling and mitotic progression. It is becoming apparent that the nuclear envelope defines not only nuclear organization but also that of the cytoskeleton and, in this way, integrates both nuclear and cytoplasmic architecture.

The nuclear envelope (NE) represents the interface between the nucleus and cytoplasm and is essential in maintaining the unique identity of each compartment (*1*). To perform this role, the NE contains channels (the nuclear pores) capable of mediating selective exchange of macromolecules. In fact, the NE displays the properties of a molecular sieve. Small molecules, corresponding to globular proteins of less than ~40 kD, may pass across the NE relatively unimpeded. Larger molecules, however, need to display specific signals to enter or exit the nucleus (*2*).

The NE is composed of several elements (Fig. 1), the most prominent of which are inner and outer nuclear membranes (INM and ONM). These are separated by the perinuclear space (PNS), a regular gap of 30 to 50 nm. Annular junctions between the INM and ONM form channels or pores that traverse the NE (*3*). These channels are occupied by nuclear pore complexes (NPCs). Each NPC, of which there are several thousand in vertebrate somatic cells, contains multiple copies of ~30-protein subunits or nucleoporins (Nups) and weighs in at more than 60 megadaltons (MD). Although NPCs were first recognized in the 1960s (*4*), their suggested role as mediators of nucleocytoplasmic transport was finally definitively demonstrated 20 years later (*5*).

Despite their continuities, the nuclear membranes are biochemically distinct. The INM contains a unique array of integral membrane proteins (*6*, *7*), whereas the ONM shares many of its functions with the peripheral endoplasmic reticulum (ER), to which it has multiple connections. Thus the ER, ONM, and INM represent discrete domains within a single membrane system, with the PNS being an extension of the ER lumen.

The final feature of the NE is the nuclear lamina (*8*). In vertebrate somatic cells, this is a 10- to 20-nm-thick protein meshwork associated with the nuclear face of the INM and is primarily composed of A- and B-type lamins. These are members of the intermediate filament (IF) family and, as do all IF proteins, feature a coiled coil flanked by nonhelical head and tail domains. In *Xenopus* oocytes, the lamina consists of a network of IF-like filaments (*9*). However, the generality of this organization is uncertain, because the oocyte contains only a single major lamin species, whereas somatic cells can contain up to five. This issue is more than just academic because lamin defects are linked to several human diseases (see below).

The standard view of the NE has been that its functions are largely passive: as a selectively permeable container for the genome and as a bystander that needs to be moved out of the way during mitosis. Recent developments, however, reveal that the NE plays far more active roles throughout the cell cycle. The recognition that certain diseases are linked to defects in both lamins and INM proteins has highlighted an essential purpose for the NE in defining interphase nuclear architecture. Related studies reveal that the NE also functions as a signaling node with an active role in mechanotransduction. Moreover, changes in nuclear lamina organization lead to altered cytoplasmic mechanics. The implication is that the NE integrates both nuclear and cytoplasmic architecture by providing a dynamic link between nuclear components and the cytoskeleton.

Mitotic Events

During the "open" mitosis of higher cells, the NE undergoes major structural reorganization (*10*). Because the mitotic spindle is assembled in the cytoplasm, the NE must be partially or completely disassembled, a process that is mediated by phosphorylation of multiple NE components. NE disassembly, in this way, permits spindle microtubules to gain access to the mitotic chromosomes. On completion of chromatid segregation, all of the disassembled

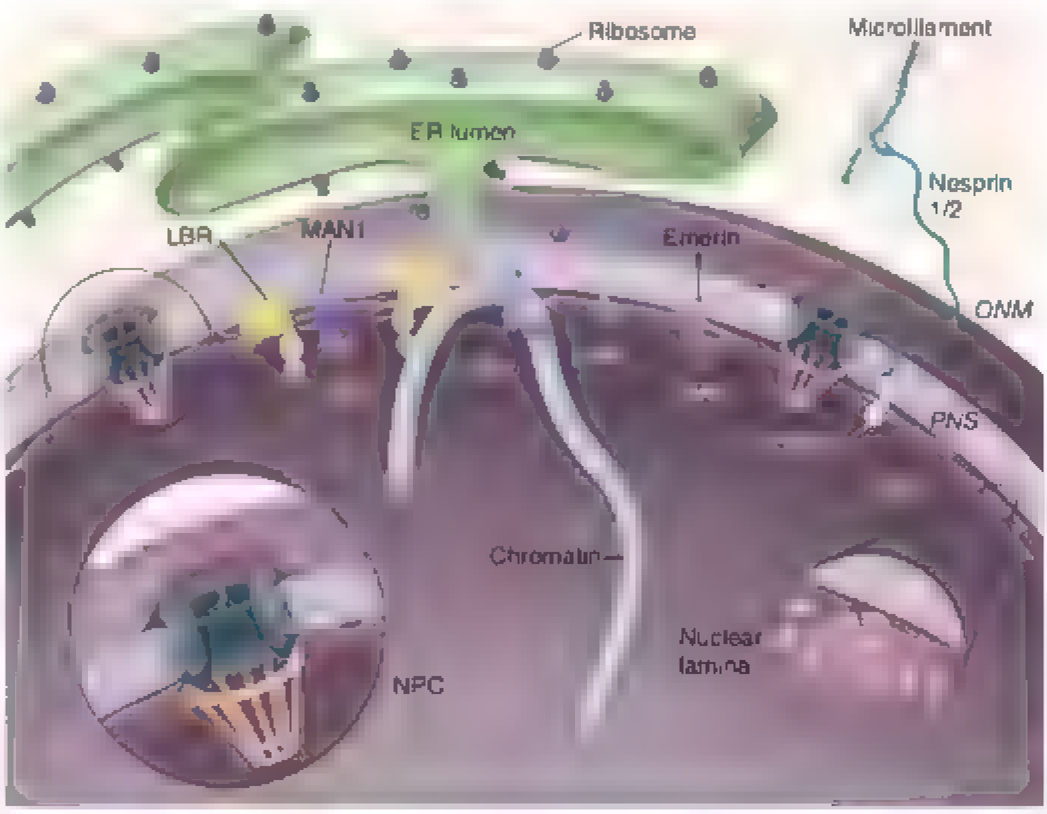

Fig. 1. Overview of nuclear envelope organization. Some selected INM proteins, including lamina-associated polypeptides 1 and 2 (LAP1 and LAP2) and LBR, are shown; these proteins interact with HP1 and BAF and provide links to chromatin. Lamin filaments are thought to form the basic structure of the nuclear lamina. Continuities between the INM and ONM at the periphery of each NPC are shown. The ONM, which is continuous with the ER, is characterized by cytoskeleton-associated nesprin proteins that are tethered by Sun1 and Sun2 in the INM.

[1]Institute of Medical Biology, 61 Biopolis Drive, Proteos, Singapore 138668, Singapore. [2]Department of Anatomy and Cell Biology, The University of Florida, 1600 Southwest Archer Road, Gainesville, FL 32610–0235, USA.

*To whom correspondence should be addressed. E-mail: bburke@ufl.edu

NE components are reutilized to assemble NEs in each daughter cell.

Disruption of the nuclear membranes and dispersal of their constituents throughout the peripheral ER is facilitated by astral microtubules and ONM-associated cytoplasmic dynein, a microtubule motor protein (*11*). There is also a poorly understood involvement of COPI, a vesicle coat protein complex associated with the Golgi apparatus (*12*, *13*). COPI displays an arrangement of structural motifs, featuring β-propeller and α-solenoid folds, that is also found in the Nup107-Nup160 complex of nucleoporins, a component of the NPC central framework. This raises intriguing questions about the evolutionary and mechanistic relations among these proteins (*14*).

An emerging theme is the display of dual-interphase versus mitotic functions of several NE components. Both A- and B-type lamins are dispersed throughout the cell during mitosis. Although A-type lamins behave as soluble proteins, B-type lamins, which are constitutively farnesylated, remain largely membrane-associated (*15*). Surprisingly, the B-type lamins play an active role in mitotic progression by contributing to the formation of a spindle matrix (*16*).

Some Nups also display such dual functions. Nup358 is a component of short filaments that form the cytoplasmic aspect of the NPC. Following NE breakdown (NEB), however, Nup358 relocates to kinetochores (*17*). In the absence of Nup358, kinetochores are malformed, which leads to chromatid segregation defects (*18*, *19*). The Nup107-Nup160 complex exhibits similar mitotic behavior (*20*, *21*). Evidently, there is a reciprocal relation between the spindle and the NE. On the one hand, dynein and astral microtubules facilitate NEB; on the other, disassembled NE components contribute to maturation of a functional spindle.

Because budding yeast uses an intranuclear spindle, it does not undergo NEB. Nonetheless, NE rearrangements still play an essential role in yeast mitotic progression. The NPC subunit Nup53 is involved in the regulation of cytokinesis through SUMOylation of septin proteins in the bud neck (*22*, *23*). Furthermore the kinetochore-associated checkpoint proteins MAD1 and MAD2 are immobilized at NPCs during interphase and evidently contribute to NPC functionality (*24*). The latter findings, as well as those in vertebrates, raise some fundamental questions about evolutionary relations between kinetochores and NPCs.

NE reassembly commences in anaphase, with stepwise recruitment of NE components. The earliest event involves association of the Nup107-Nup160 complex with the chromatin surface (*10*). This is followed by the appearance of INM proteins and the formation of a continuous double membrane. These membrane components originate in the peripheral ER network (*25*). NPC proteins also play a crucial role in membrane assembly. Interplay between Nup107-160 and the NPC membrane protein POM121 seems to function as a membrane assembly checkpoint, which ensures that a sealed NE does not form in the absence of functional NPCs (*26*).

The Nuclear Envelope and Disease

The past decade has seen the emergence of links between the NE and both infectious and hereditary diseases. Viruses, in particular, have developed strategies for subverting, and even bypassing, host-cell nuclear transport pathways. Both adenovirus and influenza A employ virally encoded adaptor proteins to import their genomes into the nucleus (*27*, *28*). Parvovirus, in contrast, resorts to transient disruption of the nuclear membranes to achieve the same result (*29*). Nuclear export of HIV RNA uses the leucine-rich nuclear export signal receptor exportin-Crm1, by using the HIV Rev protein as an adaptor (*30*). However, herpes simplex virus capsids, which are assembled within the nucleoplasm, exit the nucleus by budding through the lamina and INM into the PNS (*31*). In this way, herpesvirus capsids bypass NPCs and conventional export pathways. Even vesicular stomatitis virus, the replication of which is exclusively cytoplasmic, preys on the nucleocytoplasmic transport system. It uses its own matrix protein (M) to block cellular mRNA export. M protein forms a ternary complex with Rae1, an mRNA export factor, and Nup98. To counter this, both Rae1 and Nup98 expression is up-regulated by interferon (*32*). In this way, the NE is one of several fronts on which antiviral warfare is fought.

Undoubtedly, it is the identification of about eight different diseases (laminopathies) resulting from mutations within the lamin A (*LMNA*) gene, along with a further seven diseases or anomalies due to defects in other NE proteins, that has revitalized interest in the NE (*33*). The laminopathies can be grouped into three categories: those primarily affecting striated muscle (skeletal and cardiac) and peripheral nerves, those affecting skeletal and fat development and homeostasis, and those resulting in premature aging or progeria (*33*). *LMNA* is unique in that mutation of no other gene results in so many diverse phenotypes. This is all the more puzzling because *LMNA* is expressed in most adult cell types, yet different mutations result in tissue-specific pathologies. It is surprising that only one disease (autosomal dominant leukodystrophy) is linked to the *LMNB1* gene (a duplication) (*34*). This implies that mammals may be more sensitive to perturbations of the constitutively expressed B-type lamins, a notion supported by the late embryonic or perinatal lethality observed in *Lmnb1*-null mice (*35*).

An intriguing aspect of laminopathies is that most of the pathologies only become apparent after birth, despite the fact that *LMNA* expression commences during embryogenesis (*36*). This has led to speculation that A-type lamins are important in postnatal tissue homeostasis, particularly those of mesenchymal origin that undergo steady turnover during postnatal life (*37*). Lamins might therefore be involved in regulating the balance between stem cell turnover and differentiation. Nevertheless, we still do not fully understand how different mutations result in tissue-specific pathologies. Clues have come from the study of cells derived from mice engineered to carry the same mutations in their *Lmna* gene as those causing disease in humans. Mutations causing muscle laminopathies, such as autosomal-dominant Emery-Dreifuss muscular dystrophy (EDMD2) and dilated cardiomyopathy (CMD1A), are found throughout *LMNA* and frequently disrupt lamin assembly (*38*). There are several consequences to this. First, mechanical integrity of the nucleus is compromised; the nucleus becomes weaker and more susceptible to mechanical stress (*39*). Second, disruption of the lamina affects mechanical properties of the cytoplasm, which results in reduction in cytoplasmic elasticity and viscosity (*39*, *40*). Third, the centrosome is lost from the vicinity of the nucleus (*40*). Last, a disrupted lamina results in redistribution of heterochromatin and NPCs and affects the retention of some nuclear membrane proteins. The best example of the latter is emerin, an INM protein, which may relocate to the peripheral ER in *LMNA* mutant cells (*41*). Indeed, the X-linked form of EDMD is linked to mutations in the emerin gene (*EMD*) (*42*). This suggests that loss of emerin from the nucleus contributes to some of the dystrophic and cardiac conduction-defect laminopathies. Precisely what function (or functions) emerin performs at the NE is unclear, although evidence from mice lacking emerin suggests that it may be important for the proper function of retinoblastoma protein (pRb) and MyoD in muscle differentiation (*43*). Other proteins such as Sun2 and certain nesprin isoforms may also be lost from the NE when A-type lamin expression is compromised (*44*, *45*). Their mislocalization may be linked to the changes in cytoplasmic mechanics and centrosome positioning (see below).

A fifth consequence of disrupting lamina assembly is that signaling systems, such as the stress-responsive nuclear factor κB pathway, are compromised, which makes the affected cells less resistant to mechanical stresses (*46*). The pleiotropic effects of lamina disruption may help explain why the muscle-based laminopathies display such variation in severity and penetrance. It may also suggest why some 50% of individuals diagnosed with EDMD carry no mutations in either the *LMNA* or *EMD* genes, and therefore, nonmuscle laminopathy may arise from defects in other proteins whose function is directly or indirectly dependent on an intact lamina (*47*).

At present, we have few insights into the molecular bases of the nonmuscle laminopathies, including peripheral neuropathy (CMT2B1), lipodystrophy (FPLD), and mandibuloacral dysplasia (MAD). In contrast to the muscle lamino-

pathies, each of these diseases is associated with specific amino acid changes. None appears to affect lamina assembly, although posttranslational processing of lamin A may be affected in FPLD (*48*, *49*). Because the amino acids that are mutated are at the surface of either the rod domain (CMT2B1) or the C-terminal globular domain (FPLD and MAD), it is possible that these may perturb interactions with other nuclear proteins. If so, such proteins remain to be identified, although for FPLD the lipogenic activator, sterol regulatory element binding protein (SREBP-1), has been suggested as a possible candidate (*50*).

The last and perhaps most fascinating group of laminopathies are the progeric diseases, Hutchinson-Gilford progeria syndrome (HGPS) and atypical Werner's syndrome. The most common mutation resulting in HGPS causes an in-frame deletion of 50 amino acids in the lamin A protein, resulting in the removal of a critical endoproteolytic cleavage site (*51*, *52*). Consequently, posttranslational processing of lamin A is impaired, with the truncated lamin protein (progerin) retaining a farnesyl residue at its C terminus. Expression of progerin has devastating consequences, with affected children displaying growth retardation, skeletal and skin defects, and alopecia. Death occurs in the mid-teens due to arteriosclerosis. The principal cellular effects of progerin are an accumulation and thickening of the lamina and impaired mitosis (*53*, *54*). These alterations may be associated with defects in DNA repair mechanisms, as well as alterations to chromatin, all of which may contribute to a decline in cell proliferation observed in cultured fibroblasts from progeric patients (*55*–*57*). Any decrease in proliferative capacity could result in a failure of some tissues to regenerate, which may be the underlying basis of progeria. Programs are under way to determine the efficacy of farnesyl transferase inhibitors in treating progeria. However, it is worth noting that we have not addressed the cellular and molecular consequences of other even more rare *LMNA* mutations that are associated with HGPS or atypical Werner's and whether they, too, feature defective farnesylation (*58*).

The Emerging Role of the NE in Cellular Signaling

The recognition of multiple human diseases linked to defects in NE proteins has led to the reevaluation of the NE as a signaling platform. There is abundant evidence for NE involvement in the regulation of DNA replication (*59*) and RNA polymerase II–dependent gene expression (*60*, *61*). Lamins are known to associate with gene regulatory proteins such as pRb (*62*–*64*), barrier-to-autointegration factor (BAF) (*65*), histones (*66*), SREBP-1 (*48*, *50*), and c-Fos (*67*). In addition, several integral INM proteins such as emerin, lamin B receptor (LBR), MAN1, and lamina-associated polypeptide 2β (Lap2β) interact with transcriptional repressors and/or chromatin modifiers (*61*). Emerin alone associates with gene-regulatory proteins such as BAF (*66*), germ cell less (GCL) (*65*), β-catenin (*69*), Btf (*70*), YT521-B (*71*), and Lmo7 (*72*). These interactions may all serve to modulate gene expression and cell differentiation. A case in point is the nuclear retention and protection from proteasomal degradation of the hypophosphorylated active form of the tumor suppressor, pRb (*73*). This probably occurs through interaction of pRb with Lap2α and A-type lamins (*74*).

The best-characterized example of an INM protein involved in cell signaling is MAN1 (*75*). A highly conserved region of the MAN1 nucleoplasmic C-terminal domain mediates interaction with the MH2 domain of the R-Smads, transcriptional regulators downstream of transforming growth factor β (TGFβ) and bone morphogenic protein (BMP) (*76*–*80*). MAN1 binding of R-Smads attenuates TGFβ-BMP signaling. Although the exact mechanism for this remains unclear, it likely involves interference in Smad hetero-oligomerization and/or phosphorylation, both necessary for Smad function (*75*). Mutations in MAN1 are linked to osteopoikilosis, Buschke-Ollendorff syndrome, and melorheostosis (*76*), three autosomal dominant diseases with the shared pathology of increased bone density, they could be accounted for, in part, by reduced capacity to modulate TGFβ-BMP signaling, as well as hyperactivation of Smad transcriptional activity (*78*).

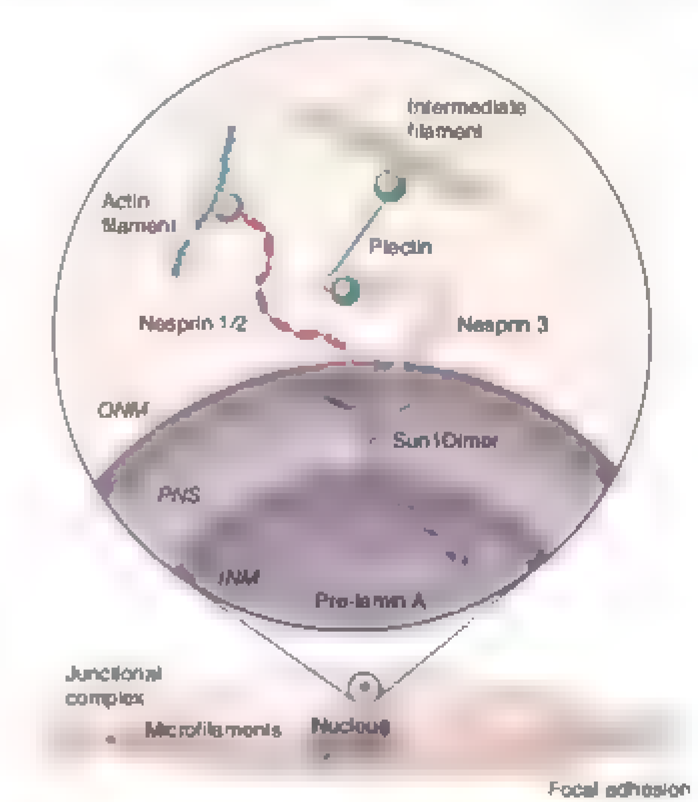

Fig. 2. The LINC complex in vertebrate cells may integrate nuclear components, including chromatin domains (blue), with cell surface and extracellular structures, including focal adhesions and junctional complexes. This is mediated by elements of the cytoskeleton, including both microfilaments and intermediate filaments. The LINC complex contains ONM nesprins that are tethered, via translumenal interactions, by INM SUN proteins. Sun1, shown in the diagram, likely exists as a dimer. Its nucleoplasmic domain binds A-type lamins and histone H2B, as well as the chromatin modifier hALP (*108*).

Of the dozen or so INM proteins characterized to date, virtually all interact with regulatory molecules, chromatin components, or both. However, there is limited evidence of their contribution to cell physiology in either health or disease. The situation will likely become even more complex as ~60 additional, largely uncharacterized, nuclear membrane proteins (*81*), possibly including INM calcium channels (*82*, *83*), are included in the equation. It seems increasingly clear that the signaling and regulatory pathways that form a nexus at the NE will be deciphered using systems-based approaches.

Two recently characterized classes of INM and ONM transmembrane proteins interact across the PNS and associate with both the lamina and cytoskeleton (Fig. 2). The notion of such translumenal interactions arose from studies in *Caenorhabditis elegans*, where localization of a large ONM actin-binding protein, Anc-1, was found to be dependent on Unc-84, an INM protein (*84*). Unc-84 is a member of the SUN domain family of proteins (*85*), of which there are at least five in vertebrates. Two of these, Sun1 and Sun2, are INM proteins and are expressed in somatic cells. Both Sun1 and Sun2 interact with A-type lamins (*44*, *45*, *86*, *87*) and function as tethers for members of the nesprin family of spectrin-repeat proteins in the ONM. The nesprins (also known as Syne proteins), Anc-1, and a *Drosophila* ONM protein, Klarsicht, all feature a short, highly conserved C-terminal KASH domain (Klarsicht, Anc-1, Syne homology), which resides within the PNS (*88*). It is the KASH domain that interacts with the Sun1/2 lumenal domain and forms a translumenal link analogous to that proposed for Unc-84 and Anc-1. The nesprins are encoded by at least three genes and encompass a bewildering array of splice variants (*89*–*92*). The largest isoforms (up to 1 MD) of nesprins 1 and 2 contain N-terminal actin-binding domains, whereas nesprin 3 contains a binding site for plectin, an IF-associated cytolinker. Some smaller nesprin isoforms are also found in the

INM. Together, SUN proteins and ONM nesprins comprise the LINC complex (linker of nucleoskeleton and cytoskeleton) (*44, 45, 86, 87*). Emerin might also be considered a peripheral component of the LINC complex because it associates with both INM nesprins (*93–95*) and lamins (*68, 96*), as well as with nuclear actin (*97–99*), nuclear myosin I, and αII-spectrin (*100*). Despite similarities, Sun1 and Sun2 are segregated within the INM. Sun1, in particular, is concentrated in a halo around NPCs (*101*). Although the significance of this localization is not understood, it does provide an explanation for the reported association of microfilaments and IFs with NPCs (*102*).

A decade ago, mechanical coupling of the nucleus and extracellular matrix (ECM) was observed (*103*). Physical displacement of cell surface integrins caused deformation of the nucleoplasm at a distance of several microns. The LINC complex now provides a mechanism to explain these observations and contributes to a model in which the cytoskeleton and ECM are in physical association with the NE and nucleoplasmic contents. This has obvious implications in terms of mechanotransduction and could provide a molecular basis for the changes in cytoplasmic organization and mechanics that are observed in certain laminopathy models (*39, 40*). Conversely, extracellular cues could directly modulate nuclear positioning, chromatin remodeling, or even gene expression. Perturbation of LINC complex proteins alters positioning of nuclei in skeletal muscle (*104, 105*). During cell migration, is the nucleus simply a passenger or a central anchor on which the cytoskeleton can organize to extend or retract processes? Deciphering the mechanisms behind such relations and their role in cell physiology seems likely to occur during the next phase in our ongoing quest to understand the NE.

Conclusions

With the exception of its periodic convulsion during mitosis, the NE presents us with a seemingly bland façade, which buttresses the widely held view that the role of the NE is largely passive. However, studies from several quarters have led to a reevaluation and expansion of our understanding of NE function. The link between human diseases and NE proteins has provided unexpected insight into their roles in normal cellular physiology. Although A-type lamins have been considered little more than NE structural proteins, such a simplistic view is incapable of accounting for all of the laminopathy-associated pathologies. Studies on *LMNA*-associated disease mechanisms have led to the finding that alterations in nuclear lamina organization can cause cytoskeletal changes potentially involving the LINC complex of SUN proteins and nesprins. This opens up possibilities of signaling routes across the NE that may bypass NPCs. On the other hand, certain nucleoporins display alternate mitotic functions that are essential for mitotic progression. We are also beginning to recognize a complex interplay between disparate NE components. Assembly of NPCs during telophase is coupled to membrane assembly by what has all the hallmarks of a Nup-dependent checkpoint. Sun1 and, hence, a subpopulation of LINC complexes are associated with NPCs and provide them with a connection to both the nuclear lamina and the cytoskeleton. This synopsis only scratches the surface of the complex networks of interactions that are being revealed at the nuclear periphery. During the coming years, we may anticipate further elucidation of both structural and signaling networks at the nuclear margins and renewed vision of the NE as a central element in cellular physiology.

Note added in proof: Two recent papers by P. Muhlhausser and U. Kutay (*106*) and G. Salpingidou *et al.* (*107*) further enhance our view of NE-cytoskeletal interactions.

References and Notes

1. M. A. D'Angelo, M. W. Hetzer, *Cell. Mol. Life Sci.* **63**, 316 (2006).
2. N. Fried, U. Kutay, *Cell. Mol. Life Sci.* **60**, 1659 (2003).
3. H. G. Callan, S. G. Tomlin, *Proc. R. Soc. Lond. B. Biol. Sci.* **137**, 367 (1950).
4. J. G. Gall, *J. Cell Biol.* **32**, 391 (1967).
5. C. M. Feldherr, E. Kallenbach, N. Schultz, *J. Cell Biol.* **99**, 2216 (1984).
6. E. C. Schirmer, R. Foisner, *Exp. Cell Res.* **313**, 2167 (2007).
7. E. C. Schirmer, L. Gerace, *Trends Biochem. Sci.* **30**, 551 (2005).
8. Y. Gruenbaum, A. Margalit, R. D. Goldman, D. K. Shumaker, K. L. Wilson, *Nat. Rev. Mol. Cell Biol.* **6**, 21 (2005).
9. U. Aebi, J. B. Cohn, L. Buhle, L. Gerace, *Nature* **323**, 560 (1986).
10. M. W. Hetzer, T. C. Walther, I. W. Mattaj, *Annu. Rev. Cell Dev. Biol.* **21**, 347 (2005).
11. B. Burke, J. Ellenberg, *Nat. Rev. Mol. Cell Biol.* **3**, 487 (2002).
12. A. J. Prunuske, K. S. Ullman, *Curr. Opin. Cell Biol.* **18**, 108 (2006).
13. J. Liu, A. J. Prunuske, A. M. Fager, K. S. Ullman, *Dev. Cell* **5**, 487 (2003).
14. D. Dreier *et al.*, *Proc. Natl. Acad. Sci. U.S.A.* **103**, 2172 (2006).
15. L. Gerace, G. Blobel, *Cell* **19**, 277 (1980).
16. M. Y. Tsai *et al.*, *Science* **311**, 1887 (2006).
17. J. Joseph, S. H. Tan, T. S. Karpova, J. G. McNally, M. Dasso, *J. Cell Biol.* **156**, 595 (2002).
18. J. Joseph, S. T. Liu, S. A. Jablonski, T. J. Yen, M. Dasso, *Curr. Biol.* **14**, 611 (2004).
19. D. Salina, P. Enarson, J. B. Rattner, B. Burke, *J. Cell Biol.* **162**, 991 (2003).
20. M. Belgareh *et al.*, *J. Cell Biol.* **154**, 1147 (2001).
21. I. Loiodice *et al.*, *Mol. Biol. Cell* **15**, 3333 (2004).
22. T. Makhnevych, C. Ptak, C. P. Lusk, J. D. Aitchison, R. W. Wozniak, *J. Cell Biol.* **177**, 39 (2007).
23. T. Makhnevych, C. P. Lusk, A. M. Anderson, J. D. Aitchison, R. W. Wozniak, *Cell* **115**, 813 (2003).
24. T. Iouk, O. Kerscher, R. J. Scott, M. A. Basrai, R. W. Wozniak, *J. Cell Biol.* **159**, 807 (2002).
25. D. J. Anderson, M. W. Hetzer, *Nat. Cell Biol.* **9**, 1160 (2007).
26. W. Antonin, C. Franz, U. Haselmann, C. Antony, I. W. Mattaj, *Mol. Cell* **17**, 83 (2005).
27. H. Wodrich *et al.*, *J. Virol.* **80**, 9608 (2006).
28. W. W. Wu, Y. H. Sun, N. Pante, *Virol. J.* **4**, 49 (2007).
29. S. Cohen, A. R. Behzad, J. B. Carroll, N. Pante, *J. Gen. Virol.* **87**, 3209 (2006).
30. U. Fischer, J. Huber, W. C. Boelens, I. W. Mattaj, R. Luhrmann, *Cell* **82**, 475 (1995).
31. T. C. Mettenleiter, *Vet. Microbiol.* **113**, 163 (2006).
32. B. M. Fontoura, P. A. Faria, D. R. Nussenzveig, *IUBMB Life* **57**, 65 (2005).
33. H. J. Worman, G. Bonne, *Exp. Cell Res.* **313**, 2121 (2007).
34. O. S. Padiath *et al.*, *Nat. Genet.* **38**, 1114 (2006).
35. L. Vergnes, M. Peterfy, M. O. Bergo, S. G. Young, K. Reue, *Proc. Natl. Acad. Sci. U.S.A.* **101**, 10428 (2004).
36. C. Stewart, B. Burke, *Cell* **51**, 383 (1987).
37. K. L. Wilson, *Trends Cell Biol.* **10**, 125 (2000).
38. W. H. Raharjo, P. Enarson, T. Sullivan, C. L. Stewart, B. Burke, *J. Cell Sci.* **114**, 4447 (2001).
39. J. Lammerding *et al.*, *J. Clin. Invest.* **113**, 370 (2004).
40. J. S. Lee *et al.*, *Biophys. J.* **93**, 2542 (2007).
41. T. Sullivan *et al.*, *J. Cell Biol.* **147**, 913 (1999).
42. S. Bione *et al.*, *Nat. Genet.* **8**, 323 (1994).
43. G. Meinke *et al.*, *Hum. Mol. Genet.* **15**, 637 (2006).
44. M. Crisp *et al.*, *J. Cell Biol.* **172**, 41 (2006).
45. V. C. Padmakumar *et al.*, *J. Cell Sci.* **118**, 3419 (2005).
46. J. Lammerding *et al.*, *J. Cell Biol.* **170**, 781 (2005).
47. G. Bonne *et al.*, *Neuromuscul. Disord.* **13**, 508 (2003).
48. C. Capanni *et al.*, *Hum. Mol. Genet.* **14**, 1489 (2005).
49. M. Caron *et al.*, *Cell Death Differ.* **14**, 1759 (2007).
50. D. J. Lloyd, R. C. Trembath, S. Shackleton, *Hum. Mol. Genet.* **11**, 769 (2002).
51. A. De Sandre-Giovannoli *et al.*, *Science* **300**, 2055 (2003).
52. M. Eriksson *et al.*, *Nature* **423**, 293 (2003).
53. T. Dechat *et al.*, *Proc. Natl. Acad. Sci. U.S.A.* **104**, 4955 (2007).
54. R. D. Goldman *et al.*, *Proc. Natl. Acad. Sci. U.S.A.* **101**, 8963 (2004).
55. J. M. Bridger, I. R. Kill, *Exp. Gerontol.* **39**, 717 (2004).
56. Y. Liu, A. Rusinol, M. Sinensky, Y. Wang, Y. Zou, *J. Cell Sci.* **119**, 4644 (2006).
57. P. Scaffidi, T. Misteli, *Nat. Med.* **11**, 440 (2005).
58. A. B. Csoka *et al.*, *J. Med. Genet.* **41**, 304 (2004).
59. E. P. Spann, R. D. Moir, A. E. Goldman, R. Stick, R. D. Goldman, *J. Cell Biol.* **136**, 1201 (1997).
60. T. P. Spann, A. E. Goldman, C. Wang, S. Huang, R. D. Goldman, *J. Cell Biol.* **156**, 603 (2002).
61. S. Shaklai, N. Amariglio, G. Rechavi, A. J. Simon, *FEBS J.* **274**, 1383 (2007).
62. M. A. Mancini, B. Shan, J. A. Nickerson, S. Penman, W. H. Lee, *Proc. Natl. Acad. Sci. U.S.A.* **91**, 418 (1994).
63. T. Ozaki *et al.*, *Oncogene* **9**, 2649 (1994).
64. B. Shan *et al.*, *Mol. Cell. Biol.* **12**, 5620 (1992).
65. J. M. Holaska, K. K. Lee, A. K. Kowalski, K. L. Wilson, *J. Biol. Chem.* **278**, 6969 (2003).
66. N. Taniura, C. Glass, L. Gerace, *J. Cell Biol.* **131**, 33 (1995).
67. C. Ivorra *et al.*, *Genes Dev.* **20**, 307 (2006).
68. K. K. Lee *et al.*, *J. Cell Sci.* **114**, 4567 (2001).
69. E. Markiewicz *et al.*, *EMBO J.* **25**, 3275 (2006).
70. T. Haraguchi *et al.*, *Eur. J. Biochem.* **271**, 1035 (2004).
71. F. L. Wilkinson *et al.*, *Eur. J. Biochem.* **270**, 2459 (2003).
72. J. M. Holaska, S. Rais-Bahrami, K. L. Wilson, *Hum. Mol. Genet.* **15**, 3459 (2006).
73. B. R. Johnson *et al.*, *Proc. Natl. Acad. Sci. U.S.A.* **101**, 9677 (2004).
74. E. Markiewicz, T. Dechat, R. Foisner, R. A. Quinlan, C. J. Hutchison, *Mol. Biol. Cell* **13**, 4401 (2002).
75. L. Bengtsson, *FEBS J.* **274**, 1374 (2007).
76. J. Hellemans *et al.*, *Nat. Genet.* **36**, 1213 (2004).
77. F. Lin, J. M. Morrison, W. Wu, H. J. Worman, *Hum. Mol. Genet.* **14**, 437 (2005).
78. S. Osada, S. Y. Ohmori, M. Taira, *Development* **130**, 1783 (2003).
79. D. Pan *et al.*, *J. Biol. Chem.* **280**, 15992 (2005).
80. G. P. Raju, N. Dimova, P. S. Klein, H. C. Huang, *J. Biol. Chem.* **278**, 428 (2003).
81. E. C. Schirmer, L. Florens, T. Guan, J. R. Yates III, L. Gerace, *Science* **301**, 1380 (2003).
82. J. P. Humbert, N. Matter, J. C. Artault, P. Koppler, A. N. Malviya, *J. Biol. Chem.* **271**, 478 (1996).
83. L. Santella, K. Kyozuka, *Cell Calcium* **22**, 11 (1997).
84. D. A. Starr, M. Han, *Science* **298**, 406 (2002).
85. K. K. Lee *et al.*, *Mol. Biol. Cell* **13**, 892 (2002).
86. F. Haque *et al.*, *Mol. Cell. Biol.* **26**, 3738 (2006).
87. S. Hasan *et al.*, *FEBS Lett.* **580**, 1263 (2006).
88. D. T. Warren, Q. Zhang, P. L. Weissberg, C. M. Shanahan, *Expert Rev. Mol. Med.* **7**, 1 (2005).
89. Y. Y. Zhen, T. Libotte, M. Munck, A. A. Noegel, E. Korenbaum, *J. Cell Sci.* **115**, 3207 (2002).
90. Q. Zhang *et al.*, *J. Cell Sci.* **114**, 4485 (2001).

91. E. D. Apel, R. M. Lewis, R. M. Grady, J. R. Sanes, *J. Biol. Chem.* **275**, 31986 (2000).
92. J. M. Mislow, M. S. Kim, D. B. Davis, E. M. McNally, *J. Cell Sci.* **115**, 61 (2002).
93. J. M. Mislow *et al.*, *FEBS Lett.* **525**, 135 (2002).
94. M. A. Wheeler *et al.*, *Exp. Cell Res.* **313**, 2845 (2007).
95. Q. Zhang *et al.*, *J. Cell Sci.* **118**, 673 (2005).
96. M. Sakaki *et al.*, *J. Biochem.* (Tokyo) **129**, 321 (2001).
97. E. A. Fairley, J. Kendrick-Jones, J. A. Ellis, *J. Cell Sci.* **112**, 2571 (1999).
98. J. M. Holaska, A. K. Kowalski, K. L. Wilson, *PLoS Biol.* **2**, E231 (2004).
99. G. Lattanzi *et al.*, *Biochem. Biophys. Res. Commun.* **303**, 764 (2003).
100. J. M. Holaska, K. L. Wilson, *Biochemistry* **46**, 8897 (2007).
101. Q. Liu *et al.*, *J. Cell Biol.* **178**, 785 (2007).
102. R. Goldman *et al.*, *Ann. N. Y. Acad. Sci.* **455**, 1 (1985).
103. A. J. Maniotis, C. S. Chen, D. E. Ingber, *Proc. Natl. Acad. Sci. U.S.A.* **94**, 849 (1997).
104. R. M. Grady, D. A. Starr, G. L. Ackerman, J. R. Sanes, M. Han, *Proc. Natl. Acad. Sci. U.S.A.* **102**, 4359 (2005).
105. X. Zhang *et al.*, *Development* **134**, 901 (2007).
106. F. Mühlhäusser, U. Kutay, *J. Cell Biol.* **178**, 595 (2007).
107. G. Salpingidou *et al.*, *J. Cell Biol.* **178**, 897 (2007).
108. Y. H. Chi, K. Haller, J. M. Peloponese Jr., K. T. Jeang, *J. Biol. Chem.* **282**, 27447 (2007).
109. This work was supported by a grant from the NIH to B.B.

10.1126/science.1142034

REVIEW

Crossing the Nuclear Envelope: Hierarchical Regulation of Nucleocytoplasmic Transport

Laura J. Terry, Eric B. Shows, Susan R. Wente*

Transport of macromolecules between the nucleus and cytoplasm is a critical cellular process for eukaryotes, and the machinery that mediates nucleocytoplasmic exchange is subject to multiple levels of control. Regulation is achieved by modulating the expression or function of single cargoes, transport receptors, or the transport channel. Each of these mechanisms has increasingly broad impacts on transport patterns and capacity, and this hierarchy of control directly affects gene expression, signal transduction, development, and disease.

In eukaryotic cells, physical separation of the nuclear genomic material from the other intracellular compartments necessitates controlled nuclear entry and exit to carry out basic biological processes. The nucleocytoplasmic transport mechanism uses specific cellular factors and macromolecular complexes to regulate such bidirectional trafficking of RNA and protein cargoes. The timely translocation of specific cargo across the nuclear envelope is especially critical for correct cell division and gene expression. The importance of faithful nuclear import and export is underscored by the role transport plays in coordinating embryonic development. Furthermore, deregulation or hijacking of transport pathways is also central to various disease states. Here we highlight the multitiered strategies for regulating nuclear influx and efflux of proteins and RNAs and the impacts of dynamic intra- and extracellular cues.

Cellular Machinery for Nuclear Import and Export

Entrance into and exit from the nucleus occurs via the nuclear pore complexes (NPCs), >60 MD macromolecular structures that form channels spanning the double lipid bilayer of the nuclear envelope (Fig. 1, A and B) (*1*, *2*). Each NPC is equipped to facilitate both import and export of proteins and RNAs (Fig. 1C) (*3*). The constituent proteins of the NPC, nucleoporins (Nups), serve precise roles in NPC assembly and function (*4*). Structural Nups contribute to the overall NPC architecture, and pore membrane proteins (Poms) anchor the NPC in the nuclear envelope. FG-Nups constitute a third class of Nups; they contain discrete domains with multiple phenylalanine-glycine (FG), GLFG (L, leucine), or FxFG (x, any) repeat motifs, separated by charged or polar spacer sequences (*5*). The FG-Nups presumably line the central NPC channel and extend filaments on both the cytoplasmic and nucleoplasmic faces (Fig. 1B). Additionally, the unfolded nature of the FG domains might allow multiple topological positions in the NPC (*6*–*8*).

Movement of ions, metabolites, and other small molecules through the NPC occurs via passive diffusion, but the translocation of cargoes larger than ~40 kD generally requires specific transport receptors (*9*, *10*). The FG-Nups are considered to play an intimate role in generating this NPC permeability barrier, although roles for structural Nups in formation of the barrier have also been reported (*11*, *12*). FG-Nups are essential components of the active translocation scaffold through the NPC (*13*). Transport receptors are thought to engage in multiple stochastic, low-affinity interactions with FG repeats during translocation. The series of interactions between an FG-Nup and a transport receptor during docking and translocation are energy-independent, with nucleotide hydrolysis apparently required only during terminal release and directionality steps (*10*).

The biophysical nature of the permeability barrier and the mechanism of translocation remain controversial and poorly understood (*13*). At the core of the debate is whether the NPC permeability barrier is physical or energetic, and recent studies suggest that either or both could be the case (*1*, *8*, *13*–*15*). As a physical barrier, the FG-Nups would interact to form a gelatinous meshwork through which only small molecules could passively diffuse (*14*). Translocation through such a meshwork would be mediated by transport receptors that locally dissolve the barrier and permit passage of receptor-cargo complexes. As an energetic barrier, the NPC would form a repulsive gate, repelling non–FG-binding molecules (*1*, *8*). Receptor binding to FG-repeats would effectively allow concentration of transport complexes at the NPC, overcoming the entropic barrier and increasing the probability of transport. Finally, a two-dimensional walk model has been proposed, with a selective barrier to passive diffusion formed by the hydrophilic spacer sequences between FG repeats or other Nups (*16*). This would result in the organization of a continuous FG surface allowing transport receptor-cargo complexes to dock and pivot along neighboring FGs. The intrinsic translocation and barrier properties are critical to the regulatory role of the NPC in intracellular transport and signaling, and further biophysical and cellular studies will be required to differentiate between the proposed mechanisms.

Transport receptors themselves are central to the nuclear import and export steps of recognizing signal-bearing cargoes, interacting with the NPC, and delivering cargo to its destination compartment (Fig. 1B) (*17*). The largest group of transport receptors comprise structurally related members of the karyopherin-β/importin-β (Kapβ/Impβ) protein family (importins, exportins, or transportins). Most Kapβs bind cargoes directly, although Kapβ1 commonly uses adaptors to recognize cargo. Specifically, Kapα isoforms serve as adaptors between Kapβ1 and cargo (*18*). Directionality of transport for Kapβ family members is accomplished via the small guanosine triphosphatase (GTPase) Ran (Fig. 1B) (*10*) and might also be affected by Nup-Kapβ binding sites (*13*). Non-Kapβ transport receptors include the Ran guanosine diphosphate (RanGDP) import factor Ntf2 and the general mRNA export receptor—yMex67 in yeast, mNxf1/Tap in metazoans—that functions as a heterodimer with yMtr2 or mNxt1/p15, respectively (*10*). Some cargoes also require more than one transport re-

Department of Cell and Developmental Biology, Vanderbilt University Medical Center, Nashville, TN 37232, USA.

*To whom correspondence should be addressed. E-mail: susan.wente@vanderbilt.edu

ceptor, such as the *Saccharomyces cerevisiae* 60S ribosomal subunit (*19*). Additionally, a limited number of cargoes undergo receptor-independent transport; for example, the Wnt signaling molecule β-catenin directly interacts with FG-repeats to mediate its own import (*20*).

It is increasingly clear that the regulation of nucleocytoplasmic transport encompasses multiple levels of control and involves all the key transport components: the NPC transport channel, the transport receptors, and the transport cargo itself. As described here, the use of multiple regulation strategies allows for hierarchical levels of impact on the overall transport process (Fig. 2). Regulation at the level of cargo usually leads to small-scale changes involving only that particular cargo, whereas modifications of transport receptor or adaptor function have an intermediate effect, potentially affecting all cargoes recognized by that receptor. Changes at the NPC level are more global and are positioned to influence multiple receptors and thus large numbers of cargo simultaneously.

Regulation at the Level of Individual Cargo

The signals displayed by cargo molecules and recognized by transport receptors are termed nuclear localization (import) sequences (NLSs) and nuclear export sequences (NESs) (*10*). These have classically been defined as primary amino acid motifs that are both necessary and sufficient for transport. However, it is now clear that such signals are composed of primary sequence and secondary or tertiary structural elements, and that they are present in both proteins and RNAs. The precise sequence and the substructural context of an NLS or NES defines its specificity for the various Kaps (*21*). Furthermore, the receptor-protein and receptor-RNA interactions that mediate cargo localization are governed by multiple posttranscriptional and posttranslational modifications (Fig. 2, cargo). This allows for specific transport regulation of individual cargo.

Control of nuclear localization by transport signals is fully demonstrated by classic examples from metazoan NF-κB and p53 signaling. Nuclear import of the transcription factor NF-κB heterodimer p65-p50 is regulated by intermolecular masking of its NLS (*22*). Crystal structure studies reveal that the NF-κB inhibitor IκBα directly occludes the NLS of p65-p50 (*23, 24*). This results in the cytoplasmic localization of the heterodimer; however, in response to proinflammatory stimuli, IκBα is subsequently degraded and NF-κB is released for nuclear import (Fig. 3A) (*22*). The tumor suppressor p53 shuttles between the nucleus and the cytoplasm in a cell cycle dependent manner (*25*). In response to cellular stress, p53 is retained in the nucleus via an "NES masking" mechanism whereby p53 homotetramerizes, burying the NESs and blocking interaction with the export Kapβ Crm1 (Fig. 3A). The nucleocytoplasmic shuttling of p53 is further abrogated by stress-induced poly(ADP-ribosyl)ation that prevents p53 interaction with Crm1 (*26*). Defects in p53 nuclear retention are associated with a number of neoplasms (*27*), illustrating the importance of proper cellular localization for single cargoes.

The affinity of a protein cargo for its cognate Kapβ receptor or Kapα adaptor influences its nucleocytoplasmic transport efficiency (*28*) and represents a subtle effector of transport regulation. However, cargo-receptor binding that is too strong impedes cargo delivery and release (*29*). More broadly, cargo-receptor complex formation can be directly affected by posttranslational changes that involve specific modifications to NLSs or NESs. The *S. cerevisiae* transcription factor Pho4 undergoes phosphorylation-dependent interactions with Kapβs to regulate its localization in response to phosphate availability (*30*). For cyclin B1, phosphorylation of its NES at the onset of mitosis leads to nuclear retention by blocking interaction with Crm1 (*31*). In addition to phosphorylation, posttranslational modifications such as methylation and ubiquitination can regulate the localization of a cargo. Methylation of the NLS in RNA helicase A is crucial for its proper import (*32*). The phosphatase and tumor suppressor PTEN is efficiently imported after monoubiquitination of specific lysine residues (*33*). Interestingly, the ubiquitin-conjugating enzyme UbcM2 is imported only when charged with ubiquitin, implicating proper enzyme activation as a transport "trigger" (Fig. 3B) (*34*). Thus, the use of posttranslational modifications to regulate protein transport allows cyclical and timely responses to cellular states.

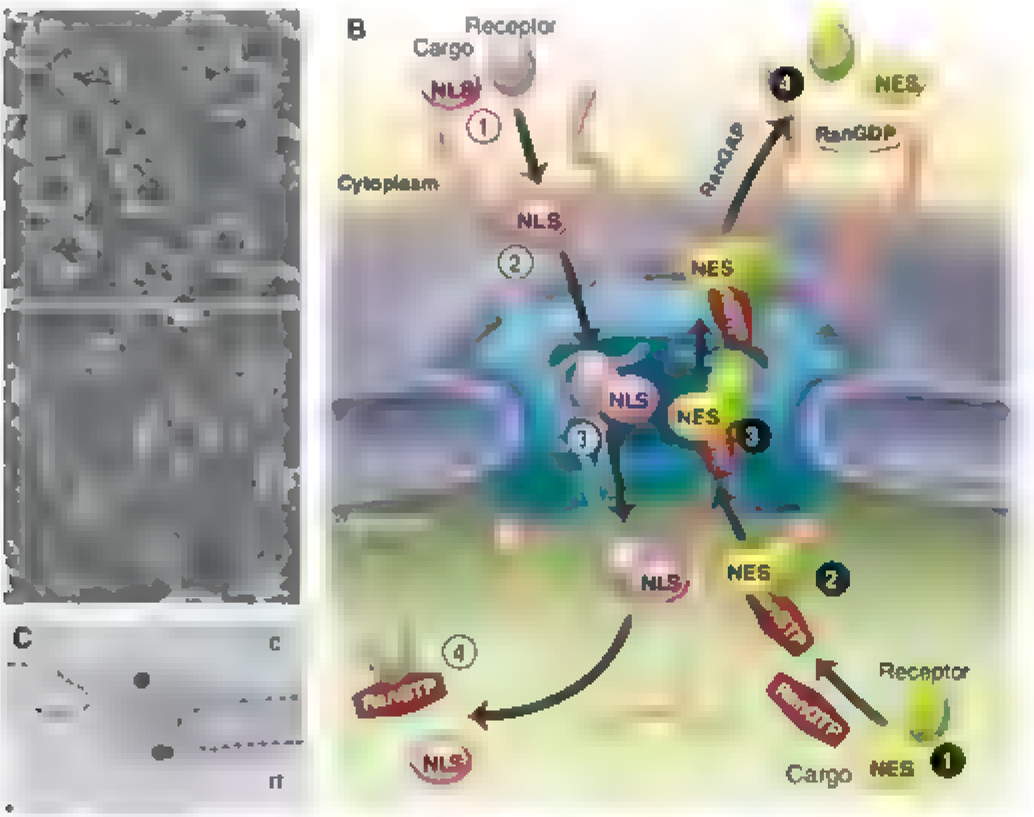

Fig. 1. The NPC mediates bidirectional nucleocytoplasmic trafficking. **(A)** Scanning electron micrograph of NPC structures from the cytoplasmic (upper panel) and nucleoplasmic (lower panel) sides of a *Xenopus laevis* oocyte nuclear envelope. The sample was a prepared as described in (*80*). [Image courtesy of M. Goldberg, Durham University, and R. Stick, University of Bremen] **(B)** Receptor-mediated transport involves sequential steps. A transport receptor recognizes a signal-bearing cargo and forms a receptor-cargo complex (1). The receptor-cargo complex then docks on the near side of the NPC (2) before engaging in sequential, stochastic, low-affinity interactions with FG-Nups during translocation (3). At the far side of the NPC, the receptor-cargo complex is disassembled (4) to deliver the cargo. For Kapβ import, complex disassembly is initiated by nuclear binding of RanGTP to the receptor. For Kapβ nuclear export, RanGTP in the export receptor-cargo complex is hydrolyzed to RanGDP by the Ran GTPase activating protein (RanGAP), resulting in complex disassembly. The Ran guanine nucleotide exchange factor (RanGEF) is localized to the nucleus and generates high RanGTP concentrations, and RanGDP is imported into the nucleus by Ntf2 (not shown). **(C)** Individual NPCs are capable of bidirectional movement of both proteins and RNA. Immuno–electron microscopy of a single nuclear pore from a *X. laevis* oocyte is shown after microinjection with gold-labeled transport substrates. Nucleoplasmin-gold (120 to 220 Å) was injected into the cytoplasm (c) and tRNA-gold (20 to 50 Å) was injected into the nucleus (n). The nuclear membranes are highlighted by the dotted blue lines. [Reprinted from (*3*) with permission]

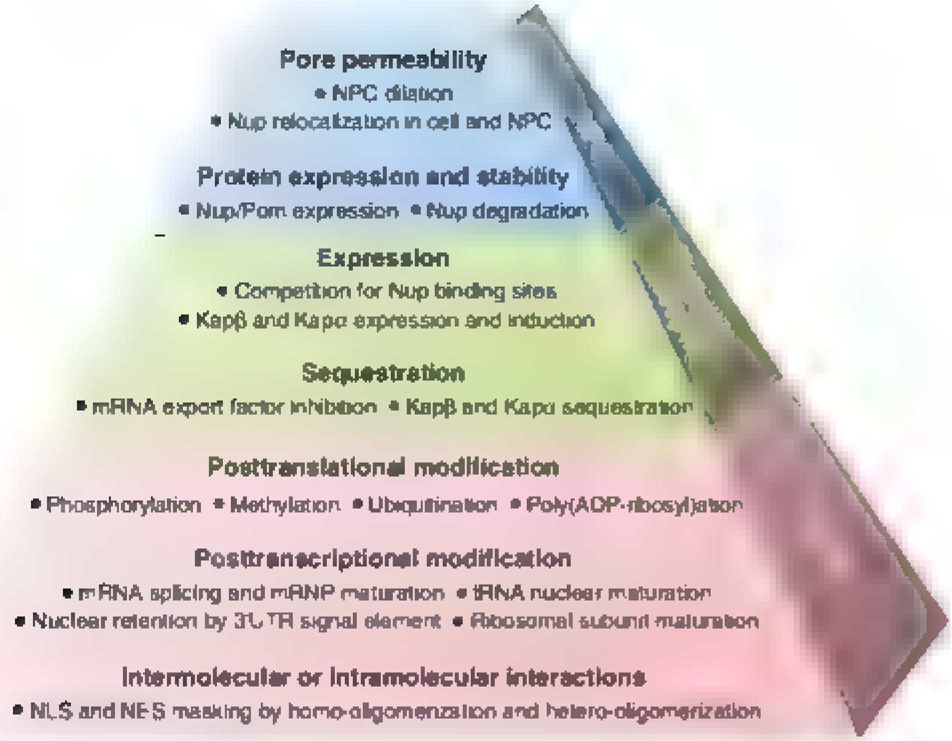

Fig. 2. Nucleocytoplasmic transport is regulated at the level of the NPC, transport receptors, and individual cargoes. The pyramid shows the hierarchy of levels used to regulate nucleocytoplasmic transport, with control at higher levels (right side) having broader impacts on trafficking. Each level is controlled by multiple mechanisms, with selected in vivo examples listed (front) and illustrated in Fig. 3.

The paradigm of discrete signal elements that regulate nuclear transport is also readily evident for various RNA cargoes. tRNA functions in the cytoplasm, and its export via direct interaction with the Kapβ exportin-t is tightly linked to its maturation state (*35*). Nuclear export of a subset of mRNAs is directly regulated by cis-acting RNA signal elements. Type D retroviral transcripts use a constitutive transport element (CTE), which directly binds the mNxf1 transport receptor (*10*). Curiously, a CTE also exists within a splice variant of the mRNA encoding mNxf1 (*36*). The mRNAs for some gene products linked to cell cycle control harbor a unique, conserved structural element in their 3' untranslated region (3'UTR) that is recognized by the translation initiation factor eIF4E (*37*). Binding of eIF4E to this element targets these mRNAs to an mNxf1-independent export pathway. In addition to promoting export, nucleic acid sequence elements regulate RNA nuclear retention and effectively modulate gene expression. The mRNA of the tumor-associated cytokine MSF contains a 3' UTR signal element that mediates nuclear retention until posttranscriptional processing in response to transforming growth factor β1 signaling triggers export (*38*). Similarly, a 3'UTR element in an alternate transcript of the amino acid transporter mCAT2 results in nuclear retention until stress conditions allow posttranscriptional processing and export (*39*). RNA signal elements can also direct nuclear import; a hexameric sequence within the microRNA miR-29b is both necessary and sufficient for its import (*40*). Sequence and structural elements therefore directly affect transport of specific RNAs.

Essential to the maturation of mRNAs and ribosomal subunits is a series of regulated, large-scale processing steps that control interactions with appropriate transport receptor(s). This ensures that only mature, fully processed cargo is exported. For mRNA, specific proteins are cotranscriptionally recruited to form a messenger ribonucleoprotein particle (mRNP) with serial changes to the mRNP during splicing, capping, and polyadenylation (*19*). Regulated mRNP maturation is required for export, with deficiencies resulting in nuclear mRNP retention (Fig. 3B). A critical step in the mRNP export process is the recruitment of the transport receptor yMex67-Mtr2 (mNxf1-Nxt1) and targeting to the NPC (*19*). Controlled, directional release of the mRNP into the cytoplasm, and alterations to the mRNP composition during export, are potentially coordinated by spatial activation of the RNA-dependent ATPase yDbp5 through NPC-associated yGle1 and inositol hexakisphosphate (*41*, *42*). The requirement for a soluble inositide in mRNA export might also allow modulation of transport by phospholipase C signaling (*43*). In a parallel manner, ribosomal subunits undergo sequential, regulated processing in the nucleolus and nucleoplasm to form rRNA-protein complexes that are selectively exported to the cytoplasm (*19*). Hence, cargo signals, modifications, and composition can play essential roles in controlling the transport of individual proteins, RNAs, and RNA-protein complexes.

Control via Modulation of Transport Receptors

Although changing the transport dynamics of a single cargo is accomplished in several ways, the regulation of a suite of cargoes can perhaps be more effectively accomplished by altering distinct transport receptors. *S. cerevisiae* has at least 17 different transport receptors, including the 14 Kapβ family members, a single Kapα, yNtf2, and the yMex67-Mtr2 heterodimer (*16*, *17*). Metazoa have ~20 known Kapβ family members, multiple Kapα isoforms, mNtf2, and up to four known mNxf family members (*17*, *44*). Each of these receptors recognizes a specific subset of NLSs and/or NESs and thereby governs the transport of select cargoes.

Several studies have documented that transport might be regulated by changes in receptor or adaptor expression levels (Fig. 2, transport receptor). Differences in transport receptor expression patterns during development have been observed in *Caenorhabditis elegans* and *Drosophila melanogaster* (*22*). Tissue-specific expression of the three *Drosophila* Kapαs during gametogenesis and early embryogenesis directly regulates the cargoes that are imported (Fig. 3C) (*18*). Indeed, aberrant Kapα expression patterns result in defects in fertility and embryogenesis. Human Kapαs also show tissue-specific expression patterns (*45*–*47*). Coordinated switching between Kapα subtypes has been implicated in regulating the neural differentiation of mouse embryonic stem cells (*48*). In this case, the temporal expression of Kapαs is critical for stage-specific nuclear import of transcription factors associated with developmental progression. Not only do Kapαs allow regulation of which cargoes are imported (Fig. 3C), but use of a Kapα adaptor with Kapβ broadens the dynamic range of import above that which a Kapβ can accomplish alone (*49*).

Deregulation of transport receptor shuttling pathways occurs in several disease states. Overexpression of Kapβ and/or Kapα family members is detected in colon, breast, and lung cancers (*50*, *51*), and deregulation of Kapα2 expression in melanoma cells and breast cancers correlates with poor survival and prognosis (*51*, *52*). However, it is unclear what cargoes are redistributed in cells overexpressing Kapα2 and how this affects tumor progression. In viral pathogenesis, sequestration of Kapα1 or Kapα2 by Ebola virus or SARS-CoV, respectively, impedes the cellular antiviral response (*53*, *54*). Thus, spatiotemporal control of transport receptor levels directly affects development and is linked to disease mechanisms.

The interplay between Kapβs for NPC binding sites is also emerging as a mechanism for regulating transport. As the abundance of a Kapβ and its cognate cargo(es) varies, so too does the efficiency of nuclear import (*55*–*57*).

Increasing the Kapβ level increases transport rates (55, 57), however, the process is saturable for a given Kapβ (58). It is also possible that different individual transport receptors compete for a limited number of NPC binding sites. Import rates measured in intact cells are lower than rates in permeabilized cells by a factor of ~10, presumably because most competing Kapβs are removed from the in vitro system (55). Transport receptors also show preferences for different FG domains both in vivo and in vitro, as summarized in (59, 60). Genetic manipulation of the NPC FG-repeat composition in *S. cerevisiae* further reveals that perturbations of single transport receptors are associated with specific FG deletions (59, 60). This indicates that the NPC has multiple independent FG pathways, each used by different transport receptors. Moreover, with up- or down-regulation of transport receptor levels, nucleocytoplasmic translocation could also be affected by competition of transport receptors for FG pathways.

Large-Scale Regulatory Mechanisms at the NPC

The FG-Nups establish avenues for efficient trafficking of specific transport receptors, as highlighted above. In addition, the structural and barrier properties of NPCs broadly influence the transport of multiple receptors and cargoes simultaneously (Fig. 2, NPC). The integrity of this NPC barrier is potentially regulated by changes in Nup composition. Both the filamentous fungus *Aspergillus nidulans* and the starfish *Asterina miniata* undergo a semi-open mitosis (i.e., incomplete nuclear envelope breakdown) and disassemble only a fraction of their Nups during mitosis (12). The specific Nups are presumably targeted for disassembly by phosphorylation and result in mitotic NPCs that are more permeable. Furthermore, organisms that undergo a closed mitosis, such as *S. cerevisiae*, initiate changes to the NPC structure in a cell cycle–dependent, Nup phosphorylation–mediated mechanism to alter specific transport events (61, 62). The NPC substructural relocalization of yNup53 alters yKap121 binding sites, with direct consequences on nuclear import of yKap121 cargoes (61). Because yKap121 also contributes to the proper subcellular localization of the small ubiquitin-like modifier (SUMO) protease yUlp1, this could be the basis for modified septin deSUMOylation patterns in *nup53* and *kap121* mutants (63). Such temporal variation in NPC composition also appears in several developmental scenarios, wherein expression patterns of mNup50 and the pore membrane protein gp210 are restricted to specific tissues in mice (64, 65). Similarly, expression of the Nup *mbo* (homologous to mNup88 and yNup82) is tissue-specific in *Drosophila* (66), and *mbo* expression has an inhibitory effect on Crm1-mediated export (67). Even within a single *S. cerevisiae* nucleus, the differential localization of NPC-associated proteins suggests that subsets of NPCs have specialized transport functions (68).

Nuclear entry is critical for replication of most DNA and some RNA viruses, including poliovirus, rhinovirus, influenza, and vesicular stomatitis virus (69, 70), with each virus targeting a subset of Nups for degradation or selective inhibition. Disruption of NPCs skews the efficiency of individual transport receptors to favor trafficking of viral components. For example, influenza virus selectively inhibits the mRNA export factors mNxf1-Nxt1 (Fig. 3D), mRae1-Gle2, and mE1B-AP5, and also down-regulates mNup98 (Fig. 3E) (70). Cellular mRNA export requires these export factors and a specific binding site on mNup98, and thus is effectively disrupted. However, as viral RNA export is not dependent on these host mRNA export factors or binding sites, it is unaffected, as summarized in (70). This viral mechanism is in direct competition with interferon-γ mediated up-regulation of mNup98 (71). Ultimately, the balance between mNup98 induction and degradation affects the cellular outcome of the viral infection (70).

In addition to changes in Nup association affecting the translocation of specific receptors and the permeability barrier, the physical shape of NPCs might also be linked to transport regulation. Electron microscopy studies have found that NPCs vary in diameter and structure (72–75). However, it is unclear whether these different structures represent assembly intermediates, subsets of NPCs with specific functions, changes in NPC structure, or specialized cargo.

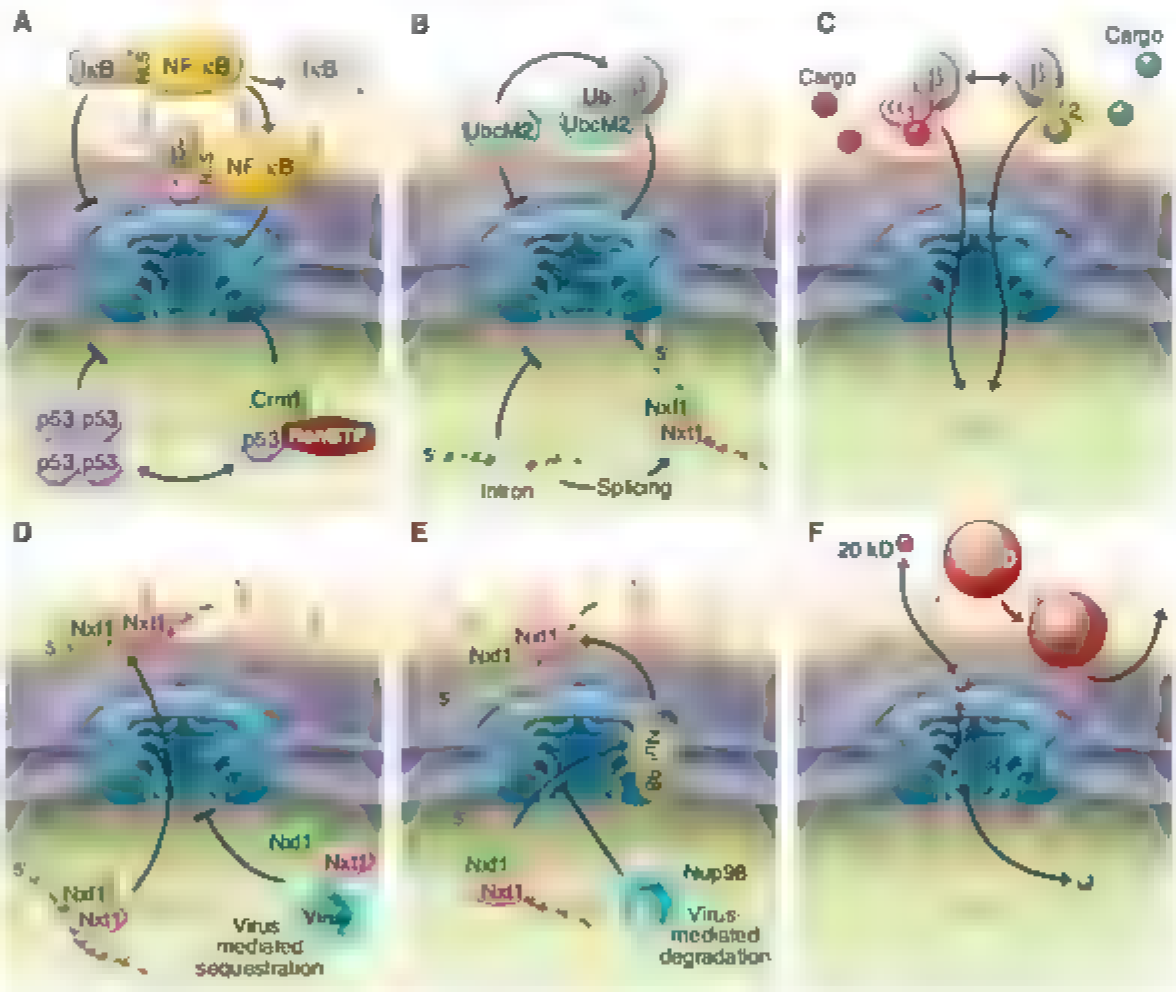

Fig. 3. Regulation of nucleocytoplasmic trafficking is dynamic and diverse. **(A)** Intermolecular and intramolecular interactions (NF-κB or p53, respectively) regulate trafficking of single cargoes. **(B)** Transport of individual cargoes is regulated by posttranslational modifications (ubiquitination of UbcM2) and posttranscriptional modifications (mRNA splicing). **(C)** Expression patterns of transport receptors alters cargo translocation. The expression of Kapα subtypes dictates which cargoes (color-coded hexagons) are imported. **(D)** Influenza virus sequesters the mRNA export receptor mNxf1-Nxt1, inhibiting cellular mRNA export. **(E)** NPC composition broadly affects transport. Influenza virus down-regulates mNup98, thus removing a key binding site for cellular mRNA export factors. **(F)** The NPC permeability barrier blocks free diffusion of large molecules (>40 kD or ~8 nm); smaller molecules move through independent of a transport receptor.

or consequences of specimen preparation. Despite a central aqueous channel diameter of ~10 nm (*76*), the NPC efficiently transports large cargoes such as 1 to 3 MD (~25 nm diameter) ribosomal subunits and proteasomal precursors (*19*, *76*). Artificial substrates up to 39 nm in diameter, such as transport receptor–coated gold particles, can also be translocated (*9*). Interestingly, the x-ray crystal structures of mNup58 and mNup45 indicate that these two Nups might slide along their common α-helical interaction surface (*77*). The interaction surface has the potential to shift by ~11 Å. Moreover, with both mNup58 and mNup45 located in the central NPC channel, circumferential Nup sliding is estimated to potentially increase the NPC diameter by up to ~30 Å, which might function to either regulate or accommodate large cargo translocation. The biophysical impact of this sliding on the interactions between other Nups is unclear, as are the mechanisms that could instigate these changes. Overall, there are multiple mechanisms by which changes to the NPC composition could broadly affect transport capacity and pore structure.

Next Steps in Understanding Transport Regulation

We have outlined the importance of regulated nucleocytoplasmic trafficking and have discussed how control is accomplished at multiple levels (Fig. 2). However, there are unanswered questions at each level. At the most fundamental stage, continued investigation is needed to further delineate the basic transport machinery. All the receptors used by various cellular cargoes and the precise signal sequences recognized are still not fully identified. Adding to the complexity, a single receptor can bind more than one signal motif without a readily identifiable primary consensus sequence (*78*). We also do not completely know how complex cargo molecules such as mRNPs are selected for targeting to the NPC through coupled maturation and quality control steps (*19*). Elucidating these cargo signals and how they are recognized by specific transport receptors will require multidisciplinary bioinformatic, structural, and cell biological approaches. As these cargoes and receptors are prime targets for regulation, this information could provide insight into a broad range of biological processes.

Given the hierarchical role of the NPC as the sole portal for nucleocytoplasmic exchange, understanding the NPC translocation mechanism is a priority. Specifically, studies are needed to resolve the biophysical nature of the permeability barrier and explain how translocation proceeds through this barrier (Fig. 3F). This will also require models that accommodate all the documented active and diffusive transport capacities of the NPC, as well as considerations of how interactions within and among cargoes, transport receptors, and Nups affect the stability of the NPC barrier. With this knowledge in hand, the field could make rational predictions and conduct tests for how transport would be affected by changes in Nup composition during viral infection, cell cycle transitions, signaling cascades, or cell differentiation.

There are clearly emerging examples of biological conditions under which cells broadly alter nuclear transport. This includes the interferon-γ–mediated up-regulation of mNup98, the cell cycle control of yNup53, and the change in cargo trafficking during neural stem cell differentiation (*48*, *61*, *71*). However, many of the mechanisms by which this occurs are not well defined. For example, it is not fully understood how heat shock–induced mRNA is preferentially exported under stress conditions in *S. cerevisiae* [as summarized in (*79*)]. Future studies of cell fate determination and development will reveal the prevalence of spatiotemporal regulation of transport receptor, adaptor, and Nup levels and the cargoes whose trafficking is affected. A further challenge is to integrate knowledge of this multitiered, hierarchical regulatory scheme involving cargoes, transport receptors, and the NPC into a global systems biology perspective of the coordination of cellular responses to internal and external stimuli.

References and Notes

1. M. P. Rout *et al.*, *J. Cell Biol.* **148**, 635 (2000).
2. J. M. Cronshaw, A. N. Krutchinsky, W. Zhang, B. T. Chait, M. J. Matunis, *J. Cell Biol.* **158**, 915 (2002).
3. S. I. Dworetzky, C. M. Feldherr, *J. Cell Biol.* **106**, 575 (1988).
4. E. J. Tran, S. R. Wente, *Cell* **125**, 1041 (2006).
5. M. P. Rout, S. R. Wente, *Trends Cell Biol.* **4**, 357 (1994).
6. B. Fahrenkrog *et al.*, *J. Struct. Biol.* **140**, 254 (2002).
7. D. P. Denning, S. S. Patel, V. Uversky, A. L. Fink, M. Rexach, *Proc. Natl. Acad. Sci. U.S.A.* **100**, 2450 (2003).
8. R. Y. Lim *et al.*, *Proc. Natl. Acad. Sci. U.S.A.* **103**, 9512 (2006).
9. N. Panté, M. Kann, *Mol. Biol. Cell* **13**, 425 (2002).
10. H. Fried, U. Kutay, *Cell. Mol. Life Sci.* **60**, 1659 (2003).
11. N. Shulga, D. S. Goldfarb, *Mol. Cell. Biol.* **23**, 534 (2003).
12. C. P. De Souza, S. A. Osmani, *Eukaryot. Cell* **6**, 1521 (2007).
13. M. Stewart, *Nat. Rev. Mol. Cell Biol.* **8**, 195 (2007).
14. S. Frey, R. P. Richter, D. Görlich, *Science* **314**, 815 (2006).
15. S. S. Patel, B. J. Belmont, J. M. Sante, M. F. Rexach, *Cell* **129**, 83 (2007).
16. R. Peters, *Traffic* **6**, 421 (2005).
17. L. F. Pemberton, B. M. Paschal, *Traffic* **6**, 187 (2005).
18. D. S. Goldfarb, A. H. Corbett, D. A. Mason, M. T. Harreman, S. A. Adam, *Trends Cell Biol.* **14**, 505 (2004).
19. A. Köhler, E. Hurt, *Nat. Rev. Mol. Cell Biol.* **8**, 761 (2007).
20. F. Fagotto, U. Gluck, B. M. Gumbiner, *Curr. Biol.* **8**, 181 (1998).
21. B. Friedrich, C. Quensel, T. Sommer, E. Hartmann, M. Köhler, *Mol. Cell. Biol.* **26**, 8697 (2006).
22. L. K. Pooe, D. A. Jans, *Traffic* **6**, 173 (2005).
23. M. D. Jacobs, S. C. Harrison, *Cell* **95**, 749 (1998).
24. T. Huxford, D. B. Huang, S. Malek, G. Ghosh, *Cell* **95**, 759 (1998).
25. J. M. Stommel *et al.*, *EMBO J.* **18**, 1660 (1999).
26. M. Kanai *et al.*, *Nat. Cell Biol.* **9**, 1175 (2007).
27. G. S. Jimenez, S. H. Khan, J. M. Stommel, G. M. Wahl, *Oncogene* **18**, 7656 (1999).
28. A. E. Hodel *et al.*, *J. Biol. Chem.* **281**, 23545 (2006).
29. D. Engelsma, R. Bernad, J. Calafat, M. Fornerod, *EMBO J.* **23**, 3643 (2004).
30. A. Komeili, E. K. O'Shea, *Science* **284**, 977 (1999).
31. J. Yang, H. Song, S. Walsh, E. S. Bardes, S. Kornbluth, *J. Biol. Chem.* **276**, 3604 (2001).
32. W. A. Smith, B. T. Schurter, F. Wong-Staal, M. David, *J. Biol. Chem.* **279**, 22795 (2004).
33. L. C. Trotman *et al.*, *Cell* **128**, 141 (2007).
34. S. M. Plafker, K. S. Plafker, A. M. Weissman, I. G. Macara, *J. Cell Biol.* **167**, 649 (2004).
35. A. K. Hopper, E. M. Phizicky, *Genes Dev.* **17**, 162 (2003).
36. Y. Li *et al.*, *Nature* **443**, 234 (2006).
37. B. Culjkovic, I. Topisirovic, L. Skrabanek, M. Ruiz-Gutierrez, K. L. Borden, *J. Cell Biol.* **175**, 415 (2006).
38. R. A. Kay *et al.*, *Cancer Res.* **65**, 10742 (2005).
39. K. V. Prasanth *et al.*, *Cell* **123**, 249 (2005).
40. H.-W. Hwang, E. A. Wentzel, J. T. Mendell, *Science* **315**, 97 (2007).
41. A. R. Alcázar-Román, E. J. Tran, S. Guo, S. R. Wente, *Nat. Cell Biol.* **8**, 711 (2006).
42. C. S. Weirich *et al.*, *Nat. Cell Biol.* **8**, 668 (2006).
43. J. D. York, A. R. Odom, R. Murphy, E. B. Ives, S. R. Wente, *Science* **285**, 96 (1999).
44. F. Stutz, E. Izaurralde, *Trends Cell Biol.* **13**, 319 (2003).
45. M. Kohler *et al.*, *Mol. Cell. Biol.* **19**, 7782 (1999).
46. M. Kohler *et al.*, *FEBS Lett.* **417**, 104 (1997).
47. M. V. Nachury, U. W. Ryder, A. I. Lamond, K. Weis, *Proc. Natl. Acad. Sci. U.S.A.* **95**, 582 (1998).
48. N. Yasuhara *et al.*, *Nat. Cell Biol.* **9**, 72 (2007).
49. G. Riddick, I. G. Macara, *Mol. Syst. Biol.* **3**, 118 (2007).
50. T. R. Kau, J. C. Way, P. A. Silver, *Nat. Rev. Cancer* **4**, 106 (2004).
51. E. Dahl *et al.*, *Clin. Cancer Res.* **12**, 3950 (2006).
52. V. Winnepenninckx *et al.*, *J. Natl. Cancer Inst.* **98**, 472 (2006).
53. S. P. Reid *et al.*, *J. Virol.* **80**, 5156 (2006).
54. M. Frieman *et al.*, *J. Virol.* **81**, 9812 (2007).
55. B. L. Timney *et al.*, *J. Cell Biol.* **175**, 579 (2006).
56. N. Mosammaparast, L. F. Pemberton, *Trends Cell Biol.* **14**, 547 (2004).
57. W. Yang, S. M. Musser, *J. Cell Biol.* **174**, 951 (2006).
58. D. S. Goldfarb, J. Gariepy, G. Schoolnik, R. D. Kornberg, *Nature* **322**, 641 (1986).
59. L. J. Terry, S. R. Wente, *J. Cell Biol.* **178**, 1121 (2007).
60. L. A. Strawn, T. Shen, N. Shulga, D. S. Goldfarb, S. R. Wente, *Nat. Cell Biol.* **6**, 197 (2004).
61. T. Makhnevych, C. P. Lusk, A. M. Anderson, J. D. Aitchison, R. W. Wozniak, *Cell* **115**, 813 (2003).
62. C. P. Lusk *et al.*, *Traffic* **8**, 647 (2007).
63. T. Makhnevych, C. Ptak, C. P. Lusk, J. D. Aitchison, R. W. Wozniak, *J. Cell Biol.* **177**, 39 (2007).
64. M. Olsson, S. Scheele, P. Ekblom, *Exp. Cell Res.* **292**, 359 (2004).
65. M. Smitherman, K. Lee, J. Swanger, R. Kapur, B. E. Clurman, *Mol. Cell. Biol.* **20**, 5631 (2000).
66. A. E. Uv *et al.*, *Genes Dev.* **14**, 1945 (2000).
67. F. Roth *et al.*, *J. Cell Biol.* **163**, 701 (2003).
68. V. Galy *et al.*, *Cell* **116**, 63 (2004).
69. K. E. Gustin, *Virus Res.* **95**, 35 (2003).
70. N. Satterly *et al.*, *Proc. Natl. Acad. Sci. U.S.A.* **104**, 1853 (2007).
71. J. Enninga, D. E. Levy, G. Blobel, B. M. A. Fontoura, *Science* **295**, 1523 (2002); published online 24 January 2002 (10.1126/science.1067861).
72. J. E. Hinshaw, R. A. Milligan, *J. Struct. Biol.* **141**, 259 (2003).
73. M. Beck *et al.*, *Science* **306**, 1387 (2004); published online 28 October 2004 (10.1126/science.1104808).
74. C. W. Akey, *J. Mol. Biol.* **248**, 273 (1995).
75. E. Kiseleva, M. W. Goldberg, T. D. Allen, C. W. Akey, *J. Cell Sci.* **111**, 223 (1998).
76. A. Lehmann, K. Janek, B. Braun, P. M. Kloetzel, C. Enenkel, *J. Mol. Biol.* **317**, 401 (2002).
77. I. Melcák, A. Hoelz, G. Blobel, *Science* **315**, 1729 (2007).
78. B. J. Lee *et al.*, *Cell* **126**, 543 (2006).
79. C. Kollenhagen, C. A. Hodge, C. N. Cole, *Eukaryot. Cell* **6**, 505 (2007).
80. M. W. Goldberg, T. D. Allen, *J. Mol. Biol.* **257**, 848 (1996).

81. We thank members of the Wente and Hardy labs for critical comments on this manuscript, and the authors who kindly provided reprints of their data in Fig. 3. We regret that space limitations prevent acknowledgement of all primary references and examples. Supported by NIH grants R01-GM51219 and R01-GM57438 (S.R.W.), National Research Service Award (NRSA) 5T32-CA009385 (L.J.T.), and NRSA 5T32-GM008554 (E.B.S.).

10.1126/science.1142204

Plants Tolerant of High Boron Levels

Kyoko Miwa,[1] Junpei Takano,[1] Hiroyuki Omori,[1] Motoaki Seki,[2] Kazuo Shinozaki,[2] Toru Fujiwara[1,3]*

Boron (B) is an essential nutrient for plants and animals, but in high concentrations it is toxic. Living organisms, including plants, must control the B distribution to maintain adequate levels of B in their cells. Reduced crop quality and yields in soils containing toxic levels of B are a worldwide problem in food production, especially in arid areas (1). By manipulating B transport, we have generated plants that are tolerant of high levels of B.

B accumulation occurs both naturally and through artificial means such as irrigation. About five million ha of soils containing greater than 15 mg kg^{-1} B, above the threshold for normal plant growth, exist in southern Australia, corresponding to 30% of the region (www.dwlbc.sa.gov.au/land/topics/mdzone/boron.html). Up to 17% of the barley yield loss in this area was estimated to be caused by B toxicity (2). B-tolerant cultivars with reduced B uptake are known for barley (3), but breeding programs have not yet produced a practical solution for B tolerance.

Arabidopsis thaliana BOR1, an efflux-type borate transporter, was the first B transporter identified in a biological system (4). BOR1 is required for the transport of B from roots to shoots under conditions of low B supply. BOR1 is capable of conferring high B tolerance to yeast by pumping boric acid out of the cell. However, in plants under high B conditions, BOR1 is degraded via endocytosis (5), and overexpression of *BOR1* does not improve plant growth in the presence of toxic levels of B (6).

We focused on *AtBOR4* (The *Arabidopsis* Information Resource code At1g15460 and GenBank code NM_101415), one of the six *BOR1* paralogs present in the *A. thaliana* genome. B transport activities of BOR4 and BOR4-green fluorescent protein (GFP) fusion were confirmed in yeast (fig. S1). We generated seven independent transgenic *A. thaliana* lines producing the BOR4-GFP fusion under the control of cauliflower mosaic virus 35S RNA promoter.

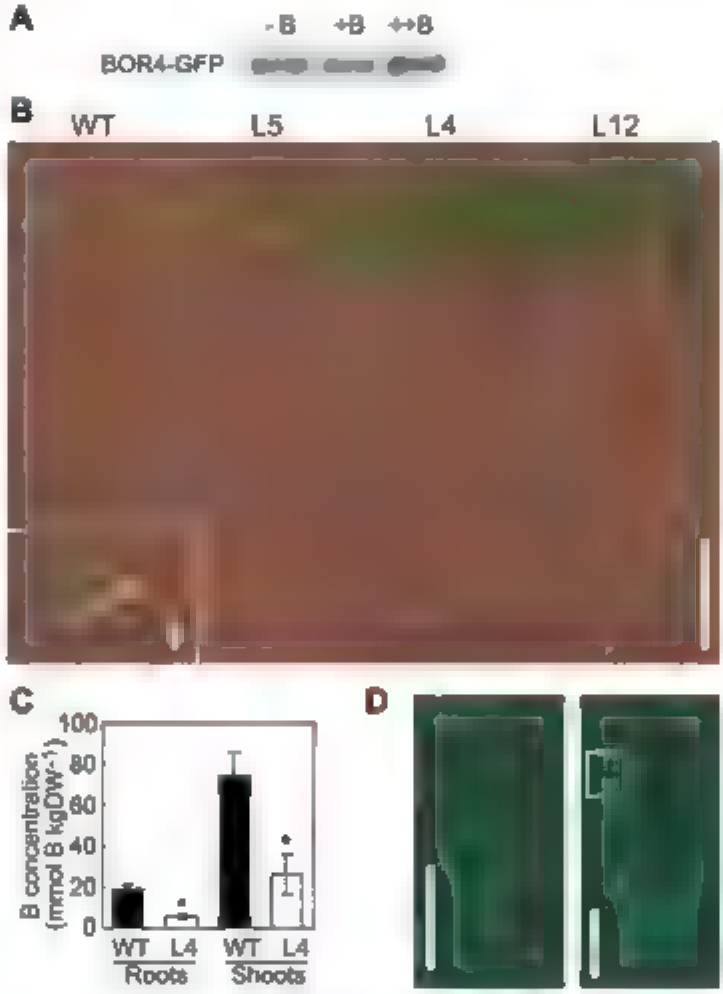

Fig. 1. Improved growth in transgenic *A. thaliana* plants overproducing BOR4 under conditions of boron toxicity. (**A**) Immunoblot analysis of transgenic plant line 4 carrying *Pro35S-BOR4-GFP*. Plants were exposed to 0.1 μM (-B), 30 μM (+B), or 3 mM (++B) boric acid for 3 days, and root microsomal proteins were subjected to immunoblotting with an antibody against GFP. (**B**) Transgenic plants grown for 17 days on solid medium containing 10 mM boric acid. Scale bar indicates 10 mm. (Inset) An enlargement of the wild-type plant (scale bar, 1 mm). WT, wild-type Col-0; L4, L5, L12, transgenic lines 4, 5, and 12, respectively, carrying the *Pro35S-BOR4-GFP* construct. (**C**) Total B concentrations in shoots and roots. Plants were grown on solid medium containing 3 mM boric acid for 18 days. Means ± SD are shown (n = 5 to 6). Asterisks indicate significant difference (P < 0.001) by Student's t test. DW, dry weight. (**D**) GFP fluorescence in roots of transgenic plants carrying the *ProBOR4-BOR4*-GFP construct. Plants were grown on solid medium containing 30 μM boric acid for 10 days. Scale bars, 25 μm (left) and 100 μm (right). The left-hand image is a magnified view of the area inside the box in the right-hand image.

Immunoblot analysis of a generated transgenic line showed that BOR4 accumulated in the presence of a high B supply (Fig. 1A), suggesting that BOR4 is exempt from the posttranslational BOR1 degradation system.

The supply of 10 mM boric acid was substantially lethal to wild-type plants, but much more vigorous root and shoot growth with varying degrees was observed in all the homozygous *Pro35S-BOR4-GFP* transgenic lines grown on solid medium containing 10 mM boric acid (Fig. 1B and fig. S2). Accumulation of BOR4-GFP and tolerance of B were positively correlated (fig. S2). The B concentrations in the roots and shoots of these transgenic plant lines were lower than that in the wild type in the presence of 3 mM boric acid (Fig. 1C). Overall tracer B uptake was also reduced in the transgenic line 4 (fig. S3). These results suggest that the overproduction of BOR4-GFP improved growth under conditions of B toxicity through B efflux.

Furthermore, GFP fluorescence derived from BOR4-GFP was strongly detected in the plasma membranes of the distal sides of epidermal cells in the elongation zone of roots of the transgenic lines carrying *ProBOR4-BOR4-GFP* (Fig. 1D). The distal localization of BOR4 is likely important for the directional export of B from the roots to the soil to prevent the accumulation of B in the xylem and growing cells. This enhanced B efflux from the roots of crop plants is expected to result in improved crop productivity in the B-toxic soils found in a number of regions of the world.

References and Notes

1. R. O. Nable, G. S. Bañuelos, J. G. Paull, *Plant Soil* **193**, 181 (1997).
2. B. Cartwright, B. A. Zarcinas, A. H. Mayfield, *Aust. J. Soil Res.* **22**, 261 (1984).
3. J. E. Hayes, R. J. Reid, *Plant Physiol.* **136**, 3376 (2004).
4. J. Takano *et al.*, *Nature* **420**, 337 (2002).
5. J. Takano, K. Miwa, L. Yuan, N. von Wirén, T. Fujiwara, *Proc. Natl. Acad. Sci. U.S.A.* **102**, 12276 (2005).
6. K. Miwa, J. Takano, T. Fujiwara, *Plant J.* **46**, 1084 (2006).
7. This work was supported in part by grants from the Japanese Society for the Promotion of Science to K.M. and the Greentechno Project from the Ministry of Agriculture, a Grant-in-Aid for Scientific Research on Priority Areas from the Ministry of Education, Culture, Sports, Science, and Technology of Japan, and a 21st Century Center of Excellence project to T.F.

Supporting Online Material

www.sciencemag.org/cgi/content/full/318/5855/1417/DC1
Materials and Methods
Figs. S1 to S3

18 June 2007; accepted 9 October 2007
10.1126/science.1146634

[1]Biotechnology Research Center, University of Tokyo, Tokyo 113-8657, Japan. [2]RIKEN Plant Science Center, Yokohama 230-0045, Japan. [3]Solution-Oriented Research for Science and Technology, Japan Science and Technology Agency, Tokyo 103-0027, Japan.

*To whom correspondence should be addressed. E-mail: atorufu@mail.ecc.u-tokyo.ac.jp

A β-Defensin Mutation Causes Black Coat Color in Domestic Dogs

Sophie I. Candille,[1*] Christopher B. Kaelin,[1*] Bruce M. Cattanach,[2] Bin Yu,[3] Darren A. Thompson,[3] Matthew A. Nix,[3] Julie A. Kerns,[1†] Sheila M. Schmutz,[4] Glenn L. Millhauser,[3] Gregory S. Barsh[1‡]

AUTHORS' SUMMARY

The marked spectrum of color and diversity of patterns that we see in mammals arises, unexpectedly, from variation in the quantity, quality, and regional distribution of just two types of pigment: black eumelanin and yellow pheomelanin. The appeal of unusual coat colors and patterns has motivated their selection in domestic animals, providing geneticists with a model for studying gene action and interaction that began a century ago and continues today. Most of the work has been carried out in laboratory mice, where studies of more than 100 different coat-color mutations have provided insight into stem cell biology (hair graying), biogenesis of intracellular organelles (pigmentary dilution), and hormone-receptor interactions (switching between the synthesis of eumelanin and pheomelanin).

The latter process—commonly known as pigment "type-switching"—is controlled primarily by the melanocortin system, in which a family of G protein–coupled receptors (identified by virtue of their response to α-melanocyte stimulating hormone or adrenocorticotropic hormone) has been implicated not only in pigmentation but also in cortisol production, body weight regulation, and exocrine gland secretion. In most mammals, pigment type-switching is controlled by two genes, the *Melanocortin 1 receptor* (*Mc1r*) and *Agouti*, which encode a seven transmembrane domain receptor and its extracellular ligand, respectively. Indeed, our current understanding of melanocortin biology stems from the identification in laboratory mice of *Mc1r* mutations as the cause of *recessive yellow* and *Agouti* mutations as the cause of *lethal yellow*.

Clarence Cook Little, who developed many of the original laboratory mouse strains and founded The Jackson Laboratory, was also one of the first dog geneticists. He recognized that dominant inheritance of a black coat was mediated differently in dogs than in other animals (*1*). Using classical linkage analysis, we realized that the *dominant black* gene represented a previously unrecognized component of the melanocortin pathway (*2*). Unexpectedly, we found the responsible gene to encode a β-defensin, a secreted protein previously studied for its role in immunity.

The identification of *dominant black* (formally, an allele of the *K* locus) rested on two major advances in dog genetics: the sequencing of the dog genome and recognition that the distinctive genetic structure of dog breeds allows for efficient gene mapping (*3*). Dogs were domesticated from wolves more than 15,000 years ago and expanded into a diverse population until the recent establishment of dog breeds. This population history is well-suited for high-resolution genetic mapping of old traits, like black coat color, that are found in multiple modern breeds. Using a combination of pedigree analysis and association studies within and among dog breeds, we identified a mutation in a β-defensin gene, *CBD103*, that correlates with black coat color in 38 different breeds. We confirmed the role of *CBD103* in pigment type-switching by demonstrating that the dog gene causes a black coat in transgenic mice. CBD103 is a member of a large family of secreted peptides with structures similar to that of Agouti and is highly expressed in dog skin.

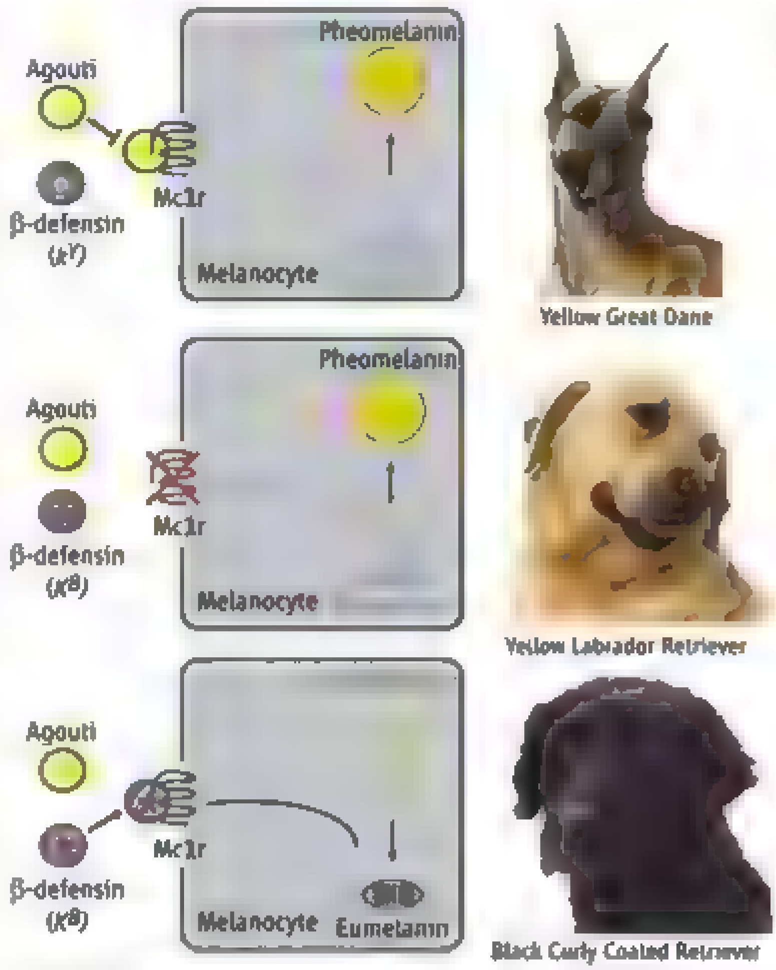

Production of yellow versus black pigment in dogs is controlled by three genes, *Mc1r*, *Agouti*, and *CBD103*. Dogs carrying wild-type alleles for all three genes have a yellow coat resulting from Agouti antagonism of Mc1r signaling in melanocytes (yellow Great Dane, top). Dogs carrying a loss-of-function mutation at *Mc1r* have a yellow coat, regardless of their genotype at *Agouti* or *CBD103* (yellow Labrador Retriever, middle). Dogs carrying wild-type alleles for *Mc1r* and *Agouti*, together with the *dominant black* allele of *CBD103* (K^B) have a black coat resulting from the interaction between a β-defensin and Mc1r (black Curly Coated Retriever, bottom).

We used biochemical and cell-based assays to show that CBD103, like Agouti, binds competitively to the Mc1r, leading to an updated model of the pigment type-switching pathway (see figure). Moreover, studies with another β-defensin and additional melanocortin receptors reveal the potential for extensive cross-talk between β-defensins and the melanocortin system. In humans and other animals, β-defensins are highly polymorphic in sequence and copy number. Current β-defensin research is focused primarily on the immune system. This stems from the early discovery of defensins in phagocytic cells and their antimicrobial properties in vitro, together with more recent work demonstrating that defensins can act as receptor-specific chemotactic agents. Our work indicates that β-defensins do more than defend and suggests that the marked molecular variation in this family supplies a diverse and rapidly evolving family of ligands for G protein–coupled receptors in many different biologic systems.

Summary References

1. C. C. Little, *The Inheritance of Coat Color in Dogs* (Comstock, Ithaca, NY, 1957).
2. J. A. Kerns *et al.*, *Genetics* **176**, 1679 (2007).
3. K. Lindblad-Toh *et al.*, *Nature* **438**, 803 (2005).

FULL-LENGTH ARTICLE

Genetic analysis of mammalian color variation has provided fundamental insight into human biology and disease. In most vertebrates, two key genes, *Agouti* and *Melanocortin 1 receptor* (*Mc1r*), encode a ligand-receptor system that controls pigment type-switching, but in domestic dogs, a third gene is implicated, the *K* locus, whose genetic characteristics predict a previously unrecognized component of the melanocortin pathway. We identify the *K* locus as β-*defensin 103* (*CBD103*) and show that its protein product binds with high affinity to the Mc1r and has a simple and strong effect on pigment type-switching in domestic dogs and transgenic mice. These results expand the functional role of β-defensins, a protein family previously implicated in innate immunity, and identify an additional class of ligands for signaling through melanocortin receptors.

Genetic analysis of model systems in laboratory animals underlies much of what we know about major signaling pathways in multicellular organisms. In mammals, coat-color mutations have proven especially fruitful, because much of the molecular machinery used by the pigmentary system is either shared by, or homologous to, genes used for other physiologic pathways (*1*).

This approach has been particularly useful for pigment "type-switching," a phenomenon in which melanocytes synthesize eumelanin (a black or brown pigment) versus pheomelanin (a red or yellow pigment), depending on the phase of the hair growth cycle, position on the body, and the genotype of several key loci (*2*). In most mammals, two genes that control pigment type-switching have been recognized: the *Mc1r*, which encodes a seven transmembrane–spanning domain protein expressed on melanocytes (*3*–*5*), and *Agouti*, which encodes a ligand for the Mc1r that is secreted by specialized dermal cells and which inhibits Mc1r signaling (*6*–*9*). Mc1r activation causes exclusive production of eumelanin, whereas Mc1r inhibition causes exclusive production of pheomelanin (*5*, *10*). Thus, gain-of-function *Mc1r* mutations cause dominant inheritance of a black coat, whereas gain-of-function *Agouti* mutations cause dominant inheritance of a yellow coat. The Mc1r was first recognized by virtue of its ability to respond to peptides derived from proopiomelanocortin (POMC), such as α-melanocyte stimulating hormone (α-MSH) (*3*, *4*); however, a null mutation of *Pomc* has no effect on pigmentation in C57BL/6 mice, leading to the suggestion that the Mc1r has high basal activity and/or additional stimulatory ligands (*11*).

In a classic series of papers in the early 1900s, Sewall Wright (*12*) concluded that genetic mechanisms for color variation were largely conserved across mammals. An exception, however, later became apparent from the work of Clarence Cook Little on domestic dogs (*13*), in which dominant inheritance of a black coat was shown to involve a locus distinct from *Mc1r*. At the time, Little posited that *dominant black* was caused by an unusual allele of *Agouti*; however, using molecular linkage analysis, we recently demonstrated the presence of a third gene in dogs that interacts with *Agouti* and *Mc1r*, which we named the *K* locus (*14*). We found that the *K* locus has three alleles with a simple dominance order [*Black* (K^B) > *brindle* (k^{br}) > *yellow* (k^y)], that the *K* locus and *Agouti* behave similarly in genetic interaction studies (*Mc1r* is epistatic to both *K* and *Agouti*), and that the genetic map position of *K* does not correspond to the predicted location of any previously known pigmentation gene. We use the distinctive evolutionary history of domestic dogs to show that the *K* locus encodes a previously unrecognized class of melanocortin receptor ligands.

Linkage and association mapping of the *K* locus. We showed previously that the K^B mutation mapped to a 12-Mb interval on the distal end of dog chromosome 16 (CFA16), between markers REN292N24 and FH3592 (*14*). We ascertained additional kindreds segregating K^B, k^{br}, and k^y to refine the map location [see supporting online material (SOM) text] and defined overlapping critical regions of 3.8 and 7.6 Mb for the K^B and k^{br} mutations, respectively (Fig. 1A and figs. S1 to S4).

We used an association-based strategy to narrow the critical region. Because most breeds were derived in the past 200 years from small founding populations (*15*), mutations within a breed are expected to be identical by descent and share extended haplotypes. In Boxers and Great Danes, we identified broad peaks of significant association (Bonferroni-corrected *P* value < 0.05) that extended over 1.9 Mb and 320 kb, respectively (Fig. 1, B to D). Sixteen genes have been annotated to the region of significant association in Great Danes, including a gene cluster that encodes 12 β-defensins (*16*), small antimicrobial peptides that are secreted mainly by epithelial cells (*17*, *18*). We sequenced the mature protein-coding regions for nine members of the β-defensin cluster (those known at the time) in dogs carrying K^B and/or k^y and identified several polymorphisms concordant with the K^B allele, including a 3–base pair (bp) deletion in the second exon of *CBD103*, the ortholog of human *DEFB103*, that predicts an in-frame glycine deletion (ΔG23).

To evaluate the extent to which the ΔG23 polymorphism distinguishes K^B versus k^y more broadly, we examined dogs from 38 breeds that could be classified into two categories with regard to their putative *K* locus genotype (SOM text). Among 454 dogs, there were 13 cases where the ΔG23 polymorphism did not correlate with coat-color phenotype. However, sequencing of *Agouti* and *Mc1r* revealed that each discordant case could be explained by known epistatic interactions (*19*, *20*) (table S3). These results indicate that K^B alleles in all breeds are probably identical by descent and suggest that the ΔG23 polymorphism or a closely linked variant in complete linkage disequilibrium (LD) is the K^B mutation.

Short-range haplotype and resequencing analysis of K^B-bearing chromosomes. By contrast to the pattern of LD within breeds, which affords a powerful approach for association mapping with megabase resolution, the pattern of LD across breeds is more fine-grained and therefore provides the opportunity for high-resolution haplotype mapping when mutations in different breeds are identical by descent (*21*). We identified 28 polymorphisms [22 single-nucleotide polymorphisms (SNPs) and six indels including the ΔG23 polymorphism] in a 20-kb interval surrounding *CBD103* that were then used to infer short-range haplotypes for 14 K^B-bearing and 16 k^y-bearing chromosomes selected from seven breeds (SOM text). We observed six "parental" k^y-bearing and five "parental" K^B-bearing chromosomes (depicted in yellow and blue, respectively, in Fig. 2A). We also identified eight chromosomes that carried a single ancestral recombination event, which together defined a maximal interval for K^B of 9146 bp (Fig. 2A). Complete resequencing of this interval (except for three homopolymer tracts) in five k^y/k^y animals, one K^B/k^y animal, and four K^B/K^B animals from seven breeds revealed two polymorphisms besides ΔG23 that are perfectly concordant with *K* locus genotype (S104 and S105) (Fig. 2A and table S2).

The 9146-bp interval contains both exons of *CBD103*, the first exon of dog expressed sequence tag (EST) CX990240, and dog EST CO665262 (Fig. 2). However, several considerations indicate that *CBD103* is, indeed, the

[1]Departments of Genetics and Pediatrics, Stanford University, Stanford, CA, USA. [2]Medical Research Council (MRC) Mammalian Genetics Unit, Harwell, Oxfordshire, OX11 0RD, UK. [3]Departments of Chemistry and Biochemistry, University of California at Santa Cruz (UCSC), Santa Cruz, CA 95064, USA. [4]Department of Animal and Poultry Science, University of Saskatchewan, Saskatoon S7N 5A8, Canada.

*These authors contributed equally to this work.
†Present address: Fred Hutchinson Cancer Research Center, Seattle, WA 98109, USA.
‡To whom correspondence should be addressed. E-mail: gbarsh@stanford.edu

K locus and that the ΔG23 deletion in *CBD103* is the K^B mutation. First, the other two transcribed elements in the critical interval are represented in the database by single ESTs and are not known to encode proteins or to be expressed in the skin. Second, S104 and S105 lie in a long terminal repeat element that is 3 kb upstream of the first exon of *CBD103* and have no effect on mRNA levels of *CBD103* (Fig. 3A). Finally, as discussed further below, *CBD103* is highly expressed in skin, the ΔG23 deletion affects CBD103 protein function, and pharmacologic studies reveal that CBD103 can modulate melanocortin signaling.

The preceding discussion has referred to K locus variation as though K^y is ancestral, whereas K^B is derived: a hypothesis based on the comparative genetic distribution of coat-color phenotypes and inheritance patterns. Considerations based on sequence alignments confirm this hypothesis. Mammalian *CBD103* orthologs that we identified from the available genome sequence are each 67 amino acids in length, and the optimal sequence similarity alignment contains no gaps or insertions (Fig. 2B), indicating that ΔG23 and consequently the K^B mutation occurred specifically within the canid lineage.

Expression of dog defensins in skin and in transfected keratinocytes. We isolated RNA from the skin of a k^y/k^y Doberman Pinscher and a K^B/k^y mixed-breed dog and surveyed the expression of the 19 β-defensin genes that are clustered on chromosomes 16 or 25 by reverse transcription polymerase chain reaction (RT-PCR) (*16*). Expression was detectable only for two genes: *CBD1* and *CBD103* (fig. S6). We then used quantitative RT-PCR to measure levels of skin mRNA from four K^B/k^y samples and four k^y/k^y samples, which were all from mixed-breed dogs, and found no effect of K locus genotype on levels of *CBD1*, *CBD103*, or *Agouti* mRNA (Fig. 3A).

Available antisera against human DEFB103 are unable to detect the endogenous dog protein by Western blotting or immunohistochemistry; therefore, we generated epitope-tagged expression constructs for each allele (CBD103V5 and CBD103ΔG23V5) and studied their patterns and levels of protein expression after transfection of cultured mouse keratinocytes.

In cell extracts analyzed by Western blotting, antisera against the V5 epitope detect a single fragment whose size (about 8 kD) corresponds to the expected molecular mass of the tagged protein after signal peptide cleavage; in media, an additional slightly smaller band is present, which suggests additional processing (Fig. 3B). The relative ratios of the two bands are similar in media from keratinocytes transfected with either construct; however, the total amount of immunodetectable protein in media was significantly greater for CBD103ΔG23V5 as compared with that for CBD103V5 (P = 0.0021, Cochran-Mantel-Haenszel chi-square test). Thus, loss of the N-terminal glycine from CBD103 does not affect intracellular processing but allows more of the mature protein to accumulate in the media and/or extracellular space.

CBD103 activity in vivo and in vitro. To further explore the function of *CBD103* in an experimental genetic system, we generated transgenic mice in which a cDNA encoding either the K^B or the k^y allele was driven by a strong and widely expressed promoter (*22*). We chose a genetic background that normally has Agouti-banded hairs and observed that two transgenic founders generated with the *CBD103ΔG23* cDNA (the K^B allele) displayed a predominantly black coat with small patches of banded hair (Fig. 4). Unexpectedly, the normal *CBD103* cDNA (the k^y allele) also produced transgenic mice with a black coat in 20 out of 21 founders (Fig. 4). Furthermore, we observed that transgenic animals were smaller than their nontransgenic littermates. By 2 weeks of age, female transgenic animals were easily recognized by their dark coat and small size; in adult mice, reduced body weight persists in both males and females (fig. S7).

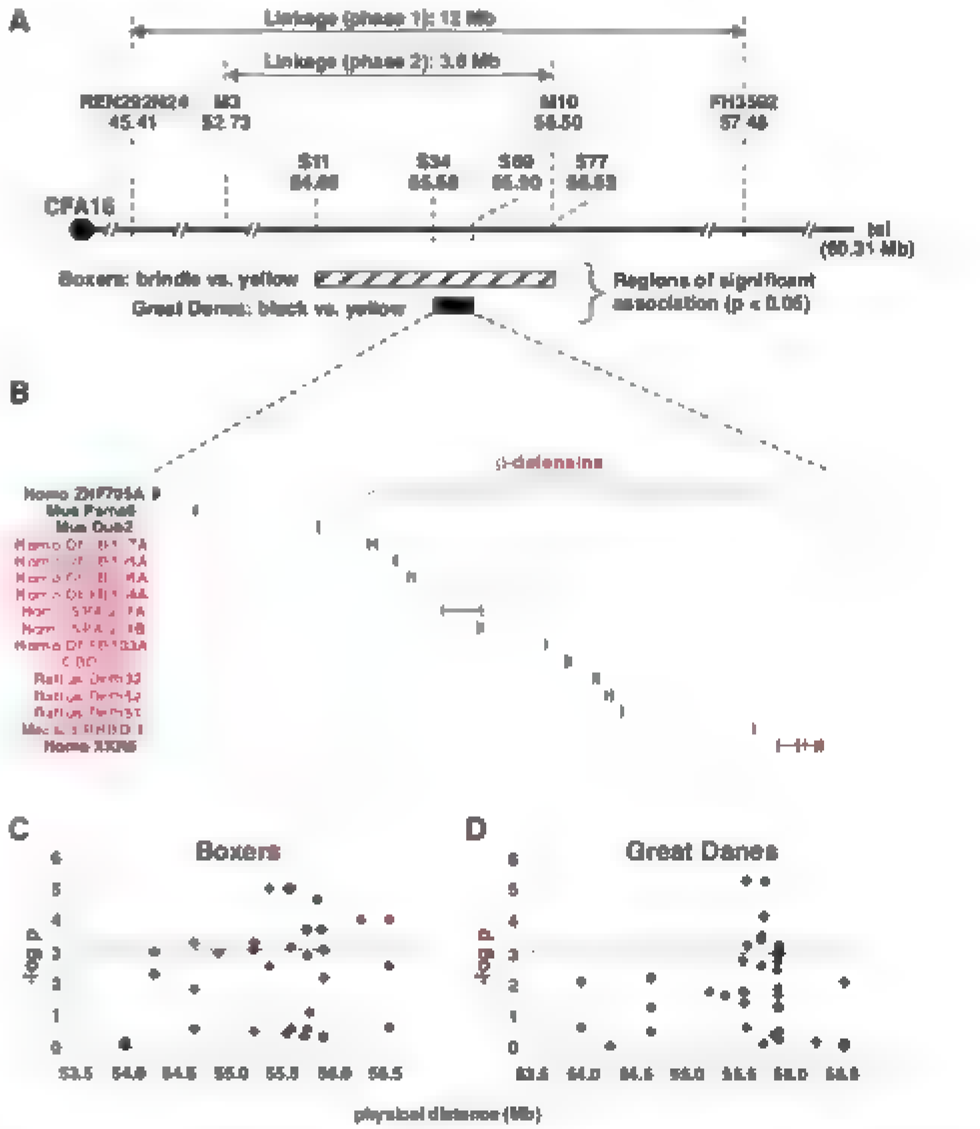

Fig. 1. Genetic mapping of the *K* locus. (**A**) Initial linkage studies [phase 1, (*14*)] defined a 12-Mb critical region for K^B; ascertainment and characterization of additional kindreds narrowed the interval to 3.8 Mb (phase 2; figs. S1 to S4). Association analysis for 60 markers in brindle (n = 12) versus yellow (n = 10) Boxers, and for 51 markers in black (n = 9) versus yellow (n = 10) Great Danes, was carried out as described in the text. (**B**) Candidate genes in the 320-kb region of greatest association in Great Danes; this region includes 12 β-defensin genes (shown in red). (**C** and **D**) Significance, plotted as –log of P values from a chi-square test of allele counts, is shown as a function of distance along CFA16 (only for SNPs present at greater than 10% frequency and genotyped in at least 75% of the samples). The dashed red line indicates a Bonferroni-corrected 5% significance level; these regions are indicated by hatched and black bars for Boxers and Great Danes, respectively, in (A). Annotation is based on the Non-dog RefSeq track in the UCSC Genome Browser, except for CBD102, identified by Patil *et al.* (*16*).

These considerations suggest three possible mechanisms by which CBD103 might act to modulate melanocortin signaling: (i) by binding to and activating the Mc1r, (ii) by binding to the Mc1r and preventing its inhibition by Agouti protein, or (iii) by binding to Agouti protein leading to its sequestration and/or degradation. To distinguish among these ideas, we generated synthetic forms of CBD103 and tested their ability to interact with the Mc1r and agouti signaling protein YY (ASIP-YY), a synthetic version of the C terminus of Agouti protein that behaves as a competitive antagonist of α-MSH at the Mc1r and Mc4r (23).

The *CBD103* k^y allele predicts a mature peptide (after signal sequence cleavage) of 45 amino acids that contains six cysteine residues and begins with the glycine that is deleted in the K^B allele (Fig. 2B). The predicted signal sequence cleavage site is supported by biochemical studies of the orthologous human protein [known as DEFB103 or human β-defensin 3 (HBD3)] purified from human tissues (*24*). We synthesized the 45-residue k^y form and 44-residue K^B form of the dog protein (hence referred to as CBD103 and CBD103ΔG23, respectively), allowed oxidative refolding, and used mass spectrometry and high-performance liquid chromatography to confirm recovery of a single congener with three intrachain disulfide bonds.

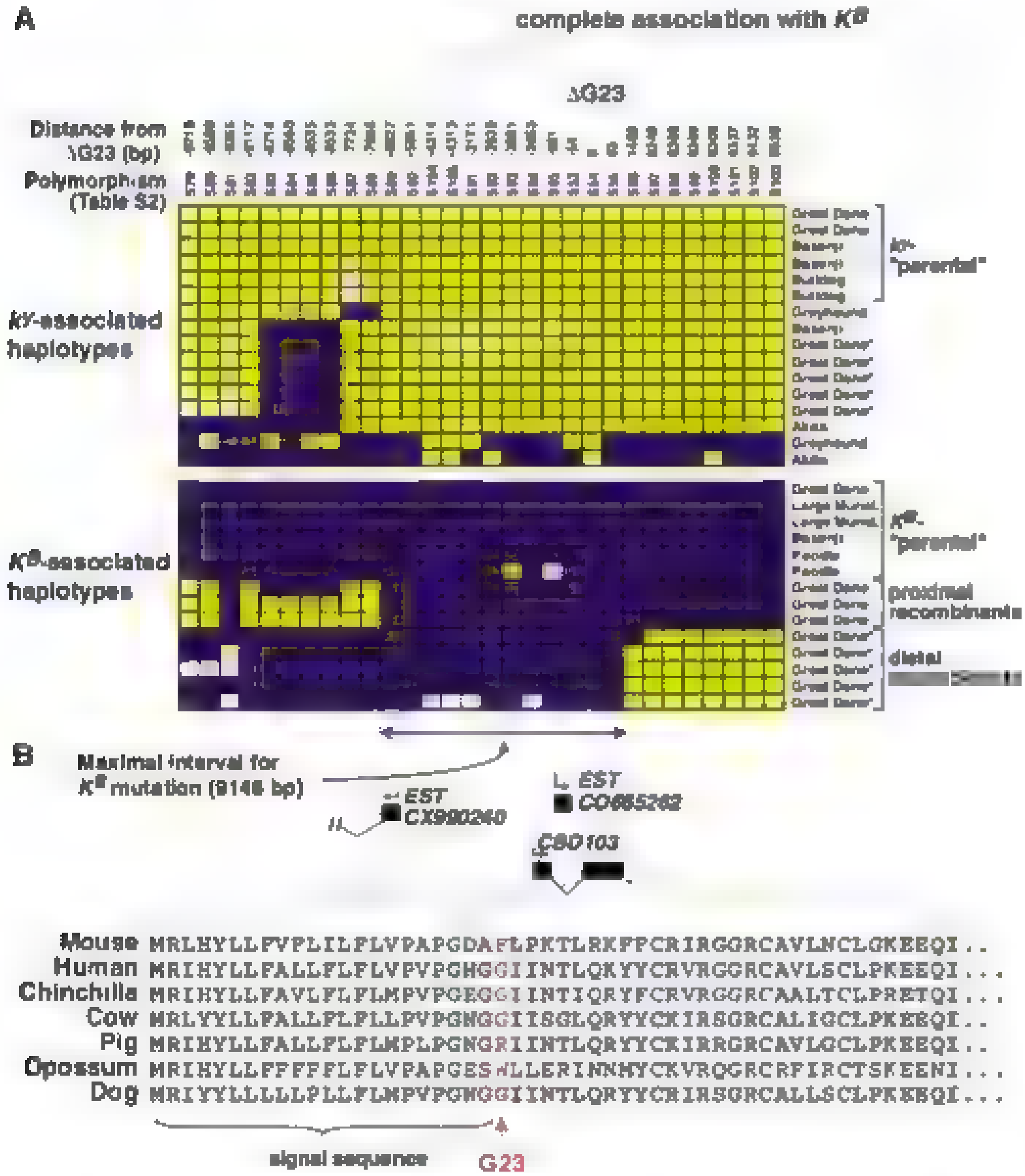

Fig. 2. Resequencing and recombinant haplotype-based mutation analysis for K^B-bearing versus k^y-bearing chromosomes. **(A)** A 20-kb region surrounding *CBD103* ΔG23 was resequenced (except for repetitive regions) in 10 dogs from 7 breeds, and haplotypes were inferred for 28 high-frequency biallelic polymorphisms. Blue and yellow squares represent the major and minor alleles in K^B-bearing chromosomes, respectively, and allow some haplotypes to be designated as "k^y-parental," "K^B-parental," or "proximal recombinant," as indicated. White squares represent missing data. Genotypes for five Great Danes (denoted by asterisks) were determined in a second resequencing round targeted specifically for distal recombinants as described in the SOM text. Within the 9.1-kb interval defined by recombinant haplotype analysis, three polymorphisms are completely associated with K^B versus k^y, as indicated in the upper part of the figure. **(B)** Exon structure of transcripts within the maximal candidate interval and alignment of selected CBD103 orthologs (*38*).

Nle^4-D-Phe^7-α-MSH (NDP-MSH), a potent derivative of α-MSH, stimulates robust accumulation of cyclic adenosine monophosphate (cAMP) in melanocytes (*25*). However, neither CBD103 nor CBD103ΔG23 has any effect on cAMP accumulation (Fig. 5A), indicating that CBD103 is not a conventional Mc1r agonist. To test for receptor binding, we transiently transfected human embryonic kidney (HEK) 293 cells with Mc1r expression constructs (*22*) and used europium-labeled NDP-MSH (Eu-NDP-MSH) as a fluorescent tracer. We used saturation binding assays to first calculate the affinity of Eu-NDP-MSH for the dog Mc1r (Fig. 5B) and then carried out displacement assays with progressively increasing concentrations of CBD103, CBD103ΔG23, or ASIP-YY. All three peptides exhibited qualitatively similar profiles characteristic for competitive binding to a single high-affinity site (Fig. 5C and Table 1). Quantitatively, inhibition constant (K_i) values estimated from the data depicted in Fig. 5C were 150.6 nM for CBD103 and 34.2 nM for CBD103ΔG23. These estimates varied according to experimental conditions, but CBD103ΔG23 consistently exhibited higher affinity for the dog Mc1r than did CBD103 (mean of fivefold across four paired experiments, Table 1). In these same experiments, ASIP-YY exhibited K_i values of 0.51 to 0.95 nM for the dog Mc1r, in the same range as reported previously for ASIP-YY at the human Mc1r (*23*). Using quantitative RT-PCR, we found that the levels of *CBD103* mRNA in total skin were ~300-fold greater than that of *Agouti* mRNA; to the extent that this difference reflects protein abundance, the levels of CBD103ΔG23 in dog skin are likely to be much greater than those of Agouti protein, which is consistent with a model in which CBD103ΔG23 competitively inhibits the ability of Agouti protein to antagonize Mc1r signaling.

Finally, we investigated a potential interaction between Agouti protein and CBD103 by preincubating ASIP-YY with either CBD103 or CBD103ΔG23 before the binding assay, and we found no evidence for a functional interaction (fig. S8). We also examined the effects of mixing the two peptides on two-dimensional nuclear magnetic resonance spectra and found no evidence for a structural interaction. Taken together, these observations indicate that CBD103 is a high-affinity ligand for the Mc1r and that the ΔG23 mutation may cause a black coat color in dogs via two different mechanisms: increased affinity for the Mc1r and increased availability of the mature protein in vivo.

Other mammals, other melanocortin receptors, and other defensins. Dogs are the only mammals known for which dominant

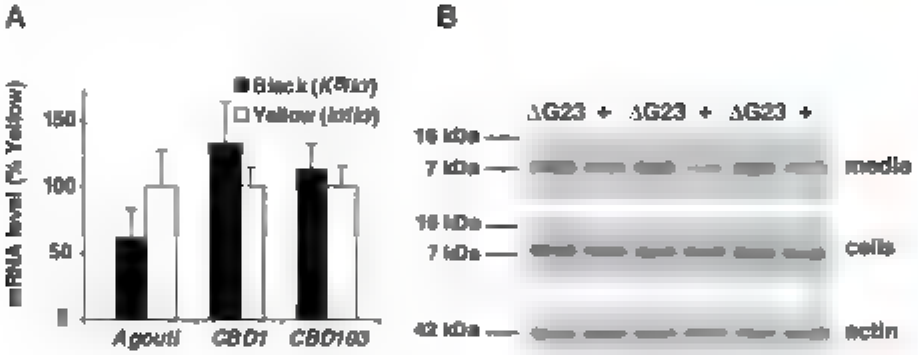

Fig. 3. Expression of β-defensin mRNA and protein in skin and in cultured keratinocytes. (**A**) Levels of *Agouti*, *CBD1*, or *CBD103* mRNA from black or yellow dog skin, as indicated, determined relative to *Bactin* by quantitative RT-PCR, and expressed as percentage of mRNA present in the yellow samples. Results shown represent the mean ± SEM of four different animals. (**B**) Expression of epitope (V5)–tagged CBD103 (+) or epitope (V5)–tagged CBD103ΔG23 (ΔG23) in cell layer and media after transfection of mouse keratinocytes as determined by Western blotting with antisera against the V5 epitope. Representative results are shown for one of four experiments; for each experiment, the two constructs were transfected in triplicate or quadruplicate.

Fig. 4. Pigmentary effects of *CBD103* in transgenic mice. Photographs of transgenic (Tg) and nontransgenic littermates, representative of 2/2 independent founders for Tg.CBD103ΔG23 and 20/21 independent founders for Tg.CBD103.

Table 1. Affinity constants for melanocortin receptor ligands. In the column for Eu-NDP-MSH, saturation binding assays as depicted in Fig. 5B were used to derive dissociation constant (K_d) values (in nM) by fitting the data to a hyperbolic dose response curve with the use of nonlinear regression. In the remaining columns, displacement binding assays as depicted in Fig. 5, C to F, were used to derive K_i values (in nM) by fitting the data to a sigmoidal dose-response curve with variable slope. For some ligand-receptor combinations, multiple experiments were carried out, in which case the mean K_i value is given followed by the range and number (in parentheses) of the separate experiments. ND, not determined.

Receptor	Eu-NDP-MSH	ASIP-YY	CBD103ΔG23	CBD103	HBD1	HBD3
Dog Mc1r	0.70	0.59 (0.51–0.95) (n = 3)	37.0 (16.4–61.1) (n = 5)	221.0 (150.6–398.7) (n = 4)	ND	ND
Mouse Mc1r	1.38	2.30	15.1 (12.4–17.0) (n = 4)	9.7 (8.9–10.4) (n = 2)	ND	ND
Human Mc1r	2.59	0.95	19.6 (12.3–26.8) (n = 2)	35.5	30.0	13.8
Human Mc4r	3.17	0.82	104.5	ND	ND	ND

inheritance of black coat color is not caused by a *Mc1r* mutation. However, we observed that both CBD103 and CBD103ΔG23 are high-affinity ligands for the mouse (Fig. 5D) and the human (Fig. 5E) Mc1r, with estimated K_i values that were, unexpectedly, lower than that observed at the dog Mc1r (Table 1). Furthermore, unlike at the dog Mc1r, the affinity of CBD103 as compared to that of CBD103ΔG23 was similar at both the mouse and the human Mc1r (Table 1), which may explain why expression of either allele caused a black coat in transgenic mice (Fig. 4).

Given the effects of the *CBD103* transgenes on body size, we investigated the potential for cross-talk between β-defensins and other melanocortin receptors. We found that CBD103ΔG23 binds to the human Mc4r with an intermediate affinity (K_i = 104.5 nM) between that of CBD103ΔG23 and CBD103 for the dog Mc1r (Table 1 and Fig. 5E). We also synthesized HBD3, the human ortholog of canine CBD103, and observed high-affinity binding (K_i = 13.8 nM) to the human Mc1r (Table 1 and Fig. 5F). Finally, we tested human β-defensin 1 (HBD1), which lies in the same cluster as HBD3 but is more distantly related; HBD1 also exhibited high-affinity binding to the human Mc1r (K_i = 30 nM) (Table 1 and Fig. 5F).

Defensins and melanocortin signaling. β-defensin genes exhibit strong signatures of diversifying selection (*26*, *27*), which is consistent with their proposed role as endogenous antibiotics. Confirming and studying this role in vivo, however, have been challenging; the results of mouse knockout experiments have been reported for only one gene, *Defb1*, and revealed no obvious effects on viability or innate defense (*28*). By contrast, the *CBD103 K^B* mutation causes a marked change in hair color that is readily apparent among a large number of dog breeds with diverse genetic backgrounds. We propose that β-defensin genes play a broader role than currently envisaged, in which the ability to modulate melanocortin receptor signaling may have been selected during vertebrate evolution to provide camouflage and/or adaptive visual cues. From this perspective, evolutionary lability of the β-defensins with regard to both diversifying selection and copy number variation (*26*, *27*, *29*) may represent a response to a shifting spectrum of environmental challenges that includes microbial pathogens, carnivorous predators, and nutrient availability. More generally, our biochemical studies indicate that at least two human β-defensins, HBD1 and HBD3, may also modulate melanocortin receptor signaling in vivo. Both genes are expressed by a broad range of epithelial and other tissues (*18*) and could therefore act not only on Mc1r but also on other melanocortin receptors, including Mc5r, for which an endogenous melanocortin ligand has not yet been identified. The range of K_i values that we observed suggests that CBD103ΔG23, and potentially HBD1 or HBD3, modulate pigmentation in the low nanomolar range; however, the antimicrobial effects of β-defensins are typically observed in the low micromolar range (*30*). Finally, several β-defensins promote chemotaxis of immune cells, and although there is controversy regarding which receptors are involved, there is a growing consensus that β-defensins contribute to adaptive as well as to innate immunity (*31*–*33*). From this perspective, several studies have pointed to a role for Mc1r signaling in immune cell function (*34*), which could be mediated by β-defensins acting as melanocortin receptor ligands.

Modulation of melanocortin receptor signaling by β-defensins may also help explain

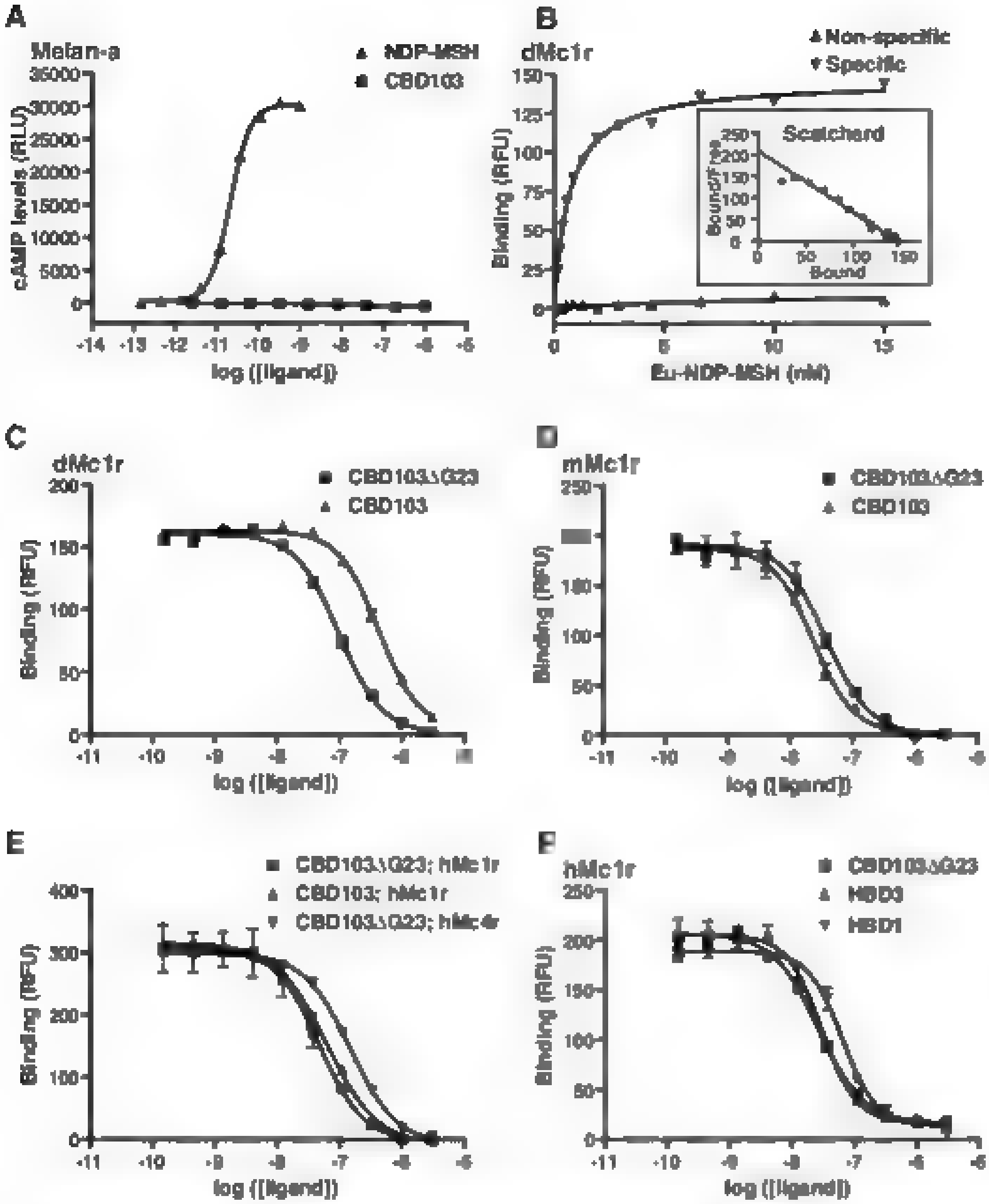

Fig. 5. Pharmacology of β-defensin action on melanocortin receptors. (**A**) Ability of NDP-MSH or CBD103 to stimulate cAMP accumulation in cultured melanocytes. (**B**) Saturation binding of Eu-NDP-MSH to HEK293 cells transiently transfected with the dog Mc1r. (**C** to **F**) Competition binding assays in which varying amounts of unlabeled synthetic β-defensins were added together with Eu-NDP-MSH tracer (at 1.8 to 3 nM) to HEK293 cells transiently transfected with dog (d), mouse (m), or human (h) melanocortin receptors, as indicated. In all panels, ligand concentration [either in nM (B) or log of the molarity [(A) and (C) to (F)]] is plotted on the abscissa; amount of cAMP formed (A) or Eu-NDP-MSH bound [(B) to (F)], measured, respectively, as relative light units (RLUs) or relative fluorescent units (RFUs), is plotted on the ordinate. Each curve represents a single experiment carried out in triplicate; error bars represent SEM.

the apparent paradox that mutations of *Pomc* have a relatively minor effect on pigmentation (*11*, *35*–*37*). These observations have been often interpreted as evidence that melanocortin receptors have high levels of constitutive activity, but our results suggest that β-defensins may raise "basal" levels of melanocortin receptor signaling in the absence of melanocortin peptides.

Much of the early work on melanocortin signaling was driven by ideas associated with the way in which *Pomc* had been discovered and named; additional biological functions of melanocortins in behavior and energy homeostasis did not become apparent for decades. An analogous situation may apply in the case of β-defensins, which underscores the utility of phenotype-driven genetics to provide an agnostic view of gene function.

References and Notes

1. D. C. Bennett, M. L. Lamoreux, *Pigment Cell Res.* **16**, 333 (2003).
2. G. S. Barsh, in *The Pigmentary System*, J. J. Nordlund *et al.*, Eds. (Blackwell, Oxford, 2006), pp. 395–410.
3. V. Chhajlani, J. E. Wikberg, *FEBS Lett.* **309**, 417 (1992).
4. K. G. Mountjoy, L. S. Robbins, M. T. Mortrud, R. D. Cone, *Science* **257**, 1248 (1992).
5. L. S. Robbins *et al.*, *Cell* **72**, 827 (1993).
6. S. E. Millar, M. W. Miller, M. E. Stevens, G. S. Barsh, *Development* **121**, 3223 (1995).
7. S. J. Bultman, E. J. Michaud, R. P. Woychik, *Cell* **71**, 1195 (1992).
8. M. W. Miller *et al.*, *Genes Dev.* **7**, 454 (1993).
9. M. M. Ollmann, M. L. Lamoreux, B. D. Wilson, G. S. Barsh, *Genes Dev.* **12**, 316 (1998).
10. H. Klungland, D. I. Vage, *Ann. N.Y. Acad. Sci.* **994**, 331 (2003).
11. A. Slominski *et al.*, *Endocrinology* **146**, 1245 (2005).
12. S. Wright, *J. Hered.* **8**, 224 (1917).
13. C. C. Little, *The Inheritance of Coat Color in Dogs* (Comstock, Ithaca, NY, 1957).
14. J. A. Kerns *et al.*, *Genetics* **176**, 1679 (2007).
15. J. Sampson, M. M. Binns, in *The Dog and Its Genome*, E. A. Ostrander, U. Giger, K. Lindblad-Toh, Eds. (Cold Spring Harbor Laboratory Press, Cold Spring Harbor, NY, 2005), pp. 19–30.
16. A. A. Patil, Y. Cai, Y. Sang, F. Blecha, G. Zhang, *Physiol. Genomics* **23**, 5 (2005).
17. T. Ganz, *Nat. Rev. Immunol.* **3**, 710 (2003).
18. M. Pazgier, D. M. Hoover, D. Yang, W. Lu, J. Lubkowski, *Cell. Mol. Life Sci.* **63**, 1294 (2006).
19. J. M. Newton *et al.*, *Mamm. Genome* **11**, 24 (2000).
20. J. A. Kerns *et al.*, *Mamm. Genome* **15**, 798 (2004).
21. K. Lindblad-Toh *et al.*, *Nature* **438**, 803 (2005).
22. For further details, see the Supporting Online Material.
23. J. C. McNulty *et al.*, *J. Mol. Biol.* **346**, 1059 (2005).
24. J. Harder, J. Bartels, E. Christophers, J. M. Schroder, *J. Biol. Chem.* **276**, 5707 (2001).
25. T. K. Sawyer *et al.*, *Proc. Natl. Acad. Sci. U.S.A.* **77**, 5754 (1980).
26. C. A. Semple, P. Gautier, K. Taylor, J. R. Dorin, *Mol. Divers.* **10**, 575 (2006).
27. A. L. Hughes, *Cell. Mol. Life Sci.* **56**, 94 (1999).
28. G. Morrison, F. Kilanowski, D. Davidson, J. Dorin, *Infect. Immun.* **70**, 3053 (2002).
29. E. J. Hollox, J. A. Armour, J. C. Barber, *Am. J. Hum. Genet.* **73**, 591 (2003).
30. H. Chen *et al.*, *Peptides* **27**, 931 (2006).
31. D. Yang *et al.*, *Science* **286**, 525 (1999).
32. A. Soruri, J. Grigat, U. Forssmann, J. Riggert, J. Zwirner, *Eur. J. Immunol.* **37**, 2474 (2007).
33. A. Biragyn *et al.*, *Science* **298**, 1025 (2002).
34. T. A. Luger, T. E. Scholzen, T. Brzoska, M. Bohm, *Ann. N.Y. Acad. Sci.* **994**, 133 (2003).
35. L. Yaswen, N. Diehl, M. B. Brennan, U. Hochgeschwender, *Nat. Med.* **5**, 1066 (1999).
36. B. G. Challis *et al.*, *Proc. Natl. Acad. Sci. U.S.A.* **101**, 4695 (2004).
37. J. C. Smart, M. J. Low, *Ann. N.Y. Acad. Sci.* **994**, 202 (2003).
38. Single-letter abbreviations for the amino acid residues are as follows: A, Ala; C, Cys; D, Asp; E, Glu; F, Phe; G, Gly; H, His; I, Ile; K, Lys; L, Leu; M, Met; N, Asn; P, Pro; Q, Gln; R, Arg; S, Ser; T, Thr; V, Val; W, Trp; and Y, Tyr.
39. This work was supported by grants from NIH to G.S.B. and to G.L.M. and by a grant from the Donald E. and Delia B. Baxter Foundation to S.I.C. We thank H. Manuel for technical assistance, Y. Kobayashi and the Stanford Transgenic Facility for advice and help with transgenic experiments; D. Bennett for melan-a cells; Y.-K. Yang for providing the Mcr expression constructs; E. A. Ostrander for providing some of the samples; and the dog owners and breeders who generously submitted DNA samples.

Supporting Online Material

www.sciencemag.org/cgi/content/full/1147880/DC1
Materials and Methods
SOM Text
Figs. S1 to S10
Tables S1 to S3
References

16 July 2007; accepted 3 October 2007
Published online 18 October 2007
10.1126/science.1147880
Include this information when citing this paper.

Charge Transfer Equilibria Between Diamond and an Aqueous Oxygen Electrochemical Redox Couple

Vidhya Chakrapani,[1] John C. Angus,[1*] Alfred B. Anderson,[1] Scott D. Wolter,[2] Brian R. Stoner,[3] Gamini U. Sumanasekera[4]

AUTHORS' SUMMARY

In 1989, Maurice Landstrass and K. V. Ravi observed a curious phenomenon—undoped diamond, known to be an exceedingly good insulator, showed substantial conductivity when exposed to air (1). The source of the conductivity has been uncertain and a matter of controversy since that time, which is surprising for such an important and long-studied material. Resolution of the problem is of inherent scientific interest and could be important for applications of diamond and in other contexts as well. Subsequent studies confirmed that the conductivity was confined to a near-surface region, carried by positive charge carriers (holes), and that the change occurred only when the diamond was covered with chemically bound hydrogen. Numerous proposals were made to explain the phenomenon; none has received wide acceptance. One recent proposal was that the effect occurred when electrons were transferred from the diamond to an electrochemical couple in an adsorbed water film (2). This proposal has received limited support, in part because it posited an adsorbed water film on an extremely hydrophobic substrate, and also because the energetics and dynamics of the proposed electrochemical couple were problematic.

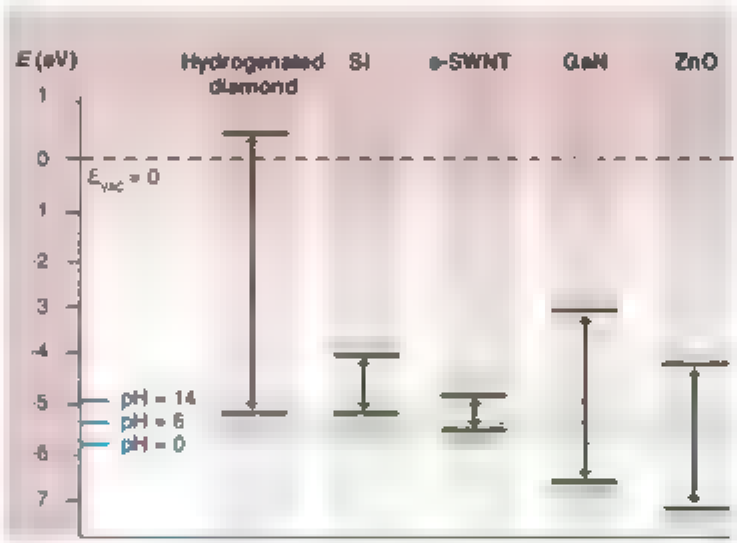

Electron energies of various solids. The vertical bars show the band gap. The continuous blue line is the electron energy of the oxygen couple in humid air (pH = 6), the lower dashed line is the value for pH = 0, the upper dashed line for pH = 14.

In this paper we describe a series of controlled experiments to explore this effect in which the presence of an aqueous phase is unambiguous. We hydrogenated diamond particles and measured the changes in pH and oxygen concentrations when the particles were added into aqueous solutions. These experiments show that electron exchange systematically occurs between diamond and the aqueous redox couple $O_2 + 4H^+ + 4e^- \rightleftharpoons 2H_2O$, which results in the consumption or formation of O_2. This electron exchange influences other properties—both the contact angle of water with the diamond surface and the amount and sign of the charge on diamond particles change in a predictable way by changing the extent of reaction that takes place. Adhesion of water to diamond is enhanced by electrostatic attraction after the charge transfer, which enhances the ability of water films to adsorb on otherwise hydrophobic surfaces.

These results imply that this process is a more general, unrecognized phenomenon that can influence a wide range of materials and processes. The key components are all derived from normal humid air. The water film provides both a medium for the electrochemical reaction as well as the O_2 and the H^+ (the protons arise from acidity generated by CO_2 that is present in air). This means that the effect can occur whenever semiconductors or other solids are exposed to humid air.

The atmosphere thus provides a source of electrons whose electrochemical potential (Fermi energy) is fixed by the oxygen redox couple. If the atmosphere is in contact with a solid phase, electrons will transfer between the adsorbed water film and the solid in a direction that tends to bring the Fermi energy of the solid equal to that of the ambient film. The process is similar to that at a metal-semiconductor contact, except that a water film replaces the metal.

The electron energies of several solids and the oxygen redox couple in humid air are shown in the figure. In equilibrium in air, the couple fixes the Fermi energy of diamond at the top of the valence band, which generates positive charge carriers (holes). The energy range of the couple spans the band gap of semiconducting single-walled carbon nanotubes (s-SWNTs). For GaN, the electron potential of the redox couple lies near the states in the middle of the energy gap responsible for its ubiquitous "yellow band" luminescence (see the figure). Other experiments suggest that the conductivity of carbon nanotubes can be changed from that based on electrons to that based on holes, and that the intensity of luminescence from GaN can be modulated by changing the electrochemical potential of the ambient air (3).

Several caveats are in order. For the ambient air to fix the Fermi energy of a solid, there must be a large reservoir of reactants and facile reaction kinetics at the interface. The air provides quasi-infinite sources of O_2, H_2O, and CO_2; however, several factors can inhibit equilibration of the Fermi energies. An oxide layer, e.g., on silicon, or a thin film of adsorbed hydrocarbon can block electron exchange. The reduction of O_2 in the aqueous redox couple may require trace metallic impurities on the surface. Chemical ionization of oxidized surfaces, not involving electron transfer, and intrinsic conductivity in small band gap semiconductors and metals can both mask the effect.

It is highly likely that the effects of electrochemically mediated charge transfer have remained unrecognized in many common situations. In this light, it will be of great interest to reexamine the literature on mechanical sliding friction and contact electrification, both of which depend in complex ways on relative humidity and impurities in the ambient air. Even more speculative is the possibility that certain animals and insects have evolved the capability of modulating the electrochemical potential in their feet to change the adhesive force to solid surfaces. Charge transfer to nanostructures not only can affect their properties, but also will vary with the size of the structure because of quantum confinement effects.

Summary References

1. M. I. Landstrass, K. V. Ravi, *Appl. Phys. Lett.* **55**, 975 (1989).
2. F. Maier, M. Riedel, J. Mantel, J. Ristein, L. Ley, *Phys. Rev. Lett.* **85**, 3472 (2000).
3. V. Chakrapani, J. C. Angus, A. B. Anderson, G. Sumanasekera, *Mater. Res. Soc. Symp. Proc.* **956**, paper J15-01 (2007).

FULL-LENGTH ARTICLE

Undoped, high-quality diamond is, under almost all circumstances, one of the best insulators known. However, diamond covered with chemically bound hydrogen shows a pronounced conductivity when exposed to air. This conductivity arises from positive-charge carriers (holes) and is confined to a narrow near-surface region. Although several explanations have been proposed, none has received wide acceptance, and the mechanism remains controversial. Here, we report the interactions of hydrogen-terminated, macroscopic diamonds and diamond powders with aqueous solutions of controlled pH and oxygen concentration. We show that electrons transfer between the diamond and an electrochemical reduction/oxidation couple involving oxygen. This charge transfer is responsible for the surface conductivity and also influences contact angles and zeta potentials. The effect is not confined to diamond and may play a previously unrecognized role in other disparate systems.

A highly unusual property of undoped, hydrogen-terminated diamond is the appearance of p-type surface conductivity when exposed to air (*1*). Sheet carrier concentration and mobility (*2–4*) have been measured and sensors and field effect transistors have been fabricated on the basis of this effect (*5–7*). Several mechanisms for the p-type conductivity have been proposed, including deep-level passivation by surface hydrogen (*1*), formation of shallow acceptors by subsurface hydrogen (*3, 8, 9*), oxidation by adsorbed gas molecules (*2*), and surface transfer doping to the H_2/H^+ redox couple in an adsorbed water layer (*10, 11*). Larsson and co-workers presented a theoretical investigation of surface transfer doping to an acidic, adsorbed water film and gave a short review of other mechanisms (*12, 13*). Recently Ristein (*14*) discussed surface transfer doping in the context of a new way of doping semiconductors, and Qi *et al.* (*15*) demonstrated surface transfer doping of diamond by tetrafluorotetracyanoquino-dimethane. However, despite much effort, no mechanism has received wide acceptance. Here, we present experimental evidence of electrochemically mediated charge transfer between diamond and macroscopic aqueous solutions. We also discuss the relevance of this effect for other material systems.

Rationale for experiments. The surface transfer doping mechanism involving the H_2/H^+ redox couple, as originally proposed (*10, 11*), is in general agreement with the experimental observations of surface conductivity in diamond. However, it relies on the presence of an adsorbed water film on hydrophobic, hydrogen-terminated diamond. Adsorbed water films on solids exposed to humid atmospheres are common (*16*), but experimental evidence for water films on diamond is tenuous. In addition, the H_2/H^+ redox couple is unlikely to fix the potential in an adsorbed film because of the very low levels of H_2 in air. Finally, the absolute position of the H_2/H^+ couple is above the valence band maximum of hydrogen-terminated diamond that is exposed to air-saturated water and therefore unlikely to accept electrons from the valence band of diamond.

In the light of the above, experiments testing the surface transfer doping mechanism when the presence of an aqueous phase is unambiguous are attractive. Furthermore, experiments in which the dissolved oxygen concentration can be controlled and measured can distinguish between the H_2/H^+ redox couple (*10, 11*) and the O_2 couple suggested by Foord *et al.* (*17*) and Chakrapani *et al.* (*18*). Because fluorinated and oxidized diamond have similar electron affinities, but very different surface chemistries, we opted to explore fluorinated as well as oxidized and hydrogenated samples.

The sheet concentration of holes in diamond exposed to moist air has been estimated to be on the order of 10^{12} to 10^{13} cm^{-2} (*2, 3*). If this charge arises from electrochemical transfer doping, a straightforward calculation shows that addition of high surface area diamond powder to small, but macroscopic, amounts of aqueous solution will produce measurable changes in pH and in dissolved oxygen concentration. Furthermore, the direction of these changes will differ depending on whether the Fermi level of the diamond is above or below the electrochemical potential of the aqueous solution.

Electron transfer between diamond and aqueous solutions should produce other macroscopic effects as well. The contact angle of aqueous solutions with diamond should decrease at low pH because of increased electrostatic attraction between the positive accumulation layer in the diamond and compensating negative ions in the adjacent solution. The sign of the zeta potential, which is related to the sign of the net charge on a particle, should vary in a similar systematic way with pH, i.e., greater positive surface charge at lower pH.

Electrochemical potentials and band line-up. According to the electrochemical transfer doping model, a p-type accumulation layer forms in diamond when the Fermi level of the diamond is higher than the electrochemical potential, μ_e, of an adsorbed water layer on the diamond surface (*10, 11*). Electrons transfer from the diamond to the water layer, resulting in a positive space charge layer in the diamond and compensating anions in the water layer. The electrochemical potential of the film is determined by electrochemical redox couples involving dissolved oxygen in equilibrium with air (*17, 18*).

$$O_2 + 4H^+ + 4e^- \rightleftharpoons 2H_2O \quad \text{dominates at acidic conditions} \qquad (1)$$

$$O_2 + 2H_2O + 4e^- \rightleftharpoons 4OH^- \quad \text{dominates at basic conditions} \qquad (2)$$

The reactions in Eq. 1 and 2 are not independent, but are related by the water equilibrium, Eq. 3.

$$H_2O \rightleftharpoons H^+ + OH^- \qquad (3)$$

Although electrons are not present as separate entities in the aqueous phase, their electrochemical potential, μ_e, is well defined and is given by the Nernst equation. The reactions in Eqs. 1 and 2 have expressions for μ_e given, respectively, in Eqs. 4 and 5

$$\mu_e(\mathrm{eV}) = -4.44 + (-1)(+1.229) + \frac{0.0592}{4}(4\mathrm{pH} - \log_{10} p_{O_2}) \qquad (4)$$

$$\mu_e(\mathrm{eV}) = -4.44 + (-1)(+0.401) + \frac{0.0592}{4}(4\mathrm{pOH} + \log_{10} p_{O_2}) \qquad (5)$$

Here, μ_e (eV) is referred to the vacuum level, the activity of H_2O is assumed to be unity, the ideal gas approximation is used, the temperature $T = 298$ K, and the partial pressure of O_2, p_{O_2}, is in bar. The electrochemical potential of electrons in the standard hydrogen electrode (SHE) relative to the vacuum level is $\mu_{e(SHE)} = -4.44$ eV (*19, 20*). The standard electrode potentials of the reactions in Eqs. 1 and 2 are +1.229 V and +0.401 V versus SHE, respectively (*21*). The relation between pH and pOH is simply pH + pOH = 14.

Mott-Schottky measurements (*22*) and theoretical considerations (*23*) indicate that the electron affinity, EA, of hydrogen-terminated diamond in contact with water or moist air is approximately +0.30 eV, which is 1 eV more positive than the value obtained in vacuum (*24*). Because the diamond band gap is 5.5 eV, this shift places the top of the diamond valence band at approximately −5.2 eV. This estimate was used to give the position of the band edges of diamond in Fig. 1. Also shown in Fig. 1 are the electrochemical potentials for the oxygen redox couple calculated from Eqs. 4 and 5 for p_{O_2} = 0.21 bar and pH = 0 and pH = 14. These energies, −5.66 eV and −4.83 eV, respectively, straddle the estimated position of the valence band maximum of diamond.

The band line-up shown in Fig. 1 is for hydrogen-terminated diamond in contact with an aqueous phase. Oxygen and fluorine are both

[1]Case Western Reserve University, Cleveland, OH 44106, USA. [2]Duke University, Raleigh-Durham, NC 27708, USA. [3]Research Triangle Institute, Research Triangle Park, NC 27709, USA. [4]University of Louisville, Louisville, KY 40291, USA.

*To whom correspondence should be addressed. E-mail: john.angus@case.edu

more electronegative than carbon in contrast to hydrogen, which is more electropositive than carbon. Therefore, surface termination with either oxygen or fluorine induces a surface dipole that will increase the electron affinity, opposite to the effect in hydrogen-terminated diamond. The electron affinity of an oxidized diamond surface is about 1 eV more positive than hydrogenated surfaces (*24*, *25*), and the effect of fluorine is expected to be similar. This lowering of the diamond energy bands by ≈ 1 eV places the valence band maximum at $E \approx -6.2$ eV, below the electrochemical potential of the aqueous phase at all pH's.

Electrochemically mediated charge transfer. Water in equilibrium with air has a pH ≈ 6 from the naturally occurring CO_2 in the air, which corresponds to an electrochemical potential of $\mu_e \approx -5.3$ eV from Eq. 4. Lowering the pH lowers μ_e. Therefore, addition of hydrogenated diamond powder equilibrated with moist air to a solution with pH < 6 leads to $\mu_e(\text{dia}) > \mu_e(\text{aq})$ and electrons transfer from the diamond to the solution until $\mu_e(\text{dia}) = \mu_e(\text{aq})$. The reaction in Eq. 1 proceeds in the forward direction, which results in consumption of protons. However, when diamond powder equilibrated with moist air is brought in contact with a basic solution, $\mu_e(\text{dia}) < \mu_e(\text{aq})$, electrons transfer from the solution into the diamond, which drives the reaction in Eq. 2 in the reverse direction. Hydroxyl ions are consumed and the solution becomes more acidic. If these are the only processes taking place at the interface, the protons consumed plus the hydroxyl ions formed are equal to the number of electrons transferred from the diamond to the solution. Reduction in the concentration of electrochemical acceptors, i.e., the dissolved oxygen, should decrease the amount of electron transfer from the diamond and suppress the changes of pH of the solution.

The overall stoichiometry of the electrochemically mediated charge transfer at moderate pH can be written as Eq. 6 (*18*):

$$4(e^- h^+)_{dia} + O_{2,air} + 2H_2O_{air} + 4CO_{2,air} \leftrightarrow$$
$$4h^+_{dia} + 4HCO_{3,aq}^- \qquad (6)$$

Equation 6 describes the situation when the acidity is generated by atmospheric CO_2. In this case, the counterions in the aqueous phase are dominantly HCO_3^-. The type of counterion will depend on the ambient. For example, in the presence of HCl vapors, the counterions will be predominantly Cl^-.

We note that the electron affinity of the aqueous oxygen redox couple is much greater than that of molecular oxygen and other gas-phase oxidants in the absence of water. For example, the electron affinity of O_2 is 0.451 eV (*26*), which places the energy at $E = -EA = -0.451$ eV, far above the energy of the oxygen redox couple at any pH (Fig. 1). The electron affinities of other highly oxidizing gas-phase species, e.g., NO_2, O_3, and F, are respectively, 2.273, 2.103, and 3.4 eV (*26*) and thus are also not sufficient to directly oxidize diamond. Therefore, direct electron transfer from diamond to gas-phase species in the absence of water is thermodynamically improbable.

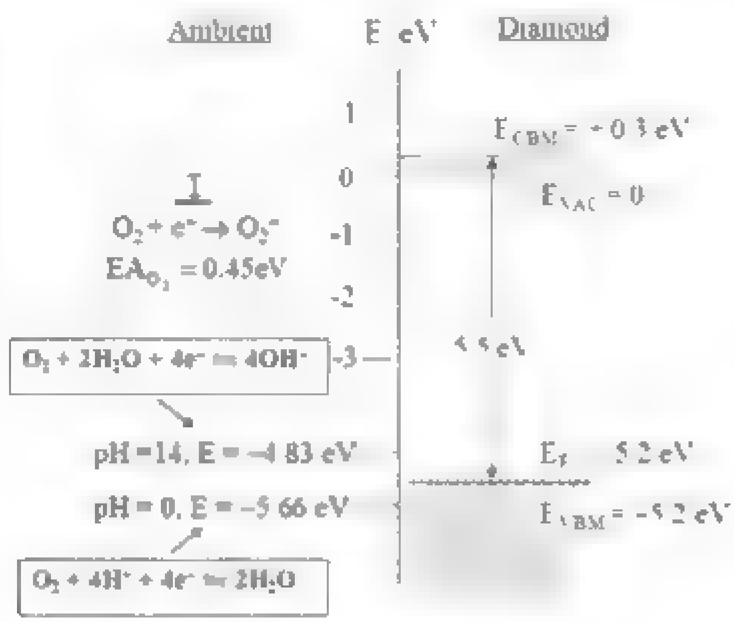

Fig. 1. Estimated band lineup of hydrogen-terminated diamond in contact with an aqueous solution. The electrochemical potentials of the oxygen redox couple are shown at pH = 0 and pH = 14. The electron affinity of gaseous O_2 is also shown (E = − EA = − 0.451 eV)

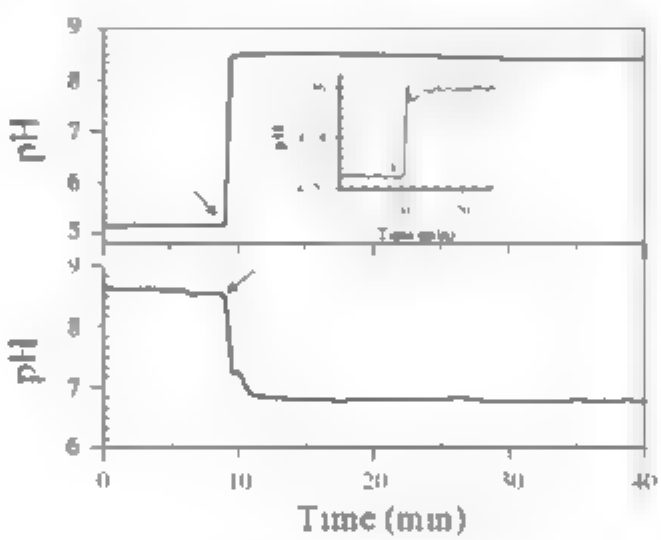

Fig. 2. Changes in pH upon addition of 1 g of hydrogen-terminated natural diamond powder, equilibrated with air, to separate 20-ml aqueous solutions with pH = 5.2 and pH = 8.5. The arrows indicate the point where the diamond powder was added. For the former, μ_e (dia) > μ_e (aq) and electrons transfer into the liquid, thereby consuming protons and raising the pH. For the latter, μ_e (dia) < μ_e (aq), and electrons transfer out of the solution, lowering the pH. The inset shows the result when hydrogen-terminated diamond powder is added to a solution deoxygenated with N_2 and $NaHSO_3$. Note the expanded vertical scale.

Titration of diamond powder. Natural diamond powder with a nominal size range of 0.5 to 1.0 μm was purchased from Advanced Abrasives Corp. The as-purchased powder was oxidized and was therefore hydrogenated at 700°C for 4 hours in a 2.45-GHz microwave plasma reactor supporting a hydrogen plasma at 750 W, at a gas flow rate of 196 standard cubic centimeters per minute and pressure of 35 torr. The powder was cooled in hydrogen gas to room temperature, stirred, and the process then repeated two times to ensure good hydrogen coverage. X-ray photoelectron spectroscopy (XPS) analysis indicated that the surface oxygen concentration was lowered from 8.5 to 1.4% by this process. Because the samples were transferred in air, the bulk of the residual oxygen likely arose from physically adsorbed species.

Diamond powder was fluorinated in a planar inductively coupled 13.56-MHz plasma reactor at 800 W with a dc bias of −307 V. A source gas of SF_6 at 25 sccm was used to maintain a pressure of 0.035 torr for 10 min. The substrate temperature was maintained at 20°C. Subsequent XPS analysis of the powder showed both fluorine and oxygen on the surface in approximately a 5:1 atomic ratio.

In all of the titration experiments with diamond powder, 1 g of powder was added to 20 ml of solution. The solution was stirred continuously before and after addition of the diamond powder. The pH and dissolved oxygen concentration measurements were made with an Accumet XL60 meter. Analytical-grade chemicals (HCl, NaOH, and $NaHSO_3$) were used in all experiments, and solutions were filtered through a 0.1-μm filter before use. Air-saturated water was used for most experiments. In some cases, the dissolved oxygen concentration was reduced by bubbling nitrogen through the solution for 4 hours and then

adding sodium bisulfite up to a concentration of 0.5 M. The original dissolved oxygen concentration of air-saturated water was ~7 mg/liter; the concentration after the nitrogen purge and bisulfite treatment was less than the sensitivity of the dissolved oxygen probe (0.01 mg/liter). For experiments with sodium bisulfite, the chamber was closed to isolate the solution from the open air, and nitrogen was continuously purged through the chamber.

Figure 2 shows the changes in pH when 1 g of hydrogenated diamond powder is added separately to 20 ml of air-saturated aqueous solutions, one at pH = 5.2 and the other at pH = 8.5. The pH increases upon addition of the hydrogenated diamond to the acidic solution and decreases upon addition of the diamond powder to the basic solution. These changes are in the expected directions described above. The inset in Fig. 2 shows the change in pH when hydrogenated diamond powder is added to a solution that has been deoxygenated with N_2 and $NaHSO_3$. The change in pH is very small (note the magnified vertical scale). This result indicates that dissolved oxygen is necessary for charge transfer to take place.

Figure 3A shows a titration curve obtained by addition of 1 g of diamond powder equilibrated with room air to 20-ml solutions of known pH. The ordinate is the number of electrons, ΔN_{e^-}, transferred into the water and is given by Eq. 7.

$$\Delta N_{e^-} = \Delta N_{OH^-} - \Delta N_{H^+} = N_{AV} V_{H_2O} \left(10^{-14}\left(10^{pH_f} - 10^{pH_i}\right) - \left(10^{-pH_f} - 10^{-pH_i}\right)\right) \quad (7)$$

where N_{AV} is Avogadro's number, ΔN_{H^+} and ΔN_{OH^-} are the changes in number of H^+ and OH^- ions respectively, V_{H_2O} is the volume of water in liters, and pH_i and pH_f are the initial and final pH of the solution. At high pH, the first term dominates; at low pH, the second term dominates. In the flat portion of the titration curve, both protons and hydroxyl ions are present in low concentrations, and the transfer of a small number of electrons leads to large changes in pH.

The crossover point in Fig. 3, A and B, is where the electrochemical potential of the solution is equal to the Fermi level of the original diamond equilibrated with air. The electrochemical potential of the solution at this point is a direct measure of the Fermi level of diamond equilibrated with room air. The crossover point is most easily seen in Fig. 3B and is estimated to occur at pH = 6.1, which from Eq. 4 corresponds to an electron chemical potential of $\mu_e = -5.3$ eV. This value is in close agreement with independent Mott-Schottky and Kelvin probe measurements that show $\mu_e = -5.2$ eV (22, 27) for diamond in equilibrium with aqueous solutions in air.

We estimated the change in the concentration of dissolved oxygen upon addition of diamond powder by using an electrochemical biochemical oxygen demand (BOD) probe consisting of a FEP Teflon membrane covering a gold and silver electrode. When hydrogenated diamond powder, previously equilibrated with room air, is added to an acidic solution, $\mu_e(\text{dia}) > \mu_e(\text{aq})$; electrons transfer into the solution and the concentration of dissolved oxygen decreases due to the reaction in Eq. 1, which proceeds in the forward direction. When hydrogenated diamond powder is added to a basic solution, $\mu_e(\text{dia}) < \mu_e(\text{aq})$, and the concentration of dissolved oxygen increases. In this latter case electrons leave the solution, driving the reaction in Eq. 2 in the reverse direction, thus increasing the concentration of dissolved oxygen. The results are summarized in Table 1. In both cases, the change in dissolved oxygen concentration is in the expected direction. Furthermore, the estimated change in number of moles of dissolved oxygen agrees with the change in number of molecules of protons and hydroxyl ions calculated from the pH change within the expected error of the oxygen measurement.

Zeta potential measurements. Zeta potentials are obtained by measurement of the electrophoretic velocity of dispersed solids in a liquid. The magnitude and sign of the zeta potential depend on the net amount and sign of the charge within the shear boundary separating the mobile liquid from the stagnant layer near the solid surface. A positive zeta potential indicates a net positive charge within the shear boundary; a negative zeta potential indicates a net negative charge (28). Here we use measurements of the zeta potential as confirmation of the direction of electron transfer between diamond powder and water.

We performed zeta potential measurements with a ZETAMASTER-S using 1-μm nominal-size natural diamond powder purchased from NJK-5, Kay Industrial Diamond Corp. Hydrogenation and fluorination of the powder were performed as described earlier. The diamond powder was equilibrated with room air before the zeta potential measurements were made.

From Fig. 4 it is evident that hydrogen-terminated diamond powder shows a positive zeta potential at all pH values less than 7. This result is consistent with electron transfer from the diamond, which increases with decreasing pH as predicted by the transfer doping model. The slightly negative zeta potentials for the hydrogen-terminated diamond at pH > 8 are consistent with a low concentration of residual oxygen-containing surface functional groups on the surface compared to the nonhydrogenated samples.

The zeta potentials for both oxidized and fluorinated diamond powder differ markedly

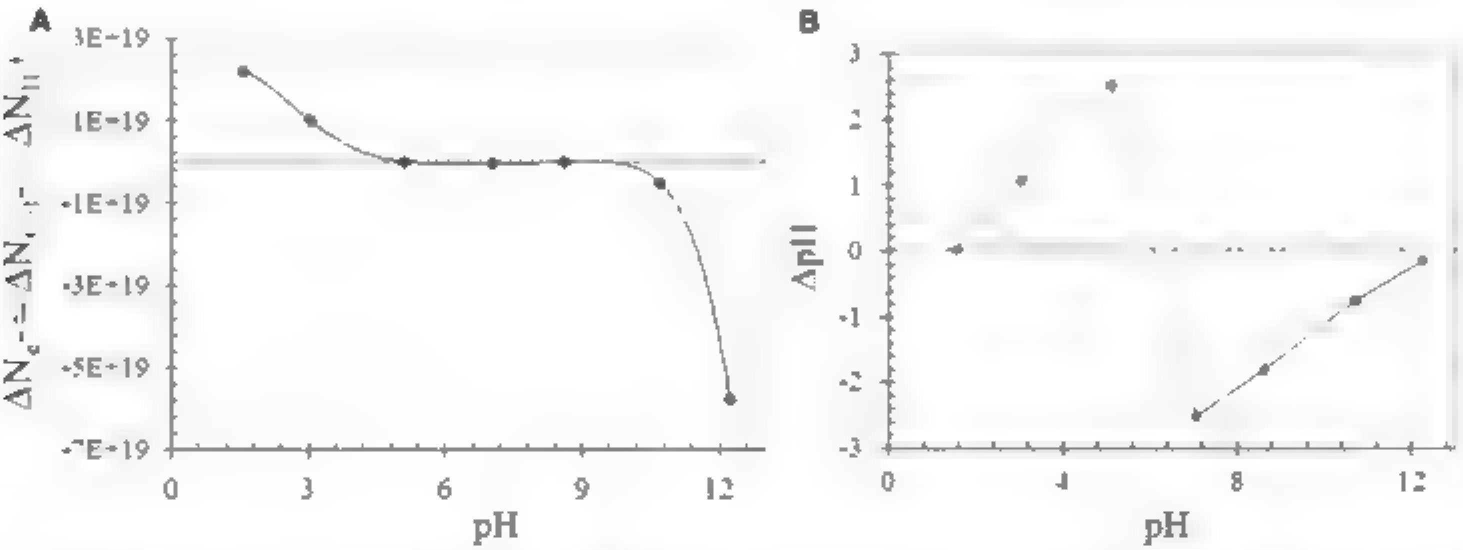

Fig. 3. (**A**) Number of electrons transferred from the diamond upon addition of 1 g of hydrogen-terminated natural diamond powder equilibrated in air to 20-ml aqueous solutions of varying initial pH. The crossover point is where the Fermi level of the diamond equals the chemical potential of electrons in equilibrium with the electrochemical couple. (**B**) Change of pH upon addition of 1 g of hydrogen-terminated natural diamond powder equilibrated in air to 20-ml solutions of varying initial pH.

from those of the hydrogen-terminated powder. The potentials for these samples are similar in magnitude and negative at all pH values greater than 1. The negative charge can arise either from transfer of electrons to the diamond or ionization of residual oxygen-containing functional groups on the surface, e.g., carboxylic acids and hydroxyl radicals. The similarity of the results for the oxidized and fluorinated samples indicates that the charging process is similar despite the different surface chemistry of the two types of samples.

Contact angle measurements. Advancing contact angles on hydrogen-terminated, 3-mm diamond macles in solutions of different pH were determined. Macles are natural, triangular, unpolished, twinned single crystals of diamond. We measured the contact angles on the (111) facets of these crystals by the Wilhelmy plate technique (29) using a KRÜSS K100 Processor Tensiometer. The diamond samples were first hydrogenated under conditions described above for diamond powders for a period of 2 hours. After hydrogenation, they were cleaned ultrasonically in Milli-Q water for 10 min and dried under flowing N_2.

The macles were suspended by a corner from the arm of the electrobalance and immersed in the solution at a constant rate of 3 mm/min while we measured the force on the sample due to wetting. The contact angle was calculated from the measured force, wetted length of the sample, and the surface tension of the solution, γ_{LV} (29). Extrapolation of the results to zero immersion depth eliminated the effect of variation of the length of the wetted perimeter. The surface tension of the solution was measured with a roughened platinum plate, which is wetted with a contact angle of virtually 0°. By measuring the force acting on the plate when immersed in the solution, we calculated γ_{LV}.

Table 1. Summary of results showing changes in the concentration of dissolved oxygen (DO) and pH with the addition of 1 g of hydrogenated natural diamond powder equilibrated with air to 20 ml of solution. The change in number of ions of H^+ and OH^- is from Eq. 7.

	Steady-state value before addition	Steady-state value after addition	Change in no. of molecules	No. of e^- transferred
DO (mg/liter)	7.8	7.3	1.9×10^{17} of O_2	$+7.6 \times 10^{17}$
pH	4.1	5.3	8.9×10^{17} of H^+ and OH^-	$+8.9 \times 10^{17}$
DO (mg/liter)	6.9	7.5	2.3×10^{17} of O_2	-9.2×10^{17}
pH	7.3	4.4	4.8×10^{17} of H^+ and OH^-	-4.8×10^{17}

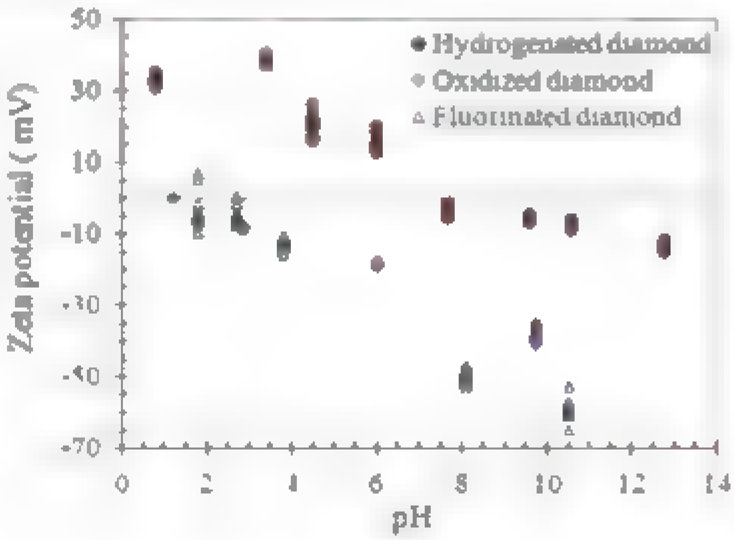

Fig. 4. Zeta potential as a function of pH for hydrogenated, oxidized, and fluorinated natural diamond powder. Hydrogen-terminated diamond shows a positive zeta potential (positive surface charge) at pH < 7. Fluorinated and oxidized diamond powders show negative zeta potentials (negative surface charge) at all pH's.

The advancing contact angles of a hydrogen-terminated diamond macle in contact with aqueous solutions of varied pH and dissolved oxygen content are shown in Fig. 5A. We attribute the decrease of the contact angle at low pH to the electrostatic attraction between the positive space charge layer in the diamond and the compensating anions in the aqueous phase (18). The solvated anions provide a mechanism for binding a water film to the hydrogen-terminated, hydrophobic diamond surface.

Reduction in the concentration of electrochemical acceptors, i.e., the dissolved oxygen, should decrease the electron transfer from the diamond and reduce the effect of pH on contact angle. First, we lowered the dissolved oxygen concentration in the water by bubbling nitrogen through the solution. Further removal of dissolved oxygen was achieved by reduction with sodium bisulfite (30). From Fig. 5A, it is clear that the contact angle increased as the concentration of dissolved oxygen decreased. Furthermore, the dependence of contact angle on pH essentially disappeared after the addition of excess sodium bisulfite, which reduces the dissolved oxygen concentration to very low levels.

The work of adhesion, W_{adh}, which is the energy required to separate the liquid and solid

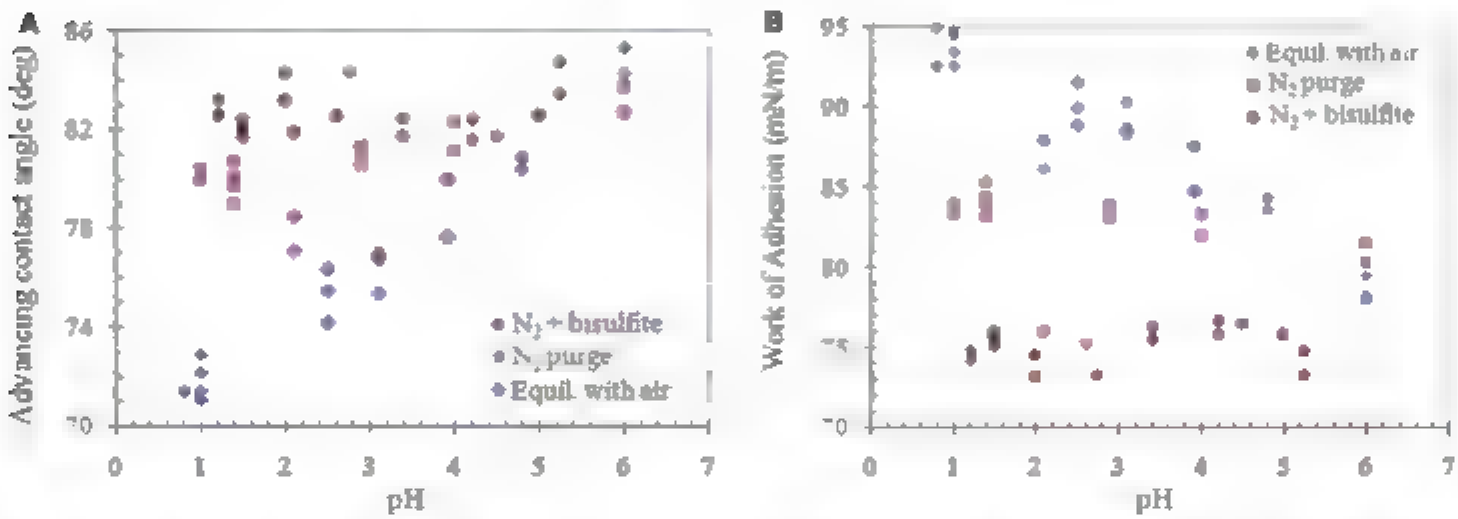

Fig. 5. (**A**) Advancing contact angles on a (111) surface of a hydrogen-terminated diamond macle as a function of pH. Experiments were performed with water in equilibrium with air, water purged with N_2, and water purged with N_2 and treated with $NaHSO_3$. (**B**) Changes in the work of adhesion calculated from the contact angles. Experiments were performed with water in equilibrium with air, water purged with N_2, and water purged with N_2 and treated with $NaHSO_3$.

phases, is related to the contact angle, θ, through the Young-Dupre equation (*16*), (Eq. 8).

$$W_{ad} = \gamma_{LV}(1 + \cos\theta) \qquad (8)$$

Figure 5B shows the work of adhesion as a function of pH of the solution. Higher work of adhesion is found at lower pH for air-saturated solutions; the work of adhesion for deoxygenated solutions is reduced and is independent of pH, as expected.

Role of oxygen. Our results support the surface transfer doping mechanism (*10, 11*), but are consistent with charge transfer between diamond and an electrochemical redox couple involving O_2 in the adjacent water phase as suggested by Foord *et al.* (*17*) and Chakrapani *et al.* (*18*), rather than the H_2/H^+ couple as originally proposed.

Fixing the electrochemical potential and pinning the Fermi level in the diamond require facile electron transport between the diamond and the adjacent aqueous phase. The redox reactions (Eqs. 1 and 2) must be sufficiently rapid to permit measurable charge exchange within the time of the measurements. The relatively large concentration of O_2 (compared to H_2) in air-equilibrated water facilitates the reaction kinetics of Eqs. 1 and 2. The reduction of O_2 in the aqueous redox couple may require trace metallic impurities on the surface to proceed at appreciable rates. Furthermore, an adsorbed organic film can displace the aqueous phase and suppress the effect (*18*). The use of epoxy resins to insulate electrical contacts may provide such a barrier.

We emphasize that under certain conditions, other processes not involving electron transfer may take place. For example, surface field effect devices have been constructed with the use of induced charge (*7*). Also, on an oxidized diamond surface, functional groups such as carboxylic acid and hydroxyl can ionize (Eqs. 9, 10).

$$(dia)\text{-}COOH \rightleftharpoons (dia)\text{-}COO^- + H^+ \qquad (9)$$

$$(dia)\text{-}OH \rightleftharpoons (dia)\text{-}O^- + H^+ \qquad (10)$$

The total number of sites on a (111) diamond surface is $\sim 10^{15}$ cm^{-2}. Therefore, even a 1% surface coverage with ionizable sites can mask the effects of transfer doping, which gives rise to sheet charge densities of $\sim 10^{12}$ to 10^{13} cm^{-2} (*2–4*).

Because the reactions in Eqs. 9 and 10 do not involve electrons, their equilibria do not depend on the chemical potential of electrons, μ_e. However, these reactions do involve protons, so their equilibria depend on the chemical potential of protons, i.e., on pH. The reaction in Eq. 9 will proceed to the right if the pH of the aqueous phase meets the condition pH > pK_a ≈ 4; similarly, the reaction in Eq. 10 will proceed if pH > pK_a ≈ 10. Here pK_a is the acid dissociation constant of the functional groups. If these conditions are met, protons transfer into the solution, lowering the pH. This effect is illustrated in Fig. 6. The pH of a solution, initially at pH ≈ 5, decreases upon addition of oxidized diamond powder. In contrast, when hydrogenated diamond is added to a solution with pH ≈ 5, surface transfer doping causes the pH to increase.

All of the experiments have been performed with natural type IA diamond, which contains appreciable quantities of nitrogen. However, the nitrogen in natural diamond is present as aggregates and, as such, does not provide active donor centers (*31, 32*). In contrast, in type Ib synthetic diamond, single substitutional nitrogen atoms are present, which have a donor level 1.6 eV below the conduction band minimum (*33*). If present, these donor centers can ionize and compensate holes generated by electron transfer to the aqueous phase (*34*). In this situation, positively charged donor sites and holes are charge-balanced by excess anions in the aqueous phase. Because all of our experiments were conducted with type IA diamond, which has negligible substitutional nitrogen, compensation by nitrogen donors does not occur. Indeed, we found that the surface conductance of the type IA diamond is four orders of magnitude greater than the conductance of type Ib, 2 × 2 mm (100) synthetic diamond crystals (Sumitomo, HTHP).

Electrochemically mediated charge transfer in other material systems. Electrochemically mediated transfer doping was first noted in diamond (*1*) because the effect on conductivity is so striking. However, the phenomenon should occur in many other systems if the band line-up is appropriate. Furthermore, the electrostatic attraction between the resulting space charge layer in the solid and the compensating ions in the adsorbed film will enhance the formation of adsorbed water films.

The electron affinity of semiconducting single-walled nanotubes (SWNTs) has been reported to be 4.8 eV (*35*). Also, SWNTs have a band gap of 0.4 to 0.6 eV and a work function of 4.8 to 5.1 eV (*36, 37*). These values place the Fermi level above the electrochemical potential of the aqueous redox couple (Eq. 1) for air-saturated water, which is −5.3 eV. Hence, when SWNTs are exposed to humid air, electrons can transfer out of the SWNTs into an adsorbed water film.

Several studies have observed an abrupt change in sign of the Seebeck coefficient from negative to positive when SWNTs that were previously annealed in vacuum were exposed to air at room temperature (*38, 39*). These results show a change in the dominant charge carrier from electrons to holes consistent with the electrochemical transfer doping mechanism. Furthermore, small concentrations of gases such as NO_2, NH_3, O_3, and H_2O change the conductivity of SWNTs (*40–43*) in the directions predicted by our model.

The electron affinity of a clean GaN surface is reported to be 3.0 ± 0.3 eV (*44, 45*). Therefore, with a band gap of 3.4 eV, the conduction band minimum is at $E \approx -3$ eV and the valence band maximum is at $E \approx -6.4$ eV. The electrochemical potentials of the oxygen redox couples (−4.83 eV to −5.66 eV) are therefore in the mid-gap region of GaN rather than near the valence band edge as in the case with diamond. Changes in the chemical potential of aqueous redox couples in an adsorbed water film can therefore change the occupancy of the mid-gap surface states that are believed to play a role in the ubiquitous yellow-band emission from GaN. This electrochemical mechanism may be responsible for the enhancement of yellow-band emission in the presence of HCl vapors and diminishment in the presence of NH_3 vapors (*46, 47*).

Charge transfer between polymers and metals (contact electrification) is a well-known, but not fully understood, phenomenon that depends on the difference in work functions of the contacting materials, presence of surface states, relative humidity, atmospheric adsorbates, humidity, and pH of the ambient environment (*48, 49*). Sliding friction is another complex phenomenon depending in some situations on the ambient. We suggest that charge transfer to electrochemical acceptors in adsorbed water films may mediate these processes and should be considered when interpreting results. Furthermore, charge transfer to electrochemical acceptors in adsorbed films may influence the properties of nanoparticles and other nanometer-scale structures. This point is of particular interest because the electron energies in small nanopar-

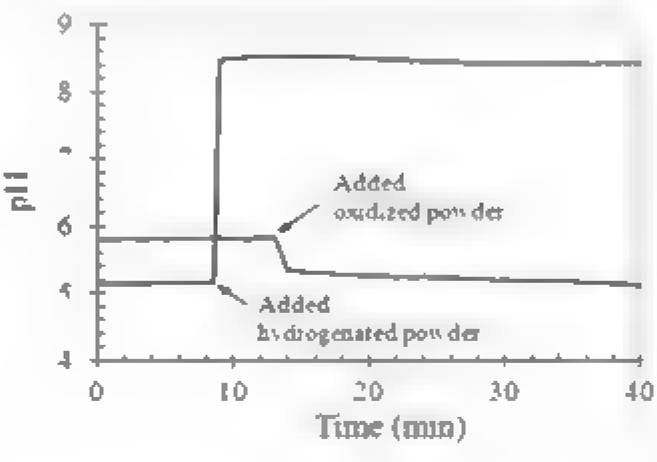

Fig. 6. Changes in pH upon addition of 1 g of hydrogen-terminated natural diamond powder and 1 g of oxidized natural diamond powder, each equilibrated with air, to separate 20-ml solutions with pH ≈ 5. The arrows indicate the point where the diamond powder was added.

ticles will depend on size due to quantum confinement effects.

References and Notes

1. M. Landstrass, K. V. Ravi, *Appl. Phys. Lett.* **55**, 975 (1989).
2. B. S. Gi *et al.*, *Jap. J. Appl. Phys. Part 1* **38**, 3492 (1999).
3. K. Hayashi, S. Yamanaka, H. Okushi, K. Kajimura, *Appl. Phys. Lett.* **68**, 376 (1996).
4. H. J. Looi *et al.*, *Diamond Relat. Mater.* **7**, 550 (1998).
5. R. S. Gi *et al.*, *Jap. J. Appl. Phys. Part 1* **36**, 2057 (1997).
6. A. Denisenko, A. Aleksov, E. Kohn, *Diamond Relat. Mater.* **10**, 667 (2001).
7. H. Kawarada, Y. Araki, T. Sakai, T. Ogawa, H. Umezawa, *Phys. Status Solidi* **185**, 79 (2001).
8. K. Hayashi *et al.*, *J. Appl. Phys.* **81**, 744 (1997).
9. T. Maki *et al.*, *Jap. J. Appl. Phys.* **31**, L1446 (1992).
10. F. Maier, M. Riedel, J. Mantel, J. Ristein, L. Ley, *Phys. Rev. Lett.* **85**, 3472 (2000).
11. J. Ristein, M. Riedel, L. Ley, *J. Electrochem. Soc.* **151**, E315 (2004).
12. K. Larsson, J. Ristein, *J. Phys. Chem. B* **109**, 10304 (2005).
13. D. Petrini, K. Larsson, *J. Phys. Chem. C* **111**, 13804 (2007).
14. J. Ristein, *Science* **313**, 1057 (2006).
15. D. Qi *et al.*, *J. Am. Chem. Soc.* **129**, 8084 (2007).
16. A. W. Adamson, *Physical Chemistry of Surfaces* (Wiley, New York, 1982).
17. J. S. Foord *et al.*, *Diamond Relat. Mater.* **11**, 856 (2002).
18. V. Chakrapani, S. C. Eaton, A. B. Anderson, M. Tabib-Azar, J. C. Angus, *Electrochem. Solid-State Lett.* **8**, E4 (2005).
19. A. J. Bard, R. Memming, B. Miller, *Pure Appl. Chem.* **63**, 569 (1991).
20. Yu. Ya. Gurevich, Yu. V. Pleskov, *Elektrokhimiya* **18**, 1477 (1982).
21. *C. R. C. Handbook of Chemistry and Physics*, D. R. Lide, Ed. (CRC Press, Boca Raton, FL, ed. 84, 2003).
22. Yu. V. Pleskov, A. Ya. Sakharova, M. D. Krotova, L. L. Bouilov, B. V. Spitsyn, *J. Electroanal. Chem.* **228**, 19 (1987).
23. G. Piantanida *et al.*, *J. Appl. Phys.* **89**, 8259 (2001).
24. F. Maier, J. Ristein, L. Ley, *Phys. Rev. B* **64**, 165411 (2001).
25. T. N. Rao, D. A. Tryk, K. Hashimoto, A. Fujishima, *J. Electrochem. Soc.* **146**, 680 (1999).
26. J. A. Dean, *Lange's Handbook of Chemistry* (McGraw-Hill, New York, ed. 15, 1999).
27. B. Rezek *et al.*, *Appl. Phys. Lett.* **82**, 2266 (2003).
28. P. C. Hiemenz, R. Rajagopalan, *Principles of Colloid and Surface Chemistry* (Dekker, New York, ed. 3, 1997).
29. A. W. Neumann, R. J. Good, *Techniques of Measuring Contact Angles, Surface and Colloid Science*, vol. II, *Experimental Methods*, R. J. Good, R. R. Stromberg, Eds. (Plenum, New York, 1979).
30. N. Matsuka, Y. Nakagawa, M. Kurihara, T. Tonomura, *Desalination* **51**, 163 (1984).
31. G. S. Woods, in *Properties and Growth of Diamond*, G. Davies, Ed. (EMIS Datareviews Ser. 9, Institution of Chemical Engineers, London, 1994), pp. 83–84.
32. T. Evans, in *The Properties of Natural and Synthetic Diamond*, J. E. Field, Ed. (Academic Press, London, 1992), p. 259.
33. A. T. Collins, E. C. Lightowlers, in *Properties of Diamond*, J. E. Field, Ed. (Academic Press, London, 1979), p. 99.
34. J. Ristein, M. Riedel, M. Stammler, B. F. Mantel, L. Ley, *Diamond Relat. Mater.* **11**, 350 (2002).
35. S. Kazaoui, N. Minami, N. Matsuda, H. Kataura, Y. Achiba, *Appl. Phys. Lett.* **78**, 3433 (2001).
36. J. Zhao, J. Han, J. Lu, *Phys. Rev. B* **65**, 1934011 (2002).
37. D. Lovall, M. Buss, E. Graugnard, R. P. Andres, R. Reifenberger, *Phys. Rev. B* **61**, 5683 (2000).
38. K. Bradley *et al.*, *Phys. Rev. Lett.* **85**, 4361 (2000).
39. G. U. Sumanasekera, C. K. W. Adu, S. Fang, P. C. Eklund, *Phys. Rev. Lett.* **85**, 1096 (2000).
40. P. G. Collins, K. Bradley, M. Ishigami, A. Zettl, *Science* **287**, 1801 (2000).
41. J. Kong *et al.*, *Science* **287**, 622 (2000).
42. S. Picozzi *et al.*, *J. Vac. Sci. Technol. A* **22**, 1466 (2004).
43. A. Zahab, L. Spina, P. Poncharal, C. Marliere, *Phys. Rev. B* **62**, 10000 (2000).
44. K. M. Tracy, P. J. Hartlieb, R. F. Davis, E. H. Hurt, R. J. Nemanich, *J. Appl. Phys.* **94**, 3939 (2003).
45. V. M. Bermudez, *J. Appl. Phys.* **80**, 1190 (1996).
46. V. Chakrapani, thesis, Case Western Reserve University, Cleveland, OH (2007).
47. V. Chakrapani, J. C. Angus, A. B. Anderson, G. Sumanasekera, *Mater. Res. Soc. Symp. Proc.* **956**, paper 0956-J15-01 (2007).
48. J. A. Wiles, M. Fialkowski, M. R. Radowski, G. M. Whitesides, B. A. Grzybowski, *J. Phys. Chem. B* **108**, 20296 (2004).
49. S. Trigwell, N. Grable, C. U. Yurteri, R. Sharma, M. K. Mazumder, *IEEE Trans. Ind. Appl.* **39**, 79 (2003).

50. We thank J. Adin Mann and D. J. Lacks for useful discussions. C. C. Hayman provided invaluable experimental support. Financial support of the NSF (grant CHEM 0314688) and Case Western Reserve University is gratefully acknowledged.

6 August 2007; accepted 16 October 2007
10.1126/science.1148841

REPORTS

Coherent Control of a Single Electron Spin with Electric Fields

K. C. Nowack,*† F. H. L. Koppens,† Yu. V. Nazarov, L. M. K. Vandersypen*

Manipulation of single spins is essential for spin-based quantum information processing. Electrical control instead of magnetic control is particularly appealing for this purpose, because electric fields are easy to generate locally on-chip. We experimentally realized coherent control of a single-electron spin in a quantum dot using an oscillating electric field generated by a local gate. The electric field induced coherent transitions (Rabi oscillations) between spin-up and spin-down with 90° rotations as fast as ~55 nanoseconds. Our analysis indicated that the electrically induced spin transitions were mediated by the spin-orbit interaction. Taken together with the recently demonstrated coherent exchange of two neighboring spins, our results establish the feasibility of fully electrical manipulation of spin qubits.

Spintronics and spin-based quantum information processing provide the possibility of adding new functionality to today's electronic devices by using the electron spin in addition to the electric charge (*1*). In this context, a key element is the ability to induce transitions between the spin-up and spin-down states of a localized electron spin and to prepare arbitrary superpositions of these two basis states. This is commonly accomplished by magnetic resonance, whereby bursts of a resonant oscillating magnetic field are applied (*2*). However, producing strong oscillating magnetic fields in a semiconductor device requires specially designed microwave cavities (*3*) or microfabricated striplines (*4*), and this has proven to be challenging. In comparison, electric fields can be generated much more easily, simply by exciting a local gate electrode. In addition, this allows for greater spatial selectivity, which is important for local addressing of individual spins. It would thus be highly desirable to control the spin by means of electric fields.

Although electric fields do not couple directly to the electron spin, indirect coupling can still be realized by placing the spin in a magnetic field gradient (*5*) or in a structure with a spatially varying g tensor, or simply through spin-orbit interaction, present in most semiconductor structures (*6*, *7*). Several of these mechanisms have been used to electrically manipulate electron spins in two-dimensional electron systems (*8*–*11*), but proposals for coherent electrical control at the level of a single spin (*5*, *12*–*15*) have so far remained unrealized.

We demonstrate coherent single spin rotations induced by an oscillating electric field. The electron is confined in a gate-defined quantum dot (Fig. 1A), and we use an adjacent quantum dot, containing one electron as well, for readout. The ac electric field is generated through excitation of one of the gates that form the dot, thereby

Kavli Institute of Nanoscience, Delft University of Technology, Post Office Box 5046, 2600 GA Delft, the Netherlands.

*To whom correspondence should be addressed. E-mail: k.c.nowack@tudelft.nl, l.m.k.vandersypen@tudelft.nl

†These authors contributed equally to this work.

periodically displacing the electron wave function around its equilibrium position (Fig. 1B).

The experiment consists of four stages (Fig. 1C). The device is initialized in a spin-blockade regime where two excess electrons, one in each dot, are held fixed with parallel spins (spin triplet), either pointing along or opposed to the external magnetic field [the system is never blocked in the triplet state with antiparallel spins, because of the effect of the nuclear fields in the two dots combined with the small interdot tunnel coupling; see (16) for details]. Next, the two spins are isolated by a gate voltage pulse, such that electron tunneling between the dots or to the reservoirs is forbidden. Then, one of the spins is rotated by an ac voltage burst applied to the gate, over an angle that depends on the length of the burst (17) (most likely the spin in the right dot, where the electric field is expected to be strongest). Finally, the readout stage allows the left electron to tunnel to the right dot if and only if the spins are antiparallel. Subsequent tunneling of one electron to the right reservoir gives a contribution to the current. This cycle is repeated continuously, and the current flow through the device is thus proportional to the probability of having antiparallel spins after excitation.

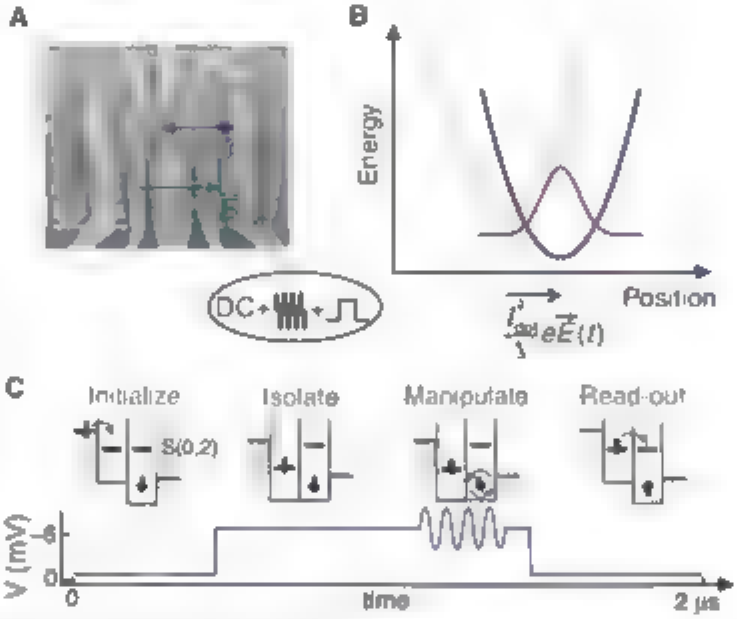

Fig. 1. (**A**) Scanning electron micrograph of a device with the same gate structure as the one used in this experiment. Metallic Ti/Au gates are deposited on top of a GaAs heterostructure that hosts a two-dimensional electron gas 90 nm below the surface. Not shown is a coplanar stripline on top of the metallic gates, separated by a dielectric [not used in this experiment; see also (4)]. In addition to a dc voltage, we can apply fast pulses and microwaves to the right side gate (as indicated) through a homemade bias-tee. The orientation of the in-plane external magnetic field is as shown. (**B**) The electric field generated upon excitation of the gate displaces the center of the electron wave function along the electric field direction and changes the potential depth. Here, Δ is the orbital energy splitting, $l_{dot} = \hbar/\sqrt{m^*\Delta}$ the size of the dot, m^* the effective electron mass, $\hbar$ the reduced Planck constant, and **E**(*t*) the electric field. (**C**) Schematic of the spin manipulation and detection scheme, controlled by a combination of a voltage pulse and burst *V*(*t*), applied to the right side gate. The diagrams show the double dot, with the thick black lines indicating the energy cost for adding an extra electron to the left or right dot, starting from (0,1), where (*n*,*m*) denotes the charge state with *n* and *m* electrons in the left and right dot. The energy cost for reaching (1,1) is (nearly) independent of the spin configuration. However, for (0,2), the energy cost for forming a singlet state [indicated by S(0,2)] is much lower than that for forming a triplet state (not shown). This difference is exploited for initialization and detection, as explained further in the main text.

To demonstrate that electrical excitation can indeed induce single-electron spin flips, we apply a microwave burst of constant length to the right side gate and monitor the average current flow through the quantum dots as a function of external magnetic field $\mathbf{B}_{ext}$ (Fig. 2A). A finite current flow is observed around the single-electron spin resonance condition, i.e., when $\mathbf{B}_{ext} = hf_{ac}/g\mu_B$, with h Planck's constant, f_{ac} the excitation frequency, and μ_B the Bohr magneton. From the position of the resonant peaks measured over a wide magnetic field range (Fig. 2B), we determine a *g* factor of $|g| = 0.39 \pm 0.01$, which is in agreement with other reported values for electrons in GaAs quantum dots (18).

In addition to the external magnetic field, the electron spin feels an effective nuclear field B_N arising from the hyperfine interaction with nuclear spins in the host material and fluctuating in time (19, 20). This nuclear field modifies the electron spin resonance condition and is generally different in the left and right dot (by ΔB_N). The peaks shown in Fig. 2A are averaged over many magnetic field sweeps and have a width of about 10 to 25 mT. This is much larger than the expected linewidth, which is only 1 to 2 mT as given by the statistical fluctuations of B_N (21, 22). Looking at individual field sweeps measured at constant excitation frequency, we see that the peaks are indeed a few mT wide (Fig. 2C), but that the peak positions change in time over a range of ~20 mT. Judging from the dependence of the position and shape of the averaged peaks on sweep direction, the origin of this large variation in the nuclear field is most likely dynamic nuclear polarization (4, 23–26).

To demonstrate coherent control of the spin, we varied the length of the microwave bursts and monitored the current level. In Fig. 3A we plot the maximum current per magnetic field sweep as a function of the microwave burst duration, averaged over several sweeps (this is a more sensitive method than averaging the traces first and then taking the maximum) (17). The maximum current exhibits clear oscillations as a function of burst length. Fitting with a cosine function reveals a linear scaling of the oscilla-

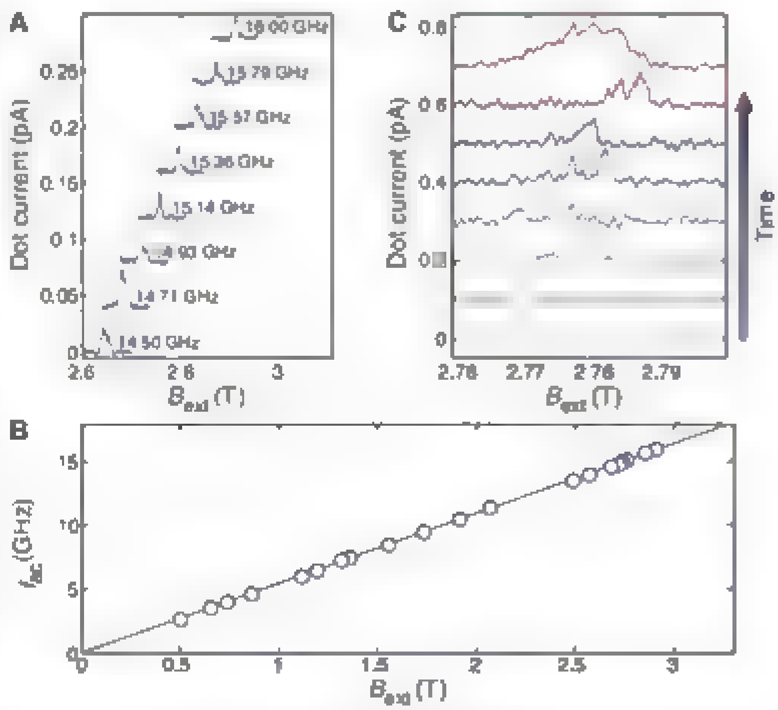

Fig. 2. (**A**) The current averaged over 40 magnetic field sweeps is given for eight different excitation frequencies, with a microwave burst length of 150 ns. The traces are offset for clarity. The microwave amplitude V_{mw} was in the range 0.9 to 2.2 mV, depending on the frequency (estimated from the output power of the microwave source and taking into account the attenuation of the coaxial lines and the switching circuit used to create microwave bursts). (**B**) Position of the resonant response over wider frequency and field ranges. Error bars are smaller than the size of the circles. (**C**) Individual magnetic field sweeps at f_{ac} = 15.2 GHz measured by sweeping from high to low magnetic field with a rate of 50 mT/min. The traces are offset by 0.1 pA each for clarity. The red trace is an average over 40 sweeps, including the ones shown and scaled up by a factor of 5.

tion frequency with the driving amplitude (Fig. 3B), a characteristic feature of Rabi oscillations and proof of coherent control of the electron spin via electric fields.

The highest Rabi frequency we achieved is ~4.7 MHz (measured at f_{ac} = 15.2 GHz), corresponding to a 90° rotation in ~55 ns, which is only a factor of 2 slower than those realized with magnetic driving (4). Stronger electrical driving was not possible because of photon-assisted tunneling. This is a process whereby the electric field provides energy for one of the following transitions: tunneling of an electron to a reservoir or to the triplet with both electrons in the right dot. This lifts spin blockade, irrespective of whether the spin resonance condition is met.

Small Rabi frequencies could be observed as well. The bottom trace of Fig. 3A shows a Rabi oscillation with a period exceeding 1.5 μs (measured at f_{ac} = 2.6 GHz), corresponding to an effective driving field of only about 0.2 mT, one-tenth the amplitude of the statistical fluctuations of the nuclear field. The oscillations are nevertheless visible because the dynamics of the nuclear bath are slow compared to the Rabi period, resulting in a slow power-law decay of the oscillation amplitude on driving field (27).

We next turn to the mechanism responsible for resonant transitions between spin states. First, we exclude a magnetic origin because the oscillating magnetic field generated upon excitation of the gate is more than two orders of magnitude too small to produce the observed Rabi oscillations with periods up to ~220 ns, which requires a driving field of about 2 mT (17). Second, we have seen that there are in principle a number of ways in which an ac electric field can cause single-spin transitions. What is required is that the oscillating electric field give rise to an effective magnetic field, $\mathbf{B}_{eff}(t)$, acting on the spin, oscillating in the plane perpendicular to $\mathbf{B}_{ext}$, at frequency $f_{ac} = g\mu_B \mathbf{B}_{ext}/h$. The g-tensor anisotropy is very small in GaAs, so g-tensor modulation can be ruled out as the driving mechanism. Furthermore, in our experiment there is no external magnetic field gradient applied, which could otherwise lead to spin resonance (5). We are aware of only two remaining possible coupling mechanisms: spin-orbit interaction and the spatial variation of the nuclear field.

In principle, moving the wave function in a nuclear field gradient can drive spin transitions (5, 28), as was recently observed (26). However, the measurement of each Rabi oscillation lasted more than 1 hour, much longer than the time during which the nuclear field gradient is constant (~100 μs to a few s). Because this field gradient and, therefore, the corresponding effective driving field, slowly fluctuates in time around zero, the oscillations would be strongly damped, regardless of the driving amplitude (26). Possibly, a (nearly) static gradient in the nuclear spin polarization could develop as a result of electron-nuclear feedback. However, such polarization would be parallel to $\mathbf{B}_{ext}$ and thus cannot be responsible for the observed coherent oscillations.

In contrast, spin-orbit mediated driving can induce coherent transitions (12), which can be understood as follows. The spin-orbit interaction in a GaAs heterostructure is given by $H_{SO} = \alpha(p_x\sigma_y - p_y\sigma_x) + \beta(-p_x\sigma_x + p_y\sigma_y)$, where α and β are the Rashba and Dresselhaus spin-orbit coefficients, respectively, and $p_{x,y}$ and $\sigma_{x,y}$ are the momentum and spin operators in the x and y directions (along the [100] and [010] crystal directions, respectively). As suggested in (12), the spin-orbit interaction can be conveniently accounted for up to the first order in α, β by applying a (gauge) transformation, resulting in a position-dependent correction to the external magnetic field. This effective magnetic field, acting on the spin, is proportional and orthogonal to the field applied

$$\mathbf{B}_{eff}(x,y) = \mathbf{n} \otimes \mathbf{B}_{ext}, n_x = \frac{2m^*}{\hbar}(-\alpha y - \beta x); \quad n_y = \frac{2m^*}{\hbar}(\alpha x + \beta y); n_z = 0 \qquad (1)$$

An electric field $\mathbf{E}(t)$ will periodically and adiabatically displace the electron wave function (Fig. 1B) by $\mathbf{x}(t) = (el_{dot}^2/\Delta)\mathbf{E}(t)$, so the electron spin will feel an oscillating effective field $\mathbf{B}_{eff}(t) \perp \mathbf{B}_{ext}$ through the dependence of $\mathbf{B}_{eff}$ on the position. The direction of $\mathbf{n}$ can be constructed from the direction of the electric field as shown in Fig. 4C and together with the direction of $\mathbf{B}_{ext}$ determines how effectively the electric field couples to the spin. The Rashba contribution always gives $\mathbf{n} \perp \mathbf{E}$, while for the Dresselhaus contribution this depends on the orientation of the electric field with respect to the crystal axis. Given the gate geometry, we expect the dominant electric field to be along the double dot axis (Fig. 1A), which here is either the [110] or [1$\bar{1}$0] crystallographic direction. For these orientations, the Dresselhaus contribution is also orthogonal to the electric field (Fig. 4C). This is why both contributions will give $\mathbf{B}_{eff} \neq 0$ and lead to coherent oscillations in the present experimental geometry, where $\mathbf{E} \perp \mathbf{B}_{ext}$. In (26), a very similar gate geometry was used, but the orientation of $\mathbf{B}_{ext}$ was different, and it

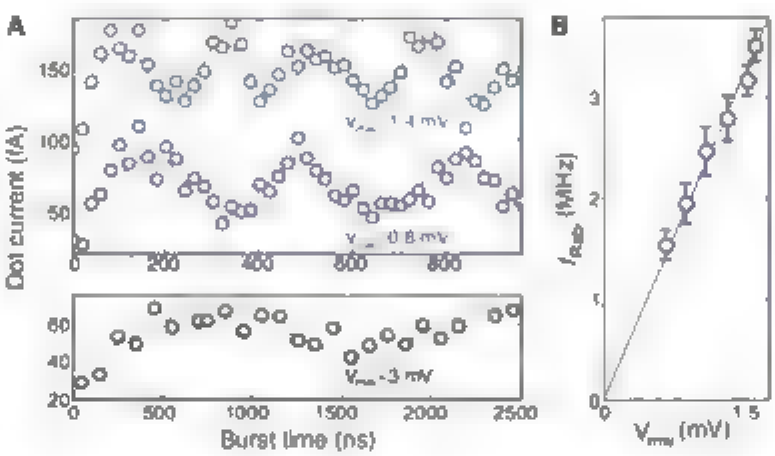

Fig. 3. (A) Rabi oscillations at 15.2 GHz (blue, average over five sweeps) and 2.6 GHz (black, average over six sweeps). The two oscillations at 15.2 GHz are measured at different amplitudes of the microwaves V_{mw}, leading to different Rabi frequencies. (B) Linear dependence of the Rabi frequency on applied microwave amplitude measured at f_{ac} = 14 GHz.

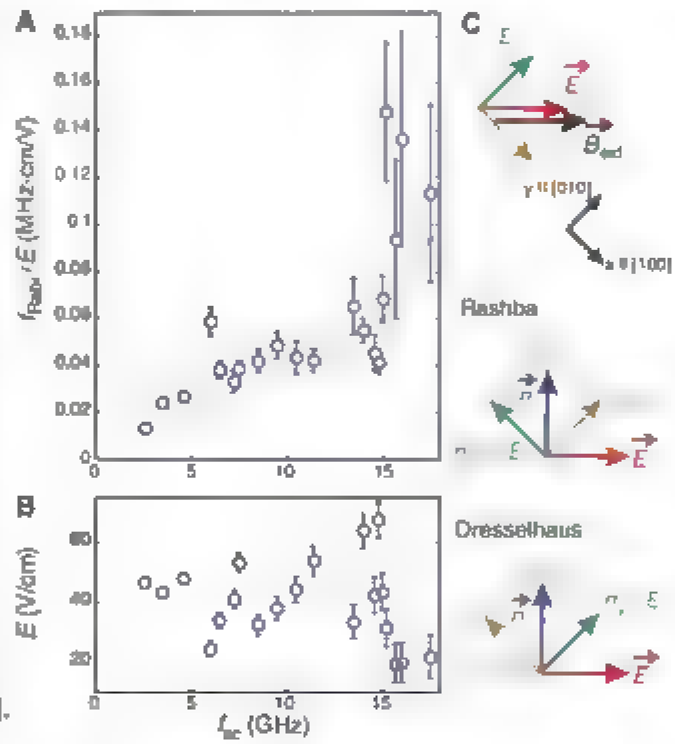

Fig. 4. (A) Rabi frequency rescaled with the applied electric field for different excitation frequencies. The error bars are given by

$$f_{Rabi}/E \sqrt{(\delta E/E)^2 + (\delta f_{Rabi}/f_{Rabi})^2}$$

where δf_{Rabi} and δE are the error in the Rabi frequency and electric field amplitude, respectively. The gray lines are the 95% confidence bounds for a linear fit through the data (weighting the data points by the inverse error squared). (B) Estimated electric field amplitudes at which the Rabi oscillations of (A) were measured at the respective excitation frequencies (17). (C) Construction of the direction of $\mathbf{n}$ resulting from the Rashba and Dresselhaus spin-orbit interaction for an electric field along [110] following Eq. 1. The coordinate system is set to the crystallographic axis [100] and [010].

can be expected that $\mathbf{E} \perp \mathbf{B}_{eff}$. In that experiment, no coherent oscillations were observed, which is consistent with the considerations here.

An important characteristic of spin-orbit–mediated driving is the linear dependence of the effective driving field on the external magnetic field, which follows from Eq. 1 and is predicted in (*12, 13, 29*). We aim to verify this dependence by measuring the Rabi frequency as a function of the resonant excitation frequency (Fig. 4A), which is proportional to the external magnetic field. Each point is rescaled by the estimated applied electric field (Fig. 4B). Even at fixed output power of the microwave source, the electric field at the dot depends on the microwave frequency due to various resonances in the line between the microwave source and the gate (caused by reflections at the bonding wires and microwave components). However, we use the photon-assisted tunneling response as a probe for the ac voltage drop across the interdot tunnel barrier, which we convert into an electric field amplitude by assuming a typical interdot distance of 100 nm. This allows us to roughly estimate the electric field at the dot for each frequency (*17*). Despite the large error bars, which predominantly result from the error made in estimating the electric field, an overall upward trend is visible in Fig. 4A.

For a quantitative comparison with theory, we extract the spin-orbit strength in GaAs, via the expression of the effective field $\mathbf{B}_{eff}$ perpendicular to $\mathbf{B}_{ext}$ for the geometry of this experiment (*12*)

$$\mathbf{B}_{eff}(t) = 2\mathbf{B}_{ext}\frac{l_{dot}}{l_{SO}}\frac{eE(t)l_{dot}}{\Delta} \quad (2)$$

with l_{SO} the spin-orbit length (for the other definitions, see Fig. 1B). Here, $l_{SO}^{-1} = m^*(\alpha \mp \beta)/\hbar$ for the case with the gate symmetry axis along $[1\bar{1}0]$ or $[110]$, respectively. Via $f_{Rabi} = g\mu_B B_{eff}/2h$, the confidence interval of the slope in Fig. 4A gives a spin-orbit length of 28 to 37 μm (with a level splitting Δ in the right dot of 0.9 meV extracted from high-bias transport measurements). Additional uncertainty in l_{SO} is due to the estimate of the interdot distance and the assumption of a homogeneous electric field, deformation effects of the dot potential (*15*), and extra cubic terms in the Hamiltonian (*7*). Still, the extracted spin-orbit length is of the same order of magnitude as other reported values for GaAs quantum dots (*18*).

Both the observed trend of $\mathbf{B}_{eff}$ with f_{ac} and the extracted range for l_{SO} are consistent with our supposition (by elimination of other mechanisms) that spin transitions are mediated by spin-orbit interaction. We note that also for relaxation of single electron spins in which electric field fluctuations from phonons couple to the spin, it is by now well established that the spin-orbit interaction is dominant at fields higher than a few 100 mT (*12, 18, 28, 29*). It can thus be expected to be dominant for coherent driving as well.

The electrically driven single-spin resonance reported here, combined with the so-called $\sqrt{SWAP}$ gate based on the exchange interaction between two neighboring spins (*30*), brings all-electrical universal control of electron spins within reach. Whereas the $\sqrt{SWAP}$ gate already operates on subnanosecond time scales, single-spin rotations still take about 100 ns (the main limitation is photon-assisted tunneling). Faster operations could be achieved by suppressing photon-assisted tunneling (e.g., by increasing the tunnel barriers or operating deeper into Coulomb blockade), by working at still higher magnetic fields, by using materials with stronger spin-orbit interaction, or through optimized gate designs. Furthermore, the electrical control offers the potential for spatially selective addressing of individual spins in a quantum dot array, because the electric field is produced by a local gate. Finally, the spin rotations were realized at magnetic fields high enough to allow for single-shot read-out of a single spin (*31*), so that both elements can be integrated in a single experiment.

References and Notes

1. D. Awschalom, D. Loss, N. Samarth, *Semiconductor Spintronics and Quantum Computation* (Springer Verlag, Berlin, 2002).
2. C. Poole, *Electron Spin Resonance* (Wiley, New York, ed. 2, 1983).
3. B. Simović *et al.*, *Rev. Sci. Instrum.* **77**, 064702 (2006).
4. F. H. L. Koppens *et al.*, *Nature* **442**, 766 (2006).
5. Y. Tokura, W. G. van der Wiel, T. Obata, S. Tarucha, *Phys. Rev. Lett.* **96**, 047202 (2006).
6. Y. A. Bychkov, E. I. Rashba, *J. Phys. C* **17**, 6039 (1984).
7. G. Dresselhaus, *Phys. Rev.* **100**, 580 (1955).
8. Y. Kato, R. C. Myers, A. C. Gossard, D. D. Awschalom, *Nature* **427**, 50 (2003).
9. Y. Kato *et al.*, *Science* **299**, 1201 (2003).
10. G. Salis *et al.*, *Nature* **414**, 619 (2001).
11. M. Schulte, J. G. S. Lok, G. Denninger, W. Dietsche, *Phys. Rev. Lett.* **94**, 137601 (2005).
12. V. N. Golovach, M. Borhani, D. Loss, *Phys. Rev. B* **74**, 165319 (2006).
13. L. Levitov, E. Rashba, *Phys. Rev. B* **67**, 115324 (2003).
14. S. Debald, C. Emary, *Phys. Rev. Lett.* **94**, 226803 (2005).
15. J. Walls, *Condens. Matter* http://arxiv.org/abs/0705.4231 (2007).
16. F. H. L. Koppens *et al.*, *J. Appl. Phys.* **101**, 081706 (2007).
17. Supporting material is available on *Science* Online.
18. R. Hanson, L. P. Kouwenhoven, J. R. Petta, S. Tarucha, L. M. K. Vandersypen, *Rev. Mod. Phys.* **79**, 1217 (2007).
19. A. V. Khaetskii, D. Loss, L. Glazman, *Phys. Rev. Lett.* **88**, [illegible].
20. I. A. Merkulov, A. L. Efros, M. Rosen, *Phys. Rev. B* **65**, 205309 (2002).
21. A. C. Johnson *et al.*, *Nature* **435**, 925 (2005).
22. F. H. L. Koppens *et al.*, *Science* **309**, 1346 (2005).
23. J. Baugh, Y. Kitamura, K. Ono, S. Tarucha, *Phys. Rev. Lett.* **99**, 096804 (2007).
24. M. S. Rudner, L. S. Levitov, *Phys. Rev. Lett.* **99**, 036602 (2007).
25. D. Klauser, W. A. Coish, D. Loss, *Phys. Rev. B* **73**, 205302 (2006).
26. E. A. Laird *et al.*, *Condens. Matter*, http://arxiv.org/abs/0707.0557 (2007).
27. F. H. L. Koppens *et al.*, *Phys. Rev. Lett.* **99**, 106803 (2007).
28. S. I. Erlingsson, Y. V. Nazarov, *Phys. Rev. B* **66**, 155327 (2002).
29. A. V. Khaetskii, Y. V. Nazarov, *Phys. Rev. B* **64**, 125316 (2001).
30. J. R. Petta *et al.*, *Science* **309**, 2180 (2005).
31. J. M. Elzerman *et al.*, *Nature* **430**, 431 (2004).

32. We thank L. P. Kouwenhoven, C. Barthel, E. Laird, M. Flatte, J. T. Vink, and T. Meunier for discussions and R. Schouten, B. van der Enden, and R. Roeleveld for technical assistance and J. H. Plantenberg and P. C. de Groot for help with microwave components. Supported by the Dutch Organization for Fundamental Research on Matter (FOM) and the Netherlands Organization for Scientific Research (NWO).

Supporting Online Material

www.sciencemag.org/cgi/content/full/1148092/DC1
Materials and Methods
SOM Text
Figs. S1 and S2
References

20 July 2007; accepted 16 October 2007
Published online 1 November 2007;
10.1126/science.1148092
Include this information when citing this paper.

Flow of Mantle Fluids Through the Ductile Lower Crust: Helium Isotope Trends

B. Mack Kennedy[1] and Matthijs C. van Soest[2]

Heat and mass are injected into the shallow crust when mantle fluids are able to flow through the ductile lower crust. Minimum $^3He/^4He$ ratios in surface fluids from the northern Basin and Range Province, western North America, increase systematically from low crustal values in the east to high mantle values in the west, a regional trend that correlates with the rates of active crustal deformation. The highest ratios occur where the extension and shear strain rates are greatest. The correspondence of helium isotope ratios and active transtensional deformation indicates a deformation-enhanced permeability and that mantle fluids can penetrate the ductile lithosphere, even in regions where there is no substantial magmatism. Superimposed on the regional trend are local, high $^3He/^4He$ anomalies indicating hidden magmatic activity and/or deep fluid production with locally enhanced permeability, identifying zones with high resource potential, particularly for geothermal energy development.

Mantle volatiles, principally water and CO_2, play an important role in lithosphere rheology and the production of buoyant fluids that can be injected into the shallow crust. Regional and local trends in the crustal occurrence of mantle volatiles provide insight into the coupling between mantle-crust tectonics (*1, 2*), heat and mass exchange between the mantle and crust (*3–5*), and the occurrence and distribution of economic resources

such as ore minerals and oil, gas, and geothermal fluids (6). Mantle-derived volatiles in the crust are traceable through He isotopic compositions of hydrologic fluids (7). Once injected into a crustal-fluid system, mantle He will be continuously diluted with radiogenic helium-4 (^{4}He) acquired from the U-Th rich crust, and therefore surface-fluid He isotopic compositions also provide a measure of the mantle He flux and the integrated permeability-fluid pressure gradient (flow rate) through the crust (1). To enter the hydrologic system, mantle He must pass through a ductile lower crust, which is believed to be an impermeable boundary because of an inability to maintain open fractures on long time scales (8–10). A general assumption is that the passage of fluids through this boundary must occur either by direct intrusion and degassing of mantle-derived magmas (6) or by diffusion through the ductile boundary layer (11). However two recent studies in areas void of recent volcanism (1, 12) have found evidence for fault-controlled advective flow of mantle fluids through the ductile boundary. How and why this occurs is not well understood.

We conducted a regional study of He isotopic compositions of thermal fluids collected from surface features and wells throughout the northern Basin and Range Province (B&R), western North America (Fig. 1 and table S1) (13). As a result of the tectonic influence exerted by the relative motion of the Pacific and North American Plates (14, 15), the B&R is a vast extended region of anomalous thermal gradients, large heat flux, high regional elevation, thin (ned) crust, and lithospheric- and asthenospheric-mantle melting. Presently, extension is accommodated by high-angle normal faults, and the locus of major extension and its associated magmatism occurs at the margins of the province (16), primarily within the Walker Lane, a narrow, 100-to-200 km wide transtensional volcanic zone along the eastern side of the Sierra Nevada that extends north into a transitional zone between the Sierra Nevada and the subduction-related volcanic arc of the Cascades. East of the Walker Lane, B&R extension occurs at a slowing rate, over a much wider area and in the absence of active or recently active volcanism. The highest extension rates in this area occur west of the central Nevada seismic belt (CNSB), a north-northeast trending belt of Holocene seismic activity.

Across the northern B&R, three general He isotope trends are apparent. First, ratios >3.0 Ra (7) occur only at the western margin of the B&R, reflecting active or recently active shallow-crustal volcanism within the Walker Lane (Coso, Long Valley, and Steamboat) and the Cascade volcanic chain (Lassen, Mount Shasta, Medicine Lake, Crater Lake, and Newberry Crater). Second, the preponderance of ratios >0.6 Ra occur in the northwest B&R in an area ranging from the CNSB west to the transition zone with the Cascade volcanics. Third, east of the CNSB, the He ratios decline, ranging from 0.1 to 0.3 Ra.

Collectively, the minimum ^{3}He/^{4}He ratios define a regional baseline trend of decreasing ratios from west to east, as illustrated by the shaded

[1]Center for Isotope Geochemistry, Earth Sciences Division, Lawrence Berkeley National Laboratory, Berkeley, CA 94720, USA. [2]Noble Gas Geochemistry and Geochronology Laboratory, School of Earth and Space Exploration, Arizona State University, Tempe, AZ 85287–1404, USA.

*To whom correspondence should be addressed. E-mail: bmkennedy@lbl.gov

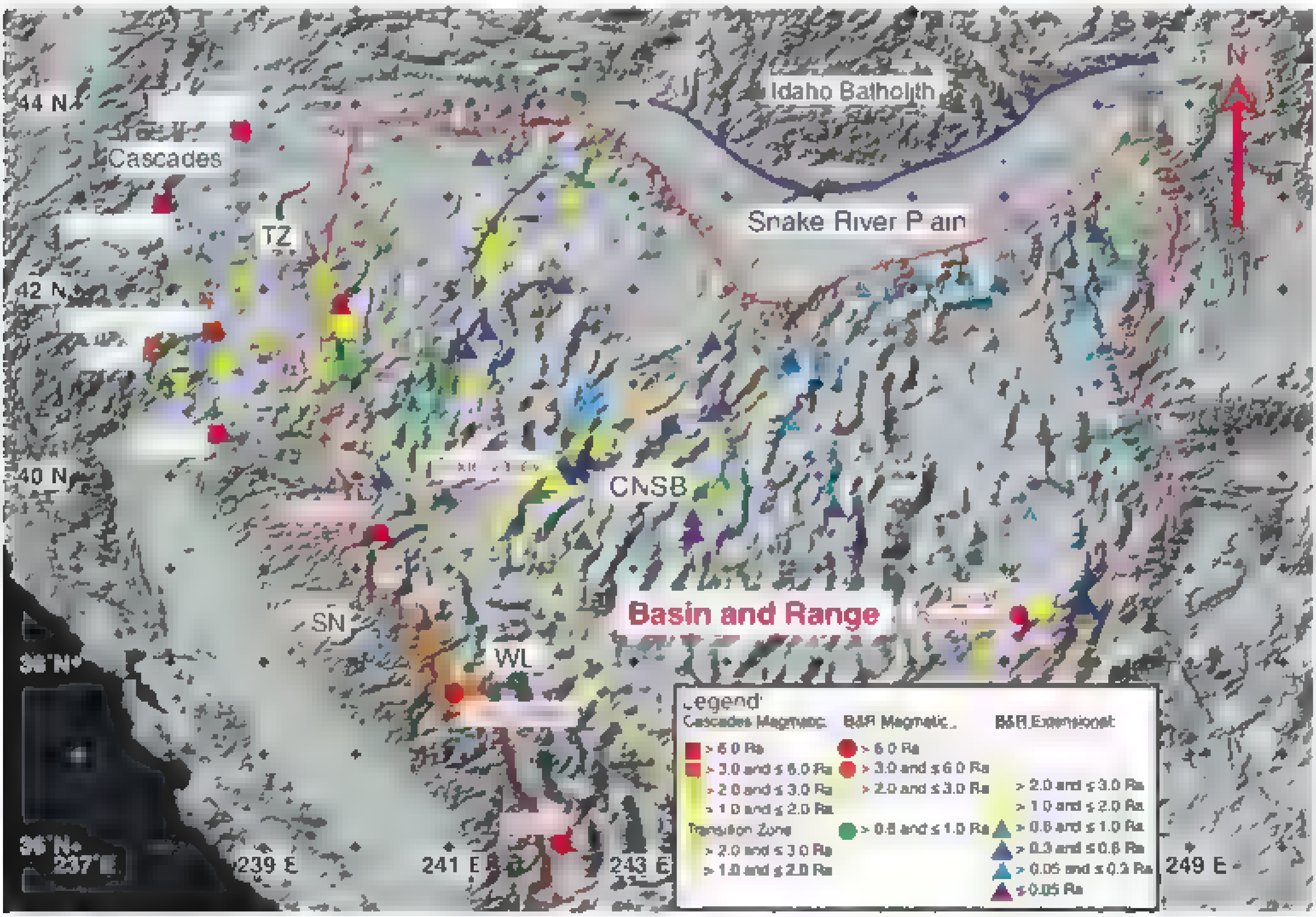

Fig. 1. Sample location map of the B&R and surrounding areas. The symbol colors delineate ^{3}He/^{4}He ratios, expressed as Rc/Ra (the air-corrected sample ratio normalized to the ratio in air), and the symbol shapes identify the type of thermal area. Tectonic zones are outlined: red, northern B&R; yellow, the Walker Lane transtensional zone (WL) and the CNSB; green, the Sierra Nevada batholith (SN); and light blue, the Cascades volcanic zone. TZ, transition zone between the Cascades, WL, and B&R.

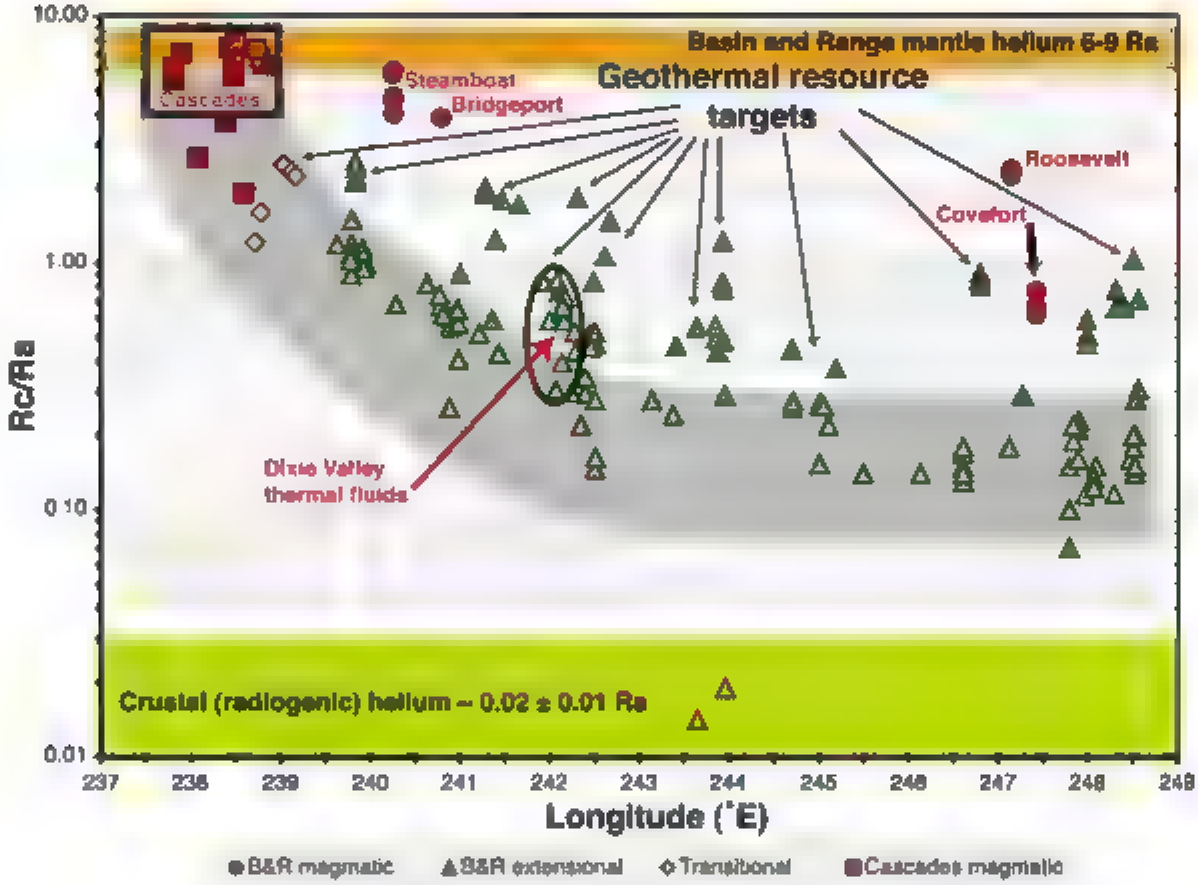

Fig. 2. Air-corrected He isotopic composition of geothermal fluids above 38°N latitude in the B&R, TZ, and Cascades, plotted as a function of longitude. The shaded curve depicts an east-to-west baseline trend defined by minima in the local $^3He/^4He$ ratios.

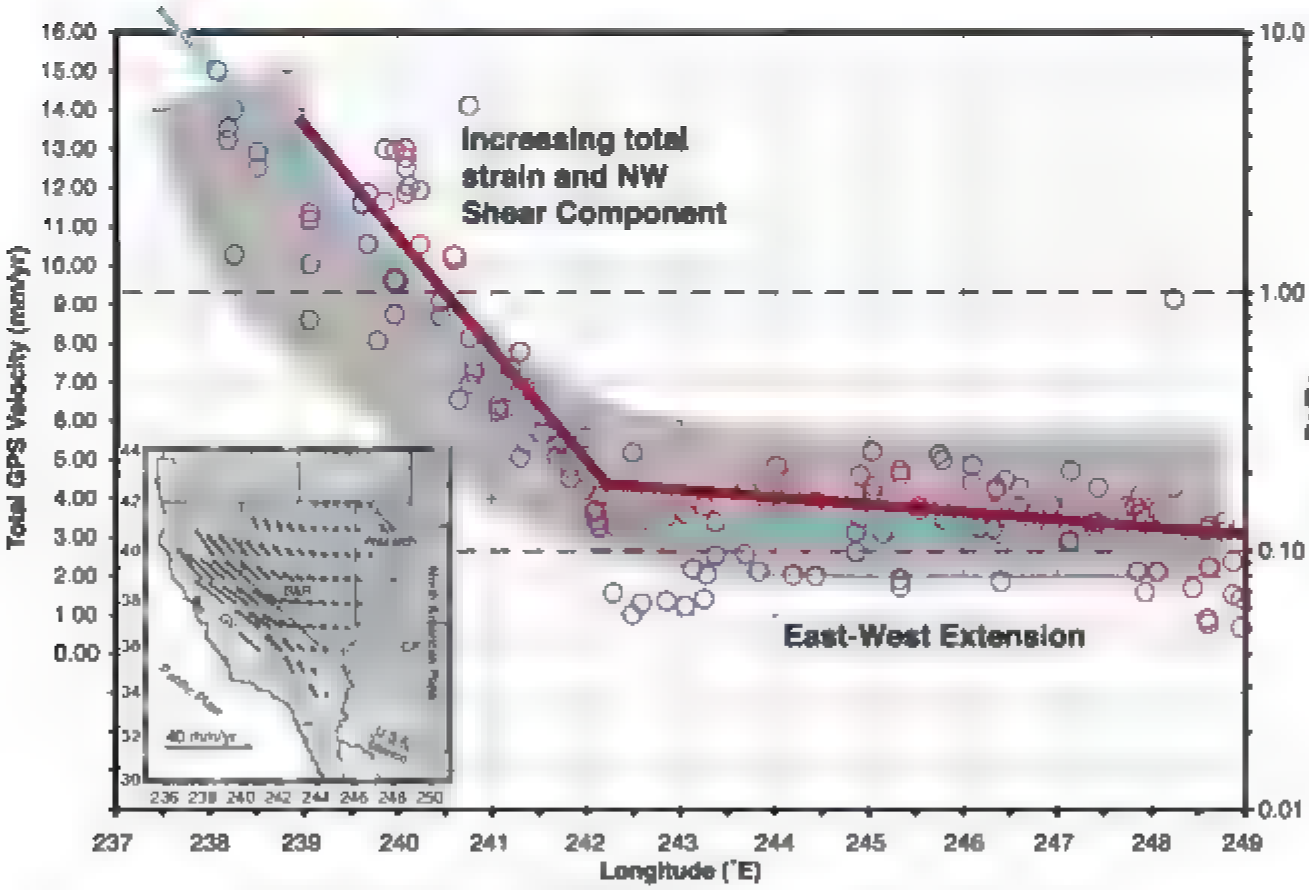

Fig. 3. Compilation of present-day GPS strain rates across the northern B&R, relative to the North America reference frame. The data are from GPS networks located in a band from 38°N to 41° N latitude (*15, 16*). West of 242°E to 242.5° E longitude, the data show a combined increase in total magnitude of strain and an increase in lateral dextral shear strain superimposed on the east-west extension. This is most evident in the Walker Lane, but it impacts most of the B&R in and to the northwest of the CNSB, as illustrated by the Fig. 3 insert taken from (*19*). The broad colored band is the regional baseline He isotope trend from Fig. 2, shown superimposed on the trends in strain rate. CP, Colorado Plateau; GV, Great Valley.

band in Fig. 2. East of the Walker Lane and Cascades, the occurrence of mantle He—as indicated by baseline $^3He/^4He$ ratios (~0.2 to 2.0 Ra) that are much greater than those of average crustal He (~0.02 Ra)—is not supported by magma intrusion, as this region has no evidence for current or recent volcanic activity. Instead, the baseline trend is strongly correlated with a change in the direction and magnitude of strain detected by present-day Global Positioning System (GPS) velocities (Fig. 3) (*17, 18*). West of the CNSB, a nearly pure east-west extension rate of ~3 mm/year shifts to N40°W and increases to 12 to 13 mm/year. The accelerating dextral shear component is driven by a drag force due to the relative movement of the Pacific and North American Plates (*19*). We hypothesize that the increase in total strain and, specifically, the northwest-orientated dextral shear component greatly enhance average fluid-flow rates, allowing for a more rapid flow of mantle fluids through the crust and preserving the high $^3He/^4He$ ratios observed at the surface. The enhanced flow rate must persist through the brittle-ductile transition, through the ductile lower crust, and into the mantle lithosphere. If, as expected, fluids passing through the ductile crust enter the base of the brittle zone at, or near, lithostatic pressure, then the east-to-west increase in the flow rate is primarily governed by an east-to-west increase in average permeability.

The high-angle normal faults that presently accommodate B&R extension and that are probably fluid-flow pathways are not expected to penetrate the ductile lower crust. In extensional regimes, because of gravitational loading, the maximum principle stress is perpendicular to the geoid. With increasing depth, the brittle-to-ductile shift in rheology refracts the maximum stress acting on the fault, resulting in nearly horizontal shear zones or detachment faults at the boundary between the high-viscosity upper crusts and low-viscosity lower crusts (*20, 21*). Strain localization induced by an increasing dextral shear component superimposed on the extensional stress field must mechanically couple the brittle and ductile crustal zones, generating vertically oriented downward fault splays that extend through the ductile crust and into the mantle. These splays would act as conduits for fluid flow. The close correspondence between He isotope ratios and the rate of dextral shear strain suggests that fluid-flow rate (and hence, permeability) through the ductile zone is a function of the rate of dextral shear strain. Once the flow has initiated, the high-pressure pore and fracture fluids may help to maintain permeability, enhancing flow through the ductile zone (*22*).

There are many sampled features that have elevated $^3He/^4He$ ratios with respect to the regional baseline trend. Although a few, such as Roosevelt Hot Spring and Cowefort, are associated with crustal magma systems (*23*), the majority are not. An example of the latter is the Dixie Valley thermal system (Fig. 2), where a detailed study (*24*) found a range in He isotope ratios (~0.3 to 0.8 Ra), with the highest ratios restricted to fluids emerging directly from the Stillwater range-front fault system, a high-angle normal fault that defines the western margin of the valley. A recent east-west high-resolution deep magnetotelluric study that crossed through Dixie Valley revealed a zone of low resistance, a possible indication of fluids at a depth of ~25 km within the mantle lithosphere (*25*), suggesting that the Dixie Valley He anomaly reflects a combination of local, deep production of mantle fluids (zone of low resistance) and a range-front fault system with enhanced permeability (high fluid-flow rates and, hence, high $^3He/^4He$ ratios). The range-front fault is the primary conduit supplying ~20 × 10^9 kg of 250°C water in support of a 62-megawatt-electric geothermal power plant (*26*). It follows that other "local He anomalies" may be indicative of similar systems and represent geothermal targets with high potential.

Our regional He isotope study of fluids across the northern B&R clearly demonstrates a strong correlation between an east-to-west increase in the magnitude of dextral shear strain and an east-to-west increase in baseline He isotope ratios. In the absence of active or recently active magmatism, the elevated He isotope ratios require amagmatic flow of mantle fluids through the ductile lower crust, suggesting that the increase in dextral shear strain rates creates and maintains permeable pathways through the ductile zone. Elevated He isotope ratios in surface fluids along amagmatic sections of the San Andreas fault (*1*) and a recently observed series of nonvolcanic tremors deep (20 to 40 km) beneath the same section of the fault provide additional support for the existence of deep-mantle fluids, their potential importance in fault mechanisms (*27*), and nonmagmatic fluid flow through the ductile zone.

The high $^3He/^4He$ anomalies superimposed on the regional trend indicate enhanced crustal permeability coupled with local zones of deep fluid production and/or hidden magmatic activity. These local anomalies may be indicative of a heterogeneous distribution of mantle volatiles that promote melt production. Assuming a $CO_2/^3He$ ratio of ~2 × 10^9 M (characteristic of mid-ocean ridge basalts) (*6*) as a proxy for mantle-derived volatiles, the calculated fluid-flow rate through the Dixie Valley geothermal system (*24*) translates into a mantle CO_2 flux of ~2 × 10^{-6} to 20 × 10^{-6} mol cm^{-2} $year^{-1}$. As of yet, no definitive geochemical or isotopic evidence for the presence of mantle CO_2 has been found, other than carbon isotopic compositions ($\delta^{13}C$ = −6.5 ± 2.5 per mil) (*22*) not dissimilar from those of mantle CO_2 (*6*). An estimated $CO_2/^3He$ ratio in Dixie Valley fluids of ~40 × 10^9 (*13*) is ~20 times the mid-ocean ridge value, suggesting that most (~95%) of the CO_2 is not mantle-derived or, alternatively, that the subcontinental mantle $CO_2/^3He$ ratio is much greater than that observed at mid-ocean ridges.

Earth's crust stores an enormous resource of thermal energy produced primarily from the radioactive decay of U, Th, and K that is dispersed throughout Earth. It has been estimated that, within the United States (excluding Hawaii and Alaska), there are ~9 × 10^{16} kilowatt-hours (kWh) of accessible geothermal energy. This is a sizable resource compared to the total energy consumption in the United States of 3 × 10^{13} kWh annually. In order for geothermal systems to develop and mine the heat source naturally, adequate fluid sources and deep permeable pathways are a necessity. The deep pathways provide access to high temperatures that can drive fluid convection cells. He isotopes provide a quantitative or, at least, a qualitative estimate of deep permeability from surface measurements, and anomalies superimposed on regional trends can identify potential resources.

References and Notes

1. B. M. Kennedy *et al.*, *Science* **278**, 1278 (1997).
2. D. L. Newell *et al.*, *GSA Today* **15**, 4 (2005).
3. F. J. Spera, *Contrib. Mineral. Petrol.* **88**, 217 (1984).
4. G. Holland, C. J. Ballentine, *Nature* **441**, 186 (2006).
5. C. J. Ballentine, B. Marty, B. S. Lollar, M. Cassidy, *Nature* **433**, 33 (2005).
6. C. J. Ballentine, R. Burgess, B. Marty, *Rev. Mineral. Geochem.* **47**, 539 (2002).
7. Without mantle influence, crustal fluids are dominated by ^4He produced from the natural radioactivity of U and Th and characterized by very low $^3He/^4He$ ratios of ~0.02 Ra (where Ra = 1.4 × 10^{-6}, the ratio in air). Mantle fluids without substantial crustal influence are strongly enriched in ^3He, with typical ratios ranging from ~6 to 35 Ra, depending on the mantle source (e.g., plume volcanism versus mid-ocean ridge basalt versus back-arc volcanism).
8. J. D. Byerlee, *Geophys. Res. Lett.* **17**, 2109 (1990).
9. J. D. Byerlee, *Geology* **21**, 303 (1993).
10. N. H. Sleep, M. L. Blanpied, *Nature* **359**, 687 (1992).
11. T. Torgersen, *J. Geophys. Res.* **98**, 16257 (1993).
12. J. T. Kulongoski, D. R. Hilton, J. A. Izbicki, *Geochim. Cosmochim. Acta* **69**, 3857 (2005).
13. Materials and methods are available as supporting material on *Science* Online.
14. C. H. Jones *et al.*, *Tectonophysics* **213**, 57 (1992).
15. M. L. Zoback, G. A. Thompson, *Geology* **6**, 111 (1978).
16. T. Parsons, in *Developments in Geotectonics 25, Publication #264 of the International Lithosphere Program*, K. H. Olsen, Ed. (Elsevier, New York, 1995), pp. 277–324.
17. R. A. Bennett, B. P. Wernicke, N. A. Niemi, A. M. Friedrich, J. L. Davis, *Tectonics* **22**, 1008 (2003).
18. W. C. Hammond, W. Thatcher, *J. Geophys. Res.* **109**, B08403 (2004).
19. L. M. Flesch, W. E. Holt, A. J. Haines, B. Shen-Tu, *Science* **287**, 834 (2000).
20. G. A. Bradshaw, M. D. Zoback, *Geology* **16**, 271 (1988).
21. H. J. Melosh, *Nature* **343**, 331 (1990).
22. S. F. Cox, *Earth Planets Space* **54**, 1121 (2002).
23. D. L. Nielson, J. N. Moore, *Geotherm. Resour. Counc. Trans.* **3**, 503 (1979).
24. B. M. Kennedy, M. C. van Soest, *Geothermics* **35**, 26 (2006).
25. P. E. Wannamaker, W. M. Doerner, D. P. Hasterok, *Geol. Soc. Am. Abstr. Prog.* **37**, 495 (2005).
26. D. D. Blackwell, B. Gollan, D. Benoit, *Geotherm. Resour. Counc. Trans.* **24**, 223 (2000).
27. R. M. Nadeau, D. Dolenc, *Science* **307**, 389 (2005); published online 9 December 2004 (10.1126/science.1107142).

28. This work was supported by the U. S. Department of Energy, Office of Basic Energy Sciences and Office of Geothermal Technologies under contract DE-AC02-05CH11231.

Supporting Online Material

www.sciencemag.org/cgi/content/full/318/5855/1433/DC1
Materials and Methods
Table S1
References

9 July 2007; accepted 17 October 2007
10.1126/science.1147537

In Situ Determination of the Nanoscale Chemistry and Behavior of Solid-Liquid Systems

Santhana K. Eswaramoorthy,[1] James M. Howe,[1*] Govindarajan Muralidharan[2]

Many fundamental questions in crystal-growth behavior remain unanswered because of the difficulties encountered in simultaneously observing phases and determining elemental concentrations and redistributions while crystals nucleate and grow at the nanoscale. We show that these obstacles can be overcome by performing energy-dispersive x-ray spectroscopy on partially molten Al-Si-Cu-Mg alloy particles during in situ heating in a transmission electron microscope. Using this technique, we were able to (i) determine that the aluminum and silicon concentrations change in a complementary and symmetric manner about the solid-liquid interface as a function of temperature; (ii) directly measure the solid- and liquid-phase compositions at equilibrium and in highly undercooled conditions for quantitative comparison with thermodynamic calculations of the liquidus and solidus phase boundaries; and (iii) provide direct evidence for homogeneous nucleation of the aluminum-rich solid.

Crystal growth is an important technological process affecting fields from metallurgy to solid-state physics and applications ranging from the production of metal-alloy ingots for buildings and aircraft to single-crystal semiconductors and oxides for electronic and optical devices (*1, 2*). It is also involved in everyday natural phenomena such as the freezing of water and biomineralization of living organisms (*3*), and in geological processes such as the formation of stalactites and stalagmites in caves (*4*). Understanding fundamental phenomena such as the structure and composition of the solid-liquid interface, the partitioning of elements between the solid and liquid phases during crystal growth, and critical factors involved in the nucleation of phases is essential to solidification science and the development of new material structures under equilibrium and nonequilibrium conditions (*1, 5–7*). The challenges of directly determining these features have been largely beyond the capabilities of experimentalists (*8*), although recent progress has been made in determining the atomic structure of the solid-liquid interface (*9–11*). This problem is particularly severe in inorganic engineering materials, which usually have high melting points (typically greater than 800 K) and are optically opaque.

Turnbull and Cech (*12*) showed that heterogeneous nucleation on impurities could be eliminated during the freezing of metals and semi-metals by using liquid droplets a few tens of micrometers in diameter. Since then, investigators have found that solidification of alloy droplets under conditions far from equilibrium has the potential to produce metastable phases with novel properties and to broaden the study of solidification processes (*7, 13*). Al-based alloys have received attention as model systems because it is possible to produce large undercoolings in atomized liquid droplets less than 20 μm in diameter (*7*). In these studies, the aforementioned difficulties have precluded direct observation of the nucleation and growth behavior of phases, or measurements of the local compositions present during solidification (or melting). The closest experiments of this type have involved in situ heating of submicrometer-diameter binary Al-Si alloy particles to obtain qualitative elemental profiles across solid-liquid interfaces (*14, 15*) in the transmission electron microscope (TEM). In this study, we used a newly designed thermal shield on a conventional TEM heating holder (*16*) to obtain quantitative chemical compositions across a solid-liquid interface and in the undercooled liquid phase as a function of temperature.

The sample chosen for this investigation was a multicomponent commercial, Al-Si base alloy (AA 390) powder obtained from Valimet (*17*). The alloy is typically used in aerospace and automobile applications because of its high strength-to-weight ratio and good wear and corrosion resistance. The alloy is mainly Al, with intentional additions of 17.87 Si, 1.83 Cu, and 0.6 Mg (here and henceforth, all compositions are in atomic percent). Additional minor impurities in the alloy such as Fe and Mn are generally present at lower amounts and are not relevant to the present study. The powder particles were suspended in ethanol and dispersed on an ultrathin

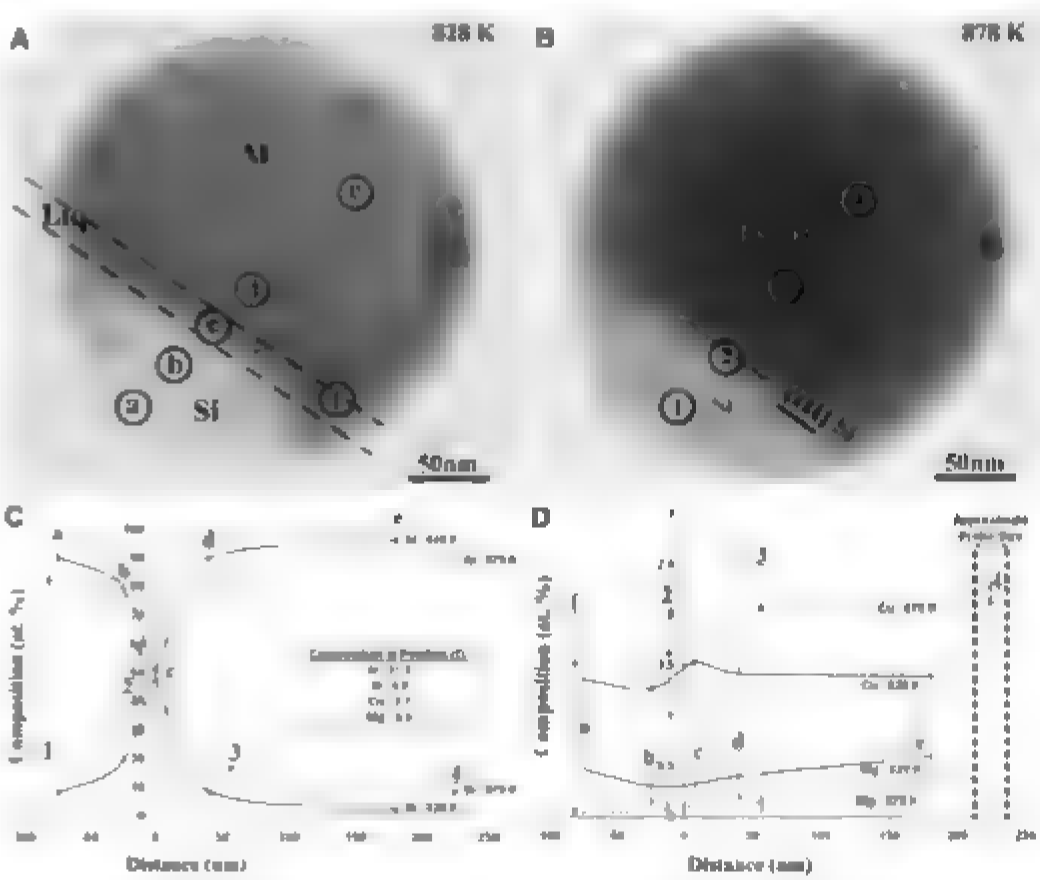

Fig. 1. (**A**) Bright-field TEM image of a partially molten Al-Si-Cu-Mg powder particle taken at a temperature of 828 K. The faint, dashed line parallel to the interface indicates the approximate appearance of the column of material sampled by the electron beam normal to the plane of the figure. Circles a through f indicate where x-ray spectra were acquired. [Reprinted from (*16*) courtesy of the Microscopy Society of America and Cambridge University Press] (**B**) Bright-field TEM image of the same powder particle after further heating to 878 K. Circles 1 through 4 indicate where x-ray spectra were acquired. (**C**) Concentration profiles of Al and Si obtained from x-ray spectra taken at 828 K (solid lines) and at 878 K (dashed lines). (**D**) Concentration profiles of Cu and Mg obtained from x-ray spectra taken at 828 K (solid lines) and at 878 K (dashed lines).

[1]Department of Materials Science and Engineering, University of Virginia, 140 Chemistry Drive, Charlottesville, VA 22904–4745, USA. [2]Materials Science and Technology Division, Oak Ridge National Laboratory, 1 Bethel Valley Road, Oak Ridge, TN 37831–6132, USA.

*To whom correspondence should be addressed. E-mail: jh9s@virginia.edu

carbon film supported on a copper-mesh TEM grid. The in situ heating experiments were performed at 200 kV in a JEOL 2000FX-II TEM with a Gatan double-tilt heating holder. A thermocouple in the holder maintained the specimen temperature to within ±5 K. Chemical compositions were determined by energy-dispersive x-ray spectroscopy (EDXS) with a Gresham high-angle x-ray detector and an incident electron beam diameter (probe size) of about 25 nm. Details regarding quantification of the x-ray spectra and the accuracy of the compositional measurements, which are generally better than ±0.2%, are provided in the Supporting Online Material.

Figure 1A shows a bright-field TEM image of an Al-Si-Cu-Mg powder particle about 350 nm in diameter, taken at a temperature of 828 K. The particle is partially molten, containing a faceted primary Si particle on the lower left and an oval-shaped solid Al-rich particle that is surrounded by Al-rich liquid phase in the upper right. An amorphous aluminum oxide film several nanometers thick forms naturally on the particle surface, and this oxide shell prevents the liquid phase from evaporating in the TEM vacuum (18). The thin oxide is highly transparent and barely visible in the TEM images. The coexistence of two solid phases and a liquid in equilibrium at 828 K is consistent with Gibb's phase rule (19), because there are four major elements (Al, Si, Cu, and Mg) in the alloy. X-ray spectra were obtained at five positions, indicated by circles a to e in Fig. 1A (the size of the circle represents the approximate probe size), and the resulting compositions are plotted in Fig. 1, C and D. One additional composition obtained in the liquid phase only, circle f in Fig. 1A, is also given in Fig. 1C. Several important features are evident from these figures. The composition on the right side of the particle, at position e, contains approximately 96.0 Al, 1.9 Si, 1.3 Cu, and 0.5 Mg, while that in the Si on the far left, at position a, is about 90.2 Si, 7.9 Al, 1.3 Cu, and 0.4 Mg, indicating that the Cu and Mg levels are similar in the two solid phases at this temperature. As the thin, liquid interface between the two solid phases is approached from either side, the Al and Si concentrations change in a complementary and symmetric manner. The Cu and Mg levels do not change appreciably except at position c, where the Cu concentration increases slightly. This increase is likely due to prior partitioning of Cu during solidification, because the first liquid formed during heating in the TEM was the last Cu-enriched liquid to solidify in the particle.

Figure 1B shows the same particle after further heating to a temperature of 878 K. The particle contains only two phases, solid Si in the lower left and Al-rich liquid in the remaining volume. Similar to Fig. 1A, x-ray spectra were obtained at four positions indicated by circles 1 to 4, and the resulting compositions are plotted in Fig. 1, C and D. As at 828 K, the Al and Si concentrations change in a complementary and symmetric manner about the solid-liquid interface as it is approached from either side. The Al concentration in the liquid on the far right has decreased to about 89.2, while the levels of Cu and Si have increased to about 2.1 and 8.1, respectively, due to partial dissolution of the solid Si and increased solubility of the Cu in the liquid phase with temperature (20, 21). Also, the partially dissolved Si particle has become highly faceted along [illegible] planes (determined by electron diffraction), indicated in Fig. 1B. In contrast to the behavior observed at 828 K,

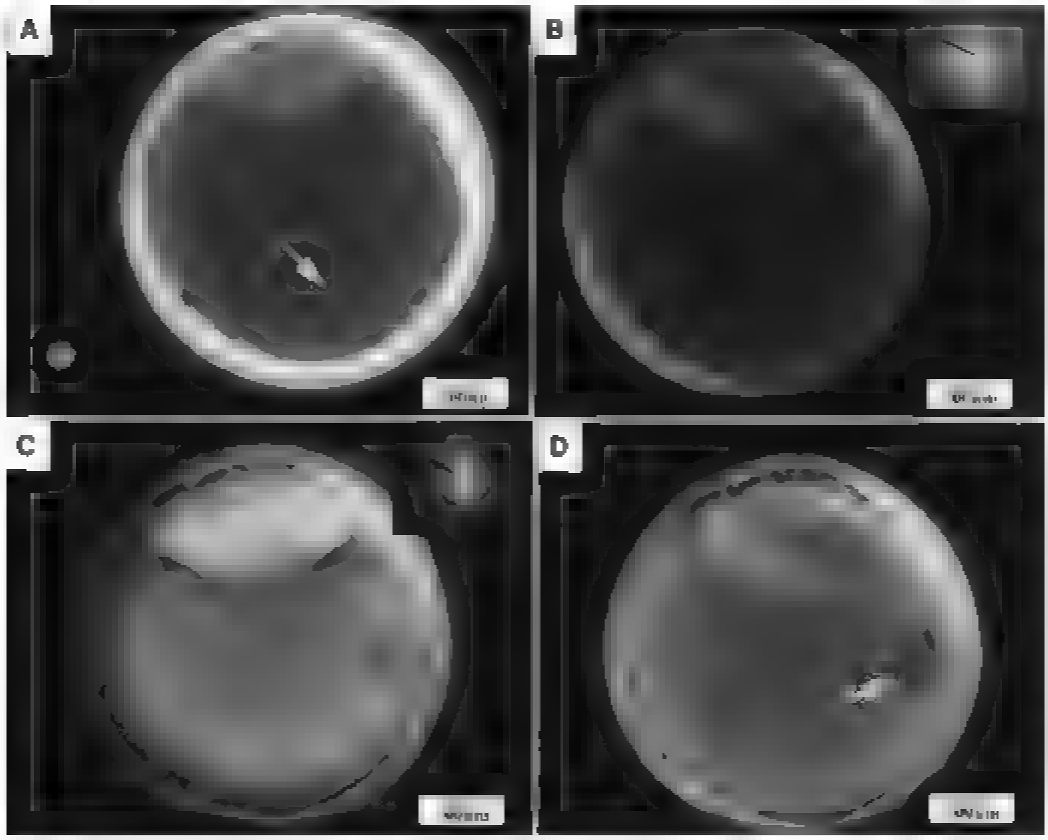

Fig. 2. (**A**) Bright-field TEM image of a second particle at 833 K. An arrow points to the position of the electron probe in the liquid in the analysis, and the bright spot in the lower-left corner is an image of the actual probe used. (**B**) Image at 753 K with an inset electron diffraction pattern showing the diffuse ring pattern corresponding to the liquid phase as well as Si reflections. (**C**) Image at 743 K with an inset electron diffraction pattern showing additional spots due to the formation of crystalline Al-rich phase. Faint rings in the diffraction pattern correspond to a small fraction of remaining liquid. (**D**) Image at 743 K taken with a lower electron beam brightness to eliminate beam heating. Arrow points to the Al_2Cu phase identified by EDXS. The electron beam is condensed to just illuminate the particle in all of the images, so that the remaining background appears dark. The contrast visible in the Si crystal is due to defects, which change their orientation and contrast slightly with temperature.

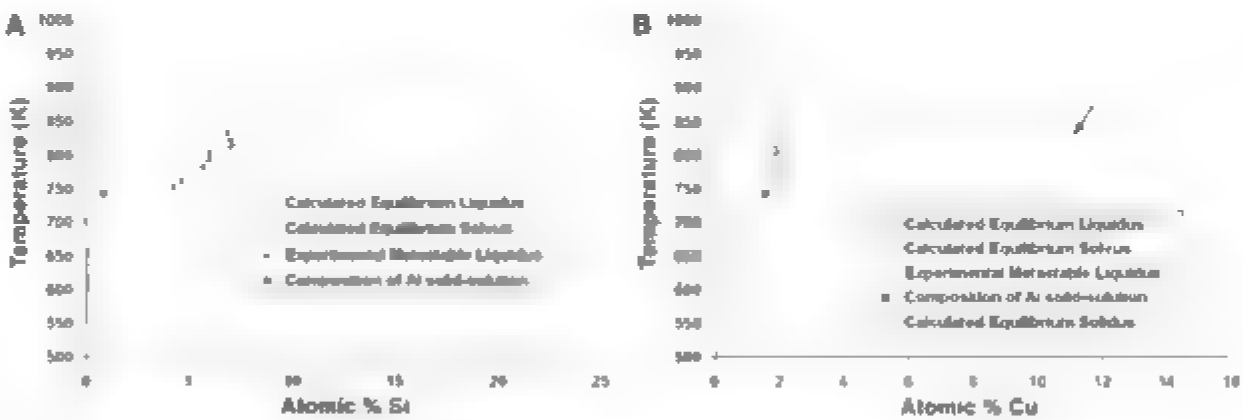

Fig. 3. (**A**) Si and (**B**) Cu concentrations in the undercooled liquid phase plotted as a function of temperature in pseudobinary phase diagrams along with the calculated equilibrium liquidus, solidus, and solvus lines for the elements.

the Cu and Mg concentrations both decrease in going from the Al-rich liquid phase to the solid Si phase at 878 K, reflecting the increased solubility in the Al-rich liquid.

Comparison of the results from the chemical analyses taken across the solid-liquid interface and in the liquid phase in the in situ TEM experiments with values obtained from thermodynamic calculations generally yielded good qualitative agreement but limited quantitative agreement. According to the calculations, the Si concentration in the liquid should increase with temperature because of the progressive dissolution of the solid Si into the liquid phase. This is in good agreement with observations from the in situ experiments. Quantitatively, the in situ results showed an increase in Si concentration from 4.6 to 8.1 when the sample was heated from 828 to 878 K, whereas the calculations yielded a change in Si concentration from 8.3 to 12.1 for the same temperatures. The experimental Cu and Mg concentrations also qualitatively followed the calculated predictions. For example, the calculations predicted a decrease in concentration from 8.8 to 1.9 in Cu and from 2.9 to 0.6 in Mg when the temperature was raised from 828 to 878 K. In comparison, the in situ experiments showed a decrease from 2.7 to 2.1 Cu and from 0.9 to 0.3 Mg. The composition of the Al solid-solution (Fig. 1, C and D) at 828 K measured in the in situ TEM experiment was 96.0 Al, 1.3 Cu, 0.5 Mg, and 1.9 Si. This is in reasonably good agreement with the calculated value of 97.3 Al, 1.0 Cu, 0.3 Mg, and 1.1 Si. The slightly higher levels of Cu, Mg, and Si in the experiment may be due to a thin layer of liquid phase between the Al and oxide at location e.

Thermodynamic calculations predict that the Si phase does not have any solid solubility for Al, Mg, or Cu at any temperature. However, experimentally, the composition of the silicon phase was 90.2 Si, 7.9 Al, 1.3 Cu, and 0.4 Mg at 828 K. This difference could be partly due to a thin layer of liquid phase that overlaps the solid Si crystal through the specimen thickness in projection, but this process cannot account for the entire difference, because with 7.9 Al, the concentrations of Cu and Mg would be about 1.0 and 0.1, respectively. Hence, the experimental results indicate that the Si phase does have some solubility for Cu and Mg (and perhaps Al) at elevated temperatures. In situ, high-temperature composition measurements in the TEM thus provide valuable information that would enable more accurate descriptions of the thermodynamics of phases and hence phase equilibria.

To investigate metastable phase equilibria, we heated the sample in situ in the TEM and determined the lowest temperature at which the liquid phase was in equilibrium with primary Si on melting. This temperature was found to be about 833 K, and the corresponding bright-field image is shown in Fig. 2A. The temperature was then decreased from 833 K in 10 K steps, and x-ray spectra were acquired from the liquid and Si phase at the same positions on the particle (indicated for the liquid by an arrow in Fig. 2A). This process was repeated until homogeneous nucleation of the Al solid-solution phase was observed to occur at 743 K, representing a cumulative undercooling of about 90 K.

A bright-field image of the sample at 753 K, just before nucleation, is shown in Fig. 2B. The corresponding electron diffraction pattern for the particle inset in Fig. 2B reveals a diffuse ring pattern due to short-range order in the liquid phase, verifying that the sample is in an undercooled metastable state. The crystalline spots also seen in the pattern correspond to the primary Si crystal. Further cooling by 10 to 743 K was sufficient to nucleate the crystalline Al-rich phase, and the electron diffraction pattern inset in Fig. 2C displays additional crystalline spots corresponding to this Al phase. The electron diffraction pattern also has fainter rings due to the small fraction of remaining liquid. A small amount of liquid phase can still be observed in Fig. 2C because the focused electron beam heats the particle slightly (*22*). Upon decreasing the brightness of the beam to eliminate this heating, the remaining liquid solidified, and the fully solid particle is shown in Fig. 2D. A small crystal with dark contrast (arrow) can be seen in the Al phase, and this was determined to be the Al_2Cu phase by EDXS.

The nucleation and growth of the solid Al-rich phase occurred and reached a size of about 800 nm in less than 0.03 s, the minimum time step of the TV camera, which records at 30 frames per second. This result suggests that the interface velocity during growth was at least 1.3×10^{-5} m/s and potentially much faster, given that the temperature gradient during solidification was on the order of 2.3×10^{7} K/m. Faster recording devices and/or TEMs specially designed to achieve ultrafast time resolution (*23*) are needed to follow the movement of such solid-liquid interfaces under these high driving force, highly undercooled conditions.

The Si and Cu concentrations in the undercooled liquid phase are plotted in Fig. 3 as a function of temperature in pseudobinary phase diagrams, along with the computed equilibrium liquidus, solidus, and solvus lines for the elements. The quaternary system is plotted as a pseudobinary phase diagram to facilitate comparison between the experimental metastable liquidus lines (i.e., phase boundaries) and the calculated equilibrium liquidus/solvus lines. The experimental data for Si in Fig. 3A show that the composition of the metastable liquid phase qualitatively follows an extrapolation of the equilibrium liquidus line although some quantitative differences occur. The Si concentration does not change during the first three temperature steps. This could be due to the highly faceted nature of portions of the Si-liquid interface seen in Fig. 2A, which require a two-dimensional nucleation and growth process (*5*, *6*) to absorb Si from the liquid. Owing to the kinetic barrier associated with this growth mechanism, it is possible that the liquid composition remained constant until there was sufficient undercooling for two-dimensional nucleation to occur, thereby allowing the Si crystal to grow and absorb Si from the liquid phase with further undercooling. The composition at the lowest-temperature data point for the solid Al-rich phase is also given in Fig. 3A and qualitatively agrees with the calculated equilibrium solvus. The Cu concentrations also follow a line that is parallel to an extension of the equilibrium liquidus line and are substantially less than the compositions of the liquid that would be in equilibrium with the Al-rich phase (arrow in Fig. 3B). This occurs because Cu remains incorporated in the undercooled liquid until nucleation of the Al-rich phase occurs. Once the Al-rich phase nucleates, Cu is rejected from the growing solid phase, and the Cu concentration in the liquid rapidly increases. In the Al-rich solid, it abruptly changes to within a few tenths of a percent of the calculated equilibrium Cu solvus line (lowest temperature data point in Fig. 3B).

In addition to compositional measurements at the nanoscale, the approach used here enables direct observations to be performed on the behavior of solid-liquid interfaces. For example, the presence of the liquid phase surrounding the solid Al phase in Figs. 1A and 2C indicates that it is energetically unfavorable for the Al-rich solid to form an interface with either the solid Si or the oxide shell (i.e., the contact angle (*6*, *19*) is 180°). This provides direct evidence that neither of these phases could have acted as a catalyst in the nucleation of the Al-rich solid. This result is in contrast to the inference of Turnbull and Cech (*12*) and agrees with more recent findings of Das *et al.* (*7*). Further, the oval shape of the solid Al seen in Figs. 1A and 2C is due to its conformance to the cavity created by the solid Si and surrounding oxide shell, rather than its unconstrained equilibrium shape, which is a sphere. In contrast, the solid Si particle has an anisotropic solid-liquid interfacial energy, because it displays clear facets. These morphological observations agree with the predictions of Jackson's α-parameter calculation (*5*, *6*, *24*), which yields α values for Si and Al of 3.6 and 1.4, respectively (based on their molar entropies of melting of 29.8 and 11.4 J/K), indicating that Si should facet and Al should not. It also agrees with other, more sophisticated, calculations predicting the same behavior (*25*).

Analyses like those shown above can be performed on all Al-base alloys prepared in powder form, because the thin aluminum oxide shell contains the molten metal in the high vacuum of the TEM. Nonpowder forms can be examined by using special TEM specimen-preparation methods (*26*). Low vapor pressure allows containing elements such as In and Sn, or the recently studied Au-Ge alloys (*27*, *28*), can also be observed in high vacuum. For other metals and materials that have a high vapor pressure and do not form a structurally stable oxide layer, some way of containing the liquid phase has to be realized. Special liquid-cell holders have been developed for the TEM (*29*, *30*) and in combination with a heating and cooling capability may be able to accommodate these materials in the future. For materials with higher melting temperatures (e.g., greater than about 900 K), further improvements in the

temperature capability of the heating-holder-x-ray detector system are needed. The use of smaller, brighter electron beams in state-of-the-art TEMs (31) can provide chemical resolutions approaching atomic dimensions. Having such direct morphological information, combined with high spatial resolution chemical analysis, illustrates the potential for solving many important questions in crystallization science. Examples include whether the fundamental assumption of local equilibrium at solid-liquid interfaces in thermodynamic and kinetic models is valid, whether solid-liquid interface compositions change with crystal orientation, and if segregation occurs at solid-liquid interfaces. Clarification of the formation mechanisms shown in recent studies of nanodroplets (27) and nanowire growth (28) may also be possible.

References and Notes

1. M. Rappaz, C. Beckermann, R. Trivedi, Eds., *Solidification Processes and Microstructures: A Symposium in Honor of Prof. W. Kurz* (The Minerals, Metals and Materials Society, Warrendale, PA, 2004).
2. K. Byrappa, T. Ohachi, Eds., *Crystal Growth Technology* (William Andrew, New York, 2003); available at www.knovel.com/knovel2/Toc.jsp?BookID=75&VerticalID=0.
3. M. Sarikaya, C. Tamerler, A. K.-Y. Jen, K. Schulten, F. Baneyx, *Nat. Mater.* **2**, 577 (2003).
4. W. Dreybrodt, *Boreas* **28**, 347 (1999).
5. M. C. Flemings, *Solidification Processing* (McGraw-Hill, New York, 1974).
6. W. A. Tiller, *The Science of Crystallization: Microscopic Interfacial Phenomena* (Cambridge Univ. Press, Cambridge, UK, 1991).
7. S. K. Das, J. H. Perepezko, R. I. Wu, G. Wilde, *Mater. Sci. Eng. A* **304-306**, 159 (2001).
8. E. Johnson, *Science* **296**, 477 (2002).
9. H. Reichert *et al.*, *Nature* **408**, 839 (2000).
10. S. E. Donnelly *et al.*, *Science* **296**, 507 (2002).
11. S. H. Oh, Y. Kauffmann, C. Scheu, W. D. Kaplan, M. Ruehle, *Science* **310**, 661 (2005).
12. D. Turnbull, R. E. Cech, *J. Appl. Phys.* **21**, 804 (1950).
13. R. P. Liu, D. M. Herlach, M. Vandyoussefi, A. L. Greer, *Metall. Mater. Trans.* **35A**, 607 (2004).
14. S. Arai, S. Tsukimoto, H. Miyai, H. Saka, *J. Electron Microsc. (Tokyo)* **48**, 317 (1999).
15. G. A. Steraska, K. T. Moore, J. M. Howe, *Philos. Mag. A* **84**, 2619 (2004).
16. S. K. Eswaramoorthy, J. M. Howe, F. Phillipp, *Microsc. Microanal.* **13**, 291 (2007).
17. Valmet, 431 East Sperry Road, Stockton, CA 95206, USA.
18. G. A. Steraska, J. M. Howe, *Mater. Sci. Eng. A* **368**, 183 (2004).
19. C. Lupis, in *Chemical Thermodynamics of Materials* (Elsevier Science, New York, 1983), pp. 169–344, 373–375, 437–502.
20. L. F. Mondolfo, in *Aluminum Alloys: Structure and Properties* (Butterworths, London, 1976), pp. 368–376, 533–535, 644–651.
21. F. N. Rhines, *Phase Diagrams in Metallurgy: Their Development and Application* (McGraw-Hill, New York, 1956), pp. 5–6, 220–242.
22. T. Yokota, J. M. Howe, M. Murayama, *Phys. Rev. Lett.* **91**, 265504 (2003).
23. W. E. King *et al.*, *J. Appl. Phys.* **97**, 111101 (2005).
24. K. A. Jackson, *Liquid Metals and Solidification* (American Society for Metals, Cleveland, 1958).
25. K. A. Jackson, *Interface Sci.* **10**, 159 (2002).
26. J. Chang, T. Sakai, H. Saka, *Philos. Mag.* **A 85**, 247 (2005).
27. P. W. Sutter, E. A. Sutter, *Nat. Mater.* **6**, 363 (2007).
28. S. Kodambaka, J. Tersoff, M. C. Reuter, F. M. Ross, *Science* **316**, 729 (2007).
29. E. L. Dauton, B. L. Little, K. Lowe, J. Jones-Meehan, *J. Microbiol. Methods* **50**, 39 (2002).
30. M. J. Williamson, R. M. Tromp, P. M. Vereecken, R. Hull, F. M. Ross, *Nat. Mater.* **2**, 532 (2003).
31. S. J. Pennycook, M. Varela, C. J. D. Hetherington, A. I. Kirkland, *MRS Bull.* **31**, 36 (2006).

32. This research was supported by the NSF under grants DMR-9908855 and DMR-0554792. The part of this work done at Oak Ridge National Laboratory was supported by the Assistant Secretary for Energy Efficiency and Renewable Energy, Office of FreedomCAR and Vehicle Technologies, Automotive Propulsion Materials Program, U.S. Department of Energy, under contract DE-AC05-00OR22725 with the University of Texas–Battelle, LLC. Use of instrumentation in the Nanoscale Materials Characterization Facility at UVA for this research is gratefully acknowledged.

Supporting Online Material
www.sciencemag.org/cgi/content/full/318/5855/1437/DC1
Materials and Methods
SOM Text
References

14 June 2007; accepted 11 October 2007
10.1126/science.1146511

Fluctuation Superconductivity in Mesoscopic Aluminum Rings

Nicholas C. Koshnick,[1] Hendrik Bluhm,[1] Martin E. Huber,[2] Kathryn A. Moler[1]*

Fluctuations are important near phase transitions, where they can be difficult to describe quantitatively. Superconductivity in mesoscopic rings is particularly intriguing because the critical temperature is an oscillatory function of magnetic field. There is an exact theory for thermal fluctuations in one-dimensional superconducting rings, which are therefore expected to be an excellent model system. We measured the susceptibility of many rings, one ring at a time, by using a scanning superconducting quantum interference device that can isolate magnetic signals that are seven orders of magnitude smaller than applied flux. We find that the fluctuation theory describes the results and that a single parameter characterizes the ways in which the fluctuations are especially important at magnetic fields where the critical temperature is suppressed.

Superconductivity requires both electron pairing and the coalescence of the pairs into a macroscopic quantum state with long-range phase coherence, usually described as a single wave function. In restricted geometries, thermal energy allows contributions from multiple wave functions to dramatically change the behavior of the system (1–3). Experimental knowledge of such fluctuations in one dimension (1D) is largely derived from transport measurements (4), which require electrical contacts and an externally applied current. We used a contactless technique to study fluctuation effects in isolated, quasi-1D rings in the temperature range where the circumference is comparable to the temperature-dependent Ginzburg-Landau (G-L) coherence length, $\xi(T)$.

With use of a scanning micro-superconducting quantum interference device (SQUID), we detected the current in many individual quasi-1D aluminum rings, paying particular attention to small currents near each ring's superconducting transition temperature, T_c. Such measurements have many advantages. In 1D, the current about a ring, I, is related to the free energy, F, via $I = -\partial F/\partial \Phi_a$, where Φ_a is the flux through the ring from an applied magnetic field. Measuring I as a function of Φ_a thus tests a fundamental thermodynamic variable and our understanding of the ring's state. If there are superconducting pairs that are coherent about the ring's circumference L, the ring's current near zero applied field is proportional to the density of pairs. Deviations from this mean field solution provide information about amplitude and phase fluctuations in the ring.

The mean field G-L solution predicts that the current near zero field should decrease linearly to zero as the temperature, T, approaches T_c. For small rings, we find a measurable current above T_c, a clear signature of fluctuations. The quasi-1D geometry allows a full numeric solution of thermal fluctuations in a G-L framework that includes non-Gaussian effects (5, 6). Previous results on a single ring at zero applied field (7) disagreed strongly with that theory. We studied fluctuations in 15 rings and found that 13 rings agree quantitatively with a full numeric solution, which was numerically intractable for the other 2 rings [Supporting Online Material (SOM) text].

The results in an applied field are particularly interesting. Little and Parks (8) showed experimentally that T_c varies as a periodic function of Φ_a, $T_c(\Phi_a)$. At half-integer multiples of the superconducting flux quantum, Φ_0, the energetic cost of maintaining the flux-induced supercurrent can be larger than the condensation energy, destroying superconductivity. Previous results (9–11) indicate qualitatively that fluctuations are especially important in this regime. We find an enhanced response at $\Phi_a = \Phi_0/2$ that can be quantitatively explained by G-L thermal fluctuations and demonstrate that a single parameter can characterize the Gaussian and non-Gaussian

[1]Department of Applied Physics, Stanford University, Stanford, CA 94305, USA. [2]Department of Physics, University of Colorado Denver, Denver, CO 80204, USA.

*To whom correspondence should be addressed. E-mail: kmoler@stanford.edu

regimes and determines where the Little-Parks effect is entirely washed out by fluctuations.

Unlike stationary sensors, a scanning sensor (Fig. 1) can measure many samples during a single cool-down. We report measurements on rings with radii (R) of 0.35, 0.5, 1, and 2 μm; annulus widths (w) from 65 to 180 nm; and thickness (d) = 60 nm. The scanning SQUID also allows excellent background cancellation (*12*). After background subtraction, the signal (Fig. 2) is proportional to current in the ring.

Many of the features in Fig. 2 can be explained with the mean field response obtained by the minimization of a 1D G-L functional. By assuming a homogenous line width of negligible width, this process gives the ring current (*7*),

$$I_n = \frac{wd\Phi_0}{\lambda(T)^2 L\mu_0}(\Phi_a - \Phi_0 n)P$$
$$P = \max\left(1 - \frac{\xi(T)^2}{R^2}(\Phi_a/\Phi_0 - n)^2, 0\right) \quad (1)$$

where $1/\lambda(T)^2$ represents the superfluid density and n is the phase winding number imposed by the single-valuedness of the macroscopic wave function. The different n states result in periodic I-Φ_a curves. The Φ_a-linear term is the London response, where $1/\lambda(T)^2 \propto T_c(0) - T$ below $T_c(0)$ in the temperature range of interest and 0 when $T > T_c(0)$. P describes pair-breaking due to an Aharonov-Bohm phase around the ring, which leads to a downturn of the response at finite field when $\xi(T) \geq R$. In small rings, this effect occurs well below $T_c(0)$ (Fig. 2, A to C). The Little-Parks effect occurs in the temperature range where $\xi(T) > 2R$, bringing P to zero for a range of applied flux. The dashed green line in Fig. 2, C and D, shows the best match to Eq. 1 at T = 1.22 K. The data's large remnant response in the region in which the mean field curve vanishes is a clear demonstration that fluctuation effects are important in this regime. In large rings (Fig. 2D), fluctuations dominate the response before the effect of the pair-breaking term is apparent.

In the theoretical framework of (*5*), the current is given by $I = -\partial F/\partial\Phi_a = k_B T \frac{\partial}{\partial\Phi_a}\ln Z_{sc}$, where the superconducting partition function, Z_{sc}, is the path integral over all possible wave functions and k_B is the Boltzmann constant. As shown in (*5*, *6*) (SOM text), Z_{sc} can be written as $Z_{sc} = \sum_{l=-\infty}^{\infty}\exp(-il2\pi\Phi_a/\Phi_0)\sum_{n=0}^{\infty}\exp(-\gamma^{1/3}E_{n,l})$, where $E_{n,l}$ are the eigenvalues of the 2D single-particle Hamiltonian, $H = -\frac{1}{2}\nabla^2 + \frac{8\pi}{\gamma^{1/2}}\frac{T-T_c(0)}{E_c/k_B}r^2 + \frac{1}{2}r^4$, l is the angular momentum index and r is a fictitious position coordinate. This formulation allows a numerical calculation of I that is exact up to truncation errors. We emphasize the parameter

$$\gamma = \frac{42\zeta(3)}{\pi^5}\frac{k_B T_c}{M_{eff}E_c} \approx \frac{0.87\,L^2}{M_{eff}\,\xi_{T=0}^2} \quad (2)$$

where $E_c = \pi^2\hbar v_F \ell_e/3L^2$ is the correlation or Thouless energy, ζ is the Riemann zeta function, v_F is the Fermi velocity, ℓ_e is the mean free path, and ξ_0 is the Pippard zero temperature coherence length. w and d enter into the effective number of channels, $M_{eff} = (\ell_e/L)(k_F^2 wd/4\pi)$, where k_F is the Fermi wavelength. This combination of parameters characterizes the size of the ring. Temperature only appears in the second term of the Hamiltonian, which can be rewritten using $8\pi k_B(T - T_c(0))/E_c = L^2/\xi(T)^2$ to illustrate the relation to the pair-breaking term of Eq. 1 and to indicate the region where $T \approx T_c(\Phi_0/2)$ in Fig. 3C. Thus, once the correct E_c and $T_c(0)$ are known for a given ring, the current as a function of Φ_a and T is entirely determined by γ.

The data points in Fig. 3 were derived from I-Φ_a curves (e.g., Fig. 2) by fitting low order polynomials near Φ_a = 0 and $\Phi_a = \pm\Phi_0/2$. We have compared these susceptibilities as a function of temperature to the theory by using the measured geometry factors, the k_F and v_F of bulk aluminum, and three parameters chosen by hand: ℓ_e, $T_c(0)$, and $M_{S,R}$, the mutual inductance between the SQUID and the ring. ℓ_e is identified by the shape of the curve as a function of temperature, $M_{S,R}$ is determined by the magnitude of the response, and $T_c(0)$ is chosen to allow the theory to match the linear temperature dependence of the Φ_a = 0 susceptibility below $T_c(0)$. The $T_c(0)$ of the rings varied from 1.237 to 1.268 K, with up to 7 mK difference for nominally identical line-width rings. The fitted $M_{S,R}$ lie within 15% of the inductance calculated with a model based on a 0.75-μm ring-sensor-loop separation. The fitted ℓ_e varies between 14 and 25 nm with an increasing dependence on line width. We attribute this dependence to oxygen absorbed during the fabrication process and, to a lesser extent, the observed 20% variations in w (*12*). The four nominally identical line-width rings shown in Fig. 3 have ℓ_e = 19.5 ± 0.5 nm. The agreement with the 1D models we have discussed demonstrates that the finite line-width effects are not essential to our physical result and that small variations in w do not qualitatively change the response above $T_c(\Phi_a)$.

Near $T_c(\Phi_a)$, γ characterizes the non-Gaussian fluctuations that interpolate between the mean field behavior far below T_c and the Gaussian fluctuations that dominate at high temperatures. Non-Gaussian fluctuations are important when quadratic expansions of the free energy cannot describe the physical result. This is particularly apparent at $T_c(\Phi_a)$, where any Gaussian approx-

Fig. 1. (**A**) Diagram of the direct current SQUID susceptometer. One field coil applies up to 50 Gauss of field to the sample, whose response couples a magnetic flux into the 4-μm pickup loop. A second counter-wound (C-W) loop cancels the SQUID's response to the applied field to within one part in 10^4. Additional modulation coils maintain the optimum working point. (**B**) The SQUID's pickup loop (white) and field coil (blue) are positioned over a single micrometer-scale aluminum ring. In situ background measurements allow the magnetic flux induced by currents in the ring to be unambiguously distinguished from the applied field, which is up to seven orders of magnitude larger.

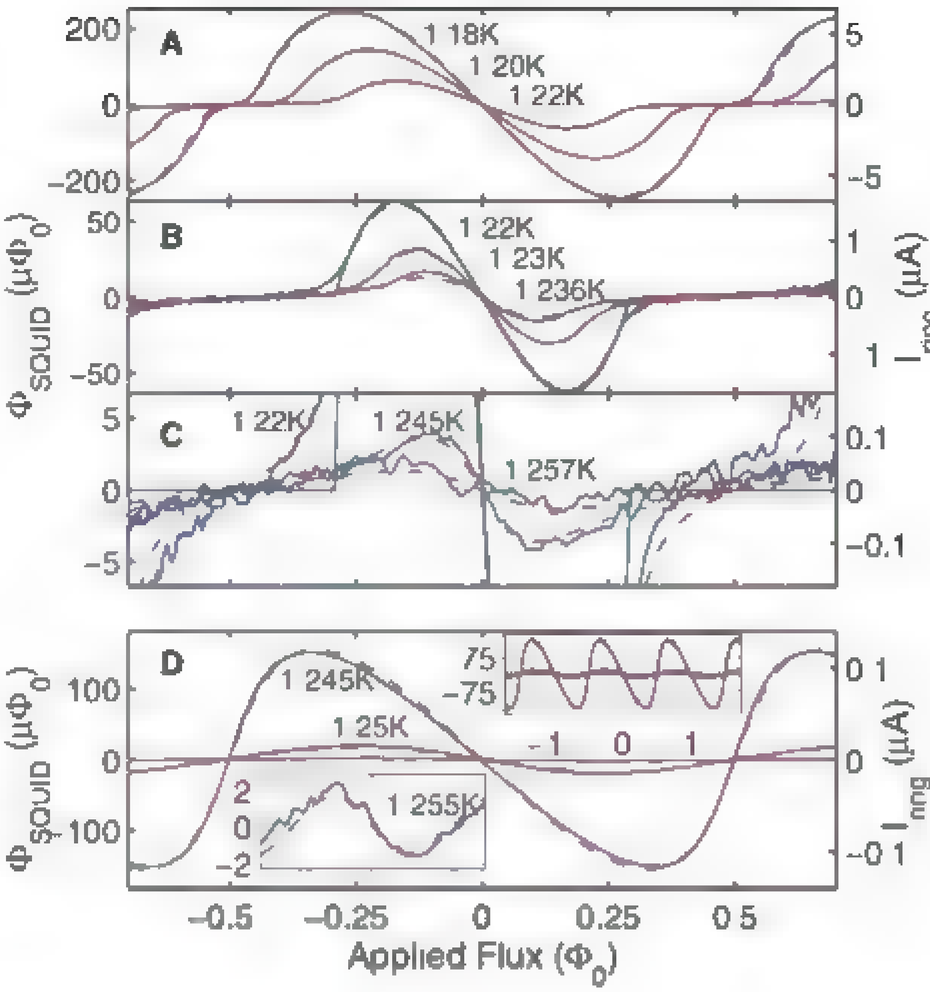

Fig. 2. SQUID signal (left axis) and ring current (right axis) as a function of applied flux Φ_a for two rings, both with $d = 60$ nm and $w = 110$ nm. The fluctuation theory (dashed red) was fit to the data (blue) through the temperature analysis shown in Fig. 3. (**A** to **C**) $R = 0.35$ μm, fitted $T_c(\Phi_a{=}0) = 1.247$ K, and $\gamma = 0.075$. The green line is the theoretical mean field response for $T = 1.22$ K and shows the characteristic Little-Parks line shape, in which the ring is not superconducting near $\Phi_a = \Phi_0/2$. The excess persistent current in this region indicates the large fluctuations in the Little-Parks regime. (**D**) $R = 2$ μm, fitted $T_c(\Phi_a{=}0) = 1.252$ K, and $\gamma = 13$. The periodic response (right inset) shows 1D treatment is appropriate and can be approximated by a thermal average over mean field G-L fluxoid states (Eq. 1 and SOM text) until additional fluctuations contribute near T_c.

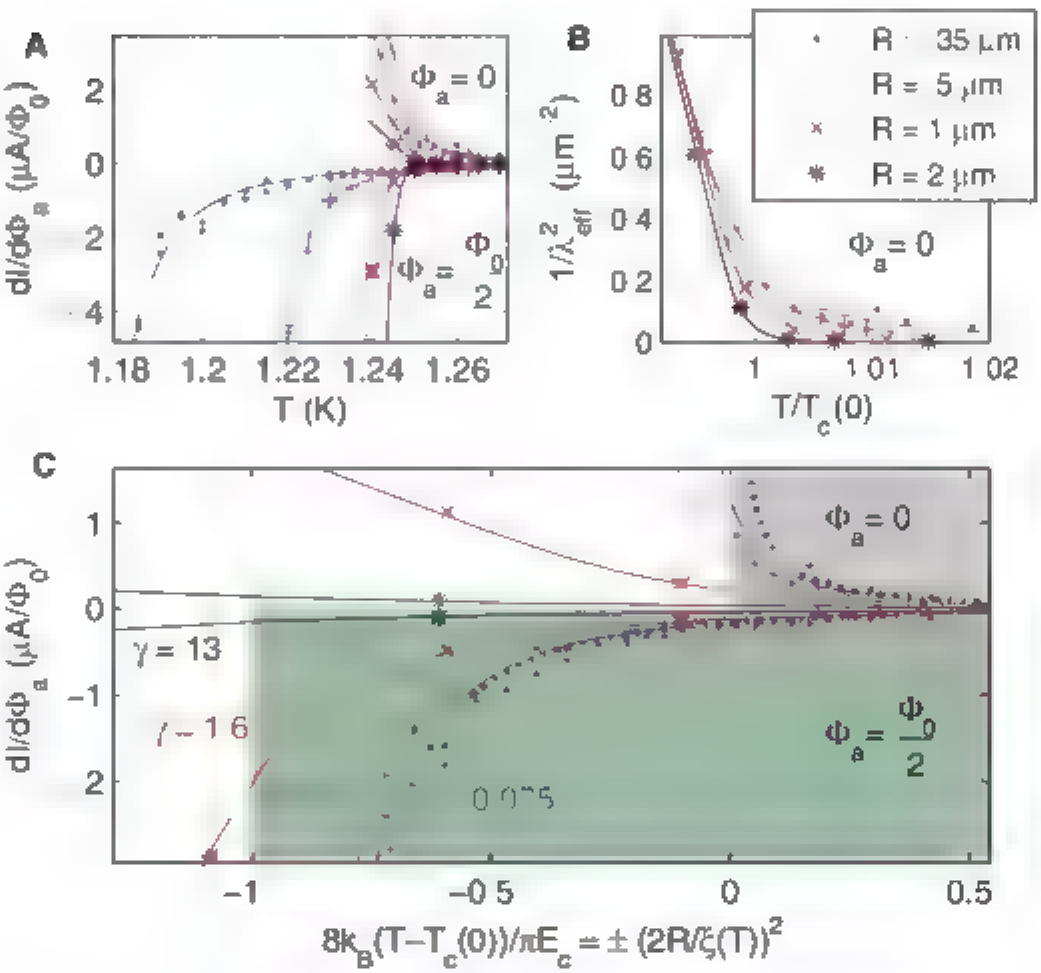

Fig. 3. Susceptibility data (symbols) and fits (lines) at $\Phi_a = 0$ (positive values) and $\Phi_0/2$ (negative values) for 110-nm-wide 60-nm-thick rings with various values of R. (**A**) Smaller rings have a larger temperature region where the Little-Parks criterion $\xi(T) > 2R$ is satisfied and thus have a larger region with a reduced $\Phi_a = \Phi_0/2$ response. (**B**) $\Phi_a = 0$ susceptibility scaled with the cross section and radius to show the effective mean field superfluid density around T_c. Smaller rings have an enhanced fluctuation response. (**C**) When the temperature is scaled by the correlation energy, E_c, the susceptibility is uniquely determined by the size parameter γ. The gray and green shaded regions indicate the temperature above $T_c(\Phi_a)$ when $\Phi = 0$ and $\Phi_0/2$, respectively. The fluctuation response above $T_c(\Phi_a)$ is enhanced for $\Phi_a = \Phi_0/2$. The dotted line shows a Gaussian prediction (SOM text) that is valid at some γ-dependent temperature above $T_c(\Phi_a)$. When $\gamma \gtrsim 1$, the response at $\Phi_a = 0$ and the response at $\Phi_a = \Phi_0/2$ are comparable in the Little-Parks regime, which corresponds to a fluctuation-dominated sinusoidal $I - \Phi_a$ response.

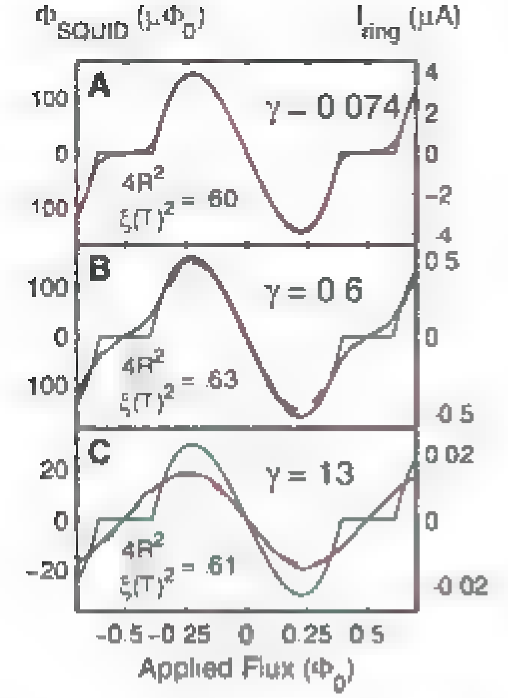

Fig. 4. Mean field theory (green), fluctuation theory (dashed red), and data (blue) for three rings with different γ parameters. The mean field response is derived from the fluctuation theory parameters for each ring at the given temperature. **(A)** T = 1.20 K. In small γ rings, the Little-Parks line shape is clearly observable. **(B)** T = 1.25 K. When γ ≈ 1, the reduction of the response due to the Little-Parks effect is significantly suppressed. **(C)** T = 1.25 K. In large γ rings, the Little-Parks effect is completely washed out by fluctuations, which affect the responses at all flux values.

ization would predict a divergent susceptibility (Fig. 3A). By using Eq. 1 to define an effective superfluid density from the zero field response, $1/\lambda_{eff}^2 = (\mu_0 L/wd)\partial I/\partial\Phi_a|_{\Phi_a=0}$, one can see (Fig. 3B) that fluctuations make the susceptibility deviate from the mean field response below $T_c(0)$, gradually smoothing the transition. Our parameterization of the theory shows that γ is the only sample-dependent parameter at $T = T_c(0)$. The temperature range where non-Gaussian fluctuations are important is typically parameterized through the Ginzburg parameter as $|T - T_c(\Phi_a)|/T_c(\Phi_a) < Gi$, where $|T - T_c(\Phi_a)|/E_c \approx \frac{T_c(\Phi_a)}{E_c} Gi \approx \sqrt{\gamma}$ (13). Inside this range, γ determines the magnitude of the response. Far above this range, Gaussian fluctuations dominate, and the susceptibility is a function of $[T - T_c(0)]/E_c \propto L^2/\xi^2$ alone.

The theory's dependence on γ allows us to state the criterion for the visibility of the Little-Parks effect in the context of fluctuations. The region that is shaded in green in Fig. 3C is above $T_c(\Phi_0/2)$ because $\xi(T) > 2R$. The susceptibility would be zero in this regime if fluctuation effects were not considered. When γ ≪ 1, the distinct Little-Parks shape is visible in that the susceptibility is smaller at $\Phi_a = \Phi_0/2$ than at $\Phi_a = 0$. However, when γ ≫ 1, the Little-Parks shape is entirely washed out by fluctuations (Fig. 4). For sufficiently large γ, the susceptibilities at $\Phi = 0$ and $\Phi_0/2$ are equal and opposite even below $T_c(\Phi_a = \Phi_0/2)$, so the response appears sinusoidal. This dependence on γ, rather than L and $\xi(T)$ alone, is the reason why the Little-Parks line shape does not occur in the ring shown in Figs. 2A and 4C.

Several factors contribute to the large fluctuation response near $\Phi_a = \Phi_0/2$ above $T_c(\Phi_a)$. First, the Gaussian fluctuations between $T_c(\Phi_a = 0)$ and $T_c(\Phi_a)$ have a large magnitude, which is due to the interplay between adjacent phase winding states. In small γ rings, the non-Gaussian fluctuation region in Fig. 3C is small. Thus, there is a large region where the magnitude of the persistent current near $\Phi_a = \Phi_0/2$ is strictly a function of $k_B[T - T_c(0)]/E_c$. In large γ rings, non-Gaussian fluctuations play an increased role in the phase diagram, and multiple phase winding modes need to be considered (13), indicating the importance of phase fluctuations. In all rings, nonhomogeneous wave functions may have a nonnegligible contribution to the final currents because of their vanishing energy cost near $T_c(\Phi_a)$. Small variations in width (SOM text) make nonhomogeneous wave functions more important (14) and would be important to include in an extended theory.

Fluctuation effects play a important role in 1D superconducting structures. Our analysis explicitly demonstrates how Gaussian and non-Gaussian fluctuations affect the persistent current in rings with various diameters and cross sections, as a function of applied magnetic flux. A single parameter, γ, characterizes the fluctuations for a given ratio of the temperature-dependent coherence length to the circumference. When γ is large, the signature of a Little-Parks flux-dependent $T_c(\Phi_a)$ is entirely washed out by fluctuations. When γ is small, the susceptibility in the non-Gaussian region near $T_c(\Phi_a)$ is enhanced, and Gaussian fluctuations are clearly visible between $T_c(\Phi_a)$ and $T_c(0)$ for $\Phi_a \approx \Phi_0/2$. This new framework for understanding Little-Parks fluctuations is supported by our data on fluctuation-induced currents in rings.

References and Notes

1. V. Emery, S. Kivelson, *Nature* **374**, 434 (1995).
2. J. M. Kosterlitz, D. J. Thouless, *J. Phys. C* **6**, 1181 (1973).
3. J. S. Langer, V. Ambegaokar, *Phys. Rev.* **164**, 498 (1967).
4. C. N. Lau, N. Markovic, M. Bockrath, A. Bezryadin, M. Tinkham, *Phys. Rev. Lett.* **87**, 217003 (2001).
5. F. von Oppen, E. K. Riedel, *Phys. Rev. B* **46**, 3203 (1992).
6. D. J. Scalapino, M. Sears, R. A. Ferrell, *Phys. Rev. B* **6**, 3409 (1972).
7. X. Zhang, J. C. Price, *Phys. Rev. B* **55**, 3128 (1997).
8. W. A. Little, R. D. Parks, *Phys. Rev. Lett.* **9**, 9 (1962).
9. Y. Liu *et al.*, *Science* **294**, 2332 (2001).
10. M. M. Rosario *et al.*, *Physica B* **329–333**, 1415 (2003).
11. M. Hayashi, H. Ebisawa, *Physica C* **352**, 191 (2001).
12. Materials and methods are available as supporting material on *Science* Online.
13. M. Daumens, C. Meyers, A. Buzdin, *Phys. Lett. A* **248**, 445 (1998).
14. J. Berger, J. Rubinstein, *Phys. Rev. Lett.* **75**, 320 (1995).

15. We acknowledge support from the Packard Foundation and NSF grants no. DMR-0507931, DMR-0216470, ECS-0210877, ECS-9731293, and PHY-0425897. We thank J. Price, Y. Imry, M. R. Beasley, Y. Oreg, and especially G. Schwiete for helpful discussions and A. Bachar for the illustration in Fig. 1B.

Supporting Online Material
www.sciencemag.org/cgi/content/full/318/5855/1440/DC1
Materials and Methods
SOM Text
Tables S1 and S2

3 August 2007; accepted 16 October 2007
10.1126/science.1146758

Extended Male Growth in a Fossil Hominin Species

Charles A. Lockwood,[1,2]* Colin G. Menter,[3] Jacopo Moggi-Cecchi,[2,4] Andre W. Keyser[2]

In primates that are highly sexually dimorphic, males often reach maturity later than females, and young adult males do not show the size, morphology, and coloration of mature males. Here we describe extended male development in a hominin species, *Paranthropus robustus*. Ranking a large sample of facial remains on the basis of dental wear stages reveals a difference in size and robusticity between young adult and old adult males. Combined with estimates of sexual dimorphism, this pattern suggests that male reproductive strategy focused on monopolizing groups of females, in a manner similar to that of silverback gorillas. However, males appear to have borne a substantial cost in the form of high rates of predation.

Sexual dimorphism is the only direct skeletal evidence available for reconstructing the evolution of human social behavior, and as such it is routinely analyzed and debated when seen in extinct hominin species (1–6). The expectation is that higher levels of sexual dimorphism correlate with higher levels of male-male competition and social systems in which males control mating access to multiple females (7). However, partly due to the limitations of small fossil samples, estimates of dimorphism have led to divergent inferences about social behavior in fossil hominins, ranging from monogamous to highly polygynous groups. Here we combine analysis of dimorphism with another aspect of life history—differences between males and females in the timing of maturity (8)—and use the results to reconstruct social behavior.

We focus on *Paranthropus robustus*, a South African robust australopithecine, because there are a large number of specimens available (35 were used in our study). This species is known primarily from the Swartkrans site, Kromdraai, and recent finds from Drimolen (*9*, *10*). The *P. robustus* deposits at these sites have been dated to 1.5 to 2.0 million years ago (*10*–*12*). In order to compare size to relative age among adults, we only considered individuals with (i) M3 erupted, (ii) sufficient parts of the face and mandible preserved to compare size, and (iii) postcanine teeth well enough preserved to determine age from the relative degree of tooth wear. This selection resulted in 19 specimens of the face or maxilla, 17 of which are from Swartkrans, and 1 each from Drimolen and Kromdraai. For mandibles, 16 specimens meet the criteria, of which 10 are from Swartkrans, 5 from Drimolen, and 1 from Kromdraai (Table 1). Because many specimens are fragmentary, we determined a nonparametric ranking of individuals based on overall size rather than a specific measurement (*13*). Age ranks were determined on the basis of tooth wear of the postcanine row, following generally accepted methods (*13*, *14*). The sample represents nearly every stage of dental wear from young adulthood to old age (*15*).

From this analysis, we infer that maximum (presumably male) size was greater among old adults than young adults (Fig. 1). Old adults in the higher size ranks also had the most well-developed morphology with respect to features diagnostic of the *P. robustus* face, such as the anterior pillars and maxillary trigon (*16*) (Fig. 2). Based on the ontogeny of sexual dimorphism in modern primates (*17*), we interpret this pattern as continued growth in males between early skeletal adulthood and full maturity. Minimum size, on the other hand, occurs throughout the age range. For example, SK 21 is the oldest specimen in the sample of maxillas, but also the smallest. Because small, relatively gracile individuals occur at every age, we conclude that females have reached full skeletal size by the time M3 has erupted or soon thereafter.

Extended male growth occurs in primates when male reproductive success is concentrated in a period of dominance resulting from intense male-male competition (*17*, *18*). Climbing the dominance hierarchy typically involves not only an increase in size but also changes in soft-tissue anatomy and, in some taxa, coloration (*18*). Bimaturism can be interpreted as part of a male strategy to delay competition with high-ranking males until the likelihood of success is greatest (*17*, *19*, *20*).

In primates showing bimaturism, sexual dimorphism in the eruption of the last permanent tooth (M3 or the canine) is clearly less than the differences in reaching maturity in body mass. For example male and female gorillas complete dental emergence at similar times (*21*, *22*), but gorilla male growth in body mass continues for years (*17*), and male gorillas do not become socially adult until as much as 5 or 6 years after females (*23*). In a more extreme case, eruption of the permanent teeth in mandrills is completed in males before females (*24*), but males continue to grow in body mass and body length for several years (*25*). Differences between dentally mature males and physically or socially mature males are thus well-recognized in modern primates.

Understanding sexual dimorphism in *P. robustus* has been aided by the discovery of DNH 7, a complete skull from Drimolen (*9*, *10*). It is substantially smaller than the well-preserved skulls of *P. robustus* from Swartkrans (such as SK 12, SK 46, SK 48, and SK 83) and Kromdraai (TM 1517) (table S1). Differences between DNH 7 and larger individuals are consistent with those expected between females and males. For example, the larger individuals have sagittal crests reaching onto the frontal bone, as well as deeply projecting mastoid processes, whereas DNH 7 lacks a sagittal crest and has reduced mastoid regions. The degree of size difference between DNH 7 and larger, presumably male specimens can be explained by a gorillalike level of sexual dimorphism but not the lower levels of dimorphism seen in chimpanzees and modern humans (supporting online material). Furthermore, it is unlikely that any of the other relatively complete skulls are female. In comparison to extant hominoids, the difference between even the smallest of the previously known crania (TM 1517) and DNH 7 is statistically greater than would be expected within the range of variation of females (supporting online text and table S2). The size of DNH 7, in combination with an understanding of male life history, helps resolve the sex of specimens such as SK 48 and TM 1517 (*26*, *27*). The two latter specimens are best regarded as young adult males.

A bias toward males among the well-preserved skulls is also reflected in the sample of maxillas as a whole (*28*). Specimens such as SK 21, SK 821, and SKW 8 are similar in size and proportions to DNH 7 and are probably females (these are size ranks 1 and 2 in Fig. 1), whereas all other specimens show male size and/or morphology (supporting online material). We conclude that the maxillofacial specimens represent 4 females and 15 males overall, and 3 females and 14 males for the Swartkrans sample only. This distribution deviates significantly from random sampling of an unbiased population (using a two-tailed binomial test and assuming a 50:50 ratio, $P = 0.0192$ for the overall sample and $P = 0.0127$ for Swartkrans).

An abundance of males is perhaps not surprising in a fossil sample that resulted largely from predation. Direct evidence of carnivore activity is present on several hominin specimens at Swartkrans, and member 1 of this site is among the most definitive examples of a predator-accumulated assemblage of hominins (*27*, *29*). In dimorphic primates, nondominant males spend more time alone, on the periphery of a social group, or in small all-male bands (*30*). Solitary behavior places males at risk (*31*, *32*). For example, when male baboons disperse, they suffer a mortality rate at least three times as great as that of group-living males or females (*32*). Thus

Table 1. Ranking of size and age (displayed in Fig. 1). Swartkrans member 1 (M1) includes all specimens from deposits referred to as the lower bank and the hanging remnant [see (*12*) for explanation].

Maxillas				Mandibles			
Specimen	**Provenience**	**Age**	**Size**	**Specimen**	**Provenience**	**Age**	**Size**
SKW 11	Swartkrans M1	1	3	TM 1517	Kromdraai B	1	1
TM 1517	Kromdraai B	1	4	SKW 5	Swartkrans M1	1	2
SK 48	Swartkrans M1	1	6	DNH 8	Drimolen	1	4
SK 49	Swartkrans M1	1	6	SKX 5013	Swartkrans M2	2	1
SK 821	Swartkrans M1	2	2	SK 23	Swartkrans M1	2	2
SK 65	Swartkrans M1	2	4	SK 34	Swartkrans M1	2	4
SK 57	Swartkrans M1	2	7	SK 858	Swartkrans M1	2	5
SKW 29	Swartkrans M1	2	7	DNH 7	Drimolen	3	3
DNH 7	Drimolen	3	1	DNH 21	Drimolen	4	2
SK 11	Swartkrans M1	4	5	SK 844	Swartkrans M1	4	3
SK 826/877	Swartkrans M1	4	8	SK 74A	Swartkrans M1	5	3
SKW 12	Swartkrans M1	4	9	DNH 19	Drimolen	5	6
SKW 8	Swartkrans M1	5	2	SK 1586	Swartkrans M1	5	6
SK 46	Swartkrans M1	5	5	SK 81	Swartkrans M1	5	6
SK 79	Swartkrans M1	5	6	DNH 6	Drimolen	6	5
SK 1512	Swartkrans M1	5	8	SK 12	Swartkrans M1	6	7
SK 83	Swartkrans M1	6	7				
SK 12	Swartkrans M1	6	8				
SK 21	Swartkrans M1	7	1				

[1]Department of Anthropology, University College London, Gower Street, London WC1E 6BT, UK. [2]Institute for Human Evolution, University of the Witwatersrand, WITS 2050, Johannesburg, South Africa. [3]Department of Anthropology and Development Studies, University of Johannesburg, Post Office Box 524 Auckland Park, Johannesburg, South Africa. [4]Laboratori di Antropologia, Dipartimento di Biologia Animale e Genetica, and Museo di Storia Naturale, Università di Firenze, 12 via del Proconsolo, 50122 Firenze, Italy.

*To whom correspondence should be addressed. E-mail: c.lockwood@ucl.ac.uk

degree of difference in mortality matches the male bias at Swartkrans. Females were apparently more shielded from predation. Putting this observation together with the conclusions about bimaturism and sexual dimorphism, we infer that the distribution of food sources allowed stable groups of *P. robustus* females to form in response to predation pressure, and males in turn sought to monopolize reproductive access to these groups (33). If females emigrated from their natal groups, then it is likely that they spent little time alone and transferred directly to a male or an established group [as occurs in gorillas (30, 34)].

The *P. robustus* pattern contrasts with that of some other australopithecine collections. For example, the sample of *Australopithecus africanus* is either biased toward females or shows no bias (4). The *A. africanus* accumulation from Sterkfontein member 4 may also be the product of predator behavior, but this conclusion is less certain than for the Swartkrans sample (27, 35). If both Swartkrans member 1 and Sterkfontein member 4 hominin collections are largely attributable to carnivore activity, the difference in sex bias raises the possibility that *P. robustus* and *A. africanus* differed in social structure.

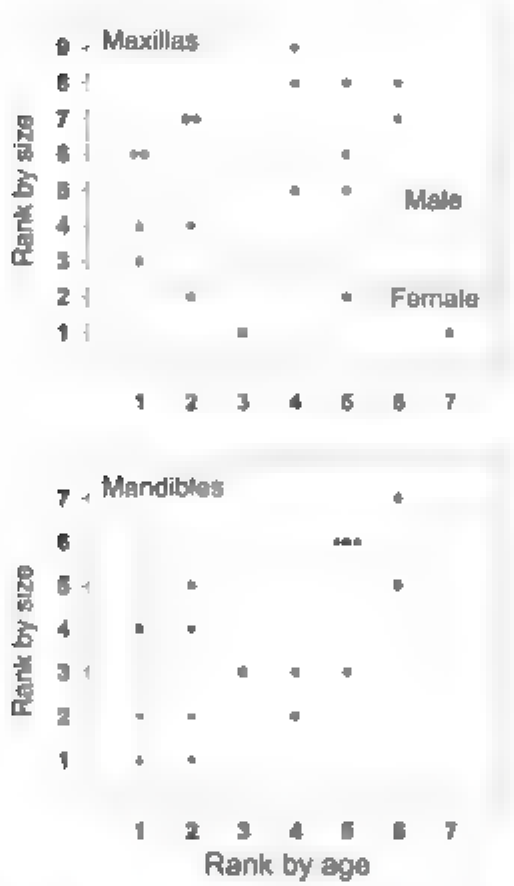

Fig. 1. Comparison of size ranks to age ranks for adult maxillofacial and mandibular specimens (Swartkrans, diamonds; Drimolen, squares; Kromdraai, triangles). Table 1 lists the specimens used here. The lowest age rank contains individuals with M3 recently erupted. The largest individuals are more advanced in age, showing at least some dentine exposure on M2. When a randomization test of correlation coefficients is used, age and size are significantly correlated among the male maxillofacial specimens ($r = 0.52$; $P = 0.027$ one-tailed test, 5000 permutations).

References and Notes

1. J. M. Plavcan, C. P. van Schaik, *J. Hum. Evol.* **32**, 345 [redacted]
2. H. M. McHenry, *J. Hum. Evol.* **27**, 77 (1994).
3. R. A. Foley, P. C. Lee, *Science* **243**, 901 (1989).
4. C. A. Lockwood, *Am. J. Phys. Anthropol.* **108**, 97 (1999).
5. P. L. Reno, R. S. Meindl, M. A. McCollum, C. O. Lovejoy, *Proc. Natl. Acad. Sci. U.S.A.* **100**, 9404 (2003).
6. We refer to differences in skull size and morphology between males and females, which have been shown to correlate with sexual dimorphism in body mass (36).
7. J. M. Plavcan, *Yrbk. Phys. Anthropol.* **116**, 25 (2001).
8. Bimaturism, defined as sex differences in the timing of cessation of growth (17).
9. A. W. Keyser, *S. Afr. J. Sci.* **96**, 189 (2000).
10. A. W. Keyser, C. G. Menter, J. Moggi-Cecchi, T. R. Pickering, L. R. Berger, *S. Afr. J. Sci.* **96**, 193 (2000).
11. E. S. Vrba, in *Hominid Evolution: Past, Present and Future*, P. V. Tobias, Ed. (Liss, New York, 1985), pp. 195–200.
12. C. K. Brain, in *Swartkrans: A Cave's Chronicle of Early Man*, C. K. Brain, Ed. (Monograph 8, Transvaal Museum, Pretoria, South Africa, 1993), pp. 23–33.
13. Further information on materials and methods is available as supporting material on *Science* Online.
14. S. Hillson, *Teeth* (Cambridge Univ. Press, New York, ed. 2, 2005).
15. In specimens with M3 recently erupted (such as SK 48 (M 1517) and DNH 80, small dentine islands are present on the M1s. Given schedules of dental development in *P. robustus* [M1 erupted at 3 years and M3 erupted at approximately 9 years (37)], this implies that tooth wear on M1 began to expose dentine after 6 years. M2 erupted approximately halfway between M1 and M3. If it underwent comparable amounts of wear to M1, then individuals of age rank 4 (which have exposed dentine on M2) are at least 3 years older than those in age rank 1.
16. Y. Rak, *The Australopithecine Face* (Academic Press, New York, 1983).
17. S. R. Leigh, *Am. J. Phys. Anthropol.* **97**, 339 (1995).
18. J. M. Setchell, P. C. Lee, in *Sexual Selection in Primates*, P. M. Kappeler, C. P. van Schaik, Eds. (Cambridge Univ. Press, Cambridge, 2004), pp. 175–195.
19. P. J. Jarman, *Biol. Rev.* **58**, 485 (1983).
20. C. H. Janson, C. P. van Schaik, in *Juvenile Primates: Life History, Development, and Behavior*, M. E. Pereira, L. A. Fairbanks, Eds. (Oxford Univ. Press, Oxford, 1993), pp. 57–74.
21. M. C. Dean, B. A. Wood, *Folia Primatol. (Basel)* **36**, 111 (1981).
22. B. H. Smith, T. L. Crummett, K. L. Brandt, *Yrbk. Phys. Anthropol.* **37**, 177 (1994).
23. D. P. Watts, A. E. Pusey, in *Juvenile Primates: Life History, Development, and Behavior*, M. E. Pereira, L. A. Fairbanks, Eds. (Oxford Univ. Press, Oxford, 1993), pp. 148–177.
24. J. M. Setchell, E. J. Wickings, *Folia Primatol. (Basel)* **75**, 121 (2004).
25. J. M. Setchell, E. J. Wickings, L. A. Knapp, *Am. J. Phys. Anthropol.* **131**, 498 (2006).
26. M. H. Wolpoff, in *Paleoanthropology: Morphology and Paleoecology*, R. Tuttle, Ed. (Mouton, The Hague, Netherlands, 1975), pp. 245–284.
27. C. K. Brain, *The Hunters or the Hunted? An Introduction to African Cave Taphonomy* (Univ. of Chicago Press, Chicago, 1981).

[redacted] We do not assign sexes to mandibles, because they are generally more fragmentary and there is greater overlap in male and female mandible size in sexually dimorphic hominoids.

29. K. J. Carlson, T. R. Pickering, *J. Hum. Evol.* **44**, 431 (2003).

[redacted] A. Pusey, C. Packer, in *Primate Societies*, B. B. Smuts, D. L. Cheney, R. M. Seyfarth, R. W. Wrangham, T. T. Struhsaker, Eds. (Univ. of Chicago Press, Chicago, 1987), pp. 250–266.

[redacted] G. Cowlishaw, *Behaviour* **131**, 293 (1994).

32. S. C. Alberts, J. Altmann, *Am. Nat.* **145**, 279 (1995).
33. E. H. M. Sterck, D. P. Watts, C. P. van Schaik, *Behav. Ecol. Sociobiol.* **41**, 291 (1997).
34. E. J. Stokes, R. J. Parnell, C. Olejniczak, *Behav. Ecol. Sociobiol.* **54**, 329 (2003).

[redacted] T. R. Pickering, R. J. Clarke, J. Moggi-Cecchi, *Am. J. Phys. Anthropol.* **125**, 1 (2004).

36. J. M. Plavcan, *J. Hum. Evol.* **42**, 579 (2002).

[redacted] M. C. Dean, in *Evolutionary History of the "Robust" Australopithecines*, F. E. Grine, Ed. (Aldine de Gruyter, New York, 1988), pp. 43–53.

Fig. 2. Size and morphological comparisons among DNH 7, SK 48, SK 12, and SKW 12 (from left to right). They are aligned approximately on the cementum-enamel junction of the molars, indicated by the lower line. Upper lines indicate the level of the inferior nasal margin as a general size comparison. DNH 7 is the most well-preserved female specimen of *P. robustus* (the mandible and cranial vault are not shown here). SK 48 is one of the largest young adult males. SK 12 and SKW 12 are older adult males. Drawings for SK 12 and SKW 12 are for schematic purposes only. Scale bar, 3 cm.

38. This work stems from excavations at Drimolen, supported by grants from the L. S. B. Leakey Foundation and the Department of Science and Technology in South Africa. Further financial support was provided to C.A.L. by the Royal Society, UK. A.W.K. and C.G.M. thank D. and J. Smith, on whose property Drimolen is situated, for permission to conduct the excavation and for their assistance. J.M.C. received support from the Italian Ministry of Foreign Affairs (Direzione Generale per la Promozione e la Cooperazione Culturale, ufficio V, Archaeology), and the Italian Embassy and Italian Cultural Institute in Pretoria. We also thank D. Shima and D. Xekane for their continued help with the Drimolen excavation; B. Zipfel and S. Potze for assistance with specimens; and Z. Alemseged, B. Bradley, C. Dean, W. Kimbel, S. Leigh, M. Plavcan, J. Setchell, J. Scott, and F. Spoor for discussion and comments.

Supporting Online Material
www.sciencemag.org/cgi/content/full/318/5855/1443/DC1
SOM Text
Tables S1 and S2
References

14 August 2007; accepted 24 October 2007
10.1126/science.1149211

Boron-Toxicity Tolerance in Barley Arising from Efflux Transporter Amplification

Tim Sutton,* Ute Baumann, Julie Hayes, Nicholas C. Collins, Bu-Jun Shi, Thorsten Schnurbusch, Alison Hay, Gwenda Mayo, Margaret Pallotta, Mark Tester, Peter Langridge

Both limiting and toxic soil concentrations of the essential micronutrient boron represent major limitations to crop production worldwide. We identified *Bot1*, a *BOR1* ortholog, as the gene responsible for the superior boron-toxicity tolerance of the Algerian barley landrace Sahara 3771 (Sahara). *Bot1* was located at the tolerance locus by high-resolution mapping. Compared to intolerant genotypes, Sahara contains about four times as many *Bot1* gene copies, produces substantially more *Bot1* transcript, and encodes a Bot1 protein with a higher capacity to provide tolerance in yeast. *Bot1* transcript levels identified in barley tissues are consistent with a role in limiting the net entry of boron into the root and in the disposal of boron from leaves via hydathode guttation.

Of all plant nutrient elements, boron has the narrowest range between deficient and toxic soil solution concentration (*1*), and both boron deficiency and toxicity severely limit crop production worldwide (*2*, *3*). Toxicity is more difficult to manage agronomically and is best dealt with by using boron-tolerant varieties. Genetic variation for boron-toxicity tolerance is known for a number of crop plant species. Tolerance is most commonly associated with the ability to maintain low boron concentrations in the shoot (*4*–*6*). In barley (*Hordeum vulgare*), the non-agronomic but highly boron-tolerant Algerian landrace Sahara 3771 (Sahara) was identified as a potential source of tolerance for variety improvement (*4*, *7*). In a cross between Sahara and the boron-intolerant Australian malting variety Clipper, several quantitative trait loci (QTL) controlling tolerance were identified (*8*). The major locus on chromosome 4H affects leaf symptom expression (Fig. 1A), boron accumulation (Fig. 1B), root length response, and dry matter production under boron-toxic conditions (*8*). The ability of Sahara to maintain lower shoot boron accumulation is at least partially due to a mechanism of active boron efflux from the root (*9*).

We followed a map-based approach to isolate the 4H boron-tolerance gene. Using a population representing 6720 meioses and gene colinearity with the syntenic region on rice chromosome 3 to generate markers, we delimited the tolerance locus to a 0.15-centimorgan interval between markers *xBM178* and *xBM162* (Fig. 2A and fig. S1) (*10*). The corresponding 112-kb interval in rice contains two intact copies and one 3′-truncated version of a gene showing similarity to a family of adenosine monophosphate (AMP)–dependent synthetases and ligases and no other predicted gene. Barley expressed sequence tags (ESTs) most closely matching one of the intact copies were used to derive the marker *xBM160*, which cosegregated with the tolerance locus.

In a parallel approach, we also mapped several candidate genes in barley. These were barley genes showing similarity to the *Arabidopsis* NIP5;1 major intrinsic protein (*11*) and the *Arabidopsis* BOR1 efflux transporter that is related to bicarbonate transporters in animals (*12*, *13*). Both *Arabidopsis* genes are required for healthy growth under conditions of low boron supply. However, in plants the genes involved in boron-toxicity tolerance may be related to those shown to function in boron efficiency. Comparisons of barley ESTs revealed four *BOR1* (At2g47160.1)–related genes. Mapping localized one of the barley genes (*Bot1*) to the region of the boron-tolerance QTL on 4H (*8*). Subsequently, a marker developed from the 3′ end of *Bot1* was found to cosegregate perfectly with the tolerance locus in our high-resolution mapping population (Fig. 2A), strongly suggesting that *Bot1* encodes the boron tolerance from the 4H locus. Although barley-rice gene colinearity was found to be high in the region (Fig. 2A), the corresponding interval on rice chromosome 3 lacks a *BOR1* ortholog, and the rice gene most closely resembling *Bot1* (Os01g08040) (Fig. 2B) resides on chromosome 1.

Southern hybridization with the use of a Clipper-derived *Bot1* probe gave a stronger signal in Sahara than in Clipper and other boron-intolerant genotypes, indicating the occurrence of additional *Bot1* copies in Sahara (fig. S2). A number of restriction enzyme digests revealed hybridizing Sahara fragments of mostly a single size (e.g.

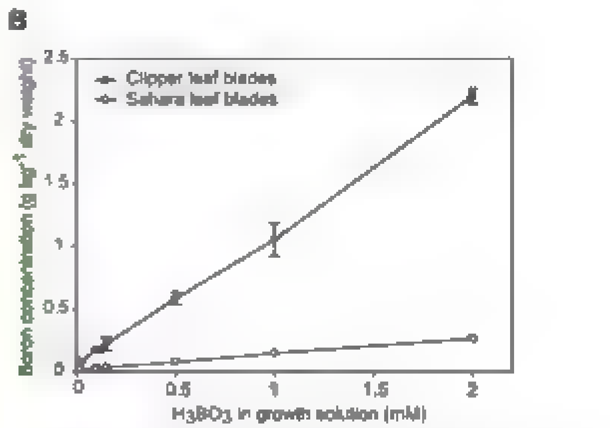

Fig. 1. Genetic variation for boron tolerance in barley. **(A)** Boron-toxicity symptoms in leaf blades of boron-intolerant (Clipper) and boron-tolerant (Sahara) barley plants. Approximately eight of the oldest leaf blades from single plants are shown 14 days after boron treatment. **(B)** Sahara accumulates less boron in leaf blades after growing for 14 days in a range of solution concentrations. Data are means ± SEM (*n* = 3 plants).

Australian Centre for Plant Functional Genomics, School of Agriculture, Food and Wine, University of Adelaide, Waite Campus, Private Mail Bag 1, Glen Osmond, South Australia 5064, Australia.

*To whom correspondence should be addressed. E-mail: tim.sutton@acpfg.com.au

Dra I (fig. S2), suggesting that the *Bot1* copies in Sahara are highly similar. With *Dra* I, which distinguishes the *Bot1* Clipper copy from the Sahara copies, all *Bot1* genes could be mapped and were found to cosegregate with boron tolerance in the Clipper-by-Sahara F_1 derived doubled-haploid population, indicating that these genes occur in a cluster. Quantitative real-time fluorescence polymerase chain reaction (QPCR) analyses using genomic DNA as the template indicated that Sahara contains about four times (3.8 ± 0.17) more copies of the gene than Clipper.

QPCR performed using cDNA as a template revealed that *Bot1* transcript levels in Sahara were ~160- and 18-fold higher in roots and leaf blades, respectively, as compared with Clipper (fig. S3). This increase in *Bot1* transcript levels exceeds the ~fourfold increase in the *Bot1* copy number in Sahara, suggesting that factors additional to gene duplication may contribute to increased *Bot1* transcript levels in Sahara. We performed a comparative promoter analysis between the Clipper and Sahara *Bot1* alleles to search for differences that could account for the observed genotypic variation in transcript levels. Over a ~3 kb region upstream of the mRNA transcription start site, the Clipper and Sahara *Bot1* promoter regions are 96% identical. On the basis of database searches, no substantial differences were detected in known regulatory elements. More work will be required to determine the actual effect of these changes on *Bot1* transcription in barley. In any case, the greater transcript levels in Sahara, relative to Clipper, offer an explanation for the functional difference between boron-tolerance and -intolerance alleles and provide additional evidence supporting *Bot1* as the gene controlling boron tolerance at the 4H locus. In both roots and leaf blades, transcript levels were unaltered by exposure to a range of boron concentrations (fig. S3). Lack of transcriptional activation of a boron-tolerance mechanism is consistent with the rapid boron efflux from Sahara roots observed after the addition of either nontoxic or toxic quantities of boron (*9*) and the similar rank order of shoot boron accumulation in different genotypes grown over a range of boron concentrations (*4*).

The ability of Bot1 to function as a boron transporter was confirmed in yeast (*Saccharomyces cerevisiae*). Initially, we screened ~2 million clones from a Sahara root cDNA expression library for their ability to confer boron tolerance to yeast. Three clones corresponding to *Bot1* were obtained that allowed yeast to grow on high boron media. The *Bot1* clones contained complete open reading frames (ORFs) and were identical in sequence. In yeast, we then compared the ability of Sahara *Bot1* with that of Clipper *Bot1* or *Arabidopsis BOR1* to confer boron tolerance. Yeast expressing Sahara *Bot1* grew better than yeast expressing Clipper *Bot1* in the presence of high boron on both a solid medium (Fig. 3) and in liquid culture (fig. S4). Cells expressing either Sahara *Bot1* or Clipper *Bot1* also maintained ~24 or 20% less cellular boron, respectively, than cells expressing the empty vector control (fig. S4). This is in spite of the fact that at physiological pH boron exists principally as undissociated boric acid (pK_{a1} to pK_{a3} = 9.2 to 13.8, where K_a is the acid dissociation constant), to which membranes are relatively permeable (*14*). Additionally, as compared with BOR1 of *Arabidopsis*, we could show that Sahara Bot1 has higher boron efflux transport activity and capacity to provide tolerance (fig. S5). These results confirmed that *Bot1*, like *BOR1* of *Arabidopsis*, encodes a functional boron efflux transporter and that Sahara Bot1 has a higher capacity to provide boron tolerance in yeast than Clipper Bot1 or BOR1. None of the clones identified by the library screen corresponded to the tolerance cosegregating gene *BM160*, further supporting the notion that *Bot1* and not *BM160* is the tolerance gene (*15*).

The Sahara *Bot1* mRNA (accession number EF660435) is predicted to encode a 666 amino acid protein with 10 to 12 putative transmembrane helices (fig. S6). Within the ORF, Clipper *Bot1* (accession number EF660437) differs by 11 nucleotides, 2 of which result in differences to the translated protein: $Leu^{305} \rightarrow Ser^{305}$ and $Asp^{592} \rightarrow Gly^{592}$. Residue change 305 [Leu (hydrophobic) to Ser (polar)] in transmembrane helix eight may impart a conformation change, and residue change 592 [Asp (polar) to Gly (no side chain)] is likely to be located within the intracellular carboxyl terminus. Both changes could affect boron transport. Bot1 showed greater sequence similarity to several other *Arabidopsis* BOR1-related proteins than to BOR1 itself (Fig. 2B and fig. S7), consistent with *Bot1* serving a

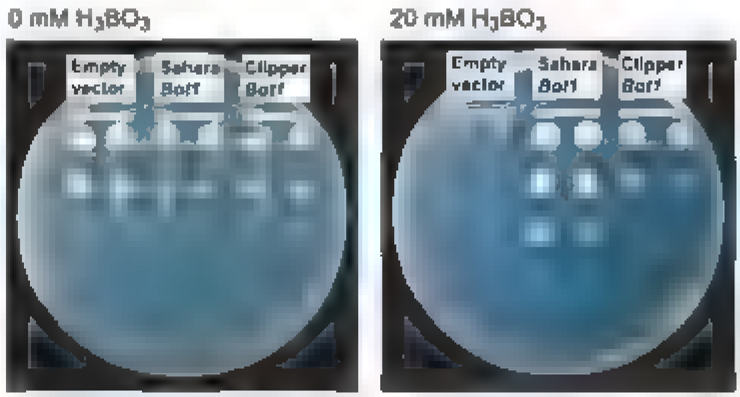

Fig. 3. *Bot1* provides boron tolerance in yeast. Growth of *S. cerevisiae* on a solid medium containing **(left)** 0 or **(right)** 20 mM supplemental H_3BO_3. Each plate shows two independent yeast clones containing either empty vector, Sahara *Bot1*, or Clipper *Bot1* (left to right in each panel). Plating was a 10 μl aliquot of 10-fold serial dilutions down the plate (top to bottom in each panel).

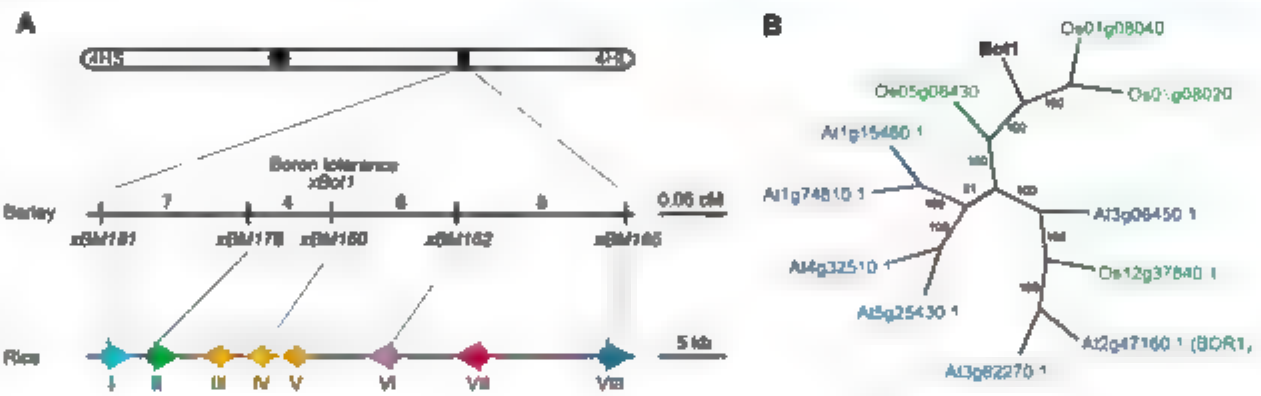

Fig. 2. *Bot1* mapping and phylogenetic analysis. **(A)** Barley/rice comparative mapping of the boron toxicity–tolerance locus on chromosome 4H. Numbers indicate recombinants identified for each marker interval. The related rice chromosome 3 (AP008209) interval spans the position from base pairs 1,861,805 to 1,873,065. Colored arrows I to VIII denote the position and orientation of predicted rice genes Os03g0133300 (hypothetical protein), Os03g0133400 (peptidoglycan-binding LysM domain–containing protein), Os03g0133500 [AMP binding protein 1 (AMPBP1)], Os03g0133600 (AMP-dependent synthetase and ligase domain–containing protein), Os03g0133800 (AMPBP1), Os03g0133900 (serine acetyltransferase), Os03g0134000 (MuDR transposase domain–containing protein), and Os03g0134300 (adenosine triphosphate phosphoribosyl transferase), respectively. Accession numbers are: *xBot1*, BV723959; *xBM160*, BV723960; *xBM165*, BV723961; *xBM178*, BV723962; *xBM181*, BV723963; and *xBM162*, BV723964. **(B)** Phylogenetic tree including Bot1 and BOR1-like proteins from rice (green) and *Arabidopsis* (blue), constructed using PHYLIP (*28*). Numbers separating junctions are bootstrap values. The closest rice ortholog of *Bot1* is Os01g08040. Locus accession numbers are according to Gramene (*29*).

different role than *BOR1*, which is required for boron efficiency. Overexpression of one of these *BOR1*-related genes in *Arabidopsis* improved boron tolerance (*16*), further supporting our hypothesis. The genomic sequence of a *Bot1* gene (accession number EF660436) was obtained from a clone (accession number EU176161) of a bacterial artificial chromosome library we constructed from a barley doubled-haploid line containing the Sahara 4H boron-tolerance allele. This sequence was identical to the cDNA in the coding sequence, and it contained 13 exons and 12 introns, including a 941–base pair intron in the 5′ untranslated region (fig. S6).

Bot1 mRNA was localized by in situ hybridization to barley-root and leaf blade tissue sections (Fig. 4, A to J). In roots, staining was strongest in all cell types of the meristematic and elongation zones at the tip (Fig. 4, I and J). Within cylindrical-sheath tissues (Fig. 4, G and H) staining was strong in all cells of the youngest leaf blades. QPCR from 10-mm segments taken along the root revealed that *Bot1* mRNA level, expressed as a proportion of total RNA content, was slightly greater in more mature root segments than in end segments containing root tips (Fig. 4K). The lower levels of staining in mature roots may reflect the proportionally lower volume of cytoplasm in these cells, but the significant transcript levels nevertheless observed by QPCR in mature roots indicate a role for the transporter in both growing and mature sections of the roots. The *Bot1* mRNA detected in young cells could potentially serve the dual role of limiting symplastic boron concentration (and hence toxicity) and helping to maintain a high boron supply to newly forming primary cell walls where boron forms an essential component of the pectic polysaccharide rhamnogalacturonan II (*17*). It is probable that *Bot1* mRNA localization in mature roots helps to efflux boron from the roots. In older leaf blades, *Bot1* mRNA staining was strong in mesophyll adjacent to enlarged vessels near the margins and was strongest at the tips (Fig. 4, A and B). In barley, leaf-blade tips are the site of guttation by hydathodes. *Bot1* mRNA localization here suggests an additional role of Bot1 in facilitating boron removal from the leaf blade via guttation fluid and hence in reducing boron toxicity in the leaves (*18*–*20*). Guttation has previously been shown to be a route by which substantial amounts of boron can be removed from leaves (*18*). In field conditions, rainfall decreases boron concentrations in shoots of barley (*21*) and wheat (*22*).

In Australian barley crops, grain yield has been estimated to be reduced by 17% as a result of boron toxicity (*23*). The importance of boron tolerance throughout Central and West Asia and North Africa is based on an observation that landraces of barley and wheat sourced from these regions tend to show high levels of tolerance—for example, the line used in the current study (Sahara) and lines from Turkey (*24*), Iraq, and Afghanistan (*25*). Poor adoption of modern varieties in some of these areas (*26*) may be associated with boron intolerance. There is also evidence that boron toxicity will become an increasing problem on irrigated land, coincident with salinity (*5*).

Barley breeding programs in Australia have used linked molecular markers to introgress the Sahara *Bot1* allele into commercial barley cultivars. However, lines carrying the introgression can potentially be lower-yielding than the recipient cultivars (*27*). We currently do not know if this potential yield reduction is the result of pleiotropic effects of Bot1 itself or is due to linked deleterious alleles from the otherwise unadapted landrace Sahara. To help break unwanted associations, lines carrying recombination events directly adjacent to *Bot1* have been identified and supplied to breeders. The identification of *Bot1* as the gene controlling the 4H QTL now offers new paths for dealing with boron toxicity. Diagnostic markers are being developed for use in barley breeding and selection strategies. It should also be possible to generate boron-tolerant plants by transformation. The ability of Bot1 to confer tolerance in yeast and barley suggests that, under appropriate transcriptional regulation, the gene may be of value in engineering tolerance in a wide range of plant species.

References and Notes

1. S. Goldberg, *Plant Soil* **193**, 35 (1997).
2. U. C. Gupta, *Boron and Its Role in Crop Production*, U. C. Gupta, Ed. (CRC Press, Boca Raton, FL, 1993).
3. R. O. Nable, J. G. Paull, in vol. 10 of *Current Topics in Plant Biochemistry and Physiology*, D. D. Randall, D. G. Blevins, C. D. Miles, Eds. (Univ. of Missouri Press, Columbia, MO, 1991), pp. 257–273.
4. R. O. Nable, *Plant Soil* **112**, 45 (1988).
5. R. O. Nable, G. S. Banuelos, J. G. Paull, *Plant Soil* **193**, 181 (1997).
6. R. O. Nable, R. C. M. Lance, B. Cartwright, *Ann. Bot. (London)* **66**, 83 (1990).
7. R. O. Nable, B. Cartwright, R. C. Lance, in *Aspects of Plant Mineral Nutrition*, M. E. Bassam, M. Dambroth, B. Loughman, Eds. (Kluwer Academic, Dordrecht, Netherlands, 1990), pp. 243–251.
8. S. P. Jefferies *et al.*, *Theor. Appl. Genet.* **98**, 1293 (1999).
9. J. E. Hayes, R. J. Reid, *Plant Physiol.* **136**, 3376 (2004).
10. Materials and methods are available as supporting material on *Science* Online.
11. J. Takano *et al.*, *Plant Cell* **18**, 1498 (2006).
12. J. Takano, K. Miwa, L. X. Yuan, N. von Wirén, T. Fujiwara, *Proc. Natl. Acad. Sci. U.S.A.* **102**, 12276 (2005).
13. J. Takano *et al.*, *Nature* **420**, 337 (2002).
14. C. Dordas, P. H. Brown, *J. Membr. Biol.* **175**, 95 (2000).
15. Because *ABM160* cosegregates with the tolerance locus, we cannot rule out a role of the corresponding gene in boron tolerance.

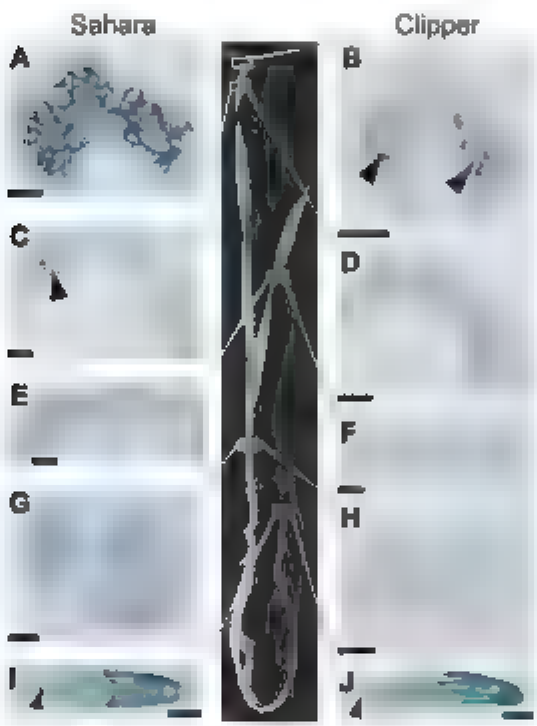

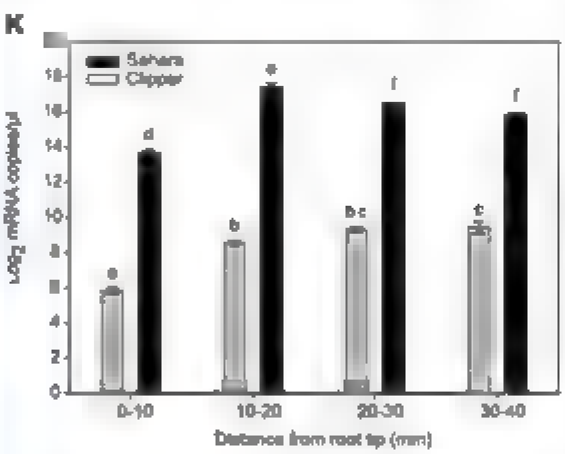

Fig. 4. Localization of *Bot1* mRNA in barley. In situ localization of *Bot1* mRNA in transverse (**A** to **H**) and longitudinal (**I** and **J**) sections of Sahara [(A), (C), (E), (G), and (I)] and Clipper [(B), (D), (F), (H), and (J)] barley tissues grown at 1 mM H_3BO_3, probed with antisense *Bot1*. *Bot1* mRNA staining is strong at the tips of leaf blades [(A) and (B)] in mesophyll surrounding the enlarged vessels [arrowheads in (B)]. Relative to the leaf-blade tip, staining is reduced 2 cm back from the tip [(C) and (D)], but remains specific to mesophyll surrounding the enlarged vessels in Sahara [arrowhead in (C)]. At the middle of the youngest fully emerged leaf blade [(E) and (F)], this pattern was not evident. *Bot1* mRNA staining is also strong in the youngest tissue of the cylindrical sheath [(G) and (H)] and root tip [(I) and (J)]. In roots, staining extended into the mature stele [arrowheads in (I) and (J)]. A quantitative difference in staining between Sahara and Clipper leaf tissue sections is evident. (A to H) Transmission electron microscopy fixative. (I and J) Formalin–acetic acid–alcohol fixative. Sense hybridizations were performed for all tissue sections and produced no detectable signal. The plant at center is a 10-day-old Clipper seedling. Scale bars, 100 μm in (A) to (F), 500 μm in (G) to (J). (**K**) *Bot1* mRNA levels in 10-mm root segments taken along the root were analyzed by QPCR. The different letters above each bar represent statistically significant differences (analysis of variance, $P < 0.05$, post hoc Tukey test). Data are means ± SEM ($n = 3$ plants).

16. K. Miwa, J. Takano, H. Omori, T. Fujiwara, *Plant Cell Physiol.* **48**, 589 (2007).
17. T. Matoh, *Plant Soil* **193**, 59 (1997).
18. J. J. Oertli, *Soil Sci.* **94**, 214 (1962).
19. J. J. Oertli, *Agrochimica* **13**, 212 (1969).
20. K. Warington, *Ann. Bot. (London)* **37**, 629 (1923).
21. R. O. Nable, J. G. Paull, B. Cartwright, *Plant Soil* **128**, 225 (1990).
22. R. O. Nable, D. B. Moody, *Plant Soil* **140**, 311 (1992).
23. B. Cartwright, B. A. Zarcinas, A. H. Mayfield, *Aust. J. Soil Res.* **22**, 261 (1984).
24. M. Avci, T. Akar, *Turk. J. Agric. For.* **29**, 377 (2005).
25. S. K. Yau, *Barley Newsl.* **40** (1996), http://wheat.pw.usda.gov/ggpages/BarleyNewsletter.
26. J. Dixon *et al.*, *J. Agric. Sci.* **144**, 489 (2006).
27. J. K. Eglinton *et al.*, *Czech. J. Genet. Plant Breed.* **40**, 166 (2004).
28. J. Felsenstein, PHYLIP (Phylogeny Inference Package) version 3.63 (distributed by the author, Department of Genome Sciences, Univ. of Washington, Seattle, WA, 2005).
29. www.gramene.org

30. This work was funded by the Australian Research Council, the South Australian government, and the Grains Research and Development Corporation. We thank N. Shirley, M. Hrmova, A. Milligan, K. Gustafson, and R. Lovell for contributions to various aspects of the work and T. Fujiwara for providing yeast strains.

Supporting Online Material

www.sciencemag.org/cgi/content/full/318/5855/1446/DC1
Materials and Methods
Figs. S1 to S7
Table S1
References

21 June 2007; accepted 9 October 2007
10.1126/science.1146853

Genome-Wide Experimental Determination of Barriers to Horizontal Gene Transfer

Rotem Sorek,[1,2] Yiwen Zhu,[2] Christopher J. Creevey,[3] M. Pilar Francino,[2] Peer Bork,[3] Edward M. Rubin[1,2]*

Horizontal gene transfer, in which genetic material is transferred from the genome of one organism to that of another, has been investigated in microbial species mainly through computational sequence analyses. To address the lack of experimental data, we studied the attempted movement of 246,045 genes from 79 prokaryotic genomes into *Escherichia coli* and identified genes that consistently fail to transfer. We studied the mechanisms underlying transfer inhibition by placing coding regions from different species under the control of inducible promoters. Our data suggest that toxicity to the host inhibited transfer regardless of the species of origin and that increased gene dosage and associated increased expression may be a predominant cause for transfer failure. Although these experimental studies examined transfer solely into *E. coli*, a computational analysis of gene-transfer rates across available bacterial and archaeal genomes supports that the barriers observed in our study are general across the tree of life.

The rapidly accumulating sequenced genomes of bacteria and archaea reveal the role of horizontal gene transfer (the nonsexual exchange of genes across hierarchal boundaries) in shaping noneukaryotic genomes (*1*, *2*). Gene exchange has been documented for nearly all types of genes and at all phylogenetic distances (*3*). These observations have sparked debates about whether microbial genes can be used for phylogenetic classification, because the proposed lack of barriers to gene transfer between genomes suggests that a treelike classification of microorganisms might be impossible (*4*, *5*).

Identifying the limitations of gene transfer is hampered because nearly all transfer events have been inferred on the basis of sequence analysis of microbial genomes. Computational approaches, including detection of nucleotide or codon compositional biases and atypical distribution of genes, identify signatures of transfer events predicted to have occurred millions of years ago (*6*). On the basis of such studies, specific categories of genes were suggested as less prone to transfer, and hence potentially useful as phylogenetic markers (*7*, *8*), but the validity of this idea relies nearly exclusively on computational evidence (*1*). The paucity of experimental and quantitative data on horizontal gene transfer, therefore, impedes our ability to understand the extent and limitations of this phenomenon.

Natural gene transfer is largely mediated by naked DNA uptake (transformation), viruses (transduction), and plasmids (conjugation) (*9*). When a microbial genome is being sequenced, multiple copies of the genome are randomly sheared into overlapping fragments of DNA (typically to libraries sized 3 kb and 8 kb), and plasmids containing the cloned fragments are transformed into an *E. coli* cell (*10*). The ends of the cloned fragments are then sequenced, and overlapping sequences are used for genome assembly. Because cloned fragments contain the full set of genes belonging to the sequenced organism, microbial genome sequencing can be viewed as a large-scale experiment in horizontal gene transfer to *E. coli*, where each gene in a given genome undergoes multiple transfer attempts to the host with an extrachromosomal plasmid. In the course of nearly all prokaryotic sequencing projects, a small fraction of the organism's genome fails to clone in *E. coli*, resulting in sequence gaps. The sequence for these gaps is acquired during a clone-independent stage termed "finishing," eventually producing an unbroken sequence of the organism's genome (*11*).

We explored the limits to horizontal transfer by studying the nature of unclonable (untransferable) genomic regions. Of the 85 finished microbial genomes with accessible original sequence reads, we selected 79 (including 75 bacterial and 4 archaeal) with sufficient clone coverage for detailed analysis (SOM Text and table S1) (*12*). We used the original sequencing data to map the clone positions on these genomes. Overall, this data set included 1,873,649 clones spanning more than 8.9 billion bases of genomic DNA fragments successfully transferred into an *E. coli* host.

We next explored the transfer of the individual genes residing in the 79 analyzed genomes. For each of the 287,884 annotated genes contained in these genomes, we calculated the number of clones fully spanning the gene on the

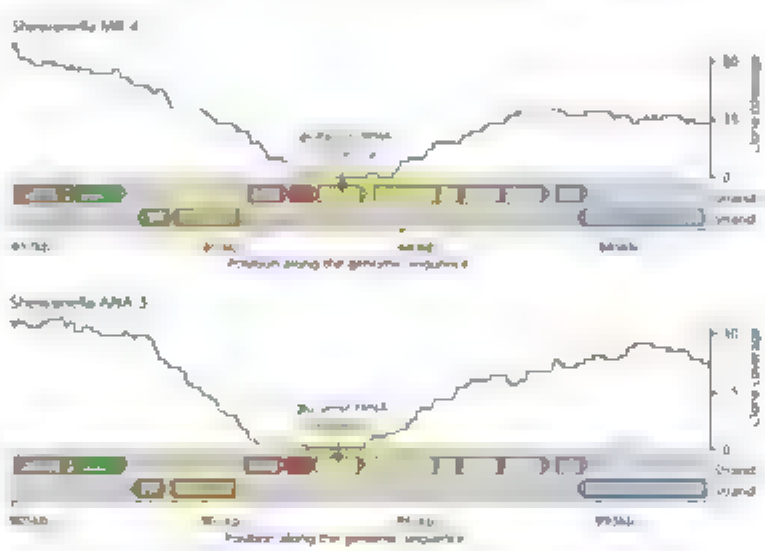

Fig. 1. Coverage plots created on the Artemis genome browser (*20*) of a syntenic 14-kb genomic region in two closely related *Shewanella* bacteria species. (**top**) *S.* sp. *MR-4*; (**bottom**) *S.* sp. *ANA-3*. Colored rectangles represent genes, with colors denoting functional categories; arrow direction indicates whether the gene is on the forward or reverse strand. Coverage is measured per nucleotide

[1]Department of Energy, Joint Genome Institute, 2800 Mitchell Drive, Walnut Creek, CA 94598, USA. [2]Genome Sciences Department, Lawrence Berkeley National Laboratory, Berkeley, CA 94720, USA. [3]European Molecular Biology Laboratory, Meyerhofstrasse 1, 69012 Heidelberg, Germany.

*To whom correspondence should be addressed. E-mail: EMRubin@lbl.gov

basis of the mapped clone positions. We considered only genes 1.5 kb or less (246,045 genes, representing 85% of all annotated genes), because larger genes are less likely to be covered to their full length by multiple clones. The average number of clones covering each of these 246,045 genes to its full length was 22.57, indicating that each gene underwent, on average, more than 22 independent transfer attempts to the host

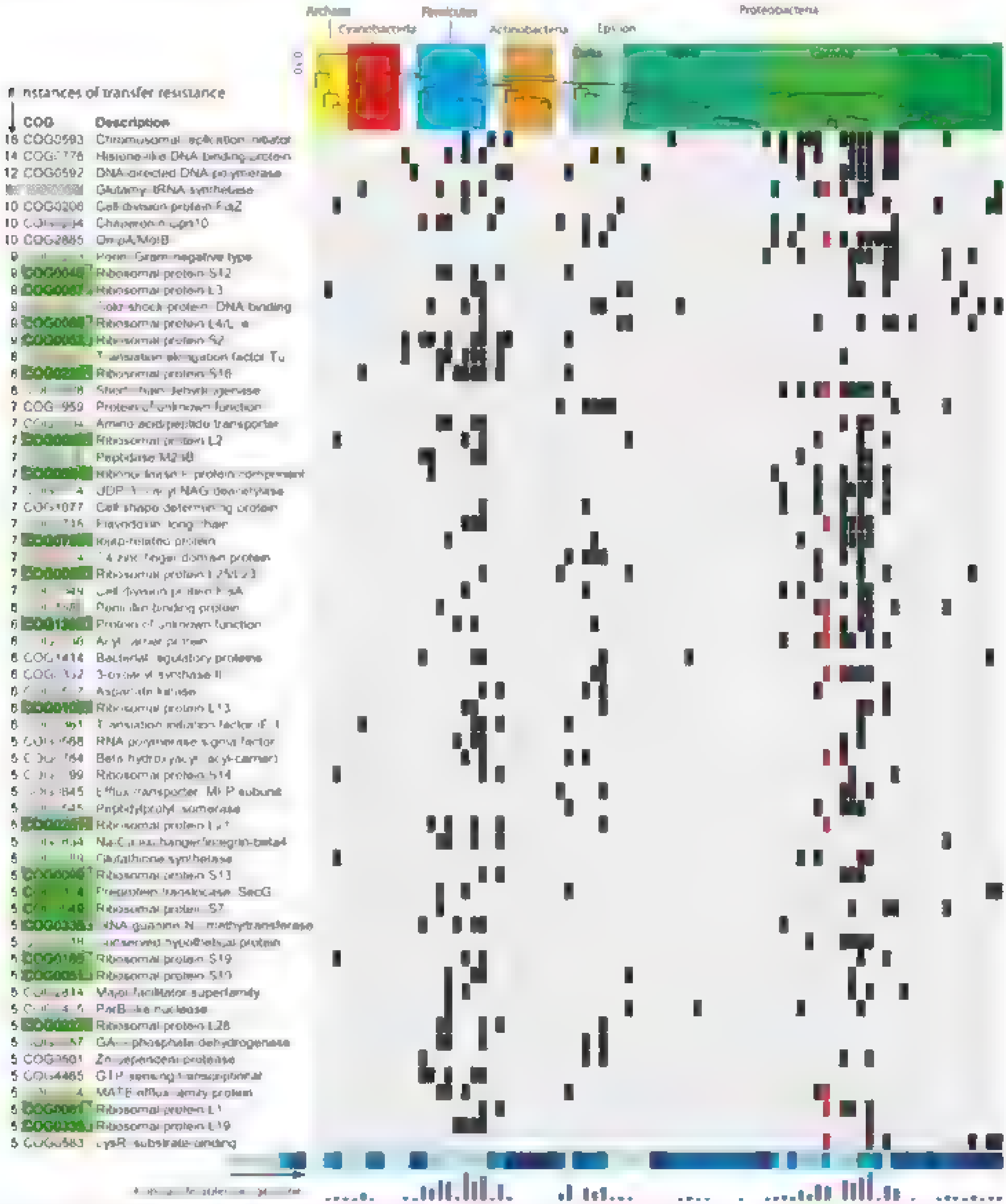

Fig. 2. Genes that cannot be cloned into *E. coli* from five or more genomes. Rows are genes, according to their COG classification (*21*). Columns represent the 79 microbial genomes analyzed, arranged by their phylogenetic relationships as determined by a Maximum Likelihood tree analysis of 16S rRNA sequences (*12*). Uncionable genes are denoted by black boxes. The leftmost column indicates the number of genomes from which the gene was not able to be transferred. Universally single-copy genes are highlighted in green. *E. coli* (Gammaproteobacteria) genes that could not be cloned into the *E. coli* sequencing strain even when originating from an *E. coli* HS genome are marked red. Percentage of GC for each of the genomes is color coded at the bottom of the figure. Darker colors indicate a higher GC content. The histogram below depicts the number of unclonable genes per genome (table S1).

We used the clone coverage distribution to identify genes unclonable into the *E. coli* host. To exclude the possibility that cloning biases are random or human-introduced, we compared clone coverage among genomes of closely related species. These genomes presented relatively similar coverage patterns, with the same sets of orthologous genes from several different organisms absent from sequenced clones, supporting the idea that clone deficiency is largely gene-dependent. Comparison of four *Shewanella* species offers an example for the high reproducibility of clone deficiency: 73 of 99 (74%) *Shewanella sp. MR-4* genes found to be unclonable into *E. coli* were also unclonable when transferred from at least one of the three other *Shewanella* species examined (Fig. 1).

Of the genes inspected, we recorded 1402 instances (642 different genes) in which an annotated gene was not fully represented in any single clone and marked these as untransferable to *E. coli* [with an estimated false positive prediction rate of 0.9% to 1.3% (*12*)]. In 1064 (76%) of these events, the same gene was unclonable to *E. coli* from two or more different genomes. Sixty-one genes (477 events, 34% of total events) could not be cloned from five or more different genomes into *E. coli* (Fig. 2). The high transfer failure rate for certain gene families across several genomes further suggests that specific genes, rather than the experimental protocol or random biases, may cause this lack of horizontal transfer.

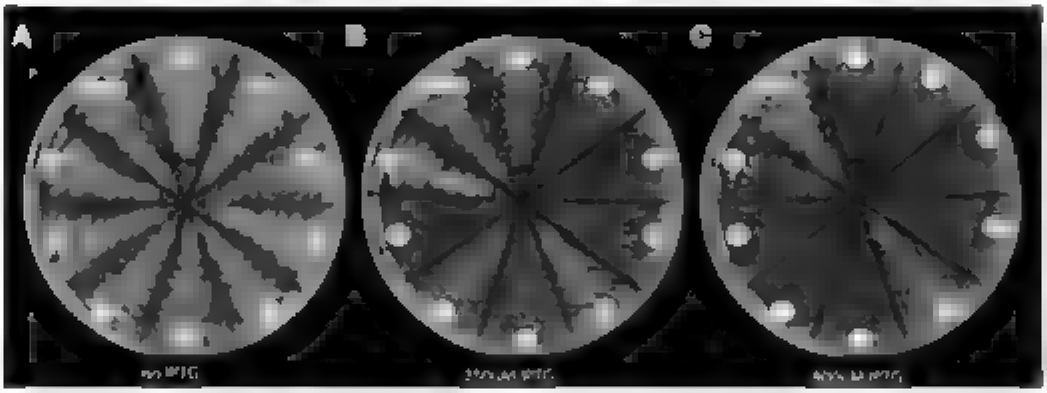

Fig. 3. Toxicity results for the first nine genes tested (table S2) and a control gene (Beta-galactosidase from *E. coli*). The coding regions of predicted unclonable genes were cloned into the pET11 vector under the control of a T7 promoter, transformed into *E. coli* BL21(DE)pLysS cells, and streaked on LB plates. Cells grown (**A**) without the expression-inducer IPTG, (**B**) with 250 μM IPTG, and (**C**) with 800 μM IPTG. 1, Replication initiator DnaA from *Shewanella denitrificans*; 2, Histone-like DNA binding from *Psychrobacter cryohalolentis*; 3, DNA polymerase III, beta subunit from *Deinococcus geothermalis*; 4, Cell division protein FtsZ from *P. cryohalolentis*; 5, Chaperonin Cpn10 from *Nitrosococcus oceani*; 6, OmpA/MotB from *N. oceani*; 7, Ribosomal protein S12 from *Rhodoferax ferrireducens*; 8, Ribosomal protein L4/L1e from *Burkholderia sp. strain 383*; 9, Ribosomal protein L3 from *P. cryohalolentis*.

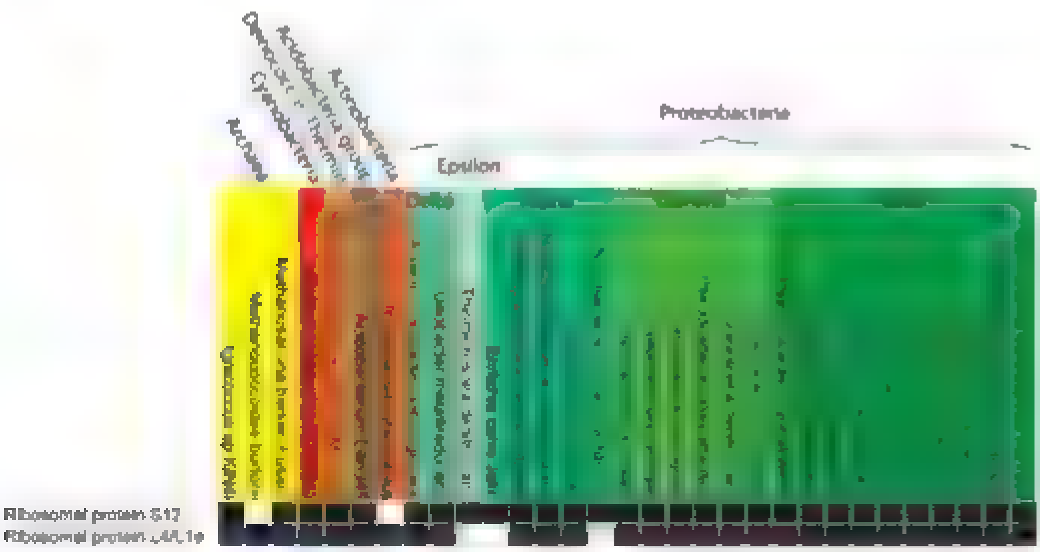

Fig. 4. Toxicity of ribosomal protein S12 (COG0048) (top row) and ribosomal protein L4/L1e (COG0088) (bottom row) from 31 microbial genomes. Columns represent species, arranged by phylogenetic classification, with different colors representing different groups (names indicated above). ORFs were cloned into the pET11 vector adjacent to a T7 promoter and transformed into *E. coli* BL21(DE)pLysS cells. Colony growth was tested without gene expression and after induction of expression with various concentrations of IPTG. Black boxes indicate growth inhibition after activation of expression; white boxes indicate that no growth inhibition was observed (details in table S3).

Whereas gene transfer in the wild is believed to be mediated by the transfer of single as well as multiple copies of the DNA, the cloning vectors used in most small-insert sequencing libraries exist in 20 to 100 copies per cell (*13*, *14*). We examined the impact of single- versus multiple-copy transfers by studying the subset of 35 sequenced genomes where, in addition to the small-insert libraries, large fragments (35 kb) of the microbial genome were propagated in fosmids, which typically exist in a single copy per *E. coli* cell (*15*) (table S1). In 124 out of 483 (26%) inspected genes in these genomes, the genes were also covered by zero (22%) or statistically fewer (4%) fosmids than expected (fig. S1) (*12*). The consistency of functional results obtained with multicopy plasmids and with single-copy fosmids suggests that a considerable portion of the observed lack of transfer is not solely due to high copy number and that the barriers described in this study are gene copy number independent.

We selected 40 genes that resisted transfer from two or more genomes into *E. coli* and were able to clone the coding regions of 39 of these genes into an expression vector system that strongly suppresses the expression of the cloned gene in the absence of the expression inducer isopropyl-β-D-thiogalactopyranoside (IPTG) (table S2 and SOM Text). In the absence of inducer, bacterial growth was observed. However, upon induction of expression, 32 of the 39 genes (82%) inhibited *E. coli* growth, indicating that the products of these genes are toxic to the host (Fig. 3 and table S2), which explains the lack of transfer observed in the genome sequencing data.

Although we identified genes that were transfer-resistant from a wide range of prokaryotes, no single gene was untransferable among all genomes examined (reflected by the absence of a horizontal line of black squares running across the complete list of organisms in Fig. 2). This was coupled with the observation that the resistance to transfer of genes tended to be similar among closely related organisms (Fig. 2). A possible explanation is that promoters (usually found adjacent to the gene and hence transferred with it) from some species may be recognized by the host *E. coli* transcriptional machinery and may drive the expression of the foreign gene leading to growth inhibition, whereas promoters of other species are not active in the *E. coli* cell. Indeed, sequences from Firmicutes were previously shown to drive strong expression when tested as promoters in *E. coli* (*16*), which is consistent with Firmicutes having high numbers of transfer resistant genes (Fig. 2). GC-rich genomes tended to have fewer untransferable genes, again consistent with observations that promoters recognized by *E. coli* are GC-poor (*17*). Therefore, we predicted that some of the genes cataloged as nontoxic would be toxic if their promoters were active in *E. coli*.

To test this, we examined two relatively transfer-resistant genes, ribosomal protein L4/L1e (COG0088) and ribosomal protein S12 (COG0048). Each of these genes did not transfer

in 9 of 79 genomes (Fig. 2). We isolated the coding sequences of these genes from 31 microorganisms for which genomic DNA was readily obtainable, including 26 organisms in which transfer resistance had not been observed on the basis of genome sequencing, and cloned them into the inducible expression system described above. Clones holding these genes grew normally in the absence of inducer. However, growth inhibition was observed in 53 of 62 (85%) clones when expression of the cloned gene was induced by low IPTG concentrations (100 μM to 600 μM) and in 57 of 62 clones (92%) in higher (800 μM) IPTG (Fig. 4 and table S3). Such a high frequency of growth inhibition was not observed in a survey of 15 randomly selected putative negative control genes, of which 2 of 15 (13%) and 7 of 15 (47%) inhibited growth in low and high IPTG, respectively (SOM Text and table S4). These results suggest that some of the genes we identified are almost universally toxic when expressed, suggesting that they face a near absolute, phylum-independent barrier to horizontal transfer into *E. coli*. We expect that the small number of putative negative control genes found to be toxic are not true negatives due to the possibility that they possess endogenous promoters inactive in the conditions in which the sequencing *E. coli* strain was grown. In these cases, such toxic genes would escape our detection method.

We compared the clusters of orthologous groups (COG) functions of the 61 genes identified as highly unclonable (those untransferable from five or more genomes) to the COG functions of all genes in our data set. These genes were significantly enriched in genes involved in ribosomal structure and translation ($P < 2 \times 10^{-9}$, Fisher's exact test corrected for multiple testing) (fig. S2). This observation is consistent with previous computational analyses that suggested that genes involved in translation tend to be underrepresented in genes postulated to have undergone horizontal transfer (*7*, *8*). The toxicity of ribosomal proteins observed here possibly stems from an incompatibility with the *E. coli* molecular machinery, as they have multiple interactions within the ribosome (*7*). We found that ribosomal proteins that resisted transfer from a large number of genomes also had more surface area in contact with the rRNA ($P = 0.023$, Spearman's test) (fig. S3).

An additional possible mechanism for explaining some of the observed transfer resistance is intolerance of the host to increased dosage of the transferred gene in addition to the endogenous homolog. To test this hypothesis, we examined data from the *E. coli HS* (*18*) genome project, in which clones containing fragments of the *E. coli HS* genome were transferred into a standard *E. coli* sequencing strain (*DH10B*). Despite the near identity between the transferred genes and the host genes, 43 *E. coli HS* genes (all of them conserved in *E. coli K12* in >98% identity) could not be cloned into the host *E. coli*. Therefore, this subset of genes cannot be tolerated in high dosage. Thirty-four (80%) of these 43 genes were also untransferable to *E. coli* from at least one additional foreign genome (Fig. 2), suggesting that their lack of transfer was also due to dosage intolerance. Moreover, 32% of the genes that were untransferable to *E. coli* from five or more genomes were universal single-copy genes, never duplicated in any of the genomes we tested (compared with 3% universal single-copy genes out of the entire gene population), providing additional support that an increased dosage and the associated increased expression of these genes is likely detrimental to most microbes (Fig. 2). The tendency of transfer-resistant genes to universally exist in a single copy provides further support that the barriers described in this study are gene copy–number independent.

Although our analysis of the experimental data from 246,045 genes transferred to *E. coli* suggests that there is a specific set of genes that are unclonable regardless of their genome of origin, it does so for a single recipient organism, the *E. coli* host. To explore whether these results are general, and whether these genes are untransferable to other recipient species, we used a tree-based computational method to predict gene transfer in 191 sequenced genomes across the entire tree of life (*19*) (SOM Text). We found a strong correlation ($P = 0.008$, Wilcoxon Mann-Whitney Test) between genes that we experimentally characterized as unclonable to *E. coli* and single-copy genes that were computationally predicted to be less transferred across the tree of life (fig. S4). These results suggest that the genes we experimentally characterized in a single host are generally transfer-resistant among most bacteria and archaea, and would be expected to be predominately vertically transmitted in prokaryotes.

Our experiments in horizontal transfer used plasmids as the vessel of transfer, imitating the conjugation process. Transfer through transduction and naked DNA uptake were not examined, but because the detected transfer barriers are caused by post-transfer gene toxicity, the vessel of transfer is not expected to play an important role for the effect of these barriers. In addition, homologous recombination between the transferred gene and its endogenous homolog might circumvent the toxicity imposed by expression of the transferred gene, thus enabling transfer. Our observation that the genes we experimentally characterized as unclonable to *E. coli* do not demonstrate transfer among most microorganisms suggests that this scenario had occurred only very rarely, if ever.

Instead, our results suggest that there are universal gene-transfer barriers, regardless of whether transfer occurs among closely or distantly related microorganisms, and that these barriers may be associated with toxicity of the transferred gene to the host. The number of untransferable genes identified in this study probably reflects a lower limit, because the genes we studied were physically forced into the host, plasmid maintenance was aggressively selected for with antibiotics, and additional natural barriers were not taken into account. In addition, transfer-resistant genes larger than 1.5 kb, as well as toxic genes whose promoters are not active in *E. coli*, escaped our detection. Our observation that many unclonable genes are universally found as a single copy (never duplicated in any sequenced bacteria) suggests that the increased expression of these genes inhibits growth in a wide range of bacteria. Accordingly, molecules that would increase the expression of any of these genes might function as broad-range antibiotics.

References and Notes

1. J. P. Gogarten, J. P. Townsend, *Nat. Rev. Microbiol.* **3**, 679 (2005).
2. T. Dagan, W. Martin, *Proc. Natl. Acad. Sci. U.S.A.* **104**, 870 (2007).
3. J. P. Gogarten, W. F. Doolittle, J. G. Lawrence, *Mol. Biol. Evol.* **19**, 2226 (2002).
4. W. F. Doolittle, *Science* **284**, 2124 (1999).
5. H. Philippe, C. J. Douady, *Curr. Opin. Microbiol.* **6**, 498 (2003).
6. B. F. Smets, T. Barkay, *Nat. Rev. Microbiol.* **3**, 675 (2005).
7. R. Jain, M. C. Rivera, J. A. Lake, *Proc. Natl. Acad. Sci. U.S.A.* **96**, 3801 (1999).
8. M. C. Rivera, R. Jain, J. E. Moore, J. A. Lake, *Proc. Natl. Acad. Sci. U.S.A.* **95**, 6239 (1998).
9. C. M. Thomas, K. M. Nielsen, *Nat. Rev. Microbiol.* **3**, 711 (2005).
10. Joint Genome Institute sequencing protocols, www.jgi.doe.gov/sequencing/protocols/prots_production.html.
11. D. Gordon, C. Desmarais, P. Green, *Genome Res.* **11**, 614 (2001).
12. Materials and methods are available as supporting material on *Science* Online.
13. D. Summers, *Mol. Microbiol.* **29**, 1137 (1998).
14. A. C. Y. Chang, S. N. Cohen, *J. Bacteriol.* **134**, 1141 (1978).
15. U. J. Kim, H. Shizuya, P. J. de Jong, B. Birren, M. I. Simon, *Nucleic Acids Res.* **20**, 1083 (1992).
16. J. P. Dillard, J. Yother, *J. Bacteriol.* **173**, 5105 (1991).
17. M. E. Mulligan, W. R. McClure, *Nucleic Acids Res.* **14**, 109 (1986).
18. M. M. Levine *et al.*, *Lancet* **1**, 1119 (1978).
19. F. D. Ciccarelli *et al.*, *Science* **311**, 1283 (2006).
20. K. Rutherford *et al.*, *Bioinformatics* **16**, 944 (2000).
21. R. L. Tatusov *et al.*, *Nucleic Acids Res.* **29**, 22 (2001).

22. We thank A. Lapidus for providing biological material, F. Warnecke for technical assistance; S. Prabhakar for statistical help; and T. Woyke and A. Visel for graphic assistance and discussion, along with L. Pennacchio, J. Eisen, S. Green Tringe, P. Hugenholtz, T. Doerks, L. Jensen, I. Letunic, T. Dagan, and J. Bristow. This work was performed under the auspices of the U.S. Department of Energy's Office of Science, Biological and Environmental Research Program and by the University of California, Lawrence Livermore National Laboratory under contract W-7405-Eng-48, Lawrence Berkeley National Laboratory under contract DE-AC02-05CH11231, and Los Alamos National Laboratory under contract DE-AC02-06NA25396.

Supporting Online Material

www.sciencemag.org/cgi/content/full/1147112/DC1
Materials and Methods
SOM Text
Figs. S1 to S4
Tables S1 to S10
References

27 June 2007; accepted 9 October 2007
Published online 18 October 2007
10.1126/science.1147112
Include this information when citing this paper.

A Melanocortin 1 Receptor Allele Suggests Varying Pigmentation Among Neanderthals

Carles Lalueza-Fox,[1*†] Holger Römpler,[2,10*] David Caramelli,[3] Claudia Stäubert,[2] Giulio Catalano,[3,4] David Hughes,[9] Nadin Rohland,[9] Elena Pilli,[3] Laura Longo,[5] Silvana Condemi,[6] Marco de la Rasilla,[7] Javier Fortea,[7] Antonio Rosas,[8] Mark Stoneking,[9] Torsten Schöneberg,[2] Jaume Bertranpetit,[4] Michael Hofreiter[9]†

The melanocortin 1 receptor (MC1R) regulates pigmentation in humans and other vertebrates. Variants of MC1R with reduced function are associated with pale skin color and red hair in humans of primarily European origin. We amplified and sequenced a fragment of the MC1R gene (*mc1r*) from two Neanderthal remains. Both specimens have a mutation that was not found in ~3700 modern humans analyzed. Functional analyses show that this variant reduces MC1R activity to a level that alters hair and/or skin pigmentation in humans. The impaired activity of this variant suggests that Neanderthals varied in pigmentation levels, potentially on the scale observed in modern humans. Our data suggest that inactive MC1R variants evolved independently in both modern humans and Neanderthals.

One gene responsible for skin and hair color variation in humans is the *melanocortin 1 receptor* (*mc1r*), which encodes a seven-transmembrane heterotrimeric GTP-binding protein (G protein)–coupled receptor (GPCR) (Fig. 1) (*1*). Red hair and pale skin result from both complete and partial loss-of-function alleles in human MC1R (huMC1R) because they alter the balance between eumelanin and pheomelanin synthesis (*2*). Thus, we hypothesize that the retrieval of *mc1r* sequences from extinct species can potentially provide information on their phenotypic traits.

Neanderthals are an extinct hominid group that lived in Eurasia ~400,000 to 28,000 years ago (*3*). Recently, metagenomic approaches recovered about 1 megabase of the Neanderthal genome (*4*, *5*), implying that amplification of nuclear DNA by the polymerase chain reaction (PCR) may be feasible in well-preserved Neanderthal remains. We studied two Neanderthal fossils, Monti Lessini (Italy) (*6*) and El Sidrón 1252 (Spain) (*7*). Both samples have a low degree of amino acid racemization (<0.10) and high amino acid content (>20,000 parts per million), suggesting good DNA preservation (*8*). Amplifications of the hypervariable region 1 of the mitochondrial DNA showed that endogenous Neanderthal DNA was preserved in these individuals (*6*, *9*).

We assumed that retrieval of Neanderthal nuclear DNA sequences from these samples was possible if the amplicon length was short and large numbers of clones were generated. Because of the low level of divergence between Neanderthals and modern humans, it is impossible to distinguish contamination if the sequences are identical or polymorphisms are shared between the species (*10*). Therefore, we focused on identifying Neanderthal-specific substitutions. We successfully amplified a 128–base pair (bp) fragment of *mc1r* (*11*) from the Monti Lessini sample. Most clones were identical to the modern human sequence, most likely representing contamination of the Neanderthal bone with modern human DNA. However, 1 of the 25 clones had an A-to-G substitution at nucleotide position 919, resulting in an Arg-to-Gly change at amino acid position 307, which was not previously observed in modern humans (*12*, *13*). We hypothesized that this was not due to PCR error because most errors are C-to-T (or G-to-A) changes, due to cytosine deaminations in the template DNA (*14*, *15*).

Because the number of amplifiable ancient DNA molecules increases exponentially with decreasing amplification length (*16*), we designed primers to amplify a shorter DNA fragment and performed four different amplifications for El Sidrón 1252 and one for Monti Lessini. We sequenced at least 10 clones per reaction

[1]Departament de Biologia Animal, Universitat de Barcelona, Spain. [2]Department of Molecular Biochemistry, Medical Faculty, University of Leipzig, Leipzig, Germany. [3]Department of Animal Biology and Genetics, Laboratory of Anthropology, University of Florence, Italy. [4]Unitat de Biologia Evolutiva, Universitat Pompeu Fabra, Barcelona, Spain. [5]Dipartimento di Scienze Ambientali, Università di Siena, Siena, Italy. [6]Unité d'Anthropologie, CNRS, UMR 6578, Marseille, France. [7]Área de Prehistoria, Universidad de Oviedo, Spain. [8]Departamento de Paleobiología, Museo Nacional de Ciencias Naturales, CSIC, Madrid, Spain. [9]Department of Evolutionary Genetics, Max Planck Institute for Evolutionary Anthropology, Leipzig, Germany. [10]Department of Organismic and Evolutionary Biology, Harvard University, Cambridge, MA, USA.

*These authors contributed equally to this work.
†To whom correspondence should be addressed. E-mail: clalueza@ub.edu (C.L.-F.); hofreite@eva.mpg.de (M.H.)

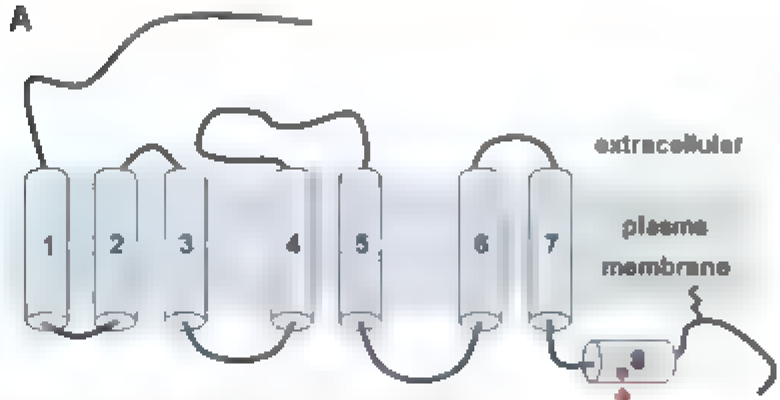

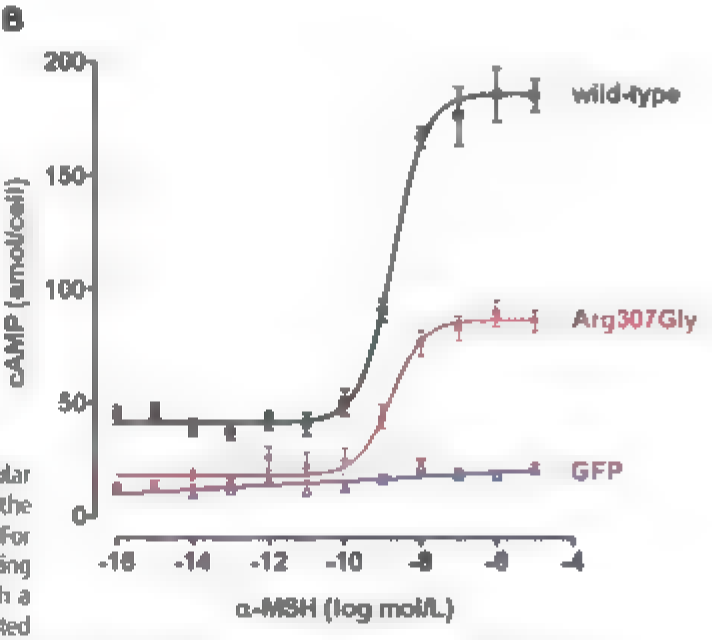

Fig. 1. Structure and activity of MC1R. **(A)** Depicted are the seven transmembrane helices of MC1R. The R307G mutation, found in two Neanderthals, is positioned within helix 8, or the fourth intracellular loop. This amphipathic helix contains many conserved basic residues and is part of the intracellular receptor C terminus. **(B)** Partial loss of function of the R307G variant. For functional characterization, COS-7 cells were transiently transfected with constructs coding for the wild type (huMC1R) and the R307G variant. As a control, cells transfected with a plasmid encoding green fluorescent protein (GFP) were used. Transfected cells were tested for agonist-induced cAMP accumulation (*11*). Shown are the mean ± SEM of three independent representative assays, each performed in duplicate.

The $Arg^{307} \rightarrow Gly^{307}$ (R307G) substitution was present in all amplification products at frequencies ranging from 7 to 25% (fig. S1). Because the humanlike sequences probably at least partially represent contamination with modern human DNA, we cannot decide whether the two individuals are homozygous for R307G or heterozygous. Thus, we concentrated on authentication of the R307G variant. The likelihood of an incorrect nucleotide, due to postmortem damage or PCR errors, decreases as the number of independent amplifications increases (14). Therefore, we amplified a different Monti Lessini extract in two additional laboratories with different primer sets. The R307G substitution was found in all three laboratories for the Monti Lessini sample but only in Barcelona for the El Sidrón sample. Altogether, we observed this substitution in 9 of 12 amplifications, with frequencies ranging from 4 to 36% (table S1). Moreover, there is no known damage in ancient DNA resulting in A-to-G substitutions (15). Even if our results were due to a previously unknown kind of template damage that occurs at the same frequency as cytosine deamination (2%) (14), the probability of obtaining the same result in 9 out of 12 independent amplifications is $\sim 10^{-13}$ (11). These results suggest that the R307G substitution is a reproducible, albeit minority, sequence not attributable to damage.

The R307G substitution has not been described in more than 2800 modern humans that have been fully sequenced for *mc1r* (12, 13). We genotyped this polymorphism in the CEPH Human Genome Diversity Panel (17) (fig. S2), as well as in all people involved in the excavation and genetic analysis, to determine whether this variant exists in extant humans (11). No individual had the R307G allele. If the R307G allele occurs in modern humans, it must be at a very low frequency, and it is unlikely that such a rare variant would appear as contamination in three separate laboratories. We additionally investigated whether nonhuman contamination could explain this result. BLASTN was used to compare the longest sequence with the R307G variant and showed that it was most like human with 98% sequence similarity, followed by primate sequences with progressively decreasing identity (table S4). None of the sequences in GenBank matched perfectly to the R307G variant, and nonprimate mammalian sequences differ considerably, excluding other common sources of contamination as possible origins of the sequence. Therefore, we concluded that the R307G substitution is an endogenous Neanderthal sequence.

The R307G mutation is positioned at the cytoplasmatic surface of MC1R within the so-called helix 8 or fourth intracellular loop (18, 19) (Fig. 1A). Mutations of conserved basic residues within this amphipathic helix alter receptor function in numerous GPCRs (19, 20). Although Arg^{307} is replaced by Lys in fox, cow, and sheep and by Met in mouse (21), the position has been shown to be intolerant of most mutations (22) (fig. S5). To investigate whether the R307G substitution affects the function of huMC1R, both wild-type MC1R and the R307G variant were expressed in COS-7 cells, and basal and agonist-induced intracellular cyclic adenosine monophosphate (cAMP) levels were determined. huMC1R responded to the natural agonist α-melanocyte-stimulating hormone (α-MSH) with an ~fourfold increase in intracellular cAMP levels (Fig. 1B and table S2). In contrast, cells expressing the R307G variant had intracellular cAMP levels that were ~40% of the wild-type levels and were 50% less than wild-type levels when activated by an agonist. Whereas basal cAMP levels of the wild type strongly correlated with the amount of transfected plasmid DNA, this was not the case for the basal activity of R307G (fig. S3). Analysis of the stimulation curves (Fig. 1B) showed that the median effective concentration values did not differ between the human and R307G variants. To exclude the possibility that the observed differences resulted from overexpression in COS-7 cells, we established stable cell lines with a single expression cassette of either MC1R variant at a predefined locus (11). These stably transfected CHOK1 cells also showed reduced agonist-induced cAMP levels for the R307G variant (table S2).

In order to determine whether these reduced basal and agonist-induced cAMP levels observed in R307G were caused by either lower cell-surface expression levels (fig. S4) or reduced G-protein coupling properties, we determined MC1R protein expression levels with an enzyme-linked immunosorbent assay and performed binding assays on intact cells (11). Total expression of the full-length receptor protein did not differ between the two variants (table S3). In contrast, radioligand binding and ligand-binding independent measurements revealed substantially reduced cell-surface expression of the R307G variant (table S3). However, we observed no difference in the ability of both receptor variants to bind α-MSH (table S3). Altogether, our data support the idea that the R307G allele has a partial loss of function caused by reduced cell-surface expression of receptor protein (23, 24) and altered G protein–coupling efficacy.

Alleles conferring partial loss of function of MC1R have been associated with pale skin color and red hair in humans (1, 12). We tested a functional cAMP assay on extant partially functional huMC1R alleles associated with pale skin color and red hair. We confirmed partial activity of these variants, indistinguishable from that of R307G (table S2). Pale skin color and lighter hair are more likely when MC1R alleles are in a homozygote or compound heterozygote stage. Although we cannot decide currently whether the Neanderthal individuals analyzed were homozygous for R307G or heterozygous, we can obtain a minimum frequency for this variant in Neanderthals. If we assume that both individuals were heterozygous, we obtain a minimum allele frequency for R307G of 50% for the two individuals investigated. From this figure, the minimum frequency of the mutation in all Neanderthals that is compatible with observing two mutant alleles when four alleles are sampled at random is 0.1 for $P > 0.05$. This translates into at least 1% of homozygous Neanderthal individuals that may have had reduced pigmentation levels, possibly even similar to the pale skin color and/or red hair observed in modern humans. These results once more raise the question of whether reduced pigmentation may have been advantageous in Europe, for example via ultraviolet-light mediated vitamin D synthesis, or whether it just reflects a loss of constraint for the *mc1r* gene in regions of reduced solar irradiation (25). Our data do not support the hypothesis that phenotypic similarities between these two human groups are explained by gene flow (26) and do support the hypothesis of convergent evolution of reduced-function MC1R alleles, as suggested between modern European and Asian populations (27, 28).

References and Notes

1. J. L. Rees, *Annu. Rev. Genet.* **37**, 67 (2003).
2. J. L. Rees, *Pigment Cell Res.* **13**, 135 (2000).
3. C. Finlayson *et al.*, *Nature* **443**, 850 (2006).
4. R. E. Green *et al.*, *Nature* **444**, 330 (2006).
5. J. P. Noonan *et al.*, *Science* **314**, 1113 (2006).
6. D. Caramelli *et al.*, *Curr. Biol.* **16**, R630 (2006).
7. A. Rosas *et al.*, *Proc. Natl. Acad. Sci. U.S.A.* **103**, 19266 (2006).
8. D. Serre *et al.*, *PLoS Biol.* **2**, e57 (2004).
9. C. Lalueza-Fox *et al.*, *Curr. Biol.* **16**, R629 (2006).
10. S. Pääbo, *Trends Biochem. Sci.* **24**, M13 (1999).
11. Materials and methods are available as supporting material on *Science* Online.
12. F. H. Wong, J. L. Rees, *Peptides* **26**, 1965 (2005).
13. M. R. Gerstenblith, A. M. Goldstein, M. C. Fargnoli, K. Peris, M. T. Landi, *Hum. Mutat.* **28**, 495 (2007).
14. M. Hofreiter, V. Jaenicke, D. Serre, A. v. Haeseler, S. Pääbo, *Nucleic Acids Res.* **29**, 4793 (2001).
15. M. Stiller *et al.*, *Proc. Natl. Acad. Sci. U.S.A.* **103**, 13578 (2006).
16. H. N. Poinar *et al.*, *Science* **311**, 392 (2006).
17. H. M. Cann *et al.*, *Science* **296**, 261b (2002).
18. E. Okuno, T. Yokomizo, T. Hori, M. Miyano, T. Shimizu, *J. Biol. Chem.* **280**, 32049 (2005).
19. M. M. O. Santos, L. A. Gardner, S. W. White, S. W. Bahouth, *J. Biol. Chem.* **281**, 12896 (2006).
20. M. Tetsuka, Y. Saito, K. Imai, H. Doi, K. Maruyama, *Endocrinology* **145**, 3712 (2004).
21. B. K. Rana *et al.*, *Genetics* **151**, 1547 (1999).
22. P. A. Kanetsky *et al.*, *Cancer Epidemiol. Biomarkers Prev.* **13**, 808 (2004).
23. K. A. Beaumont *et al.*, *Hum. Mol. Genet.* **14**, 2145 (2005).
24. B. L. Sánchez-Laorden, J. Sánchez-Más, M. C. Turpín, J. C. García-Borrón, C. Jiménez-Cervantes, *Cell Mol. Biol.* **52**, 39 (2006).
25. R. M. Harding *et al.*, *Am. J. Hum. Genet.* **66**, 1351 (2000).
26. M. H. Wolpoff, J. H. R. Caspari, *Am. J. Phys. Anthropol.* **112**, 129 (2000).
27. S. Myles, M. Somel, K. Tang, J. Kelso, M. Stoneking, *Hum. Genet.* **120**, 613 (2007).
28. H. L. Norton *et al.*, *Mol. Biol. Evol.* **24**, 710 (2007).

29. We thank C. Green for many suggestions and critical reading of the manuscript; S. Plak for help with the statistical analysis; and the Ministry of Education and Science of Spain and the Generalitat de Catalunya (C.L.F. and J.B.), the Max Planck Society (D.H., N.R., M.S., and M.H.), the Deutsche Forschungsgemeinschaft, Bundesministerium für

Bildung und Forschung, the IZKF Leipzig (H.R., C.S., and T.S.), and the Studienstiftung des Deutschen Volkes (C.S.) for financial support. The excavation at El Sidrón is supported by the Autonomous Government of Asturias. The study of the Monti Lessini Neanderthal is framed into a research project on human fossil remains at the Verona Natural History Museum. The Neanderthal *mc1r* sequence has been deposited at GenBank, accession number EU204643.

Supporting Online Material
www.sciencemag.org/cgi/content/full/1147417/DC1
Materials and Methods
Figs. S1 to S5
Tables S1 to S4
References

5 July 2007; accepted 12 October 2007
Published online 25 October 2007;
10.1126/science.1147417
Include this information when citing this paper.

5′-Triphosphate–Dependent Activation of PKR by RNAs with Short Stem-Loops

Subba Rao Nallagatla,[1*] Jungwook Hwang,[2*] Rebecca Toroney,[1] Xiaofeng Zheng,[1,3] Craig E. Cameron,[2,4]† Philip C. Bevilacqua[1]†

Molecular patterns in pathogenic RNAs can be recognized by the innate immune system, and a component of this response is the interferon-induced enzyme RNA-activated protein kinase (PKR). The major activators of PKR have been proposed to be long double-stranded RNAs. We report that RNAs with very limited secondary structures activate PKR in a 5′-triphosphate–dependent fashion in vitro and in vivo. Activation of PKR by 5′-triphosphate RNA is independent of RIG-I and is enhanced by treatment with type 1 interferon (IFN-α). Surveillance of molecular features at the 5′ end of transcripts by PKR presents a means of allowing pathogenic RNA to be distinguished from self-RNA. The evidence presented here suggests that this form of RNA-based discrimination may be a critical step in mounting an early immune response.

The innate immune response offers the host early protection from foreign organisms and viruses (*1*). As part of this response, the double-stranded RNA (dsRNA) activated protein kinase (PKR) becomes activated through autophosphorylation in the presence of viral RNA (*2*). Subsequently, PKR phosphorylates eukaryotic initiation factor 2α (eIF2α), which inhibits translation initiation, thus preventing pathogen replication (*2*).

PKR can be both activated and inhibited through its interaction with RNA, which is mediated by dsRNA-binding motifs (dsRBMs) (Fig. 1A) that also exist in other diverse proteins, including RNA-specific adenosine deaminases (ADARs), Dicer, and ribonuclease III (*3*). This interaction with dsRNA is sequence-independent (*4*, *5*), and although at least 16 base pairs (bp) of dsRNA are required for inhibition of PKR, 33 bp are needed for activation (*4*, *6*). We have previously shown that short dsRNAs with single-stranded tails (ss-dsRNAs) activate PKR, with the length of the tail providing a critical determinant (*6*). This motif has an imperfect stem of 16 bp and is flanked by single-stranded tails (Fig. 1B), and because it was prepared by transcription, it contains a 5′-triphosphate (*7*). This raises the question of what features of the tail might be important in activating PKR.

In our initial experiments, we observed that a 79-bp perfectly dsRNA (dsRNA-79) led to potent activation of PKR, with an RNA-dependency factor of ~35 (Fig. 1C) (*8*). PKR was also activated by ss-dsRNAs and gave the expected ~10-nucleotide (nt) tail-length dependence (*6*) (Fig. 1C). Maximal activation by ss-dsRNA was as intense as that by dsRNA-79, albeit requiring ~10-fold more RNA. The ss-dsRNA(9,11) (having 5′ and 3′ tails of 9 and 11 nt, respectively) transcript (Fig. 1B) was next treated with calf intestinal phosphatase (CIP) to remove the 5′-triphosphate (fig. S1), leading to abrogation of activation even at higher concentrations (Fig. 1C). Furthermore, chemically synthesized ss-dsRNA(9,11) having a 5′ hydroxyl (fig. S2) also failed to activate PKR. The presence of the 5′-triphosphate led to 100-fold higher PKR activation than occurred in its absence (fig. S2) (*8*). A mixture of CIP-treated and untreated transcripts showed full activation of PKR (fig. S3), indicating that the reason why CIP-treated RNAs do not activate PKR is not because CIP treatment renders PKR incapable of activation.

To test whether the presence of 5′-triphosphate also affects the ability of long dsRNAs to activate PKR, top and bottom strands of dsRNA-79 were CIP-treated and annealed (fig. S4). Unlike ss-dsRNA, CIP-treated as well as untreated dsRNA could activate PKR, with a standard bell-shaped dependence on RNA concentration (fig. S4D) (*6*). Thus, long dsRNA does not require 5′-triphosphate, suggesting that the contribution of this motif to PKR activation is dependent on RNA structure.

Given that ss-dsRNAs have functionally important non–base-paired elements (*6*), we next tested activation by the single strands of dsRNA-79, which also have secondary structure (fig. S4, A and B). CIP-treated ssRNA-79TS (TS, top

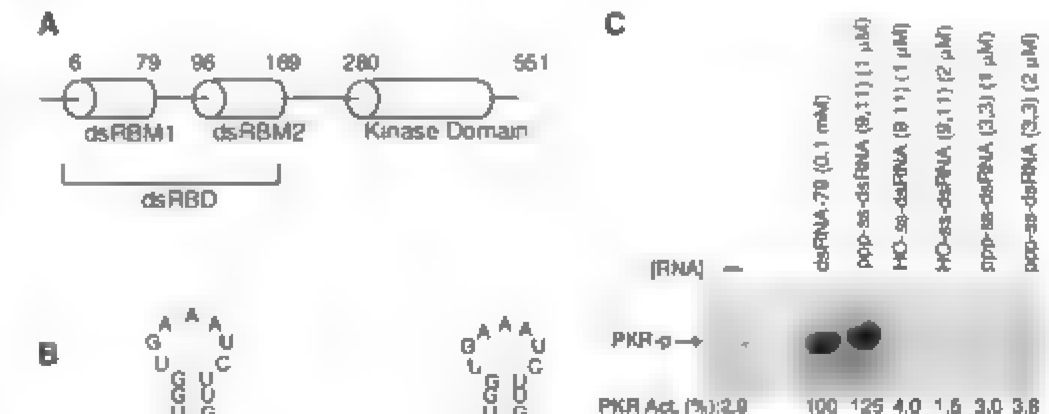

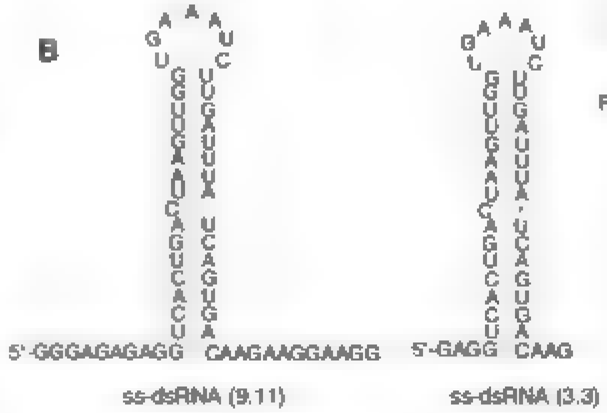

Fig. 1. Activation of PKR by ss-dsRNA is 5′-triphosphate–dependent. **(A)** PKR has two dsRBMs (the dsRBD) and a kinase domain. **(B)** Experimental structures of ss-dsRNAs (*6*). **(C)** Activation assays using ss-dsRNAs [10% SDS–polyacrylamide gel electrophoresis (PAGE)]. RNAs were transcribed and untreated (5′-ppp) or CIP-treated (5′-OH). A no-RNA lane (–) is provided. Phosphorylation activities are normalized to 0.1 μM dsRNA-79 (no CIP).

[1]Department of Chemistry, Pennsylvania State University, University Park, PA 16802, USA. [2]Integrative Biosciences, Pennsylvania State University, University Park, PA 16802, USA. [3]Department of Biochemistry and Molecular Biology, Life Sciences College, Peking University, Beijing 100871, China. [4]Department of Biochemistry and Molecular Biology, Pennsylvania State University, University Park, PA 16802, USA.

*These authors contributed equally to this work.
†To whom correspondence should be addressed. E-mail: pcb@chem.psu.edu (P.C.B.); cec9@psu.edu (C.E.C.)

strand) and ssRNA 79BS (BS, bottom strand) transcripts (8) were poor activators, whereas untreated transcripts activated PKR at levels similar to those produced by dsRNA-79 (fig. S4, E and F), with a measurable 5′-triphosphate dependence. The experiments thus far suggest that triphosphate makes the greatest contribution when the 5′ end is unstructured. To examine this further, 47- and 110-nt transcripts with minimal secondary structure were prepared (fig. S5), and despite having only a small number of short stem-loops, both transcripts activated PKR at levels close to those produced by dsRNA-79 (fig. S4, G and H). CIP treatment greatly reduced activation, confirming dependence on 5′-triphosphate.

Many viral and bacterial RNAs possess 5′-triphosphates (9, 10), whereas most cellular transcripts have a 7-methyl-guanosine (7mG) cap or a 5′-monophosphate. Thus, it is possible that PKR uses the 5′ end of mRNA as part of a quality control mechanism (11). 5′-monophosphate or 5′-hydroxyl termini, prepared by chemical synthesis of ssRNA-47, were at least 50-fold less effective than a 5′-triphosphate terminus, yielding no detectable activation (8) [Fig. 2 and supporting online material (SOM) text]. Transcripts primed with a 7mG cap or guanosine diphosphate (GDP) also failed to induce measurable PKR activation (Fig. 2, B to D). Parallel experiments on ssRNA-110 gave similar results (figs. S4G and S6), indicating that longer transcripts also have a dependence on 5′-triphosphate for activation of PKR.

Short 5′-triphosphate double-stranded small interfering RNAs, which induce an interferon response (12), as well as related short ssRNAs, failed to activate PKR (fig. S7 and SOM text). This suggested a minimal length of ssRNA required for activation, which we determined to be ~47 nt (fig. S8). In addition, a short (5-bp) stem-loop enhanced the magnitude of the response as well as the dependence on triphosphate (figs. S9 and S10). We also observed that the optimal positioning of the stem-loop in otherwise unstructured ssRNA was 21 to 46 nt from the 5′ end (figs. S9 and S10). One possible reason for this is that short stem-loops assist PKR binding, an idea that is supported by data on a dsRNA-binding domain (dsRBD) binding to 20-bp dsRNA that is consistent with a site size of 6 to 7 bp per dsRBD (13). As for other support, RNA-PKR binding assays revealed a correlation between RNA binding and kinase activation (fig. S8, B and C).

One of the biological substrates of PKR is eIF2α, the function of which in translation initiation is inhibited upon phosphorylation of Ser[51] (2). Upon activation by 5′-triphosphate ssRNA, PKR efficiently phosphorylated eIF2α (figs. S11 and S12 and SOM text), with each activated PKR molecule phosphorylating more than 100 eIF2α molecules with a PKR:eIF2α stoichiometry of 1:1. These results are consistent with a recent crystal structure, which showed each monomer in a PKR dimer interacting with an eIF2α protein (14).

To explore the biological relevance of our findings thus far, three cell lines were selected to test components of the innate immune response: Huh-7, Huh-7.5, and Vero (Fig. 3). All are responsive to interferon (IFN-α) but produce different levels of IFN-α/β in response to RNA virus (Fig. 3A). Transfection of dsRNA-79 into Huh-7 cells induced activation of PKR and increased levels of eIF2α phosphorylation (Fig. 3B, lane 2). Phosphorylated PKR was not observed in mock-transfected cells, although some eIF2α-p was detected (Fig. 3B, lane 1). For the ssRNA, a 110-nt oligomer was selected, which has the same 5′-end requirements as the 47-nt oligomer (Fig. 2 and fig. S6), because longer RNAs possess superior transfection properties. Although 110-nt oligomer ppp-ssRNA (ppp-

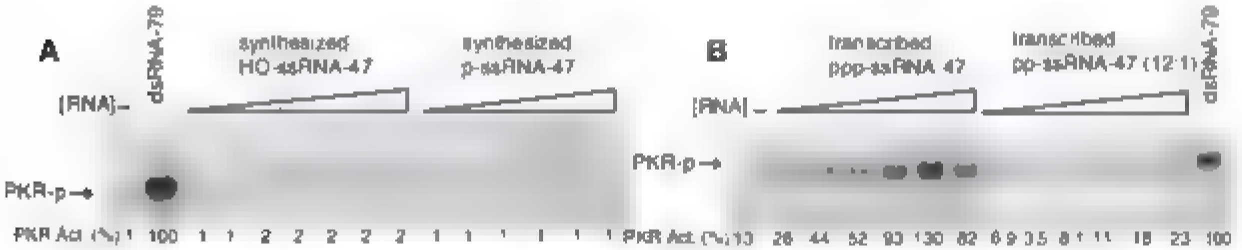

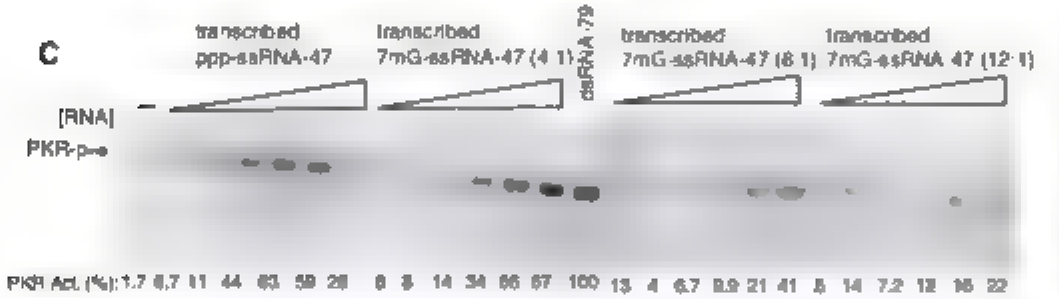

Fig. 2. Activation of PKR by ssRNA is 5′-triphosphate-dependent in vitro. **(A)** Effects of 5′-OH and 5′-p on PKR activation. ssRNA-47 was synthesized with 5′-OH or 5′-p, and concentrations were 0.1, 0.5, 1, 2, 3, 5, and 10 μM (0.1 μM is omitted for 5′-p). **(B)** Effects of 5′-pp and 5′-ppp on PKR activation. ssRNA-47 was transcribed with guanosine triphosphate (GTP) only or with a GDP:GTP ratio of 12:1 and tested for PKR activation. RNA concentrations were 0.16, 0.31, 0.63, 1.25, 2.5, and 5 μM. **(C)** Effect of a 7mG cap on PKR activation. ssRNA-47 was transcribed with a 7mGpppG:GTP ratio of 4:1, 8:1, or 12:1. RNA concentrations were 0.16, 0.31, 0.63, 1.25, 2.5, and 5 μM. **(D)** PKR phosphorylation data from (C). The ratio of 7mGpppG:GTP was 0 (solid line, black circles); 4 (dashed line, white circles); 8 (solid line, black boxes); and 12 (dashed line, white boxes). Phosphorylation activities are normalized to 0.1 μM dsRNA-79 (no CIP).

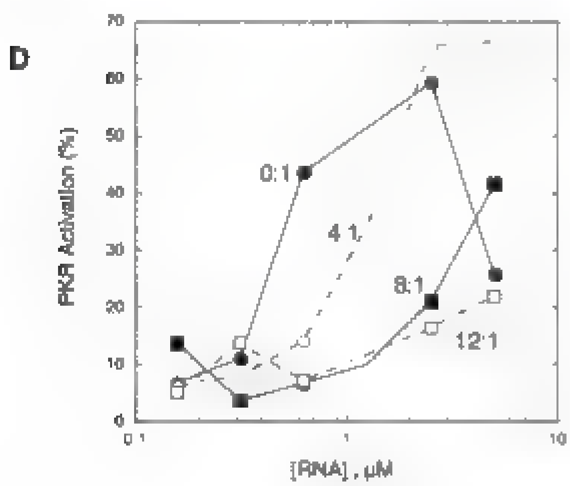

5′-triphosphate) failed to activate PKR to a detectable level, a significant increase in eIF2α-p was nevertheless observed (Fig. 3B, lane 3) relative to mock-transfected cells. The response required the triphosphate, because the CIP-treated ssRNA transcript showed only background levels of eIF2α-p (Fig. 3B, lane 4). These results suggest that ssRNA requires a 5′-triphosphate for PKR-mediated phosphorylation of eIF2α intracellularly.

The helicase and innate immune sensor RIG-I has also recently been shown to be activated by ssRNA with a 5′-triphosphate (15, 16). To determine whether activation of RIG-I contributes to PKR activation by 5′-triphosphate ssRNA, we used the Huh-7.5 subline of Huh-7, which lacks a functional RIG-I signaling pathway (17). Activated PKR was not detected in this cell line in response to dsRNA (Fig. 3C, lane 2) or ppp-ssRNA (Fig. 3C, lane 3), although a subtle yet reproducible increase in the amount of eIF2α-p was observed in response to dsRNA treatment (Fig. 3C, lane 2).

It was possible that a requirement for RIG-I for activation of PKR might be due to a need for IFN-α/β production. To test this, Vero cells, which are incapable of producing IFN-α/β, were tested, revealing activation of PKR by dsRNA (Fig. 3D, lane 2) but not ppp-ssRNA (Fig. 3D, lane 3). These data show that activation of PKR by dsRNA is independent of IFN-α/β production. Activation of PKR by ppp-ssRNA may use an alternative mechanism, requiring functional RIG-I signaling and/or IFN-α/β production.

All three cell lines we used are known to respond to IFN-α treatment (Fig. 3A). To further dissect the need for RIG-I signaling from IFN-α/β production, the experiments were repeated in cells treated with IFN-α. In all cell lines, dsRNA activated PKR on the basis of detection of both PKR-p and eIF2α-p (Fig. 3, B to D, lane 6). These experiments demonstrate that RIG-I signaling is not required for PKR activation by dsRNA. Likewise, ppp-ssRNA activated PKR in all cell lines treated with IFN-α, with both PKR-p and eIF2α-p being detected (Fig. 3, B to D, lane 7), indicating that RIG-I signaling is not required for PKR activation by ppp-ssRNA either. CIP-treated ssRNA did not produce significant levels of PKR-p, although this RNA led to some increase in eIF2α-p in Huh-7 cells (Fig. 3, B to D, lane 8), which is probably due to residual triphosphate (8). We conclude that ssRNA activates PKR in a 5′-triphosphate–dependent fashion in cells.

The data thus far are consistent with the existence of a "primed" form of cellular PKR, which is induced by IFN-α treatment and required for effective activation of PKR by ppp-ssRNA. This conclusion is based on the observation that PKR activation by 5′-triphosphate ssRNA shows a strict dependency on IFN (Fig. 3, B to D, lanes 3 and 7) whereas PKR activation by dsRNA does not (Fig. 3, B and D, lanes 2 and 6). ppp-ssRNA is more potent than dsRNA in activating PKR in IFN-α–treated Huh-7 cells (Fig. 3B, lanes 6 and 7). Alternatively, it is possible that a higher PKR concentration, which is stimulated by IFN, is required for ppp-ssRNA–mediated activation of PKR.

For ssRNA-110, only a transcript with a 5′-triphosphate was capable of activating PKR intracellularly, and it also showed the greatest potency of activation of eIF2α (Fig. 3E). [The low levels of activation of eIF2α that were present for 5′-hydroxyl and the 7mG cap may be due to residual triphosphate (8).] In agreement with in vitro experiments, activation of PKR by ssRNA-79TS was 5′-triphosphate dependent whereas activation by dsRNA-79 was not (Fig. 3F). Activation by ssRNA-79BS RNA was not 5′-triphosphate–dependent in cells, however; this transcript has a complex secondary structure (fig. S4A), which may facilitate the 5′-triphosphate–independent mode of activation. Indeed, a few RNAs with complex secondary structures are known to activate PKR, including RNA from hepatitis delta virus, the 3′ untranslated region from human alpha-tropomyosin, and various aptamers to PKR's dsRBD (18–20).

The results presented here reveal that ssRNAs with very limited secondary structures have the ability to activate PKR in a 5′-triphosphate–dependent fashion. These activators differ from classical dsRNA activators. In particular, we have found that activation in a cellular context requires just 5 bp of RNA and is IFN-α–dependent but independent of RIG-I signaling (15, 16). There is evidence that a number of ssRNA viruses use non-dsRNA to activate PKR in vivo (21). In particular, influenza virus has a 5′-triphosphorylated single-stranded viral RNA that activates PKR (22) and does not produce detectable levels of dsRNA during replication (16). It is also notable that several virus families have evolved use of a protein primer that bypasses the presence of a triphosphate at the 5′ end of RNA (9), which might represent a mechanism to evade PKR activation. 5′-triphosphate

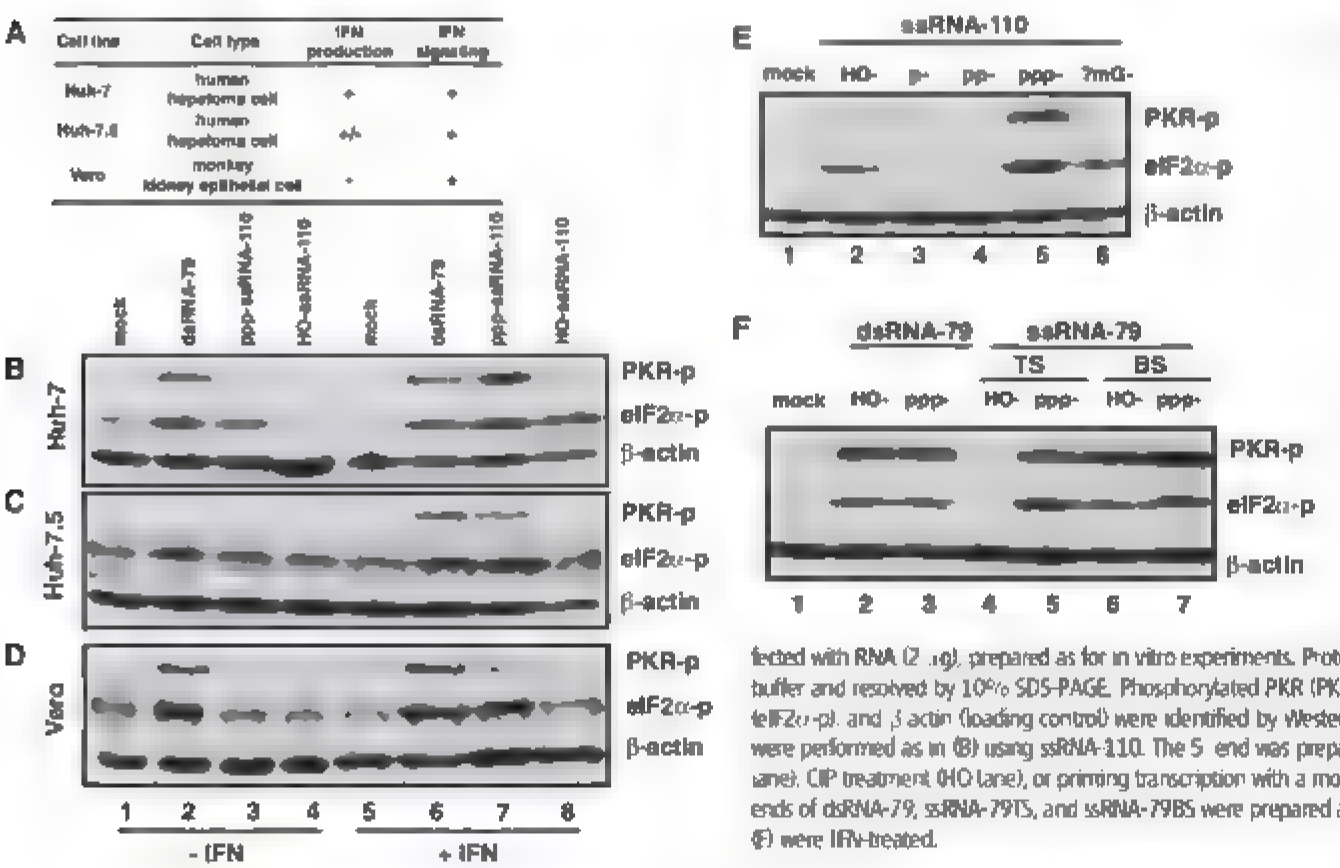

Fig. 3. Activation of PKR by ssRNA is 5′-triphosphate–dependent in vivo. (A) Origin of cell line, capacity to produce IFN-α/β, and capacity to signal from the IFN-α/β receptor are indicated. A block of IFN-α/β production in Huh-7.5 cells is observed only if RIG-I signaling is required (17). The IFN-α/β gene cluster is deleted in Vero cells (23). (B to D) Cells were plated 24 hours before transfection in the absence (lanes 1 to 4) or presence (lanes 5 to 8) of 1000 units of IFN-α per milliliter. Cells were transfected with RNA (2 μg), prepared as for in vitro experiments. Proteins were denatured in SDS buffer and resolved by 10% SDS-PAGE. Phosphorylated PKR (PKR-p), phosphorylated eIF2α (eIF2α-p), and β-actin (loading control) were identified by Western blotting. (E) Experiments were performed as in (B) using ssRNA-110. The 5′ end was prepared by no treatment (ppp-lane), CIP treatment (HO-lane), or priming transcription with a modified guanosine. (F) The 5′ ends of dsRNA-79, ssRNA-79TS, and ssRNA-79BS were prepared as in (E). Samples in (E) and (F) were IFN-treated.

dependent activation of PKR by ssRNA may be a major pathway for sensing and responding to viral infection in vivo.

References and Notes

1. G. R. Stark, I. M. Kerr, B. R. Williams, R. H. Silverman, R. D. Schreiber, *Annu. Rev. Biochem.* **67**, 227 (1998).
2. T. E. Dever, A. C. Dar, F. Sicheri, in *Translational Control in Biology and Medicine*, M. B. Mathews, N. Sonenberg, J. W. Hershey, Eds. (Cold Spring Harbor Laboratory Press, Cold Spring Harbor, NY, 2007), pp. 319–344.
3. B. Tian, P. C. Bevilacqua, A. Diegelman-Parente, M. B. Mathews, *Nat. Rev. Mol. Cell Biol.* **5**, 1013 (2004).
4. L. Manche, S. R. Green, C. Schmedt, M. B. Mathews, *Mol. Cell. Biol.* **12**, 5238 (1992).
5. P. C. Bevilacqua, T. R. Cech, *Biochemistry* **35**, 9983 (1996).
6. X. Zheng, P. C. Bevilacqua, *RNA* **10**, 1934 (2004).
7. J. F. Milligan, D. R. Groebe, G. W. Witherell, O. C. Uhlenbeck, *Nucleic Acids Res.* **15**, 8783 (1987).
8. Materials and methods are available as supporting material on *Science* Online.
9. *Fields Virology*, D. Knipe, P. M. Howley, Eds. (Lippincott Williams & Wilkins, Philadelphia, PA, ed. 5, 2007).
10. C. D. Bieger, D. P. Nierlich, *J. Bacteriol.* **171**, 141 (1989).
11. L. E. Maquat, G. G. Carmichael, *Cell* **104**, 173 (2001).
12. D. H. Kim *et al.*, *Nat. Biotechnol.* **22**, 321 (2004).
13. J. W. Ucci, J. L. Cole, *Biophys. Chem.* **108**, 127 (2004).
14. A. C. Dar, T. E. Dever, F. Sicheri, *Cell* **122**, 887 (2005).
15. V. Hornung *et al.*, *Science* **314**, 994 (2006).
16. A. Pichlmair *et al.*, *Science* **314**, 997 (2006).
17. R. Sumpter Jr. *et al.*, *J. Virol.* **79**, 2689 (2005).
18. H. D. Robertson, L. Manche, M. B. Mathews, *J. Virol.* **70**, 5611 (1996).
19. S. Davis, J. C. Watson, *Proc. Natl. Acad. Sci. U.S.A.* **93**, 508 (1996).
20. P. C. Bevilacqua, C. X. George, C. E. Samuel, T. R. Cech, *Biochemistry* **37**, 6303 (1998).
21. J. O. Langland, J. M. Cameron, M. C. Heck, J. K. Jancovich, B. L. Jacobs, *Virus Res.* **119**, 100 (2006).
22. E. Hatada, S. Saito, R. Fukuda, *J. Virol.* **73**, 2425 (1999).
23. J. M. Emery, M. J. Morgan, *J. Gen. Virol.* **43**, 247 (1979).

24. We thank B. Golden, D. Herschlag, and J. Reese for helpful comments and the following sources for funding: NIH grant GM58709 (P.C.B.) and the Martarano and Berg endowments of the Eberly College of Science (C.E.C.).

Supporting Online Material
www.sciencemag.org/cgi/content/full/318/5855/1455/DC1
Materials and Methods
SOM Text
Figs. S1 to S14
References

3 July 2007; accepted 31 October 2007
10.1126/science.1147347

Direct Observation of Chaperone-Induced Changes in a Protein Folding Pathway

Philipp Bechtluft,[1]* Ruud G. H. van Leeuwen,[2]*† Matthew Tyreman,[2]* Danuta Tomkiewicz,[1] Nico Nouwen,[1]‡ Harald L. Tepper,[2]§ Arnold J. M. Driessen,[1] Sander J. Tans[2]‖

How chaperone interactions affect protein folding pathways is a central problem in biology. With the use of optical tweezers and all-atom molecular dynamics simulations, we studied the effect of chaperone SecB on the folding and unfolding pathways of maltose binding protein (MBP) at the single-molecule level. In the absence of SecB, we find that the MBP polypeptide first collapses into a molten globulelike compacted state and then folds into a stable core structure onto which several α helices are finally wrapped. Interactions with SecB completely prevent stable tertiary contacts in the core structure but have no detectable effect on the folding of the external α helices. It appears that SecB only binds to the extended or molten globulelike structure and retains MBP in this latter state. Thus during MBP translocation, no energy is required to disrupt stable tertiary interactions.

Folding pathways are traditionally studied with isolated proteins, even though the cellular environment often presents interactions with other molecules during the folding process. For instance, interactions with chaperones are often crucial to guide folding, to prevent aggregation, and to facilitate protein translocation across membranes (*1*, *2*). However, how folding pathways are affected by chaperones remains poorly understood. For instance, it is unclear which steps of the folding process are affected by chaperones, whether the protein-chaperone structure is stable and well defined, and whether native or alternative tertiary interactions are formed in the presence of chaperones.

We addressed these questions by using optical tweezers to induce the mechanical unfolding and refolding of a single protein molecule in the absence and the presence of molecular chaperones. Single-molecule techniques can reveal folding transitions, as has been shown for isolated molecules (*3*–*7*), although they cannot directly correlate the transitions with molecular-level changes in protein structure. To obtain structural insights into the chaperone-free folding pathway, we combined all-atom molecular dynamics (MD) simulations with optical tweezers measurements.

We studied the unfolding and folding of *Escherichia coli* maltose binding protein (MBP) and its dependence on the chaperone SecB (*8*, *9*). The interaction between SecB and MBP has been extensively studied by bulk biochemical assays, making it an ideal system for exploration at the single-molecule level. The known physiological effects of SecB are to reduce aggregation (*10*), to promote translocation across membranes (*11*), and to delay formation of the native state (*12*, *13*). SecB binds to hydrophobic peptide regions (*14*, *15*) and does not require a signal sequence for interaction (*16*). Although the structure of MBP in complex with SecB is unknown, it has been suggested that MBP forms tertiary structure elements in the presence of SecB (*17*). Such elements would need to be disrupted during translocation because only an extended chain can pass through the narrow SecYEG channel (*18*).

Individual MBP molecules were tethered between two polystyrene spheres ~2 μm in diameter by using a 2553–base pair DNA molecular spacer to prevent undesired bead-bead interactions (Fig. 1A). Connections to the N- and C-terminal ends of wild-type MBP were obtained via an engineered biotin group and a quadruple c-myc tag, respectively. Purified constructs, here referred to as MBP, retained their ability to bind to an amylose resin, indicating proper folding. The DNA-protein tether was stretched by displacement of the pipette bead, and the resulting force on the second bead trapped in the laser focus was measured. These experiments yielded force-extension curves (Fig. 1B) showing a sudden change in extension at an average applied force of 25 ± 8 (SD) pN. When MBP was replaced with a plain biotinylated c-myc tag, there were no sudden extension changes (fig. S1), showing that they correspond to MBP unfolding events. After the unfolded MBP was relaxed by moving the beads together, it folded back to its native state, as evidenced by a second stretching experiment that yielded a similar curve. This unfold-refold cycle was reproducible several times on a single molecule until a linkage in the tether broke.

Stretching curves of a second construct composed of four tandem MBP repeats (4MBP) reproduced the unfolding at an average force of 23 ± 4 pN (Fig. 2, A and B). As previously reported for atomic force microscopy experiments on proteins with repeated domains (*3*, *6*), a sawtooth pattern was observed, corresponding to the separate unfolding events of the repeats. Interestingly, however, after the force had been lowered to allow refolding, in the second stretching curve the protein often failed to unfold at the normal 25 pN

[1]Department of Molecular Microbiology, Groningen Biomolecular Sciences and Biotechnology Institute and the Zernike Institute for Advanced Materials, University of Groningen, Kerklaan 30, 9751 NN Haren, Netherlands. [2]FOM Institute for Atomic and Molecular Physics (AMOLF), Kruislaan 407, 1098 SJ Amsterdam, Netherlands.

*These authors contributed equally to this work.
†Present address: Philips Research, High Tech Campus 36, 5656 AE Eindhoven, Netherlands.
‡Present address: Laboratoire de Symbioses Tropicales et Méditerranéennes, TA A-82/J, Campus International de Baillarguet, 34398 Montpellier cedex 5, France.
§Present address: McKinsey and Company, Amstel 344, 1017 AS Amsterdam, Netherlands.
‖To whom correspondence should be addressed. E-mail: tans@amolf.nl

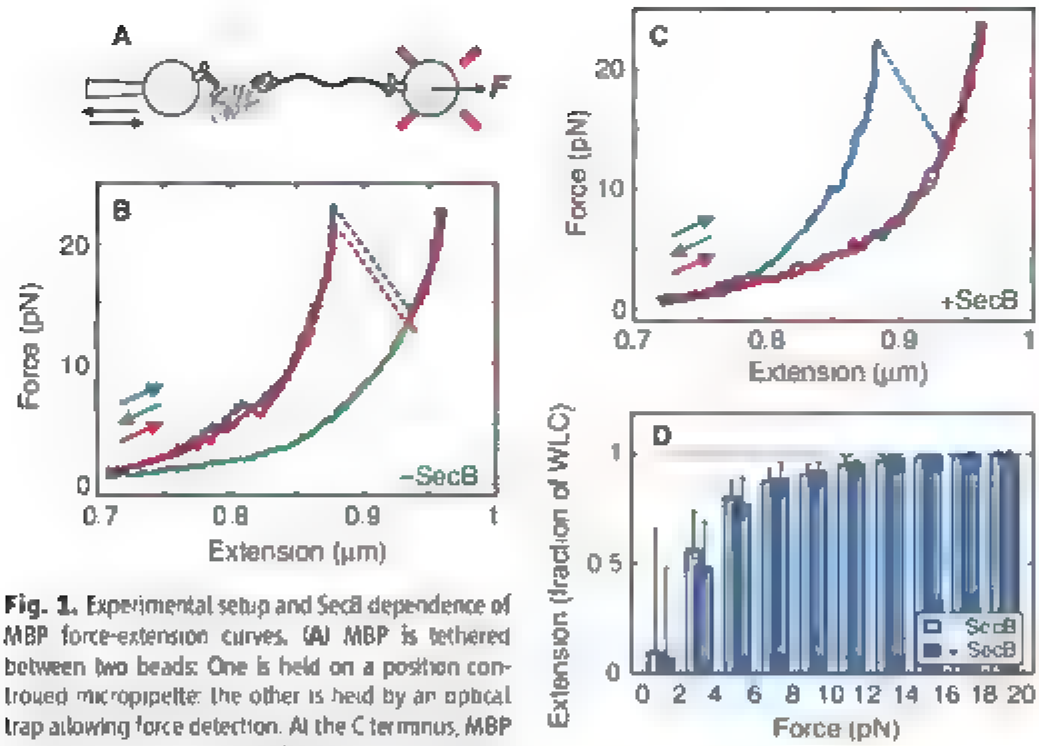

Fig. 1. Experimental setup and SecB dependence of MBP force-extension curves. **(A)** MBP is tethered between two beads: One is held on a position-controlled micropipette; the other is held by an optical trap allowing force detection. At the C terminus, MBP is attached via an antibody-myc-tag connection, whereas at the N terminus it is attached via streptavidin-biotin linkages to a DNA tether, which in turn is attached to the bead surface via an antibody-digoxigenin connection. **(B)** Force-extension curves in the absence of SecB showing unfolding at high force (red), refolding at low forces (green), and again unfolding at high force (blue). **(C)** Force-extension curves in the presence of SecB (0.1 µM). The second stretching curve (red) lacks the typical unfolding features, showing that stable tertiary interactions are absent. **(D)** Comparison between relaxation curves and WLC model. Indicated is the average extension from several curves within a force window, normalized to the extension expected from the WLC model (fig. S2). At higher forces, data and model overlap, whereas a lower value points to additional compaction of the polypeptide. The error bars indicate the standard deviations of the extension from various refolding curves.

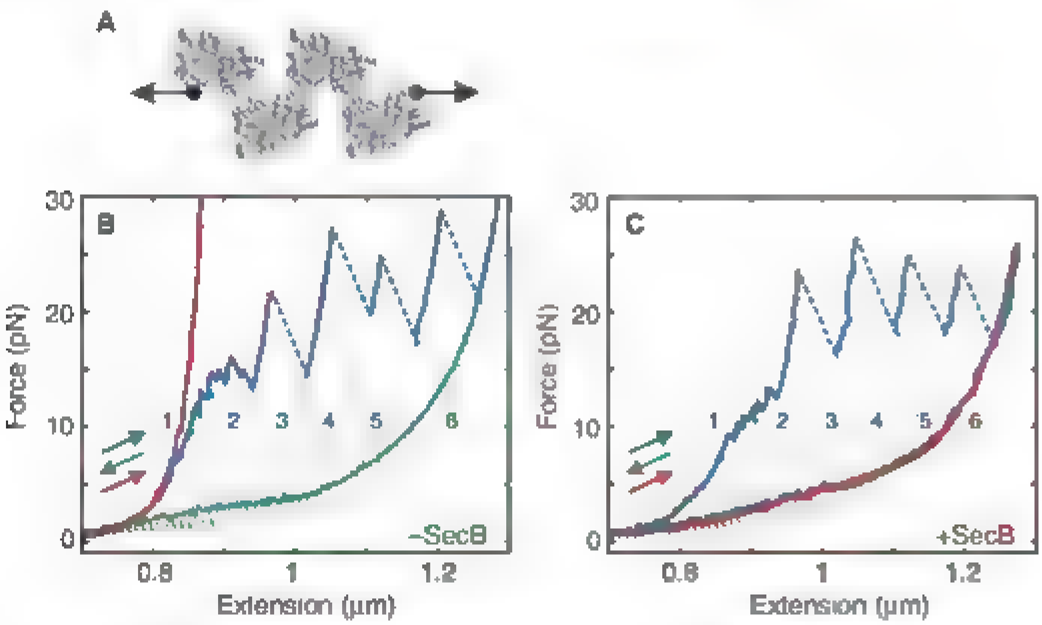

Fig. 2. **(A)** Schematic illustration of the 4MBP construct. **(B)** Force-extension curves in the absence of SecB. Dotted lines represent the theoretical WLC compliance of the DNA-protein construct in various stages of unfolding, as predicted by MD simulations: curve 1, DNA tether alone, representing the native or aggregated MBP state; curve 2, DNA tether plus compliant polypeptide of four times 91 residues, representing four folded MBP cores and their unfolded external α helices; and curve 3, polypeptide length is increased by 279 residues, representing the unfolding of one core structure. For each subsequent curve (4, 5, and 6) the length is increased by one additional unfolded core. After full unfolding (6) and subsequent relaxation to low force, the stretch data (red trace) follow WLC curve 1, indicating 4MBP has misfolded into a tight aggregate. **(C)** Force-extension curves in the presence of SecB (0.1 µM). Aggregation is prevented during relaxation, as evidenced by the low forces required for extending the polypeptide (red trace). The 4MBP results are consistent with the single MBP repeat data.

(Fig. 2B, red trace), instead requiring over 40 pN. Thus, the high local concentration likely promoted aggregation (19) of the MBP repeats to produce a structure more stable than the native state.

Once proper folding behavior was established in the single MBP construct, the chaperone SecB was flowed into the fluidic chamber of the optical tweezers. The first stretching curve (Fig. 1C) is similar to those without chaperone present, exhibiting a comparable average unfolding force of 24 ± 4 pN. SecB thus does not promote unfolding of native MBP, even when it is held under tension. Subsequent stretching curves did not overlap with the first stretching curve but rather followed the relaxation curve and lacked features typical of breaking tertiary interactions. SecB thus only binds fully unfolded MBP and when bound prevents the formation of any stable tertiary interactions in MBP. In addition, the MBP-SecB complex appears to form more rapidly than the fastest folding event (8). Similarly, in the aggregation transition the second stretching curve for 4MBP overlapped with the previous relaxation curve (Fig. 2C), showing that despite their stability, the aggregation interactions cannot form because of interference by SecB.

The force-extension curves show more detailed features, and the challenge is to relate these to structural changes. For example, a gradual extension increase involving several small substeps is observed below 15 pN, before full unfolding at ~25 pN (Figs. 1 and 2). The low- and high-force transitions cannot reflect a separate unfolding of structural domains; the two lobes of MBP (20) cannot unfold independently because the polypeptide runs back and forth between them.

To identify structural changes associated with transitions in the force-extension curves, we used molecular dynamics (MD) to simulate the unfolding of native MBP. When a force was applied on the MBP termini (Fig. 3A and movie S1), a five-residue segment at the N terminus unfolded first, followed by the C-terminal α helix. Continuing such unfolding simulations is problematic, because the increasing protein extension makes the simulation volume computationally intractable. To circumvent this, we deleted unfolded segments and then continued the simulations on the new construct. This method relies on the assumption that unfolded segments remain extended and do not fold back, which is reasonable given the force applied on the termini. The subsequent simulations showed that another four C-terminal α helices located on the exterior of the structure were sequentially unfolded, until in total 91 residues had unfolded and a stable core structure remained (Fig. 3B). Note that the simulations involve pulling at much faster time scales (21) and therefore act as a hypothesis that we will test against the experiments.

The stability of the simulated intermediate core structure implies that it might be observed as a distinct state in the tweezers measurements. The theoretical force-extension relation for this state

based on the worm-like chain (WLC) model (22) indeed overlaps with the data after the low-force unfolding below 15 pN (Fig. 2 and fig. S2), indicating a good agreement between simulated and measured length changes. Also the gradual nature of the low-force extension increases is consistent with the simulated sequential unfolding. The 4MBP data show an increase in length that is four times larger at low force compared with that of native MBP, indicating that all external α helices unfold before the first core unfolding. The length changes of the high-force unfolding events agree with the unfolding of a single 279-residue core, showing that MBP fully unfolds. We note that reported stability-decreasing MBP mutations (23) are all positioned near the N terminus of the predicted core intermediate structure.

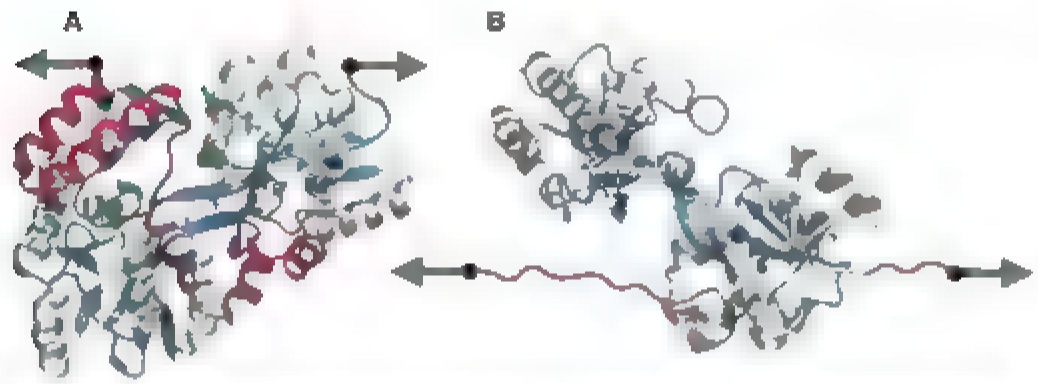

Fig. 3. Results from all-atom MD simulations. (A) MBP native state. After applying a force to the C and N terminus, the red segments sequentially detached until a stable core structure remained (B). Unfolded segments were deleted from the structure to keep the simulation volume computationally tractable.

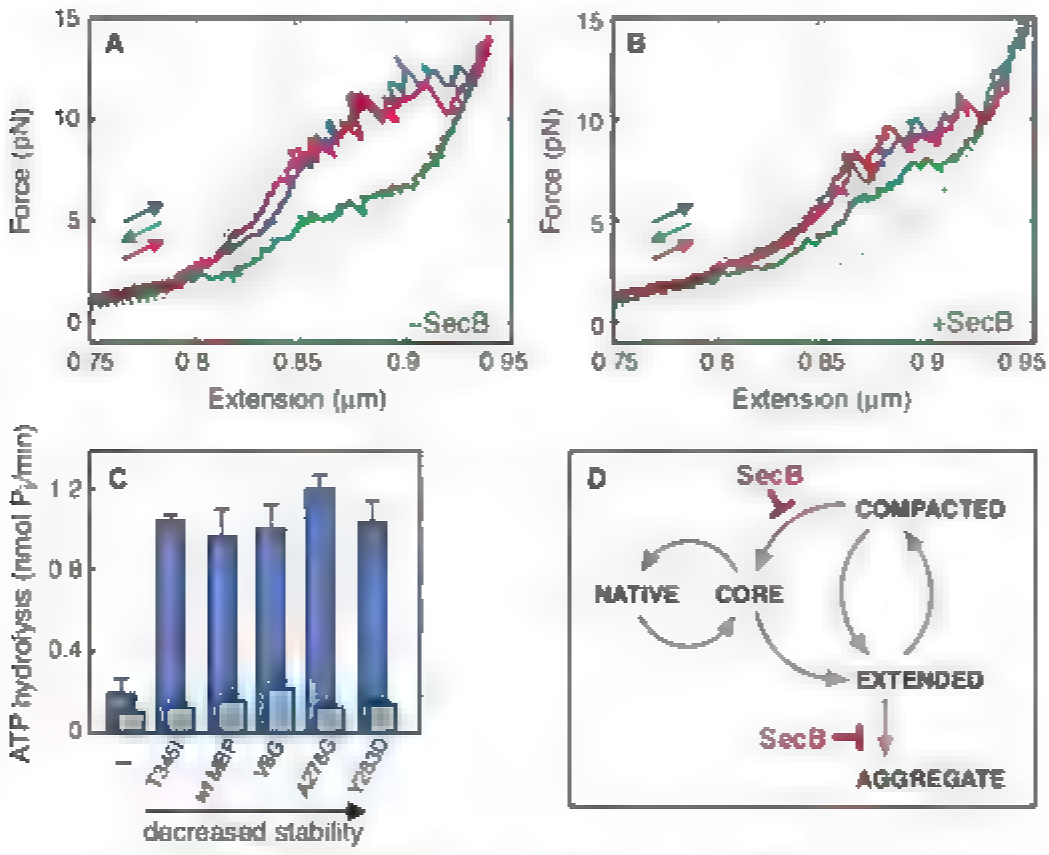

Fig. 4. Low-force unfolding and refolding and translocation assay results. (A) Force-extension curves of 4MBP in absence of SecB. The construct was first stretched, resulting in the predicted gradual unfolding of the external α helices (Fig. 3), and then relaxed before the core structures would unfold. During relaxation the near-equilibrium refolding of the same α helices was observed directly as a shortening of the tether. The dotted lines indicate the WLC behavior: The first denotes the DNA alone, whereas in the second a 4x91 residue-compliant polypeptide was added, representing the unfolded external α helices (also fig. S2). (B) Force-extension curves of 4MBP in presence of SecB (0.1 μM). The SecB interactions do not alter this refolding transition. (C) ATPase activity during translocation of MBP stability mutants. Folding stability in kcal/mol is, respectively: 11.2 [Thr^{345}→Ile^{345} (T345I)], 10.5 (wild type), 9.4 [Val^{8}→Gly^{8} (V8G)], 9 [Ala^{276}→Gly^{276} (A276G)], and 7.3 [Tyr^{283}→Asp^{283} (Y283D)]. All mutants exhibited a similar energy requirement for SecB-mediated translocation (dark blue). The preMBP translocation kinetics was similar in the presence of SecB. Controls without SecB (light blue) or MBP showed low ATPase activity and translocation as expected. The error bars indicate the standard deviations. (D) Force-induced MBP folding and unfolding transitions observed in the experiments and their dependence on SecB.

The sequential detachment of the external α helices suggests that the reverse folding process, in which they would zip back onto the core surface, might be directly observable in the force-extension experiments. We tested this idea by stopping the stretch experiment after the low-force unfolding and then bringing the beads together again. A gradual refolding of the external α helices was indeed detected directly as a near-equilibrium process, as evidenced by the shortening of the tether at nonzero loads (Fig. 4A). The native state was recovered after relaxation, as seen by the characteristic unfolding features in the subsequent stretching curve. Note that after full unfolding (Figs. 1 and 2) one does not directly observe refolding of the core nor of the external α helices during relaxation, which is consistent with the proposed folding pathway in which the slowly folding core structure must form first.

The external α helices refolded with similar dynamics in the presence of SecB (Fig. 4B). SecB apparently does not affect this transition, despite the existence of a putative SecB binding site on the unfolded external α helices, as identified in peptide binding assays (14). These results may indicate that this refolding transition occurs faster than SecB binding. Alternatively, SecB may only bind sites buried within the core structure (15) and not efficiently bind the putative binding site on the external α helices, possibly because of the nearby bulky core.

In the experiments without SecB, when the polypeptide is relaxed after being fully unfolded (Fig. 1B), the measured extension increasingly deviates from the WLC behavior showing lengths that are over two times smaller at the lowest forces (fig. S2 and Fig. 1D). This compaction of the polypeptide is consistent with previous bulk studies indicating an MBP molten globulelike state (23, 24), a compacted form that is held together by unstable tertiary and secondary intramolecular interactions. When such a relaxation experiment was rapidly followed by a second stretching experiment, the two resulting curves overlapped (fig. S3), which indicates that the transition is near equilibrium and that the tertiary interactions are unstable.

The curve shape for relaxation to low forces is similar in the presence of SecB (Fig. 1, C and D), showing that protein-SecB interactions do not result in an additional compaction. The MBP-SecB complex has been shown to have a strict 1:1 stoichiometry (25) and likely involves multiple contacts (26). One might therefore anticipate that their rupturing during stretching would also show up as sudden extension changes. The lack of such features suggests that MBP-SecB con-

facts are not stable or alternatively that binding occurs effectively at a single MBP site.

Next, we followed the transition from the compacted molten globulelike state to the natively folded state. Considering this transition as a single-barrier process, the probability to fold within a waiting time t is $P(t) = 1 - e^{-kt}$, where k is the folding rate. This probability can be estimated by performing multiple stretch-relaxation cycles, in which the polypeptide is allowed to refold at zero load in the waiting time between the relaxation and the stretching curve. Whether folding had occurred was determined from the unfolding features during the subsequent stretching. We obtained a folding rate of $0.76 \pm 0.19\ s^{-1}$ in the absence of SecB (fig. S4). This value is similar to MBP folding rates found in bulk (*23, 24*), which is consistent with the idea that it is the slowest folding step. We could not quantify the refolding rate in the presence of SecB because this required waiting times in the order of minutes. It is clear, however, that SecB-MBP interactions maintain MBP in the molten globulelike compacted state by perturbing the formation of stable tertiary interactions.

The single-molecule results have a direct implication for MBP translocation across the cellular membrane. Whether stable tertiary interactions are actively disrupted by the translocation machinery is a matter of debate (*17, 27*). Our data suggest that SecB efficiently prevents any stable tertiary interactions in MBP. To test this prediction in a translocation reaction, we measured the adenosine triphosphatase (ATPase) activity during the translocation of MBP mutants with altered folding stability (*17, 23*). We indeed found that all mutants displayed ATPase activity similar to that of wild-type preMBP (precursor form of MBP with the signal sequence) (Fig. 4C). Control experiments lacking MBP or SecB showed low ATPase activity as expected. These results support our hypothesis that for SecB-mediated translocation only limited energy is required to disrupt SecB-MBP interactions as well as tertiary intramolecular interactions in MBP. The single-molecule data provide an estimate for this energy requirement of ~$25k_BT$ (fig. S2), which roughly corresponds to the hydrolysis of one ATP molecule.

Taken together, the data indicate a folding pathway with a large variety of transitions and modes of folding (Fig. 4D), which are each affected differently by SecB: (i) The extended peptide is compacted to a molten globule state in either the presence or the absence of SecB. (ii) In the absence of SecB, folding proceeds from the molten globule to a core intermediate, but SecB prevents the formation of stable tertiary interactions, thereby maintaining the molten globulelike state. This effect may well be more general and apply also to other chaperones such as GroEL, for which there is support from other studies (*28, 29*). (iii) Once the core intermediate has formed, SecB cannot bind, and it therefore has no effect on the folding of the external α helices onto the surface of the core structure. Folding from the core to the fully folded state exhibits similarities with a nucleation-growth mode of folding (*30, 31*) and contrasts with the complex conformational search in the molten globulelike phase that characterizes the folding of the core. (iv) SecB also prevents the stable aggregation interactions that occur at high local MBP concentrations.

The results provide an important first step in understanding how a protein folding landscape is altered by contacts with a secondary protein. The approach is general and can be applied to interrogate other proteins and chaperone systems.

References and Notes

1. F. U. Hartl, M. Hayer-Hartl, *Science* **295**, 1852 (2002).
2. C. M. Dobson, *Nature* **426**, 884 (2003).
3. M. Rief, J. Pascual, M. Saraste, H. E. Gaub, *J. Mol. Biol.* **286**, 553 (1999).
4. R. B. Best, B. Li, A. Steward, V. Daggett, J. Clarke, *Biophys. J.* **81**, 2344 (2001).
5. A. F. Oberhauser, C. Badilla-Fernandez, M. Carrion-Vazquez, J. M. Fernandez, *J. Mol. Biol.* **319**, 433 (2002).
6. I. E. Fisher, P. E. Marszalek, J. M. Fernandez, *Nat. Struct. Biol.* **7**, 719 (2000).
7. C. Cecconi, E. A. Shank, C. Bustamante, S. Marqusee, *Science* **309**, 2057 (2005).
8. P. Fekkes, A. J. M. Driessen, *Microbiol. Mol. Biol. Rev.* **63**, 161 (1999).
9. Z. Xu, J. D. Knafels, K. Yoshino, *Nat. Struct. Biol.* **7**, 1172 (2000).
10. S. H. Lecker, A. J. M. Driessen, W. Wickner, *EMBO J.* **9**, 2309 (1990).
11. F. U. Hartl, S. Lecker, E. Schiebel, J. P. Hendrick, W. Wickner, *Cell* **63**, 269 (1990).
12. D. N. Collier, V. A. Bankaitis, J. B. Weiss, P. J. Bassford, *Cell* **53**, 273 (1988).
13. S. J. Hardy, L. L. Randall, *Science* **251**, 439 (1991).
14. N. F. M. Knoblauch *et al.*, *J. Biol. Chem.* **274**, 34219 [illegible]
15. T. B. Topping, L. L. Randall, *Protein Sci.* **3**, 730 (1994).
16. L. L. Randall, T. B. Topping, S. J. Hardy, *Science* **248**, 860 (1990).
17. H. de Cock, L. L. Randall, *Mol. Microbiol.* **27**, 469 (1998).
18. B. van den Berg *et al.*, *Nature* **427**, 36 (2004).
19. A. F. Oberhauser, P. E. Marszalek, M. Carrion-Vazquez, J. M. Fernandez, *Nat. Struct. Biol.* **6**, 1025 (1999).
20. X. Duan, J. A. Hall, H. Nikaido, F. A. Quiocho, *J. Mol. Biol.* **306**, 1115 (2001).
21. Materials and methods are available on *Science* Online.
22. J. F. Marko, E. D. Siggia, *Macromolecules* **28**, 8759 (1995).
23. S. Y. Chun, S. Strobel, P. Bassford, L. L. Randall, *J. Biol. Chem.* **268**, 20855 (1993).
24. K. Beena, J. B. Udgaonkar, R. Varadarajan, *Biochemistry* **43**, 3608 (2004).
25. P. Fekkes, C. van der Does, A. J. M. Driessen, *EMBO J.* **16**, 6105 (1997).
26. J. M. Crane *et al.*, *J. Mol. Biol.* **363**, 63 (2006).
27. G. P. Liu, T. B. Topping, W. H. Cover, L. L. Randall, *J. Biol. Chem.* **263**, 14790 (1988).
28. R. Horst *et al.*, *Proc. Natl. Acad. Sci. U.S.A.* **102**, 12748 (2005).
29. G. Stan, G. H. Lorimer, D. Thirumalai, B. R. Brooks, *Proc. Natl. Acad. Sci. U.S.A.* **104**, 8803 (2007).
30. A. R. Fersht, V. Daggett, *Cell* **108**, 573 (2002).
31. A. R. Fersht, *Curr. Opin. Struct. Biol.* **7**, 3 (1997).

32. We thank P. R. ten Wolde, C. Tischer, and M. Dogterom for critical reading of the manuscript; S. Tănase-Nicola for discussions; and D. Rozeveld for technical assistance. This work was funded by the European Community Biomach program, NanoNed, a national nanotechnology program coordinated by the Dutch Ministry of Economic Affairs, and the Organization for Fundamental Research on Matter (FOM) and the Foundation for Life Sciences (ALW), which are both financially supported by the Netherlands Organization for Scientific Research (NWO). H.L.T. was supported by a VENI grant from NWO.

Supporting Online Material

www.sciencemag.org/cgi/content/full/318/5855/1458/DC1
Materials and Methods
Figs. S1 to S4
References

11 May 2007; accepted 17 October 2007
10.1126/science.1144977

Carbon Dioxide Activation at the Ni,Fe-Cluster of Anaerobic Carbon Monoxide Dehydrogenase

Jae-Hun Jeoung and Holger Dobbek*

Anaerobic CO dehydrogenases catalyze the reversible oxidation of CO to CO_2 at a complex Ni-, Fe-, and S-containing metal center called cluster C. We report crystal structures of CO dehydrogenase II from *Carboxydothermus hydrogenoformans* in three different states. In a reduced state, exogenous CO_2 supplied in solution is bound and reductively activated by cluster C. In the intermediate structure, CO_2 acts as a bridging ligand between Ni and the asymmetrically coordinated Fe, where it completes the square-planar coordination of the Ni ion. It replaces a water/hydroxo ligand bound to the Fe ion in the other two states. The structures define the mechanism of CO oxidation and CO_2 reduction at the Ni-Fe site of cluster C.

The biological redox transformations of CO_2, N_2, and H_2 are essential processes in global biogeochemical cycles and are catalyzed by enzymes containing complex metal clusters based on iron and sulfur whose detailed function is still poorly understood (*1, 2*). Carbon monoxide dehydrogenases (CODHases) are the biological catalysts for the reversible oxidation of CO to CO_2, with water as the source of oxygen: $CO + H_2O \rightleftharpoons CO_2 + 2e^- + 2H^+$ (Eq. 1). Two principal types of CODHases have been described that differ in their cofactor composition, structure, and stability in the presence of dioxygen. Anaerobic bacteria and archaea use oxygen-sensitive Ni- and Fe-containing CODHases, whereas aerobic, carboxydotrophic bacteria use a Cu-, Mo-, and Fe-containing flavoenzyme (*3*). The Ni,Fe-CODHases are monofunctional or bifunctional enzymes associated with Ni,Fe-containing acetyl–coenzyme A (CoA) synthases (ACS) (*4, 5*) [for review, see (*3, 6*)].

CO oxidation and CO_2 reduction at the active site, cluster C, of Ni,Fe-CODHases are proposed to require three different oxidation states differing by one electron (C_{red1}, C_{int}, and C_{red2}) (6). In this model, the C_{red1} state of cluster C converts CO to CO_2 and is formed at redox potentials below −200 mV (7). At pH = 7.0, the midpoint potential for the conversion of C_{red1} to C_{red2} is −530 mV (8, 9), similar to the normal potential of the CO_2-CO couple of −558 mV (10). Consequently, C_{red2} is generated by a two-electron reduction of the C_{red1} state via C_{int} (11). The structure of cluster C was revealed by crystallographic analysis of CODHases isolated from *Carboxydothermus hydrogenoformans* ($CODHII_{Ch}$) and *Rhodospirillum rubrum* ($CODH_{Rr}$) at 1.6 and 2.8 Å resolution, respectively (12, 13). Cluster C in $CODHII_{Ch}$ has been described as an asymmetric $[NiFe_4S_5]$ center, which comprises an integral Ni ion coordinated by four sulfur ligands with square-planar geometry (12). An asymmetrically coordinated Fe ion (Fe1) is found close to the Ni ion. In CO-treated $CODH_{Rr}$, cluster C has a similar structure with a cubane $[NiFe_3S_4]$ center linked to a mononuclear Fe site (13). Corresponding structures of cluster C were also identified in the crystal structures of bifunctional ACS/CODH isolated from *Moorella thermoacetica* ($CODH_{Mt}$) (4, 5). Mechanisms proposed for the reversible oxidation of CO to CO_2 posit the activation of H_2O and CO as well as the stabilization of a metal-bound COO(H) intermediate. However, the structure of these states remained elusive. We describe how H_2O and CO_2 are bound and activated and propose a structure-based model for CO oxidation and CO_2 reduction at the Ni-Fe1 site of cluster C.

An expression system for $CODHII_{Ch}$ established in *Escherichia coli* enables a one-step purification of active enzyme. Crystals of recombinant $CODHII_{Ch}$ diffract up to 1.40 Å resolution on a rotating anode x-ray generator (table S1). The overall structure of recombinant $CODHII_{Ch}$ is identical to the structure of native $CODHII_{Ch}$ (12). $CODHII_{Ch}$ crystals were held at a defined redox potential of −600 mV for 3 hours with use of Ti(III) citrate. These crystals were either directly frozen in liquid nitrogen, generating the −600 mV state; oxidized via incubation with methylviologen (MV_{ox}) and dithiothreitol (DTT) and then incubated with DTT to give the −320 mV state; or incubated in the −600 mV solution with $NaHCO_3$ as the CO_2 source, generating the −600 mV+CO_2 state. The −600 mV state (equivalent in its redox potential to the C_{red2} state) and the −320 mV state (equivalent to the C_{red1} state) display practically identical structures for cluster C (Fig. 1, A and C). In both structures, the Ni ion is coordinated by three sulfur ligands with distorted T-shaped coordination geometry (Fig. 1, A and C, and table S3). Fe1 is coordinated by His[261] (H261), Cys[295] (C295), a μ_3-sulfido ligand, and a monoatomic ligand (Fig. 1, A and C, and figs. S2 and S4). A weakly occupied alternative position for Fe1 (Fe1B) is observed in both states (Fig. 1 and table S2). The monoatomic ligand is a distance of 2.7 Å from the Ni ion and occupies the position that would complete the square-planar coordination of the Ni. The electron density of the ligand can be modeled as a light atom (C, N, or O) with occupancies of about 60 to 70% or a sulfur atom with 30% occupancy. The observed Fe-ligand bond lengths of 1.93 to 1.95 Å are atypical for Fe-S bonds, whereas a H_2O/OH^- ligand is consistent with the refined bond length, the relative occupancies of ligand and Fe1 (table S2), and spectroscopic investigations of the C_{red1} state. The long distance between Ni and the ligand suggests a weak Ni-OH_x interaction. A H_2O/OH^- ligand has been detected bound to a high-spin Fe^{2+} ion called ferrous component II (FCII) in the C_{red1} state (14, 15), so the crystal structure is consistent with Fe1 in the −320 mV state being FCII.

In the presence of appropriate reducing agents, Ni,Fe-CODHases can catalyze the reduction of CO_2 (16). The structure of $CODHII_{Ch}$ with CO_2 (−600 mV+CO_2 state) reveals a triatomic ligand bridging Ni and Fe1, which replaces the water/hydroxo ligand at Fe1 (Fig. 1B). Modeling the ligand as CO_2 fully satisfies the observed electron density maps, whereas modeling with one or two

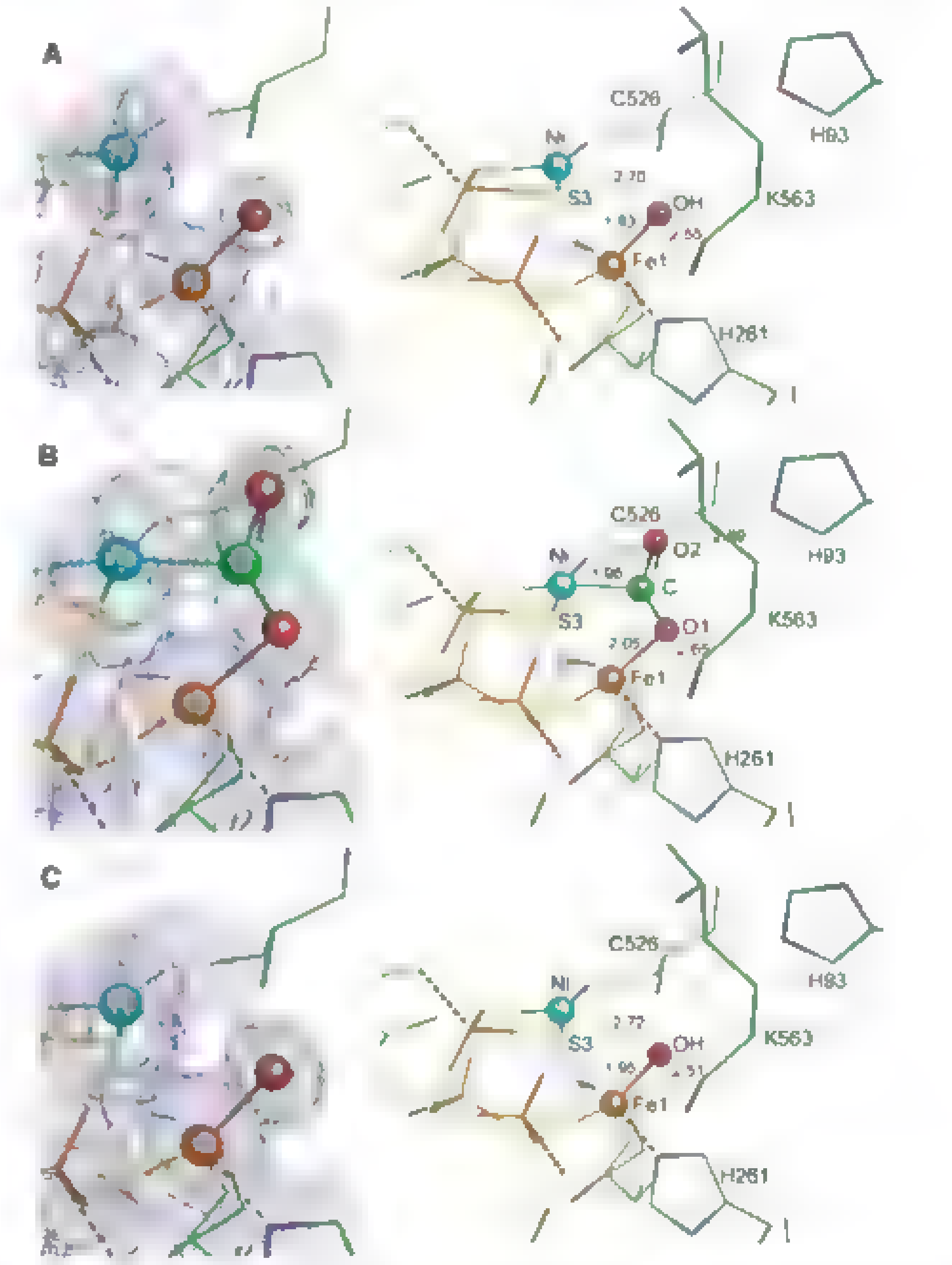

Fig. 1. The −600 mV (**A**), −600 mV+CO_2 (**B**) and −320 mV (**C**) states of cluster C. $2F_{obs} - F_{calc}$ maps in blue are contoured at 1σ, and $F_{obs} - F_{calc}$ maps in green are contoured at 4.5σ. For the calculation of the $F_{obs} - F_{calc}$ map, the OH_x ligand (A) and (C) and the CO_2 ligand (B) have been removed from the model. An alternative position found for Fe1, termed Fe1B, is depicted in transparent light gray. The occupancies for the alternative position have been estimated to 10 to 30%. Selected distances are shown in A. For more details on the geometry of the three states, see figs. S2 to S4. All pictures were prepared by using PyMol (23).

Laboratorium Proteinkristallographie and Forschungszentrum für Bio-Makromoleküle, Universität Bayreuth, D-95440 Bayreuth, Germany.

*To whom correspondence should be addressed. E-mail: holger.dobbek@uni-bayreuth.de

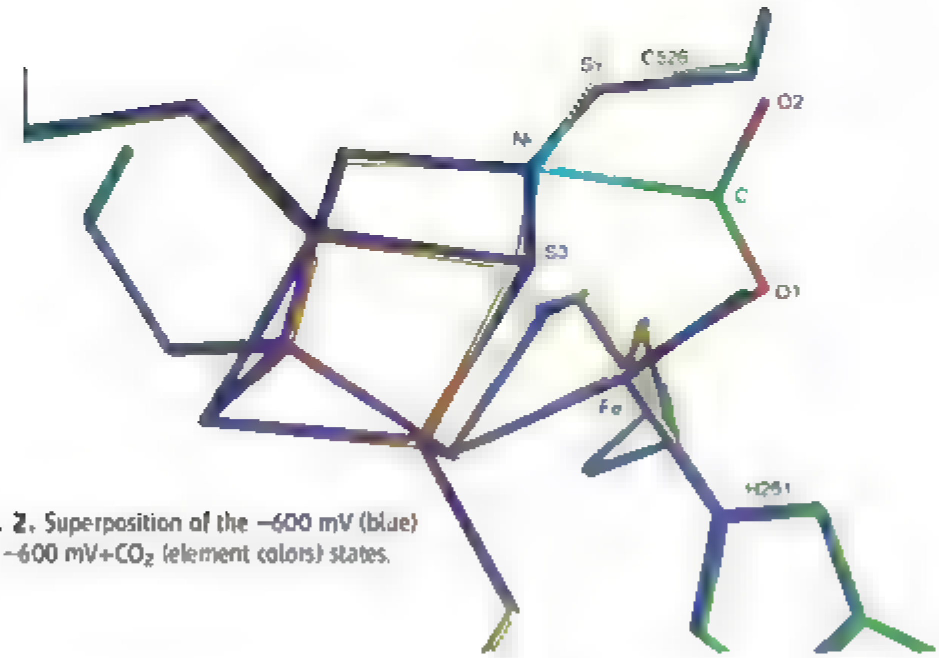

Fig. 2. Superposition of the −600 mV (blue) and −600 mV+CO_2 (element colors) states.

atoms does not. CO_2 bound to cluster C acts as a η^1 OCO ligand at Ni^{2+} with a Ni-C distance of 1.96 Å and completes the square-planar coordination geometry typically found for Ni^{2+} ions. CO_2 acts as a η^1 OCO ligand at Fe1 with an Fe1-O1 distance of 2.05 Å, resulting in a μ_2-η^2 binding mode of CO_2 bridging the Ni-Fe1 site (Fig. 1B). Like the H_2O/OH^- ligand in the −600 mV and −320 mV states, O1 of CO_2 is in hydrogen-bonding distance to Lys[563] (K563) (Fig. 1B). O2 is in hydrogen-bonding distance to His[93]. CO_2 binding to cluster C causes only minor changes in the geometry of the cluster (Fig. 2). The change of the distorted T-shaped to the square-planar coordination at the Ni ion induces a small shift in the Ni position of about 0.2 Å and widens the Cys[526]S1-Ni-S_3 angle (table S3).

The ability of CO_2 to coordinate transition metal complexes is well documented (17). Coordination of CO_2 at the carbon atom results in a net electron transfer from the metal into the anti-

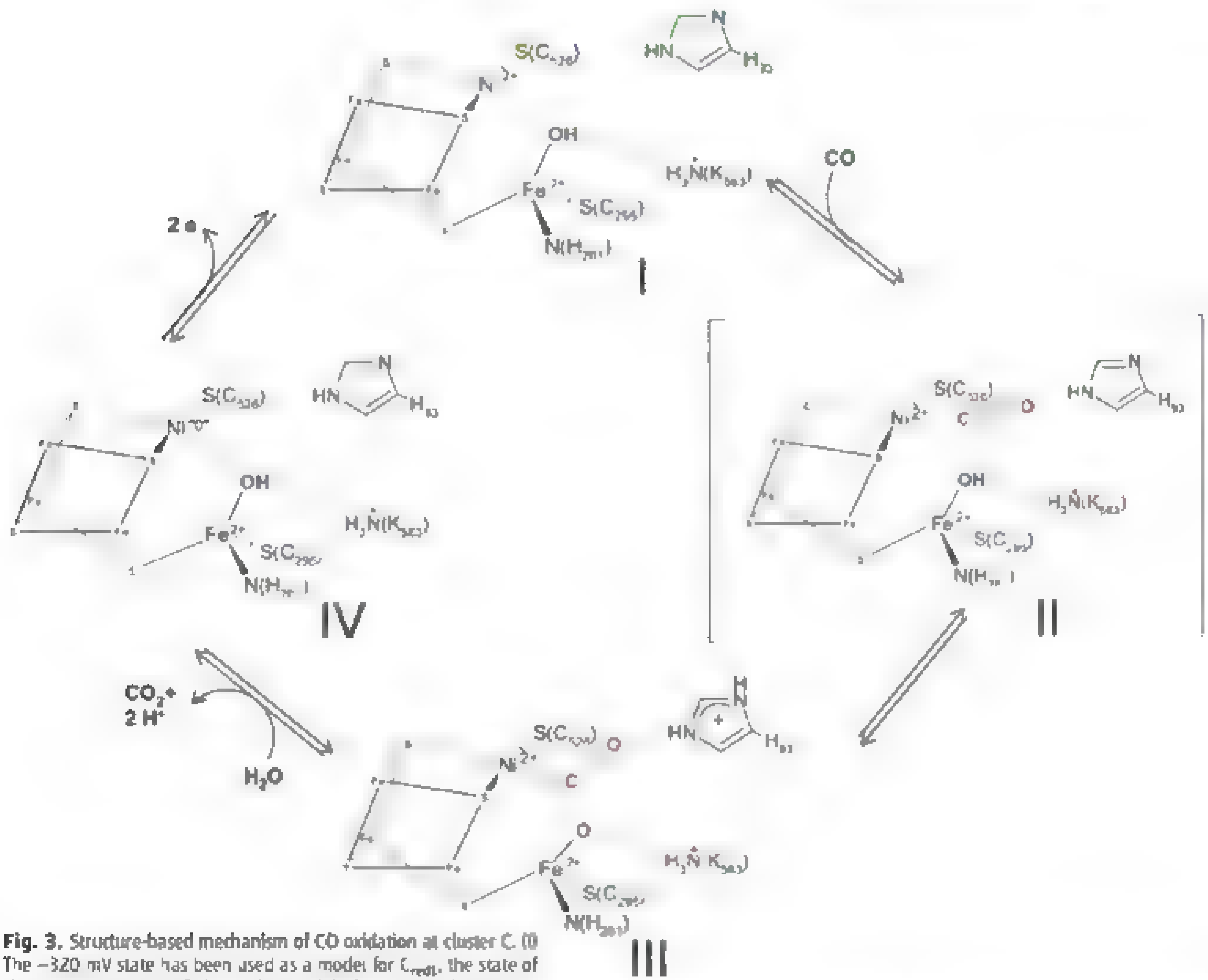

Fig. 3. Structure-based mechanism of CO oxidation at cluster C. (I) The −320 mV state has been used as a model for C_{red1}, the state of cluster C competent of CO oxidation. (II) The proposed transition state of the reaction in which CO binds to the Ni^{2+} ion and reacts with the Fe1 bound OH group. (III) The −600 mV+CO_2 state is used as a model for the stabilization of the metal carboxylate state. (IV) The −600 mV state is used as a model for the C_{red2} state, which is supposed to contain two additional electrons compared with the C_{red1} state, denoted as a formal change of the oxidation state of the Ni^{2+} ion.

bonding lowest unoccupied molecular orbital of CO_2. This activation of CO_2 increases the negative partial charges at the oxygen atoms, which are stabilized by binding to electron-deficient centers like transition metals or by forming hydrogen bonds (*17*). In the cluster C-CO_2 complex, Ni acts as the Lewis base, and Fe1 is the Lewis acid that together with K563 stabilizes the negative partial charge on O1. The deviation from linearity along the O-C-O axis [O-C-O ~133° (table S3)] is in agreement with the activation of CO_2 by binding to cluster C.

In previous structural characterizations of native preparations of $CODHII_{Ch}$, we identified a μ-sulfido ligand (S2) bridging Ni and Fe1 (*12*, *18*). The enzyme used for crystallization as well as dissolved crystals had high specific activities of ~14 000 units mg^{-1}, and on the basis of a positive correlation between the presence of the S2 ligand and enzyme activity it was postulated that S2 is essential for the catalytic CO oxidation (*18*, *19*). However, the necessity of the S2 ligand for catalysis was debated when sulfide was shown to reversibly inactivate $CODH_{Rr}$ and $CODH_{Mt}$, leading to short lag phases (*20*), and no S2 ligands were identified in the crystal structures of $CODH_{Rr}$ and $CODH_{Mt}$ (*5*, *13*). Here, we describe the structures of $[NiFe_4S_4(OH_x)(CO_2)]$ clusters without S2 ligand in crystals with high specific CO oxidation activities (11,000 to 13,500 units mg^{-1}), showing that the presence of S2 is not necessary for catalysis. Furthermore, the S2 ligand occupies the binding site of two substrates of Ni,Fe-CODHases, water, and CO_2. The H_2O/OH^- ligand identified requires the same coordination site at Fe1 as the bridging S2 ligand (fig. S5), and CO_2 binds to the two open coordination sites of Ni and Fe1. Thus, we suggest that the S2 ligand between Ni and Fe1 is absent in catalytically competent enzyme species and can be reductively or chemically replaced, activating the enzyme.

The three presented structures offer direct insight into the reaction mechanism (Fig. 3). The $[NiFe_4S_4OH_x]$ cluster determined in the −320 mV state is the functional state that activates CO and contains the H_2O/OH^- ligand. The Ni^{2+} ion is positioned at the end of the substrate channel, and its three sulfido ligands act as π donors to the metal, enabling CO to bind to the Ni^{2+} ion (*21*). The Ni^{2+} ion has two open coordination sites, allowing either an apical binding of CO to form a distorted tetrahedral geometry or CO binding equatorially to complete the square-planar coordination geometry. Binding of CO in the apical position has been proposed for CO-treated crystals of $CODH_{Rr}$ and $CODH_{Mt}$ (*5*, *13*). Modeling of CO in the apical position places the CO-carbon atom more than 3.5 Å apart from the H_2O/OH^- ligand and makes further rearrangements necessary for the reaction to proceed. In contrast, CO binding to complete a distorted square-planar coordination of the Ni^{2+} ion results in a OC–OH_x distance of less than 2 Å (Fig. 3, step II). The binding of CO to a weakly backdonating metal like Ni^{2+} results in an electrophilic carbon atom and facilitates its reaction with the Fe1-bound H_2O/OH^- ligand to a metal-carboxylate species as observed in the −600 mV+CO_2 state (Figs. 1B and 3, step III). Product release may be assisted by the reversible ligand exchange of CO_2 against H_2O at Fe1 and is accompanied by a two-electron reduction of cluster C, generating the C_{red2} state. The H_2O/OH^- ligand can be replenished by a neighboring network of solvent molecules (fig. S6). A comparison of the $[NiFe_4S_4OH_x]$ and $[NiFe_4S_4(CO_2)]$ states reveals the positions of Ni and Fe1 to be largely unaffected by the presence or absence of the CO_2 ligand (Fig. 2). The $[Fe_3S_4]$ site of cluster C provides a solid metal-sulfur frame in which Ni and Fe1 are held in place and serves as an electronic buffer to compensate for the electronic changes at Ni and Fe1 during the catalytic cycle. The small structural changes of cluster C agree well with the low reorganization energy expected for a reaction with turnover rates of 31,000 s^{-1} and a ratio of k_{cat} (catalytic rate constant)/K_m (Michaelis constant) of 1.7×10^9 $M^{-1} s^{-1}$ at 70°C (*22*).

The structure-based mechanism outlined agrees in all central aspects with the bimetallic mechanism proposed on the basis of electron paramagnetic resonance (EPR), electron nuclear double-resonance (ENDOR), and Mössbauer spectroscopy (*14*, *15*).

References and Notes

1. D. C. Rees, *Annu. Rev. Biochem.* **71**, 221 (2002).
2. D. C. Rees, J. B. Howard, *Science* **300**, 929 (2003).
3. S. W. Ragsdale, *Crit. Rev. Biochem. Mol. Biol.* **39**, 165 (2004).
4. T. I. Doukov, T. M. Iverson, J. Seravalli, S. W. Ragsdale, C. L. Drennan, *Science* **298**, 567 (2002).
5. C. Darnault *et al.*, *Nat. Struct. Biol.* **10**, 271 (2003).
6. P. A. Lindahl, *Biochemistry* **41**, 2097 (2002).
7. J. Feng, P. A. Lindahl, *Biochemistry* **43**, 1552 (2004).
8. P. A. Lindahl, E. Münck, S. W. Ragsdale, *J. Biol. Chem.* **265**, 3873 (1990).
9. P. A. Lindahl, S. W. Ragsdale, E. Münck, *J. Biol. Chem.* **265**, 3880 (1990).
10. D. A. Grahame, E. DeMoll, *Biochemistry* **34**, 4617 (1995).
11. D. M. Fraser, P. A. Lindahl, *Biochemistry* **38**, 15706 (1999).
12. H. Dobbek, V. Svetlitchnyi, L. Gremer, R. Huber, O. Meyer, *Science* **293**, 1281 (2001).
13. C. L. Drennan, J. Heo, M. D. Sintchak, E. Schreiter, P. W. Ludden, *Proc. Natl. Acad. Sci. U.S.A.* **98**, 11973 (2001).
14. Z. Hu *et al.*, *J. Am. Chem. Soc.* **118**, 830 (1996).
15. V. J. DeRose, J. Telser, M. E. Anderson, P. A. Lindahl, B. M. Hoffman, *J. Am. Chem. Soc.* **120**, 8767 (1998).
16. S. A. Ensign, *Biochemistry* **34**, 5372 (1995).
17. W. Leitner, *Coord. Chem. Rev.* **153**, 257 (1996).
18. H. Dobbek, V. Svetlitchnyi, J. Liss, O. Meyer, *J. Am. Chem. Soc.* **126**, 5382 (2004).
19. S. W. Ha *et al.*, *J. Biol. Chem.* **282**, 10639 (2007).
20. J. Feng, P. A. Lindahl, *J. Am. Chem. Soc.* **126**, 9094 (2004).
21. S. A. Macgregor, Z. Lu, O. Eisenstein, R. H. Crabtree, *Inorg. Chem.* **33**, 3616 (1994).
22. V. Svetlitchnyi, C. Peschel, G. Acker, O. Meyer, *J. Bacteriol.* **183**, 5134 (2001).
23. PyMol, W. L. DeLano, DeLano Scientific, San Carlos, CA.

24. We thank W. Buckel and O. Einsle for critical reading of the manuscript and acknowledge the Deutsche Forschungsgemeinschaft (DFG grant DO 785/1) and the Fonds der chemischen Industrie (FCI) for funding. V. Svetlitchnyi is acknowledged for providing *C. hydrogenoformans* Z-2901 (strain DSM 6008) for genomic DNA preparation. Coordinates and structure factors have been deposited in the Protein Data Bank (www.pdb.org) as entries 3B51 (−600 mV state), 3B52 (−600 mV+CO_2 state), and 3B53 (−320 mV state).

Supporting Online Material
www.sciencemag.org/cgi/content/full/318/5855/1461/DC1
Materials and Methods
SOM Text
Figs. S1 to S6
Tables S1 and S2
References

30 July 2007; accepted 31 October 2007
10.1126/science.1148481

Solvent Tuning of Electrochemical Potentials in the Active Sites of HiPIP Versus Ferredoxin

Abhishek Dey,[1] Francis E. Jenney Jr.,[2] Michael W. W. Adams,[2] Elena Babini,[3] Yasuhiro Takahashi,[4] Kenichi Fukuyama,[4] Keith O. Hodgson,[1,5]* Britt Hedman,[5]* Edward I. Solomon[1,5]*

A persistent puzzle in the field of biological electron transfer is the conserved iron-sulfur cluster motif in both high potential iron-sulfur protein (HiPIP) and ferredoxin (Fd) active sites. Despite this structural similarity, HiPIPs react oxidatively at physiological potentials, whereas Fds are reduced. Sulfur K-edge x-ray absorption spectroscopy uncovers the substantial influence of hydration on this variation in reactivity. Fe-S covalency is much lower in natively hydrated Fd active sites than in HiPIPs but increases upon water removal; similarly, HiPIP covalency decreases when unfolding exposes an otherwise hydrophobically shielded active site to water. Studies on model compounds and accompanying density functional theory calculations support a correlation of Fe-S covalency with ease of oxidation and therefore suggest that hydration accounts for most of the difference between Fd and HiPIP reduction potentials.

Proteins containing Fe_4S_4 clusters catalyze one-electron transfer processes and are ubiquitous in nature (*1*–*4*). These proteins have evolved into two classes that have large differences in their electrochemical potentials: high potential iron-sulfur proteins (HiPIPs) and bacterial ferredoxins (Fds) (*5*–*8*). Physiological conditions support a reduction potential window ranging from about −600 to +500 mV (*9*). Spectroscopic and electrochemical measure-

ments have shown that the resting state in both classes of protein is $[Fe_4S_4]^{2+}$ and that HiPIPs react by oxidation to $[Fe_4S_4]^{3+}$ (with an associated oxidation potential ranging from 150 mV to 350 mV) whereas Fds are reduced to $[Fe_4S_4]^{+}$ (with an associated reduction potential ranging from −250 mV to −400 mV) (10–14). The corresponding Fd oxidation and HiPIP reduction potentials lie outside the physiological window, and so the associated processes are not biologically active.

The geometric and spectroscopic features of the $[Fe_4S_4]^{2+}$ resting states are identical in both protein classes (15–18), and no significant differences in their electronic structures emerged from quantum mechanics (QM) (19) and molecular mechanics (MM) simulations (20, 21). Thus, the difference in electrochemical behavior appears to arise from environmental factors at the respective active sites. Crystallographic data indicate that the Fe_4S_4 cluster is buried in a hydrophobic core in HiPIP with ~five conserved H-bonding interactions to the cluster ligands from the backbone, whereas Fds are exposed to solvent, with eight protein H-bonding interactions, and have a highly conserved CXXCXXC loop (where C is Cys and X is any amino acid) (18). Structurally congruent synthetic inorganic complexes have been reported for the three oxidation states observed in HiPIPs and Fds (3, 22, 23). Whereas the oxidation of synthetic $[Fe_4S_4]^{2+}$ complexes has a similar potential to those observed in HiPIPs, the reduction of the $[Fe_4S_4]^{2+}$ model complex has ~1 V more negative potential than that of the Fds (24). Holm and co-workers reported significant variations in the $[Fe_4S_4]^{2+}$ reduction potential for these complexes with varying solvent dielectric, nature of the thiolate, and presence of charged residue near the cluster; however, the reduction potentials of these models were still very negative and mostly below the physiological range (25). Electrostatic and MM calculations suggested that large dipolar interactions from peptide residues and intercalated water molecules in the Fd environment shift the $[Fe_4S_4]^{2+}$ reduction potential by 1.4 V above that in HiPIP while at the same time disfavoring oxidation by shifting that potential 1.5 V below the corresponding HiPIP couple (21, 26). However, so far there are no experimental data that determine the relative contributions of these effects on the electrochemical potentials of these proteins.

Direct determination of electrochemical potentials in perturbed (lyophilized, unfolded, etc.) protein active sites using voltametric techniques is challenging at best. Our previous results have shown that, in a series of model complexes, the electrochemical potential varies linearly with the extent of Fe-S covalency in the cluster, which can be directly measured experimentally with use of sulfur K-edge x-ray absorption spectroscopy (XAS). In this study, we systematically varied the solvent exposure to the active sites of these proteins in an effort to quantify the impact of hydration of these active sites on their electronic structure and electrochemical potential.

With use of S K-edge XAS, we previously observed a large decrease in Fe-S bond covalency in Fd relative to HiPIP, although the origin of this difference was not determined at that time (27). Sulfur K-edge XAS is a direct experimental probe of ligand-metal bond covalency (28). The primary feature at the S K edge is the S 1s → 4p transition. The lower energy transitions from ligand 1s orbitals to the unoccupied metal-based 3d antibonding orbitals are disallowed, but they obtain absorption intensity if these 3d orbitals mix with S_{3p} orbitals because the sulfur-based 1s → 3p ($\Delta L = 1$, where L represents the orbital angular momentum) transition is electric-dipole allowed (29, 30). This pre-edge intensity is directly proportional to the percent of S_{3p} mixing in the Fe_{3d} orbitals and hence provides an experimental measure of ligand-metal bond covalency (31). This method was previously used to analyze the electronic

[1]Department of Chemistry, Stanford University, Stanford, CA 94305, USA. [2]Department of Biochemistry and Molecular Biology, University of Georgia, Athens, GA 30602, USA. [3]University of Bologna, Campus Universitario di Scienze degli Alimenti Via Ravennate, 1020, 47023 Cesena, Italy. [4]Department of Biological Sciences, Graduate School of Science, Osaka University, Toyonaka, Osaka 560-0043, Japan. [5]Stanford Synchrotron Radiation Laboratory (SSRL), Stanford Linear Accelerator Center (SLAC), Stanford University, Menlo Park, CA 94025, USA.

*To whom correspondence should be addressed. E-mail: hodgson@ssrl.slac.stanford.edu (K.O.H.); hedman@ssrl.slac.stanford.edu (B.H.); edward.solomon@stanford.edu (E.I.S.)

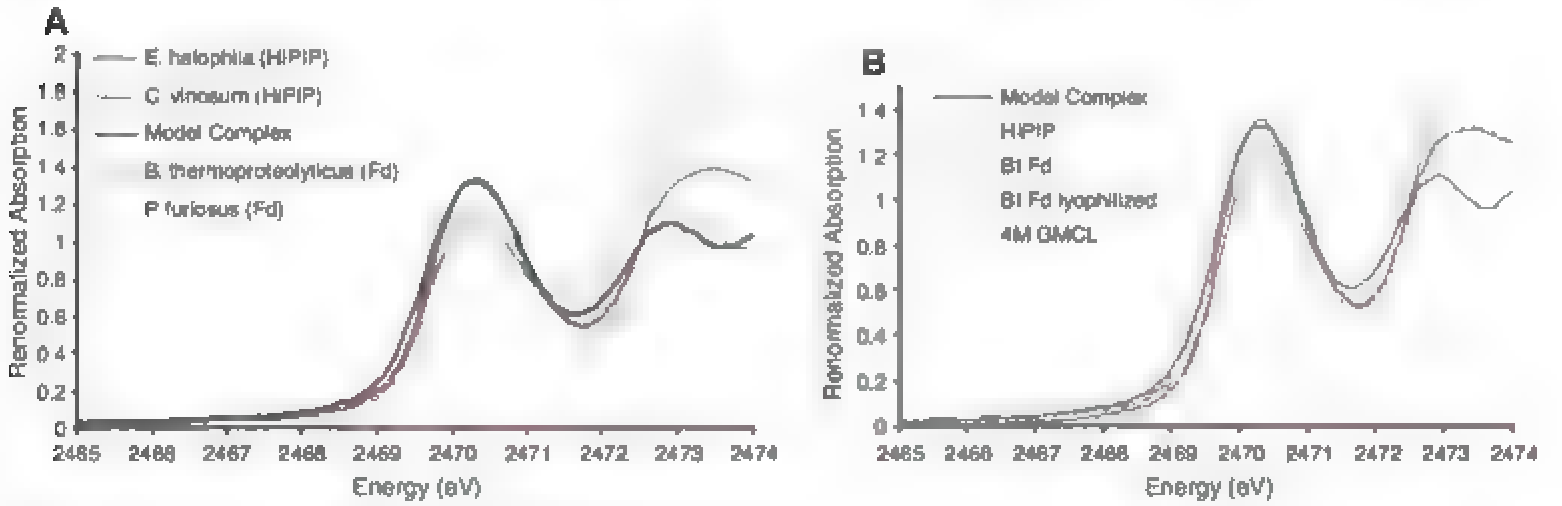

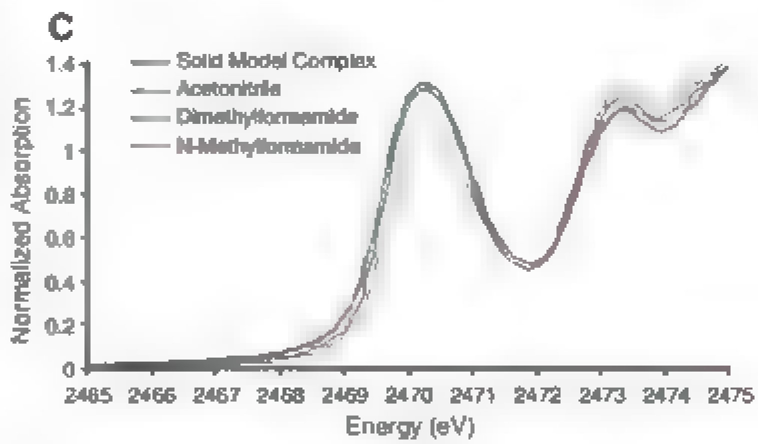

Fig. 1. (**A**) S K-edge x-ray absorption spectra of $(NEt_4)_2[Fe_4S_4(SEt)_4]$ (black), HiPIP from *C. vinosum* (blue), HiPIP from *E. halophila I* (light blue), Fd from *Bt* (red), and Fd from *Pf* (orange). (**B**) Pre-edge region of the absorption spectra for the model (black), WT *C. vinosum* HiPIP (blue), unfolded *C. vinosum* HiPIP (dashed brown), WT *Bt* Fd (red), and lyophilized *Bt* Fd (dashed green). (**C**) X-ray absorption spectra of $(NBu_4)_2[Fe_4S_4(SPh)_4]$ as a solid (black) and in acetonitrile (green), N,N-dimethylformamide (blue), and N-methylformamide (red) solutions.

structure and bonding of models and active sites of mononuclear Fe-S (rubredoxins), binuclear Fe_2S_2 (spinach ferredoxin and Rieske protein), trinuclear (bacterial ferredoxin), and tetranuclear (HiPIPs and ferredoxins) proteins (27, 28, 30, 32). In most cases, the Fe-S bonds in the protein active sites were found to be less covalent than those in the structurally congruent corresponding model complexes (30, 33, 34).

The S K-edge spectrum of $(NEt_4)_2[Fe_4S_4(SEt)_4]$ (Fig. 1A), where Et indicates an ethyl group, serves as an appropriate reference for the Fe_4S_4 clusters in proteins because an aliphatic ethyl thiolate ligand has a bonding interaction with the cluster similar to that of the cysteine ligands in the proteins. Its absorption spectrum (Fig. 1A black) shows a pre-edge peak at 2470.2 eV. Previous S K-edge data on clusters with S^{2-} substituted by Se^{2-} and RS^- (where R is an alkyl or an aryl substituent) substituted by Cl^- have shown that the four $S_{sulfide}$ and the four $S_{thiolate}$ pre-edge transitions are centered at 2470.0 eV and 2471.0 eV, respectively (30). From fits to the black spectrum in Fig. 1A and its second derivative, the peak intensity reflects 168% thiolate and 480% sulfide 3p characters mixed into the unoccupied valence orbitals of the Fe_4S_4 cluster (28). In the following text, the total intensity of this peak, i.e., the total covalency of this model complex, is used as a reference for the decreases observed in the proteins. The additional rising-edge feature at 2472 to 2473 eV represents the background $S_{1s} \rightarrow C\text{-}S_{\sigma^*}$ transitions for all cysteine and methionine residues in the model or protein (thus, these vary between different models and proteins).

The XAS data for representative HiPIPs from *Chromatium vinosum* (Fig. 1A, blue) and *Ectothiorhodospira halophila I* (Fig. 1A, light blue) show pre-edge intensities very similar to each other and only slightly lower than that of the model complex. The fits to the HiPIP data indicate that the total Fe-S covalencies are 95% to 96% of that of the model complex (Table 1). In contrast, the S K-edge data for representative Fds from *Bacillus thermoproteolyticus* (*Bt*) (Fig. 1A, red) and *Pyrococcus furiosus* (*Pf*) (35) (Fig. 1A, orange) have significantly less pre-edge intensity than the model complex (Fig. 1A, black) and the HiPIPs (Fig. 1A, blue and light blue). These data indicate that the Fe-S bonds in Fds are less covalent than those of the model complex and of the HiPIPs. The fitted intensities for the Fds give total Fe-S covalencies of 86% to 85% of that of the model complex. Both the $\mu_3S_{sulfide}$ and the $S_{thiolate}$ covalencies are significantly reduced in the Fd active sites relative to those of the HiPIP active sites (Table 1).

Table 1. Fe-S covalency in Fe_4S_4 and proteins and a model from S K-edge XAS. Covalencies were summed over 1800% total Fe_{3d}-based orbitals, where each of the 18 unoccupied orbitals is worth 100%.

	Covalency ($\%S_{3p}$)			Relative to model complex
	$\mu_3S_{sulfide}$	$S_{thiolate}$	Total	
$(NEt_4)_2[Fe_4S_4(SEt)_4]$	480 ± 10	168 ± 7	648 ± 10	100%
C. vinosum (HiPIP)	468 ± 8	156 ± 9	624 ± 21	96%
C. vinosum (unfolded)	444 ± 16	140 ± 8	581 ± 23	89%
E. halophila I (HiPIP)	468 ± 9	148 ± 7	613 ± 17	95%
Bt Fd	420 ± 14	136 ± 12	557 ± 25	86%
Bt Fd (lyophilized)	468 ± 11	152 ± 8	617 ± 20	95%
Pf Fd	396 ± 18	124 ± 16	551 ± 25	85%

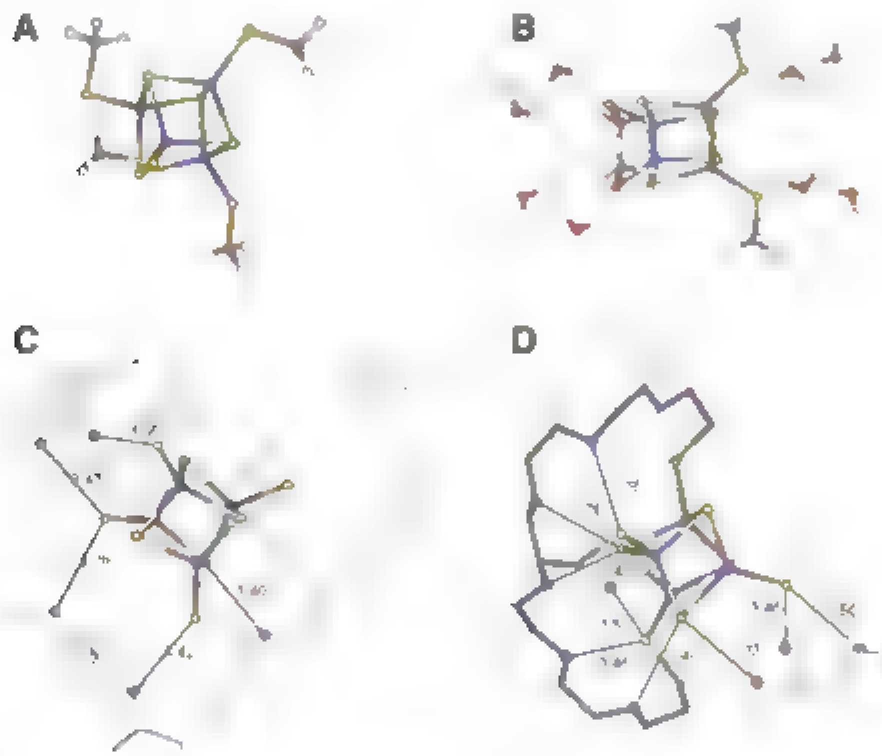

Fig. 2. Computational structures simulating (**A**) isolated model complex, (**B**) H-bonded model complex, (**C**) HiPIP active site (the NH···S distances are indicated), and (**D**) Fd active site (the CXXCXXC loop of the backbone is highlighted).

The weakening of Fe-S bonds in Fds relative to HiPIPs could stem from differences in the H bonding from the peptide backbone (five in HiPIP versus eight in Fd) as well as differences in solvent exposure (HiPIP is buried in a hydrophobic core, and Fd is solvent-exposed) (10). To gauge the effect of hydration in Fe-S covalency, we subjected a lyophilized sample of *Bt* Fd to XAS. The data (Fig. 1B, dashed green) show a marked increase in pre-edge intensity relative to the pre-edge of *Bt* Fd in aqueous solution (Fig. 1B, red), although the rising edge remains relatively unaffected (for details, see fig. S1A). The reduction of the pre-edge intensity in buffered aqueous solution is reversible (fig. S1A) and indicates that the Fd cluster forms H bonds directly with water molecules, thereby reducing its covalency. Quantification indicates that the total covalency increases from 86% in *Bt* Fd (Table 1, row 5) to 95% of that of the model complex upon lyophilization (Table 1, row 6).

In a complementary experiment, the *C. vinosum* HiPIP was treated anaerobically with 4 M guanidinium hydrochloride, which has been shown to partially and reversibly unfold this HiPIP, to expose the cluster to water without further chemical modification (36). The XAS data for unfolded HiPIP (Fig. 1B, dashed brown) show a decrease in the pre-edge intensity relative to that of folded *C. vinosum* HiPIP (Fig. 1B, blue). This process is reversible (fig. S1B), and the similar rising edges between these spectra (Fig. 1B, blue line and brown dashed line) indicate that the cluster in HiPIP remains intact during this conversion. Fits to the data show that the total Fe-S covalency decreases from 96% of the model in wild-type (WT) *C. vinosum* HiPIP to 89% in the unfolded protein and that the Fe-$\mu_3S_{sulfide}$ and Fe-$S_{thiolate}$ bond covalencies are equally affected. The result of unfolding the HiPIP protein is complementary to the lyophilization of the *Bt* Fd protein, with both indicating that hydration of the cluster is the major source of reduction of Fe-S bond covalency.

To gauge the relative impacts of solvent dielectric and H bonding independently on Fe-S covalency, we dissolved a well-characterized Fe_4S_4 model complex $(NBu_4)_2[Fe_4S_4(SPh)_4]$, where Bu is a butyl group and Ph is a phenyl group, in a

variety of solvents with different dielectric constants (acetonitrile and *N,N*-dimethylformamide DMF) and capacities for H bonding (*N*-methyl formamide, NMF). The model complex is stable in all three solvents. The S K-edge data for the solid $(NBu_4)_2[Fe_4S_4(SPh)_4]$ complex (Fig. 1C, black) are very similar to the data for the complex in acetonitrile (Fig. 1C, green) and DMF (Fig. 1C, blue). These results suggest that there is little impact on covalency from changes in dielectric constant around the cluster. However, the data for the same complex in NMF (Fig. 1C, red), which can act as an H-bond donor, show a large decrease in the pre-edge intensity. Fits to the data indicate that the total Fe-S covalency decreases by 15% in NMF (fig. S2). This decrease in covalency due to H bonding from solvent parallels the results observed on perturbing water access to the protein active sites (lyophilized *Bt* Fd and unfolded *C. vinosum* HiPIP) and confirms that H bonding of the water to the S ligands is the direct contribution to this effect.

The above results were compared to density functional theory (DFT) calculations on the model complex and protein active sites. The $(NBu_4)_2[Fe_4S_4(SPh)_4]$ complex was modeled with an $[Fe_4S_4(SMe)_4]^{2-}$ (where Me indicates a methyl group) cluster (Fig. 2A) to which eight water molecules were added (Fig. 2B). The HiPIP active site was approximated with a 210-atom molecule whose coordinates were taken from a high-resolution (1.2 Å) crystal structure of the *C. vinosum* protein from the Protein Data Bank (PDB identification code 1CKU) (Fig. 2C). A 140-atom model of the *Bt* Fd active site with and without seven H_2O molecules was similarly simulated (PDB identification code 1IQZ) (Fig. 2D) (31).

Upon forming H bonds to eight water molecules, the simulated $[Fe_4S_4(SMe)_4]^{2-}$ compound evidenced a total Fe-S covalency reduction of 10% S_{3p} (table S1), which is in reasonable agreement with the experimentally observed decrease of 15% S_{3p} in an H-bonding solvent (*vide supra*). The calculations also indicate that both the Fe-$\mu_3S_{sulfide}$ and the Fe-$S_{thiolate}$ bond covalencies are reduced as observed in the experiment (fig. S2B). The calculation on the *Bt* Fd (without H_2O molecules) and HiPIP active sites show 3% and 2% reduction in the Fe-S bond covalency (table S1), respectively, relative to the reference model. This result is consistent with the limited 5% and 4% decrease of Fe-S bond covalency observed in lyophilized *Bt* Fd and HiPIP (Table 1, rows 6 and 2). These decreases are largely localized in Fe-$S_{thiolate}$ moieties (table S1), which is consistent with the larger number of H bonds donated to the $S_{thiolate}$ atoms relative to the $S_{sulfide}$ atoms from the backbone. When the amide groups in the simulated backbone are replaced with ester groups (i.e., the dipolar interaction of the C=O is still present, but there is no H bonding from the N-H groups), no decrease in Fe-S bond covalency is observed (table S1, row 4). Including seven H_2O molecules in the solvent-exposed side of the Fd model shows a 10% decrease in Fe-S covalency [in both Fe-$\mu_3S_{sulfide}$ and Fe-$S_{thiolate}$ (table S1, row 5)] relative to the model complex, which is close to (although less than) the experimentally observed 15% decrease in Fe-S covalency in Fds relative to the model complex (Table 1, row 5).

Thus, both the experimental and theoretical results show that Fe-S covalency is a sensitive probe of electrostatic interactions present in protein active sites. This decrease of covalency due to H bonding would correspond to the solute polarization term in a total energy calculation (37, 38). In both HiPIPs and Fds, H bonding from the peptide backbone causes only a limited reduction in Fe-S bond covalency. Rather the hydration causes two-thirds of the large decrease in the Fe-S bond covalency that is observed in the solvent-exposed Fd active site relative to an alkyl thiolate model.

Relative to the model complex (in DMF scaled to the normal hydrogen electrode (NHE)), the reduction potential of Fd is raised from −1100

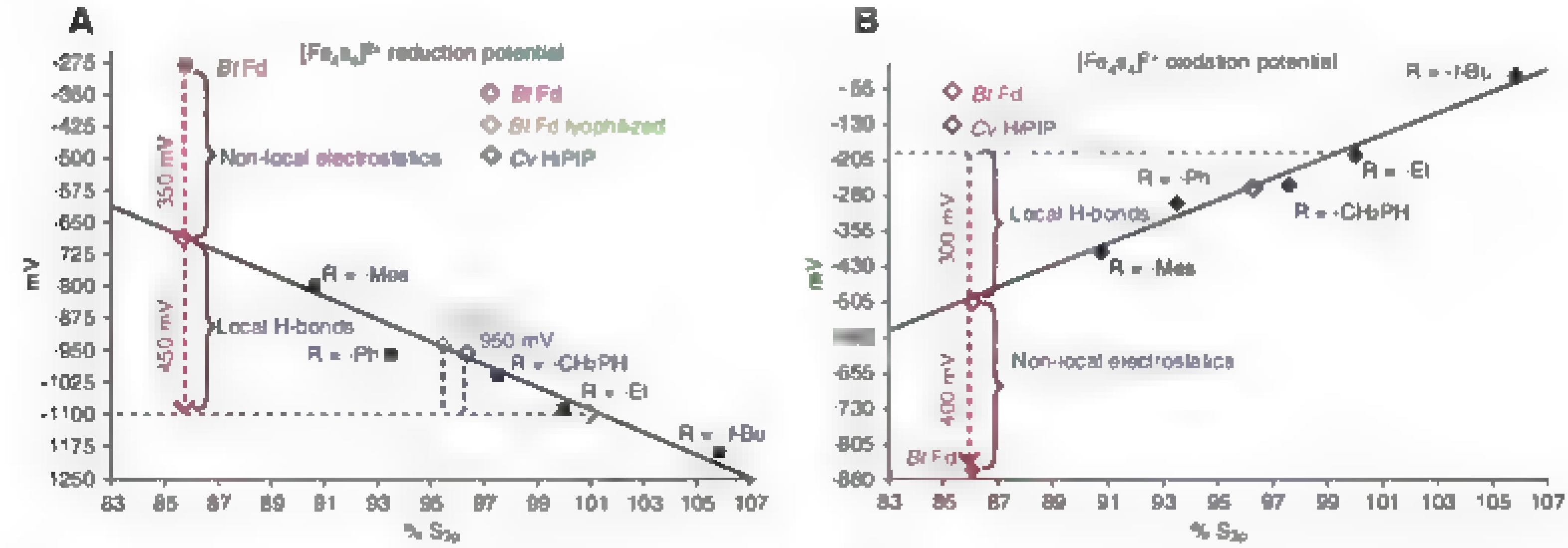

Fig. 3. Plot of total Fe-S covalency as a function of $[Fe_4S_4]^{2+}$ (**A**) reduction potential and (**B**) oxidation potential versus NHE for a series of $[Fe_4S_4(SR)_4]$ complexes (solid black) and *Bt* Fd (solid red). The open squares represent the predicted (using covalency) $[Fe_4S_4]^{2+}$ electrochemical potentials. The $[Fe_4S_4]^{2+}$ reduction-oxidation potential for the reference complex $[Fe_4S_4(SEt)_4]^{2-}$ is indicated by the horizontal dashed gray line.

Fig. 4. Schematic representation of $[Fe_4S_4]^{2+}$ reduction potential tuning by desolvation

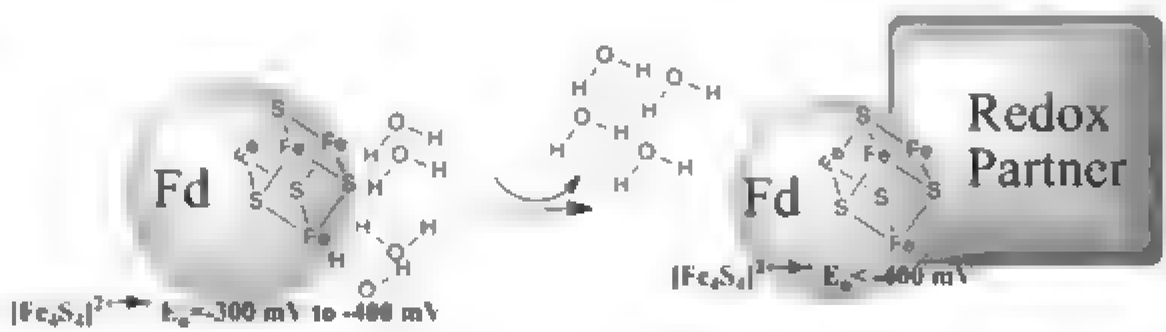

mV to −300 mV (black and red points in Fig. 3A). From our past studies, the electrostatic effect of water H-bonded to S ligands will decrease their covalent interaction with the Fe and weaken the Fe-S bonds. This will raise the reduction potential by destabilizing the oxidized state more than the reduced state (*40*). An estimate of this effect on the reduction potential of the Fe_4S_4 clusters is given in Fig. 3A, in which the covalencies derived from S K-edge XAS intensities for a series of $[Fe_4S_4(SR)_4]^{2-}$ complexes with varying thiolates (solid black squares) are plotted relative to their corresponding $[Fe_4S_4]^{2+}$ one-electron reduction potentials (measured in DMF scaled to NHE). This plot shows a linear correlation, and the negative slope indicates that it is easier to reduce the $[Fe_4S_4]^{2+}$ cluster as the Fe-S covalency decreases (*34*). For the Fe_4S_4 cluster in HiPIP, the experimental covalency decreases by 5% relative to the model, which corresponds to a +150 mV shift in its $[Fe_4S_4]^{2+}$ reduction potential (open blue diamond). Consistent with this extrapolation, the one-electron reduction of the $[Fe_4S_4]^{2+}$ resting form of HiPIP from *C. vinosum* has been experimentally estimated to be −950 mV, which is outside the physiological window (*39*).

For Fd in aqueous solution, the electrostatic effect of the local H bonds on the thiolate and sulfide ligands of the Fe_4S_4 cluster decreases the covalency by 15% relative to the model complex. The plot in Fig. 3A gives an estimated change of the reduction potential of +450 mV associated with this Fe-S covalency change. The remaining +350 mV contribution to the observed reduction potential of Fd would result from the additional stabilization of the reduced state by the asymmetric electrostatic field around the H-bonded cluster. One face of the cluster is exposed to the high dielectric of water and the other to the dipoles in the CXXCXXC peptide loop, which is highly conserved in all the bacterial Fds (Fig. 2D, highlighted in bold and fig. S3) (*40*). The CXXCXXC dipoles were found to make the dominant contribution to the protein dipolar stabilization term in the calculations of Warshel and co-workers (*21*, *26*).

For the HiPIP $[Fe_4S_4]^{2+}$ oxidation couple, an analogous plot of the measured total S_{3p} character for a series of $[Fe_4S_4(SR)_4]^{2-}$ complexes with different thiolate ligands versus the $[Fe_4S_4]^{2+}$ oxidation potential (*41*, *42*) also shows a linear correlation (Fig. 3B). The protein data points on this plot show essentially the same features as observed for the $[Fe_4S_4]^{2+}$ reduction couple in Fig. 3A). The predicted $[Fe_4S_4]^{2+}$ oxidation potential for HiPIP (Fig. 3B, blue open diamond at ~265 mV) shows a limited shift because of the 5% decrease in covalency relative to the alkyl thiolate model couple (~200 mV). Alternatively, the $[Fe_4S_4]^{2+}$ oxidation potential in the Fd protein active site is lowered by ~700 mV relative to the model complex, into the nonphysiological ~800 to ~900 mV range (Fig. 3B, solid red) (*41*); ~300 mV because of the electrostatic effect of local H bonds, which decrease the covalency; and ~400 mV because of nonlocal protein electrostatics.

Thus, the same factors that shift the $[Fe_4S_4]^{2+}$ reduction potential in the Fd active site by ~−600 mV relative to HiPIP (from −900 mV to −300 mV), bringing it into physiological range, also shift the $[Fe_4S_4]^{2+}$ oxidation potential of Fds by ~500 mV relative to HiPIP (from ~350 mV to ~850 mV) and out of physiological range.

Our results indicate that H bonding from water in a solvent-exposed Fd site can tune the $[Fe_4S_4]^{2+}$ reduction potential up by at least +300 mV. This phenomenon may provide a regulation mechanism for electron transfer in Fe-S cluster proteins. As examples, Fds are proposed to catalyze the reduction of formyl dehydrogenase ($E°$ = −530 mV) by hydrogenase ($E°$ = −414 mV) in methanogenic bacteria (*43*), and DNA binding is proposed to lower the $[Fe_4S_4]^{2+}$ reduction potential by >300 mV in endonuclease III (*44*). As illustrated in Fig. 4, interaction with an electron transfer partner may lead to a partial desolvation of the active site that can shift the reduction or oxidation potential of the Fd $[Fe_4S_4]^{2+}$ cluster. Indeed, the large surface area of docking (1000 Å^2) and the close contact between the active sites (10 Å to 12 Å) in a nuclear magnetic resonance structure of a protein or protein complex of a Fd with its redox partner cytochrome c_{553} (from *Desulfovibrio norvegicum*) (*45*) are consistent with this possibility. Thus, solvent tuning may play an important role in protein-protein and protein-DNA interactions.

References and Notes

1. T. G. Spiro, Ed., *Iron-Sulfur Proteins*, vol. IV of *Metal Ions in Biology* (Wiley, New York, 1982).
2. S. C. Lee, R. H. Holm, *Chem. Rev.* **104**, 1135 (2004).
3. P. V. Rao, R. H. Holm, *Chem. Rev.* **104**, 527 (2004).
4. K. Fukuyama, in *Handbook of Metalloproteins*, A. Messerschmidt, R. Huber, T. L. Poulos, K. Wieghardt, Eds. (Wiley, New York, 2004), p. 543.
5. One ferredoxin has been reported to have a potential of −650 mV (*6*).
6. H. S. Gao-Sheridan, H. R. Pershad, F. A. Armstrong, B. K. Burgess, *J. Biol. Chem.* **273**, 5514 (1998).
7. H. Sticht, P. Rösch, *Prog. Biophys. Mol. Biol.* **70**, 95 (1998).
8. K. Fukuyama, *Photosynth. Res.* **81**, 289 (2004).
9. All potentials in this report are referenced relative to the normal hydrogen electrode (NHE).
10. C. W. J. Carter *et al.*, *Proc. Natl. Acad. Sci. U.S.A.* **69**, 3526 (1972).
11. H. Beinert, R. H. Holm, E. Münck, *Science* **277**, 653 (1997).
12. J. J. Girerd, P. Glous, B. B. Lamotte, J.-J. M. Mouesca, G. Rius, *J. Am. Chem. Soc.* **116**, 1953 (1994).
13. J. J. Glous, P. Glous, *J. Am. Chem. Soc.* **117**, 7513 (1995).
14. L. L. LePape, B. B. Lamotte, J.-J. M. Mouesca, G. Rius, *J. Am. Chem. Soc.* **119**, 9757 (1997).
15. G. Backes *et al.*, *J. Am. Chem. Soc.* **113**, 2055 (1991).
16. R. S. Czernuszewicz, K. A. Macor, M. K. Johnson, A. Gewirth, T. G. Spiro, *J. Am. Chem. Soc.* **109**, 7178 (1987).
17. M. R. Orme-Johnson *et al.*, *Biochim. Biophys. Acta* **748**, 68 (1983).
18. R. P. Sheridan, L. C. Allen, C. W. J. Carter, *J. Biol. Chem.* **256**, 5052 (1981).
19. R. A. Torres, T. Lovell, L. Noodleman, D. A. Case, *J. Am. Chem. Soc.* **125**, 1923 (2003).
20. R. Langen, G. M. Jensen, U. Jacob, P. J. Stephens, A. Warshel, *J. Biol. Chem.* **267**, 25625 (1992).
21. G. M. Jensen, A. Warshel, P. J. Stephens, *Biochemistry* **33**, 10911 (1994).
22. T. O'Sullivan, M. M. Millar, *J. Am. Chem. Soc.* **107**, 4096 (1985).
23. B. A. Averill, T. Herskovitz, R. H. Holm, J. A. Ibers, *J. Am. Chem. Soc.* **95**, 3523 (1973).
24. R. E. Johnson, G. C. Papaefthymiou, R. B. Frankel, R. H. Holm, *J. Am. Chem. Soc.* **105**, 7280 (1983).
25. C. Zhou, J. W. Raebiger, B. M. Segal, R. H. Holm, *Inorg. Chim. Acta* **300-302**, 892 (2000).
26. P. J. Stephens, D. R. Jollie, A. Warshel, *Chem. Rev.* **96**, 2491 (1996).
27. T. Glaser *et al.*, *J. Am. Chem. Soc.* **123**, 4859 (2001).
28. E. I. Solomon, B. Hedman, K. O. Hodgson, A. Dey, R. K. Szilagyi, *Coord. Chem. Rev.* **249**, 97 (2005).
29. F. Neese, B. Hedman, K. O. Hodgson, E. I. Solomon, *Inorg. Chem.* **38**, 4854 (1999).
30. T. Glaser, B. Hedman, K. O. Hodgson, E. I. Solomon, *Acc. Chem. Res.* **33**, 859 (2000).
31. Detailed materials and methods are available on *Science* Online.
32. A. Dey *et al.*, *J. Am. Chem. Soc.* **128**, 533 (2006).
33. N. Ueyama, Y. Yamada, T. Okamura, S. Kimura, A. Nakamura, *Inorg. Chem.* **35**, 6473 (1996).
34. A. Dey *et al.*, *J. Am. Chem. Soc.* **127**, 12046 (2005).
35. The [Fe4S4] Fd from *Pf* is coordinated by an aspartate (Asp[14]) residue at one Fe. Thus, an Asp[14] → Cys[14] mutant, which has been characterized to have four cysteines coordinating the four Fe atoms of the cluster, has been used for this study.
36. D. Bentrop *et al.*, *Biochemistry* **38**, 4669 (1999).
37. J. Florian, A. Warshel, *J. Phys. Chem. B* **101**, 5583 (1997).
38. V. Luzhkov, A. Warshel, *J. Comput. Chem.* **13**, 199 (1992).
39. H. A. Heering, Y. B. M. Bulsink, W. R. Hagen, T. E. Meyer, *Eur. J. Biochem.* **232**, 811 (1995).
40. C. W. J. Carter, *J. Biol. Chem.* **252**, 7802 (1977).
41. F. A. Armstrong, H. A. O. Hill, N. J. Walton, *FEBS Lett.* **150**, 214 (1982).
42. H. L. Blonk *et al.*, *Inorg. Chem.* **30**, 3231 (1991).
43. U. Deppenmeier, *Prog. Nucleic Acid Res. Mol. Biol.* **71**, 223 (2002).
44. E. M. Boon, A. L. Livingston, N. H. Chmiel, S. S. David, J. K. Barton, *Proc. Natl. Acad. Sci. U.S.A.* **100**, 12543 (2003).
45. X. Morelli *et al.*, *Biochemistry* **39**, 2530 (2000).

46. This research was supported by NSF grants CHE-0446304 (E.I.S.), RR-01209 (K.O.H.), and GM 60329 (M.W.W.A.). A.D. received an Evelyn McBain Fellowship from Stanford University. SSRL operations are supported by the U.S. Department of Energy, Office of Basic Energy Sciences. The SSRL Structural Molecular Biology Program is supported by the NIH, National Center for Research Resources, Biomedical Technology Program and by the U.S. Department of Energy, Office of Biological and Environmental Research. The project described was supported by grant number P41 RR-001209 from the National Center for Research Resources (NCRR), a component of the NIH, and its contents are solely the responsibility of the authors and do not necessarily represent the official view of NCRR or NIH. J. Brauman is acknowledged for suggestions on the manuscript.

Supporting Online Material

www.sciencemag.org/cgi/content/full/318/5855/1464/DC1

Materials and Methods

Figs. S1 to S3

Table S1

References

13 July 2007; accepted 18 October 2007

10.1126/science.1147753

The Obesity-Associated *FTO* Gene Encodes a 2-Oxoglutarate–Dependent Nucleic Acid Demethylase

Thomas Gerken,[1] Christophe A. Girard,[2*] Yi-Chun Loraine Tung,[3*] Celia J. Webby,[1†] Vladimir Saudek,[3†] Kirsty S. Hewitson,[1,4†] Giles S. H. Yeo,[3†] Michael A. McDonough,[1†] Sharon Cunliffe,[4†] Luke A. McNeill,[1,4†] Juris Galvanovskis,[5†] Patrik Rorsman,[5] Peter Robins,[6] Xavier Prieur,[3] Anthony P. Coll,[3] Marcella Ma,[3] Zorica Jovanovic,[3] I. Sadaf Farooqi,[3] Barbara Sedgwick,[6] Inês Barroso,[7] Tomas Lindahl,[6] Chris P. Ponting,[8‡§¶] Frances M. Ashcroft,[2‡§¶] Stephen O'Rahilly,[3§¶] Christopher J. Schofield[1‡§¶]

Variants in the *FTO* (fat mass and obesity associated) gene are associated with increased body mass index in humans. Here, we show by bioinformatics analysis that FTO shares sequence motifs with Fe(II)- and 2-oxoglutarate–dependent oxygenases. We find that recombinant murine Fto catalyzes the Fe(II)- and 2OG-dependent demethylation of 3-methylthymine in single-stranded DNA, with concomitant production of succinate, formaldehyde, and carbon dioxide. Consistent with a potential role in nucleic acid demethylation, Fto localizes to the nucleus in transfected cells. Studies of wild-type mice indicate that *Fto* messenger RNA (mRNA) is most abundant in the brain, particularly in hypothalamic nuclei governing energy balance, and that *Fto* mRNA levels in the arcuate nucleus are regulated by feeding and fasting. Studies can now be directed toward determining the physiologically relevant FTO substrate and how nucleic acid methylation status is linked to increased fat mass.

Recent studies have revealed a strong association between common variants in the first intron of *FTO* and obesity in both children and adults, with ~16% of studied populations homozygous for the risk alleles (*1*–*4*). As adults, these individuals weigh ~3 kg more than those homozygous for the low-risk alleles as a result of a specific increase in fat mass (*2*). *FTO* mRNA is expressed in a wide range of human tissues (*2*). The *Fto* gene was first cloned after identification of a fused-toe mutant mouse whose phenotype results from a 1.6-Mb deletion of six genes, including *Fto* (*5*).

Sequence analysis predicts that FTO protein contains a double-stranded beta-helix (DSBH) fold homologous to those of Fe(II) and 2-oxoglutarate (2OG) oxygenases [for a review of these enzymes, see (*6*)] (Fig. 1). The predicted DSBH fold of FTO contains four conserved residues characteristic of Fe(II) and 2OG binding sites (*7*, *8*), and its sequence is highly conserved in organisms ranging from mammals to green algae (Fig. 1 and fig. S1). 2OG oxygenases are involved in diverse processes, including DNA repair, fatty acid metabolism, and posttranslational modifications, for example, proline hydroxylation and histone lysine demethylation [reviewed in (*6*, *9*)]. They require nonheme iron [Fe(II)] as a cofactor, use oxygen and, almost always, 2OG as cosubstrates, and produce succinate and carbon dioxide as by-products.

To determine whether FTO is a 2OG oxygenase, we expressed the murine *Fto* gene in *Escherichia coli* and purified N-terminally hexa-His tagged Fto (*10*). Some 2OG oxygenases catalyze 2OG turnover without a "prime" substrate provided that a reducing agent, typically ascorbate, is present (uncoupled turnover). 2OG uncoupled turnover assays with Fto, monitoring conversion of [1-^{14}C]-2OG into [^{14}C]-carbon dioxide (*10*), revealed that Fto catalyzed 2OG decarboxylation, a reaction that was stimulated by ascorbate and $FeSO_4$ (fig. S2A). 2OG turnover was inhibited by known 2OG oxygenase inhibitors (fig. S2B) and by the absence of Fe(II) and ascorbate.

We next considered the identity of the prime FTO substrate. Among 2OG oxygenases with known substrates, the FTO sequence is most similar to that of the *E. coli* enzyme AlkB (*11*) and its eukaryotic homologs. Members of the

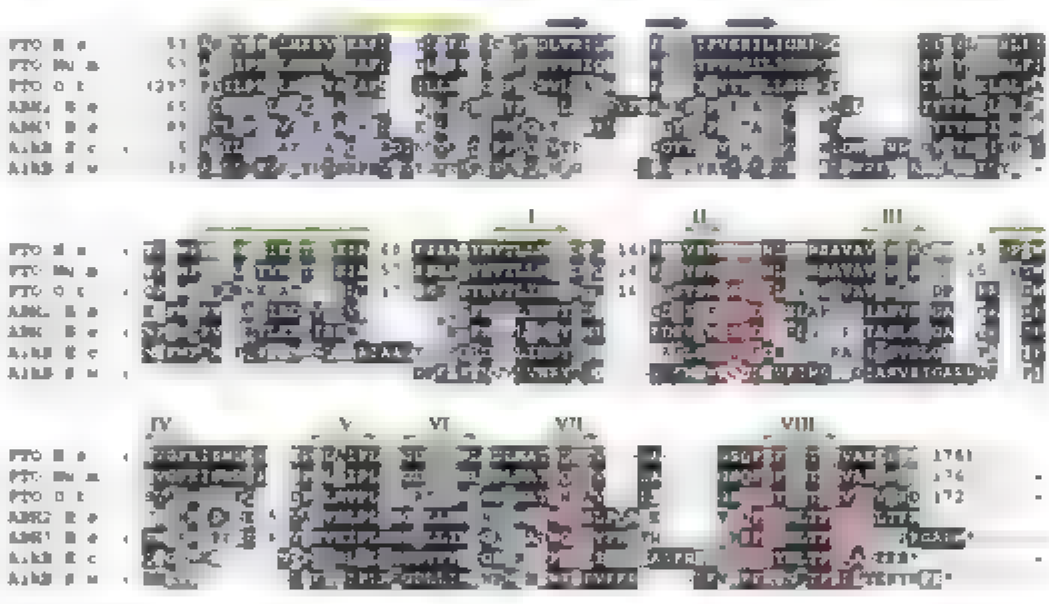

Fig. 1. Multiple sequence alignment of FTO from human (*Homo sapiens*, Hs), mouse (*Mus musculus*, Mm) and green algae (*Ostreococcus tauri*, Ot) with *Escherichia coli* (Ec) and *Shewanella woodyi* (Sw) AlkB and human ABH2 and ABH3. A comparison of Ot FTO with the nonredundant protein sequence database at the National Center for Biotechnology Information using PSI-BLAST (*28*) revealed significant similarity ($E < 0.005$) between human FTO, bacterial AlkB, and its human homologs, within two iterations. Conserved residues highlighted in red are histidine and carboxylate (Asp or Glu) Fe(II) binding residues of 2OG oxygenases (His-228/231, Asp-230/233, and His-304/307 in murine Fto/human FTO, respectively), as well as an arginine (Arg-313/316), which binds the 2OG C-5 carboxylate in a 2OG oxygenase subfamily (*7*, *8*). The cylinders and arrows represent α helices and β strands, respectively, assigned as in a crystal structure of ABH3 (*29*). Secondary structure in yellow represents the N-terminal region, blue strands represent an assigned (*29*) substrate binding lid for ABH3, green strands labeled with roman numerals identify the eight β strands that form the conserved double-stranded beta-helix of the 2OG oxygenases. GenInfo numbers: human FTO: 122937263, mouse Fto: 6753916, green algae FTO: 116060758; human ABH2: 48717226; human ABH3: 21040275; *E. coli* AlkB: 113638; *S. woodyi* AlkB: 118070714.

[1]Chemistry Research Laboratory and Oxford Centre for Integrative Systems Biology, University of Oxford, 12 Mansfield Road, Oxford, Oxon OX1 3TA, UK. [2]Department of Physiology, Anatomy and Genetics, University of Oxford, Parks Road, Oxford, Oxon OX1 3PT, UK. [3]University of Cambridge, Metabolic Research Laboratories, Institute of Metabolic Science, Addenbrooke's Hospital, Cambridge CB2 0QQ, UK. [4]ReOx Ltd., Magdalen Centre, The Oxford Science Park, Oxford, Oxon OX4 4GA, UK. [5]Oxford Centre for Diabetes, Endocrinology and Metabolism, Churchill Hospital, Oxford, Oxon OX3 7LJ, UK. [6]Cancer Research UK London Research Institute, Clare Hall Laboratories, South Mimms, Hertfordshire EN6 3LD, UK. [7]Metabolic Disease Group, Wellcome Trust Sanger Institute, Hinxton, Cambridge, UK. [8]MRC Functional Genetics Unit, Department of Physiology, Anatomy and Genetics, University of Oxford, South Parks Road, Oxford, Oxon OX1 3QX, UK.

*These authors contributed equally to this work.
†These authors contributed equally to this work.
‡These authors contributed equally to this work.
§These authors contributed equally to this work.
¶To whom correspondence should be addressed. E-mail: chris.ponting@dpag.ox.ac.uk (C.P.P.); frances.ashcroft@dpag.ox.ac.uk (F.M.A.); so104@medschl.cam.ac.uk (S.O.); christopher.schofield@chem.ox.ac.uk (C.J.S.)

ABH (AlkB homolog) family (Fig. 1). AlkB is a DNA repair enzyme that repairs cytotoxic 1-methyladenine (1-meA) and 3-methylcytosine (3-meC) lesions by methyl group hydroxylation, followed by a retro-aldol reaction. Among the various human ABHs, only two, ABH2 and ABH3, have been shown to exhibit DNA demethylation activity analogous to that of AlkB (*12*, *13*). ABH 2 and ABH3 are ubiquitously expressed, and their expression is not known to be altered by physiological stimuli.

We screened potential Fto substrates, including a synthetic single-stranded 1-methyl adenine (1-meA) methylated oligonucleotide, Lys-9 methylated histone H3, hypoxia-inducible factor-1α (HIF-1α) subunit fragments, IκBα, coenzyme A derivatives, and other known substrates of human 2OG oxygenases (*10*). Only the 1-meA methylated oligonucleotide stimulated turnover of 2OG above control levels (Fig. 2A). This activity was inhibited by *N*-oxalylglycine, fumarate, and succinate, which were also inhibitors in the 2OG uncoupled turnover assays (Fig. 2C).

Using a liquid chromatography mass spectrometry assay that directly monitors DNA demethylation [without the need for radiolabeled (co-)substrates or coupled assays (*10*)], we demonstrated that Fto catalyzes Fe(II)- and 2OG-dependent DNA demethylation. This activity was stimulated by ascorbate, as observed for other 2OG oxygenases (*6*) (Fig. 2B). Significantly reduced turnover was observed when the reaction was

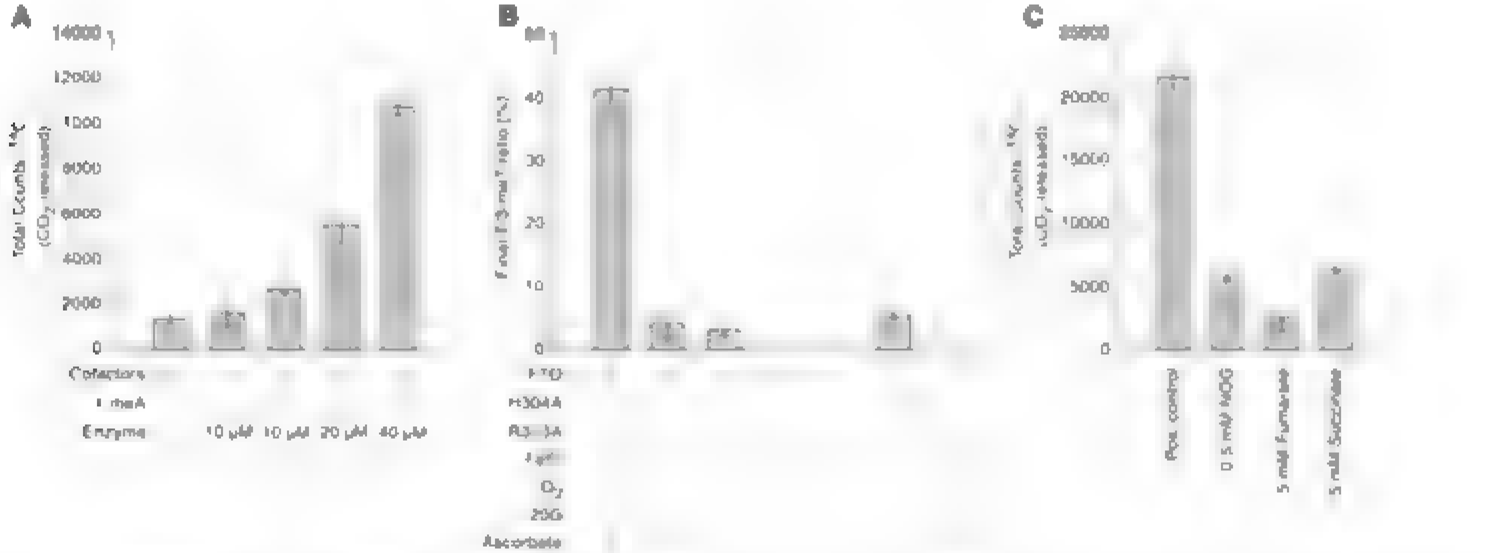

Fig. 2. Fto is a 2-oxoglutarate–dependent DNA demethylase in vitro. **(A)** Demethylation of 1-meA is dependent on Fto in 2OG decarboxylation assays. **(B)** Cofactor/cosubstrate dependence of FTO activity on a 3-meT substrate shown by LC-MS. Data shown represent ratios of thymine to 3-meT in ss-DNA. The oxygen control reaction was carried out in an atmosphere of <1% O_2. **(C)** Inhibition of Fto-catalyzed 1-meA demethylation in 2OG decarboxylation assays. All assays were performed in triplicate, at least, with error bars denoting ±SD.

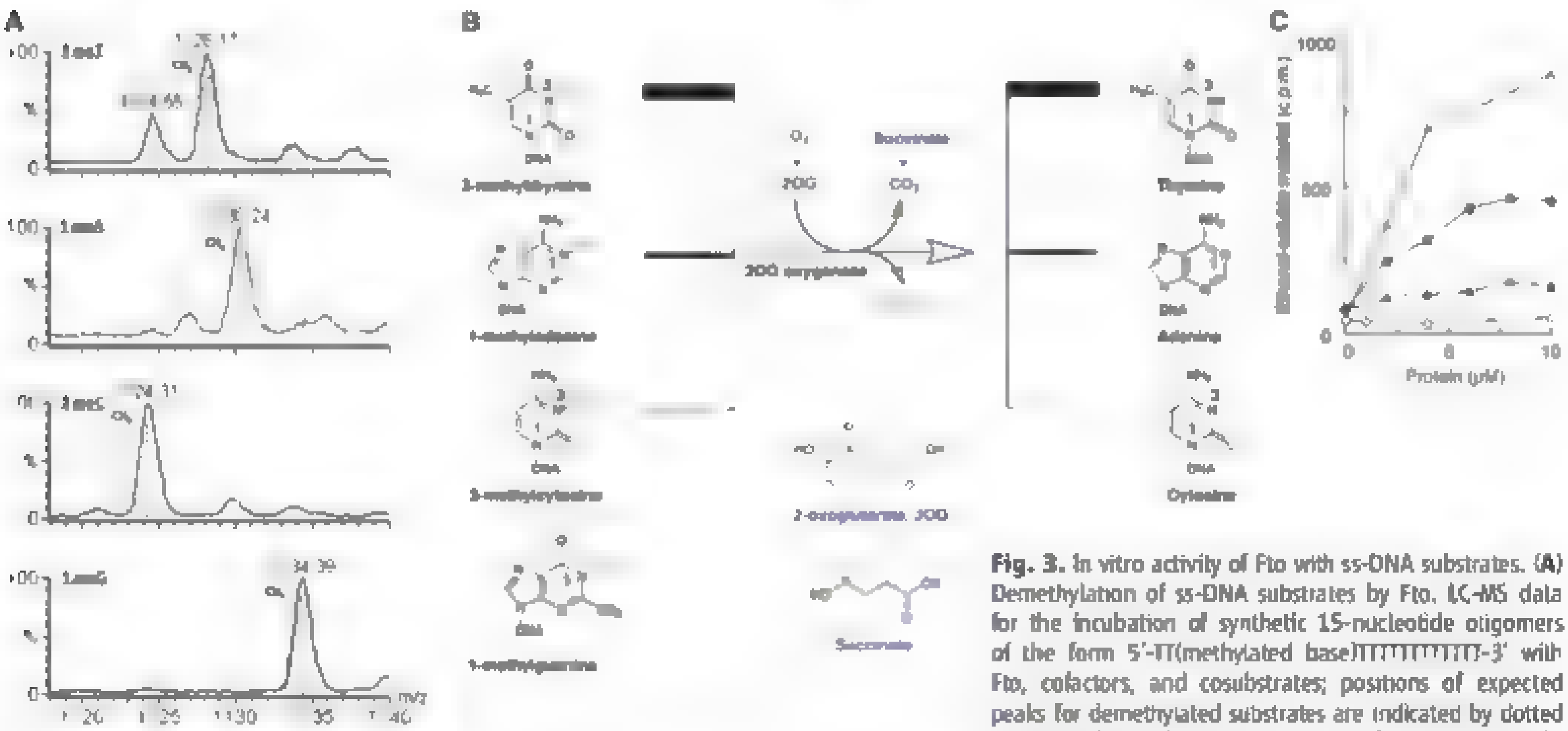

Fig. 3. In vitro activity of Fto with ss-DNA substrates. **(A)** Demethylation of ss-DNA substrates by Fto. LC-MS data for the incubation of synthetic 15-nucleotide oligomers of the form 5′-TT(methylated base)TTTTTTTTTTTT-3′ with Fto, cofactors, and cosubstrates; positions of expected peaks for demethylated substrates are indicated by dotted lines. Smaller peaks at higher masses than reactant peaks probably arise from Na^+ and K^+ adducts of the methylated oligonucleotides. m/z = mass-to-charge ratio, shown in units of Dalton. **(B)** Stoichiometry of the Fto reaction. **(C)** Release of formaldehyde from methylated poly(dA) and poly(dT). FTO and ABH3 were assayed for demethylase activity by incubation with [^{14}C]-methylated poly(dA) or [^{14}C]-methylated poly(dT) [total counts per minute (c.p.m.) 1000 or 800, respectively] at 37°C for 15 min. Release of ethanol-soluble [^{14}C]-formaldehyde was monitored. FTO (○, ●); ABH3 (△, ▲); [^{14}C]-methylated poly(dA) (○, △); [^{14}C]-methylated poly(dT) (●, ▲). In the absence of 2OG, no significant activity was detected; the ethanol soluble material released by FTO or ABH3 was at background level (less than 100 c.p.m).

performed under reduced oxygen conditions. The production of succinate was verified by ^{1}H nuclear magnetic resonance (400 MHz) analyses and that of formaldehyde was confirmed by derivatization with pentafluorophenylhydrazine.

To test the predicted role of the assigned Fe(II) binding and 2OG 5-carboxylate binding residues, His-304 and Arg-313 alanine substitution mutants were constructed (10) (fig. S3). The His-304 mutant showed reduced 2OG turnover, whereas the Arg-313 mutant ablated activity (Fig. 2B), consistent with observations on other 2OG oxygenases.

We next investigated Fto activity with single-stranded oligonucleotides (ss-DNA) methylated at a single position: 1-methyladenine (1-meA), 1-methylguanine (1-meG), 3-methylcytosine (3-meC), and 3-methylthymine (3-meT) (Fig. 3B). Under the assay conditions at pH 7.5, Fto exhibited a preference for 3-meT over 1-meA or 3-meC in ss-DNA. 1-meG was not an Fto substrate (Fig. 3A). The preference of Fto for 3-meT substrates was also observed in assays measuring the release of formaldehyde from randomly methylated poly(dA) and poly(dT) (Fig. 3C). Consistent with previous reports (14, 15) we found that recombinant ABH3 demethylated 1-meA, with only very low levels of 3-meT demethylation observed under our conditions (Fig. 3C).

A protein with nucleic acid demethylase activity might be expected to localize to the cell nucleus. Indeed, confocal imaging of COS-7 cells (from simian kidney) transfected with a plasmid encoding for yellow fluorescent protein (YFP)–tagged Fto, or with YFP alone, revealed that YFP-Fto is concentrated in the nucleus, whereas YFP is present only in the cytoplasm (10) (Fig. 4A). YFP-Fto did not colocalize with mitochondria (Fig. 4A).

The *FTO* SNPs associated with adiposity are intronic and may exert functional effects through altered expression of *FTO* mRNA. If FTO regulates energy homeostasis, it might be more highly expressed in tissues involved in the control of energy balance and be influenced by nutritional signals. We examined *Fto* mRNA levels in multiple murine tissues by quantitative reverse transcription polymerase chain reaction (Fig. 4B). Consistent with human data (2), mouse *Fto* mRNA was detected in all tissues studied, with the highest expression in the brain. Within the brain, high levels were found in the hypothalamus, an area that plays a key role in the control of energy homeostasis. In situ hybridization of hypothalamic slices revealed that *Fto* mRNA was highly expressed in arcuate (ARC), paraventricular (PVN), dorsomedial (DMN), and ventromedial (VMN) nuclei, all sites of critical importance for the control of energy balance (Fig. 4C).

To determine whether *Fto* mRNA expression is nutritionally regulated, we examined *Fto* mRNA levels in laser-dissected hypothalamic nuclei (ARC, VMN, and PVN) from three groups of mice (freely feeding, fasted for 48 hours, and 48 hours fasted treated with daily intraperitoneal injections of leptin, respectively). The leptin-supplemented group was included to examine

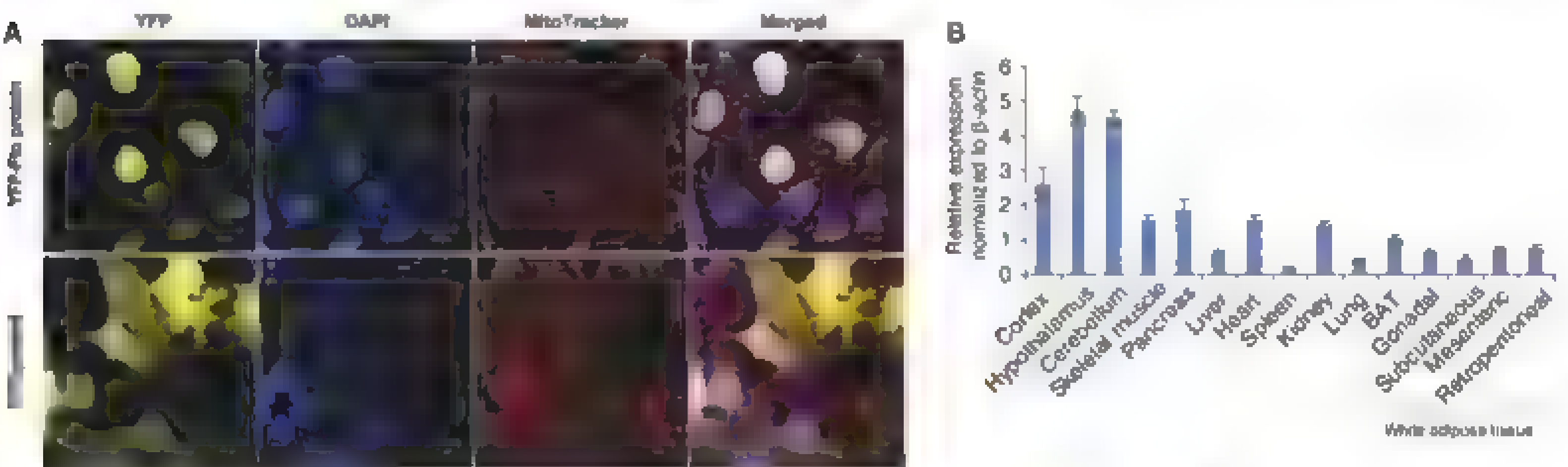

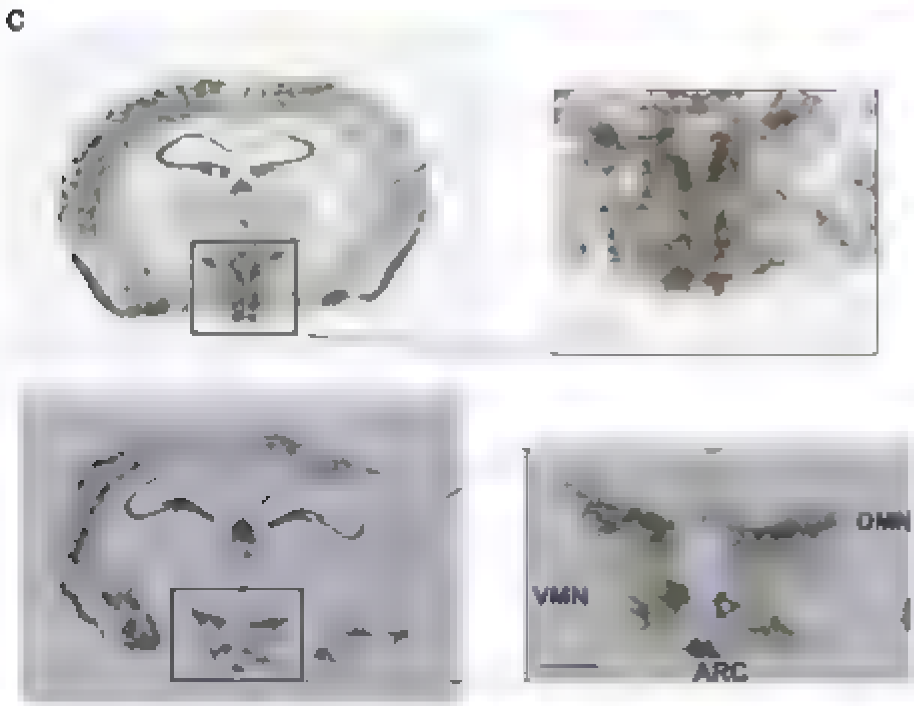

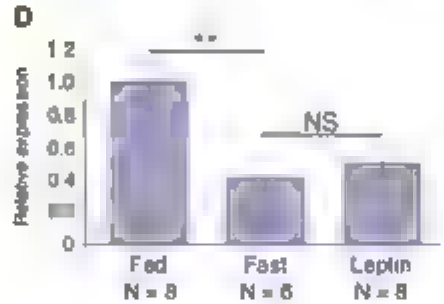

Fig. 4. Expression studies of Fto protein and mRNA in mice. (**A**) Subcellular localization of murine Fto in COS-7 cells. Confocal fluorescence images of COS-7 cells expressing YFP-Fto or YFP show YFP-Fto localizing to the nucleus. Nuclei were visualized with 4′,6-diamidino-2-phenylindole (DAPI) staining and mitochondria with MitoTracker. Colocalization of YFP (yellow) and DAPI (blue) in the merged images produces a white signal. (**B**) Relative expression of *Fto* mRNA in different tissues. Bar graphs show the relative expression of *Fto* mRNA normalized to β actin across a panel of different tissues. Data are represented as the mean (±SE) of six independent mice per tissue. (**C**) In situ hybridization of murine Fto in brain. PVN, paraventricular nucleus; VMN, ventromedial nucleus; DMN, dorsomedial nucleus; ARC, arcuate nucleus; scale bar = 500 μm. (**D**) Nutritional regulation of *Fto* mRNA expression in ARC. Bar graphs show the change in expression of *Fto* mRNA in the arcuate nucleus of the hypothalamus in the fed, fasted, and leptin-treated–while-fasted state. Response is expressed in terms of fold induction of the fasted and leptin-treated expression over the fed expression. The *P* value was calculated using a two-tailed distribution unpaired Student's *t* test. $^{**}P < 0.01$. Data are represented as the mean (±SE) of at least six independent mice per group.

whether any changes associated with fasting were caused by the reduction of circulating leptin that occurs during starvation (16). In the arcuate nucleus, *Fto* mRNA levels were reduced by ~60% in fasted mice and were not rescued by leptin supplementation (Fig. 4D). *Fto* mRNA levels in the PVN and VMN were unchanged (10).

2OG oxygenase catalyzed posttranslational hydroxylation is central to transcriptional regulation in the hypoxic response (17, 18), and 2OG oxygenases catalyze histone demethylation (19). The catalytic activity of FTO may similarly regulate the transcription of genes involved in metabolism by nucleic acid demethylation. Alternatively, it is possible that FTO, as proposed for ABH2, can act as a nucleic acid repair enzyme (20). There is evidence that breakdown of genomic repair processes leads to obesity and metabolic syndrome (21–23).

Under our assay conditions at physiological pH, the preferred substrate of FTO was 3-methylthymine in DNA, a minor but stable lesion that is generated upon exposure of DNA to methylating agents. Verification of whether this methylated base in DNA, or an as-yet-uninvestigated modification of DNA or possibly RNA, is the physiologically relevant substrate(s) of FTO is a key objective of future work. It is noteworthy that although both *E. coli* AlkB and human ABH3 demethylate both DNA and RNA (24, 25), it remains unclear whether RNA demethylation is physiologically relevant.

It is now important to determine whether altered FTO demethylase activity underlies the enhanced fat mass associated with the *FTO* gene variant and whether this alteration in activity is associated with increased food intake, decreased energy expenditure, or both. The majority of human genetic defects associated with obesity have their principal impact on the function of the hypothalamus (26), and our findings with respect to its hypothalamic expression and nutritional regulation suggest that this may also be the case for FTO. Fto is inhibited by Krebs cycle intermediates, in particular fumarate (Fig. 2C), as proposed for the HIF-1α hydroxylases (27). Disease states with elevated fumarate/succinate levels may therefore modulate FTO activity. Further functional studies of Fto may lead to new insights into the pathogenesis of obesity and possibly new avenues for treatment.

References and Notes

1. C. Dina *et al.*, *Nat. Genet.* **39**, 724 (2007).
2. T. M. Frayling *et al.*, *Science* **316**, 889 (2007).
3. L. J. Scott *et al.*, *Science* **316**, 1341 (2007).
4. A. Scuteri *et al.*, *PLoS Genetics* **3**, e115 (2007).
5. T. Peters, K. Ausmeier, R. Dildrop, U. Rüther, *Mamm. Genome* **13**, 186 (2002).
6. L. J. Clifton *et al.*, *J. Inorg. Biochem.* **100**, 644 (2006).
7. K. Valegård *et al.*, *Nature* **394**, 805 (1998).
8. L. Aravind, E. Koonin, *Genome Biol.* **2**, research0007.1 (2001).
9. R. P. Hausinger, *Crit. Rev. Biochem. Mol. Biol.* **39**, 21 (2004).
10. Materials and methods and supplementary data are available on *Science* Online.
11. S. C. Trewick, T. F. Henshaw, R. P. Hausinger, T. Lindahl, B. Sedgwick, *Nature* **419**, 174 (2002).
12. P. A. Aas *et al.*, *Nature* **421**, 859 (2003).
13. T. Duncan *et al.*, *Proc. Natl. Acad. Sci. U.S.A.* **99**, 16660 (2002).
14. P. Koivisto, P. Robins, T. Lindahl, B. Sedgwick, *J. Biol. Chem.* **279**, 40470 (2004).
15. J. C. Delaney, J. M. Essigmann, *Proc. Natl. Acad. Sci. U.S.A.* **101**, 14051 (2004).
16. R. S. Ahima *et al.*, *Nature* **382**, 250 (1996).
17. M. Ivan *et al.*, *Science* **292**, 464 (2001).
18. P. Jaakkola *et al.*, *Science* **292**, 468 (2001).
19. R. J. Klose *et al.*, *Nature* **442**, 312 (2006).
20. J. Ringvoll *et al.*, *EMBO J.* **25**, 2189 (2006).
21. V. Vartanian *et al.*, *Proc. Natl. Acad. Sci. U.S.A.* **103**, 1864 (2006).
22. I. van der Pluijm *et al.*, *PLoS Biol.* **5**, e2 (2007).
23. R. Mostoslavsky *et al.*, *Cell* **124**, 315 (2006).
24. B. Ougland *et al.*, *Mol. Cell* **16**, 107 (2004).
25. D. H. Lee *et al.*, *J. Biol. Chem.* **280**, 39448 (2005).
26. I. S. Farooqi, S. O'Rahilly, *Annu. Rev. Med.* **56**, 443 (2005).
27. M. A. Selak *et al.*, *Cancer Cell* **7**, 77 (2005).
28. A. A. Schaller *et al.*, *Nucleic Acids Res.* **29**, 2994 (2001).
29. O. Sundheim *et al.*, *EMBO J.* **25**, 3389 (2006).

30. We thank J. M. Claverie, C. Notredame, Z. Kostrouch, and A. Hatterdey for useful discussions; R. Read and G. Chavali for SF9 cells, the PMB vector, and technical advice; and D. Rimmington and D. Lyon for additional technical help. This work was supported by the Biochemical and Biological Research Council, the Medical Research Council, Cancer Research UK, European Community FP6 LSHM-CT-503041/518153/512013, and the Wellcome Trust. F.M.A. is a Royal Society Research Professor. C.J.S. is a cofounder of ReOx, a company that aims to exploit the hypoxic response for therapeutic benefit.

Supporting Online Material
www.sciencemag.org/cgi/content/full/1151710/DC1
Materials and Methods
Figs. S1 to S4
References

22 August 2007; accepted 30 October 2007
Published online 8 November 2007;
10.1126/science.1151710
Include this information when citing this paper.

Expression and Function of Junctional Adhesion Molecule–C in Myelinated Peripheral Nerves

Christoph Scheiermann,[1,2] Paolo Meda,[3] Michel Aurrand-Lions,[4] Rime Madani,[3] Yiangos Yiangou,[5] Peter Coffey,[6] Thomas E. Salt,[6] Dominique Ducrest-Gay,[3] Dorothée Caille,[3] Owain Howell,[7] Richard Reynolds,[7] Alexander Lobrinus,[3] Ralf H. Adams,[8] Alan S. L. Yu,[9] Praveen Anand,[5] Beat A. Imhof,[3]* Sussan Nourshargh[1,2]*†

JAM-C is an adhesion molecule that is expressed on cells within the vascular compartment and epithelial cells and, to date, has been largely studied in the context of inflammatory events. Using immunolabeling procedures in conjunction with confocal and electron microscopy, we show here that JAM-C is also expressed in peripheral nerves and that this expression is localized to Schwann cells at junctions between adjoining myelin end loops. Sciatic nerves from JAM-C–deficient [having the JAM-C gene knocked out (KO)] mice exhibited loss of integrity of the myelin sheath and defective nerve conduction as indicated by morphological and electrophysiological studies, respectively. In addition, behavioral tests showed motor abnormalities in the KO animals. JAM-C was also expressed in human sural nerves with an expression profile similar to that seen in mice. These results demonstrate that JAM-C is a component of the autotypic junctional attachments of Schwann cells and plays an important role in maintaining the integrity and function of myelinated peripheral nerves.

JAM-C is a member of an immunoglobulin subfamily of junctional adhesion molecules, composed (as far as is known) of JAM-A, -B, -C, JAM4, ESAM, and CAR, which are specifically enriched at tight junctions of cell-cell contacts (1–3). To date, human JAM-C has been reported to be expressed on the cell surface of platelets and certain leukocyte subtypes, as well as at junctions between endothelial cells (ECs) and intestinal epithelial cells, and has largely been investigated in the context of inflammatory and vascular events (1–8). In addition, JAM-C plays an important role in establishing cell polarity and the formation of endothelial tight junctions (1–3, 5, 9).

As part of our investigations into the functional role of JAM-C in leukocyte transmigration, we detected in vivo, using immunofluorescence analysis of cremaster muscles from wild-type (WT) mice, low-level expression of JAM-C in microvessels at EC junctions colocalizing with the EC marker platelet endothelial cell adhesion molecule 1 (PECAM-1) (10) (Fig. 1A). In addition, a strong and specific expression of JAM-C was detected at discrete sites within nerve bundles (Fig. 1A and fig. S1). Another member of the JAM family, JAM-A, was also found to be expressed at EC junctions and localized to junctions of perineural cells surrounding JAM-C positive nerves (Fig. 1B). The costaining of mouse spinal cords (CNS) and its ventral roots [i.e., peripheral nervous system (PNS)] for JAM-C and neurofilament or the CNS- and PNS-specific myelin proteins, myelin oligodendrocyte glycoprotein (MOG) or protein zero (P_0), respectively, demonstrated that neural JAM-C was restricted to the PNS (Fig. 1C).

In the PNS, myelinating Schwann cells wrap around axons in such a way as to organize the axonal membrane into distinct domains known as nodes of Ranvier (*11*, *12*), sites important for rapid saltatory conduction. To facilitate efficient conduction propagation, tight interactions exist between the axon and the glial cells at regions that flank the nodes of Ranvier (axo-glial paranodal junctions) and between adjacent membrane layers of individual glial cells (*12*). Our observations of teased sciatic nerve fibers immunostained for JAM-C and laminin γ1 indicated that JAM-C was strongly expressed in Schwann cells, at sites characteristic of junctional regions of noncompact myelin. These sites are paranodal regions on either side of the node of Ranvier from where mesaxonal bands, most likely the inner mesaxon, could be seen connecting the internodal Schmidt-Lanterman incisures (Fig. 1D and schematically illustrated in fig. S2A) (*12*–*14*). Analysis of JAM-C expression during development indicated localization at paranodal junctions from postnatal day P5 onward (fig. S3).

Costaining with neurofascin 155, a molecule involved in the formation of axo-glial paranodal junctions (*11*), revealed a broader distribution pattern of JAM-C at the paranodal regions (Fig. 1E). Furthermore, JAM-C was more distally located from the node than E-cadherin, a marker of adherens junctions (*15*), but colocalized with the tight junctional molecule claudin-19 (*16*) (Fig. 1E). None of the molecules analyzed were mislocalized in JAM-C knockout (KO) mice [(Fig. 1E and fig. S2B) for the gap junction component connexin 32 (*14*) and for myelin-associated glycoprotein (MAG) and E-cadherin at incisures].

The node of Ranvier is organized on either side by two Schwann cells, whose cytoplasm increases at paranodal regions (noncompact myelin) to form terminal loops that closely interact with the axon (at paranodal junctions) and the lateral myelin lamellae (fig. S4A). Immunogold staining of longitudinal sections of WT sciatic nerve fibers showed that JAM-C was located at the lateral sides of adjacent myelin lamellae of terminal paranodal loops. However, JAM-C was not expressed in the axon or regions of compact myelin and could not be detected at axo-glial paranodal junctions or tight junctional domains (Fig. 2A and fig. S4, A to C). It is interesting that the findings of these studies indicated expression of JAM-C along the whole length of paranodal terminal loops, a distribution pattern that has not been reported for other tight junctional markers, which suggests that colocalization between JAM-C and claudin-19 is only partial (see Fig. 1E). Expression of JAM-C that is not at the tight junction has also been reported in other cell types (*3*), which implies that the characteristics of junctional localization of JAM-C may be cell-specific. The ligand with which JAM-C is interacting in this scenario is at present unknown, but it is highly probable that the interaction is mediated by JAM-C:JAM-C autotypic adhesion between adjacent terminal loops, because expression of JAM-B, its major binding partner in endothelial cells, was not detected.

The above immunoelectron studies also identified an important, though mild, morphological defect in JAM-C KO sciatic nerve fibers. Perfusion-fixed samples indicated a profile of sequential terminal myelin loops that were misaligned, suggesting a defective adhesive contact between these structures in fibers of similar caliber [(Fig. 2B and fig. S4D); 95.8 and 78.9% of the terminal paranodal loops closely interacted with the axon, in WT and JAM-C KO mice, respectively, for four to six mice with 168 and 279 terminal loops from 15 to 23 nodes of Ranvier counted for WT and KO, respectively]. These findings suggest an important role for JAM-C in maintaining the organization of the paranodal terminal loops, but the relatively low incidence of the noted defect under conditions of JAM-C deletion suggests the existence of compensatory

Fig. 1. JAM-C is expressed in junctional regions of Schwann cells in peripheral nerves. **(A)** Confocal images of WT cremaster muscles immunostained for PECAM-1 (red) and JAM-C (green) show expression of JAM-C in nerves (n) and vascular EC junctions (v). **(B)** Cremaster muscles stained for JAM-A (red) and JAM-C (green) show that JAM-A localizes to EC junctions and surrounds JAM-C–positive nerves (arrows). **(C)** Longitudinal sections of mouse spinal cord (CNS) and its ventral roots (PNS) immunostained for JAM-C (green) and, in red, neurofilament (NF), P_0 (marker for PNS), or MOG (marker for CNS) showing restriction of neural JAM-C expression to the PNS. **(D)** Teased sciatic nerve fibers stained for JAM-C (green) and laminin γ1 (red). JAM-C is restricted to junctional regions of Schwann cells, i.e., the paranodes (arrows) surrounding the nodes of Ranvier (asterisks), Schmidt-Lanterman incisures (single arrowheads), and mesaxonal bands (double arrowheads). **(E)** Teased sciatic nerve fibers stained for JAM-C (green) and, in red, neurofascin 155 (NF 155), E-cadherin (E-cad), or claudin-19 (Cld-19) in WT and JAM-C–KO mice showing normal distribution of the latter molecules in KO mice. Scale bars: (A, B, D, E) 10 μm, (C) 20 μm.

[1]National Heart and Lung Institute, Imperial College London, London, UK. [2]William Harvey Research Institute, Barts and the London School of Medicine and Dentistry, Charterhouse Square, London EC1M 6BQ, UK. [3]Centre Medical Universitaire (CMU), Medical Faculty, University of Geneva, Geneva, Switzerland. [4]INSERM UMR 599, Institut Paoli-Calmettes, Marseille, France. [5]Peripheral Neuropathy Unit, Division of Neurosciences and Mental Health, Imperial College London, London, UK. [6]Institute of Ophthalmology, University College London, London, UK. [7]Department of Cellular and Molecular Neuroscience, Division of Neurosciences and Mental Health, Imperial College London, London, UK. [8]London Research Institute, Cancer Research UK, London, UK. [9]Nephrology Division, Department of Medicine, Keck School of Medicine, University of Southern California, Los Angeles, CA, USA.

*These authors contributed equally to this work.
†To whom correspondence should be addressed. E-mail: s.nourshargh@qmul.ac.uk

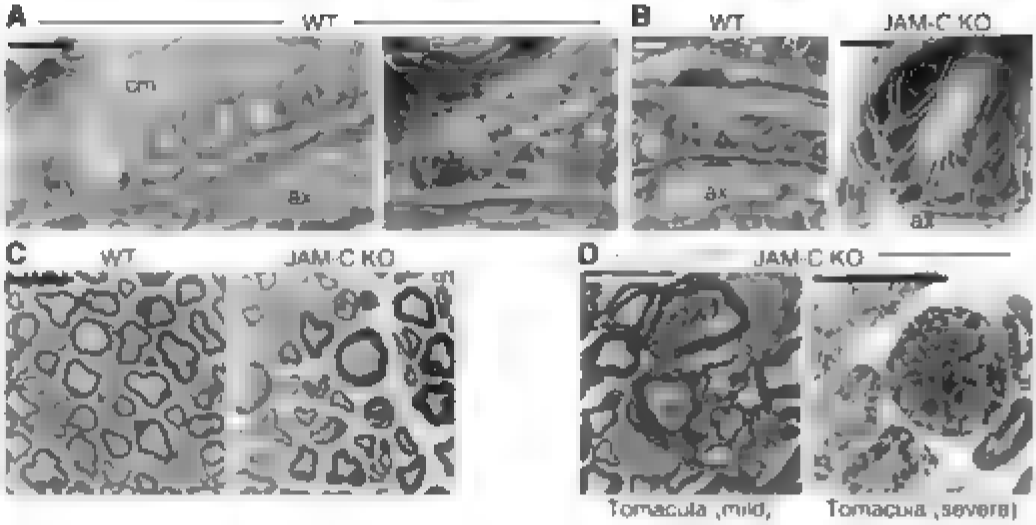

Fig. 2. JAM-C deficiency alters the integrity of the myelin sheath. (**A**) Immunoelectron microscopy of longitudinal sections of WT sciatic nerves revealed JAM-C expression at lateral sides of adjacent myelin lamellae in noncompact, paranodal myelin, but not in the axon (ax) or compact myelin (cm). (**B**) Ultrastructural analysis of longitudinal sections of sciatic nerves from WT and JAM-C–KO mice (16 weeks old) prepared for immunoelectron microscopy (without antibodies to JAM-C) indicated that a proportion of KO terminal loops exhibited an apparent looser adhesion to adjacent loops and axon. (**C** and **D**) Ultrastructural analysis of transverse sections of sciatic nerves from WT and JAM-C–KO mice (16 weeks old) revealed abnormalities in the myelin sheath of a proportion of KO fibers (~7%) exhibiting layers of loose myelin that form mild and severe tomacula. Scale bars, (A) 190 nm, (B) 120 nm, and (C and D) 10 μm.

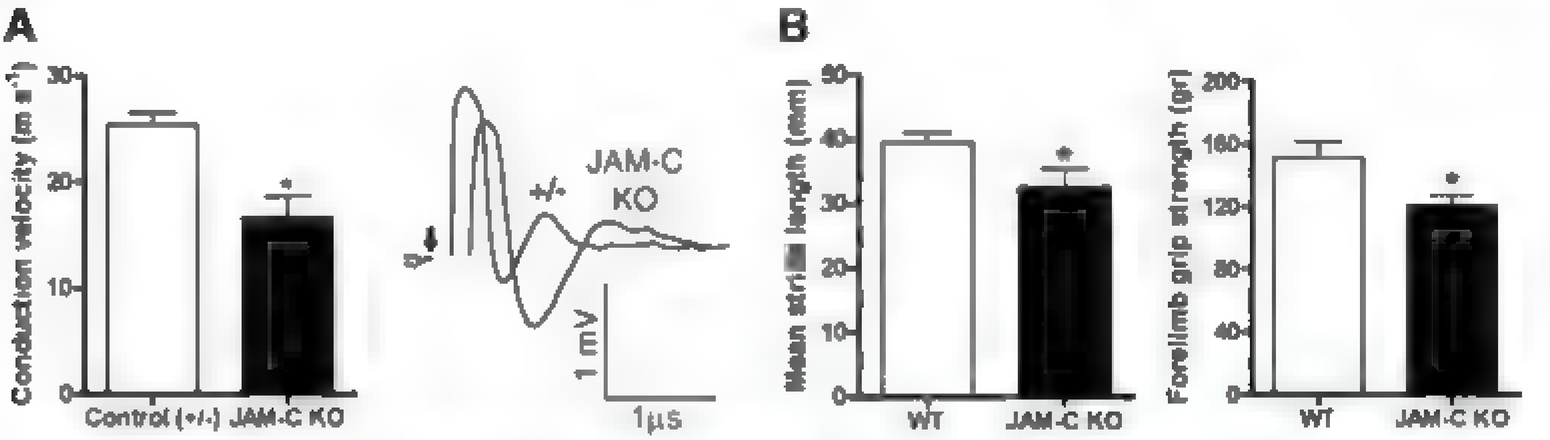

Fig. 3. JAM-C–deficient mice exhibit electrophysiological and behavioral defects. (**A**) Isolated sciatic nerves from control littermates (+/–) and JAM-C–KO mice revealed significantly reduced conduction velocities in the KO (*$P < 0.05$, n = four to eight nerves) and a lag in their CAPs with reduced amplitudes compared with control nerves. (**B**) JAM-C–KO mice exhibited significantly reduced stride length (*$P < 0.05$, n = 13 to 18 mice) and grip strength (*$P < 0.05$, n = 8 to 9 mice). Experiments were performed by a blinded examiner.

mechanisms in the KO mice, such as enhanced expression and/or function of other adhesion pathways. Furthermore, ultrastructural analysis of transverse sections from sciatic nerves revealed that, whereas most KO fibers showed a normal phenotype (Fig. 2C), a proportion exhibited accumulated layers of loose myelin within the periaxonal space forming tomacula [1.2 ± 0.8 and 6.9 ± 2.1% tomacula formation in WT and KO mice, respectively, $P < 0.05$, for seven to nine mice with [illegible] WT and 4222 KO fibers counted (Fig. 2D)]. This thickening of the myelin sheath is a characteristic feature of nerve fibers from patients with hereditary neuropathy with liability to pressure palsies (HNPP). Together, these observations suggest that the abnormal myelin phenotypes detected in JAM-C–deficient mice are caused by the loss of JAM-C–mediated autotypic interactions between myelin lamellae at the paranodal regions, as well as potentially at Schmidt-Lanterman incisures. Of note, whereas JAM-C–KO mice can exhibit a number of defects such as megaesophagus or high susceptibility to lung infections (often fatal) and some of them are smaller in size during early phases of their life span (3 to 8 weeks) ([illegible]), the young adult mice chosen for the studies detailed here (ages 8 to 16 weeks) were of normal health status and were matched by weight with the controls.

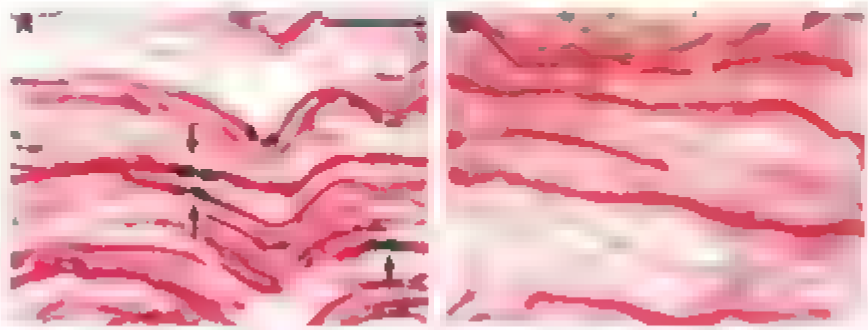

Fig. 4. JAM-C is expressed in human peripheral nerves. Double-staining of human sural nerves for JAM-C (black) and neurofilament (red) obtained from a healthy limb (**A**) and a patient with a clinical and histopathological diagnosis of chronic inflammatory demyelinating polyneuropathy (**B**). JAM-C is expressed at paranodal regions (arrows) in healthy nerves, and the number of JAM-C–positive paranodes was significantly reduced in nerves from patients in accordance with the demyelinated state of the fibers ($P < 0.01$, for six healthy subjects and five patients with neuropathy; the images shown are representative of all samples analyzed). Scale bar, 50 μm.

Because defective JAM-C–mediated adhesion may directly or indirectly lead to reduced paranodal sealing, we assessed whether JAM-C–KO mice exhibited neurological defects. KO sciatic nerves displayed reduced conduction velocity

A DELICATE TOUCH

The notion of a cell membrane serving to contain a large mixture of proteins randomly moving about in a cytosol may once have been the grade school introduction to cellular biology. However, when one considers the nature and coordination of cellular activities, it becomes evident that random collisions between proteins could not result in the spatial and temporal reaction and information-carrying cascades now known to occur in cells. Proteins must interact in very specific ways in order to coordinate nearly all cellular processes including DNA replication and transcription, RNA splicing and translation, protein modification and secretion, cell cycle control, and apoptosis as well as signal transduction and gene expression. Therefore, a disruption in the interaction of proteins is likely to contribute to the onset of disease and is the reason so much research effort is focused on understanding the nuances and implications of such interactions. By Alfred Doig

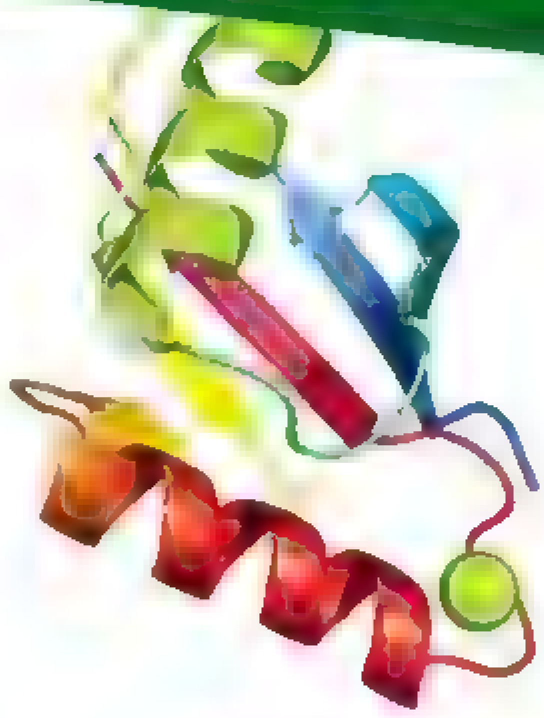

Protein-protein interactions (PPIs) occurring on the exterior of the cell membrane provide signals as to the cell's external environment. Within the cell membrane such signals are propagated by other specialized PPIs that serve to deliver the message to one or more of the compartmentalized cell structures, such as the nucleus or mitochondria, which might result in, for example, a change in gene expression or ATP production.

PPIs are very diverse but all protein interactions occur in a highly specific manner determined by structural and physiochemical properties of the interacting proteins. At the molecular level PPIs can be characterized by their binding strength (permanent or transient), specificity (specific or nonspecific), the location of interacting segments (within one or more polypeptide chains), and the degree of similarity between interacting protein subunits.

Experimental Approaches

PPIs are affected by a number of variables including protein concentrations—as determined by protein synthesis and degradation—and the location of the interacting protein participants within the cell. In recent years, innovations in software, reagents, and instrumentation as well as improvements to experimental protocols have given a clearer understanding of the biological roles of many PPIs.

Methods available to study PPIs extend from very qualitative approaches to highly quantitative measurements. The methods of choice are determined by the nature of the experimental study and can range from the desire to discover new PPIs to determining the dissociation kinetics between well established interacting pairs. There exist a number of in vivo and in vitro methods used to identify and characterize PPIs. The techniques are based on a variety of biological, biophysical, or physiochemical measurements and some lend themselves to high throughput format development.

Biological Methods

If a yes/no answer regarding the significance of a suspected two protein interaction is required, a synthetic lethality approach may be appropriate. This method involves the construction of cells containing two mutations, one in each of a suspected PPI pair. Neither of the mutations alone results in loss of cell viability, but if both should occur in the same cell, death results. Another established method used in PPI research is the two-hybrid approach, first demonstrated using yeast strains and subsequently adapted for use with mammalian and human cell lines. The yeast two-hybrid methodology utilizes a nutrient-dependent yeast strain into which separate bait and prey plasmids are introduced. One plasmid produces a known protein (the bait) with a fused DNA-binding domain (BD) fragment while the other plasmid produces a protein product in which an activation domain (AD) fragment is fused onto

"In recent years, innovations in software, reagents, and instrumentation as well as improvements to experimental protocols have given a clearer understanding of the biological roles of many PPIs."

Look for these Upcoming Articles
Robotics/Automation — January 18
Mass Spectrometry — February 22
Proteomics 1 — March 7

Inclusion of companies in this article does not indicate endorsement by either AAAS or Science, nor is it meant to imply that their products or services are superior to those of other companies.

the so-called prey protein. The prey protein can be either a single known protein or a library of known or unknown proteins. If the bait and prey proteins bind, transcription of a reporter gene takes place, indicating the formation of a PPI.

This "bait and prey" approach has been incorporated into a variety of commercial reagent formats. **BD Biosciences** markets the BD Matchmaker Two-Hybrid System 3, an enhanced GAL4 two-hybrid system. The product uses yeast strain AH109, in which four reporter genes are integrated in the host genome. A similar system, DUAL-membrane from **Dualsystems Biotech**, is specifically designed to detect interactions involving integral membrane proteins with other such proteins, membrane-associated proteins, or soluble proteins. A human cell based "bait-prey" PPI assay system, known as GRIP, is produced by **BioImage** (part of Thermo Fisher Scientific). The GRIP technology is based on the translocation of human cAMP phosphodiesterase PDE4A4 and provides a high throughput method to screen for inhibitors of protein interactions.

Another in vivo method for visualizing PPIs involves use of the fluorescence resonance energy transfer (FRET) approach. In this technique, two different fluorescent molecules (fluorophores)—the donor and acceptor—are genetically fused to the two proteins of interest. Regular fluorescence occurs when the protein bound fluorophores emit energy at the emission frequency. When the two labeled proteins interact and are stimulated by light energy at the excitation frequency for the donor fluorophore, some of this energy transfers to the acceptor, which then re-emits the light at its own emission wavelength. The result is that the donor partner in the PPI emits less light energy, while the acceptor emits more. FRET equipped microscopes and fluorescence-based cell sorter systems are used in conjunction with these FRET reagents to quantify the PPIs.

Featured Participants

Agilent Technologies www.agilent.com	**Invitrogen** www.invitrogen.com
Attana www.attana.com	**MicroCal** www.microcal.com
BD Biosciences www.bdbiosciences.com	**Panomics** www.panomics.com
BioImage (part of Thermo Fisher Scientific) www.bioimage.com	**Pierce Biotechnology (part of Thermo Fisher Scientific)** www.piercenet.com
Bio-Rad www.bio-rad.com	**Sigma-Aldrich** www.sigmaaldrich.com
Dualsystems Biotech www.dualsystems.com	**Stratagene** www.stratagene.com
GE Healthcare/Biacore www.biacore.com	**TIRF Technologies** www.tirftechnologies.com
Hypromatrix www.hypromatrix.com	**Yale University** www.yale.edu
Ingenuity Systems www.ingenuity.com	

Isolating Protein Pairs

In studies where the isolation of proteins involved in a PPI is desired, "pull down" assays can be used. **Pierce Biotechnology** (now a part of Thermo Fisher Scientific) offers its ProFound PPI pull down kits for this application. The product is based on either GST- or His-tagged fusion proteins. The tagged fusion protein is used as the "bait" protein and the pull-down process is based on a bead-based, affinity purification technique. The captured PPIs are eluted for analysis by Western blot.

For recovering interacting proteins from mammalian cells, **Stratagene, an Agilent Technologies** company, produces its InterPlay Mammalian TAP System. The method is based on expression of a protein of interest fused to two affinity tags: a streptavidin binding peptide (SBP) and a calmodulin binding peptide (CBP). "A two-step tandem affinity purification protocol yields exceptionally pure and intact interacting proteins through gentle elution and elimination of a protease digestion step," says Benjamin Pricer, the product manager for functional biology at Stratagene. "The isolated proteins," he continues, "can be identified using Western blotting or mass spectrometry."

Array Screening

Protein arrays are another, more recent addition to the PPI toolbox. As in the two-hybrid approach, a "bait and prey" strategy is used. The methods involve incubating an array of surface anchored proteins with cell supernatant, washing the assay surface, and analyzing for PPIs. A variety of anchoring methods and formats is used including glass slides, polymeric beads, and chromatographic media. **Hypromatrix** supplies a general purpose PPI screening array called the AntibodyArray, which comprises membrane tethered antibodies against hundreds of well-studied proteins. The antigenic protein binds to the antibody, thus capturing any PPIs between the antigen protein and its interacting partners. Similarly, **Invitrogen's** ProtoArray Human Protein Microarray contains approximately 8,000 unique human proteins, selected from multiple gene families and arrayed in duplicate on a 1 inch x 3 inch nitrocellulose-coated glass slide. To provide maximum flexibility, these microarrays are compatible with fluorescent, chemiluminescent, radioisotopic, and other detection methods.

Specialty arrays for PPI screening are also available and include **Sigma-Aldrich's** Panoram Human Cancer v1 Protein Array used to screen for interactions with 130 fully functional cancer proteins. Also, **Panomics'** TF Protein Array is useful for determining how a particular protein interacts with the 140 known transcription factor proteins spotted on this array.

Instrumentation for Bound Proteins

Over the past 15 years, specific instrumentation has evolved to measure the physiochemical properties of known interacting proteins. These instruments are based on crystal resonance, surface plasmon energy measurements, microcalorimetry, scanning tunneling microscopy, and total internal reflection fluorescence.

The principle of crystal resonance has been applied by **Attana** to develop a quartz crystal microbalance (QCM) technology to obtain label-free, real-time measurements of PPI kinetics, affinity, and specificity. QCM uses a piezoelectric effect to oscillate a crystal at its resonance frequency. This frequency shifts when molecules are added to or removed from the surface of the crystal. By attaching a specific bait protein to the biotin treated crystal surface, continued »

"The AFM instrument employs a sensitive probe, the deflection of which is a measure of sample surface topography."

an interaction with an introduced prey protein can be detected due to the resulting change in protein mass.

Taking a slightly different tack, two companies, **GE Healthcare/ Biacore Systems** and **Bio-Rad Laboratories**, market instrumentation based on surface plasmon resonance (SPR). These instruments use a gold foil detector surface and reflected light energy to generate surface electron charge density waves (plasmons). PPIs forming between surface-tethered proteins and introduced proteins on the detector surface interact with these plasmons resulting in measurable refractive index changes that are proportional to changes in surface mass. Stefan Löfås, chief scientist, Biacore Systems, GE Healthcare Bio-Sciences AB, explains that "the combination of label-free SPR detection, sophisticated microfluidics and a broad range of surface chemistries allows characterization of almost any type of biomolecular interaction at a very detailed level. The kinetic information obtained greatly facilitates the characterization of molecular mechanisms and biological processes."

The introduction of higher throughput screening capacities for SPR instruments is a focus for Biacore and Bio-Rad. As Cathy Mainini, senior product manager, protein function division, Bio-Rad Laboratories, points out, "We have combined surface plasmon resonance technology with an innovative 6 x 6 microfluidic design that allows one to measure an array of 36 biomolecular interactions simultaneously. This parallel approach can generate a complete kinetic profile of a biomolecular interaction in a single experiment without regeneration."

TIRF Technologies' instruments are based on total internal reflection fluorescence (TIRF). The process uses light propagating within a quartz crystal which, when it reaches an interface with a less dense aqueous solution, although fully reflected, generates an evanescent field that extends beyond the interface and into the aqueous solution. The fluorophores adsorbed, adhered, or bound to the surface will fluoresce while fluorophores in bulk solution will not. The sensitivity of the TIRF approach is reported to be 10,000 times higher than SPR-based instruments.

Based on the scanning tunneling microscopy—the inventors of which received half of the 1986 Nobel Prize in Physics—the atomic force microscope (AFM) is an imaging and measurement tool that provides a three-dimensional map of a sample's surface. The AFM instrument employs a sensitive probe, the deflection of which is a measure of sample surface topography. With the capacity to observe and manipulate biological surfaces under physiological conditions, AFM can be used to explore biological structures at the single molecule level and measure mechanical ligand-receptor interactions with 3D resolution and sensitivity down in the picoNewton (N^{-12}) range. W. Travis Johnson, senior scientist at Agilent Technologies, explains, "We are combining AFM with surface chemistry and bioconjugation chemistry in order to study individual, discrete ligand-receptor interactions far from equilibrium. This is increasing our understanding of how biological systems work at the single molecule level."

Instrumentation for Proteins in Solution

MicroCal has found a way to adapt ultrasensitive calorimetry to the study of PPIs. Utilizing isothermal titration calorimetry (ITC), the instrument measures the heat that is absorbed or generated when a biomolecular interaction occurs. Uniquely, the method does not require that the target protein be labeled or bound to a surface, allowing the proteins to be studied in solution in a native state. Ernesto Freire, Henry Walters Professor, Biology and Biophysics, Johns Hopkins University, reports his laboratory uses "ITC in all our projects involving protein-protein interactions. ITC not only provides the most accurate determination of binding affinity, but also it is the only technique that reveals the nature and magnitude of the forces involved in the binding process by being able to measure the binding enthalpy and entropy in a single experiment."

Bringing It All Together

Understanding of the physiological and disease associated importance of protein-protein interactions continues to expand. For example, researchers recently reported using a Biacore system to generate binding kinetics measurements to identify a site on the HIV-1 Env protein that may be a target for vaccine development. PPI research is moving forward aided by innovations in instrumentation, availability of reagents, and the generation of robust data sets.

PPI research is also benefitting from advances in knowledge software such as **Ingenuity Systems'** Pathways Analysis. Megan Laurance, senior scientist at Ingenuity Systems, points out "our software application contains a comprehensive network of protein-protein interactions and regulatory events [transcriptional effects, post-translational modifications, epigenetic events] manually curated from the scientific literature." This enables researchers to put the particular PPI under investigation into a broader context of normal and abnormal cellular function. As Laurance puts it, this allows them to "rapidly understand their experimental system as a whole, based on what was detected at the protein interaction level."

Emphasizing the importance of depending on multiple technologies, Michael Snyder of **Yale University** points out that in his laboratory "we use a number of methods including two-hybrid, protein arrays, affinity chromatography, and SPR to investigate the biological significance of PPIs. All of these methods have their inherent limitations; however, by integrating the resulting datasets we gain confidence in our understanding of the function and importance of specific PPIs." These technologies are enabling exciting new research on the characterization of multiprotein interactions involving "scaffold" proteins responsible for bringing other proteins together so they can interact.

Continued advancements in the ability to measure the various parameters associated with PPIs coupled with knowledge-based software will undoubtedly provide the understanding required for systems biology modeling and serve to uncover new targets for therapeutic developments.

Alfred Doig is a freelance bioscience writer and editor living in Natick, MA.

DOI: 10.1126/science.opms.p0700020

New Products

Colorful Laboratory Instruments

The new HydroFlex 3-in-1 platform and the popular Sunrise microplate reader are available in bright orange, blue, red, and green. The HydroFlex is a compact, versatile platform for automated vacuum filtration, magnetic bead separation, and microplate washing. It increases productivity by automating a range of 96-well format applications, including polymerase chain reaction cleanup and bead assays, enzyme-linked immunosorbent assays, cell assays, and protein arrays. The Sunrise system is a fast, 12-channel absorbance reader for 96-well microplates that provides all the functionality needed for numerous applications in diagnostics, biotechnology, and research laboratories. The new colors are designed to brighten up the lab and bring fun to the workplace.

Tecan Group
For information +41 44 922 81 11
www.tecan.com

Basement Membrane Extract

The PathClear Basement Membrane Extract (BME) High Protein Concentration (HC20+) has been added to the Cultrex product line. The PathClear designation means that in addition to standard sterility, endotoxin, and mouse antibody production testing, the BME is tested by polymerase chain reaction and is clear of a battery of 31 pathogens and viruses, making it suitable for in vivo applications. PathClear HC20+ was developed for use in in vivo applications in which higher protein concentrations facilitate faster gelling times, increased gel strength, and successful establishment and growth of tumor cells in nude mice. It offers lot-to-lot consistency and controlled protein concentrations to support in vivo angiogenesis assays and tumorigenicity assays.

Trevigen
For information 800-873-8443
www.trevigen.com

Trypsin Removal

Mag-Trypsin provides a method for magnetically immobilizing trypsin so it can be removed easily from a protein digestion mixture using a magnetic separator after the reaction is complete. Treatment with trypsin immobilized on magnetic beads prior to immobilization inhibits chymotrypsin activity without any effect on trypsin. Unlike agarose-linked immobilized trypsin, Mag-Trypsin does not require any centrifugation or use of columns. It provides a simple method for eliminating trypsin contamination after digesting protein samples to their peptide constituents in preparation for such techniques as mass spectroscopy or peptide enrichment.

Clontech Laboratories
For information 650-919-7382
www.clontech.com

Protein Expression Media

The ProNSO Chemically Defined (CD) Serum-free Media support maximal production of recombinant protein in NSO cells. The NSO cell line is widely used for recombinant mammalian protein expression in research and biotherapeutic applications. Two formulas are available to cover a broad range of nutritional needs, with a companion ProNSO Lipid CD Supplement also available.

Lonza
For information 800-521-0390
www.lonza.com

Human Cancer Biomarker Panel

The Beadlyte Human Cancer Biomarker Panel includes a five-plex containing the biomarkers: macrophage, migration inhibitory factor, prolactin, CA-125, leptin, and osteopontin as well as a singleplex IGF-II assay. Each of the biomarkers has been identified in various tumor types, including lung, breast, prostate, and colorectal. The panel can be used to quantify these biomarkers in serum, plasma, and cell or tissue culture supernatant samples. Each panel includes all components to run the assay, standards, and quality controls; it can be easily adapted for high throughput automation. The panel is sensitive and offers excellent intra-assay and interassay precision.

Millipore
For information 978-762-5080
www.millipore.com

Polypropylene Plates

The NUNC 384-Well Polypropylene Plates feature an improved design for achieving a secure seal when using commercially available heat seal tapes and instruments. They feature a raised rim around each well that promotes a robust, secure seal in all wells, enables plates to be resealed multiple times, and is compatible with adhesive seal tapes. Polypropylene plates are commonly used for storage and transport of chemicals, nucleic acids, and proteins because of their inherent chemical stability. The new plate construction meets the critical storage requirements that each well be completely sealed to prevent well-to-well contamination, evaporation, and loss or degradation of contents. These plates are available sterile or nonsterile in four colors: natural, white, black, and blue. The black and white plates are used for fluorescence and luminescence assays, respectively. The black plates help increase product stability by blocking light from photosensitive compounds.

Thermo Fisher Scientific
For information 800-446-2543
www.nuncbrand.com

Protein Kinase Library

The Calbiochem InhibitorSelectT Protein Kinase Library I contains 80 well-characterized, potent protein kinase inhibitors. They are supplied in a convenient 96-well plate at a concentration of 10 mM in DMSO.

Calbiochem
For information 800-854-3417
www.emdbiosciences.com/html/CBC/inhibitor_library.htm

Center for AIDS Prevention Studies University of California, San Francisco

Faculty Search-Rank Open: Social Behavioral HIV Prevention Research

The mission of the Center for AIDS Prevention Studies (CAPS) is to conduct domestic and international research to prevent the acquisition of HIV and to optimize health outcomes among HIV-infected individuals. CAPS, based in the Department of Medicine, Division of Prevention Science, at the University of California, San Francisco (UCSF), is recruiting one or more faculty members in the area of HIV/AIDS or social behavioral research applied to prevention science and the development of effective HIV prevention interventions.

UCSF seeks candidates whose experience, teaching, research, or community service has prepared them to contribute to our mission. Strong NIH funding track record and experience directing federally funded research studies required. Research expertise in the following areas sought: social psychology, sociology, epidemiology, clinical psychology, anthropology, community psychology, medical sociology, and statistics. Populations and areas of special interest include: ethnic minority populations, men who have sex with men, women, adolescents, substance users, incarcerated populations and their families, optimizing health outcomes, and biomedical approaches to prevention.

Interested candidates should submit a detailed cover letter describing their interests and experience, as well as curriculum vitae to: **Margaret Paternck, PhD, Deputy Director, UCSF Center for AIDS Prevention Studies, 50 Beale Street, 13th floor, San Francisco, CA 94105.**

UCSF seeks candidates whose experience, teaching, research, or community service has prepared them to contribute to our commitment to diversity and excellence. UCSF is an Equal Opportunity/Affirmative Action Employer. The University undertakes affirmative action to assure equal employment opportunity for underutilized minorities and women, for persons with disabilities, and for covered veterans. All qualified applicants are to apply, including minorities and women.

Head, Department of Biology

Texas A&M University College Station, Texas

A national search is underway to identify outstanding candidates for Head of Biology at Texas A&M University, one of the largest universities in the nation with an enrollment of over 46,000 students and recently rated #1 in serving the needs of the nation by Washington Monthly. Our thematically diverse department is at the research and teaching core of the basic life sciences at Texas A&M University. The department seeks an individual with a vibrant and internationally recognized research program, a sincere commitment to undergraduate and graduate education, and proven leadership skills.

The Biology Department has nearly 1800 undergraduate majors, 90 graduate students, 44 full-time faculty members, 6 joint appointments, and 7 lecturers. The university is committed to increasing the number of full-time tenured and tenure-track faculty to at least 50, including expansion of research space. Department facilities support a wide range of molecular biological, imaging, and computational technologies. Complementary expertise and specialized research facilities are available on campus. Further information about the department, its faculty, and its facilities can be found at our website: **www.bio.tamu.edu**.

Applicants should send by email a CV and a statement of research accomplishments, teaching perspective and administrative philosophy to: **Headsearch@mail.bio.tamu.edu**. Review of applications will begin **January 15, 2008**, and continue until the position is filled.

Texas A&M University is an Equal Opportunity/Affirmative Action Employer that is dedicated to the goal of building a culturally diverse and pluralistic faculty and staff who are committed to teaching and working in a multicultural environment. We strongly encourage applications from women, minorities, veterans, and individuals with disabilities. The university is particularly responsive to the needs of dual-career couples.

Center for AIDS Prevention Studies University of California, San Francisco

Search for Academic Specialists: Social Behavioral HIV Prevention Research

The mission of the Center for AIDS Prevention Studies (CAPS) is to conduct domestic and international research to prevent the acquisition of HIV and to optimize health outcomes among HIV-infected individuals. CAPS, based in the Department of Medicine, Division of Prevention Science, at the University of California, San Francisco (UCSF), is recruiting one or more academic Specialists in the area of HIV/AIDS or social behavioral research applied to prevention science and the development of effective HIV prevention interventions. The Specialist series is used for academic appointees who are engaged in research in specialized areas and who do not have any teaching responsibilities.

UCSF seeks candidates whose experience, teaching, research, or community service has prepared them to contribute to our mission. Strong NIH funding track record and experience directing federally funded research studies required. Research expertise in the following areas sought: social psychology, sociology, epidemiology, clinical psychology, anthropology, community psychology, medical sociology, and statistics. Populations and areas of special interest include: ethnic and minority populations, incarcerated populations and their families, optimizing health outcomes, MSM, IDU, and biological approaches.

Interested candidates should submit a detailed cover letter describing their interests and experience as well as curriculum vitae to: **Margaret Paternck, PhD, Deputy Director, UCSF Center for AIDS Prevention Studies, 50 Beale Street, 13th floor, San Francisco, CA 94105.**

UCSF seeks candidates whose experience, teaching, research, or community service has prepared them to contribute to our commitment to diversity and excellence. UCSF is an Equal Opportunity/Affirmative Action Employer. The University undertakes affirmative action to assure equal employment opportunity for underutilized minorities and women, for persons with disabilities, and for covered veterans. All qualified applicants are to apply, including minorities and women.

NEW JERSEY MEDICAL SCHOOL
DEPARTMENT OF ORTHOPAEDICS
NORTH JERSEY ORTHOPAEDIC INSTITUTE

BASIC MUSCULOSKELETAL SCIENTIST

The Department of Orthopaedics at the UMDNJ-New Jersey Medical School invites applications for a tenure-track faculty position. Applicants with research interest in any area of human musculoskeletal and joint disease are encouraged to apply. Research areas might include, but are not limited to: biology of bone and joint diseases, including molecular aspects, arthrosplasty science, bioengineering, biomaterials and biomechanics. Applicants must have a PhD or its equivalent and at least two years of post-doctoral experience. The successful candidate will be expected to develop a strong extramurally funded research program. Current basic science research efforts in the Department focus on the study of biomaterials for skeletal repair, the molecular biology and biomechanics of bone healing, the molecular analysis of skeletal development, control of proliferation and differential in osteoblasts, and orthopaedic oncology.

Applicants should send cover letter with CV, the names of three references and a statement of research interests to: **Elizabeth Moran, Ph.D., Professor and Director Orthopaedic Research Laboratories, Department of Orthopaedics, UMDNJ, Cancer Center, 205 South Orange Avenue, Room G1200, Newark, NJ 07103, or e-mail: strumoje@umdnj.edu.** The University of Medicine and Dentistry of New Jersey is an equal opportunity and affirmative action employer.

UMDNJ
UNIVERSITY OF MEDICINE & DENTISTRY OF NEW JERSEY